

UNITED STATES AIR FORCE  
SUMMER RESEARCH PROGRAM -- 1996  
SUMMER RESEARCH EXTENSION PROGRAM FINAL REPORTS  
VOLUME 2  
PHILLIPS LABORATORY

RESEARCH & DEVELOPMENT LABORATORIES  
5800 Uplander Way  
Culver City, CA 90230-6608

Program Director, RDL  
Gary Moore

Program Manager, AFOSR  
Major Linda Steel-Goodwin

Program Manager, RDL  
Scott Licoscas

Program Administrator, RDL  
Johnetta Thompson

Program Administrator  
Rebecca Kelly-Clemmons

Submitted to:

AIR FORCE OFFICE OF SCIENTIFIC RESEARCH  
Bolling Air Force Base  
Washington, D.C.  
December 1996

20010319 017

AQMD1-06-1064

# REPORT DOCUMENTATION PAGE

Public reporting burden for this collection of information is estimated to average 1 hour per response, including the time for reviewing instructions, searching existing data sources, gathering the required information, reviewing and collecting the information, and completing and reviewing the collection of information. Send comments regarding this burden estimate or any other aspect of this collection of information, including suggestions for reducing the burden, to Washington Headquarters Services, Directorate for Information Operations and Reports, 1215 Jefferson Davis Highway, Suite 1204, Arlington, VA 22202-4302, and to the Office of Management and Budget, Paperwork Project, Washington, DC 20503.

AFRL-SR-BL-TR-00-

0703

Reporting  
mation

1. AGENCY USE ONLY (Leave blank)		2. REPORT DATE December, 1996		3. REPORT NUMBER	
4. TITLE AND SUBTITLE 1996 Summer Research Program (SRP), Summer Research Extension Program (SREP), Final Report, Volume 2, Phillips Laboratory				5. FUNDING NUMBERS F49620-93-C-0063	
6. AUTHOR(S) Gary Moore					
7. PERFORMING ORGANIZATION NAME(S) AND ADDRESS(ES) Research & Development Laboratories (RDL) 5800 Uplander Way Culver City, CA 90230-6608				8. PERFORMING ORGANIZATION REPORT NUMBER	
9. SPONSORING/MONITORING AGENCY NAME(S) AND ADDRESS(ES) Air Force Office of Scientific Research (AFOSR) 801 N. Randolph St. Arlington, VA 22203-1977				10. SPONSORING/MONITORING AGENCY REPORT NUMBER	
11. SUPPLEMENTARY NOTES					
12a. DISTRIBUTION AVAILABILITY STATEMENT Approved for Public Release				12b. DISTRIBUTION CODE	
13. ABSTRACT (Maximum 200 words) The United States Air Force Summer Research Program (SRP) is designed to introduce university, college, and technical institute faculty members to Air Force research. This is accomplished by the faculty members, graduate students, and high school students being selected on a nationally advertised competitive basis during the summer intersession period to perform research at Air Force Research Laboratory (AFRL) Technical Directorates and Air Force Air Logistics Centers (ALC). AFOSR also offers its research associates (faculty only) an opportunity, under the Summer Research Extension Program (SREP), to continue their AFOSR-sponsored research at their home institutions through the award of research grants. This volume consists of a listing of the participants for the SREP and the technical report from each participant working at the AF Phillips Laboratory.					
14. SUBJECT TERMS Air Force Research, Air Force, Engineering, Laboratories, Reports, Summer, Universities, Faculty, Graduate Student, High School Student				15. NUMBER OF PAGES	
				16. PRICE CODE	
17. SECURITY CLASSIFICATION OF REPORT Unclassified	18. SECURITY CLASSIFICATION OF THIS PAGE Unclassified	19. SECURITY CLASSIFICATION OF ABSTRACT Unclassified	20. LIMITATION OF ABSTRACT UL		

# 1996 SREP FINAL REPORTS

## Armstrong Laboratory

### VOLUME 1

<b>Report #</b>	<b>Report Title Author's University</b>	<b>Report Author</b>
1	<b>Chlorinated Ethene Transformation, Sorption &amp; Product Distr in Metallic Iron/Water Systems: Effect of Iron Properties Washington State University, Pullman, WA</b>	<b>Dr. Richelle M Allen-King Dept. of Geology AL/EQ</b>
2	<b>Dynamically Adaptive Interfaces: A Preliminary Investigation Wright State University, Dayton, OH</b>	<b>Dr. Kevin B Bennett Dept. of Psychology AL/CF</b>
3	<b>Geographically Distributed Collaborative Work Environment California State University, Hayward, CA</b>	<b>Dr. Alexander B Bordetsky Dept. Decesion Sciences AL/HR</b>
4	<b>Development of Fluorescence Post Labeling Assay for DNA Adducts: Chloroacetaldeh New York Univ Dental/Medical School, New York, NY</b>	<b>Dr. Joseph B Guttenplan Dept. of Chemistry AL/OE</b>
5	<b>The Checkmark Pattern &amp; Regression to the Mean in Dioxin Half Life Studies University of South Alabama, Mobile, AL</b>	<b>Dr. Pandurang M Kulkarni Dept. of Statistics AL/AO</b>
6	<b>Determination of the Enzymatic Constraints Limiting the Growth of Pseudomonas University of Dayton, Dayton, OH</b>	<b>Dr. Michael P Labare Dept. of Marine Sciences AL/HR</b>
7	<b>Tuned Selectivity Solid Phase Microextraction Clarkson University, Potsdam, NY</b>	<b>Dr. Barry K Lavine Dept. of Chemistry AL/EQ</b>
8	<b>A Cognitive Engineering Approach to Distributed Team Decision Making During University of Georgia, Athens, GA</b>	<b>Dr. Robert P Mahan Dept. of Psychology AL/CF</b>
9	<b>Repetative Sequence Based PCR: An Epidemiological Study of a Streptococcus Stonehill College, North Easton, MA</b>	<b>Dr. Sandra McAlister Dept. of Biology AL/CF</b>
10	<b>An Investigation into the Efficacy of Headphone Listening for Localization of Middle Tennessee State University, Murfreesbord, TN</b>	<b>Dr. Alan D. Musicant Dept. of Psychology AL/CF</b>
11	<b>The Neck Models to Predict Human Tolerance in a G-Y CUNY-City College, New York, NY</b>	<b>Dr. Ali M. Sadegh Dept. of Mech Engineering AL/CF</b>

## 1996 SREP FINAL REPORTS

### Armstrong Laboratory

### VOLUME 1 (cont.)

<b>Report #</b>	<b>Report Title Author's University</b>	<b>Report Author</b>
12	Tracer Methodology Development for Enhanced Passive Ventilation for Soil University of Florida, Gainesville, FL	Dr. William R. Wise Dept. of Civil Engineering AL/EQ
13	Application of a Distribution-Based Assessment of Mission Readiness System for the Evaluation of Personnel Training Texas A&M University, College Station, TX	Dr. David J. Woehr Dept. of Psychology AL/HR
14	Electrophysiological, Behavioral, and Subjective Indexes of Workload when Performing Multiple Tasks Washington State University, Pullman, WA	Ms. Lisa Fournier Dept. of Psychology AL/CF
15	Methods for Establishing Design Limits to Ensure Accommodation for Ergonomic Design Miami University, Oxford, OH	Ms. Kristie Nemeth Dept. of Psychology AL/HR

# 1996 SREP FINAL REPORTS

## Phillips Laboratory

### VOLUME 2

<b>Report #</b>	<b>Report Title Author's University</b>	<b>Report Author</b>
1	Experimental Study of the Tilt Angular Anisotropy Correlation & the Effect Georgia Tech Research Institute, Atlanta, GA	Dr. Mikhail Belen'kii Dept. of Electro Optics PL/LI
2	Performance Evaluations & Computer Simulations of Synchronous & Asynchronous California State University, Fresno, CA	Dr. Daniel C. Bukofzer Dept. of Elec Engineering PL/VT
3	MM4 Model Experiments on the Effects of Cloud Shading Texas Tech University, Lubbock, TX	Dr. Chia-Bo Chang Dept. of Geosciences PL/GP
4	Miniature Laser Gyro consisting in a Pair of Unidirectional Ring Lasers University of New Mexico, Albuquerque, NM	Dr. Jean-Claude M. Diels Dept. of Physics PL/LI
5	Simulations & Theoretical Studies of Ultrafast Silicon Avalanche Old Dominion University, Norfolk, VA	Dr. Ravindra P. Joshi Dept. of Elec Engineering PL/WS
6	Theory of Wave Propagation in a Time-Varying Magnetoplasma Medium & Applications to Geophysical Phenomena University of Massachusetts Lowell, Lowell, MA	Dr. Dikshitulu K. Kalluri Dept. of Elec Engineering PL/GP
7	Thermal Analysis for the Applications of High Power Lasers in Large-Area Materials Processing University of Central Florida, Orlando, FL	Dr. Arvinda Kar Dept. of Engineering PL/LI
8	Analytical Noise Modeling and Optimization of a Phasor-Based Phase Texas Tech University, Lubbock, TX	Dr. Thomas F. Krile Dept. of Elec Engineering PL/LI
9	Mathematical Modeling of Thermionic-AMTEC Cascade System for Space Power Texas Tech University, Lubbock, TX	Dr. M. Arfin K. Lodhi Dept. of Physics PL/VT
10	Preparation & characterization of Polymer Blends Ohio State University, Columbus, OH	Dr. Charles J. Noel Dept. of Chemistry PL/RK
11	Evaluation of Particle & Energy Transport to Anode, Cathode University of Texas-Denton, Denton, TX	Dr. Carlos A. Ordonez Dept. of Physics PL/WS
12	Analysis of the Structure & Motion of Equatorial Emission Depletion Bands Using Optical All-Sky Images University of Massachusetts Lowell, Lowell, MA	Dr. Ronald M. Pickett Dept. of Psychology PL/GP

---

1996 SREP FINAL REPORTS

Phillips Laboratory

VOLUME 2 (cont.)

<u>Report #</u>	<u>Author's University</u>	<u>Report Author</u>
13.	<b>On the Fluid Dynamics of High Pressure Atomization in Rocket Propulsion</b> University of Illinois-Chicago, Chicago, IL	<b>Dr. Dimos Poulikakos</b> <b>Dept. of Mech Engineering</b> <b>PL/RK</b>
14	<b>Gigahertz Modulation &amp; Ultrafast Gain Build-up in Iodine Lasers</b> University of New Mexico, Albuquerque, NM	<b>Dr. W. Rudolph</b> <b>Dept. of Physics</b> <b>PL/LI</b>
15	<b>Inversion of Hyperspectral Atmospheric Radiance Images for the Measurement of Temperature, Turbulence, and Velocity</b> University of New Mexico, Albuquerque, NM	<b>Dr. David Watt</b> <b>Dept. of Mech Engineering</b> <b>PL/GP</b>

# 1996 SREP FINAL REPORTS

Rome Laboratory

## VOLUME 3

<b>Report #</b>	<b>Author's University</b>	<b>Report Author</b>
1	Performance Analysis of an ATM-Satellite System Florida Atlantic University, Boca Raton, FL	Dr. Valentine Aalo Dept. of Elec Engineering RL/C3
2	Reformulating Domain Theories to Improve their Computational Usefulness Oklahoma State University, Stillwater, OK	Dr. David P. Benjamin Dept. of Comp Engineering RL/C3
3	An Analysis of the Adaptive Displaced Phase Centered Antenna Lehigh University, Bethlehem, PA	Dr. Rick S. Blum Dept. Elec Engineering RL/OC
4	Effect of Concatenated Codes on the Transport of ATM-Based Traffic California Polytechnic State, San Luis Obispo, CA	Dr. Mostafa Chinichian Dept. of Engineering RL/C3
5	Development of Efficient Algorithms & Software Codes for Lossless and Near-Lossless Compression of Digitized Images Oakland University, Rochester, MI	Dr. Manohar K. Das Dept. Elec Engineering RL/IR
6	Mode-Locked Fiber Lasers Rensselaer Polytechnic Institution, Troy, NY	Dr. Joseph W. Haus Dept. of Physics RL/OC
7	Magnitude & Phase Measurements of Electromagnetic Fields Using Infrared University of Colorado, Colorado Springs, CO	Dr. John D. Norgard Dept. Elec Engineering RL/ER
8	Image Multiresolution Decomposition & Progressive Transmission Using Wavelets New Jersey Institute of Technology, Newark, NJ	Dr. Frank Y. Shih Dept. of Comp Science RL/IR
9	Investigation of Si-Based Quantum Well Intersubband Lasers University of Massachusetts-Boston, Boston, MA	Dr. Gang Sun Dept. of Physics RL/ER
10	Numerical Study of Bistatic Scattering from Land Surfaces at Grazing Incidence Oklahoma State University, Stillwater, OK	Dr. James C. West Dept. of Elec Engineering RL/ER

# 1996 SREP FINAL REPORTS

Wright Laboratory

## VOLUME 4A

<b>Report #</b>	<b>Author's University</b>	<b>Report Author</b>
1	<b>Barrel-Launched Adaptive Munition Experimental Round Research Auburn University, Auburn, AL</b>	<b>Dr. Ronald M. Barrett Dept. of Aerospace Eng WL/MN</b>
2	<b>Modeling &amp; Design of New Cold Cathode Emitters &amp; Photocathodes University of Cincinnati, Cincinnati, OH</b>	<b>Dr. Marc M. Cahay Dept. of Elec Engineering WL/EL</b>
3	<b>Unsteady Aerodynamics University of California-Berkeley, Berkeley, CA</b>	<b>Dr. Gary Chapman Dept. of Aerospace Eng WL/MN</b>
4	<b>Characteristics of the Texture Formed During the Annealing of Copper Plate University of Nebraska-Lincoln, Lincoln, NE</b>	<b>Dr. Robert J. DeAngelis Dept. of Mech Engineering WL/MN</b>
5	<b>Development of Perturbed Photorefectance, Implementation of Nonlinear Optical Parametric Devices Bowling Green State University</b>	<b>Dr. Yujie J. Ding Dept. of Physics WL/EL</b>
6	<b>Computations of Drag Reduction &amp; Boundary Layer Structure on a Turbine Blade with an Oscillating Bleed Flow University of Dayton, Dayton, OH</b>	<b>Dr. Elizabeth A. Ervin Dept. of Mech Engineering WL/PO</b>
7	<b>Low Signal to Noise Signal Processor for Laser Doppler Velocimetry North Carolina State University, Raleigh, NC</b>	<b>Dr. Richard D. Gould Dept. of Mech Engineering WL/PO</b>
8	<b>Modeling &amp; Control for Rotating Stall in Aeroengines Louisiana State University, Baton Rouge, LA</b>	<b>Dr. Guoxiang Gu Dept. of Elec Engineering WL/FI</b>
9	<b>Scaleable Parallel Processing for Real-time Rule-Based Decision Aids University of Missouri-Columbia, Columbia, MO</b>	<b>Dr. Chun-Shin Lin Dept. of Elec Engineering WL/FI</b>
10	<b>Quantitative Image Location &amp; Processing in Ballistic Holograms University of West Florida, Pensacola, FL</b>	<b>Dr. James S. Marsh Dept. of Physics WL/MN</b>
11	<b>Experimental &amp; Computational Investigation of Flame Suppression University of North Texas, Denton, TX</b>	<b>Dr. Paul Marshall Dept. of Chemistry WL/ML</b>
12	<b>Investigations of Shear Localization in Energetic Materials Systems University of Notre Dame, Notre Dame, IN</b>	<b>Dr. James J. Mason Dept. of Aerospace Eng WL/MN</b>

# 1996 SREP FINAL REPORTS

Wright Laboratory

## VOLUME 4A (cont.)

<b>Report #</b>	<b>Author's University</b>	<b>Report Author</b>
13	A Time Slotted Approach to Real-Time Message Scheduling on SCI University of Nebraska-Lincoln, Lincoln, NE	Dr. Sarit Mukherjee Dept. of Comp Engineering WL/AA
14	Dielectric Resonator Measurements on High Temperature Superconductor (HTS) Wright State University, Dayton, OH	Dr. Krishna Naishadham Dept. Elec Engineering WL/ML
15	Modeling of Initiation & Propagation of Detonation Energetic Solids University of Notre Dame, Notre Dame, IN	Dr. Joseph M. Powers Dept. of Aerospace WL/MN
16	Robust control Design for Nonlinear Uncertain Systems by Merging University of Central Florida, Orlando, FL	Dr. Zhihua Qu Dept. of Elec Engineering WL/MN

# 1996 SREP FINAL REPORTS

## Wright Laboratory

### VOLUME 4B

Report #	Author's University	Report Author
17	<b>HELPR: A Hybrid Evolutionary Learning System</b> Wright State University, Dayton, OH	<b>Dr. Mateen M. Rizki</b> Dept. of Comp Engineering WL/AA
18	<b>Virtual Materials Processing: automated Fixture Design for Materials</b> Southern Illinois University-Carbondale, IL	<b>Dr. Yiming K. Rong</b> Dept. of Technology WL/ML
19	<b>A Flexible Architecture for Communication Systems (FACS):</b> Software AM Radio Wright State University, Dayton, OH	<b>Dr. John L. Schmalzel</b> Dept. of Engineering WL/AA
20	<b>A Design Strategy for Preventing High Cycle Fatigue by Minimizing</b> Sensitivity of Bladed Disks to Mistuning Wright State University, Dayton, OH	<b>Dr. Joseph C. Slater</b> Dept. of Mech Engineering WL/FI
21	<b>Growth of Silicon Carbide Thin Films by Molecular Beam Epitaxy</b> University of Cincinnati, Cincinnati, OH	<b>Dr. Andrew J. Steckl</b> Dept. of Elec Engineering WL/FI
22	<b>Performance of Iterative &amp; Noniterative Schemes for Image Restoration</b> University of Arizona, Tucson, AZ	<b>Dr. Malur K. Sundareshan</b> Dept. of Elec Engineering WL/MN
23	<b>Improving the Tribological Properties of Hard TiC Coatings</b> University of New Orleans, New Orleans, LA	<b>Dr. Jinke Tang</b> Dept. of Physics WL/ML
24	<b>Development of Massively Parallel Epic Hydrocode in Cray T3D Using PVM</b> Florida Atlantic University, Boca Raton, FL	<b>Dr. Chi-Tay Tsai</b> Dept. of Mech Engineering WL/MN
25	<b>Supramolecular Multilayer Assemblies w/Periodicities in a Submicron Range</b> Western Michigan University, Kalamazoo, MI	<b>Dr. Vladimir V. Tsukruk</b> Dept. of Physics WL/ML
26	<b>Distributed Control of Nonlinear Flexible Beams &amp; Plates</b> w/Mechanical & Temperature Excitations University of Kentucky, Lexington, KY	<b>Dr. Horn-Sen Tzou</b> Dept. of Mech Engineering WL/FI
27	<b>A Progressive Refinement Approach to Planning &amp; Scheduling</b> University of Colorado-Denver, Denver, CO	<b>Dr. William J. Wolfe</b> Dept. of Comp Engineering WL/MT
28	<b>Development of a New Numerical Boundary condition for Perfect Conductors</b> University of Idaho, Moscow, OH	<b>Dr. Jeffrey L. Young</b> Dept. of Elec Engineering WL/FI

# 1996 SREP FINAL REPORTS

## Wright Laboratory

### VOLUME 4B (cont.)

<b>Report #</b>	<b>Author's University</b>	<b>Report Author</b>
29	<b>Eigenstructure Assignment in Missile Autopilot Design Using a Unified Spectral Louisiana State University, Baton Rouge, LA</b>	<b>Dr. Jianchao Zhu Dept. of Elec Engineering WL/FI</b>
30	<b>Design &amp; Implementation of a GNSS Software Radio Receiver Ohio University, Athens, OH</b>	<b>Dr. Dennis M. Akos Dept. of Elec Engineering</b>
31	<b>Experimental &amp; Numerical Study of Localized Shear as an Initiation Mechanism University of Notre Dame, Notre Dame, IN</b>	<b>Mr. Richard J. Caspar Dept. of Aero Engineering WL/MN</b>
32	<b>A Molecular-Level view of Solvation in Supercritical Fluid Systems State University of New York – Buffalo, Buffalo, NY</b>	<b>Ms. Emily D. Niemeyer Dept. of Chemistry WL/PO</b>
33	<b>Initiation of Explosives by High Shear Strain Rate Impact University of Notre Dame, Notre Dame, IN</b>	<b>Mr. Keith M. Roessig Dept. of Aero Engineering WL/MN</b>

# 1996 SREP FINAL REPORTS

## VOLUME 5

<b>Report #</b>	<b>Author's University</b>	<b>Report Author</b>
<b>Arnold Engineering Development Center</b>		
<b>1</b>	<b>Facility Health Monitoring &amp; Diagnosis Vanderbilt University, Nashville, TN</b>	<b>Dr. Theodore Bapty Dept. of Elec Engineering AEDC</b>
<b>Air Logistic Centers</b>		
<b>2</b>	<b>Fatigue Crack Growth Rates in Naturally-Coroded Aircraft Aluminum University of Oklahome, Norman, OK</b>	<b>Dr. James D. Baldwin Dept. of Mech Engineering OCALC</b>
<b>3</b>	<b>A Novel Artificial Neural Network Classifier for Multi-Modal University of Toledo, Toledo, OH</b>	<b>Dr. Gursel Serpen Dept. of Elec Engineering OOALC</b>
<b>4</b>	<b>Development of a Cost-Effective Organizational Information System West Virginia University, Morgantown, WV</b>	<b>Dr. Michael D. Wolfe Dept. Mgmt Science SAALC</b>
<b>5</b>	<b>Implementation of a Scheduling Software w/Shop Floor Parts Tracking Sys University of Wisconsin-Stout, Menomonie, WI</b>	<b>Dr. Norman D. Zhou Dept. of Technology SMALC</b>
<b>6</b>	<b>Development of a High Performance Electric Vehicle Actuator System Clarkson University, Potsdam, NY</b>	<b>Dr. James J. Carroll Dept. Elec Engineering WRALC</b>

---

Experimental Study of the Tilt Angular Anisoplanatic Correlation and the Effect of Stratospheric  
Turbulence on Star Image Motion

Mikhail S. Belen'kii  
Research Scientist  
Department of Electro-Optics

Georgia Tech Research Institute  
Atlanta, GA 30332

Final Report for:  
Summer Research Extension Program  
Phillips Laboratory

Sponsored by:  
Air Force Office of Scientific Research  
Bolling Air Force Base, DC

and

Phillips Laboratory

November 1996

# EXPERIMENTAL STUDY OF THE TILT ANGULAR ANISOPLANATIC CORRELATION AND THE EFFECT OF STRATOSPHERIC TURBULENCE ON STAR IMAGE MOTION

Mikhail S. Belen'kii  
Principle Research Scientists  
Electro-optics, Environment, and Materials Laboratory  
Georgia Tech Research Institute  
Atlanta, Georgia 30332-0834

## Abstract

The results of experimental studies of the effect of stratospheric turbulence on star image motion and tilt angular anisoplanatism are presented. A Polaris jitter experiment was designed and conducted to determine the effect of stratospheric inhomogeneities on star image motion. Polaris permits us to measure star image motion with a bolted telescope. In this case the mechanical telescope motion is eliminated. High resolution spatial and temporal statistics of the Polaris image motion were obtained. It was shown that the dependencies of the Polaris jitter variance on the telescope diameter have a knee. This knee cannot be explained based on the Kolmogorov model for the atmospheric turbulence. At the same time, the knee is consistent with the model which takes into account the effect of stratospheric turbulence. The dependence of the power spectra of the Polaris image jitter on the telescope diameter was also studied. It was determined that the measured spectral slopes deviate from the theoretical predictions. In the high frequency domain the  $f^{-8/3}$  and  $f^{-9/3}$  behavior was observed, whereas the  $f^{-11/3}$  behavior is predicted by the theory. In the low frequency domain the measured slope is close to -1, whereas the slope -2/3 follows from the theoretical predictions. The dependence of the knee frequency of the power spectrum on the telescope diameter, nevertheless, agrees well with the corresponding formula. The tilt temporal correlation scale increases proportionally to the telescope diameter. For the aperture of 0.1 m and 1.5 m it is in the range from 0.1 s to 1 s. To study the tilt angular anisoplanatism, a Moon edge jitter experiment was designed and carried out. By measuring the angular motion of small portions of the edge of the Moon at different angular separations, a standard deviation of the lateral tilt difference was determined. The preliminary analysis shows that the measured dependencies of the tilt difference standard deviation on the separation differ from the theoretical predictions and exceed the corresponding dependencies obtained from observations of the stars. A cross linking effect of the longitudinal tilt is considered as a possible reason. A spatial filtering technique should be applied to the measured data to eliminate this effect. The future development of the above studies is considered.

# EXPERIMENTAL STUDY OF THE TILT ANGULAR ANISOPLANATIC CORRELATION AND THE EFFECT OF STRATOSPHERIC TURBULENCE ON STAR IMAGE MOTION

Mikhail S. Belen'kii

## Introduction

Adaptive optics systems {1-3} can potentially provide us with a diffraction limited resolution for the large aperture telescopes. However, the inability of the conventional laser guide star (LGS) method to sense a global tilt across the telescope aperture greatly limits the area of the sky accessible for adaptive optics correction. To achieve full sky coverage, a tilt sensing technique with a LGS should be developed.

The technique for sensing full aperture tilt with a LGS has been suggested {4,5}. This technique exploits a laser beam transmitting through the main telescope and two auxiliary telescopes separated in transverse directions. A tilt angular anisoplanatism is exploited in this technique to eliminate a contribution of a down propagation path to the measured tilt. Due to the fact that light emitted from different portions of a laser beacon on the way to an auxiliary telescope pass through different inhomogeneities, a LGS image is wavy. The waviness scale is determined by the tilt angular correlation scale. If the FOV of the receiver is much larger than the tilt angular correlation scale, then the contribution of a down propagation path might be averaged out by averaging the LGS image motion over its angular extent. A full aperture tilt might be also measured by using a small aperture beam transmitting from behind a portion of a primary mirror {6}. Simultaneous observations of the LGS image motion with both a main and auxiliary telescope are required in this scheme.

In order to design a tilt sensing experiment with the LGS {4-6}, estimates for the tilt angular correlation scale for the site are needed. Such estimates might be obtained by using the corresponding theoretical relationship. However, that requires the data for the vertical profile of  $C_t^2(h)$  and an outer scale of turbulence. Unfortunately, there are no reliable data for the outer scale available in the literature. To overcome this difficulty an experimental study of the tilt anisoplanatism was suggested. To study the tilt angular anisoplanatism, the Moon edge jitter experiment was designed and conducted. By measuring the lateral, or transverse, angular motion of small portions of the Moon edge image, at variable separations from each other, a standard deviation of the lateral tilt difference was determined. This development was performed as a part of this project, jointly with a team of researchers at the Starfire Optical Range (SOR) at Phillips Laboratory, Albuquerque, NM.

Another important phenomenon which might affect the performance of adaptive systems is the effect of stratospheric turbulence on star image degradation. The theoretical analysis {7,8} shows that this effect is important for large aperture telescopes. To verify the theoretical predictions, a Polaris image jitter experiment was designed and carried out at SOR.

### Polaris jitter experiment

To determine the effect of non-Kolmogorov stratospheric turbulence on the star image motion, a Polaris jitter experiment was designed using a ground-based telescope. Polaris was chosen for this study for the following reason. A non-Kolmogorov stratospheric turbulence produces an effect on the star image motion, which is similar to that for uncontrolled motion of the telescope. In order to isolate the atmospheric motion, the telescope jitter should be eliminated. Because of the slow angular motion, Polaris permits us to make measurements with a bolted telescope. In this case the mechanical motion is removed.

The experiment was based on observations of the Polaris image motion by using a 64 x 64 CCD (Lincoln Lab) imaging system at the 1.5 m telescope. The five aperture masks ( $D = 0.1, 0.2, 0.5, 0.75, \text{ and } 1.5 \text{ m}$ ) in conjunction with the appropriate ND filters to keep incident flux constant and to achieve maximum flux without saturating the CCD camera were used to obtain high resolution spatial and temporal statistics of the Polaris image jitter. To assure that the measured data are not affected by internal turbulence within an optical path, the image motion of an internal source was measured with the same experimental set up. It was shown that the jitter variance of the internal source is more than one order magnitude smaller than that for a natural star.

The following observation procedure was exploited. The telescope views Polaris with a symmetrical  $42 \times 42 \text{ arcsec}$  FOV, yielding resolution of  $0.66 \text{ arcsec/pixel}$ . The telescope is first pointed toward Polaris and bolted in position such that the earth's rotation causes the image of Polaris to track horizontally across the FOV (at approximately  $1 \mu \text{ rad/sec}$ ). The data are collected with a frame rate of 200 Hz over 100 s, and with a rate of 400 Hz over 50 s, and stored. The K-mirror is used to ensure the stellar image tracks along one CCD channel without crossing into an adjacent channel. Each data run consists of 20,000 frames. Next, the telescope is unbolted and pointed at Polaris, keeping the image centered as data is collected. Comparison of the jitter statistics determined from the two data sets permits us to isolate the atmospheric and mechanical jitter. The optimum pixel size of  $0.66 \text{ arcsec}$  was determined by using a numerical simulation procedure, developed by Capt. D. Monterra. This pixel size presents an optimum tradeoff between sampling error and read noise.

### Data collection and processing procedures

The data were collected during four nights in May, June, and August, 1996. The 14 data sets corresponding to both bolted and unbolted telescope operation were collected and stored. For each experimental session the meteorological data including wind speed and direction, coherence diameter ( $r_0$ ) and isoplanatic angle ( $\theta_0$ ) were recorded, as well. During these observations a coherent diameter  $r_0$  was in the range from 3 cm to 8.5 cm.

The data processing procedure included the following steps: 1) the sky background was subtracted from the measured data, and the correction for the dome flat was performed; 2) the two one-axis (X and Y) coordinates of the centroid position were determined for each of the 20,000 frames; 3) the trends were removed from the time series for

the centroid coordinates; 4) the Polaris image jitter variance, the tilt temporal power spectrum, and tilt temporal correlation coefficient were calculated for each aperture mask.

### Results obtained

#### a) Dependence of the star jitter variance on the telescope diameter

The dependencies of one-axis Polaris image jitter variance on the telescope diameter obtained during three days are presented in Figs. 1a-c. The experimental dependencies are shown along with the two theoretical predictions. One prediction corresponds to the Kolmogorov model with infinite outer scale of turbulence, which yields the well known dependence,  $\sigma^2 \approx D^{-1/3}$  {9}. Another prediction corresponds to the finite outer scale. Even though the experimental dependencies deviate from the theoretical predictions, a larger than -1/3 slope of experimental curves for small D might be attributed to a finite outer scale.

According to both predictions based on the Kolmogorov model, a star jitter variance,  $\sigma^2$ , should gradually decrease with increasing telescope diameter. However, as it is shown in Figs. 1a-c, the experimental dependencies at  $D \geq 0.75 m$  have a knee. This knee cannot be explained on the basis of Kolmogorov model. At the same time, it can be explained by taking into account the effect of stratospheric turbulence. Indeed, according to {7,8}, the stratospheric phase structure function is approximately quadratic, and the stratospheric component of the star image motion does not depend on the telescope diameter. Due to this fact, the dependencies of the star jitter variance on the telescope diameter have a knee. Because the telescope mechanical motion in these measurements was eliminated, and the contribution of the turbulence within the optical train was negligibly small, one should assume an influence of inhomogeneities with the spectrum which differs from the Kolmogorov model to explain the knee.

#### b) Tilt Temporal Power Spectra

The temporal power spectra of one-axis components of the Polaris centroid were calculated from the time series for the data collected during the four nights of observation. About 60 power spectra for one-axis tilt components corresponding to both bolted and unbolted telescope performance and five aperture masks were calculated. For the time series with a frame repetition rate of 200 Hz the Nyquist frequency equals 100 Hz, and it is 200 Hz for the time series with a frame repetition rate of 400 Hz.

According to Kolmogorov model and frozen turbulence hypothesis, the tilt temporal power spectrum follows the dependence  $f^{-11/3}$  in the high frequency domain, whereas it obeys to the  $f^{-2/3}$  law in the low frequency range {10}. The knee frequency of the power spectrum is determined by the equation  $f_k = 0.3(V/D)$ , where V is a wind speed and D is the telescope diameter. At the knee frequency,  $f_k$ , a slope-break marks the separation between the two regimes.

The power spectra for one-axis tilt component for  $D = 0.1 \text{ m}$  and  $D = 1.5 \text{ m}$  for unbolted telescope performance are shown in Figs. 2a-b. By comparing these plots, it is easy to see that the spectra strongly depend on the telescope diameter. The power spectrum for the small aperture,  $D = 0.1 \text{ m}$ , exceeds that for the large one,  $D = 1.5 \text{ m}$ , in both low and high frequency ranges. Such a behavior corresponds to an enlargement of the Polaris jitter variance with decreasing the telescope diameter (see Figs. 1a-c). The power spectra have a slope which is close to  $-8/3 = -2.66$  in the high frequency range, and the slope is  $-1$  in the low frequency range. The knee frequency increases with decreasing the telescope diameter.

The two dependencies of the knee frequency on the telescope diameter measured at different days along with the theoretical predictions calculated from the formula  $f_k = 0.3(V/D)$  are presented in Fig. 3a and b. The knee frequency for the smallest aperture,  $D = 0.1 \text{ m}$ , in the first case is equal to 25 Hz that corresponds to the wind velocity of 8.3 m/s. In the other case the knee frequency is 45 Hz corresponding to the wind speed of 15 m/s.

To verify the fact that the measured data are not affected by the turbulence within the optical train, the temporal power spectra with an internal source were also measured. The power spectra for the internal source for  $D = 0.1 \text{ m}$  and  $1.5 \text{ m}$  are shown along with the atmospheric spectra for unbolted telescope performance in Fig. 4. It is shown, that the power spectrum for the small aperture,  $D = 0.1 \text{ m}$ , exceeds by almost two order of magnitude that for the large one,  $D = 1.5 \text{ m}$ , in the high frequency range. Both spectra for Polaris exceed that for the internal source in both low and high frequency ranges.

It is also seen that the power spectrum for a  $D = 1.5 \text{ m}$  aperture and unbolted telescope performance have a noticeable bump in the range from 70 Hz to 90 Hz. This bump, however, does not appear in the spectra for the bolted telescope performance. Therefore, the bump is associated with the mechanical telescope. The relative contribution of the bump to the Polaris jitter variance, however, is negligibly small.

The analysis shows that the majority of the spectra for the largest aperture,  $D = 1.5 \text{ m}$ , have a slope in the range from -2.3 to -2.6 with a mean value -2.45. For the smallest aperture,  $D = 0.1 \text{ m}$ , a spectral slope varies in the range from -2.6 to -3 in the high frequency domain, and it is close to -1 in the low frequency range. The implication is that the measured slopes deviate from the predictions based on the Kolmogorov model and the frozen turbulence hypothesis. In particular, the spectral slopes close to  $-8/3$  and  $-9/3$  were observed in the high frequency domain, whereas the slope  $-11/3$  was predicted. In the low frequency domain the slope  $-2/3$  was predicted by the theory, whereas the slope -1, was observed. It should be noted that the  $f^{-8/3}$  behavior in the high frequency range has been also observed in the stellar interferometric measurements [11].

There are some speculations that the theoretical  $f^{-1/3}$  high-frequency law is generally not observed because of noise and aliasing effects in wave-front sensing. An alternative explanation is that wind velocity fluctuations and turbulent inhomogeneities evolution might affect the behavior of the power spectra. Thus, the spectral slopes are not perfectly

consistent with the theoretical predictions. An additional analysis of the measured data, as well as, a more sophisticated theoretical model is needed for interpretation of the above measured dependencies.

#### c) Tilt Temporal Correlation

From the time series for the energy centroid the tilt temporal correlation coefficients were calculated. The correlation coefficients were calculated separately for the X and Y centroid for each aperture size. The correlation coefficients for one-axis tilt components corresponding to an unbolted telescope performance are shown in Figs. 5a-b. If one determines the tilt temporal correlation scale as the time lag over which the correlation coefficient decreases to the level  $e^{-1}$ , then it is shown from the data presented in Figs. 5a-b, that the tilt correlation scale for the largest aperture is about 1 s, whereas for the smallest aperture it is less than 0.1 s. It is seen that the tilt correlation scale increases proportionally to the telescope diameter.

#### Conclusion

To verify the predicted effect of the stratospheric turbulence on star image motion, the Polaris image jitter experiment was designed and carried out. Polaris image motion was measured by using both bolted and unbolted telescopes. In the bolted case the mechanical telescope motion was eliminated. High resolution spatial and temporal statistics of the Polaris image motion were obtained. It was shown that the dependencies of the Polaris jitter variance on the telescope diameter have a knee. The knee cannot be explained based on the Kolmogorov model, but it can be explained by taking into account the effect of stratospheric turbulence. The measured spectral slopes deviate from the theoretical predictions. At the same time, the dependencies of the knee frequency on the telescope diameter agree well with the corresponding formula. For the telescope diameter of 0.1 m and 1.5 m, respectively, the temporal tilt correlation scale is in the range from 0.1 s to 1 s, and it increases proportionally to the telescope diameter.

#### Future development

The current experimental design does not permit us to measure star image motion with different aperture masks simultaneously. Due to this fact, the data can suffer from rapid variations in atmospheric seeing conditions. This makes a comparison of the jitter variances for different telescope diameters difficult. A modification in the optical scheme which permits us to record the star images for the five aperture masks at the same frame has been suggested by Capt. S. Karis. The influence of the variations of the atmospheric seeing conditions in a new scheme is eliminated. Measurements of the Polaris image motion with a modified optical scheme at a 3.5 m telescope are planned.

#### Tilt angular correlation and tilt anisoplanatism

Let us consider first the theoretical predictions for the tilt angular anisoplanatism.

## Results of the theoretical analysis

The angular correlation of the tilts for two plane waves arriving at the telescope of diameter  $D$  at the angles zero and  $\theta$  is considered by using the Zernike polynomials expansion for the atmospheric wave-front distortions {12-15}. For the von Karman power spectrum of the refractive-index fluctuations  $\phi_n(K) = 0.033C_n^2(K^2 + K_{0K}^2)^{-11/6}$ , where  $K_{0K} = 3.08 / L_0$ , a tilt correlation coefficient has the form

$$b_{x,y}(\theta) = \frac{\int_0^\infty dh C_n^2(h) \cdot \int_0^\infty dK (K^2 + K_{0K}^2)^{-11/6} J_2^2(K) \left[ J_0\left(\frac{2\theta h}{D} K\right)_{-} J_2\left(\frac{2\theta h}{D} K\right)_{+} \right] / K}{\int_0^\infty dh C_n^2(h) \cdot \int_0^\infty dK (K^2 + K_{0K}^2)^{-11/6} J_2^2(K) / K}, \quad (1)$$

where  $J_0$  and  $J_2$  are the Bessel functions. The negative sign in Eq. (1) corresponds to the longitudinal, or parallel to the separation  $\theta$ , tilt, X, whereas the positive sign corresponds to the lateral tilt, Y. The tilt correlation coefficients calculated by using Eq. (1) for the vertical profile  $C_n^2(h)$  given by the model  $C_n^2(h) = C_{n0}^2 \exp(-h/\bar{h})$  are shown in Fig. 6. Here  $\bar{h}$  is the effective altitude, or characteristic scale, of the turbulent atmosphere determined by the ratio  $\bar{h} = \mu_1 / \mu_0$  of the first two moments for the vertical profile  $C_n^2(h)$ :  $\mu_0 = \int_0^\infty C_n^2(h) dh$  and  $\mu_1 = \int_0^\infty C_n^2(h) h dh$ . If the parameters  $C_{n0}^2$  and  $\bar{h}$  are equal to  $C_{n0}^2 = 2.37 \times 10^{-15} m^{-2/3}$  and  $\bar{h} = 934 m$ , respectively, the two moments  $\mu_0$  and  $\mu_1$  for the above  $C_n^2(h)$  model coincide with that for the Hufnagel-Valley (HV<sub>57</sub>) model {16,17}. For the HV-54 model these parameters equal  $C_{n0}^2 = 8.55 \times 10^{-16} m^{-2/3}$  and  $\bar{h} = 3,466 m$ . The tilt structure function, or tilt anisoplanatism,  $D_t(\theta)$ , is related to the tilt angular correlation coefficient  $b_t(\theta)$  through the equation

$$D_t(\theta) = \langle [a_x(0) - a_x(\theta)]^2 \rangle = 2\sigma_x^2 (L_0 / D) [1 - b_t(\theta / \theta_t)], \quad (2)$$

where  $\sigma_x^2$  is a one-axis tilt variance depending on the ratio  $L_0 / D$ . Therefore, one can calculate the tilt anisoplanatism by knowing the correlation coefficient  $b_t(\theta)$  and the variance  $\sigma_x^2$ .

From Fig. 6 it is shown that the tilt angular correlation gradually decreases with increasing angular distance,  $\theta$ . For small separation ( $\theta \ll \theta_t$ ) it approaches the asymptote  $b_{x,y}(\theta) \sim 1 - (\theta / \theta_t)^2$ . For large angular separation ( $\theta \gg \theta_t$ ) and for the Kolmogorov model with  $L_0 = \infty$ , the asymptote has the form  $(\theta / \theta_t)^{-1/3}$ . For a finite outer scale,  $L_0$ , and large angular separation,  $\theta$ , the correlation coefficients for the lateral and longitudinal tilt have the asymptotes,  $(\theta / \theta_t)^{-1}$ , and,  $(\theta / \theta_t)^{-2}$ , respectively. Therefore, the asymptotes and the tilt angular correlation coefficient behavior for the finite and infinite outer scale are different. The implication is that the Kolmogorov model with infinite outer scale ( $L_0 = \infty$ ) does not permit us to describe the tilt angular correlation.

One can introduce the tilt angular correlation scale,  $\theta_t$ , as the distance between the propagation paths over which the correlation coefficient,  $b_t$ , decreases to the level  $e^{-1}$  ( $b_t(\theta_t) = e^{-1}$ ). From the numerical estimates for  $b_t(\theta)$  presented in Fig. 6, it is easy to find that the tilt correlation scale  $\theta_t$  is

$$\theta_t = \alpha (L_0 / D) D / \bar{h}, \quad (3)$$

where  $\alpha$  is the coefficient of proportionality. This coefficient describes the effect of the outer scale of turbulence,  $L_0$ , on the tilt correlation scale. When  $\alpha = \text{constant}$ , the tilt correlation scale,  $\theta_t$ , is proportional to  $D$ , however, due to the dependence,  $\alpha(L_0 / D)$ , the tilt correlation scale  $\theta_t$  varies with the telescope diameter  $D$  non-linearly. The latter is seen in Table. 1, where the estimates for the tilt correlation scale,  $\theta_t$ , for different models of  $C_n^2(h)$  vertical profile and outer scale  $L_0$  are presented.

Table 1. Tilt angular correlation scale, $\theta_t$ , arcsec							
Telescope diameter, $D_t$ m		0.1	0.2	0.3	0.5	1.5	3.5
HV-54, $\bar{h}=3,466$ m	$L_0=3$ m	13	21	26	33	69	139
	$L_0=6$ m	17	27	35	46	87	172
HV <sub>57</sub> , $\bar{h}=934$ m	$L_0=3$ m	48	78	96	122	255	516
	$L_0=6$ m	63	100	130	170	323	638

The correlation scale,  $\theta_t$ , increases with increasing both the telescope diameter  $D_t$  and the outer scale  $L_0$ . The correlation scale,  $\theta_t$ , is smaller for the model HV-54 than that for the model HV<sub>57</sub>. The later is due to the fact that the HV-54 model contains stronger turbulence at high altitudes than the model HV<sub>57</sub>. The high altitude turbulence more severely degrades the tilt angular correlation than that near the ground. The implication is that one can expect the tilt correlation scale to be smaller at the sites with good seeing conditions than that at the sites with bad seeing. In Fig. 7 the tilt correlation coefficient  $b_y(\theta)$  is plotted versus  $\theta / \theta_t$  representing a universal tilt correlation curve.

### Experimental study

To study the tilt angular correlation and tilt anisoplanatism, the Moon edge experiment was designed and carried out. In this experiment the lateral, or transverse to the image, motion of the small portions of the Moon edge was measured by using a high resolution CCD camera. By selecting the two portions of the Moon edge image at different angular separations, the tilt structure function, or standard deviation of the tilt difference, was determined. Special attention in this experiment was paid to the dependence of the tilt anisoplanatism on the aperture size. For this purpose the observations were performed with the five aperture masks ( $D = 0.1, 0.2, 0.5, 0.75$ , and  $1.5$  m).

The experimental set up for the Moon edge experiment was similar to that for the Polaris jitter experiment. A  $64 \times 64$  CCD camera with angular pixel size of  $0.66$  arcsec, yielding  $42 \times 42$  arcsec FOV was used. The K-mirror was exploited to ensure the Moon edge be parallel to one CCD pixel row. The data were collated with a frame rate of  $200$  Hz during  $100$  s, and with a frame rate of  $400$  Hz during  $50$  s. The corresponding exposure times are equal  $5$  ms and  $2.5$  ms, respectively. Each data run consists of  $20000$  frames.

The data processing procedure included several steps. First, the sky background was subtracted and a flat field correction was performed. After that, the Moon edge position was calculated for each column in each frame by using a median algorithm. Then, a standard deviation of the tilt difference as a function of angular separation between the column was calculated from the sequence of 20,000 frames for the five aperture masks.

The preliminary results are shown in Fig. 8. The standard deviations of the differential centroid motion measured with a 2.4 m telescope {18} are also presented at the same plot. The latest results were obtained by measuring a differential motion of the centroids of closely spaced pairs of stars visible in the 60 arcsec wide FOV.

It is easy to see that the behavior of the experimental curves 1-3 for small angular separations differs from the theoretical prediction. According to the asymptote for the tilt correlation coefficient,  $b_{t,x}(\theta) \sim 1 - (\theta/\theta_t)^2$ , the tilt structure function for small separations should obey to the square power law:  $D_y(\theta) \approx (\theta/\theta_t)^2$ . Therefore, the tilt difference standard deviation should be proportional to the angular separation. However, the experimental curves 1-3 do not follow this prediction. Besides, the curves 1-3 exceed the corresponding standard deviations obtained from the stellar observations.

A possible reason for the above discrepancies is the influence, or cross linking effect, of the longitudinal tilt on the measurements of the lateral tilt. Because the atmospheric motion is two-dimensional, and the jitter rms is comparable with a pixel size, a longitudinal tilt might result in displacement of the portion of the Moon edge image from one column to the other. Due to this fact, an extra lateral tilt is determined by the median algorithm. The cross linking effect leads to enlargement of the tilt structure function and the standard deviation.

To eliminate the cross linking tilt effect, a spatial filtering technique should be applied to the sequence of frames with the Moon edge images, or/and the angular size of the smallest portion of the edge image should be enlarged by banding the neighboring columns. In any case, a more detailed analysis of the full set of data by using the algorithm for elimination of the cross linking effect should be performed.

### Conclusion

The Moon edge experiment was designed and carried out to study the tilt angular anisoplanatism. The data were collected and processed. The comparison with the measurements of a differential motion of the centroids of closely spaced pairs of stars and the theoretical prediction was made. The comparison shows that the measured dependencies deviate from that obtained from observations of the stars and differ from the theoretical predictions. A cross linking tilt effect is considered as a possible reason for these deviations. Further analysis of the measured data is planned to be performed by exploiting the filtering algorithm for elimination of the tilt cross linking effect.

### Acknowledgments

The author expresses his appreciation to the AFOSR RDL Summer Research Program personnel for the administrative support and to the team of researches at the SOR lead by R. Q. Fugate for fruitful collaboration.

### References

1. R. Q. Fugate, D. L. Fried, G. A. Ameer, B. R. Boeke, S. L. Browne, P. H. Roberts, R. E. Ruane, and L. M. Wopat, "Measurements of atmospheric wavefront distortion using scattering light from a laser guide-star," *Nature (London)* 353, 144-146 (1991).
2. C. A. Primmerman, D. V. Murphy, D. A. Page, B. G. Zollars, and H. T. Barclay, "Compensation of atmospheric optical distortion using a synthetic beacon," *Nature (London)* 353, 141-143 (1991).
3. R. Q. Fugate, B. L. Ellerbroek, C. H. Higgins, M. P. Jelonek, W. J. Lange, A. C. Slavin, W. J. Wild, D. M. Winker, J. M. Wynia, J. M. Spinhirne, B. R. Boeke, R. E. Ruane, J. F. Moroney, M. D. Oliker, D. W. Swindle, and R. A. Cleis, "Two generation of laser-guide-star adaptive-optics experiments at the Starfire Optical Range," *J. Opt. Soc. Am., A* 11, 310- 324 (1994).
4. M. S. Belen'kii, "Full aperture tilt measurement technique with a laser guide star," in Atmospheric Propagation and Remote Sensing IV, J. Christopher Dainty, Editor. Proc. SPIE 2471, 289-300 (1995).
5. M. S. Belen'kii, "Tilt angular anisoplanatism and full aperture tilt measurement technique with a laser guide star," submitted to *Appl. Opt.*
6. M. S. Belen'kii, "Tilt angular correlation and full aperture tilt measurement techniques with a laser guide star," The European Symposium on Satellite Remote Sensing, Taormina, Italy, September 24-26, 1996, Invited Paper.
7. A. S. Gurvich and M. S. Belen'kii, "Influence of stratospheric turbulence on infrared imaging," *J. Opt. Soc. Am., A* 12, 2517-2522 (1995).
8. M. S. Belen'kii, "Effect of the stratosphere on star image motion," *Opt. Lett.* 20, 1359-1361 (1995).
9. V. I. Tatarskii, Wave Propagation in a Turbulent Medium, McGraw-Hill Book Company, New York (1961).
10. J. M. Conan, G. Rousset and P. Y. Madec, "Wave-front temporal spectra in high-resolution through turbulence," *J. Opt. Soc. Am., A* 12, 1559-1570.
11. D. F. Buscher, J. T. Armstrong, C. A. Hummel, et.al., "Interferometric seeing measurements on Mt. Wilson: power spectra and outer scale," *Appl. Opt.*, 34, 1081-1096 (1995).
12. R. J. Noll, "Zernike polynomials and atmospheric turbulence," *J. Opt. Soc. Am.*, 63, 207-211 (1976).
13. G. C. Valley and S. M. Wandzura, "Spatial correlation of phase-expansion coefficients for propagation through atmospheric turbulence," *J. Opt. Soc. Am.*, 69, 712-717 (1979).
14. P. H. Hu, J. Stone, and T. Stanley, "Application of Zernike polynomials to atmospheric propagation problems," *J. Opt. Soc. Am. A* 6, 1595-1608 (1989).

15. R. J. Sasiela and J. D. Shelton, "Transverse spectral filtering and Mellin transform techniques applied to the effect of outer scale on tilt and tilt anisoplanatism," J. Opt. Soc. Am. A 10, 646-660 (1993).
16. The  $HV_{57}$  turbulence model was developed by modifying a conventional Hufnagel-Valley turbulence model<sup>15</sup> so that at zenith the coherence diameter equals 0.05 m and isoplanatic angle is 7 urad for  $\lambda = 0.5 \text{ } \mu\text{m}$ . This model corresponds to the conditions in the region of Albuquerque, New Mexico.
17. G. C. Valley, "Isoplanatic degradation of tilt correction and short-term imaging systems," Appl. Opt., 19, 574-577 (1980).
18. A. Sivaramakrishnan, R. J. Weymann, and J. W. Beletic, "Measurements of the angular correlation of stellar centroid motion," Astron. J. 110, 430-438 (1995).

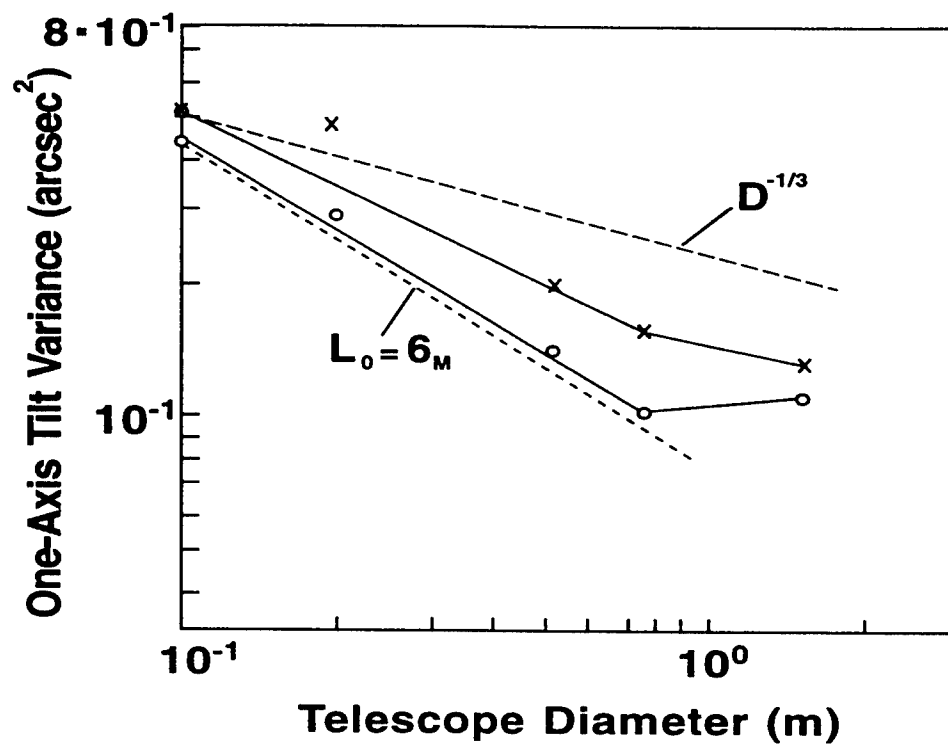


Figure 1a

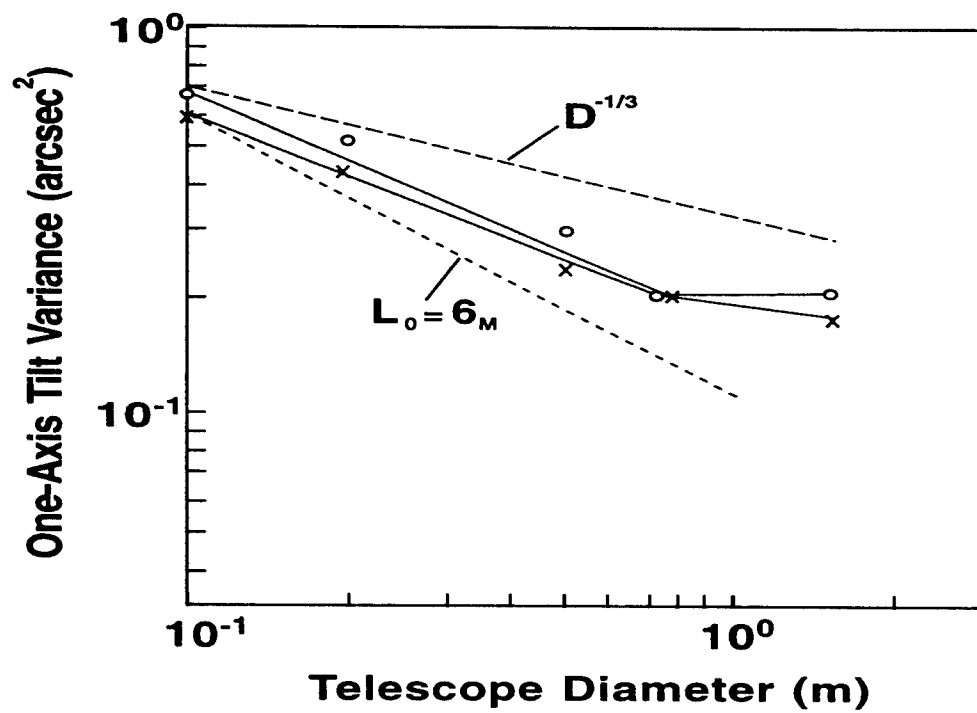


Figure 1b

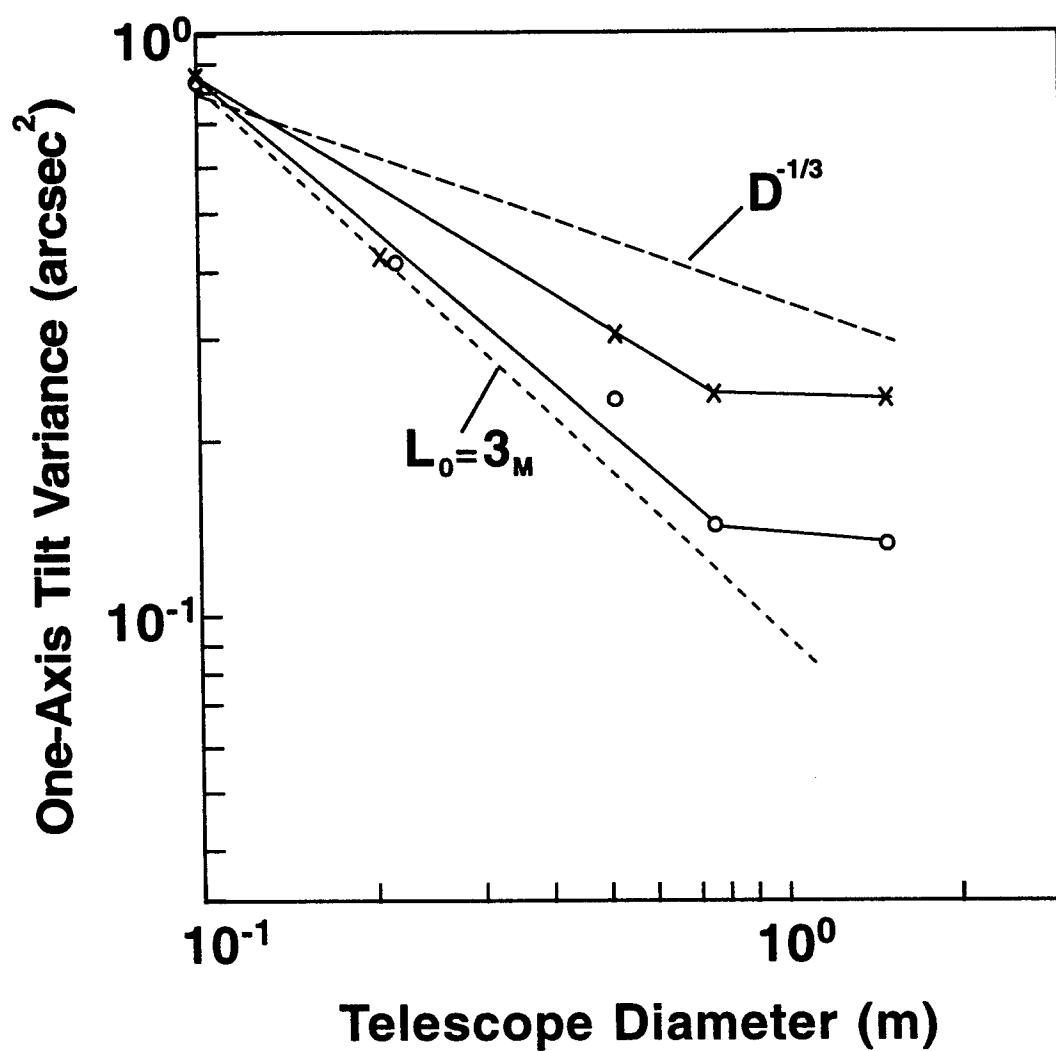


Figure 1c

Fig. 1a, b, and c. Dependence of the Polaris jitter variance on the telescope diameter.

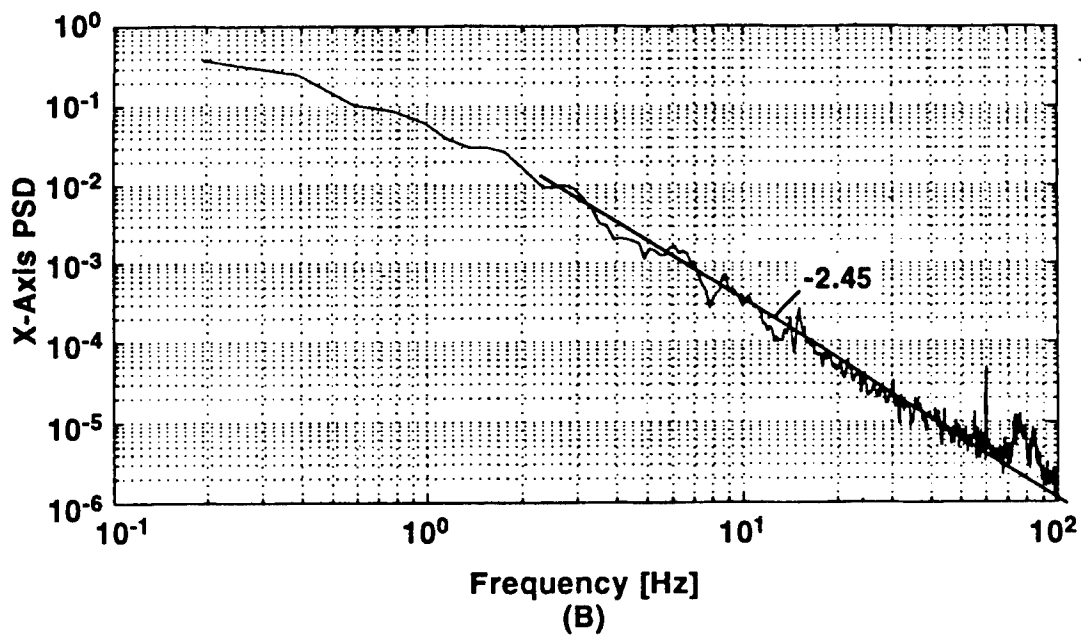
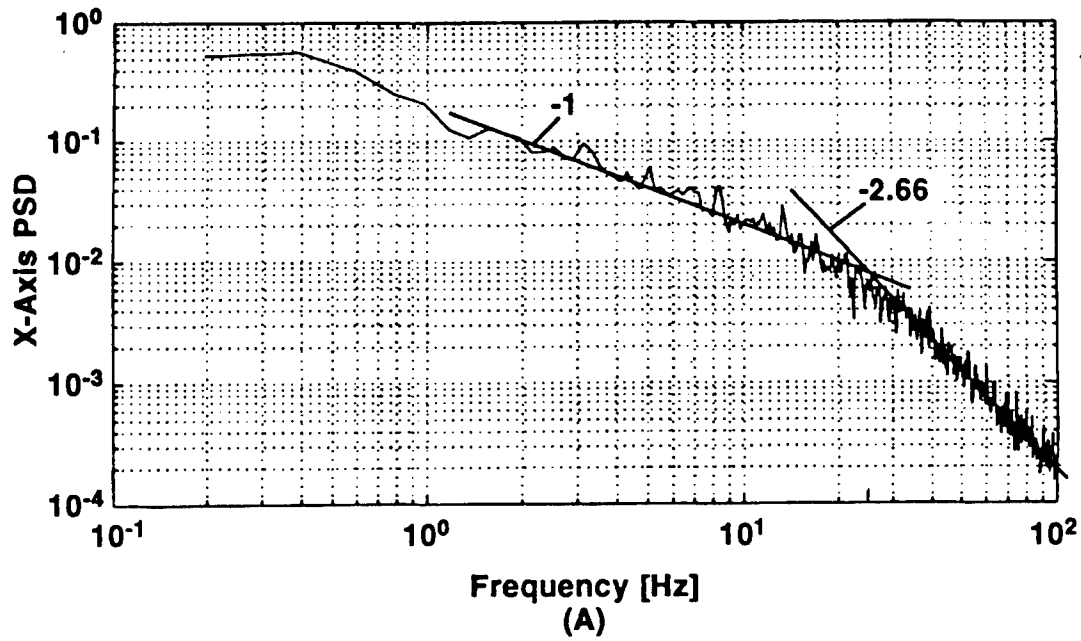


Fig. 2 a and b. Polaris image jitter power spectra for the telescope diameter of  $D = 0.1 \text{ m}$  (a) and  $D = 1.5 \text{ m}$  (b).

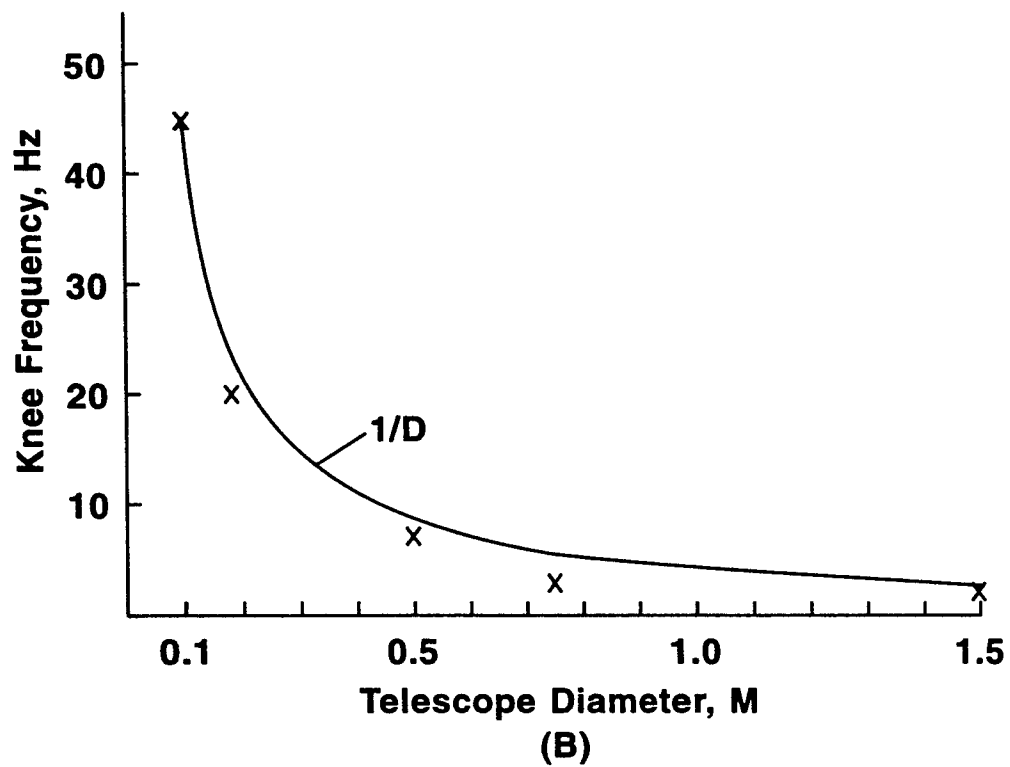
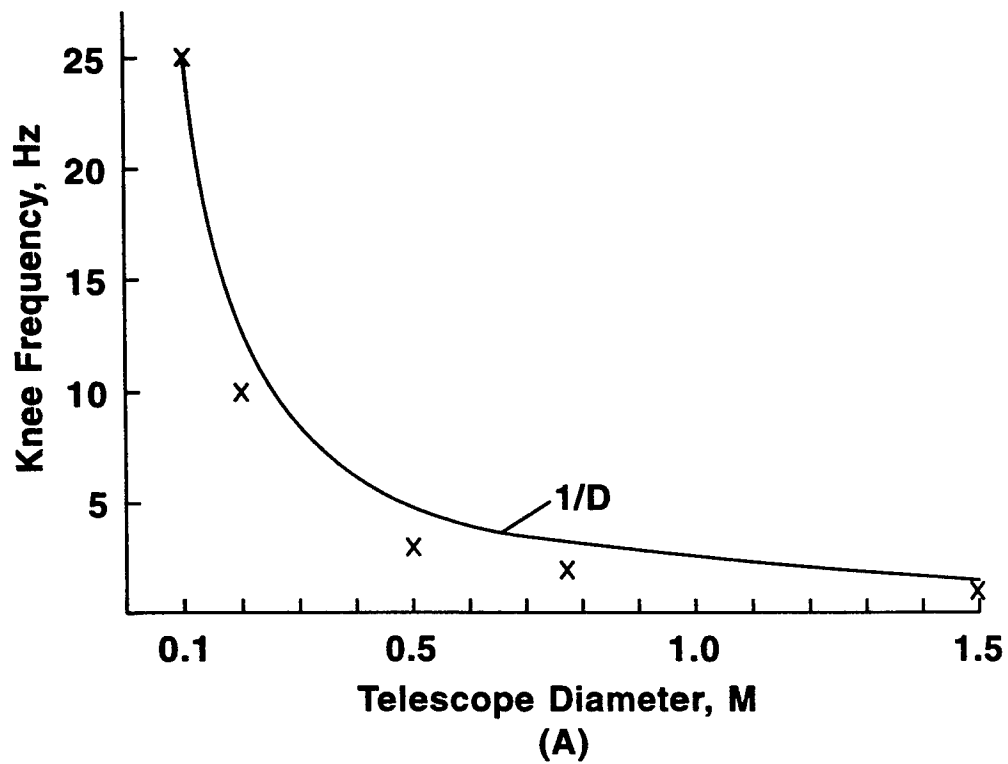


Fig. 3a and b. Dependence of the knee frequency on the telescope diameter measured in two days.

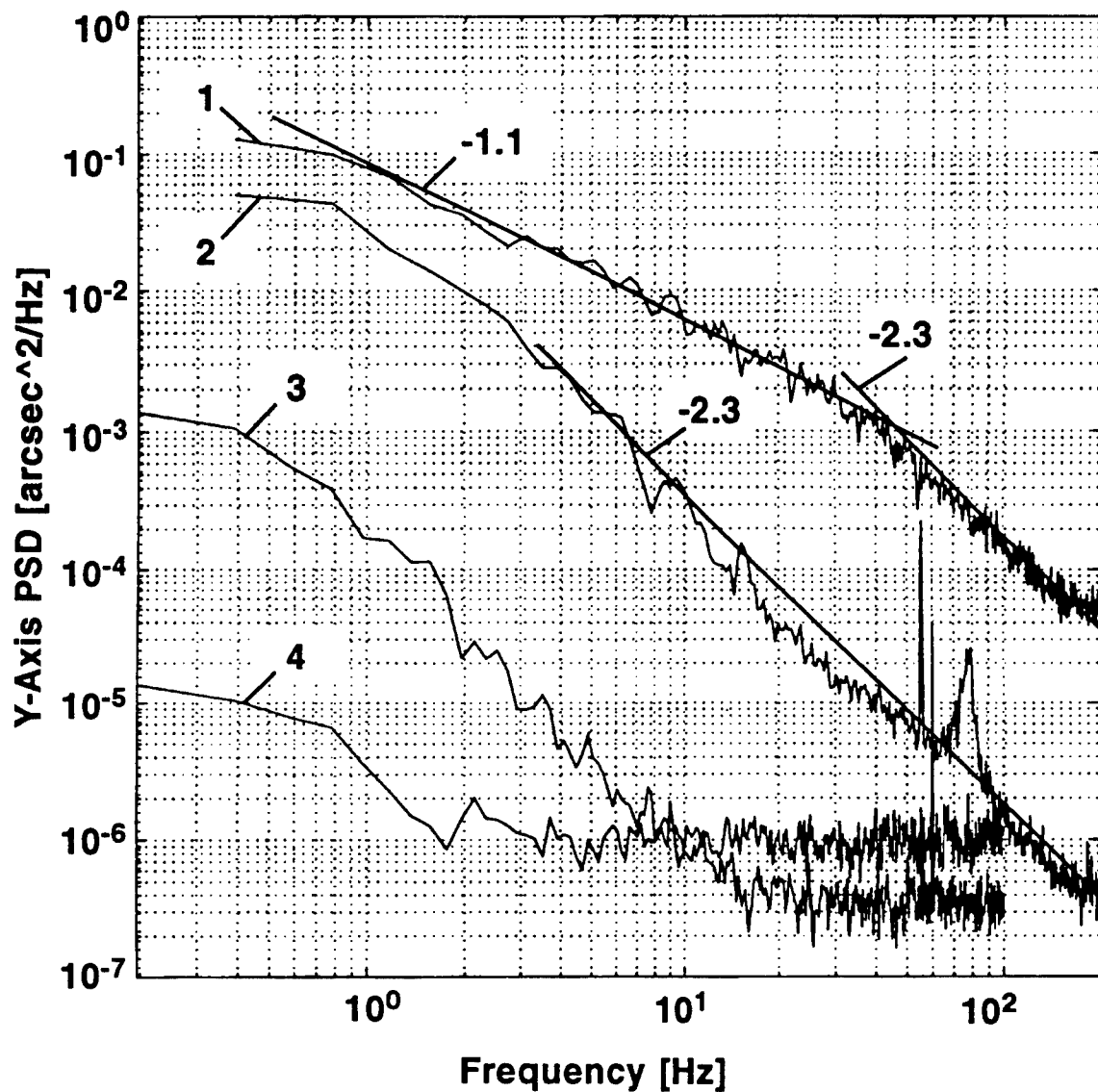


Fig. 4. Temporal power spectra for Polaris (curves 1 and 2) and an internal source (curves 3 and 4). Curves 1 and 3 correspond  $D = 0.1 \text{ m}$  and curves 2 and 4 correspond to  $D = 1.5 \text{ m}$ .

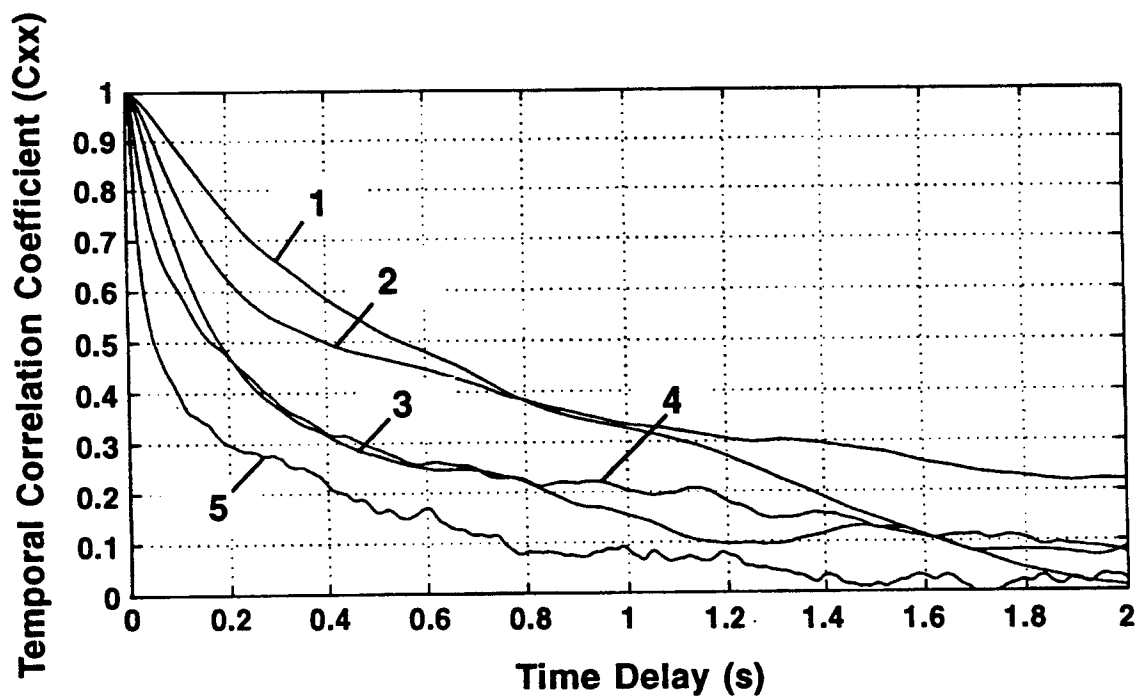
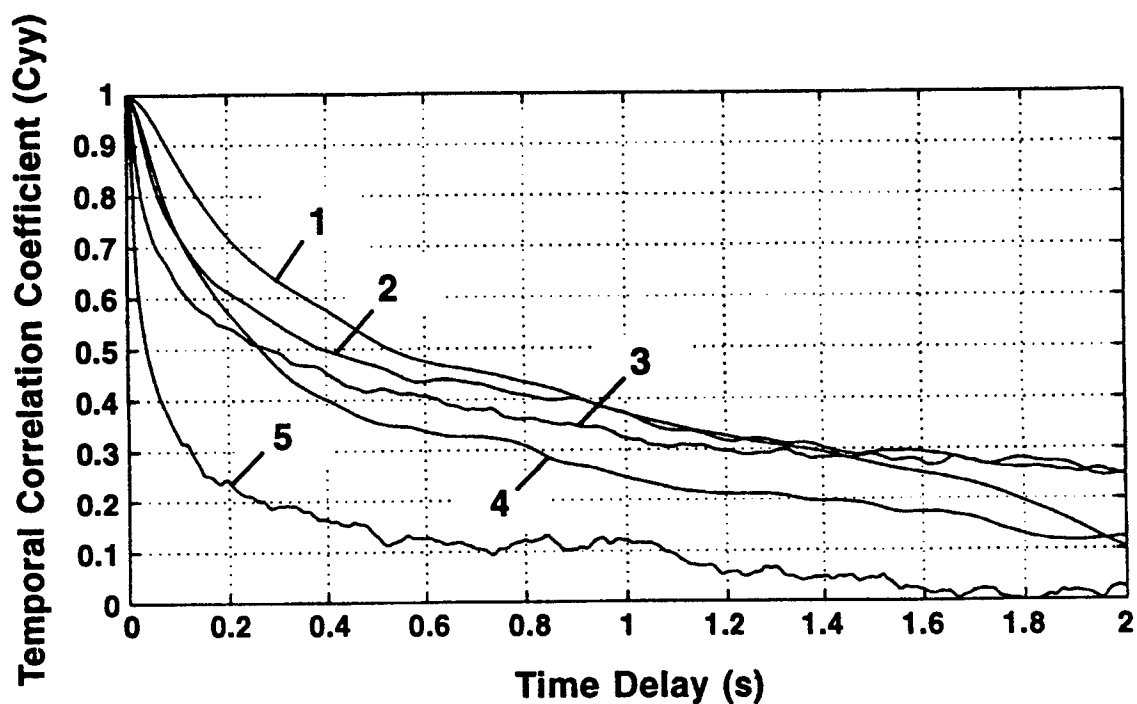


Fig. 5a and b. Temporal correlation coefficient for one-axis tilt components. Curves 1, 2, 3, 4, and 5 corresponds to  $D = 0.1, 0.2, 0.5, 0.75$ , and  $1.5$  m, respectively.

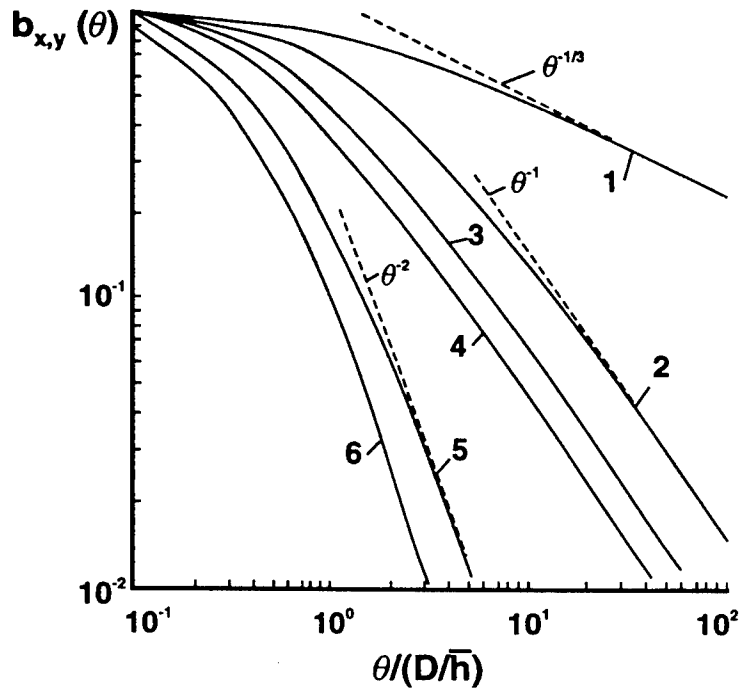


Fig. 6. Angular correlation coefficient for the lateral and longitudinal tilts on the vertical propagation path. Curves 1-4 correspond to the lateral tilt, and curves 5 and 6 correspond to the longitudinal one. Ratio  $L_0/D$  is equal to infinity for curve 1,  $L_0/D = 50$  for curve 2,  $L_0/D = 10$  for curves 3 and 5, and  $L_0/D = 3$  for curves 4 and 6.

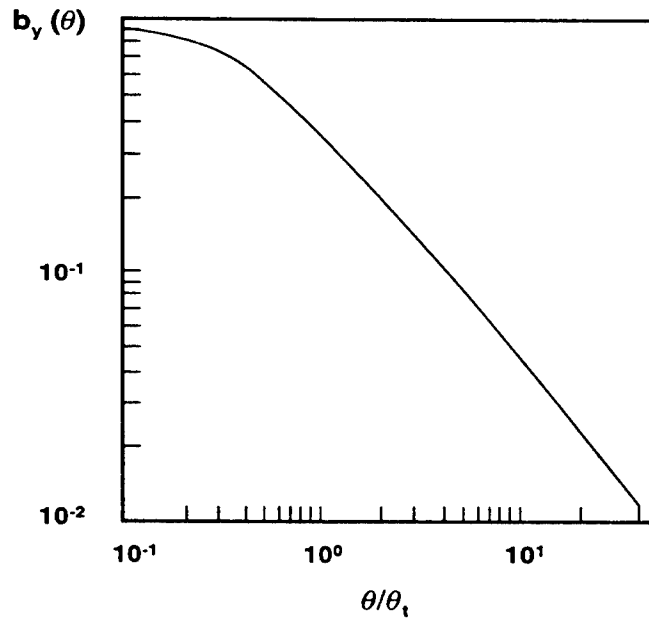


Fig. 7. Universal dependence of the tilt correlation coefficient on the angular separation.

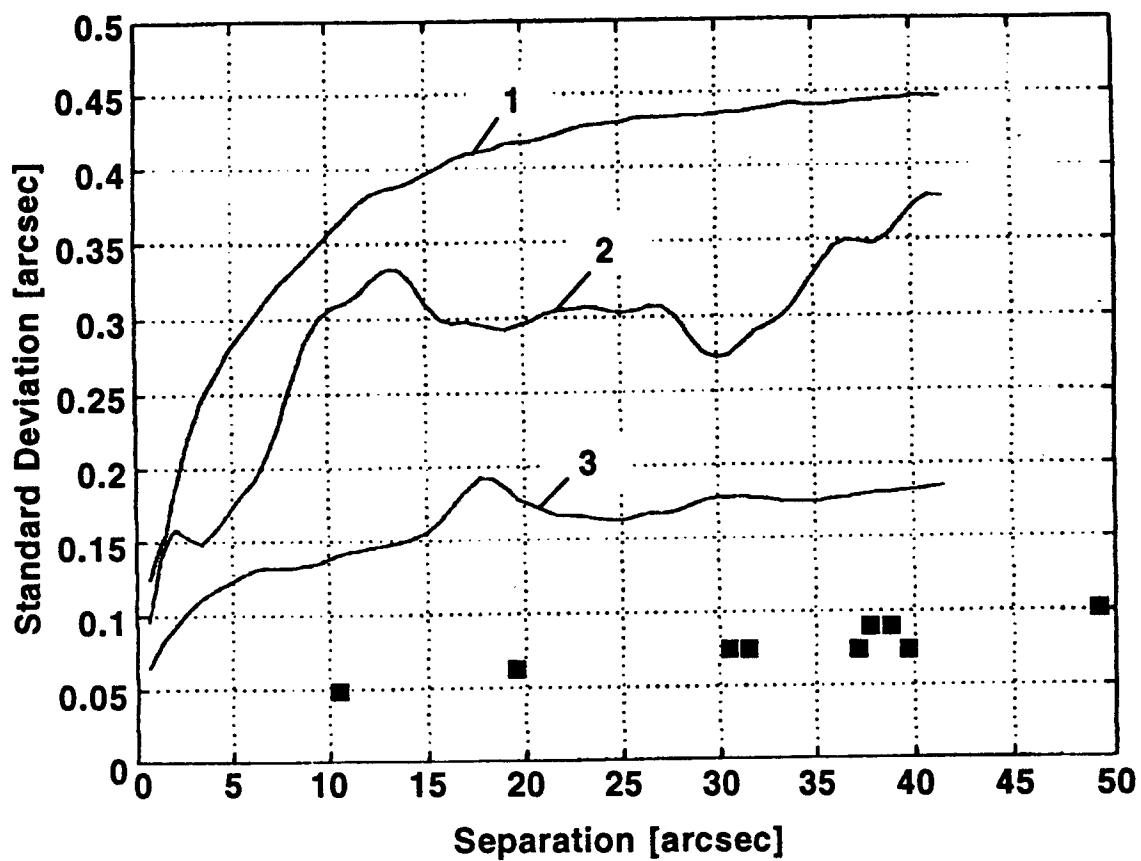



Fig. 8. Dependence of the standard deviation of the tilt difference on the angular separation. Curves 1, 2, and 3 correspond to  $D = 0.1, 0.5$ , and  $1.5$  m, respectively. Squares show the standard deviations of the centroid motion obtained from observations of the stars with a  $2.4$  m telescope {18}.

## Report of Invention

I have no inventions to report as a result of my work on the AFOSR 1996 Summer Research Extension Program.

 12. 11. 96

Mikhail S. Belen'kii

Associate Number

95-0101

Computer Simulation Results on the Performance of Multi-User Data Detection in an Optical  
Code Division Multiple Access Digital Communication System

Daniel Bukorzer  
Professor  
Department of Electrical and Computer Engineering

California State University  
Fresno, CA 93740-8030

Final Report for:  
Summer Research Extension Program  
Phillips Laboratory

Sponsored by:  
Air Force Office of Scientific Research  
Bolling Air Force Base  
Washington, D.C.

and

Phillips AFB

December 1996

# **COMPUTER SIMULATION RESULTS ON THE PERFORMANCE OF MULTI-USER DATA DETECTION IN AN OPTICAL CODE DIVISION MULTIPLE ACCESS DIGITAL COMMUNICATION SYSTEM**

**Daniel Bukofzer  
Professor and Chairman  
Department of Electrical & Computer Engineering  
California State University, Fresno**

## **- ABSTRACT -**

This report examines a specific fiber-optic code division multiple access (O-CDMA) digital communication system. Performance results on data detection for different settings of various system parameters are presented. Previous work in this area produced preliminary performance results, however the need for further investigations became evident. The simulation results presented involve a system accommodating multiple users, operating in both synchronous (same bit rate per user) and asynchronous (different user bit rates with unrelated clocks) modes. The effect of various system parameters and operating conditions, such as data rate, receiver filter characteristics, photodiode efficiency factor, and noise induced distortion have been investigated.

The report focuses on describing the simulation system implemented and presenting the results of an exhaustive evaluation of system performance as a function of the many parameters that can vary in practice. The primary emphasis centers on demonstrating the appropriate bit stream recovery for each of the users having access to the system under different operational scenarios.

Implementation (in software) of a novel Optical Orthogonal Code (OOC), used as an encoding mask for the on-off modulating carrier waves at set frequencies, proved to be successful in reducing crosstalk in systems accommodating multiple users. A DSP simulation package named "Signal Processing Workbench" (SPW) was used to obtain the computer generated performance results. SPW offers a block oriented approach to simulating the complex structure of the communication system under study. By using standard library blocks or creating user specified blocks almost any system can be thoroughly evaluated, subject to processor limitations (i.e. memory, simulation run time, etc.).

General conclusions that can be made based on the computer simulations performed are as follows. High data rates, (higher than 100 KHz for typical parameter values in the simulation) will result in errors in decoded binary data outputs. Furthermore, the filter parameters used to separate the individual frequency components in the received signal, require delicate adjustment in order to capture the exact signal energy level for each frequency component. It was found that leakage light in the sources used to generate the lightwave signals, needs to be suppressed 20 dB below the light transmitting energy level, in order to guarantee reasonable average error rates. Specific simulations show that white Gaussian noise added to the on-off keyed modulated signals, results in errors in the decoded user data for Signal to Noise Ratios below approximately 6 dB.

## **- TABLE OF CONTENTS -**

LIST OF FIGURES AND TABLES	-4-
ACKNOWLEDGMENTS	-5-
INTRODUCTION	-5-
Section 1    The O-CDMA System - General Principles	-6-
Section 2    Transmission Impairments	-8-
THE SIMULATION SYSTEM	
Section 3    User Code Masks	-12-
Section 4    Code Cross Correlation	-17-
Section 5    Unipolar and Bipolar O-CDMA Systems	-20-
Section 6    The Simulation System Blocks	-22-
SIMULATION RESULTS	
Section 7    The Simulation Results	-31-
CONCLUSIONS	-39-
REFERENCES	-40-

## - LIST OF FIGURES AND TABLES -

Fig. 1 A fiber-optic communication system	-7-
Fig. 2 Block diagram of a fiber optic code division multiple access (FO-CDMA) network in a star configuration.	-8-
Fig. 3 Inter Symbol Interference (ISI)	-9-
Fig. 4 Loss in a single-mode silica fiber as a function of wavelength	-10-
Fig. 5 Typical material dispersion for three different silica fibers	-10-
Fig. 6 PN-generator	-13-
Fig. 7 A three stage PN-generator	-14-
Fig. 8 The simulation system with four users	-23-
Fig. 9 Lower level diagram of the PN-code generator block	-25-
Fig. 10 User data for four users	-25-
Fig. 11 Lower level diagram of the encoder block (input and output)	-26-
Fig. 12 Lower level diagram of the encoder block (major components)	-27-
Fig. 13 Lower level diagram of the preliminary decoder block	-28-
Fig. 14 Lower level diagram of the decoder block	-30-
Fig. 15 Decoded output with two errors	-32-
Fig. 16 Absolute value of the signal before threshold comparison with a modified PN-sequence as code mask	-36-
Fig. 17 Absolute value of the signal before threshold comparison with a Walsh code as code mask	-36-
Table 1 Modified PN-sequences for 7 users	-17-
Table 2 Cross-correlation result between two PN-sequences	-18-
Table 3 Walsh codes for 16 users	-18-
Table 4 Cross-correlation result between two Walsh codes	-19-
Table 5 Results of varying several parameters in a synchronous system	-33-
Table 6 Result varying Signal to Noise Ratio	-34-
Table 7 Results varying filter bandwidth and transmission frequencies	-34-
Table 8 Results varying parameters data rate and "low" & "no" signal level	-35-
Table 9 Results of Walsh codes and modified PN-sequences as code masks	-37-
Table 10 Results varying the data rate in an asynchronous system	-38-

## **- ACKNOWLEDGMENTS -**

This work was supported by the U.S. Air Force Phillips Laboratory, Kirtland AFB, New Mexico, under the auspices of the Air Force Office of Scientific Research, Bolling AFB. It is the result of being awarded a summer research extension of the work carried out in the summer of 1995. The head of the U.S. Air Force of Scientific Research is recognized and thanked for supporting the SFRP and the Summer Research Extension Program which allows university faculty members and students the opportunity to become involved in projects of importance to the U.S. Air Force.

The author gratefully acknowledges the support received from both the technical and administrative staff of RDL, Inc., Culver City, Calif.

Additionally, the author recognizes the extensive work and effort as well as the many computer simulations carried out by student assistants Roy Brands, and Mirjan Bakker.

## **- INTRODUCTION -**

Due to the explosive growth of information transmission in the last 20 years, the need for high speed communication systems is evident. Computer networks, either local or wide (i.e., the internet) are well-known examples of transmission systems requiring high capacity, multi-user/multi-access capability and high data rates/throughput. Lightwave technology developments have made it possible to develop systems with such characteristics. An overview of the development of lightwave communication technology may be found in [1]. Studies in the field of lightwave communication networks with a goal of increasing transmission speed and the number of simultaneously active users while at the same time offering reliable overall system performance, have led to a better understanding of physical limitations imposed by optical and non-optical components.

In an optical communication system, information is transmitted by light propagation inside a glass fiber in the form of a coded sequence of optical pulses. The technique known as Optical Code Division Multiple Access (O-CDMA) provides a means of developing a reliable high speed multi-user communication system. There are other techniques for developing such communication systems, however a detailed explanation of the various techniques used, is beyond the scope of this report. A preliminary investigation into the possibility of carrying out computer simulations of an O-CDMA communication system has been performed. The results of this system performance investigation, (reported in [4]), were used as a starting point for this research project.

Recovery (i.e., decoding of the user signals at the input of the receiver) of encoded binary information in the O-CDMA communication system, can be performed in several ways, as described in an excellent treatment on the subject, [5].

Recovery of the binary information in the O-CDMA digital communication system under study is based on decisions made against set threshold levels and implemented with photodetectors and counters. In previous work it was found that the use of bipolar codes (as opposed to unipolar codes) in the O-CDMA communication system under study is fundamental to its practical operation. As explained in Section 5 of the report, the system's threshold for unipolar coded systems was found to be dependent on the number of active users. In practice, the number of active users at a certain time can only be determined if there is some sort of network control present. This would impose significant design challenges as in typical O-CDMA communication environments, the network controller would have to monitor the number of users and their characteristics.

Ideally the O-CDMA system should allow random access to an indefinite number of users, without having the communication channel subdivided into time or frequency slots. Additional users subscribing to the system, can be assigned unique codes and then given channel access without the need to synchronize with any of the other users. This is the essence of the system that has been investigated via computer simulations under various operational scenarios.

The advantage of assigning unique codes to each user is the security provided against possible attempted eavesdropping by unauthorized parties, to whom the signal will be unintelligible, unless the code is known. (A detailed explanation on the use of coding may be found in Section 3 in this report.) Some theoretical background on the generation of the codes used in this system simulation study can be found in [6], [7] as it relates to a maximal length PN-code and in [8] for the Walsh code. A detailed presentation on the characterization and performance of optical codes in a CDMA environment can be found in [9] and [10], whereas [11] deals with an analytical approach to describing the performance of O-CDMA systems.

## **- 1. THE O-CDMA SYSTEM - GENERAL PRINCIPLES -**

Optical code division multiple access (O-CDMA) communications provides a means to combine the vast bandwidth available in direct detection optical systems with the advantages of spread spectrum multiplexing. Non-Optical CDMA techniques utilize spread spectrum radio frequency modulation techniques based on the assignment of individual spreading codes to each of the users. By means of encoding, the binary user signals in a CDMA digital communication system are spread in the frequency domain so that each user occupies the entire bandwidth available resulting in total bandwidth utilization. The optical medium is superbly suited for spread spectrum multiple access, due to its extremely large bandwidth. In fact, because of the limited speed of electronic signal processors, the process of optical-to-electrical and electrical-to-optical conversion in a fiber optic network limits how much fiber bandwidth can be used. Once fully developed and integrated, optical components will offer much higher speeds for optical signal processing than their electronic counterparts. Due to these advantages, CDMA has been the focus of much research in the last twenty years, primarily in the radio frequency domain, but also in the optical domain.

O-CDMA is a bandwidth utilization scheme in which many users access a common fiber optic channel simultaneously, synchronously or asynchronously through the use of data encoding. This multi-access system does not use time or frequency allocation, and users may transmit without the delays inherent in multi-access protocols. The O-CDMA scheme takes advantage of excess bandwidth in single mode fibers in order to achieve the random multi-user communication access, essentially free of network control.

A typical O-CDMA system is best represented by an information data source, followed by an optical encoder containing a laser or some other optical light source, when the information is an electrical signal. An optical encoder is used to map the electrical binary information into optical sequences. These optical signals are then coupled onto a single mode fiber optic channel. At the receiving end of the O-CDMA system, the optical pulse sequences are decoded and converted back to their electrical form. Figure 1 shows a typical O-CDMA system configuration.

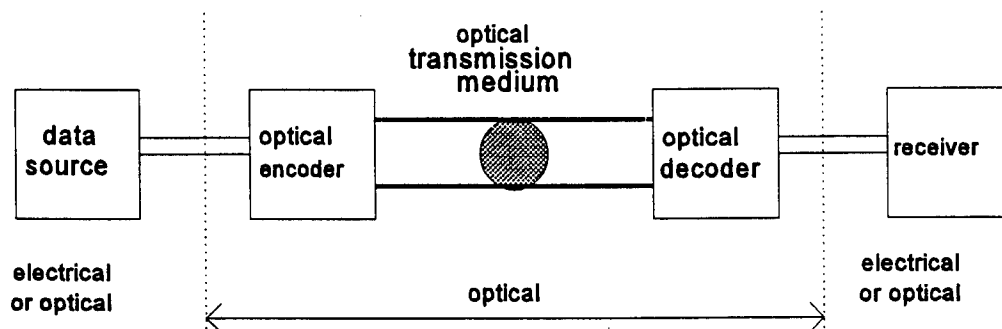


*Fig. 1 A fiber-optic communication system.*

The optical pulse sequences can be decoded in two different ways. One way involves a comparison of the received sequence to a stored replica of itself (correlation process), followed by a threshold level comparator. Another way to decode the optical sequences is to use a combination of filters centered around the different center frequencies as set in the encoder, in combination with a photodetector and counter.

In a typical O-CDMA there are "N" such transmitters (user data sources) and receiver pairs. Figure 2 shows the block diagram of a typical O-CDMA system.

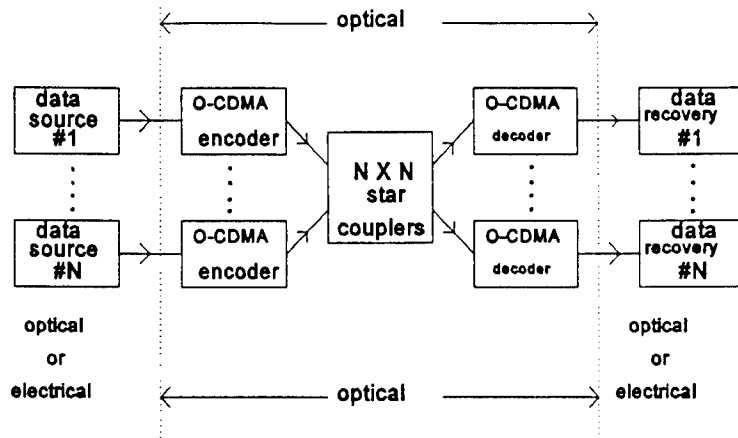


*Fig. 2 Block diagram of a fiber optic code division multiple access (FO-CDMA) network in a star configuration.*

To send information from one user to another in an O-CDMA digital communication system, the address code for the intended receiver is impressed upon the data from the transmitting data source. One of the principles of O-CDMA signals involves the ability to extract the data from the received optical signal in the presence of all other users' signals. This means that at every receiver the appropriate data, sent by the other half of the receiver-transmitter pair, needs to be decoded correctly even under the very likely scenario in which multiple user receiver-transmitter pairs are active and transmitting at the same time.

Possible interference between signals from each of the users in the single mode fiber optic transmission channel therefore needs to be minimized in order to reduce "crosstalk" between the users and thus errors in the recovered data. This will be examined in greater detail in Section 7.2 of the report.

## - 2. TRANSMISSION IMPAIRMENTS -

There are unfortunately numerous sources of transmission impairments in lightwave communication systems. The different impairments that are of importance in the design of O-CDMA systems will be discussed in this section.

### 2.1 Inter symbol interference

Inter symbol interference (ISI) is caused by signal dispersion. Dispersion can be viewed as the effect in which signal pulses are delayed with the length of the delay in the received signal varying with the signal frequency.

ISI refers to those impairments that distort and broaden the width of signal pulses, resulting in self interference in the individual user signals. This effect will limit the maximum bit rate that can be used over the transmission channel. This can be seen in Figure 3 where the broadening of the lightpulses is shown as well as its resulting interference.

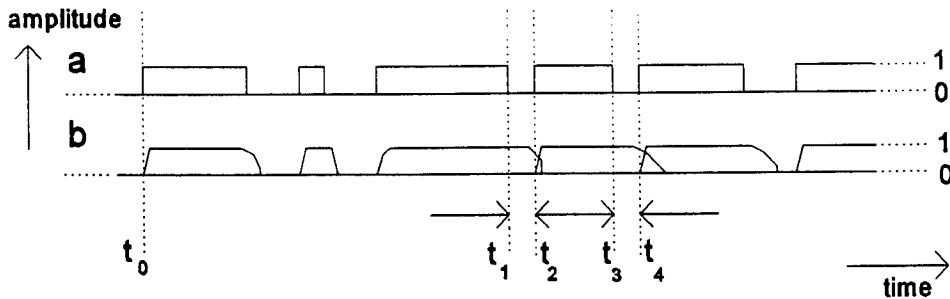


*Fig. 3 Inter symbol interference (ISI).*

The signals “a” and “b” in Figure 3 show the same information content of a binary sequence. The logic “1” in this figure implies the presence of light in the fiber, whereas the logic “0” implies the absence of light. Signal “a” represents the ideal situation where light pulses have zero rise and fall time. Signal “b” in Figure 3 represents the more realistic situation in an optical fiber. The broadening of the lightpulses may cause signal overlap between individual light pulses if the data rate is sufficiently high. This effect (ISI) can be seen between  $t_1$  and  $t_2$  as well as  $t_3$  and  $t_4$ , causing a logic “0” to be received as a logic “1”. If the effect is too severe, data errors will occur forcing data rates to be reduced. This means that the time interval between pulses (i.e. the distance between time positions  $t_3$  and  $t_4$  in Figure 3) will be larger and overlapping pulses will be less likely to occur.

The broadening of the lightwave pulses is caused by physical effects known as

1. Chromatic dispersion
2. Polarization dispersion
3. Laser nonlinearities

These three effects are briefly discussed next.

### 2.1.1 Chromatic dispersion

This effect is caused by material dispersion in the fiber optic transmission medium, because of slight impurities in the (atomic) structure of the glass fiber. The large increase in the use of lasers in communication has partly come about as result of improvements in the quality of the medium through which light energy is transmitted. (An excellent treatment on the historical development of different optical fibers can be found in [1].)

The objective of most lightwave transmission systems is to maximize the bit rate-distance product ( $BL$ ). The bit rate ( $B$ ) is limited inherently by chromatic dispersion in the fiber, which is responsible for the broadening of optical pulses during their propagation inside a single-mode fiber. The maximum distance ( $L$ ), a bit stream can be transmitted through an optical-fiber before a repeater (amplifier) is necessary on account of signal loss, also is a very important parameter associated with the optical-fiber.

The choice of operating wavelength is related to the loss and dispersion characteristics of the fiber. In order to develop a sense of the properties of single-mode fibers (as would be used in practical realizations of the simulated O-CDMA digital communication system), Figures 4 and 5 are provided. Figure 4 shows a diagram of measured loss as a function of wavelength for single-mode silica fibers. The arrows in Figure 4 indicate the wavelength regions used for optical fiber communications. Figure 5 shows the material dispersion for typical single-mode silica fibers. Data points for three different fibers are shown.

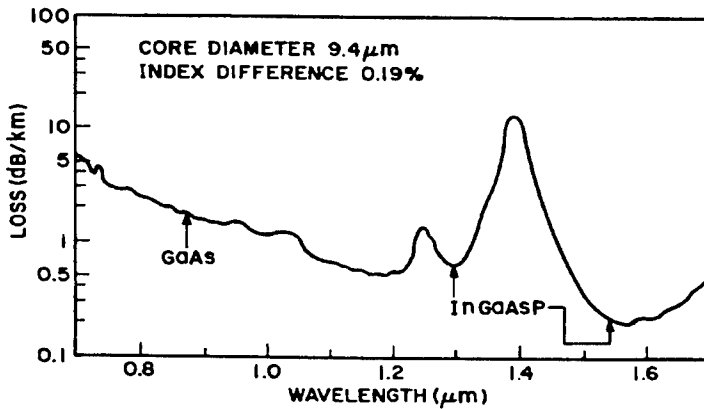


Fig. 4 Loss in a single-mode silica fiber as a function of wavelength [2].

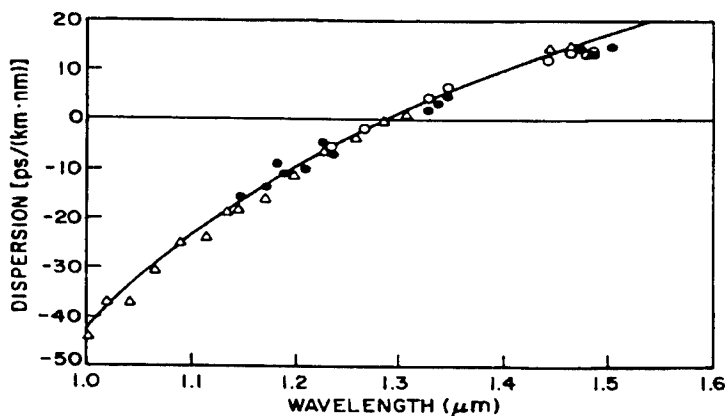


Fig. 5 Typical material dispersion for three different silica fibers [2].

As can be seen from these figures, minimum fiber loss occurs at a wavelength near  $1.55 \mu\text{m}$ . Modern optical communication systems use lasers operating at or near this wavelength. However the zero dispersion wavelength, which is at about  $1.3 \mu\text{m}$ , is different from the minimum loss region wavelength. It is however possible to shift the zero dispersion wavelength towards the desirable  $1.55 \mu\text{m}$  region, by modifying the fiber characteristics [2].

### 2.1.2 Polarization dispersion

Dispersion can be polarization dependent. Two signals of the same frequency, but with opposite polarizations, will experience different delays.

### 2.1.3 Laser nonlinearities

The first two physical effects causing dispersion, increase in severity with increasing transmission distances. The amount of delay difference between lightwaves of different frequencies due to chromatic and/or polarization dispersion, becomes larger with increasing transmission distance. Laser nonlinearities cause dispersion, independent of transmission distances. Laser nonlinearities increase with aging of the laser. The lasers used to modulate data do not produce pure signals of an exact frequency. The spectrum of a laser signal exhibits a certain small bandwidth called the linewidth. Therefore the pulse sequences have finite linewidths.

To understand the role of the spectral width  $\Delta\lambda_s$  of the laser pulse, it is known that during its propagation inside a fiber of length  $L$ , an optical pulse broadens and its width increases by an amount given by

$$\Delta\tau = D_f (\Delta\lambda_s) L \quad \text{Eq. 1}$$

In Eq. 1,  $D_f$  is the fiber dispersion coefficient having a value of  $\sim 17 \text{ ps}/(\text{km}\cdot\text{nm})$  at a wavelength of  $1.55 \mu\text{m}$  (see Fig. 5). In order for the pulse to arrive within its assigned time slot, the pulse should not be wider than  $B^{-1}$ ,  $B$  being the bit rate in Gb/s, i.e.,

$$B\Delta\tau = BLD_f (\Delta\lambda_s) < 1 \quad \text{Eq. 2}$$

A typical spectral width ( $\Delta\lambda_s$ ) for an InGaAsP laser, operating on  $1.55 \mu\text{m}$  is about  $5 \text{ nm}$ . Using realistic values for  $D_f$  and  $\Delta\lambda_s$ , it is possible to calculate the bit-rate distance product,  $BL$ . The  $BL$ -product is limited to less than  $10 \text{ GHz}\cdot\text{km}$ . This means that a repeater spacing in a transmission medium of  $100 \text{ km}$  will limit the bit-rate in the fiber to  $100 \text{ Mb/s}$ . This is considered to be small in today's long haul lightwave transmission systems.

## **2.2 Photodetector nonlinearity**

Signal dispersion is one of the impairments in the O-CDMA digital communication system. Additional impairments involve the use of photodetectors in the direct detection receiver. A direct detection O-CDMA digital communication system uses photodetectors in combination with bandpass filters. The output of the photodetectors is a measure of energy for signals of a certain frequency as determined by the bandpass filters. (A thorough discussion of the working details of the simulated O-CDMA digital communication system is presented in Section 6 of this report).

The number of photons that arrive at the photodetector are counted, used as a measure of signal strength and converted into an electric current. The efficiency of this whole process of transferring light energy to electric current is however not ideal. The number of photons counted when light impinges on a photodetector is known to be random and Poisson distributed.

## **2.3 Noise**

Noise in the received signal can consist of shot noise, thermal noise, laser phase noise, or amplified spontaneous emission noise (ASE). The latter noise is introduced in O-CDMA systems through the use of optical amplifiers. Optical amplifiers are however not used in the O-CDMA digital communication system under study. Shot noise is introduced by the photodetectors and involves photons whose number is Poisson distributed. The random variation in the phase of signals transmitted by lasers is referred to as phase noise. This phase noise results in broadening in the linewidth of the output laser spectrum. This results in dispersion of the signals in the O-CDMA system as already discussed. Thermal noise is introduced mainly by the receiver pre-amplifiers and is of additive Gaussian form.

## **- 3. USER CODE MASKS -**

There are several reasons why binary information is modulated by code masks. One of the reasons is that the information sent is not supposed to be disturbed or read by unintended users. To be sure that only the user addressed receives the information that has been sent, every user needs to be assigned a unique code. The codes to be designed have to meet two conditions:

1. each sequence should be easily distinguished from shifted versions of itself and
2. each sequence should be easily distinguished from versions of every other assigned sequence.

Codes developed with these requirements that meet orthogonality conditions are called nearly Optical Orthogonal Codes. In this section the kind of code masks used in this investigation will be explained.

### 3.1 PN-codes

A code sequence generator, that produces pseudonoise (PN)-codes, is made up of delay elements with appropriate feedback. By means of combining feedback paths with the delay elements, the generator's output can be controlled so as to produce an output sequence with certain properties. A linear binary shift register sequence generator using feedback and modulo-2 addition is used to generate binary PN-codes.

The pseudo-random generator is so called because of its repeating output sequence and the generation of what appears to be a random binary output. Every sequence consists of a certain number of bits, called "chips" before repetition sets in. The larger the number of delays used, the longer the period of its repeating output sequence. The number and placement of feedback taps are determined by the generator function. A diagram of a PN-code generator shows that it consists of nothing more than a shift register in conjunction with its appropriate logic, which feeds back a logical combination of the state of two or more of its delay elements to its input as shown in Figure 6.

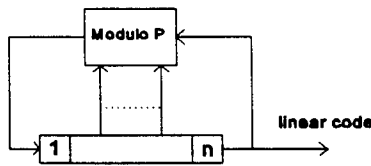


*Fig. 6 PN-generator.*

In Figure 6, n is the last delay element, normally also being the output of the generator, although the output of any delay element in the generator can be used to provide the same linear code with a certain amount of time delay. If the output is for instance taken from delay element (n-1) instead of n, the time delay or shift will be exactly one chip duration. The "modulo- P" block represents a network that modulo-P adds outputs of different delay elements together, P being the total number of delay elements added together. The output of the "modulo-P" block is then fed back to the input, which is considered to be delay element number one.

The generator will do nothing without a certain initial value in its delay elements. If any number of zeros are modulo-P added together, the result will consist of only zeros. Therefore often an initial value of "one" is given to at least one delay element and the first n-bits at the output will therefore show at most 'n'-ones, as can be seen in Figure 7 for a generator made up of 3 stages.

The generator can produce code sequences of a certain maximum period length N, where N is specified by the following formula:

$$N = 2^n - 1 \quad \text{Eq. 3}$$

That is, N is the number of chips in one period of a maximum length pseudo-random bit sequence and n is the number of delay elements in the feedback shift register system.

The statistical distribution of the ones and zeros in one period is well defined and is always the same in each sequence. Relative positions of the sequences can vary from sequence to sequence, but each repetition represents the same one-zero sequence, and the statistical distribution remains the same. To show that each generator repeats sequences after a certain time, the following example is shown. A generator consisting of 3 delay elements, in which the outputs of element 1 and 3 are fed back to the input of the first element is shown in Figure 7.

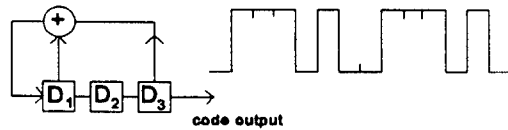


*Fig. 7 A three stage PN-generator*

The output can be seen being repeated every 7 chips. With the initial values of the delay elements being all ones, the sequence shown below can now be developed. Note that the values in columns 1 and 3 are modulo-2 added and deliver the new input value to delay element one. After exactly 7 shifts the sequence starts repeating itself. Also note that the chips in the third column form the actual output sequence, namely the PN-code.

As can be seen, the code with an initial value of ones in the delay elements, is the repeated sequence 1 1 1 0 1 0 0.

Delay element :	1	2	3	
Initial value :	1	1	1	<---
	---	0	1	1
				(1 exor 1 gives 0)
		1	0	1
		0	1	0
		0	0	1
		1	0	0
		1	1	0
		1	1	1
		1	1	1
				<-----> same as first initial value.

A 4 stage PN-generator produces a maximum code length of 15 chips, given by

1 0 0 1 1 0 1 0 1 1 1 1 0 0 0

Each user can be assigned its own unique code by shifting the PN-sequence in time. When the code above is shifted in time for other users it will appear as shown.

0 0 1 1 0 1 0 1 1 1 1 0 0 0 1	user 2
0 1 1 0 1 0 1 1 1 1 0 0 0 1 0	user 3
1 1 0 1 0 1 1 1 1 0 0 0 1 0 0	user 4 etc.

A problem arises in practice because when the information arrives at the receiver it is delayed in time as a result of finite propagation velocity. Without an absolute time reference, this means the receiver can not determine which user has sent the information.

To make every code unique for each user the PN-code is inverted and placed next to the original code, so a code of 30 chips is created that for the example case looks like this

1 0 0 1 1 0 1 0 1 1 1 1 0 0 0	original 15 chips-code user 1
0 1 1 0 0 1 0 1 0 0 0 0 1 1 1	inverted 15 chips-code user 1
1 0 0 1 1 0 1 0 1 1 1 1 0 0 0 0 1 1 0 0 1 0 1 0 0 0 0 1 1 1	30 chips-code user 1

The codes generated by this method will henceforth be called modified PN-sequences. The original code can be shifted in time 15 times which means 15 unique codes can be produced. And so with a 30 chip code, 15 users can be identified without an absolute time reference.

### 3.2 Walsh codes

Another code that has been considered in this investigation is the Walsh code. The discrete Walsh Hadamard transform involves rearrangements of discrete Hadamard matrices. A Hadamard matrix of order N is defined as an N \* N matrix, which for dimensions that are a power of two, can be constructed in the following manner

$$H_{2N} = \begin{bmatrix} H_N & H_N \\ H_N & -H_N \end{bmatrix} \quad \text{Eq. 4}$$

with  $H_1 = [1]$ . Therefore,

$$H_2 = \begin{bmatrix} H_1 & H_1 \\ H_1 & -H_1 \end{bmatrix} = \begin{bmatrix} 1 & 1 \\ 1 & -1 \end{bmatrix} \quad \text{Eq. 5}$$

and for  $N = 2$

$$H_4 = \begin{bmatrix} H_2 & H_2 \\ H_2 & -H_2 \end{bmatrix} = \begin{bmatrix} 1 & 1 & 1 & 1 \\ 1 & -1 & 1 & -1 \\ 1 & 1 & -1 & -1 \\ 1 & -1 & -1 & 1 \end{bmatrix} \quad \text{Eq. 6}$$

For N = 4

$$H_8 = \begin{bmatrix} H_4 & H_4 \\ H_4 & -H_4 \end{bmatrix} = \begin{vmatrix} 1 & 1 & 1 & 1 & 1 & 1 & 1 & 1 \\ 1 & -1 & 1 & -1 & 1 & -1 & 1 & -1 \\ 1 & 1 & -1 & -1 & 1 & 1 & -1 & -1 \\ 1 & -1 & -1 & 1 & 1 & -1 & -1 & 1 \\ 1 & 1 & 1 & 1 & -1 & -1 & -1 & -1 \\ 1 & -1 & 1 & -1 & -1 & 1 & -1 & 1 \\ 1 & 1 & -1 & -1 & -1 & -1 & 1 & 1 \\ 1 & -1 & -1 & 1 & -1 & 1 & 1 & -1 \end{vmatrix} \quad \text{Eq. 7}$$

The discrete Walsh Hadamard transform matrix H can be obtained from the Hadamard matrix by reordering the rows in increasing sequence order. The sequence of a row is half the number of sign changes in that row. In  $H_8$  the first row has no sign changes, the second row has 7 sign changes, the third row has 3 sign changes, and so on. Reordering the  $H_8$  matrix in increasing sequence order, results in

$$H = \begin{vmatrix} 1 & 1 & 1 & 1 & 1 & 1 & 1 & 1 \\ 1 & 1 & 1 & 1 & -1 & -1 & -1 & -1 \\ 1 & 1 & -1 & -1 & -1 & -1 & 1 & 1 \\ 1 & 1 & -1 & -1 & 1 & 1 & -1 & -1 \\ 1 & -1 & -1 & 1 & 1 & -1 & -1 & 1 \\ 1 & -1 & -1 & 1 & -1 & 1 & 1 & -1 \\ 1 & -1 & 1 & -1 & -1 & 1 & -1 & 1 \\ 1 & -1 & 1 & -1 & 1 & -1 & 1 & -1 \end{vmatrix} \quad \text{Eq. 8}$$

This matrix shows the Walsh codes in the correct order. Therefore, row number one of H is Walsh code one, row number two is Walsh code two and so on. The first Walsh code can not be used in this investigation because it contains no sign changes. Furthermore Walsh code 3, 5 and 7 are not used because these codes are shifted versions of respectively Walsh code 2, 4 and 6. So, when a matrix of 8 chips per code is created there are 4 useful codes in it for this investigation. The number of useful codes that can be generated is half the dimension of the H matrix. The dimension of the H matrix used for the system simulation is 32 by 32.

## - 4. CODE CROSS-CORRELATION -

The correlation properties of code sequences depend on code type, length, chip rate, and even the chip-by-chip structure of the particular code being used. Cross-correlation in communication systems is of interest in several areas, such as (a) code division multiple access systems (or any other code addressed system) in which receiver response to any signal other than the proper addressing sequence is not allowable, and (b) antijamming systems that may employ codes with extremely low cross-correlation.

Cross-correlation is a measure of similarity between two different code sequences. It is a comparison of a sequence  $a_n$  and another sequence  $b_n$  over all possible time shifts of one with respect to the other. It is evaluated from the formula

$$c_{(m)} = \sum_n a_n b_{n-m} \quad \text{Eq. 9}$$

Practically, the correlation  $c_{(m)}$  can be obtained by counting agreements and disagreements. That is, the sequences aligned in time are compared with each other. When two chips being compared are one or are zero, it is called an agreement. When the chips are different, it is called a disagreement. The greater the number of disagreements, the lower the cross-correlation is between the sequences.

The cross-correlation between Walsh codes is better than the cross-correlation between modified PN-sequences (modified PN-sequences are explained in subsection 3.1). The modified PN-sequences shown in Table 1 have been used in previous work as reported on in [4].

Table 1 Modified PN-sequences for 7 users

Modified PN-sequences									
1	1	0	0	1	1	0	1	0	1
2	0	1	0	0	1	1	0	1	1
3	0	0	1	0	0	1	1	0	1
4	0	0	0	1	0	0	1	1	1
5	1	0	0	0	1	0	1	0	1
6	1	1	0	0	0	1	1	0	1
7	1	1	1	0	0	0	1	1	0

The cross-correlation between sequence 3 and sequence 4 (one chip shifted in time), for example, gives the result shown in Table 2.

Table 2 Cross-correlation result between two PN-sequences

3	0010	0110	1011	110	1101	1001	0100	001
4	0010	0110	1011	111	1101	1001	0100	000
CR	AAAA	AAAA	AAAA	AAD	AAAA	AAAA	AAAA	AAD

A = Agreement

D = Disagreement

CR = Correlation Result

The number of chips in agreement is 28 out of 30. The more chips that agree, the higher the chance of cross-talk. This is an effect that needs to be avoided as much as possible. In this case there is always a pair of sequences that has this cross-correlation level thereby increasing the chance of cross-talk between those two signals at the receiver.

In the simulations carried out all the useful Walsh codes are implemented as user code masks (See Table 3). Note that in the Tables 3 and 4 the negative ones in the H matrix become zero in the binary Walsh code.

Table 3 Walsh codes for 16 users

Walsh codes								
1	1111	1111	1111	1111	0000	0000	0000	0000
2	1111	1111	0000	0000	1111	1111	0000	0000
3	1111	0000	1111	0000	0000	1111	0000	1111
4	1111	0000	1111	0000	1111	0000	1111	0000
5	1100	0011	1100	0011	0011	1100	0011	1100
6	1100	0011	1100	0011	1100	0011	1100	0011
7	1100	1100	1100	1100	0011	0011	0011	0011
8	1100	1100	1100	1100	1100	1100	1100	1100
9	1001	1001	1001	1001	0110	0110	0110	0110

<b>Walsh codes</b>								
10	1001	1001	0110	0110	1001	1001	0110	0110
11	1001	0110	1001	0110	0110	1001	0110	1001
12	1010	0101	1010	0101	1010	0101	1010	0101
13	1010	0101	1010	0101	0101	1010	0101	1010
14	1010	1010	0101	0101	1010	1010	0101	0101
15	1010	1010	1010	1010	0101	0101	0101	0101
16	1010	1010	1010	1010	1010	1010	1010	1010

When, for example, Walsh code 3 and Walsh code 4 (1 chip shifted in time) are compared, the number of agreements is 16 out of 32 (Table 4).

Table 4 Cross-correlation result between two Walsh codes

3	1111	0000	1111	0000	0000	1111	0000	1111
4	1110	0001	1110	0001	1110	0001	1110	0001
CR	AAAD	AAAD	AAAD	AAAD	DDDA	DDDA	DDDA	DDDA

It turns out that regardless of which Walsh codes are cross-correlated, the number of disagreements between them will always be 16. While this can be proven, it can be said that the cross-correlation between the Walsh codes is better than the cross-correlation between the modified PN-sequences, because of the number of agreements that result. As previously explained, the lower the number of agreements between the sequences, the less chance there is of cross-talk amongst the users. In subsection 7.4, simulation results that address this issue can be found.

## - 5. UNIPOLAR AND BIPOLAR O-CDMA SYSTEMS -

The codes in Section 4 are used in a O-CDMA bipolar system. In the following two subsections, both, systems using unipolar and bipolar codes are described and the advantages of one over the other are explained.

### 5.1 O-CDMA system using unipolar codes

The optical unipolar CDMA system can be described as follows. Let  $d_{ni}$  represent a (0, 1) binary bit sequence at a rate  $R$  bits/sec associated with the  $i$ th user of an  $N$  user system. Such user is assigned a spreading code or mask  $u_i$ , where  $u_i$  consists of  $K$  logic states 0 and 1. A logic 1 in  $u_i$  implies light transmission while a logic 0 implies no (or very low) light transmission. A very broadband light source is employed from which  $K$  distinct frequencies are extracted and each assigned to one of the logic states associated with the mask. When  $d_{ni}$  equals 1, those frequencies with a logic 1 state in  $u_i$  are transmitted (light is "on") while frequencies associated with a logic 0 state in  $u_i$  are not transmitted at all (or transmitted at a very low level perhaps as much as 30 dB below the "on" signal level). When  $d_{ni}$  equals 0, those frequencies associated with a logic state 1 in  $u_i$  are transmitted at a level low enough to represent leakage light (thus modeling the inability to completely turn off the light source), while those frequencies associated with a logic state 0 in  $u_i$  are not transmitted at all or at a very low level, as previously explained. This effectively produces on-off keyed modulation signals at each of the transmitted frequencies of the broadband source, which are summed to produce a composite signal that is equivalent to a wavelength multiplexed digital signal. At the receiver, the different frequency components present in the composite signal are separated, identified and extracted. Photodetectors are used to produce a photon count that is proportional to the light intensity present at each frequency. When the overall photon count associated with all frequencies that can be transmitted for a given mask exceeds a specified threshold, a logic 1 is associated with  $d_{ni}$  whereas if the threshold is not exceeded, a logic 0 is declared.

Simulations of this O-CDMA system using unipolar codes were developed and tested as part of a previous investigation. While the simulation results pointed toward a system that worked properly, it was found that key to its operation was the ability to correctly set the receiver threshold for the binary decisions. More importantly, the correct threshold setting, proved to be very much dependent on the number of users present. It was felt that unless adequate prior knowledge existed about how many users were simultaneously active, it would be difficult if not impossible to have such a system operate properly, unless very sparse user codes (or masks) were used that produced little or no interference amongst users. This, although possible, would require very long user codes  $u_i$  (because each mask would be mostly made up of logical 0 states) and therefore a very broadband source, or shorter user codes accommodating a small number of users [4]. These limitations makes the choice between a system using unipolar codes and one using bipolar codes an easy one.

## 5.2 O-CDMA system using bipolar codes

The optical bipolar CDMA system can be described as follows. As in subsection 5.1, let  $d_{ni}$  represent a (0, 1) binary bit sequence at a rate  $R$  bits/sec associated with the  $i$ th user of a  $N$  user system. Such user is assigned a spreading code or mask  $u_i$ , where  $u_i$  consists of  $K$  logic states 0 and 1. Associated with code  $u_i$  is the complementary code  $\bar{u}_i$ , where each element of the latter is the logical complement of the former. A concatenation of  $u_i$  and  $\bar{u}_i$  is formed to produce a code (or mask) of  $2K$  logical states, denoted  $U_i$ . As before, a logic 1 (in  $U_i$ ) implies light transmission while a logic 0 implies no (or very low) light transmission. A very broadband light source is employed from which  $2K$  distinct frequencies are extracted and each assigned to one of the logic states associated with the mask. When  $d_{ni}$  equals 1, those frequencies associated with a logic 1 state in  $U_i$  are transmitted (light is "on") while frequencies associated with a logic 0 state in  $U_i$  are not transmitted at all (or transmitted at a very low level perhaps as much as 30 dB below the "on" signal level). When  $d_{ni}$  equals 0, those frequencies associated with a logic state 1 in  $U_i$  are transmitted at a level low enough to represent leakage light (thus modeling the inability to completely turn off the light source), while those frequencies associated with a logic state 0 in  $U_i$  are not transmitted at all or at a very low level, as previously explained. In addition to forming a concatenated code or mask, the bipolar system differs from the unipolar one by forming the complement  $\bar{U}_i$  of the concatenated code  $U_i$ . This complement code  $\bar{U}_i$  is operated upon by  $\bar{d}_{ni}$ , the complement of the binary sequence associated with the  $i$ th user. The same  $2K$  frequencies extracted from the broadband source are assigned to each one of the logic states associated with the mask. When  $\bar{d}_{ni}$  equals 1, those frequencies associated with a logic 1 state in  $\bar{U}_i$  are transmitted (light is "on") while frequencies associated with a logic 0 state in  $\bar{U}_i$  are not transmitted at all (or transmitted at a very low level perhaps as much as 30 dB below the "on" signal level). When  $\bar{d}_{ni}$  equals 0, those frequencies associated with a logic state 1 in  $\bar{U}_i$  are transmitted at a level low enough to represent leakage light (thus modeling the inability to completely turn off the light source), while those frequencies associated with a logic state 0 in  $\bar{U}_i$  are not transmitted at all or at a very low level, as previously explained. This effectively produced on-off keyed modulation at each of the transmitted frequencies of the broadband source which are summed to produce a composite signal that is equivalent to a wavelength multiplexed digital signal. At the receiver the different frequency components present in the composite signal are separated, identified, and extracted. Photodetectors are used to produce a photon count that is proportional to the light intensity present. The overall photon count associated with all the frequencies that can be transmitted for the  $U_i$  mask is compared to the overall photon count associated with all frequencies that can be transmitted for the  $\bar{U}_i$  mask. If the former exceeds the latter, a logic 1 is associated with  $d_{ni}$  whereas if the latter exceeds the former, a logic 0 is declared. This is equivalent to subtracting the two values of the photon count and comparing that number with zero. The masks  $U_i$  were generated using, both, modified PN-sequences and Walsh codes.

The clear advantage of this method versus the (unipolar) previous one is that the threshold used to decide on the logical state associated with  $d_{ni}$  is independent of the number of users present. This important feature of the bipolar method leads to a system that is both implementable and attractive from a performance standpoint [4].

## - 6. THE SIMULATION SYSTEM BLOCKS -

In this section, the development of the computer simulation system will be discussed in detail. As previously indicated, a software simulation toolkit called SPW was used to perform computer simulations of the O-CDMA digital communication system. Using SPW, the communication system operating under many different system parameter settings, can be thoroughly evaluated. An advantage of SPW is that it is block oriented. The complete system can be subdivided into subcomponents or blocks, each performing one particular function.

Some of the simulation run times were found to be lengthy, especially as the number of users  $N$ , increased. A system constructed with 16 users was found to be the largest one whose performance could be simulated in a reasonable amount of time. Additionally, the amount of data being processed was so extensive that the computer system used, though quite modern, simply could not handle simulations involving greater number of users. With 16 users, data-swapfiles of sizes bigger than 220 Megabytes(!) were created by SPW and the hard disk was used as temporary storage for data being processed by the software. The RAM memory (32 Megabytes) in the Sparc workstations was not sufficient for some simulation runs. Expanding the simulation system to 32 users was not possible, forcing all simulations therefore to be carried out for a system of 16 users. In order to explain the different components of the simulation system, only 4 users are assumed to be present in the descriptions that follow. The number of users in the O-CDMA system can be set to any desired number, but greater computational requirements will result when carrying out simulations.

Both the synchronous and the asynchronous O-CDMA system will be discussed in this section, highlighting the differences between the two.

### 6.1 The overall system

In Figure 8, major components of the overall simulation system are shown. From this figure, it can be seen that the O-CDMA system roughly consists of three main sections. First, there is the transmitting section. The second section consists of the receiver and the third section represents the transmission medium, namely the fiber optic network, connecting the first two sections to each other. In the transmitting section, blocks labeled "PN-generator" and blocks labeled "encoder" can be discerned. The PN-generator block provides the pseudo random binary data for each individual user. The encoder block is used to convert the data into related optical sequences. The encoder blocks are user-unique, which means that each encoder assigns an individual signature to the data (in the form of a code mask) of the corresponding connected user. The output of all individual user encoder blocks are added together, representing the fiber optic channel's input.

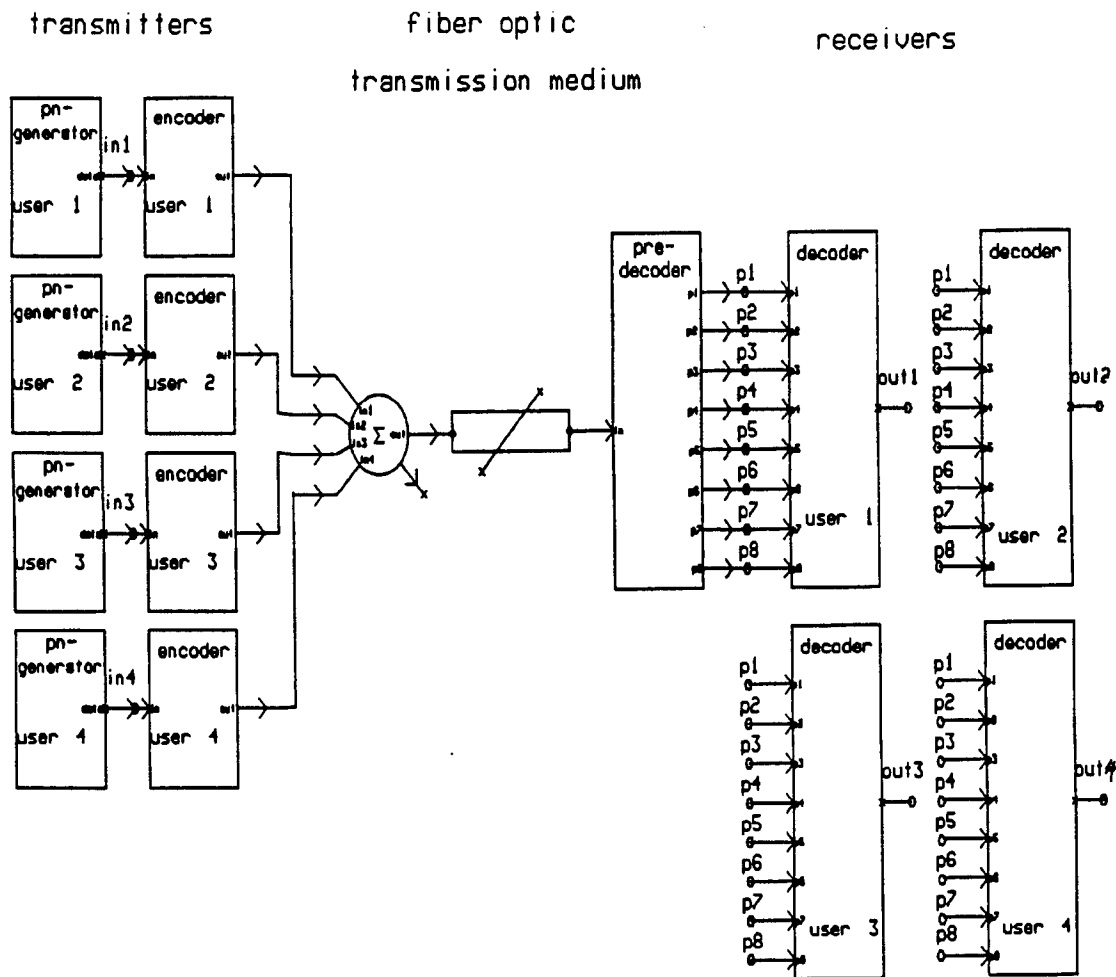


Fig. 8 The simulation system with four users.

The receiver section consists of a "pre-decoder"- block ("pre-" is short for preliminary) followed by the four user unique decoder blocks. The pre-decoder block processes the channel output by separating the frequency components via a bank of bandpass filters. The decoder blocks perform a specific signal processing operation, that is unique to each user.

The synchronous system operates on the same bit rate per user driven by a master clock, while in the asynchronous system users operate on different bit rates with unrelated clocks. Therefore, computer simulations of the asynchronous system differ from the synchronous system in the number of pre-decoder blocks present. In the synchronous system, the received signal is applied directly to the pre-decoder block, whose output feeds a separate decoder block, one for every user. The asynchronous system however, has a pre-decoder block for each user whose output is connected to individual decoder blocks.

The sampling frequency is set at 400 MHz and the data rate at 100 Kbps. In the simulation runs, these as well as other parameters were varied and their effect studied. The sampling frequency can not be chosen too large, or the system's limits in handling data will be reached. It was determined that a sampling frequency of 400 MHz offered a reasonable compromise.

The simulation results are intended to offer qualitative and quantitative information on the performance of O-CDMA digital communication systems. These results, as discussed Section 7, can be used as a starting point for the development of practical realizations of O-CDMA digital communication systems.

The individual blocks used in the overall simulation system will now be discussed.

## **6.2 The PN-data generator block**

**Function:** provides the pseudo random binary data

**Parameters:**

- sampling frequency
- data rate
- PN-formula specification

**Description:**

The transmitted data in the O-CDMA digital communication system is of random binary form. At the lower level of this block, as seen in Figure 9, a pseudo-random generator block is used to simulate the random data. In Section 3, it was indicated that PN-code sequences have periods of variable length. By setting the period length to 15 chips and assigning every user a shifted version of this PN-sequence, specific data bit streams are assigned to each of the individual users. (Note that only four shifted versions of the 15 chip length PN-sequence are needed for the 4 user system and that the 16th user in a 16 user system would have to be assigned the same version as user 1). This avoids the need to provide signal observation (i.e., signal sinks) for both the transmitted data and the recovered data of all of the individual users. This has the effect of reducing simulation run times considerably.

The PN-data generator is set to work at a certain data rate by the use of the impulse train block and the inverter block, which control the hold input of the PN-generator block. At the first simulation iteration, the first bit of the PN-sequence is produced and held for a certain amount of time determined by the value of the parameter "data rate" as set in the impulse train block.

parameters

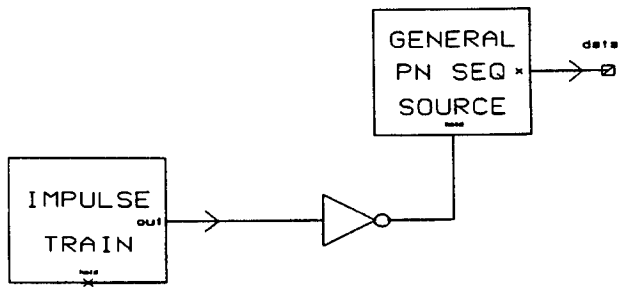
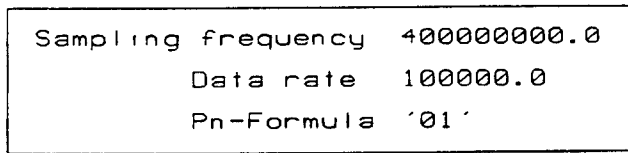


Fig. 9 Lower level diagram of the PN-code generator block.

Figure 10 shows the data signals for all users in a 4 user O-CDMA digital communication system. Four shifted versions of a PN-code having a period length of 7 chips are shown.

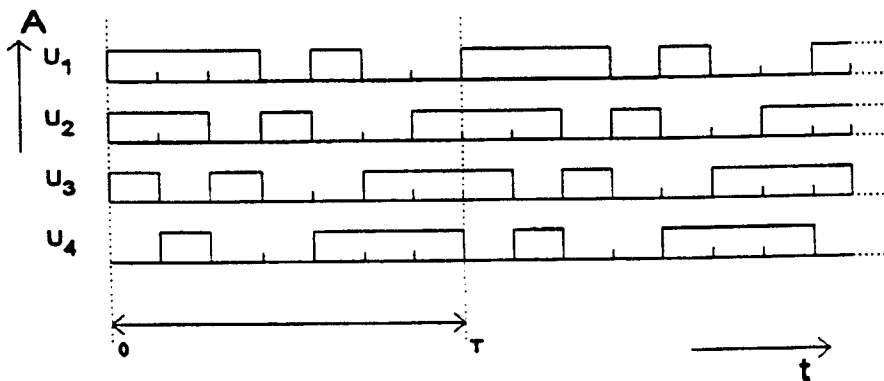


Fig. 10 User data for four users.

### 6.3 The encoder block

#### Function:

The encoder block is used to convert the binary random data into (the equivalent of) optical sequences.

**Parameters:**

- sampling frequency
- data rate
- power level for transmitting light
- power level for transmitting no light
- power level for light leakage

**Description:**

Figure 11 shows at the lower level the input and output of the encoder block. The input to the encoder block is the output of the PN-data generator block. The logical states in the binary random data input signal are converted into integer voltage levels in the "Binary to Numeric" block. Figure 12 shows at the lower level the major components of the encoder block. Complex tone generator blocks are used to create sinusoids of prescribed frequencies. The complex tone block generates a pure sine wave of a certain frequency, after which the real component is extracted and used to produce on-off keyed modulated signals. The pseudo-random data is used to control the operation of switches that allow these tones to be multiplied either by a unity factor, corresponding to a logic "1" in the mask, or a very small factor, corresponding to a logical "0" in the mask. (See also Section 5 in this report.)

Unique codes selected from the family Walsh codes provide an individual signature for each user. The binary mask is represented by the "onsig" and "lowsig" inputs, their values set at 1 and 0.01, respectively. It can be seen from Figure 12 that the system implements a bipolar code to encode the user information.

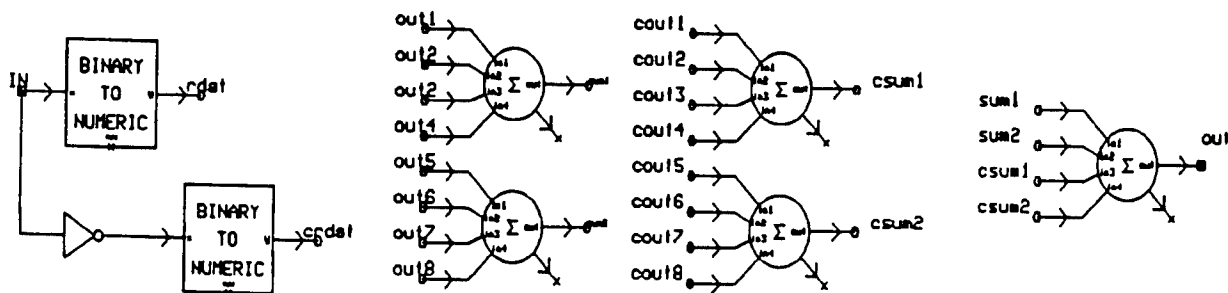


Fig. 11 Lower level diagram of the encoder block (input and output).

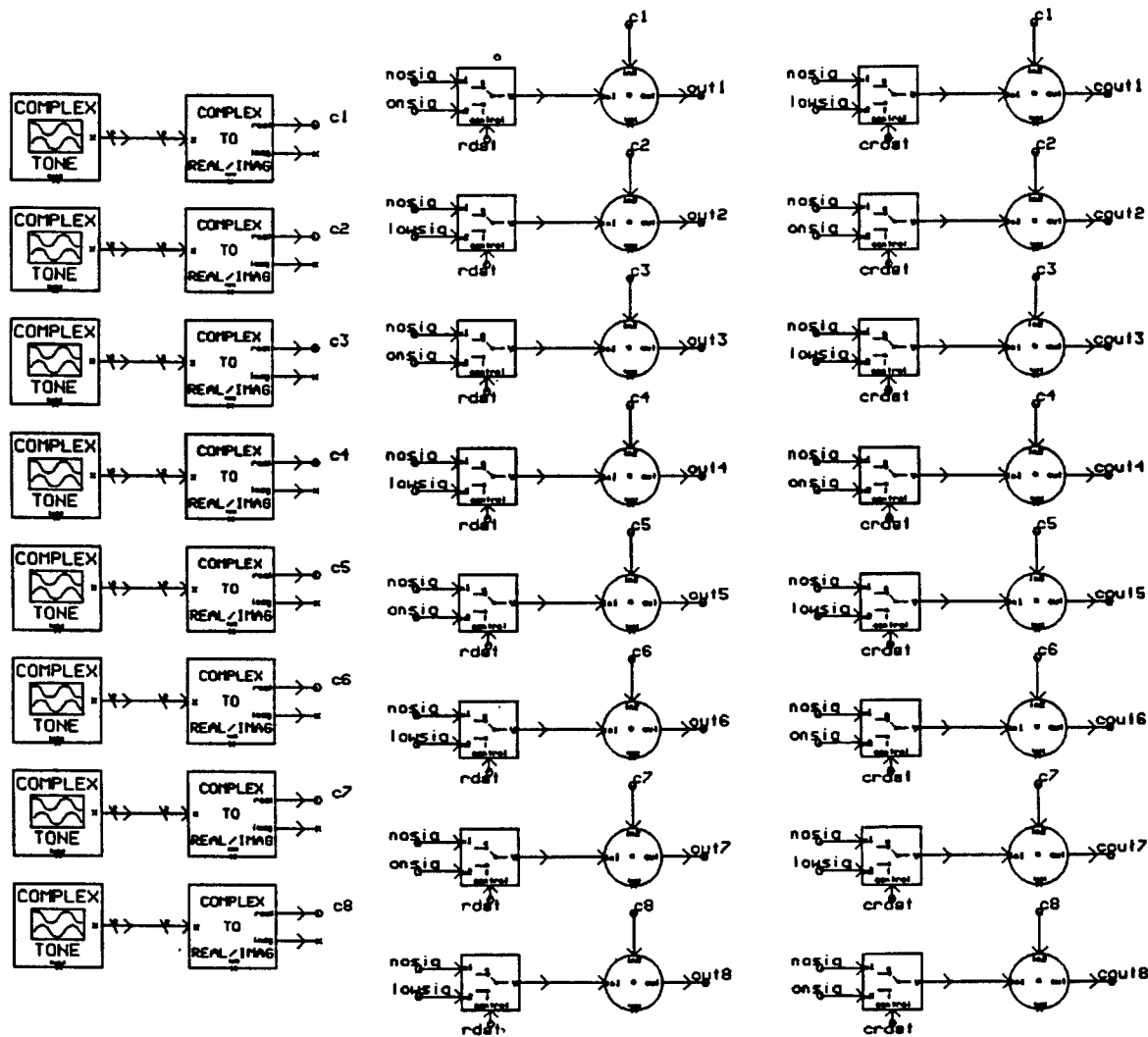


Fig. 12 Lower level diagram of the encoder block (major components).

#### 6.4. The preliminary decoder block

##### Function:

In the pre-decoder block the frequency components of the channel output are separated by a bank of Butterworth bandpass filters.

##### Parameters:

- sampling frequency
- data rate
- photo diode efficiency
- filter bandwidth

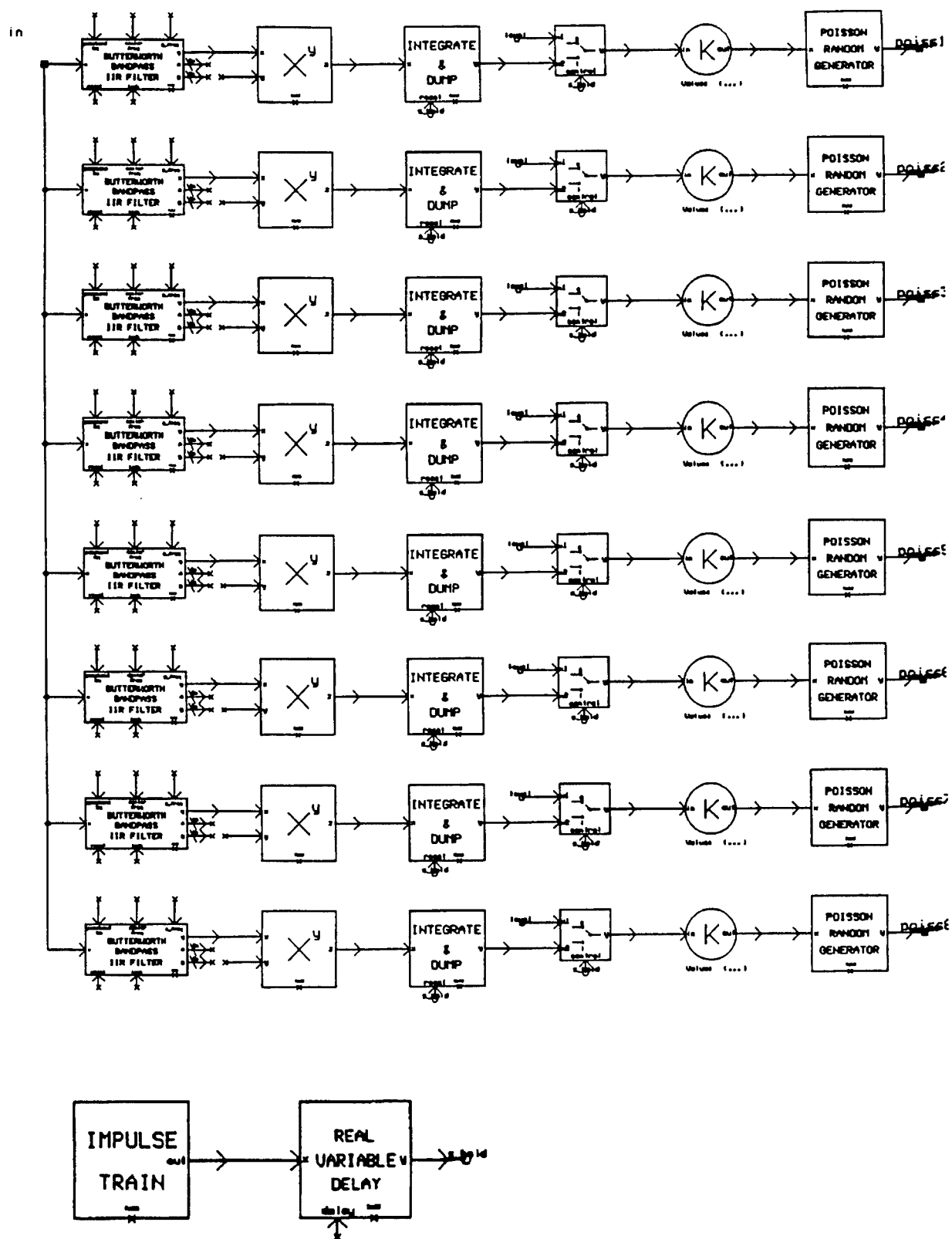


Fig. 13 Lower level diagram of the preliminary decoder block.

**Description:**

Figure 13 shows at the lower level the major components of the pre-decoder block. Each filter in the pre-decoder block of the 4 user O-CDMA system has a center frequency of  $2m$  (in MHz) in which  $m = 1, 2, \dots, 8$ . The bandwidth of the filters is made large enough to capture the energy associated with each on-off keyed modulation signal. The signal at the output of the filter is squared and integrated over the bit duration interval. This output is a measure of signal energy at each of the  $2m$  (in MHz) frequencies.

The block “impulse train” has two parameters that need to be set. One is the impulse rate or data rate and the other is the sampling frequency. The output of the block will give a pulse after a certain number of samples given by

$$\frac{f_{sample}}{d} = N \quad \text{Eq. 10}$$

In Eq. 9,  $f_{sample}$  represents the sampling frequency (in samples/sec) and  $d$  the data rate (in Bits/sec).  $N$  in this case, represents the number of samples contained in each data bit interval. In the common case where  $f_{sample} = 400 \text{ Mhz}$  and  $d = 100 \text{ kHz}$  then  $N$  equals 4000 samples/bit.

The delay block delays the signal for another 2500 samples in order to represent the delay in time between sending the information and receiving it. The pulse called “s\_hold” (sample and hold) is high at sample values 2500, 6500, 10500, 14500 etc. This impulse train is connected to the block “integrate & dump” and to the “switch” block. Every time the pulse is high the “integrate & dump” block integrates the received signal over its bit duration, stores it at the output, and is reset to zero.

Each “switch” block produces a constant output set by the parameter, which has been set to 0.00000000001 in this case. Only when the “s\_hold” pulse is high, a switch to the second input takes place and allows the value calculated by the “integrate & dump” block through. Two more blocks are added to model the photon count. Light exists as photons that impinge on a photodetector. The detector counts the number of photons in the light signal, but cannot do so exactly. To represent this non ideal nature of a photodetector, the Poisson block is added. The Poisson block produces a Poisson distributed random number, that is proportional to the input of the block. The output of this block, for each of the  $2m$  (in MHz) frequencies, represents the energy of the signal at that frequency. The scalar gain block in front of the Poisson block is placed to represent the efficiency of the energy conversion process.

**6.5. The decoder block****Function:**

Final decoding of the received lightwave signals.

**Parameters:**

- sampling frequency
- data rate

**Description:**

Figure 14 shows at the lower level the major components of the decoder. The signals represented by the ones in the  $U_i$  code mask (see Section 5.2), are added together. Also the signals represented by the ones in the complementary code mask,  $\bar{U}_i$ , are added together. After subtracting these two values, the result is compared to zero. The comparison is made by the "threshold" block. The parameters "pos thresh" and "neg thresh" are set in such a way that if the value at the input is higher than the value "pos thresh" a 1 is declared at the output, and when it is lower than the "neg thresh" value, a -1 is declared at the output. As long as the value at the input is between "pos thresh" and "neg thresh", the output remains unchanged. Both threshold parameters are set to zero in this case, which means that the output will be 1 when the input value is above zero and the output will be -1 when the input value is below zero.

The "and" block, placed after the "threshold" block, has two inputs. The first input is the output of the "threshold" block and the second input is the "s\_hold" pulse described in Section 6.4. The output of an "and" block is only 1 when both inputs are 1. In all other cases the output is 0. The last block in the schematic is a "latch" block. Its inputs are s (set) and r (reset). When s receives a 1 from the "and" output it will declare a 1 at the Q output. The output remains 1 until the r input becomes a 1, causing the Q output to become 0. The output will become 1 again when the s input is a 1, and so on. The output of this block is the decoded binary data signal.

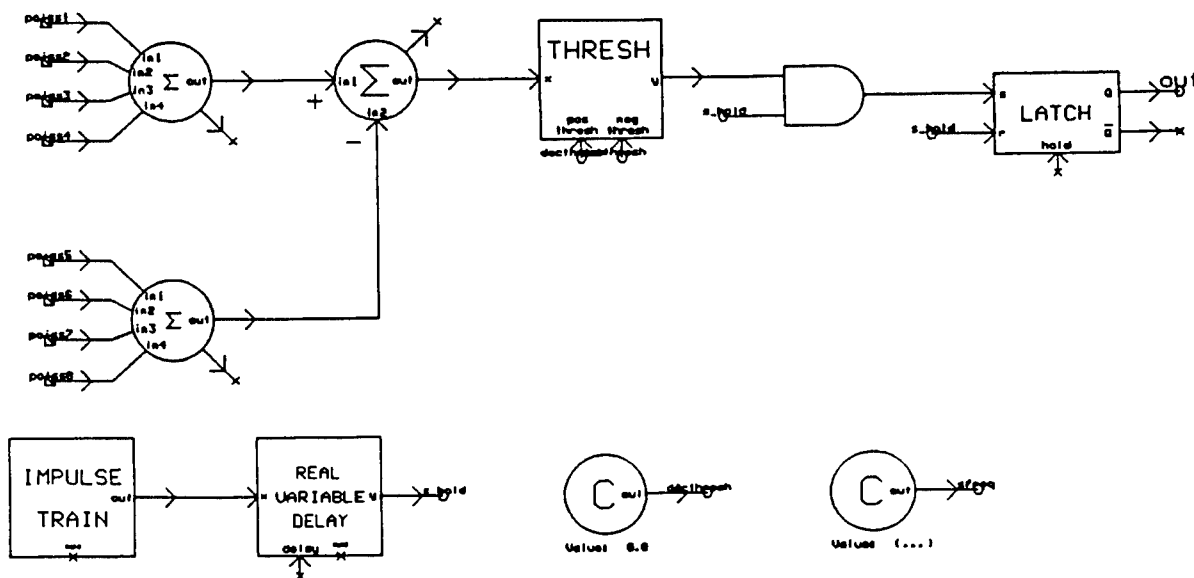


Fig. 14 Lower level diagram of the decoder block.

## 6.6. The transmission medium

The fiber optic transmission medium shown in Figure 8 is considered to be ideal in the system under study. In previous work the channel signal was allowed to propagate through a soft channel nonlinearity which for simulation purposes had been allowed to take the form  $y = A \tanh(Bx)$ , where  $x$  and  $y$  are the input and output, respectively, and  $A$  as well as  $B$  are variable parameters that control the amplitude and the degree of the curvature of the nonlinearity, respectively. After performing specific simulations in the course of this research however, it was found that the effect of the nonlinear function of the transmission block was negligible for the frequency components in the channel signal considered. For this reason and the assumed short transmission distances in the O-CDMA digital communication system under study, ideal channel propagation conditions were simulated and therefore the transmission block was not used.

## - 7. THE SIMULATION RESULTS -

Not all of the simulation results that were obtained are shown in this report. Only those results that are important to the main issues addressed in this study are described and tabulated in this section.

All the simulations are performed in an O-CDMA digital communication system for 15 or 16 users. For simulations performed with Walsh codes as code masks, the total number of users is 16. For simulations performed with modified PN-sequences as code masks, the total number of users is 15. As explained earlier, this number proved to be the largest number of users that could be simulated within reasonable computer run times. Though the system can easily be expanded to more users, this would require greater computational capabilities.

The signal labeled "Transmitted Data" shows the data that has to be transmitted for a particular user. The signal labeled "Decoded Output User" shows the decoded output signal for a specific user. The signal labeled "error" shows the number of errors in the received signal compared to the signal sent by the user. These three signals are shown in Figure 15.

The block used to count the errors in the received signal, makes a comparison at every sample time and counts the differences between the transmitted data and the decoded output signal. The number of samples per bit interval is different for simulations with different data rates. To get the actual number of errors in the decoded output signal, the number of counted errors needs to be divided by the number of samples in the bit interval. The columns labeled "Errors" in the tables show the total number of errors for the total number of users.

Each simulation has been performed for 100,000 sample points. To make a fair comparison between the results, a column "Average error rate" is added. It gives the number of errors per user, which means that the number of "Total errors" is divided by the product of the number of users and the number of bit intervals observed.

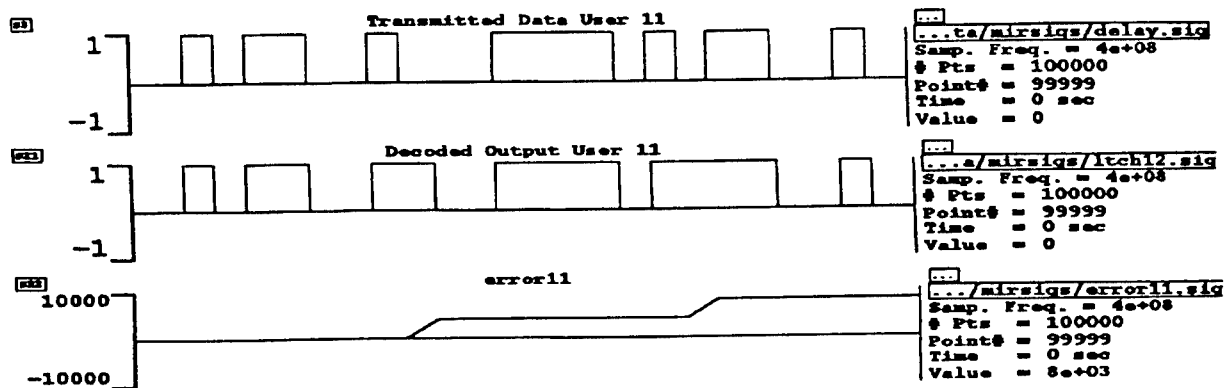


Fig. 15 Decoded output with 2 errors

## 7.1 Varying parameters in a synchronous system

Table 5 shows performance results associated with different combinations of parameters involving the data rate, filter bandwidth, and photodiode efficiency in a synchronous system with Walsh code masks. The data rate parameter is set in the main block diagram, the "pre-decoder" block, and the "decoder" block (impulse train). The photodiode efficiency and the filter bandwidth are both parameters set in the "pre-decoder" block. Parameters involving data rate, filter bandwidth, and photodiode efficiency are varied in these simulations.

### Combination of parameters that produced errorless results

The data sent is received without errors in a situation where the sampling frequency is 400 MHz, the frequency components of the masks are 2m (in MHz) with  $m = 1, 2, 3, \dots, 32$ , the data rate is 100 KHz, the filter bandwidth is 500 KHz, and photodiode efficiency is 100,000. The results of this simulation are considered the reference set. One parameter is changed at the time and the results of those simulations are compared to the results of this "reference" simulation.

### Varied parameter: data rate

The data rate is tested at lower and higher values. The higher the value of the data rate becomes, the more errors that show up at the receiver. From the results of the simulations it can be concluded that a data rate higher than 100 KHz show errors at the receivers. The simulation with a data rate of 50 KHz has been carried out to show that a lower data rate will result in perfect decoded outputs as well.

**Varied parameter: photodiode efficiency**

The simulation results show that a photodiode efficiency of less than 100,000 is not enough to let the process run without any errors. To allow the energy conversion process be efficient, the scalar gain block has to be set at a minimum of 100,000.

**Varied parameter: filter bandwidth**

The filter bandwidth parameter has been investigated exhaustively. In all of the situations considered, there are errors in the decoded output signal. The first case in which errors were found, when the bandwidth is smaller than the reference case, is at a bandwidth of 400 KHz. The bandwidth of the filters is not large enough to capture the energy associated with each on-off keyed modulation signal. In a case of a broader bandwidth, the errors first show up at the receivers when the filter bandwidth is set to 600 MHz. The errors are now caused by the fact that the filters pick up signal energy from adjacent channel users.

Table 5 Results of varying several parameters in a synchronous system

Varied parameter	Data rate (Hz)	Photodiode efficiency	Filter bandwidth (Hz)	Total errors	Average error rate
Reference	100,000	100,000	500,000	0	0
Data rate	50,000	100,000	500,000	0	0
	150,000	100,000	500,000	3	0.005
	200,000	100,000	500,000	14	0.018
Photodiode efficiency	100,000	10,000	500,000	54	0.135
	100,000	50,000	500,000	4	0.010
Filter bandwidth	100,000	100,000	200,000	197	0.493
	100,000	100,000	400,000	4	0.010
	100,000	100,000	600,000	1	0.003
	100,000	100,000	750,000	9	0.023
	100,000	100,000	1,000,000	25	0.063

**Varied parameter: Signal to Noise Ratio**

White Gaussian noise was introduced in the complex tone generators in the encoder-blocks in order to get an indication of the influence of white noise on correct decoding of the received signals. Imperfect decoding was found to be present for a Signal to Noise Ratios (SNR) smaller than 6 dB. Table 6 shows the amount of errors present with the SNR set at 3 dB.

Table 6 Result varying Signal to Noise Ratio

Data rate (Hz)	Photodiode efficiency	Filter bandwidth (Hz)	SNR (dB)	Total errors	Average error rate
100,000	100,000	500,000	3	4	0.010

**Varied parameters: filter bandwidth and transmission frequencies**

The frequency components associated with the masks are brought closer together and are tested with values at 1m (in MHz) with  $m = 2, 3, 4, \dots, 33$  (mask a), and with values at 0.5m (in MHz) with  $m = 4, 5, 6, \dots, 35$  (mask b). The only combination of parameters that shows performance results, without errors involves a data rate of 100 MHz, a filter bandwidth of 400 MHz, and a photodiode efficiency of 100,000 in a system with frequency components 1m (in MHz) with  $m = 2, 3, 4, \dots, 33$ . In all other cases, errors are detected at the receivers. The frequency components of the masks are set in the “encoder” block and in the “pre-decoder” block. The results of the simulations are shown in Table 7.

Table 7 Results varying filter bandwidth and transmission frequencies

Mask	Data rate (Hz)	Photodiode efficiency	Filter bandwidth (Hz)	Total errors	Average error rate
a	100,000	100,000	250,000	158	0.395
a	100,000	100,000	350,000	11	0.028
a	100,000	100,000	400,000	0	0
a	100,000	100,000	500,000	1	0.003
b	100,000	100,000	200,000	198	0.495

**Varied parameters: data rate and “low” signal & “no” signal levels**

In the “encoder” block, the signals “on”, “low”, and “no” can be found. The value of the “on” signal represents light transmission (light is “on”). The value of the “low” signal represents leakage of light, while the “no” signal value represents no light transmission at all. The values of the “low” signal and “no” signal are varied. Table 8 shows the effect of variations in these parameters on the decoded output signals for different data rates. The photodiode efficiency and the filter bandwidth are set at respectively 100,000 and 500 KHz for each simulation.

Table 8 Results varying parameters data rate and “low” signal & “no” signal level

Data rate (Hz)	“low” signal	“no” signal	Total errors	Average error rate
100,000	0.01	0.001	0	0
	0.05	0.005	0	0
150,000	0.01	0.001	3	0.005
150,000	0.001	0.0001	1	0.002
	0.05	0.005	3	0.005
200,000	0.01	0.001	14	0.018
	0.001	0.0001	11	0.014
	0.05	0.005	13	0.017

**7.2 Walsh codes and modified PN-sequences as code masks**

As explained in Section 4, the cross-correlation between Walsh codes is better than the cross-correlation between modified PN-sequences. From the simulation results it can be concluded that the Walsh codes used as code masks give fewer errors in the decoded output signal and therefore it is a better code to use as code mask. To make a fair comparison between the two different codes an ideal situation for sending the information is created. Ideal means that the signal transmitted and received has not been affected by non-ideal components. Randomness in the photon count, modeled by the use of the Poisson blocks in the decoder, will prevent a direct comparison. Therefore, the Poisson blocks are removed.

As explained in the Section 6.5, ahead of the threshold block the two values of the photon count are subtracted and that number is compared with zero by the threshold block to decide if the output is high (1) or low (0). For a high output, the signal energy level representing the ones in the  $U_i$  mask has to be higher than the signal energy level representing the ones in the  $\bar{U}_i$  mask. The higher the number after subtraction the less interference the signal experiences from the other signals. In Figure 16 and Figure 17 it is shown that the absolute values of the signals before the threshold comparison are larger for Walsh code masks than the values obtained for the modified PN-sequence masks. This indicates that the Walsh code used yields better code masks in the sense that there is a smaller likelihood of decoded errors.

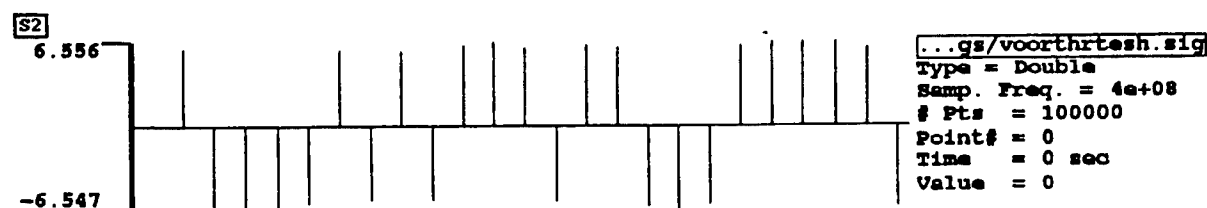


Fig. 16 Absolute value of the signal before threshold comparison with a modified PN-sequence as code mask.



Fig. 17 Absolute value of the signal before threshold comparison with a Walsh code as code mask

This simulation has been run for only one user. To prove the fact that the Walsh code yields a better code masks, a simulation with 15 users has also been run with modified PN-sequences as code masks under the same conditions as the reference case in subsection 7.1. The results are presented in Table 9.

Table 9 Results of Walsh codes and modified PN-sequences as code masks

	Data rate (Hz)	Photodiode efficiency	Filter bandwidth (Hz)	Total errors	Average error rate
Walsh codes	100,000	100,000	500,000	0	0
Modified PN-sequences	100,000	100,000	500,000	1	0.003

### 7.3 Simulation results of the asynchronous system

For the asynchronous system, only the results of the simulations in which the data rates were varied are presented. The way of tabulating the simulation results for the asynchronous system is different as seen in Table 10. Each simulation has been performed for 100,000 sample points. This means, for every user a different number of bits is observed. Therefore, the total number of errors are presented per user and there is no "Average error rate" column.

As explained in Section 6.1, each user has its own data rate. The data rate parameter is set in the "pre-decoder" blocks, and the "decoder" blocks (impulse train). In Table 10 the data rates of the first and the last user are given. The data rate increases by 2500 Hz per user. The parameters photodiode efficiency and filter bandwidth are respectively 100,000 and 500,000 for each simulation.

In the asynchronous system users operate on different data rates and in the synchronous system all users operate on the same data rate. Comparisons between the two systems are therefore difficult to make. However, it can be concluded that increasing data rates result in a larger number of total errors, both for the synchronous and asynchronous system. Furthermore, it can be concluded that in an asynchronous system the total number of errors in the decoded output signal for a certain data rate is larger compared to the corresponding data rate in the synchronous system. To illustrate this, consider the following case. In the synchronous system operating on a data rate of 150 KHz a total of three errors were present in decoded output signals (See Table 5). In the asynchronous system, the one user operating on a data rate 150 KHz experiences a total of 5 errors. The difference in these results can only be related to the presence of other users operating at different data rates.

Table 10 Results varying the data rate in an asynchronous system

Data rate (Hz)	User	Data rate user (Hz)	Total errors
62,500 - 100,000			0
82,500 - 120,000	9	102,500	1
	13	112,500	1
112,500 - 150,000	1	112,500	5
	2	115,000	6
	3	117,500	7
	4	120,000	6
	5	122,500	5
	6	125,000	6
	7	127,500	5
	8	130,000	5
	9	132,500	6
	10	135,000	6
	11	137,500	8
	12	140,000	7
	13	142,500	7
	14	145,000	6
	15	147,500	5
	16	150,000	5

## **- CONCLUSIONS -**

In this report, simulation results on user data detection under different operational scenarios in an Optical Code Division Multiple Access (O-CDMA) digital communication system are presented and the system studied is explained. The simulation results obtained, provide information on the performance of the specific O-CDMA digital communication system with 16 users. These results can be used as a guide in implementing real world realizations of an O-CDMA digital communication system. The number of users present in the O-CDMA system under study has been limited to 16, in order to remain within the hardware limitations of the computer system used to perform the simulation runs.

Potential useful codes (or masks), other than modified maximal length PN-codes have been investigated. The Walsh-codes proved to be easy to generate and additionally provide better correlation properties when compared to modified PN-codes.

Simulation results for both a synchronous and an asynchronous O-CDMA system have been presented in this report. In the synchronous system, system parameters were exhaustively varied and their effect on performance studied. In the asynchronous system, the effect of varying similar system parameters as in the synchronous system produced correspondingly equal performance results. Therefore the focus in the asynchronous system has been the effect on performance due to different data rate settings for the data signals of the 16 users.

Noise effects on user signals' decoding performance have been investigated. White Gaussian noise has been added in the on-off keyed modulating sinusoid signals in the encoder. Results show that Signal to Noise Ratios smaller than 6 dB result in errors in the decoded outputs.

Performance results focused on the total and average number of decoded errors, presented in tabular form. In general, results show that for data rates higher than 100 KHz, errors will occur in decoded outputs. Filter bandwidth settings in the pre-decoder to filter out the individual frequency components need to be adjusted with great care in accordance with the frequency component settings in the encoder. It was found that if filter bandwidths are chosen too small, not all the energy associated with each on-off keyed modulation signal is captured. On the other hand, filter bandwidth settings chosen too large, causes picking up signal energy from adjacent channel users. In both cases this causes the accumulation of significant numbers of decoded errors. This research also showed the need for a suppression of leakage light ("low" signal, representing no light transmission) to levels in the encoder blocks that are 20 dB below the "on" signal level, in order to guarantee reasonable average error rates.

## - REFERENCES-

- [1] Whinnery, John R., *Lasers, Invention to Application*, National Academy Press, 1987.
- [2] Agrawal, Govind P., Dutta, N.K., *Semiconductor Lasers*, International Thomson Publishing, 1993.
- [3] Winters, Jack H., Gitlin, Richard D., Kasturia, Sanjay, *Reducing the Effects of Transmission Impairments in Digital Fiber Optic Systems*, IEEE Communications Magazine, June 1993, pp. 68-76.
- [4] Bukozer, Daniel, C. *Computer Simulations of Synchronous and Asynchronous Multi-User Optical Code Division Multiple Access Digital Communication Systems*, August 1995.
- [5] Hui, J.Y., *Pattern Code Modulation and Optical Decoding - A novel Code Division Multiplexing Technique for Multifiber Networks*, IEEE, Journal on Selected Areas in Communications, vol. SAC-3, no.6, Nov, 1985, pp. 916-927.
- [6] Skaug, R., Hjelmstad, J.F., *Spread Spectrum in Communication*, Peter Pergrinus Ltd, 1985.
- [7] Dixon, Robert C., *Spread Spectrum Systems*, John Wiley & Sons, 1984, pp. 56-71.
- [8] Sayood, Khalid, *Introduction to Data Compression*, Morgan Kaufmann Publishers Inc., 1996.
- [9] Salehi, Jawad A., *Code Division Multiple-Access Techniques in Optical Fiber Networks - Part I: Fundamental Principles*, IEEE Transactions on Communications, vol. 37, no. 8, August 1989, pp. 824-833.
- [10] Salehi, Jawad A., *Code Division Multiple-Access Techniques in Optical Fiber Networks - Part II: Systems Performance Analysis*, IEEE Transactions on Communications, vol. 37, no. 8, August 1989, pp. 834-842.
- [11] Brady, David and Verdú, Sergio, *A Semiclassical Analysis of Optical Code Division Multiple Access*, IEEE Transactions on Communications, vol. 39, no. 1, Jan 1991, pp. 85-93.

# **MM4 MODEL EXPERIMENTS ON THE EFFECTS OF CLOUD SHADING**

**Chia-Bo Cheng  
Associate Professor  
Department of Geosciences**

**Texas Tech University  
Lubbock, TX 79409**

**Final Report for:  
Summer Research Extension Program  
Phillips Laboratory**

**Sponsored by:  
Air Force Office of Scientific Research  
Bolling Air Force Base, DC**

**and**

**Phillips Laboratory**

**December 1996**

## MM4 MODEL EXPERIMENTS ON THE EFFECTS OF CLOUD SHADING

Chia-Bo Chang  
Associate Professor  
Department of Geosciences  
Texas Tech University

### Abstract

This study examines the effects of cloud shading on mesoscale numerical weather prediction. These effects are evaluated based on real-data numerical simulation experiments using the PSU/NCAR MM4 model. Empirical formulas combining relative humidity and the dynamically predicted cloud water with a weighting factor were used to determine cloud fraction. Four simulation experiments with different weighting factors were carried out. The structure of model cloud fraction varied considerably from the experiment based on RH alone to the experiment weighted heavily on cloud water. The RH-based cloud fraction had a broad-scale structure, while the cloud fraction associated with cloud water showed small-scale features.

Among all experiments, the 12-h model simulated surface flow and temperature fields quite resemble each other despite the significant structure changes in cloud fraction. Some notable differences are shown at the 24-h simulations. These appear to contradict what anticipated. During the daytime (the first twelve hours), large changes in cloud fraction are expected to alter solar heating at the surface and hence the circulations, while at night (the second twelve hours) cloud shading is unlikely to have large influences on the surface energy budget. However, the responses of motion and thermal fields to surface heating may vary from case to case. Clearly, more case studies and analyses are needed to understand the role of cloud shading in the surface energy budget.

About the same amount of non-convective rainfalls were produced in all experiments, and convective rainfalls increased somewhat with increasing weight for cloud water in the cloud fraction equations. Unfortunately, at this time we do not have adequate data for a quantitative assessment of precipitation forecasting. In comparison with the daily weather map, which revealed very little precipitation in eastern U.S. during the 24-h period, all experiments showed the similar skill.

## Introduction

In the atmosphere, weather systems develop in response to horizontal difference in radiative heating. On the other hand, the cloud and moisture distribution associated with these systems constantly modifies the radiation budget. Clouds, the principal modulator of radiation in the atmosphere, can greatly reduce the outgoing infrared radiation and cooling at the surface. Also, a substantial depletion of insolation takes place at the cloud top because of its large albedo which, except for cirrus, is on the order of 0.5 (Stephens and Webster, 1981). This depletion process may not be significant so far as the absorption of solar radiation in the atmosphere is concerned. However, it can have a controlling effect on surface energy budget over land.

During the daytime, solar heating results in a surplus of radiative energy at the surface. Some of the surplus in energy will be transferred from ground to air in the form of sensible and latent heat fluxes. The intensity of sensible heat flux (surface heating) is largely dependent upon the characteristics of surface and the atmospheric conditions, for example, cloud cover. The disruption of radiative heat transfer due to cloud shading can significantly influence the surface temperatures as well as the thermal structure (e.g., static stability and regional baroclinicity) of the lower troposphere. Surface temperature is the essential element in defining surface energy sources for the development of weather systems in numerical weather prediction (NWP) models. Mesoscale weather systems are often sensitive to change in low-level static stability. Lipton (1993) showed that the assimilation of cloud shading derived from satellite cloud information could improve the model prediction of surface temperatures. As a result, the model was able to simulate more realistic mesoscale circulations. Chang (1995) showed that cloud shading had a direct impact on the surface temperature forecasting and mesoscale circulations over land.

This study, a continuation of the summer research effort of the principal investigator, further examines the effects of cloud shading on short-range mesoscale NWP using real-data model simulation

experiments. The mesoscale modeling system known as MM4 developed at the Pennsylvania State University (PSU) and National Center for Atmospheric Research (NCAR) is employed for the experiments.

The current MM4 parameterization of cloud fraction is based on relative humidity (RH). A modified approach involving the cloud water for determining the model cloud fraction is formulated in this study. It is intended to test the hypothesis that the inclusion of dynamically predicted cloud water will improve the estimate of cloud fraction and consequently the model prediction. This study will provide useful information for a better understanding of air-land interaction in mesoscale NWP.

#### Modeling system

A brief overview of MM4 system summarized from Gill (1992) and Grell et al. (1994) is given in this section. The MM4 dynamic prediction model is a three-dimensional primitive equation model using a  $\sigma$  grid in the vertical and a Cartesian grid casting on a Lambert conformal projection in the horizontal.

The model basic equations are the equations of motion, hydrostatic equation, first law of thermodynamics, moisture conservation equations for water vapor, cloud water, and rainwater. The model physics are as follows:

- 1) Parameterization of subgrid-scale moist convection,
- 2) Dry convective adjustment,
- 3) Microphysics in the grid-scale cloud and precipitation processes,
- 4) Planetary boundary layer (PBL) processes,
- 5) Atmospheric radiation and surface energy budget.

In this study the model initial state was obtained from the objective analysis of the National Weather Service (NWS) upper-air and surface observations. The National Meteorological Center (NMC) gridded data was used as a first guess in the analysis. The dynamic model used in this study had 29 levels with the  $\sigma$  values ranging from 1 at the surface to 0 at the model top ( $\sim 50$  mb) and a rather higher resolution in

the PBL (about 10  $\sigma$  levels below 900 mb). There were 50 x 55 grid points in the horizontal and the grid size was 45 km. The time-dependent conditions generated from the observations were imposed on the lateral boundaries. Other numerical aspects of the model including the horizontal grid structure, finite difference approximation for space and time derivatives, and lower and upper boundary conditions were summarized in the paper by Modica et al. (1994). A modified Arakawa-Schubert scheme and the associated microphysics in the model cloud water equation were employed.

In the earlier experiments (Chang, 1995), a two-way interactive nested grid was used for 12-h integration. The grid mesh sizes were 45 km and 15 km, respectively. However, the nested grid was too much time-consuming to run and the differences between the coarse-mesh and fine-mesh runs were not very significant. In this study, only the coarse-mesh model simulations with a longer time integration, 24-h instead of 12-h, were performed.

The focus this study, of course, is on how cloud shading alters the surface energy budget. The surface energy budget involved incident solar and infrared irradiance, sensible heat flux and latent heat (moisture) flux into the atmosphere, and heat conduction into the sub-surface layer. The surface heat fluxes were determined using a bulk-aerodynamical formulation. In the radiation computation, only water vapor was considered as an optically active gas in the model atmosphere, and radiative heating/cooling in the model atmosphere was neglected. The ground temperatures and heat flux were computed from the surface energy budget equation.

The cloud attenuation of solar radiation and the enhancements of infrared radiation were parameterized. The reduction of insolation at the surface would result in lower ground temperatures and consequently smaller sensible heat flux and moisture flux. Three cloud layers (low, middle, and high clouds) were considered. The original empirical formulas for cloud fraction ( $n$ ) based on RH were, respectively,

$$n = 4 \text{ RH} - 3, \quad (1)$$

for the lower atmosphere (between  $\sigma = 0.96$  and 0.75) and middle atmosphere (between  $\sigma = 0.75$  and

0.35), and

$$n = 2.5 \text{ RH} - 1.5, \quad (2)$$

for the upper atmosphere ( $\sigma \leq 0.35$ ). RH was the maximum relative humidity found in the respective layers. Note that although cloud water was predicted in the model, cloud fraction was not directly correlated with the model cloud water distribution. The evaporation of cloud water was invoked in the cloud water equation if  $\text{RH} < 1$ . Hence the existence of cloud water implied that the air was saturated and  $n$  would be 1.

The above empirical formulas for cloud fraction were modified to include model cloud water for the simulation experiments as described in the following section.

#### Methodology

The real-data model simulation experiments were conducted on the 23-24 August 1993 case. The experiments were aimed at a quantitative assessment of the role of cloud shading in regional circulation. The case study represented a weak synoptic situation. No significant meteorological event occurred in the United States during the 24-h period. This case was selected for an ongoing satellite-model coupled analysis research at Atmospheric Science Division, Phillips Laboratory. The availability of satellite cloud imageries could provide information for a qualitative verification of the model cloud cover.

The modified empirical formulas for cloud fraction ( $m$ ) for the lower, middle, and upper layers of the model atmosphere are:

$$\begin{aligned} m &= w n & 0 < c < a, \\ m &= w n + (1 - w) \sqrt{(c - a)/(b - a)} & a \leq c \leq b, \\ m &= w n + (1 - w) & c > b, \end{aligned} \quad (3)$$

where  $c$  is the layer-mean cloud water in gm/gm,  $w$  is a weighting factor ranging from 0 to 1,  $a$  and  $b$  are two threshold values. If  $c < a$ , cloud water is ignored. The impact of cloud water on cloud fraction

increases for  $a \leq c \leq b$  and levels off for  $c > b$ . For the lower and middle atmosphere,  $a = 10^{-6}$  gm/gm and  $b = 10^{-4}$  gm/gm, and  $a = 10^{-6}$  gm/gm and  $b = 5 \times 10^{-5}$  gm/gm, respectively, and  $n$  is defined in (1), while for the upper atmosphere,  $a = 10^{-6}$  gm/gm and  $b = 4 \times 10^{-5}$  gm/gm, and  $n$  is same as that defined in (2). The higher  $w$  the heavier RH is weighed in (3). For  $w = 0$ ,  $m$  is completely determined by  $c$ , while for  $w = 1$ ,  $m = n$  and cloud fraction is a function of RH only as in (1) and (2).

Consider the case of equal weight ( $w = 0.5$ ) for  $c$  and RH as an example. If  $c < a$  and  $n = 1$ ,  $m = 0.5$  or 50% of cloud cover. If  $a \leq c \leq b$  and  $n = 1$ ,  $0.5 \leq m \leq n$ , and if  $c > b$  and  $n = 1$ ,  $m = n$  or an overcast sky. In other words, 100% cloud cover occurs only when a relatively large amount of cloud water is predicted, and  $n$  is reduced to  $m$  if the model cloud water is less than  $b$ . On the other hand, if  $n < 1$  (e.g., 0.5) and  $c > a$ ,  $n$  is raised to  $m$  ( $> 0.5$ ). Note that for  $w < 1$  except that  $n = 1$  and  $c > b$   $m$  is always less than 1.

The use of  $w$  smooths out the sharp gradient in cloud fraction between the areas of cloudy and clear skies shown in the earlier experiments (Chang, 1995). The threshold values  $a$  and  $b$  are somewhat arbitrary. The constant  $a$  is more than two orders of magnitude below the typical liquid water content in stratus clouds (Rogers, 1979). Also, the MM4 model has been modified to include cloud fraction as one of the 2-D variables stored in the model output history.

The model simulation experiments conducted are as follows:

- 1) Experiment 1 (E1) was a 24-h forecast with  $w = 1$ .
- 2) Experiment 2 (E2) was similar to E1 except that  $w = 0.75$ .
- 3) Experiment 3 (E3) was similar to E1 except that  $w = 0.5$ .
- 4) Experiment 4 (E4) was similar to E1 except that  $w = 0.25$ .

E1 is regarded as a benchmark run. The model output of E1 is compared with observations (gridded fields) for a qualitative evaluation of the model performance. Different combinations of RH and cloud water used to estimate cloud fraction are tested in E2, E3, and E4. Comparisons between the individual forecast experiments are made to see which  $w$  value may be more appropriate for the

estimate of cloud fraction and consequently leads to a better model performance. The variations in surface energy sources due to any changes in cloud fraction are expected to have a greater impact on the surface than upper-air circulations. Therefore, a careful examination of the model surface winds and temperatures, and precipitation is conducted for the forecast comparisons.

#### Results of the model simulations

The model was initialized at 1200 UTC 23 August 1993 for all experiments. Figure 1 shows the model domain covering the eastern half of the United States. The Appalachian Mountains were well represented in the model terrain. Figure 2 shows the analyzed initial surface ( $\sigma = 0.995$ , approximately 50 m above the ground) vector winds and temperatures. The relatively large temperature gradient zones, one over Kansas and Missouri and the other extending from Illinois southeastward to Georgia, were associated with the surface cold and warm fronts, respectively. The wind field displayed some direction shifts across the fronts in eastern Kansas and in the southeastern states. Also, the advection of warm air from the south toward the north-central states was quite evident. The southern portions of the fronts started to dissipate in the next 12 hours. The synoptic setting suggested little upper-air forcing over the eastern United States.

Figure 3 shows the 12-h simulated surface vector winds and temperatures at 0000 UTC 24 August 1993 for E1, while Fig. 4 shows the corresponding observations. The observed temperature patterns indicated the eastward movement of cool air behind the cold front toward Illinois and Missouri. The cool air pushed the northward intrusion of warm air to the southwest of the warm front toward Indiana and Ohio. A major forecast error occurred in Illinois and Missouri where the model was 5–10°C warmer than the observation. The observed cool air centered in Illinois was misplaced too far to the west and the northeastward intrusion of warm air was not as deep in the model. The model performed better in the upper air (not shown); the forecast errors were on the order of 1°C. The basic flow patterns at the surface were well predicted. As in the case of temperature, the model overpredicted the wind speeds in Missouri, Illinois, and Indiana. Minor errors included the erroneous northerlies in

southern Alabama and the eastern lies near the west coast of Florida. Much better agreement with the observations was found over the water.

Figure 5 shows the 24-h simulated surface vector winds and temperatures at 1200 UTC 24 August 1993 for E1. During the 12-h period, some notable changes in the flow field occurred over the northeastern states, and North Carolina where a small anticyclone formed. Also, along the coastal areas of western Florida, Alabama, and Mississippi, there were clear increases in the off-shore flows resembling a land-breeze circulation. The 12-h changes in the temperature field were quite drastic. Over land there were warming near the northern boundary and cooling in other regions ranging from about 10°C over Missouri to a few degrees in the coastal areas.

Figure 6 shows the 12-h and 24-h simulated cloud fractions for E1. There was extensive low-cloud cover over the eastern states. Between 12 h and 24 h the low and middle clouds decreased considerably in the west, while an increase in high cloud in the northeast was observed. Superposing the three layers of clouds, we notice rather cloudy conditions in the east at both times. Fig. 7 shows the 24-h accumulated total and convective precipitation. Most rainfalls were non-convective except over the Great Lakes area. This was consistent with the increase of high clouds to the east of convection.

As pointed out by Chang (1995) earlier the large errors in the surface temperature forecast in E1 over Illinois and Missouri appeared to be caused by too much surface heating. It was noted that the model failed to reproduce the light rainfall (about half inch in 24 h as revealed in the daily weather maps) in Illinois and Missouri. The dry surface in conjunction with little cloud cover contributed to the high ground temperatures and too strong surface heating in the model.

Figure 8 shows the 12-h and 24-h simulated cloud fraction for E2. The basic patterns and areas of cloud cover are similar to those of E1. But for some areas where the model did not predict cloud water the sizes of cloud fraction were somewhat reduced. On the other hand, the areas with predicted cloud water, for example off the east coast of Florida, we see clear changes in cloud fraction. The 24-h

simulated total and convective precipitation (not shown) are very similar to those of E1. Also, there are no significant differences in the predicted surface temperatures and winds between E1 and E2.

Figure 9 shows the 12-h and 24-h simulated cloud fraction for E3. The use of  $w = 0.5$  greatly altered the structure of cloud fraction. Clouds oriented in lines were embedded in the broad-scale patterns. The structure suggests that in the middle and higher atmosphere the model predicted little cloud water over the western half of the domain. Figs. 10 and 11 show, respectively, the 12-h and 24-h model surface vector winds and temperatures for E3. At 12 h E1 and E2 were very similar at the surface level. At 24 h, over the eastern U.S., E3 was slightly cooler than E1. Some differences from E1 in the surface winds were found over the southeastern states (e.g., Tennessee and North Carolina). Fig. 12 shows the 24-h simulated total and convective precipitation for E3. The enhanced maximums in western Virginia and at the west coast of Florida did not exist in E1. Both were a result of convection.

Figure 13 shows the 12-h and 24-h simulated cloud fraction for E4. There are striking discrepancies in cloud fraction between E1 and E4. The areas of high cloud fraction based on RH do not agree well with those according to cloud water. The 24-h total precipitation, surface temperatures, and winds (not shown) resemble those of E3.

### Summary

Based on the real-data model simulation experiments Chang (1995) showed that the effects of cloud shading should not be overlooked in short-term mesoscale NWP. Without cloud shading the model surface temperatures were too high and consequently the model atmosphere became less stable causing erroneous convection. To resolve the essentials of shading effects in the model an accurate estimate of cloud fraction is needed.

In most NWP models, cloud fraction is parameterized based on RH. In this study, however, empirical formulas involving both RH and the dynamically predicted cloud water were used to

determine cloud fraction. It was intended to reveal whether these new formulas might provide a better estimate of cloud fraction and consequently improve the model performance. Four real-data model experiments using the formulas with different weighting factor for RH and cloud water were carried out. The structure of model cloud fraction varied considerably from the experiment based on RH alone to the experiment weighted heavily on cloud water. The RH-based cloud fraction had a broad-scale structure, while the cloud fraction associated with cloud water showed small-scale features.

Among all experiments, the 12-h model simulated surface flow and temperature fields quite resemble each other despite the significant structure changes in cloud fraction. Some notable differences are shown at the 24-h simulations. These appear to contradict what anticipated. During the daytime (the first twelve hours), large changes in cloud fraction are expected to alter solar heating at the surface and hence the circulations, while at night (the second twelve hours) cloud shading is unlikely to have large influences on the surface energy budget. However, the responses of motion and thermal fields to surface heating may vary from case to case. Clearly, more case studies and analyses are needed to understand the role of cloud shading in the surface energy budget.

About the same amount of non-convective rainfalls were produced in all experiments, and convective rainfalls increased somewhat with increasing weight for cloud water in the cloud fraction equations. Unfortunately, at this time we do not have adequate data for a quantitative assessment of precipitation forecasting. In comparison with the daily weather map, which revealed very little precipitation in eastern U.S. during the 24-h period, all experiments showed the similar skill.

#### Acknowledgements

I am grateful to RDL/AFOSR and Phillips Laboratory for the research opportunity. I wish to express my appreciation to Mr. George Modica for his technical assistance in preparing the complex modeling system and graphics used in this research. The model simulation experiments were performed on the Navy c90 computer as well as the Army CRAY-YMP computers.

## References

- Chang, C.-B., 1995: Mesoscale model experiments on cloud shading effects. Final Report, Summer Faculty Research Program, RDL/AFOSR, 20 pp.
- Gill, D. O., 1992: A user's guide to the Penn State/NCAR mesoscale modeling system. NCAR/TN-381+IA, National Center for Atmospheric Research, Boulder, CO.
- Grell, G. A., J. Dudhia, and D. R. Stauffer, 1994: A description of the fifth-generation Penn State/NCAR mesoscale model (MM5). NCAR/TN-398+IA, National Center for Atmospheric Research, Boulder CO, 107 pp.
- Lipton, A. E., 1993: Cloud shading retrieval and assimilation in a satellite-model coupled mesoscale system. *Mon. Wea. Rev.*, **121**, 3062-3081.
- Modica, G. D., S. T. Heckman, and R. M. Rasmussen, 1994: An application of an explicit microphysics mesoscale model to a regional icing event. *J. Appl. Meteor.*, **33**, 53-64.
- Rogers, R.R., 1979: A Short Course in Cloud Physics. Pergamon Press, 235 pp.
- Stephens, G. L., and P. J. Webster, 1981: Clouds and climate: Sensitivity of simple systems. *J. Atmos. Sci.*, **38**, 235-247.

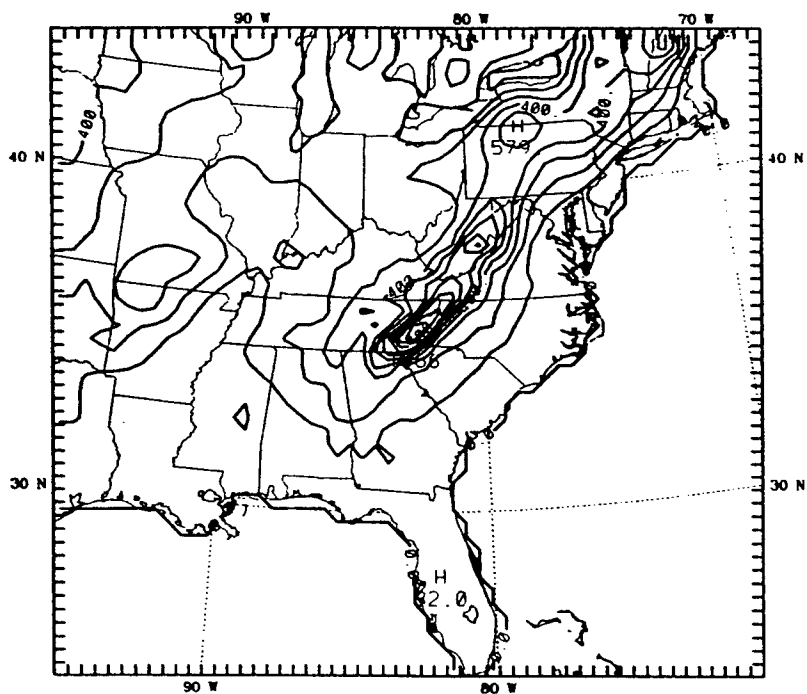
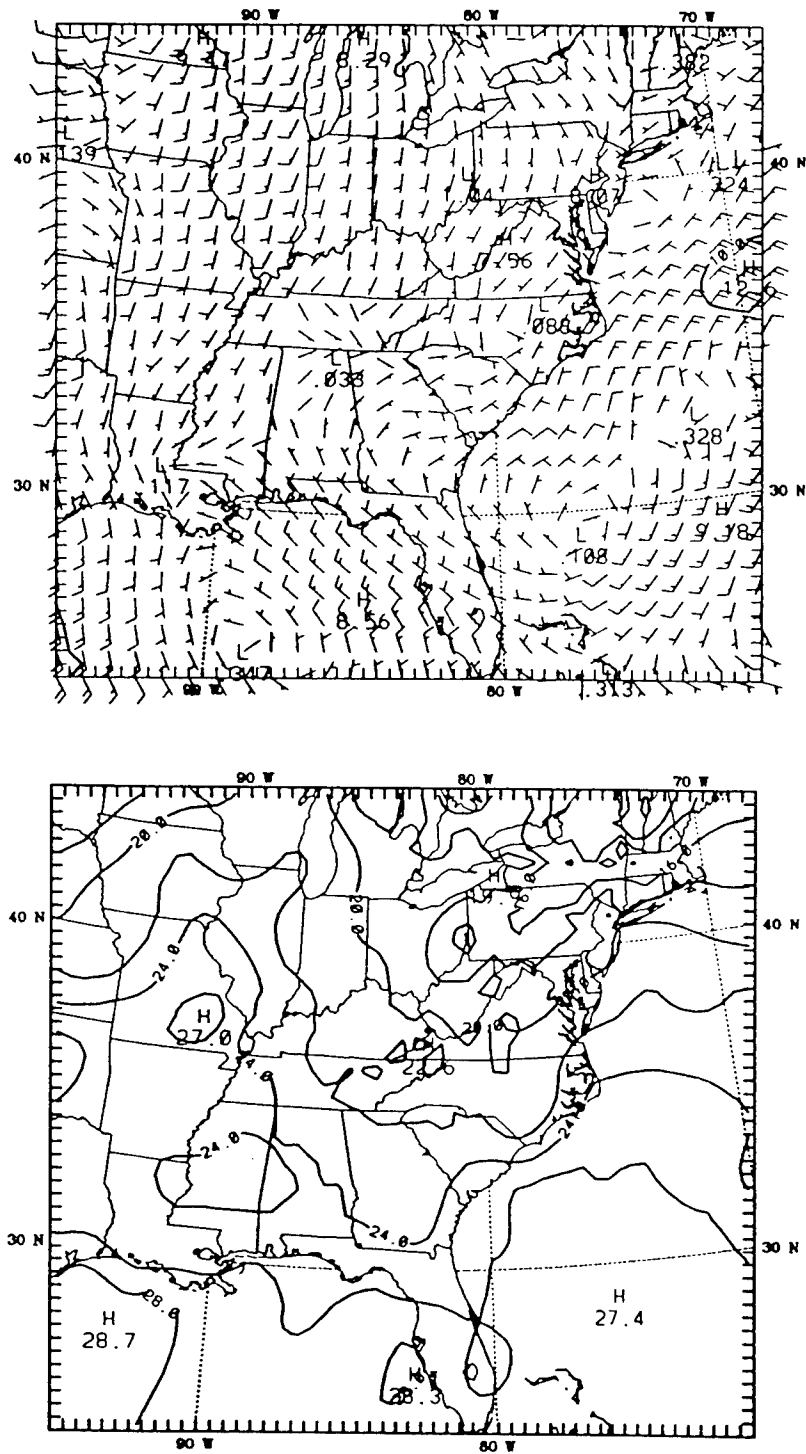


Fig. 1. The model domain and terrain (m)



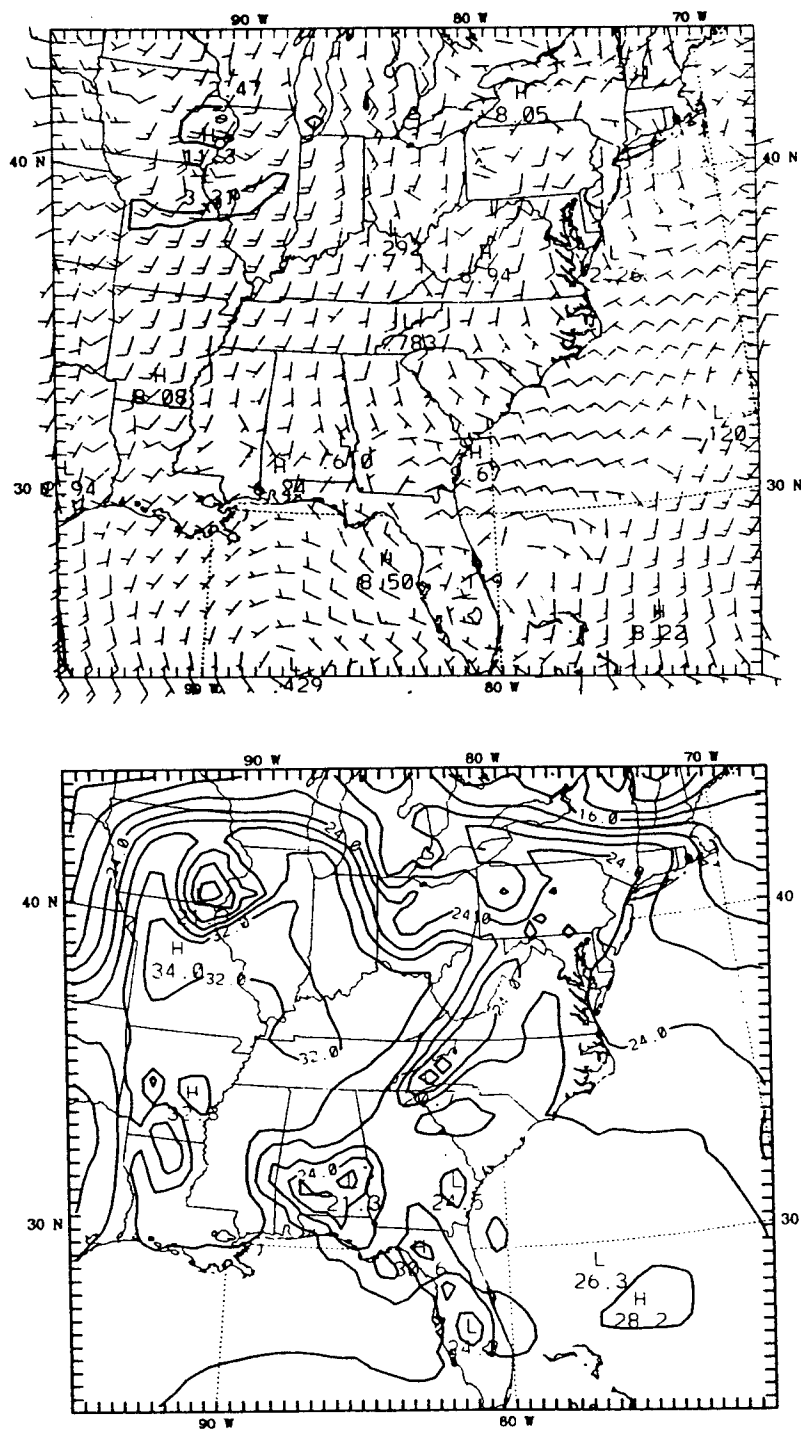


Fig. 3. The 12-h simulated model surface vector winds (knots) and temperatures (°C) for E1 at 0000 UTC 24 August 1993.

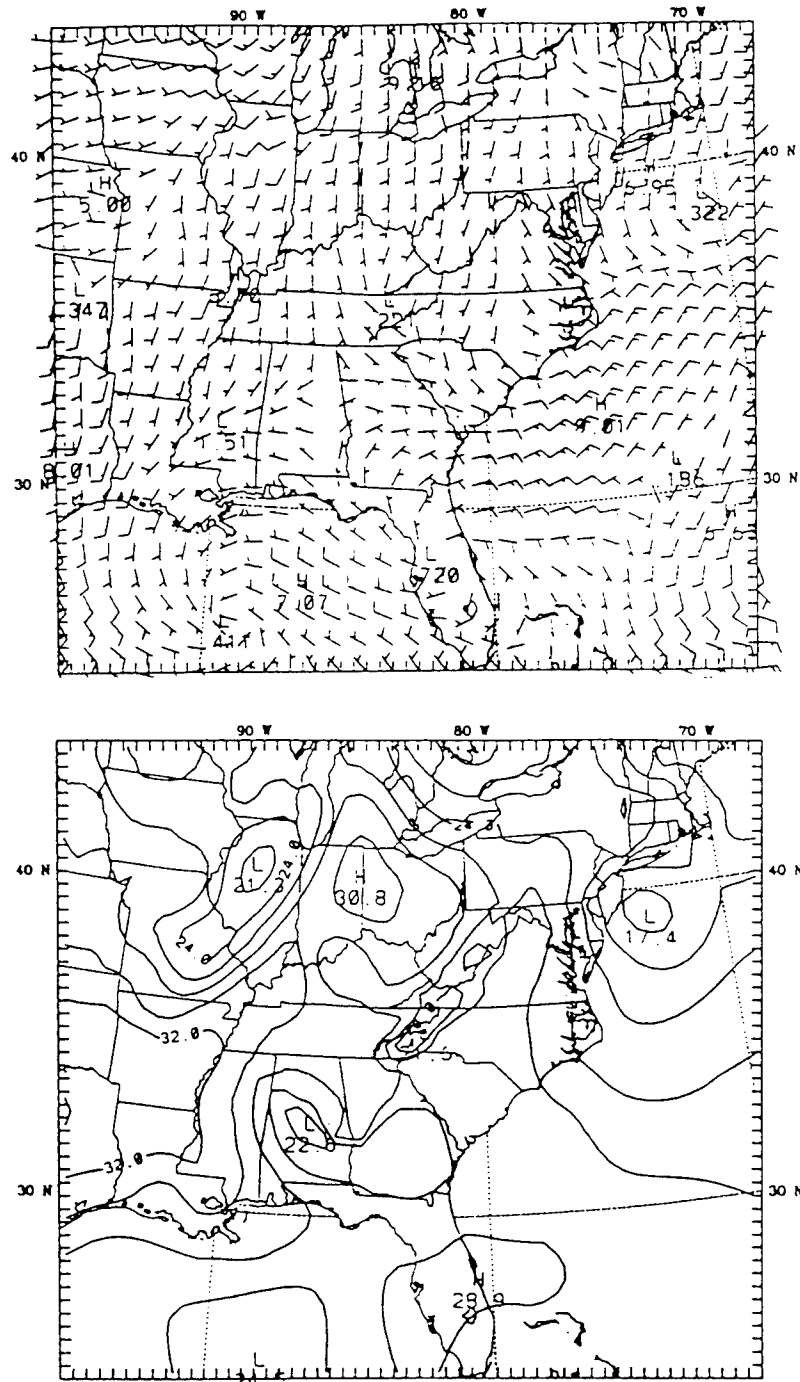


Fig. 4. The observed surface vector winds (knots) and temperatures ( $^{\circ}\text{C}$ ) at 0000 UTC 24 August 1993.

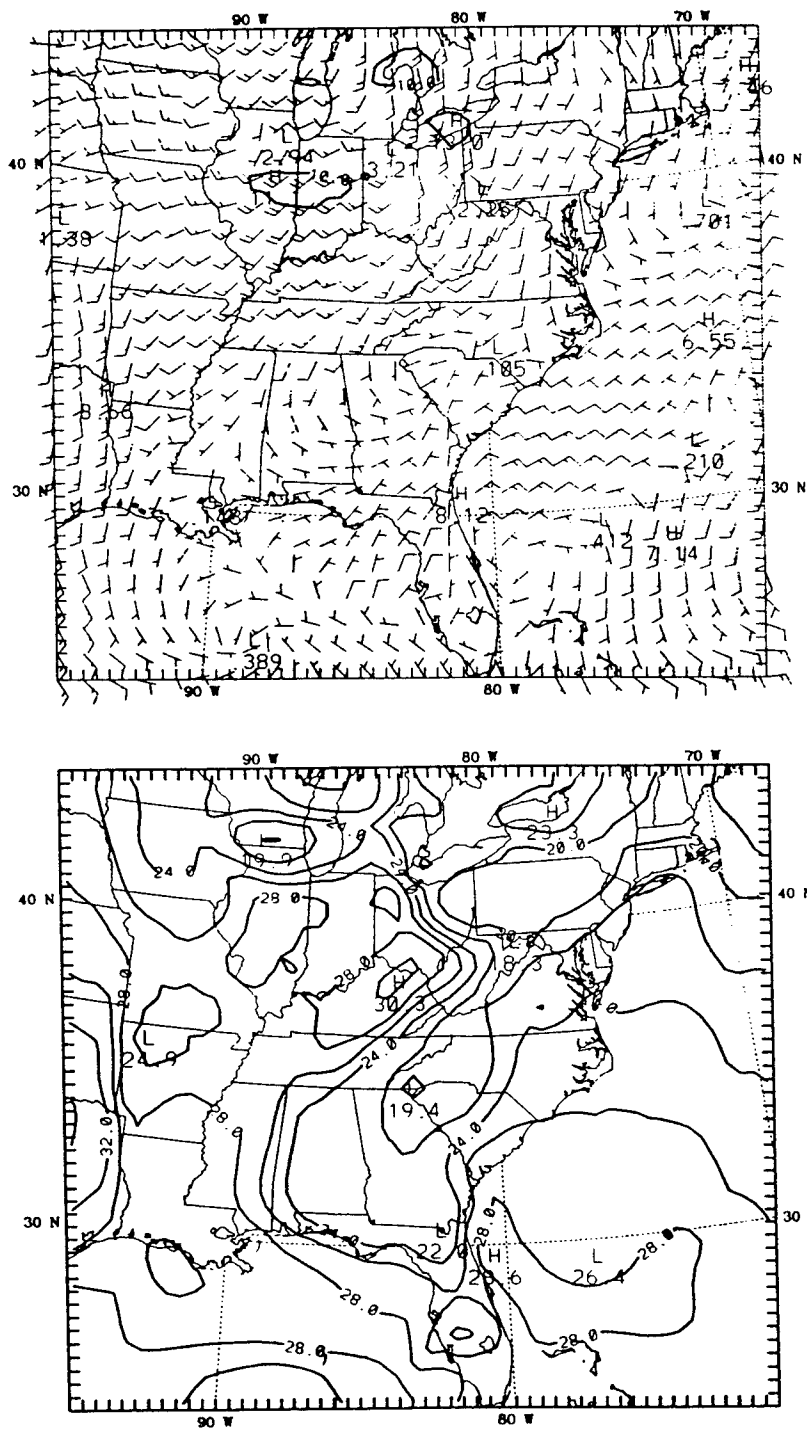


Fig. 5. The 24-h simulated model surface vector winds (knots) and temperatures ( $^{\circ}\text{C}$ ) for E1 at 1200 UTC 24 August 1993.

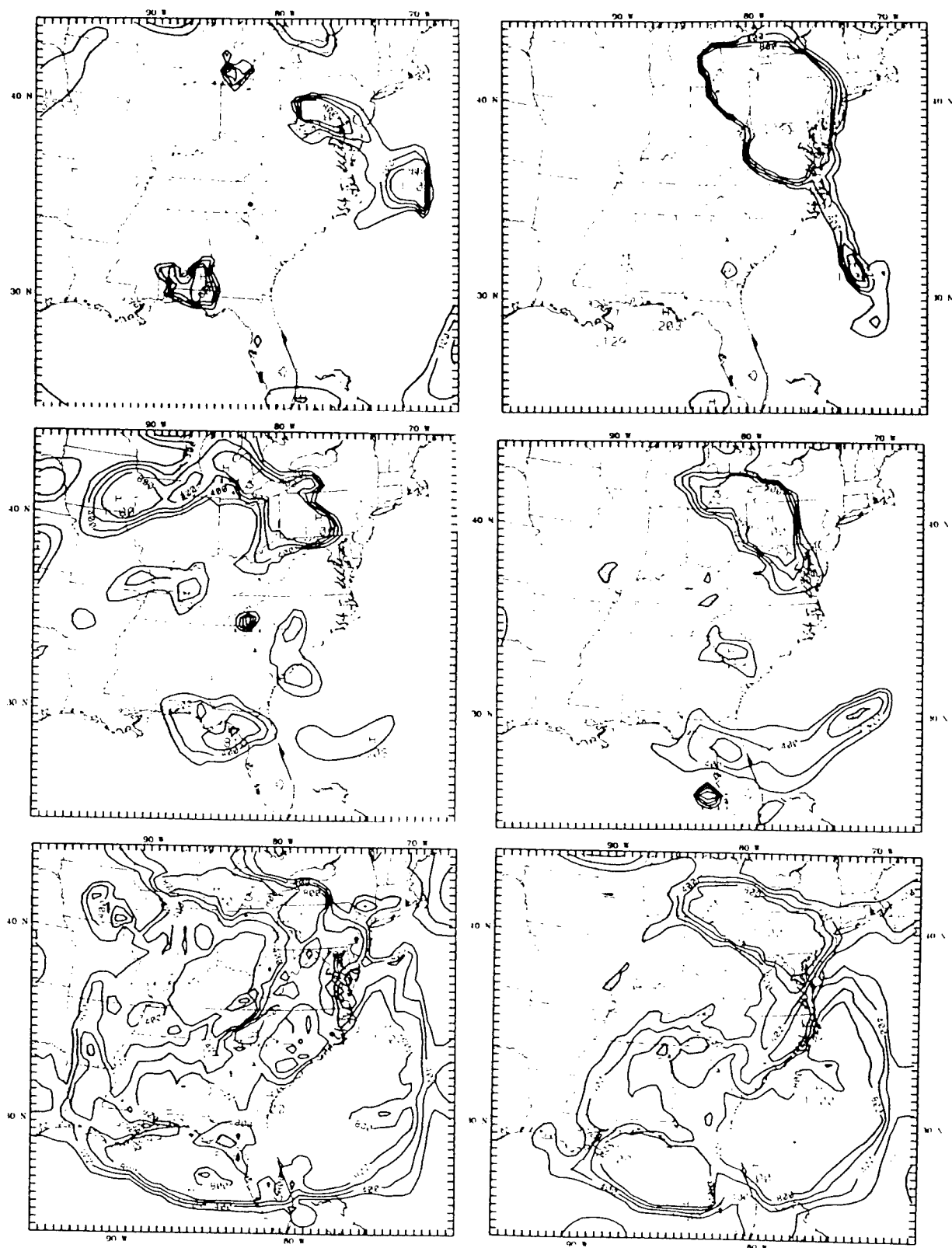


Fig. 6. The 12-h (left) and 24-h model high (upper panel), middle, and low cloud fraction for E1. The contour interval is 0.2.

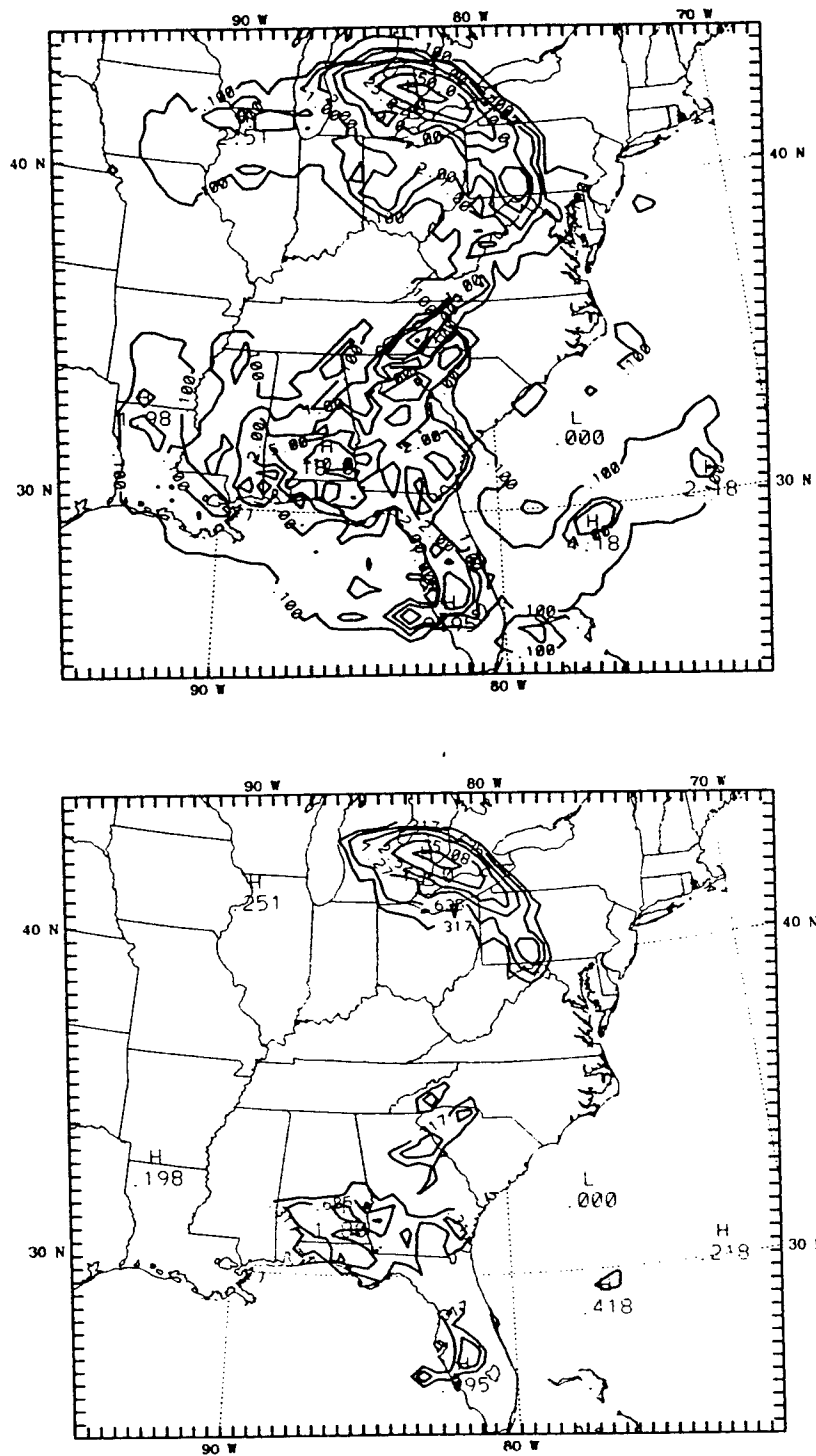


Fig. 7. The 24-h simulated accumulated total (upper panel) and convective precipitation for E1. The unit is mm.

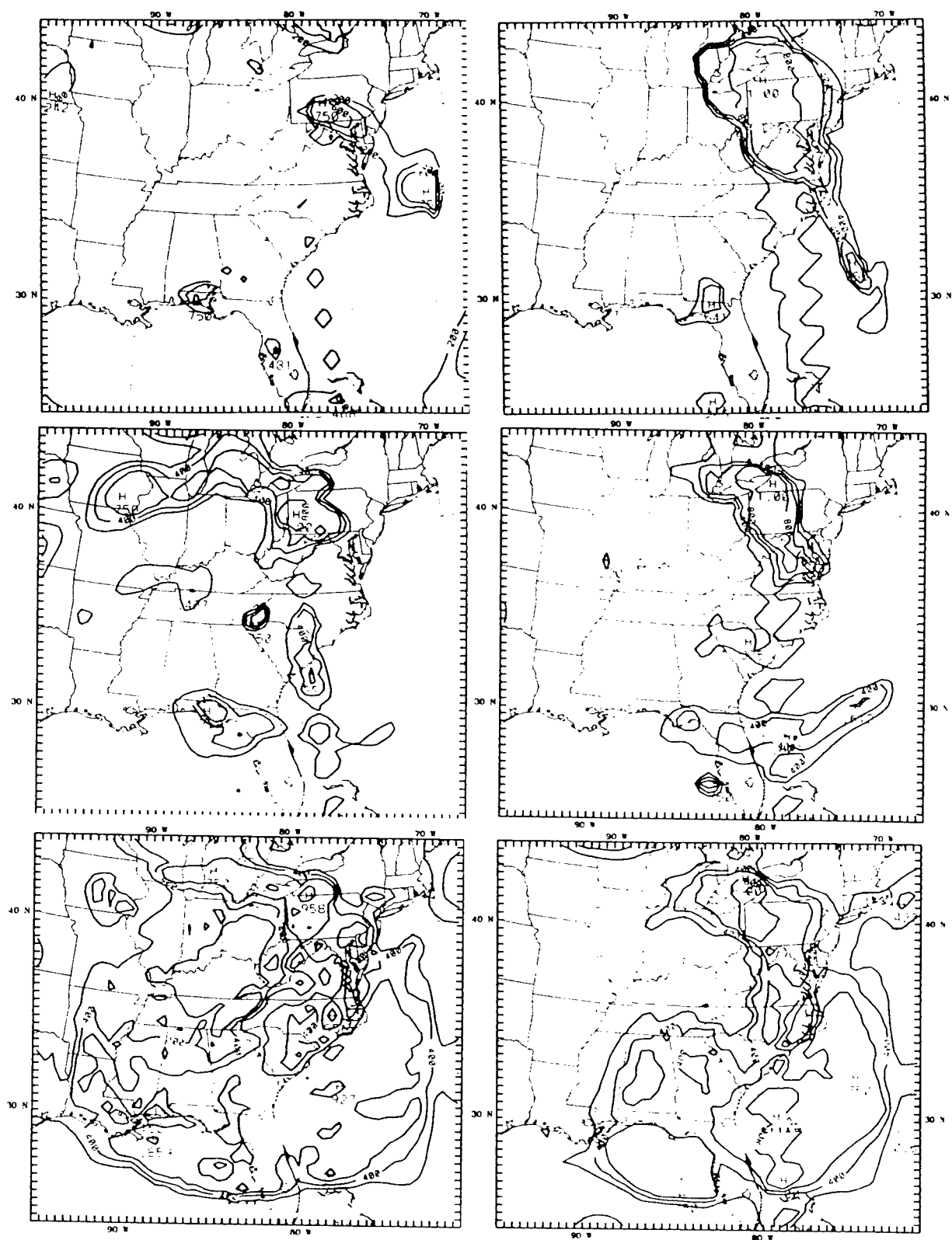


Fig 8. As in Fig 6 except for E2.

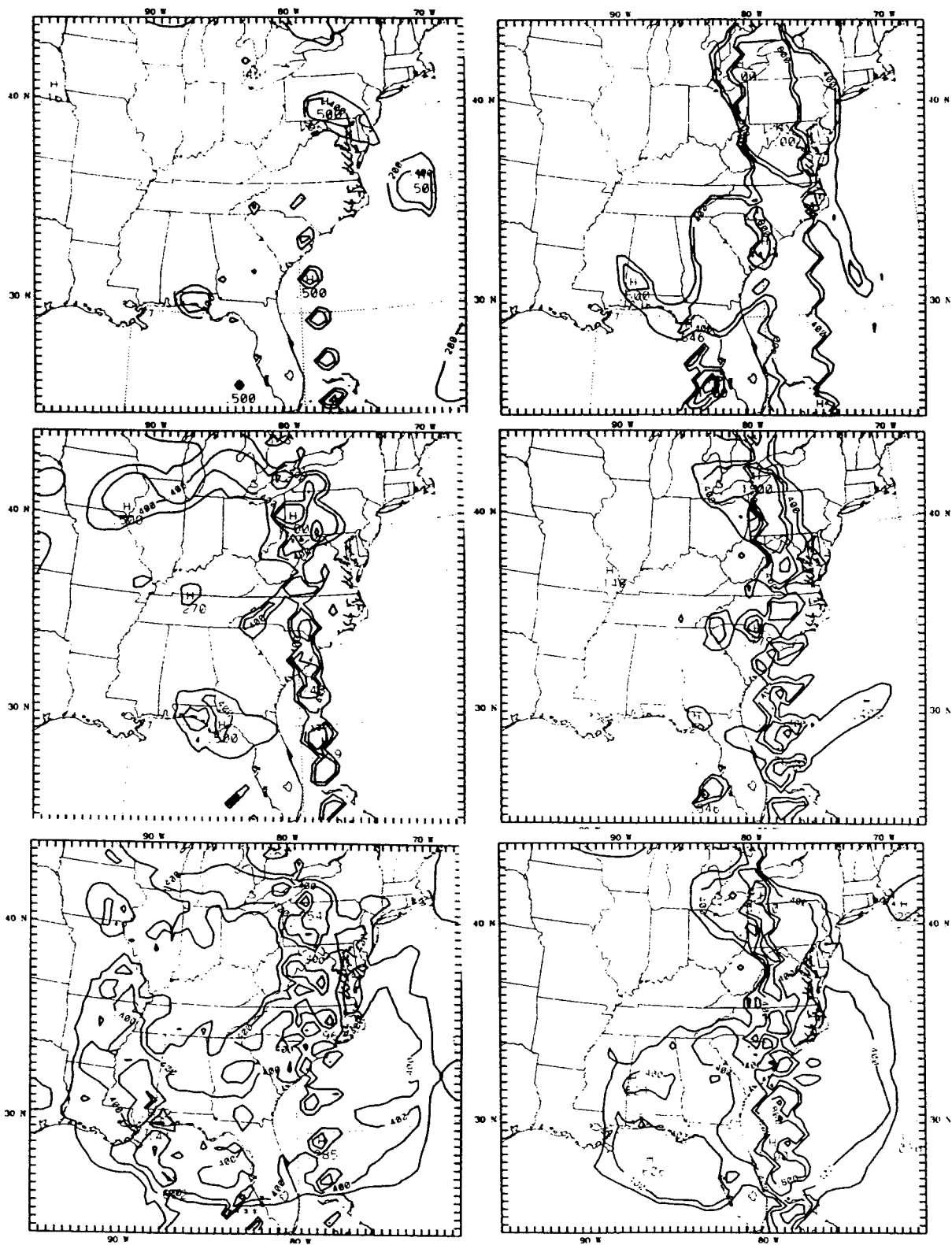


Fig. 9. As in Fig. 6 except for E3.

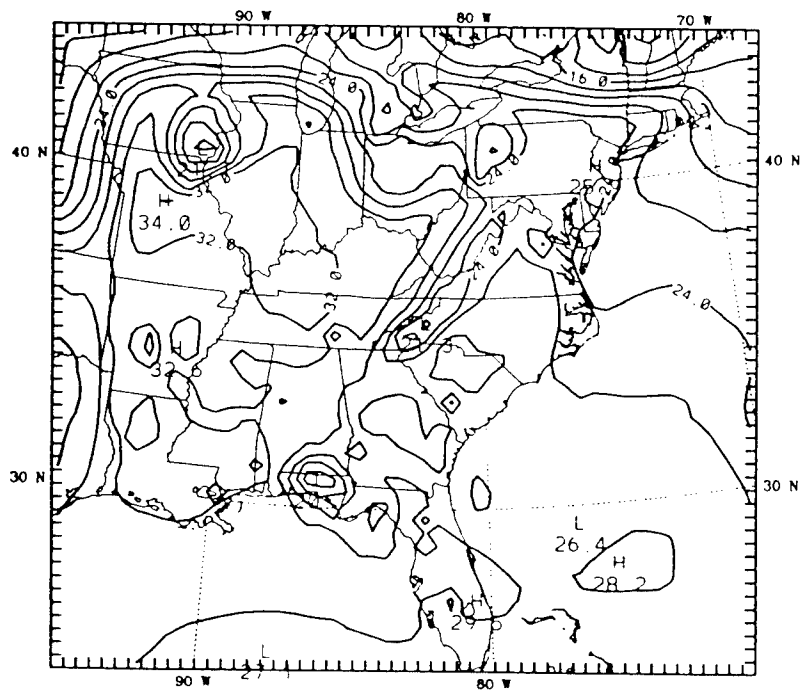
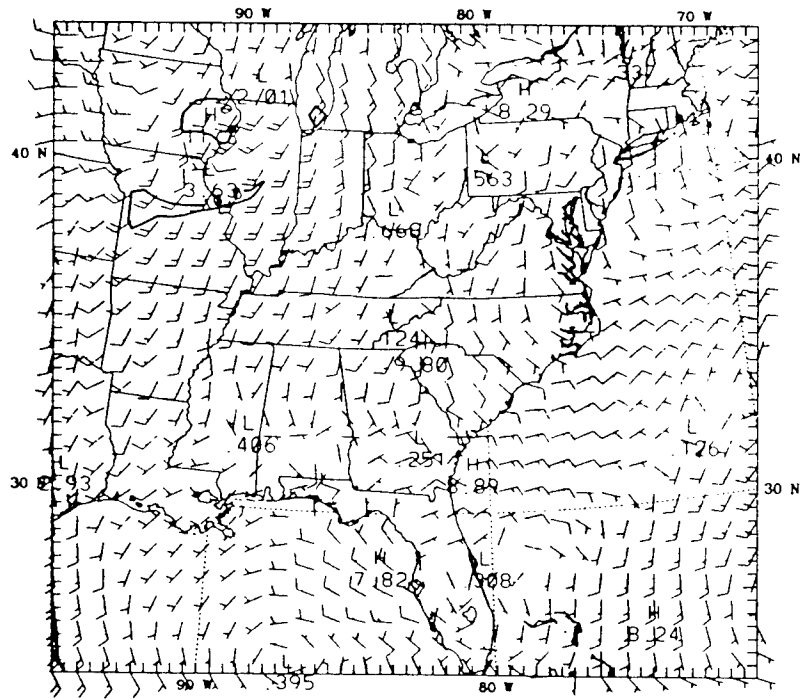


Fig. 10. As in Fig. 3 except for E3.

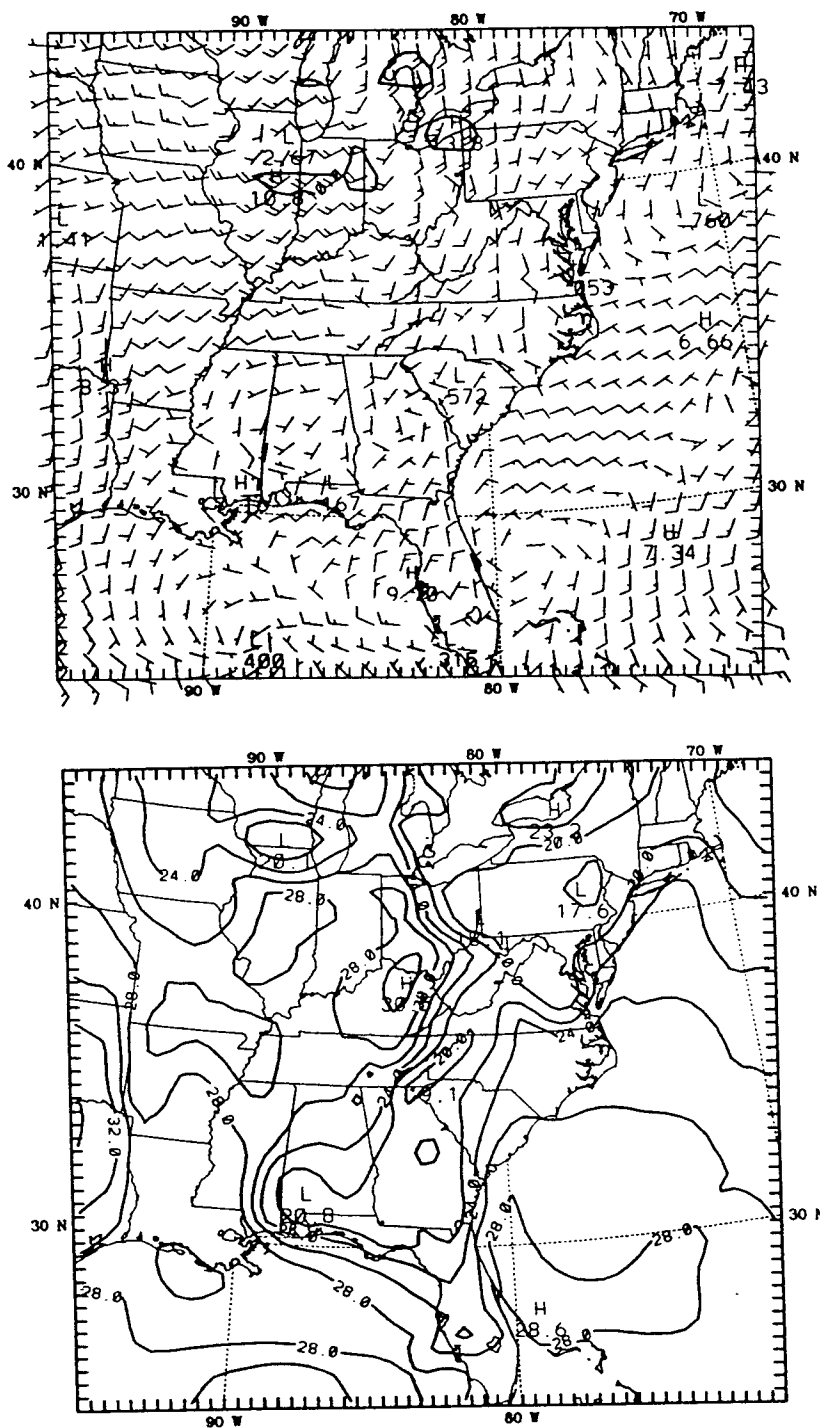


Fig. 11. As in Fig. 5 except for E3.

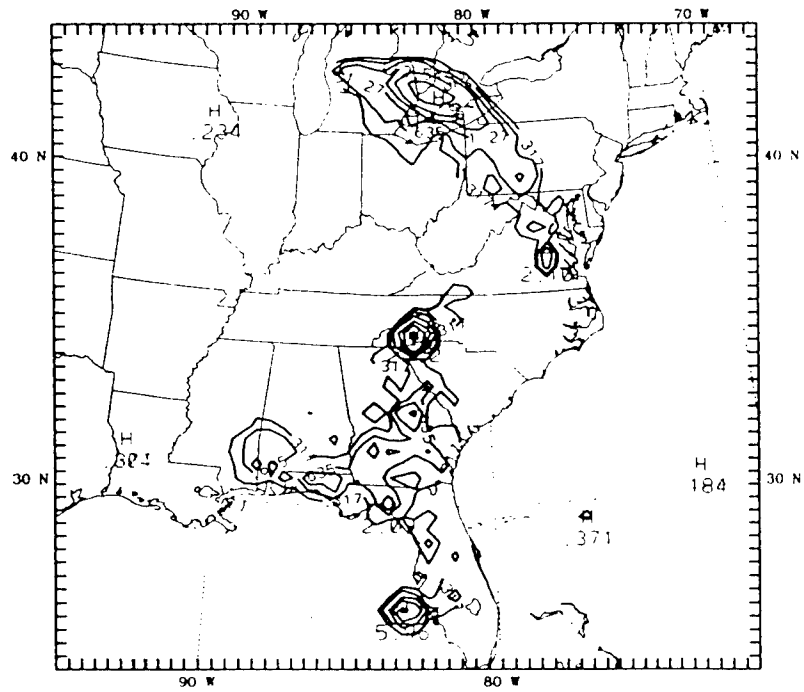
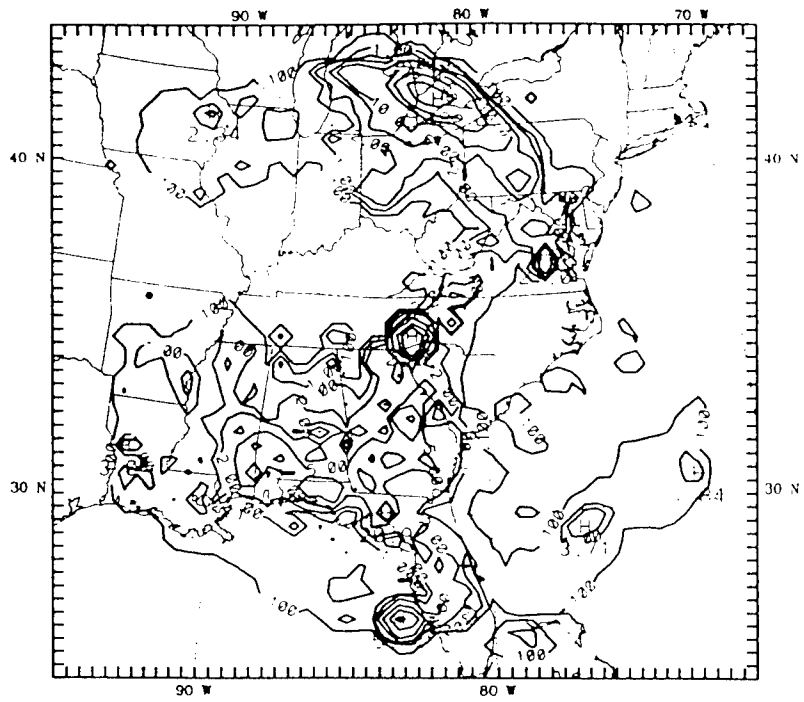


Fig. 12. As in Fig. 7 except for E3.

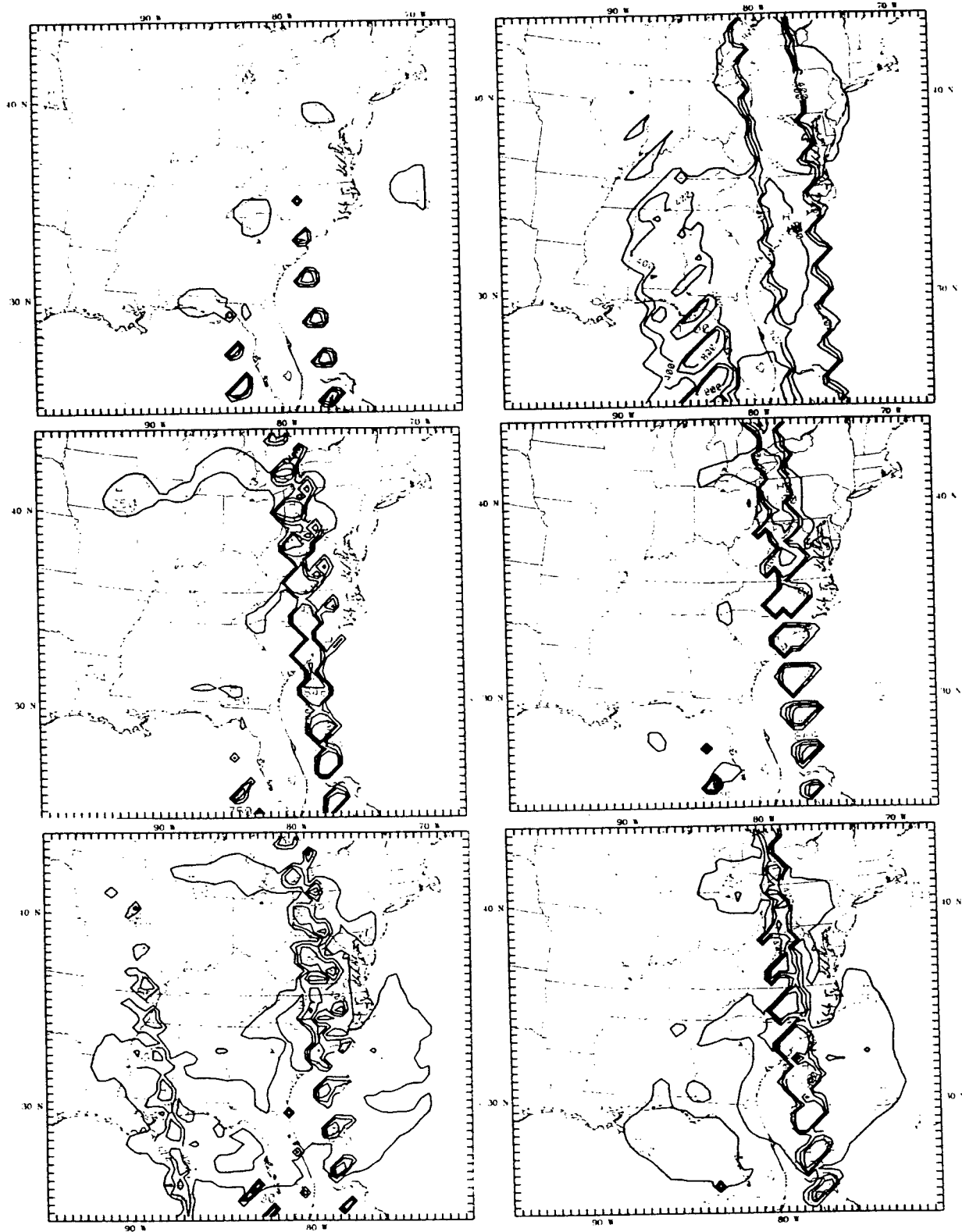


Fig. 13. As in Fig. 6 except for E4.

# Miniature Laser Gyro Consisting in a Pair of Unidirectional Ring Lasers

Jean-Claude Diels  
Professor  
Department of Physics and Astronomy

University of New Mexico  
Albuquerque, NM 87131

Final Report for:  
Summer Research Extension Program  
Phillips Laboratory

Sponsored by:  
Air Force Office of Scientific Research  
Bolling Air Force Base  
Washington, D.C.

and

Phillips AFB

December 1996

---

## Miniature Laser Gyro Consisting in a Pair of Unidirectional Ring Lasers

Jean-Claude Diels  
Professor  
Department of Physics and Astronomy  
University of New Mexico  
Albuquerque, NM 87131

### ABSTRACT

Very thin (compared to the wavelength) gain and dielectric layers have similar reflection properties, except for a phase factor of  $\pi/2$ . This particular difference makes it possible to design non-reciprocal elements, having a zero reflectivity from one direction, and a finite reflectivity from the other direction. Unidirectional operation of a ring laser, based on this property, has been demonstrated.

# MINIATURE LASER GYRO CONSISTING IN A PAIR OF UNIDIRECTIONAL RING LASERS

Jean-Claude Diels

## Objective

The short term objective was successfully achieved, i.e. is to demonstrate unidirectional operation of a ring laser with a free standing multiple quantum well structure as its gain medium.

An extension of this program could lead to a long term objective, which is to demonstrate gyro response of a dual ring laser operating on a small cube of semiconductor material.

## Principle of “non-reciprocity”

The principle of the asymmetry in reflection of the structure can best be understood by considering just a pair of two ultrathin (thickness  $\ll$  wavelength) reflecting layers, one being a dielectric “delta function”, and the other a pure gain discontinuity. This ultra-simplified pair provides a base of understanding for the more complex multilayer structure of the MQW. We will consider successively single dielectric layers, single gain layers (imbedded in a dielectric with the same real part for the dielectric constant), pairs of layers, and finally more complex structures.

Because one is used to deal with continuous structures of dimension larger than the wavelength, optical properties of such structures are counter-intuitive. For instance, the usual concept of a “self-saturation” and a “mutual saturation” does not apply to the ultrathin gain medium. The saturation is uniquely determined by the value of the *local* field at the layer, which could be the node or antinode of a standing wave. Unlike the situation in a continuous gain medium, the field reflection of the single gain layer is comparable to the field gain in transmission.

## Single layer

Let us consider first a single dielectric slab imbedded in a uniform dielectric medium, excited by a linearly polarized plane wave with electric field amplitude:

$$E(t) = \tilde{E}(t) + c.c. = \frac{1}{2} \tilde{E}(t) e^{i(\omega t - kz)} + c.c. \quad (1)$$

The slab being made of a layer of dipoles with polarizability  $\chi\epsilon_0$ , the total polarization is  $\tilde{P} = \chi\delta(z)\epsilon_0\tilde{E}$ . Inserting this polarization as a source term in Maxwell's equations:

$$\frac{\partial^2 \tilde{E}}{\partial z^2} + k^2 \tilde{E} = -\mu_0\epsilon_0\omega^2\chi\delta(z)\tilde{E} = -\frac{\omega^2}{c^2}\chi\delta(z)\tilde{E}. \quad (2)$$

We will use  $o$ ,  $r$  and  $t$  as indices for the incident, reflected and transmitted waves, respectively. Continuity of the tangential component of the field across the dielectric layer imposes that:

$$\tilde{\mathcal{E}}_o + \tilde{\mathcal{E}}_r = (1 + \tilde{r})\tilde{\mathcal{E}}_o = \tilde{\mathcal{E}}_t = \tilde{t}\tilde{\mathcal{E}}_o. \quad (3)$$

Integrating Maxwell's equation (2) across the dielectric layer:

$$\left[-ik\tilde{\mathcal{E}}_t\right] - \left[-ik\tilde{\mathcal{E}}_o + ik\tilde{\mathcal{E}}_r\right] = -\frac{\omega_t^2}{c^2}\chi\tilde{\mathcal{E}}_o(1 + \tilde{r}). \quad (4)$$

Taking into account the relation (3), we find:

$$\frac{\tilde{r}}{1 + \tilde{r}} = -i\frac{\omega_t\chi}{2nc} = -i\beta, \quad (5)$$

where  $n$  is the index of refraction of the host medium. Solving for the reflection and transmission coefficient:

$$\tilde{r} = \frac{-i\beta}{1 + i\beta} \quad (6)$$

$$\tilde{t} = \frac{1}{1 + i\beta}. \quad (7)$$

Since  $\beta$  is proportional to the susceptibility, for a gain medium, we will have a reflection and transmission of the form:

$$\tilde{r} = \frac{\alpha}{1 - \alpha} \quad (8)$$

$$\tilde{t} = \frac{1}{1 - \alpha}. \quad (9)$$

These two expressions apply as well for an absorbing medium, and have been checked numerically using matrix multiplication methods. While the agreement is excellent for small values of  $\alpha$ , there is some discrepancies for  $\alpha > 0.1$ , which is of no concern in practical cases, but points to some hidden approximation in substituting a  $\delta$  function for the polarizability. It is interesting to note the symmetry between forward and backward directions in the case of an absorbing or amplifying layer. For any value of  $\alpha$ , the field reflection is equal to the field gain (attenuation) in the forward direction. This result is consistent with a simple argument that the emitting layer being much thinner than the wavelength has no information on the direction of the field, hence has equal probability of emission in forward and backward directions. Again consistent with the semiclassical approximation, in a gain (absorbing) layer or volume of dimensions much smaller than the wavelength, the local dipole induced by the light has no space dependence, hence cannot have any "traveling wave" dependence. In the case of a macroscopic volume as a laser gain medium, atoms at different positions along  $z$  are excited in phase, hence the radiation in the forward direction has the same  $k$  vector as the exciting wave, while the radiation in the backward direction averages out. Note that it is the *field* gain, rather than the gain in energy, that is symmetric. In terms of the reflected and transmitted energy, the reflection is second order with respect to the transmission gain.

As in the case of the dielectric layer, it is the basic property that the *tangential component of a field is continuous across an interface* that has as consequence that the reflected field is equal to the gain in transmitted field. One is used to associate the gain (absorbing) medium with a discontinuity in field (i.e., a larger field at the output of the medium than at the input). This view is incorrect for layers thinner than the wavelength. For the amplifying thin layer, the dipolar radiation emits on both sides of the plane. For the absorbing layer, the induced dipoles make a “sink” for the field, bringing it down equally on both sides of the layer.

It is a peculiar coincidence that the quantum field description of stimulating emission of a single atom, being emitted exclusively in the direction of the exciting mode, is consistent with the *macroscopic* limit of the semiclassical theory, and not the microscopic one. Quantum electrodynamics cannot easily be extended from a single atom consideration to an atomic layer.

## The non-reciprocal element

The pairing of a thin gain layer with a dielectric reflecting layer leads to a structure that has non symmetric reflection properties. Let us consider, from left to right, a thin gain layer (transmission  $E_t = (1 + \alpha)E_i$ ; reflection  $E_r = \alpha E_i$ ) followed at a distance  $\ell = 3\lambda/8$  by a dielectric layer (reflection  $E_r = irE_i$ ; transmission  $E_t = \sqrt{1 - r^2}E_i$ ). The round trip between the two layers corresponds to a phase factor  $\exp\{-2ik\ell\} = i$ . Let us neglect for simplicity multiple reflections. The combined reflection from both interfaces, for a beam incident from the left, is:  $E_r = (\alpha - r)E_i$ , which is zero if  $\alpha = r$ . For a beam incident from the right:  $E_r = i(\alpha + r)E_i$ , which is finite if  $\alpha = r$ .

## A “robust” Layer structure

The properties of non-reciprocity in reflection can be generalized to more complex multiple quantum well structures. Standard matrix calculation is used to calculate the transmissivity and reflectivity of a multiple quantum well structure. Since the GaAs substrate is opaque to the design wavelength of this laser (860 nm), it will have to be etched away. From both sides, the “nonreciprocal gain structure” is bounded by an antireflection stack. It is preferable to have the AR coating included in the multilayer structure grown by MBE or MOCVD, rather than to have an additional manufacturing step.

The layer structure is designed for maximum reflectivity from one side, zero reflectivity from the other side. There is however an additional condition of the phase shift upon reflection, for the reflecting side. This condition is dictated by the potential gyro application. The performances of a laser gyro at low speed are affected by backscattering. At each round trip, some small fraction of the radiation of — for instance — the clockwise propagating beam  $\tilde{e}\tilde{E}_1 \exp\{i[\omega t - kz]\}$  is reflected into the cavity of the counterclockwise propagating beam. If the phase  $\phi_e$  of the backscattering coefficient  $\tilde{e}$  is such that the reflection has a component in phase with the counterclockwise field  $\tilde{E}_2 \exp\{i[\omega t + kz]\}$ , the latter

will be “injection locked” by the backscattering. There is no injection locking if the backscattering is  $90^\circ$  out of phase with the field  $\tilde{\mathcal{E}}_2$ .

For use in a ring laser, it is essential that the phase of the reflected wave be at  $90^\circ$  from that of the transmitted wave. This phase relationship will prevent locking of the laser gyro.

Let us consider a structure such as detailed in table 1 inserted in a ring cavity, with the clockwise beam incident first upon the face of zero reflection. Let  $\varphi_t$  be the phase shift upon transmission, and  $\varphi_r$  the phase shift upon reflection of the second surface. The resonance condition for the ring cavity is that the phase shift for the light path outside the MQW structure be  $-\varphi_t$ . The condition that counterclockwise wave reflected at the right interface be  $90^\circ$  out of phase with the transmitted phase is:

$$\begin{aligned} (-\varphi_t) + \varphi_r &= \varphi_t + \frac{\pi}{2} \\ \varphi_r - 2\varphi_t &= \frac{\pi}{2}. \end{aligned} \tag{10}$$

The last condition is that of “robustness”. Given an error on any of the growth parameter (error bar on index of refraction, layer thickness and composition), the change in structure properties should be negligible. This “robustness” of the structure was found to vary over wide ranges depending on the particular choice of parameters.

There is, at this point, no systematic method to search simultaneously for zero reflection from one direction, maximum reflection from the other, an optimum phase shift upon reflection and transmission, a maximum gain, and a robust structure. The gain in the quantum wells is proportional to the imaginary index. First, the resonant wavelength had to be determined for a GaAs quantum well layer. Knowing the thickness and the Al content in the barrier region, a good estimate of the resonant wavelength can be determined by calculating the energy levels of the quantum well. In the actual gain region, the quantum wells are separated by half a wavelength. This has been shown to increase the overlap of the anti-nodes of the internal local electric fields with the individual quantum wells [1]. The anti-reflection layers consist of a half wavelength layer followed by alternating quarter wavelength layers of AlAs and AlGaAs. The asymmetry in the structure is introduced with the “dielectric layers”, which are the four (on one side) and six (on the other side) separating the gain structure from the antireflection structure.

It should be noted that this is a unique type of vertical cavity laser because the absence of heat dissipating substrate. Because the GaAs substrate has to be etched off, all the heat dissipated in the gain layer has to be conducted away transversally through the very thin structure. To maximize heat dissipation and provide mechanical support, the thickness of the layers bordering the gain region was chosen to be in excess of one micron.

The values for the refractive index are taken from the data in [2].

There is an optimum gain (imaginary index) to attain this zero reflectivity in the CW direction. For values other than the gain used in these calculations, the reflectivity increases on either side of this optimum value. A graph of the

material	thickness (nm)	index (r)	index (i)	comment
air		1.	0.000	boundary
$Al_{0.25}Ga_{0.75}As$	126.30	3.3967	0.000	stop etch layer
$AlAs$	71.90	2.9835	0.000	
$Al_{0.25}Ga_{0.75}As$	63.15	3.3967	0.000	
$AlAs$	71.90	2.9835	0.000	AR
$Al_{0.25}Ga_{0.75}As$	63.15	3.3967	0.000	
$AlAs$	71.90	2.9835	0.000	AR
$sAl_{0.25}Ga_{0.75}As$	63.15	3.3967	0.000	
$AlAs$	71.90	2.9835	0.000	AR
$Al_{0.25}Ga_{0.75}As$	41.00	3.3967	0.000	reflector
$AlAs$	85.00	2.9835	0.000	reflector
$Al_{0.25}Ga_{0.75}As$	59.00	3.3967	0.000	spacer $r - \alpha$
$AlAs$	76.62	2.9835	0.000	(2 layers)
$Al_{0.25}Ga_{0.75}As$	59.00	3.3967	0.000	spacer $r - \alpha$
$AlAs$	76.62	2.9835	0.000	(2 layers)
$Al_{0.25}Ga_{0.75}As$	1108.78	3.3967	0.000	spacer $r - \alpha$
$GaAs$	10.00	3.6470	-0.014	Quantum well
$Ga_{0.80}Al_{0.20}As$	115.00	3.4130	0.000	pump layer
$GaAs$	10.00	3.6470	-0.014	Quantum well
$Ga_{0.80}Al_{0.20}As$	115.00	3.4130	0.000	pump layer
...	...	...	...	19 pairs total between —
$GaAs$	10.00	3.6470	-0.014	Quantum well
$Ga_{0.80}Al_{0.20}As$	115.00	3.4130	0.000	pump layer
$GaAs$	10.00	3.6470	-0.014	Quantum well
$Ga_{0.80}Al_{0.20}As$	115.00	3.4130	0.000	pump layer
$GaAs$	10.00	3.6470	-0.014	last Quantum well
$Al_{0.25}Ga_{0.75}As$	1108.78	3.3967	0.000	spacer
$AlAs$	76.62	2.9835	0.000	(1 layer)
$Al_{0.25}Ga_{0.75}As$	59.00	3.3967	0.000	spacer
$AlAs$	76.62	2.9835	0.000	(1 layer)
$Al_{0.25}Ga_{0.75}As$	35.50	3.3967	0.000	reflector
$AlAs$	71.90	2.9835	0.000	reflector
$Al_{0.25}Ga_{0.75}As$	63.15	3.3967	0.000	AR
$AlAs$	71.90	2.9835	0.000	AR
$Al_{0.25}Ga_{0.75}As$	63.15	3.3967	0.000	AR
$AlAs$	71.90	2.9835	0.000	AR
$Al_{0.25}Ga_{0.75}As$	63.15	3.3967	0.000	AR
$AlAs$	71.90	2.9835	0.000	AR
$Al_{0.25}Ga_{0.75}As$	126.30	3.3967	0.000	etch layer
$AlAs$	10.00	2.9835	0.000	1st etch
$GaAs$		3.6470	0.000	substrate

s

Table 1: Detailed constitution of the AlGaAs MQW structure optimized for zero reflection at 858 nm, and maximum robustness. Note the two layers of 1108 nm for heat sinking and mechanical rigidity.

reflectivity as a function of gain is shown in Fig. 3

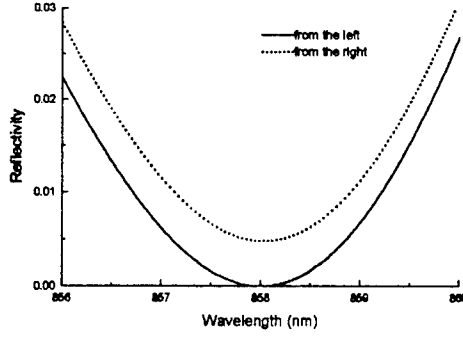


Figure 1: reflection spectrum for light incident from the right (dotted line) or the left (solid line) of the structure of table 1.

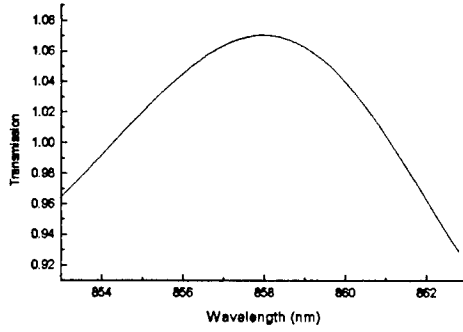


Figure 2: Transmission spectrum of the non-reciprocal structure.

## The sample

One sample was grown at the CHTM by MOCVD. The properties of that sample did not bare any resemblance with the prediction. In fact, the sample had luminescence at 960 nm instead of 860, which cannot even be explained by the sloppiness of the CHTM crystal grower.

Another sample was grown by MBE at Sandia Laboratories Etching of the substrate was made up to the last AlAs “stop-etch” layer. However, a last slow etch was made to eliminate the AlAs layer up to the  $\text{Al}_{0.25}\text{Ga}_{0.75}\text{As}$  layer, which is not so easily oxydized as AlAs. The diameter of the etched zone was kept as small as possible, compatible with the size of the pump and laser beams. For better heat removal, the etched sample was mounted on a sapphire window that has a hole drilled in it to allow passage of the beam.

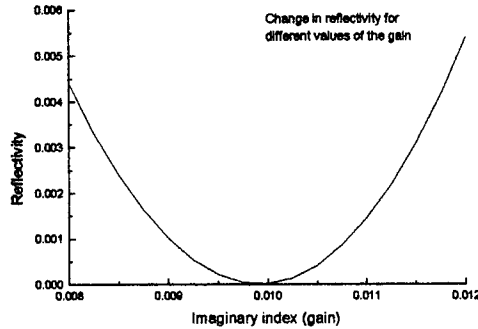


Figure 3: Reflectivity in the CW at 858 nm, as a function of the imaginary index (gain)

## The unidirectional MQW laser

### Laser cavity

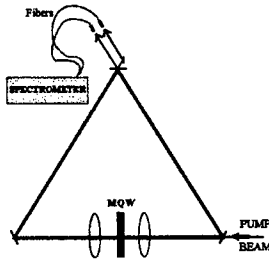


Figure 4: MQW laser cavity.

Unidirectional operation is expected for a ring laser in which the non-reciprocal MQW structure is used as a gain medium. The MQW structure is pumped with radiation from a dye laser (LDS 698 dye) which had a maximum gain in the 700 -730 nm region. This range corresponds to the optimum pumping range for the GaAs/AlGaAs quantum wells. The maximum pump power was 300 mW.

The ring laser cavity is sketched in Fig. 4)). Basically there are three mirrors that are configured to make a triangular ring cavity and two micro-lenses to focus the light into both sides of the MQW sample. The sample is being pumped collinearly through a dichroic mirror. Since heat dissipation is transverse, the transverse dimension of the gain medium is also kept to a minimum (estimated spot size of the pump beam on the sample:  $\approx 20\mu\text{m}$ ). The lenses are the most critical elements of the cavity. Because of the tight focusing ( $f = 4\text{ mm}$ ), their curvature is strong, and it becomes difficult to minimize the reflections losses at the four surfaces that are traversed at each round-trip. The

lenses used in the experiment were GelTech (originally Corning) aspheric micro lenses with a focal length of about 4 mm and a working distance of about 2 mm, with “V coat” antireflection coating (guaranteed specification  $< 0.25\%$  per surface, target specification as low as  $0.10\%$  per surface).

The mirrors were selected from VLOC, with high reflection coefficient ( $> 99.9\%$ ) centered around 860 nm and partially transmitting (80%) around 720 nm. Since the pump beam was fairly strong (a few hundred milliwatts), a 20% loss in pump transmission is acceptable. The mirrors were flat and designed for 30 degrees incidence.

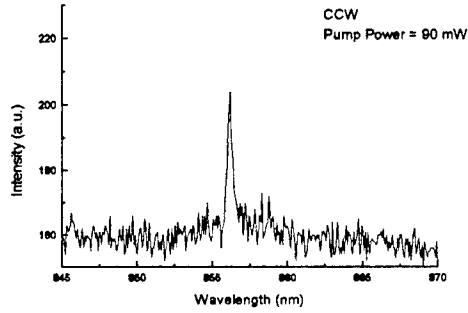


Figure 5: Unidirectional lasing in the CCW direction just above threshold

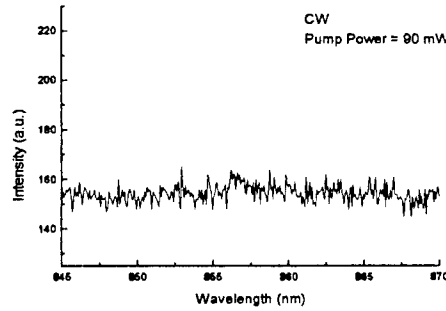


Figure 6: Lasing suppressed in the CW direction.

## Sample mounting

In order to increase the heat dissipation, the sapphire window is then placed into a copper block which is mounted onto a thermoelectric cooler. This Peltier cooler is hooked up to a Wavelength Electronics temperature controller and

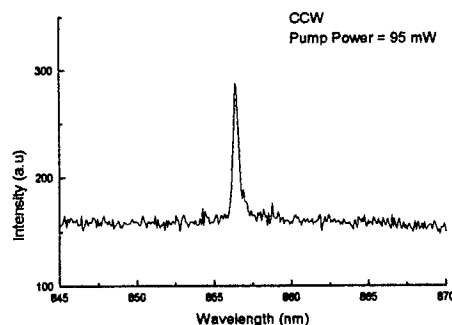


Figure 7: Stronger lasing in the CCW direction at a slightly higher pump power.

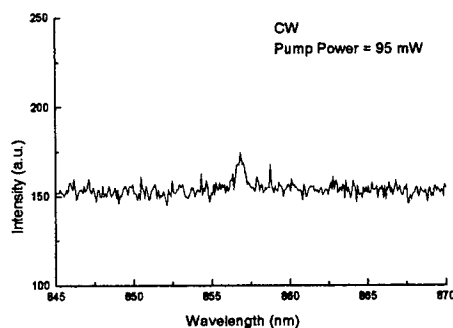


Figure 8: The onset of weak lasing in the CW direction.

driven by a Lambda power supply which limits the current. The controller can stabilize the temperature to about 0.01 C and can cool the apparatus down to the dewpoint. On most days here in this very dry state, the sample can be cooled to about 18 C and condensation can be avoided. Heating of the MQW sample is further reduced by introducing a duty cycle for the pump beam, with a chopper wheel with a small ratio of opening/closure time. A 50% duty cycle was sufficient to achieve lasing without excessive thermal load on the sample.

## Unidirectional operation

Lasing was determined by observing a large spike in the spectrum around 857 nm. The design gain per pass is about 1.6%. Since the total losses due to all of the elements in the cavity per round trip is between 1.2% and 1.4%, the alignment is obviously quite critical.

The sample is placed in the cavity with the etched side towards the pump beam. According to the design, the “zero” reflection is on the other side of the etched hole. A beam incident from that side has a smaller reflection than

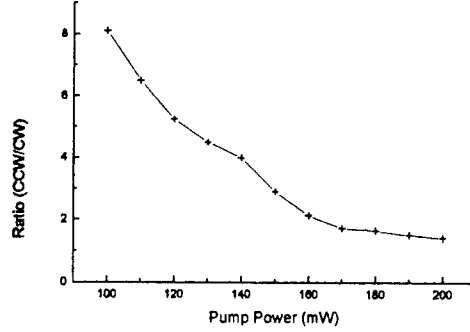


Figure 9: Ratio of the peak intensities (CCW/CW).

a beam incident on the side that was etched. The lasing wavelength is between 856 nm and 857 nm which happens to be very close to the design wavelength of the structure.

Unidirectionality is observed at low pump powers in the CCW direction with lasing suppressed in the CW direction (see figures (5) and (6)). As the pump power is turned up, the MQW starts lasing in the CW direction, but the intensity was still less than the beam going CCW (see figures (7) and (8)). The linewidth of the laser peaks increases with the power. Close to threshold ( $\sim 90$  mW), the linewidth at full width half maximum (FWHM) is measured to be around 0.5 nm, which is the resolution of the spectrometer. The degradation of unidirectionality with pump power is expected, since the design “zero reflection gain” corresponds to threshold — or even below (see figure (3)).

The ratio of the peak intensity as a function of pump power for the CCW beam to the CW beam is shown in figure (9). Above threshold, the ratio gets progressively smaller; which is consistent with the theoretical curve where the smaller reflectivity occurs at an optimum gain, with this reflectivity increasing as the gain is increased. By decreasing the differential losses, this increase in the reflectivity lowers the effectiveness of the device as a non-reciprocal structure.

## A laser cube gyro

The unidirectionality property demonstrated above can be exploited in a miniature ‘cube’ laser gyro, consisting of two  $90^\circ$  turning prisms with the MQW gain structure deposited on the hypotenuse face of one prism. The two prisms are optically contacted to form a cube (Fig. 10). Depending of the location of the pump spot (indicated by an arrow), the lasing will be clock-wise or counterclock-wise in the cross-section of the cube. With two pump spots at different height in the prisms, lasing can occur in opposite direction in adjacent planes. Since there is no coupling between the cavities, the beat frequency between the two lasing planes should exhibit a perfect gyroscopic response. The beams can be extracted from the laser by frustrated total reflection with an auxiliary prism, as indicated on the figure.

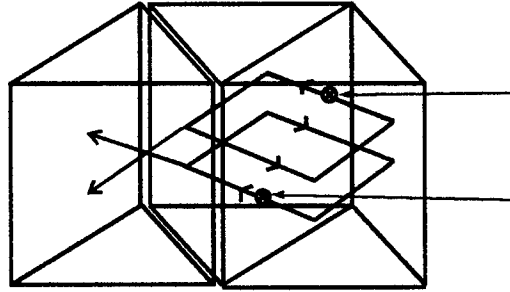


Figure 10: The cubic laser gyro. Two  $90^\circ$  turning prisms constitute the two halves of the cube. The nonreciprocal layer structure is grown on the hypotenuse plane of one of the cubes. The two prisms are optically contacted. The laser is pumped at two different heights, resulting in unidirectional operation in opposite direction in two parallel planes.

## References

- [1] M. Y. Raja, S. R. Brueck, M. Osinski, C. F. Shaus, J. G. McInerney, T. M. Brennan, and B. E. Hammons. Resonant periodic gain surface emitting semiconductor lasers. *IEEE J. Quantum Electron.*, 25:1500–1511, 1989.
- [2] A. Aspnes, S. M. Kelso, R. A. Logan, and R. Bhat. Optical properties of AlGaAs. *J. Appl. Phys.*, 60:754–766, 1986.

TWO-DIMENSIONAL SIMULATIONS OF ULTRAFAST SILICON AVALANCHE  
SHAPER (SAS) DEVICES FOR HIGH POWER SWITCHING

R. P. Joshi  
Associate Professor  
Department of Electrical and Computer Engineering

Old Dominion University  
Norfolk, VA 23529-0246

Final Report for:  
Summer Faculty Research Program  
Phillips Laboratory, Kirtland Air Force Base

Sponsored by:  
Air Force Office of Scientific Research  
Bolling Air Force Base, DC

and

Phillips Laboratory

December 1996

---

TWO-DIMENSIONAL SIMULATIONS OF ULTRAFAST SILICON  
AVALANCHE SHAPER (SAS) DEVICES FOR HIGH POWER APPLICATIONS

R. P. Joshi  
Associate Professor  
Department of Electrical and Computer Engineering  
Old Dominion University  
Norfolk, VA 23529-0246

Abstract

Silicon Avalanche Shaper devices have been projected as being important components of an inexpensive, semiconductor-based all-electrical technology for high power switching and pulse shaping applications. The primary advantage of this technology is that it is based on Silicon material which is easy to fabricate and has a well established processing technology. Unlike other high power technologies, the SAS devices do not rely on external optical triggering which eliminates the need for lasers and related optical circuitry.

The SAS based high power switching technology has been pioneered and tested by a Russian group. Though preliminary results have been very encouraging, the device reliability and its operating capability at high voltages have not been studied in detail. Furthermore, the rather large device parameter space has not been fully explored to ascertain the optimal operating point. As a result, the set of device parameters necessary to yield the desired electrical response for a given application, remains unclear. Besides, the potential for internal current filamentation and device breakdown in the Silicon Avalanche Shaper has not been analyzed. All of these aspects can best be studied and understood in a cost-effective manner through numerical simulations.

In this research, a two-dimensional simulator for the SAS device has been developed based on the drift-diffusion model. Predictions of the device electrical response have been obtained. The role of transverse variations in the doping profile have been analyzed by obtaining the transient current characteristics. The results reveal the development and propagation of internal electric field waves. The wavefront of such propagating electric waves has been shown to be non-uniform, and to depend on the details of the transverse doping. The transverse variations could either be accidental or the result of intentional inhomogeneities occurring during device fabrication. Simulation data for the conduction current distribution within the device at various time instants, clearly show evidence for the growth of filamentary modes. The filamentation, however, is strongly dependent on the transverse doping characteristics, and hence could in principle be tailored.

## TWO-DIMENSIONAL SIMULATIONS OF ULTRAFAST SILICON AVALANCHE SHAPER (SAS) DEVICES FOR HIGH POWER APPLICATIONS

R. P. Joshi

### HIGH POWER SWITCHING

High power switches are the crucial components in a variety of engineering circuits. The switches are needed for a range of applications. These include: (i) high voltage pulse generators, (ii) dc to RF conversion circuits, (iii) high energy pulsed lasers, (iv) for the generation of ultrawideband microwaves, (v) high frequency plasmatrons, (vi) impulse radar systems, and (vii) frozen waveform generators [1].

The major factors which need to be considered in the development of high power switches include: (a) the efficiency of energy delivery from the pulser to the load, (b) shaping of the output pulses, and (c) the control of the timing and its relative sequence. Aspects related to the efficiency arise from losses in the switch itself. The energy transferred to the load usually must be delivered as a pulse of given rise time and duration. In addition, the time of delivery of the pulse frequently must be controlled accurately. Also, since several switches may be used in one network to reduce the power dissipated per switch to a manageable level, close synchronization is often required [2].

Traditionally, fast high-power switching was realized with gas discharge devices. These devices, however, have a number of inherent shortcomings, and as a result, have largely been replaced in the last 15-20 years by high power semiconductors [1]. The shortcomings associated with gas discharge-based or mechanical switching include: (i) an inherently slower response, (ii) large bulk and size, and (iii) lower thermal capacity. The development of materials with non-linear resistivity in commercial quantities and a greater range of electrical characteristics, in particular those whose resistance depends upon current or temperature, gave rise to the utilization of solid state devices as closing and/or opening switches in pulse power applications [3,4]. Such semiconductor based switches have a number of potential advantages. These advantages include: (i) Compactness and small size leading to weight reductions, (ii) low jitter associated with optically triggered semiconductor switches, (iii) larger thermal capacity, (iv) ultrafast switching times and rapid repetition rates, and (v) the potential for a higher density plasma which can initiate a rapid transition into the high conducting state.

Power switching by semiconductor devices of any type occurs through a strong modulated increase in the conductivity. In the "OFF" state, the device is in its high resistive state and so effectively blocks any external potential applied to the device. This region can either be the space charge region (SCR) of a reverse-biased junction which is completely depleted of free carriers by the strong external field, or a highly resistive low-doped semiconductor region. For schemes based on highly resistive low-doped semiconductors, the "OFF" state is maintained through Schottky contacts which provide an effective barrier to carrier injection. In the "ON" state, the conductivity of this region increases dramatically as it becomes filled with an electron-hole plasma. The electron-

hole plasma can be created by any one of the following mechanisms:

- (a) Photo-excitation by an external optical source such as a laser or a light emitting diode,
- (b) Electron-beam bombardment to create a plasma,
- (c) Charge injection through device contacts by applying a circuit voltage, and
- (d) By initiating an internal avalanche breakdown process through either band-to-band or band-to-trap impact ionization.

The use of a solid state material with the resistivity changing reversibly by several orders of magnitude, provides a better alternative to high power switches. The most promising semiconductor switches appear to be those based on bulk material with carrier mobility changing throughout the entire device volume. Such materials, in principle, provide the highest volumetric efficiency since they would utilize the entire material volume uniformly on both microscopic and macroscopic scales [2]. The uniformity also works to ensure a homogeneous current density and should therefore reduce the potential for localized filamentation.

## **CHARACTERISTICS OF HIGH POWER SWITCHES**

In general, solid state switches for high power applications should exhibit the following desirable characteristics:

- The ability to withstand high electric fields and to have a large breakdown/blocking voltage.
- Low leakage currents to preserve a high-impedance "OFF" state.
- Short turn-on times attainable through high mobility charge carriers.
- A very low resistance during the "ON" state and the ability to sustain high current densities.
- Device reliability and the absence of internal instabilities such as current filamentation.
- Good thermal conductivity for heat dissipation.
- A negative temperature coefficient for suppression of thermal instabilities.
- Simple structure and ease of fabrication for cost minimization.

## **SEMICONDUCTOR SWITCH MATERIALS**

The choice of the semiconducting material to be used for a high power switch is very important for optimizing the electrical characteristics, its efficiency and overall utility. As already mentioned, the switching process has to be initiated throughout the bulk of the device. Bulk generation has the following advantages: (i) Greater current carrying capability due to the larger available area, (ii) Better uniformity in the current density distribution, (iii) easier and faster heat dissipation for improved reliability and controlled device parameters, (iv) higher energy handling capacity, (v) lower internal resistance leading to reduced internal voltage drops and lower "RC" time constants.

Given the importance of bulk switching and plasma propagation throughout the device, the choice of a

material for high power switching devices is guided by the bulk semiconductor properties. The important parameters are: (i) The material band gap which controls leakage currents, places an upper limit on the operating temperature, the intrinsic carrier concentration and the impedance of the "OFF" state. (ii) The breakdown field and dielectric strength which determine the maximum hold-off voltage. These parameters also provide a measure of the device length necessary to ensure the blockage of high voltages. (iii) The saturated drift velocity which controls the response speed and the current density levels. (iv) The ionization coefficient which determines the threshold for impact ionization and the possibility for internal carrier generation through avalanching. (v) The nature of the band-gap since, a direct bandgap semiconductor provides the possibility of optical excitation while an indirect semiconductor does not. (vi) The thermal conductivity which may become a relevant consideration for energy dissipation and in enhancing the power handling capacity. (vii) Ease of fabrication, commercial development of the semiconductor and relative costs of device manufacture.

Based on the above considerations, silicon and GaAs emerge as the materials of choice for high power switches. Of these GaAs is a direct bandgap material and is exclusive to optically based switches. Silicon, though unsuited for photoswitches, has a number of advantages over GaAs. For example, the related processing technology is very well developed and the costs involved in device manufacture are the least. It also has a much higher carrier drift velocity which ensures fast response times at high fields. The thermal conductivity is also larger than GaAs which is beneficial for high power switching. Finally, both Ohmic and Schottky contacts can be fabricated which are robust and increase the device reliability. Furthermore, Si unlike GaAs, does not exhibit the intervalley electron transfer "Gunn effect" [5] which leads to negative differential conductivity (NDC). NDC, as is well known, is detrimental to reliable device and can give rise to internal instabilities. As a result, this research focusses on Silicon based high power switches.

The high power switch studied here relies on the creation of an internal travelling electric field and the impact ionization of electron-hole pairs to trigger the device into the conducting state. For an efficient transition into the "ON" state, the associated ionization coefficient " $\alpha$ " for the material has to be large. The " $\alpha_{Si}$ " value happens to be larger than " $\alpha_{GaAs}$ ". This occurs because the impact ionization threshold energy  $E_{TH}$  which depends on the bandgap is lower for silicon. Secondly, the disparity between electron and hole effective masses is lower for silicon as compared to GaAs. As a result, **both** electrons and holes can contribute to avalanche multiplication in Si more effectively than in GaAs. These considerations again favor silicon as the material of choice over GaAs.

## RESEARCH OBJECTIVES

The transient behavior of silicon avalanche switches which are used for high-power waveform shaping applications, and function in both the "closing" and "opening" modes, are studied here. Numerical simulations have been performed to predict switching currents and examine the repetitive device response. The main research objective is to simulate two-dimensional effects and thereby probe the possibility of current filamentation and the prospects of internal non-uniform current density channels. Such localized current channels and filamentation is

known to be destructive and needs to be controlled for useful device performance. However, unless the two-dimensional effects are first understood through numerical simulations and device modeling, one cannot hope to control these effects. The simulations presented in this research address this objective.

Two-dimensional effects in devices can arise due to spatial nonuniformities. These could either be due to non-uniformities in the device geometry or due to inhomogeneous doping distributions. Spatially non-uniform traps and defects can also contribute to two-dimensional effects. In this research, only the dopant inhomogeneities will be addressed. The resulting two-dimensional current distributions which can lead to filamentation and localized heating, will be evaluated for various doping levels and profiles.

## COMPARISON BETWEEN OPTICAL AND ELECTRICAL TRIGGERING

This section briefly outlines the main comparisons between the optical and electrical triggering mechanisms for semiconductor switches. The comparison provides reasons in support of electrically triggered silicon avalanche switches (SAS) and hence, provides motivation for the present study.

- (i) Complex optical sources or external lasers and photogenerating elements are not required for electrical triggering. This reduces the size of the switching element making it more compact.
- (ii) Electrically switched elements can easily be integrated with other electronic components on a chip.
- (iii) The optical switches rely on direct band gap semiconductors such as GaAs, InP and other III-V materials. All of these are more expensive to fabricate than the indirect bandgap silicon.
- (iv) All of the direct bandgap materials used for optical switches have satellite valleys which leads to intervalley transfer. This phenomena can give rise to internal domain formation and can result in internal instabilities.
- (v) The density of the electron-hole plasma in side optically excited switches usually is non-uniform. This arises from the Beer-Lampert law which leads to an exponential distribution of electron-hole pairs internally. This inherent nonuniformity can lead to instabilities, localized current channels or current filamentation.

## THE SAS OPERATIONAL PRINCIPLE

The silicon avalanche shaper switch (SAS) was first proposed and successfully demonstrated by a Russian group [6-8]. Simple qualitative discussions of the SAS operating principle have been given in several papers by Grekhov et al. [6-9] over the years. The concept relies on the generation of a fast propagating electric field and an accompanying ionization wave within the device through the application of a rapid reverse bias across a Silicon p-n junction device. Basically the device has a  $N^+-N-P^+$  structure. The low-doped, near intrinsic "N" region is depleted of carriers during the holdoff phase and supports a large voltage drop. Initially the device is able to hold off an applied voltage and a negligible current flows in the circuit. This corresponds to the "OFF" state. This applied hold-off bias is below the critical breakdown voltage. As soon as the total applied peak bias exceeds the static breakdown voltage, the switch transitions into the "ON" state through the rapid avalanche generation of electron-hole pairs within the high-field regions of the device. The conductivity is therefore enhanced rather quickly, and the switch triggers

into the conductive "ON" state. The switch is therefore triggered by an internal avalanche process through either band-to-band or band-to-trap impact ionization. A brief summary of the important sequence of physical events is given below.

- (i) The SAS is initially in the non-conducting "OFF" state with a moderate reverse bias across the  $N^+-N-P^+$  structure. The applied voltage is held to a value below the characteristic avalanche voltage of the Si device. This hold-off voltage can, in principle, be varied by changing either the internal doping densities or the device length. Lowering the doping for example, increases the internal electric field, making it possible for the device to withstand an initiation into the avalanche mode. Similarly, increasing the device length also increases the holdoff voltage capability.
- (ii) For turn-on, a sharply reverse voltage pulse is applied. As a result, the total voltage across the SAS device then exceeds the breakdown limit. At the higher voltage, a high- field region is created across the  $P^+-N$  junction, with field strengths exceeding the critical breakdown value. Impact ionization is thus initiated in a region localized near the  $P^+-N$  junction.
- (iii) Rapid impact ionization creates a high conductivity region at the  $P^+-N$  junction. The electrons and holes thus created through impact ionization, begin to move in opposite directions. The motion of the mobile charge contributes to a current rise.
- (iv) Next, the electric field in the highly conduction region begin to collapse as the separation of mobile charge forms an internal polarization field. The electric field in the adjacent non-conducting N-region, however, increases to sustain the overall voltage drop across the device. This increase in the electric field provides the displacement current necessary to maintain exact continuity of the total current across the entire device.
- (v) As a result of the above mechanism, the electric field grows starting from the  $P^+-N$  junction, towards the  $N^+$  anode side through the N-region in the middle. A propagating electric field wave is thus set up. This propagating field, in turns, creates a travelling impact ionization front, and is responsible for the uniform turn-on of the entire device.
- (vi) The current in the SAS device can be turned off by lowering the applied bias to a level below the critical sustaining breakdown voltage. Upon lowering the external voltage, the carriers are removed through a combination of drift flush-out and recombination.

A schematic for the turn-on sequence is shown in Figure 1. The initial field in the  $N-P^+$  depletion region is below the critical value for impact ionization. Hence, the carrier concentration and the conductivity remain at a low level. On the application of a large reverse bias, the field increases beyond the critical value, and carrier generation via impact ionization is initiated. This ionization effectively increases the local conductivity, and forces the growth of the electric field in an adjoining low conductivity region. This progressive movement of the electric field away from the junction and into the low conductivity N-region continues, as carriers continually keep getting generated within the N-layer starting from the junction.

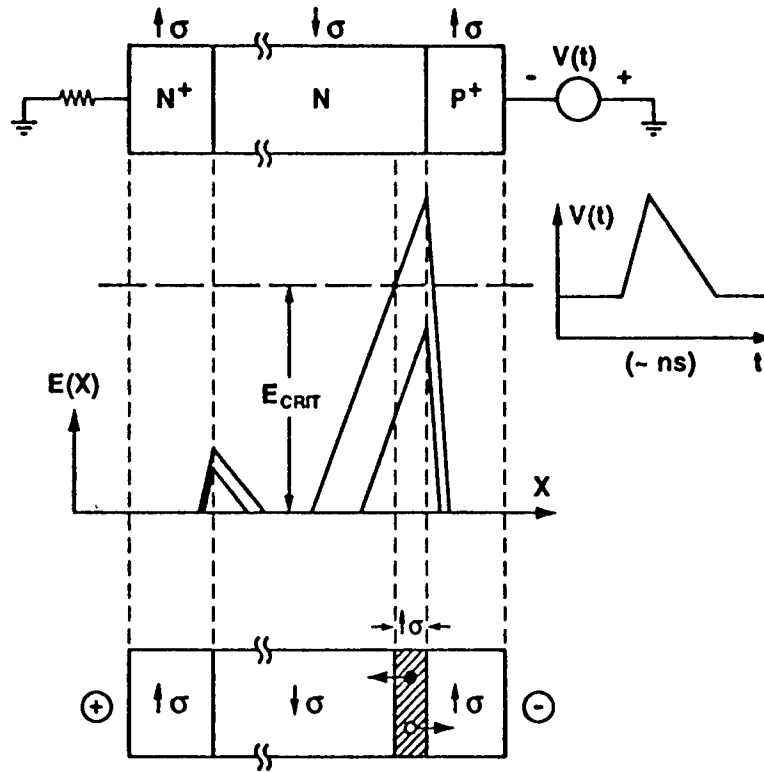


Fig. 1 Schematic of the SAS turn-on sequence.

#### ADVANTAGES AND BENEFITS OF THE SAS DEVICE

Based on the above summary of the SAS operational principle, several key advantages can be identified. These are based on the inherent operating principle and the device physics. The following is a list of important advantages for this SAS-based high power technology, which has also been discussed previously [10]:

- (i) The elimination of external lasers for triggering and turn-on. This simplifies the complexity of the circuit.
- (ii) A natural self-propagation of the electric fields within the device. This facilitates a gradual and more homogeneous turn-on. The potential for instabilities associated with spatial non-uniformities as with localized charge injection, is thus greatly reduced.
- (iii) The application of a rapidly increasing voltage pulse dramatically decreases the likelihood of current filamentation and "micro-channels". As is well known [11], such filamentation is associated with the rapid growth of the electric fields within localized regions of the device due to density fluctuations. However, in this device, the application of a fast voltage ramp increases the electric fields everywhere within the device. As a result, currents cannot remain localized within narrow channels since the rapidly increasing field creates charge in the adjacent regions through impact ionization. The carrier density is therefore enhanced over a broad area, thereby swamping the initial fluctuations (if any) in the local carrier density.
- (iv) Another advantage of this technology is its reliance on Si rather than GaAs. Silicon has the following inherent advantages over GaAs, a material which is often used in photoconducting switches. The advantages

include: (a) Ease of fabrication. (b) A higher thermal conductivity for better heat dissipation and better protection against thermal runaway. (c) A higher carrier saturation velocity which should lead to higher currents and faster turn-on. (d) A material system inherently free of Negative Differential Resistance (NDR) effect. As is well known, the NDR effect in GaAs associated with inter-valley transfer gives rise to a potential instability [12].

- (v) Furthermore, the SAS by being a p-n junction device, naturally ensures that the regions of high electric field occur within the bulk device and not at the end contacts. As a result, the device circumvents many of the "contact problems" that are associated with other devices. These problems include uncontrolled thermionic emission and carrier tunneling due to high fields at the contact, excessive heating and contact degradation.
- (vi) Finally, the SAS also offers the possibility of scaling the hold-off voltage. This could be done by stacking several such devices in series, increasing the size of the central N-region, and by decreasing the doping levels. Therefore there do not appear to be any fundamental limits on the voltage scaling.

#### **ASPECTS OF THE TWO-DIMENSIONAL RESEARCH SIMULATIONS**

There are basically two important aspects that are addressed in this research. These two areas are: (1) The issue of current filamentation, and (2) Determining the role of two-dimensional variations in the doping density on the electrical response and device stability. Both of these aspects are important in determining the reliability and usefulness of the SAS device. For instance, if the doping is not homogeneous across all of the cross-sections of the device, the internal conductivity will also be nonuniform. The nonuniform conductivity can then lead to the formation of localized current channels with the possibility of premature switch turn on.

As is well known, current filamentation arises from spatial non-uniformities across the device cross section, and is basically a two-dimensional effect. Such non-uniformities can arise from any one of the following reasons: (a) Doping inhomogeneities (either intentional or accidental) during the processing and fabrication steps. (b) The formation of spatially non-uniform defects within the semiconductor. (c) The development of non-uniform fields within the semiconductor during device operation which can lead to non-uniform impact ionization with variable charge creation. (d) Thermal effects which again can lead to non-uniform carrier generation within the device.

In order to explore these issues, a two-dimensional numerical model has been developed. The model uses the drift-diffusion approach, given its relative simplicity and modest computational requirements. Furthermore, since the dimensions of the SAS devices used in this study are well above the micrometer range and the time scale of interest are relatively large (higher than 10 ns), the more complex approaches such as the Monte Carlo method will not be necessary. The results obtained from the drift-diffusion scheme are therefore expected to be adequate.

#### **THE DRIFT-DIFFUSION TRANSPORT APPROACH**

The overall current transport in the Drift-Diffusion approach is described by the following equation:

$$J = nqv_n + pqv_p - qD_n \left( \frac{dn}{dx} \right) + qD_p \left( \frac{dp}{dx} \right) + \epsilon \frac{dE}{dt} \quad (1)$$

where E is the electric field,  $\epsilon$  is the permittivity of material, "n" and "p" are the electron and hole densities, and  $D_{n,p}$  the electron/hole diffusion coefficients. Both the conduction and displacement currents are included in this formulation. This equation is derived from the Boltzmann transport equation under the following assumptions:

- a) An isotropic and parabolic single band.
- b) Inherent assumption of the relaxation time approximation.
- c) Absence of degeneracy with no hot carrier effects.
- d) A homogeneous collision time. The validity of the drift-diffusion scheme also requires that the scattering time be significantly smaller than the simulation time scale of interest.
- e) No strong off-equilibrium effects, and
- f) An assumption that the length scales for spatial variation of the electric field and impurity concentrations are much longer than the carrier mean free path.

The model developed for the study of the SAS devices had the following salient features:

- It was based on the drift-diffusion approach.
- It explicitly solved for the two-dimensional distributions of the internal electric fields and carrier densities.
- It yielded the self-consistent transient analysis, as well as the final steady-state response.
- The model was bipolar in nature, and could treat both electron and hole transport.
- An important component of the model consists of rate equations which describe the transient dynamics of the free-carrier generation, trapping and recombination.
- An external circuit was incorporated in the model.
- The model took account of the internal displacement current.
- An added feature of the model was the inclusion of impact ionization at high electric fields. This mechanism is very important since it is at the heart of the switch "turn-on" process.
- The numerical implementation included heat generation within the device. A one-dimensional diffusive heat flow model is included, and changes in the transport parameters with any resulting temperature rise taken into account.
- Finally, carrier injection at the two contacts was implemented based on the thermionic emission model which uses the Richardson coefficient  $A^*$ . A value of  $80 \text{ A/cm}^2/\text{K}^2$  was assumed for  $A^*$ . The barrier heights at each contact were assumed fixed at a value of 0.5 eV independent of the current density.

## SEMICONDUCTOR MODEL IMPLEMENTATION AND SIMULATION SCHEME

For numerical implementation, the SAS device was spatially divided into "N" boxes each with a finite spatial extent. The mesh sizes  $\Delta x$  along the longitudinal x-direction, and  $\Delta y$  along the transverse y-direction, were chosen to be equal. The density of free carriers, ionized/unionized donors and acceptors, the average internal electric field, and device temperature were all represented by discrete values at the center of each box. Thus the above parameters were assumed to be fixed within each box, but to vary from box to simulation box during each time step of the simulation. A schematic of the device simulation region along with the circuit is shown in Fig. 2.

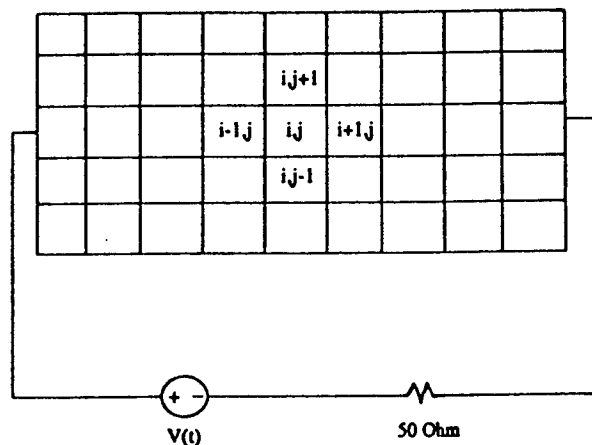


Fig. 2 Schematic of the circuit and the device simulation region.

The temporal scale was also discretized into time intervals of magnitude  $\Delta t$ . This time step  $\Delta t$  was chosen to satisfy the requirement of being greater than both the relaxation time and the internal collision times. In order to obtain numerical stability of the space-time discretization, the well known "Courant-Fredericks-Lewy" inequality condition [13] was used to limit the time step  $\Delta t$ . Thus:  $\Delta t \leq \Delta x / [2 v_{\max}]$ . The specific silicon SAS device structure used for the simulations was a  $N^+-N-P^+$  diode with dimensions of  $40\mu m$ ,  $250\mu m$  and  $50\mu m$ , respectively. A total of 150 discretized boxes were chosen along the longitudinal x-direction for the device simulations.

## RESULTS AND DISCUSSION

This section provides all the numerical simulation results that were obtained for the SAS device. The simulations were carried out to predict and gauge the electrical response characteristics. The 2D implementation of the drift-diffusion model was used to obtain the transient response for four different doping profiles along the transverse direction. These four doping profiles chosen for the simulations were as: (i) A sinusoidal shaped centrosymmetric distribution with a minimum dopant density at the two opposite surfaces and a maxima over the axial

center, (ii) A sinusoidal shaped centro-symmetric distribution with maximum dopant density at the two opposite surfaces and a minima over the axial center, (iii) A two-layer asymmetric, off-center composite distribution, and (iv) Uniform doping profiles along the transverse direction. Three-dimensional plots showing details of the dopant distribution profiles for each case are shown next along with a discussion of the results obtained for each profile.

## TWO-DIMENSIONAL RESULTS AND ANALYSIS: CASE I

The SAS device was taken to comprise of  $N^+-N-P^+$  Si material with nonuniform doping profiles along the transverse direction for each of the three regions. The same functional form was used for the doping profiles in the three constituent regions. The peak dopant density values were taken to be:  $N_D^{\max} = 5 \times 10^{16} \text{ cm}^{-3}$  in the  $N^+$  region,  $N_D^{\max} = 10^{14} \text{ cm}^{-3}$  for the lower doped N-layer, and  $N_A^{\max} = 5 \times 10^{16} \text{ cm}^{-3}$  for the  $P^+$  region. The external circuit was as shown in Figure 2. The device area was  $2 \times 10^{-2} \text{ cm}^2$  and the operating temperature was assumed to be 300 K. For simplicity, a periodic "saw-tooth" type voltage waveform as shown in Fig. 3 was assumed for the voltage source. Such a waveshape is similar to that actually used in preliminary experimental tests so far [14].

Simulation results for the initial unbiased steady state conditions within the SAS device for the first of the four doping profiles are shown in Figures 4-8. The dopant profile for this case was taken to be a sinusoidally symmetric distribution with minimum dopant density at the two opposite surfaces and a maxima on the central axis. The resulting ionized impurity concentration as obtained from the simulations is shown in Figure 4. The peak magnitude of the ionized impurity density nearly equals  $5 \times 10^{16} \text{ cm}^{-3}$  which is the maximum concentration of dopant atoms. This peak lies on the central axis of the device and the profile is symmetric. The 2D electron and hole profiles are plotted in Figures 5 and 6, respectively. Their transverse shapes follow that of the dopant distribution. In addition, some structure along the longitudinal direction is also seen at the junctions. This is due to free carrier diffusion and the formation of built-in electric fields and depletion regions at the various junctions and interfaces. The longitudinal electric field distribution  $E_x$  under unbiased steady state conditions is shown in Figure 7 and the transverse field  $E_y$  in Figure 8. A number of features associated with this plot are immediately evident. First, the magnitude of  $E_y$  is much smaller than that of  $E_x$ . This is to be expected since the steady state electric field is roughly proportional to the negative gradient of the majority carrier density " $n(x,y)$ ". This follows from the requirement of a zero net conduction current, and leads to  $E_y$  being proportional to:  $-[dn/dy]$ . Since the gradient " $dn/dy$ " is antisymmetric for the chosen doping profile, the electric field distribution  $E_y$  also has an anti-symmetric shape. Next, since the gradient of the majority carrier density and dopant distribution along the transverse "y" direction is not as large as that along the x-direction, the magnitude of  $E_y$  is smaller than  $E_x$ . Finally, since electrons and holes are oppositely charged, their diffusion along the transverse direction gives rise to built-in fields  $E_y$  which are mutually anti-parallel. This is evident from Figure 8 as the  $E_y$  direction within the  $P^+$  region on the left is opposite that of the field direction in the N and  $N^+$  regions.

The transient current corresponding to this voltage waveform of Fig. 3 is shown in Figure 9. The initial spike represents a displacement current created in response to the voltage ramp from 0 Volts to 600 Volts. Following

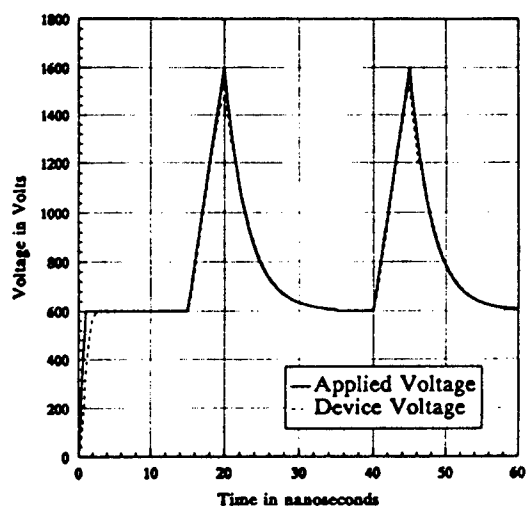


Fig. 3 Applied voltage waveform

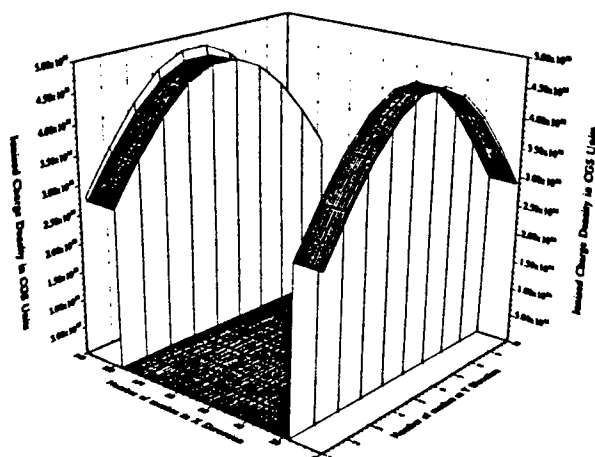


Fig. 4 Steady state ionized impurity profile for unbiased case I device

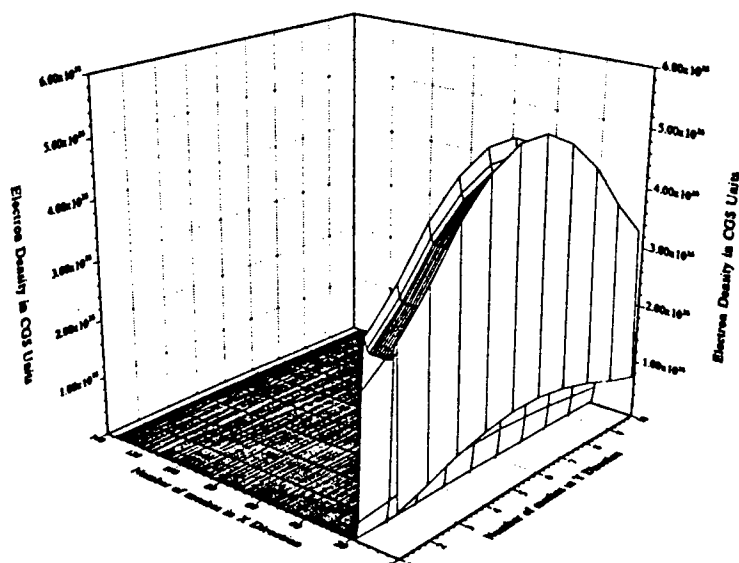


Fig. 5 Steady state electron distribution for unbiased case I device

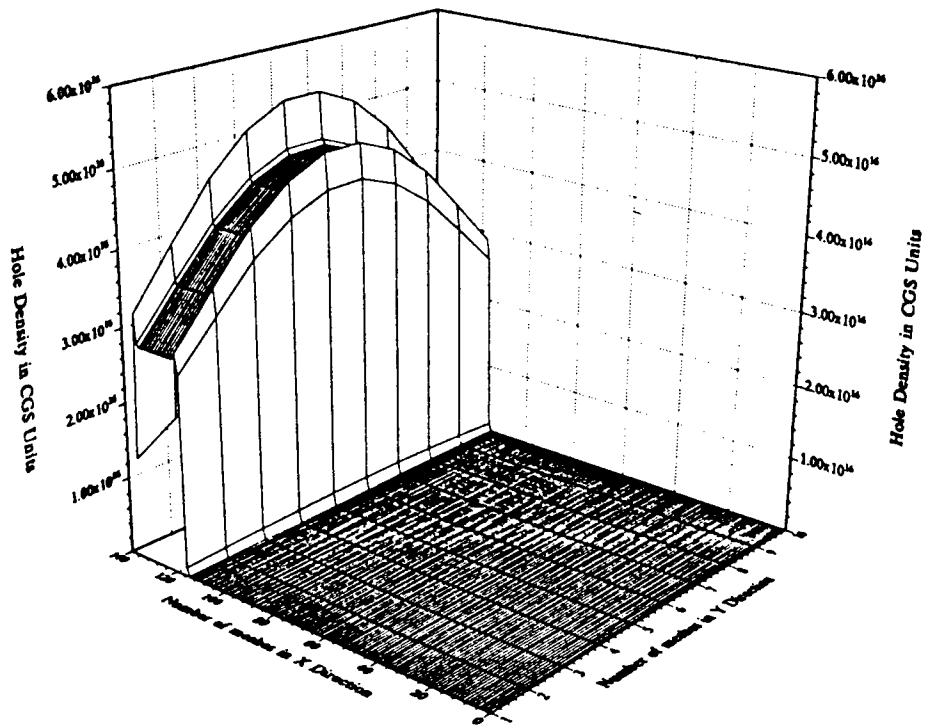


Fig. 6 Steady state hole distribution for unbiased SAS

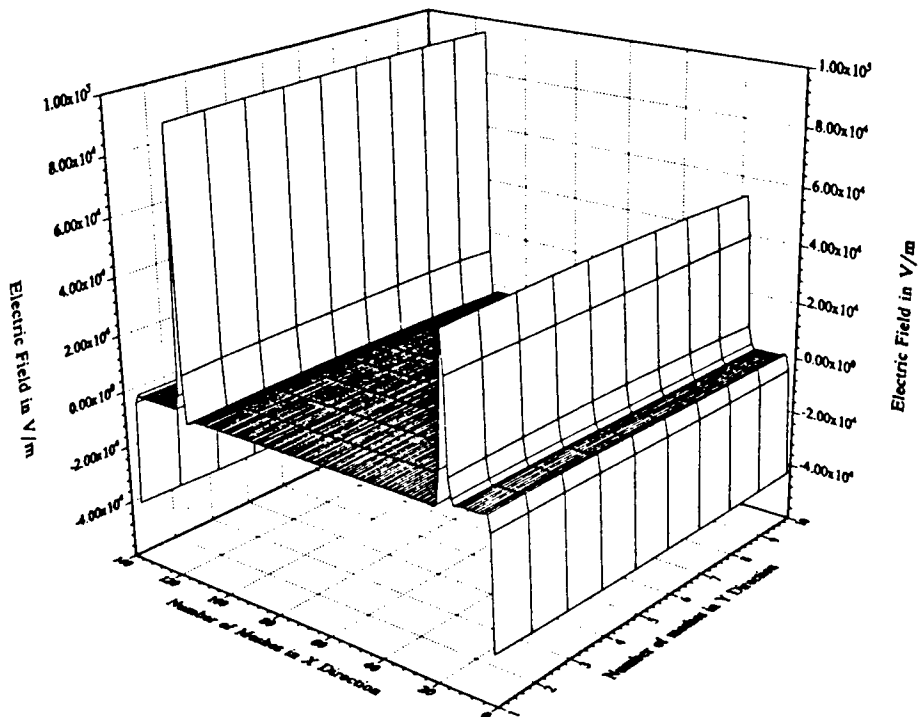


Fig. 7 Longitudinal electric field profile within the unbiased SAS device

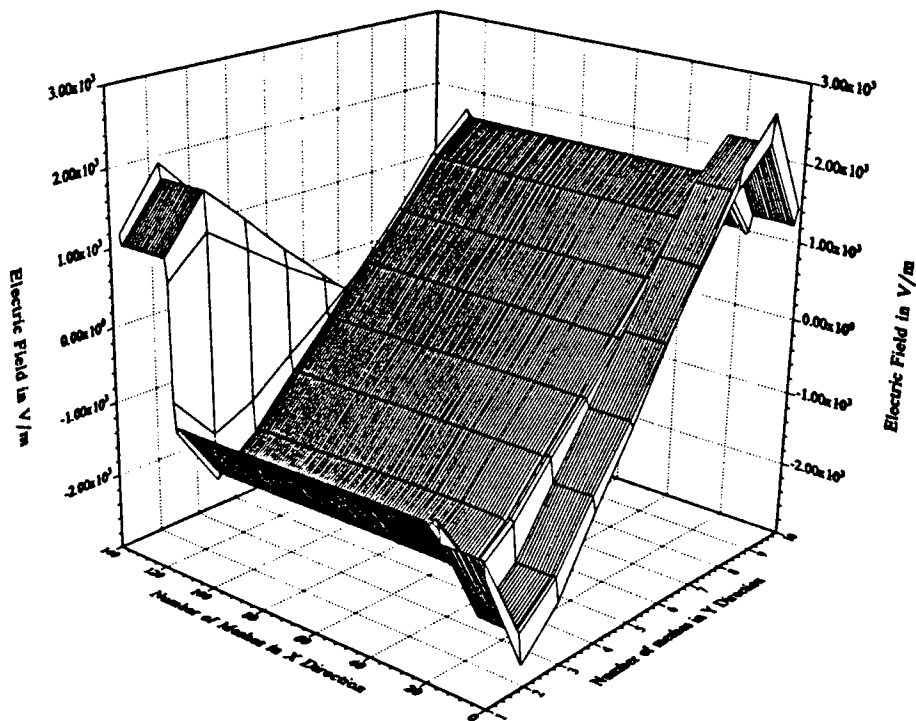


Fig. 8 Transverse electric field distribution for unbiased SAS device

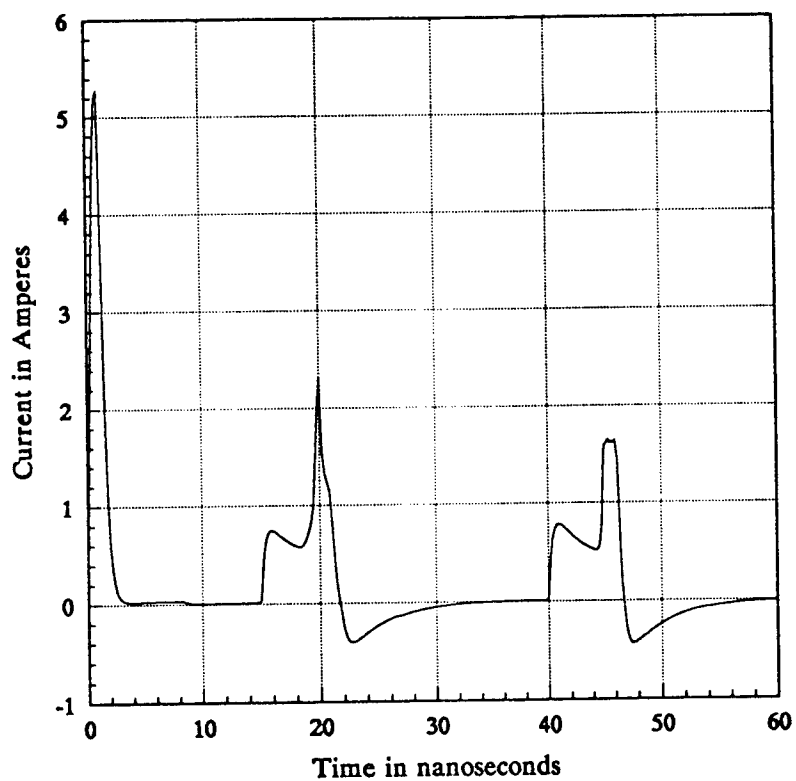


Fig. 9 Simulation results of the transient circuit current waveform

the initial build up of the internal fields and carrier densities within the device, a steady OFF state situation is reached and the current drops to near-zero levels. The current remains at this near-zero level until the application of the ionizing voltage ramp at 15 ns. The current then increases to about 0.5 Ampere, and is comprised of both the displacement and conduction components. Of these two, the displacement component gradually weakens as a steady state electric field distribution begins to be set up within the device. This gives rise to a slight decrease in the current from the 0.75 Ampere level to about 0.65 Ampere. At around 18 ns in time, the current is seen to begin increasing dramatically from its value of about 0.65 Ampere to a maximum of about 2.2 Amperes. This maximum occurs at 20 ns, and corresponds to the time at which the applied voltage is a maximum of 1600 Volts. The increased current is due to the initiation of internal impact ionization and the process of carrier avalanche.

Following a decay in the applied voltage, the current begins to decrease as expected. The current falls below zero at about 21 ns, and assumes a slight undershoot before settling to a near-zero level at around 32 ns. The negative current signifies that the SAS device is functioning as an active element and supplying power to both the resistor and the voltage element. Physically, the source of this power supply comes from the stored electromagnetic energy within the SAS device which had been built up during the applied voltage ramp. The undershoot characteristic and its duration is expected to depend on the actual circuit conditions. For instance, a higher value of the circuit resistance would lead to a quicker dissipation of the energy stored within the SAS device, and hence a less significant undershoot. Similarly, the presence of circuit inductances would also weaken the undershoot behavior.

The second current pulse appears to have a slightly lower peak than the first. This marginal variation between the first and second current pulses seems to suggest that a "short-term memory effect" is inherent in the SAS device. Such a memory effect is probably associated with the transverse propagation of both the electric field and the free carrier densities within the device during the turn-on cycle. The movement of carriers along the transverse direction distort the state of the semiconductor system. During the "turn-off" transient, changes in the electric fields are predominantly along the longitudinal direction since this is the orientation of the applied voltage. The result is a relatively fast redistribution parallel to the longitudinal axis leading to near complete recovery of the semiconductor system. However, the recovery and charge redistribution in the transverse direction is not as rapid. This occurs for two reasons. First, the electric field is changing at a very slow rate as there is no applied voltage in this direction. Second, since the values of the transverse field  $E_y$  are much smaller than those of  $E_x$ , the driving force for carrier movement and relocation is weak. Consequently, the inherent "relaxation time" or the duration necessary for bringing the semiconductor system back into the initial "OFF state" is quite large. From the simulation results, it appears that this time is more than 25 ns, since the SAS does not appear to have fully recovered at the start of the second pulse.

Results pertaining to the internal electric field are presented next. The longitudinal components of the electric field at 10 ns, 18 ns and 20 ns are presented in Figures 10-12. From these plots it is obvious that the internal field grows and propagates from the P<sup>+</sup>-N junction on applying the biasing pulse. A travelling electromagnetic wave

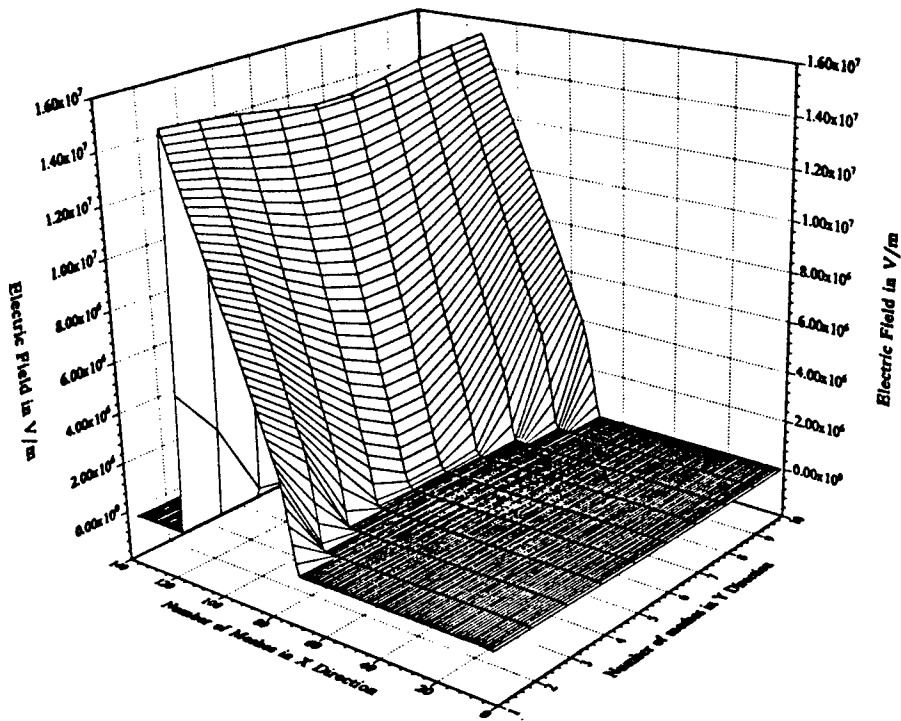


Fig. 10 Snapshot of the longitudinal electric field at 10 ns

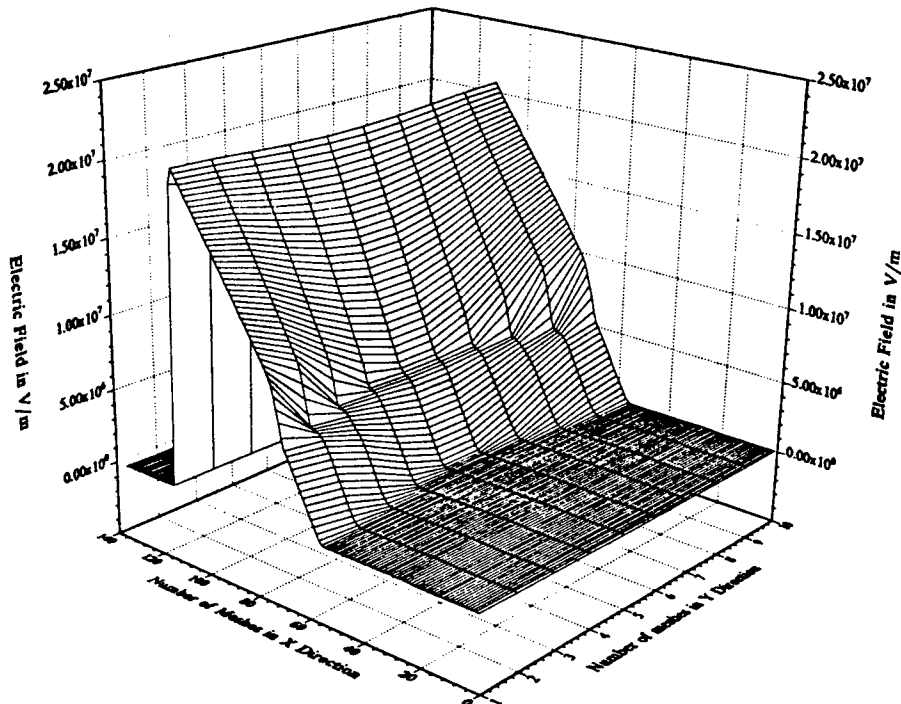


Fig. 11 Snapshot of the longitudinal electric field at 18 ns

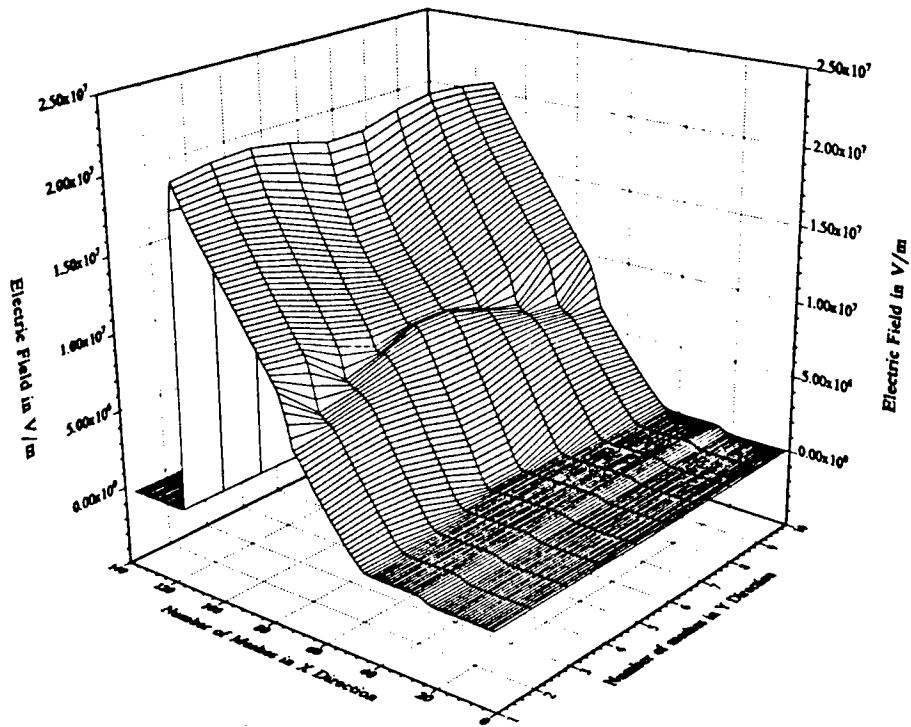


Fig. 12 Snapshot of the longitudinal electric field at 20 ns

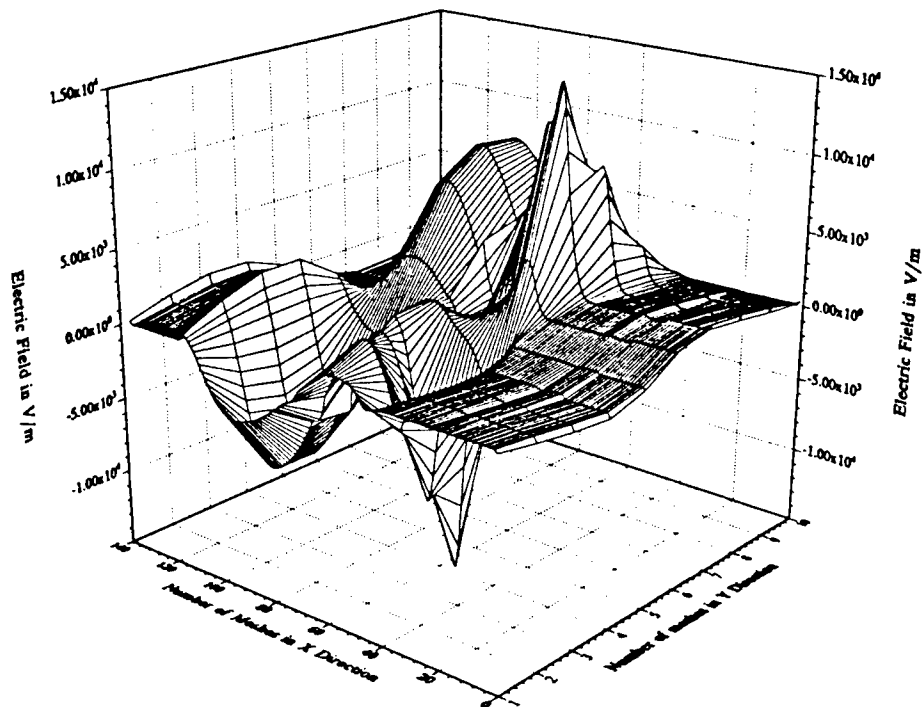


Fig. 13 Snapshot of the transverse electric field at 20 ns

is thus evident. From Figure 12, this  $E_x$  wave is seen to develop a distinct hump near the center of the device at 20 ns. As a result of this hump, the field magnitude over the central portion of the P<sup>+</sup>-N junction boundary in Figure 12 is not as high as at the two ends. This is in keeping with the requirement that the line integral of the longitudinal field  $E_x$  have a constant value across all paths parallel to the longitudinal axis. Since the electric field increases at the central portion of the device over the central axis, its value on the central axis at the P<sup>+</sup>-N junction is relatively lowered to maintain the path independent requirement.

The snapshot of the transverse field component at 20 ns has been shown in Figures 13. The values are much smaller than those of  $E_x$  at the corresponding times as may be expected. The temporal development of  $E_y$  reveals the formation and movement of an electron wave, and can be understood based on the following physical sequence of events. Application of the initial voltage ramp from 0 Volts to 600 Volts widens the depletion region as compared to the unbiased steady state. Electrons present on the N-side of the P<sup>+</sup>-N junction move away from the junction and into the N region. These carriers not only have a longitudinal motion into the N-region, but are also diffuse laterally away from the center. However, the net transverse current has to equal zero at all times since there is no conductive path in this direction. This forces a transverse electric field  $E_y$  to be built up for establishing a dynamic equilibrium with zero net current. The result is the formation of anti-symmetric peaks in Fig. 13 within the N-region, at locations away from the junction boundary. Since  $E_y$  is proportional to the negative gradient of the free carrier density, the profile is anti-symmetric relative to the central axis.

Figure 13 also reveals secondary bumps behind the anti-symmetric peaks. The secondary bumps are closer to the junction boundary and are caused by the injection of electrons into the N-region from the P<sup>+</sup>-N boundary. The bumps indicate that the transverse distribution of this wave of injected electrons is once again non-uniform leading to transverse diffusion. The bumps show that the electron injection responsible for creating the secondary  $E_y$  profile arises from impact ionization. This is based on the following argument. The P<sup>+</sup>-N junction prior to the start of the 1600 Volt voltage ramp is already in a state of depletion as a result of the 600 Volt reverse biasing voltage. It is thus incapable of supplying any free carriers. Hence, electronic injection can only arise from avalanching and impact ionization across the junction boundary.

The current distributions within the SAS device are shown in Figures 14 and 15. The longitudinal conduction current at 18 ns shown in Figure 14 is relatively large throughout the N<sup>+</sup> and the P<sup>+</sup> regions. This is expected since these regions have high carrier densities leading to large drift current contributions. The conduction current within the middle N-region, however, is negligible by comparison. Figure 15 at 20 ns reveals a general increase in the current. Within the N region, the conduction current increase is dramatic over the central axis. This can be attributed to three factors. The first arises from the movement of the existing mobile electrons within the N-region upon the application of the reversed biasing ramp. As these carriers move away, the depletion region begins to expand. Since the central region over the axis has the highest doping and hence the largest supply of mobile carriers, the conduction current is the largest over this section. The second factor arises from electron injection from the P<sup>+</sup> side into the N-region. This mainly occurs over the central axial portion which has the highest

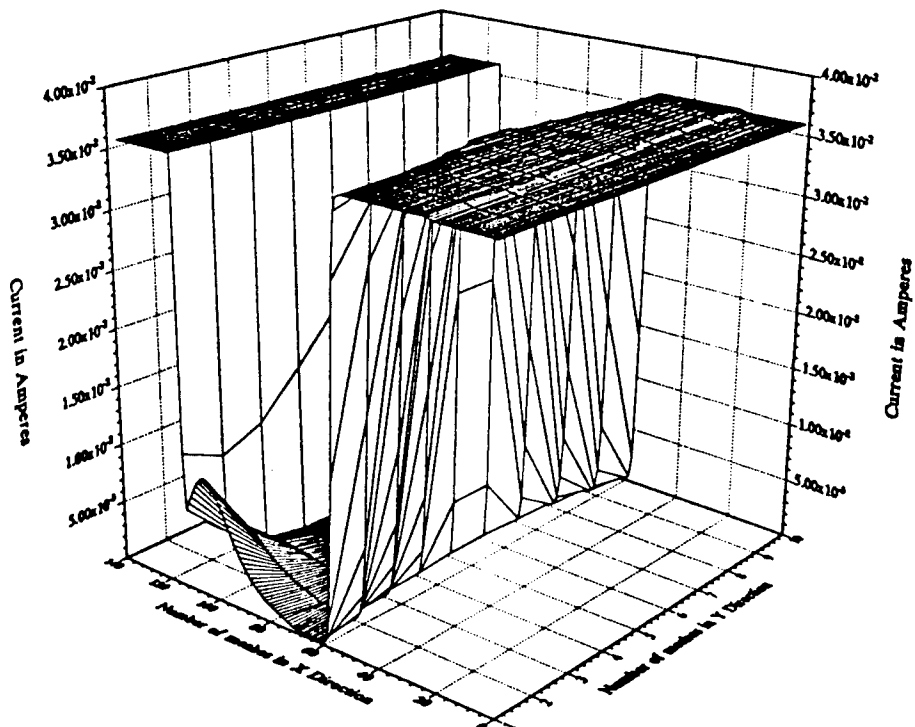


Fig. 14 Conduction current distribution within the device at 18 ns

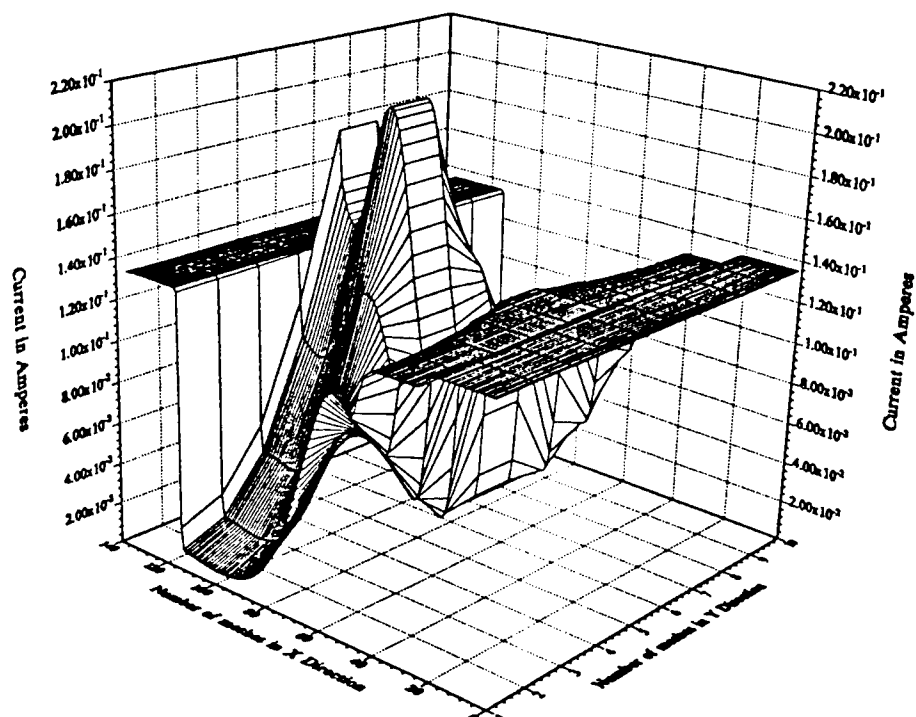


Fig. 15 Conduction current distribution within the device at 20 ns

supply of carriers to initiate impact ionization. The double humped structure on the axis is indicative of the finite time lag between the initial movement of electrons within the N-side as the depletion region increases, and the subsequent injection from the P<sup>+</sup>-N junction due to impact ionization. Thirdly, the strong increase in the longitudinal electric field  $E_x$  within the N-region, relative to the N<sup>+</sup> and P<sup>+</sup> regions also contributes to the high conduction current. This occurs because the drift velocity is appreciably enhanced as a result of the electric field increase which promotes a high drift current value. Figure 15 also reveals the presence of a highly non-uniform current distribution along the transverse dimension, and is indicative of a "filamentary mode". The central location of this current filament can be potentially detrimental, since it can lead to internal heating. Heat produced within the filament would be more difficult to dissipate through external cooling, given its central axial location. Had the filament been towards the outer boundaries, heat dissipation through external cooling schemes would be easier. The heating can potentially lead to a second breakdown and irreversible device failure. These results therefore indicate that SAS devices with large doping towards the central axis cannot be left in the "ON-state" for a long duration.

The total longitudinal current  $I_x$  as a function of the transverse direction at different times is shown in Figures 16 and 17. The plots show, as expected, that the current progressively increases as the biasing pulse is turned on. Furthermore, the longitudinal currents are all equal and there is no transverse variation. This result provides a consistency check for the 2D simulations employed here, since one expects the gradient of the total current to be zero based on the following argument. Basically, the total current has to be conserved,  $J^{\text{tot}} = J_x^{\text{tot}} + J_y^{\text{tot}} = \text{constant}$ . However,  $J_y^{\text{tot}} = 0$  since there is no conduction path along the transverse y-direction. Since  $J^{\text{tot}}$  is a constant, the curl of  $J^{\text{tot}}$  has to be zero. But the curl of  $J^{\text{tot}}$  equals:  $\mathbf{a}_z [dJ_y^{\text{tot}}/dx - dJ_x^{\text{tot}}/dy] = \mathbf{a}_z [0 - dJ_x^{\text{tot}}/dy] = -\mathbf{a}_z dJ_x^{\text{tot}}/dy$ . As a result,  $dJ_x^{\text{tot}}/dy = 0$  as borne out in the results of Figures 16-17.

## TWO-DIMENSIONAL RESULTS AND ANALYSIS: CASE II

Results for the second doping profile are examined next. This test case is the inverse of the previous profile, with the dopant density being centro-symmetric with a minimum level at the central axis and the maximum at the two end surfaces. Before discussing the results obtained, it is instructive to look at some of the obvious differences. First, we compare the average conductive ratio between the two cases by evaluating the dopant charge. Since the conductance "G" is proportional to the carrier density, a ratio of the conductances  $G_I/G_{II} = \rho_I^{\text{av}}/\rho_{II}^{\text{av}}$ . For the dopant distributions chosen here, this ratio works out to about 1.2 as given in equation (2). Designating  $L_T$  as the transverse length along the "y" axis, the conductivity ratio is given as:

$$\frac{G_I}{G_{II}} = \frac{\int_0^{L_T} dy \left[ \frac{1}{2} + \frac{1}{2} \sin\left(\frac{\pi y}{L_T}\right) \right]}{\int_0^{L_T} dy \left[ 1 - \frac{1}{2} \sin\left(\frac{\pi y}{L_T}\right) \right]} \approx 1.2 \quad (2)$$

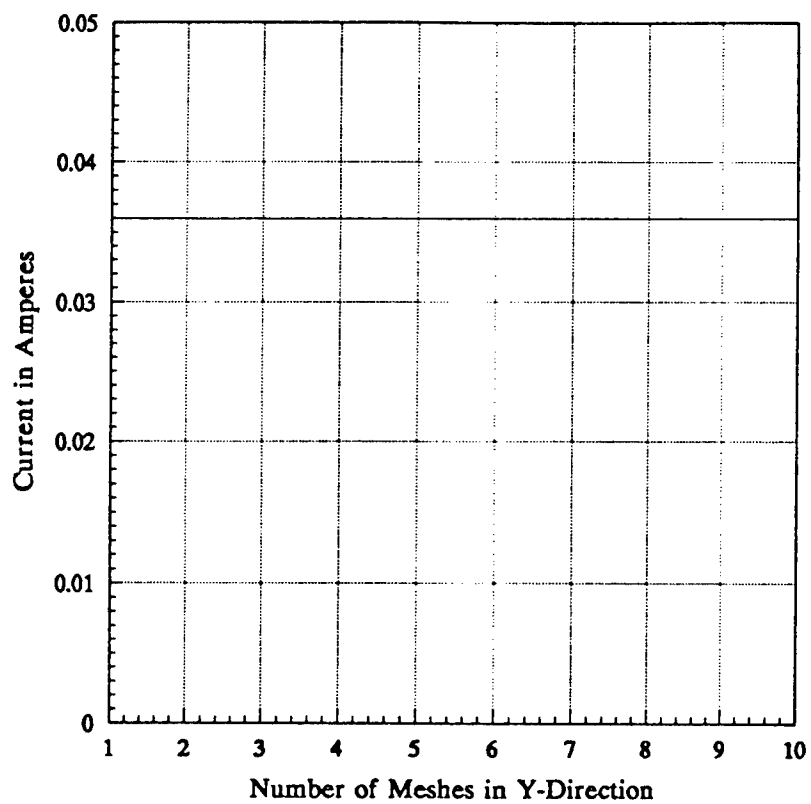


Fig. 16 Total current in the device at 18 ns as a function of the transverse axis

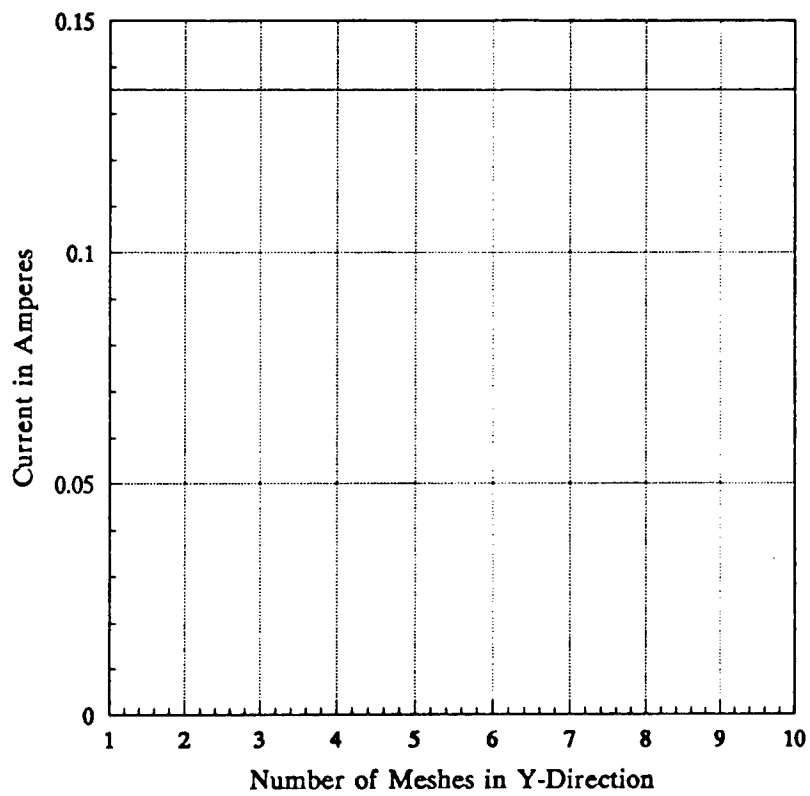


Fig. 17 Total current in the device at 20 ns as a function of the transverse axis

Hence, the average conductivity for case I is larger than that of case II. It is therefore follows that the circuit currents can be expected to be higher in case I as compared to case II. A second point pertains to anticipated relative values of the peak electric field within the device. Based on simple P-N junction theory, the maximum internal electric field  $E_{\max}$  at any voltage is a monotonically increasing function of the average doping density " $N_{\text{av}}$ ". Thus:  $E_{\max} \propto [N_{\text{av}}]^{0.5}$ . This implies that the peak electric field for case I would be higher than those for case II. As a result, impact ionization and the launching of an electron wave is expected to be relatively strong for case I and not as dominant for the case II device.

Simulation result for the initial unbiased steady state ionized density distribution within the SAS device is shown in Figure 18. This profile is in keeping with the chosen centro-symmetric distribution. The peak magnitude of the ionized impurity density nearly equals  $5 \times 10^{16} \text{ cm}^{-3}$  which is the maximum concentration of dopant atoms, and occurs at the two edges. The transient current corresponding to the voltage waveform of Fig. 3 is shown in Figure 19. This plot differs from the corresponding results for case I in two respects. (i) First, the value of the circuit currents for case II are generally lower than those for case I. For instance, the initial displacement current spike is about 5.2 Amperes in case I but only 3.6 Amperes in case II. The maximum currents during the applied voltage pulse at about 20 ns and 46 ns are also smaller for case II. These decreased current magnitudes are the result of a lower average conductance  $G_{\text{II}}$  for case II as compared with case I. Such a result is expected and was briefly discussed above through equation (2). (ii) Next, the sharp current pulses produced around 20 ns and 46 ns during the voltage ramps in case I are absent in case II. Instead, a broad current pulse having a 5 ns time duration results in case II. The production of such a broad pulse is not very useful for pulse shaping applications. The absence of a sharp current peak in case II suggests a lack of strong impact ionization and internal avalanching. This result is a direct consequence of a lower average device doping which leads to lower values of the maximum electric field  $E_{\max}$  as has been discussed above. These lower field values preclude the onset of strong avalanching, and the launching of a rapid ionization wave. Given this lack of strong internal ionization, the current waveform only displays an initial displacement current rise at around 15 ns and 40 ns as the voltage ramp is applied. This is followed by a monotonic decrease as the voltage drop across the 50 Ohm series resistor increases.

Results of the internal electric field  $E_x$  at 10 ns and 20 ns are presented in Figures 20 and 21. These plots reveal growth and propagation of an internal field. This growth and propagation occurs mainly towards the outer edges. Correspondingly, the values of the electric field over the outer portions at the  $P^+$ -N junction boundary in Figure 21 are not as high as those over the center. This is in keeping with the requirement that the line integral of the longitudinal field  $E_x$  have a constant value across all paths parallel to the longitudinal axis. The primary difference between Fig. 21 and the case I plot of Fig. 12 lies in the magnitudes of the electric field. The peak values in Fig. 21 are at about  $1.7 \times 10^7 \text{ V/m}$ , while those of Fig. 12 are at  $1.85 \times 10^7 \text{ V/m}$ . The lower values of the maximum field work to dramatically reduce the impact ionization since the process has an exponential dependence on the electric field. As a result, ionization and avalanching in the device of case II is not as strong, and does not give rise to a sharp current amplification.

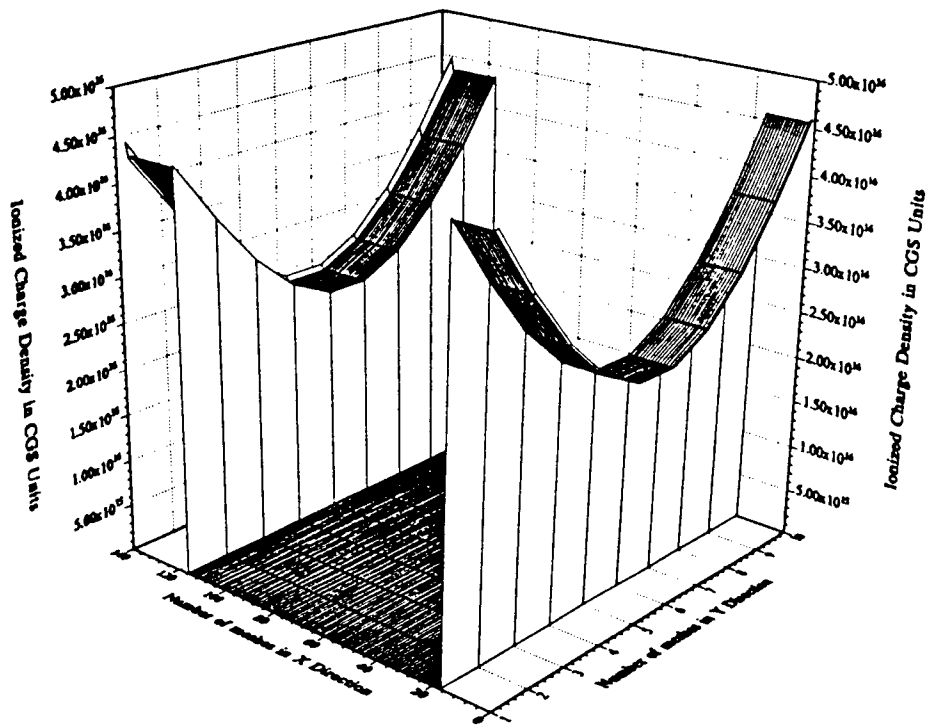


Fig. 18 Steady state ionized impurity profile for case II unbiased device

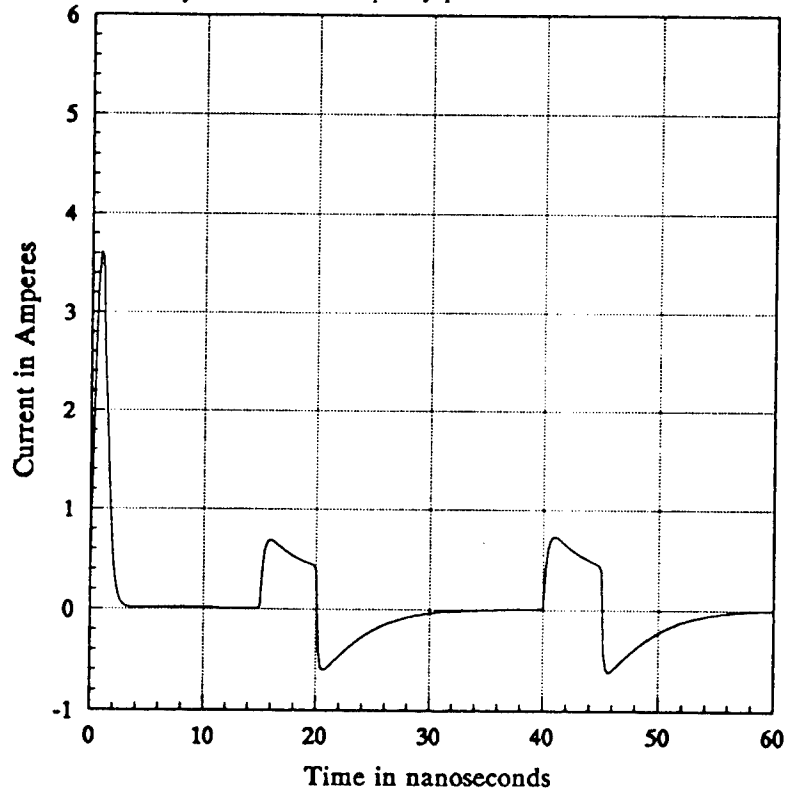


Fig. 19 Simulation results for the transient circuit current waveform

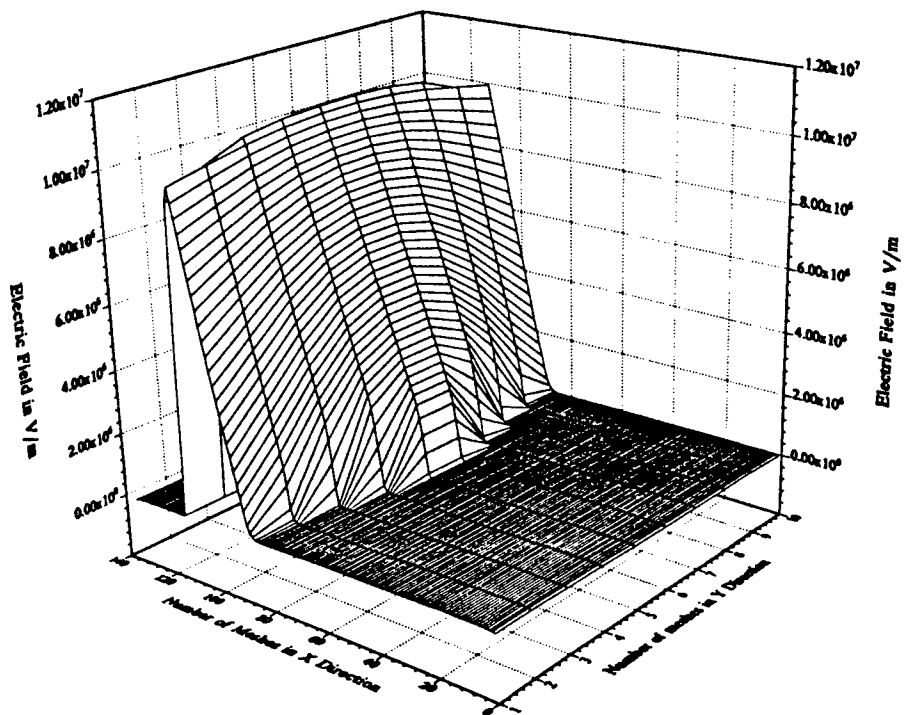


Fig. 20 Longitudinal electric field distribution at 10 ns

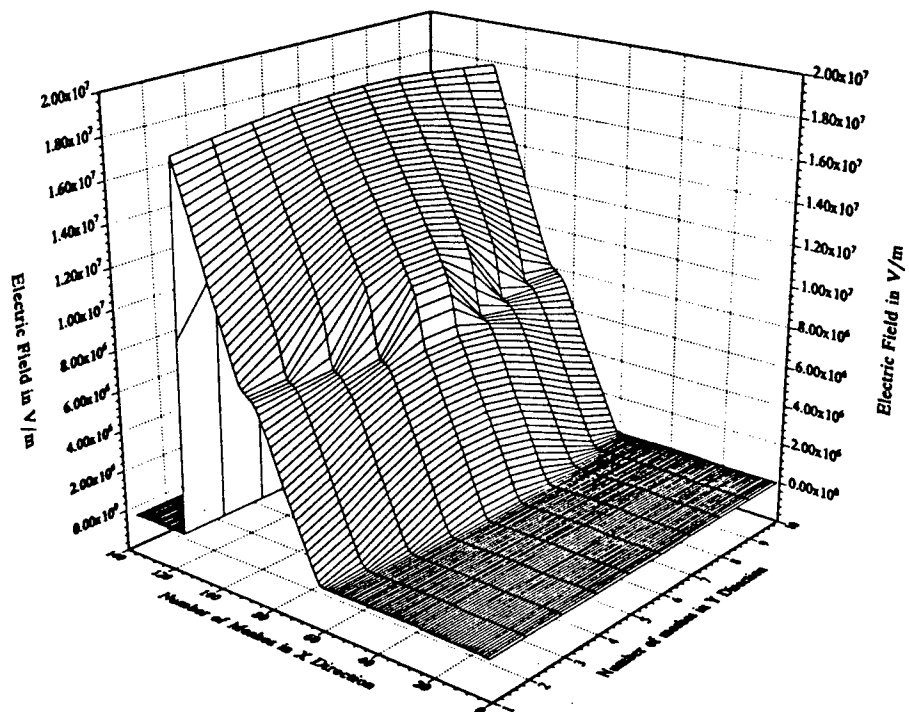


Fig. 21 Longitudinal electric field distribution at 20 ns

Snapshot of the longitudinal conduction current at 20 ns within the SAS device is shown in Figures 22. The plot shows that the conduction current is relatively large throughout the  $N^+$  and the  $P^+$  regions as expected due to the large supply of free carriers. However, in the middle N-region, the current is almost negligible. Furthermore, no filamentary growth or localized current flow enhancements are evident. This result is completely different from that obtained in Fig. 15.

### **TWO-DIMENSIONAL RESULTS AND ANALYSIS: CASE III**

Simulation results for the asymmetric doping profile are examined next. This case represents an aberration in the doping distribution. The ionized dopant distribution is shown in Fig. 23. In this case the total dopant charge inside the device is greater than both of the two previous cases. As a result, the device conductance "G" is correspondingly higher, implying that the circuit currents can be expected to be higher than previously obtained. Since the average dopant densities are higher, the peak electric field values within the device should also be larger. This is indicative of a much stronger impact ionization.

The transient SAS circuit current is shown in Figure 24. The values of the circuit current are much higher than those for cases I and II. For instance, the maximum currents during the applied voltage pulse at about 20 ns and 46 ns are about 4 and 5 Amperes, as compared to 2.2 and 1.8 Amperes for case I. Such high values of the current are associated with the large device conductance and the ability for strong impact ionization on the basis of larger electric fields.

Results of the internal electric field  $E_x$  at 18 ns and 20 ns are presented in Figures 25 and 26 which show the propagation on an internal electric field wave. The electric wave, however, does not move into the N-region in a uniform manner. Instead, its dynamics and propagation is determined by the doping non-uniformity along the transverse direction. For example, the region of highest doping occurs over a longitudinal strip located between meshes 7 and 9 along the Y-direction. The electric field at the  $P^+$ -N junction is therefore highest over Y-meshes 7 to 9, with the smallest penetration into the N-region. The small penetration is the result of a large slope in the  $E_x$  profile, since the slope is proportional to the ionized dopant density in accordance with Gauss' law. Similarly, values of the electric field maxima at the  $P^+$ -N junction, away from the strip between Y-meshes 7 through 9, are not as large. However, the field extends deeper into the N-region due to the smaller slope in  $E_x(x)$  associated with the smaller ionized dopant density. On application of the voltage pulse, the fields begin to increase in magnitude and spread into the N-region. However, the wavefront moves non-uniformly along the transverse direction. Electric field propagation into the N-region over the strip between Y-meshes 7 to 9, is the slowest because of the high doping. The peak value, on the other hand, exhibits a fast growth as seen in Fig. 25. Conversely, the propagation and spreading of the electric field over the regions outside the high doping strip is much faster, even though the peak field values do not increase quite as much. This behavior is evident in Fig. 25 which shows an  $E_x$  wave moving faster in an asymmetric fashion. At 20 ns, this non-uniform movement is even more apparent. A distinct hump is seen towards the left surface of the device roughly given by mesh coordinates  $X = 80$ ,  $Y = 2$ .

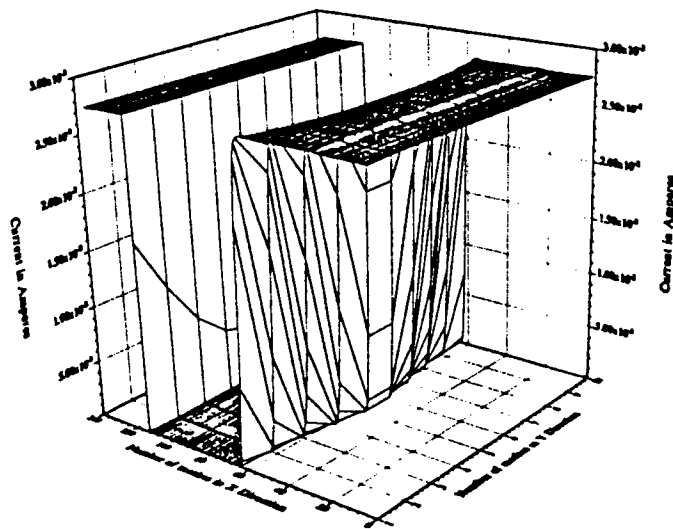


Fig. 22 Longitudinal conduction current distribution within SAS device

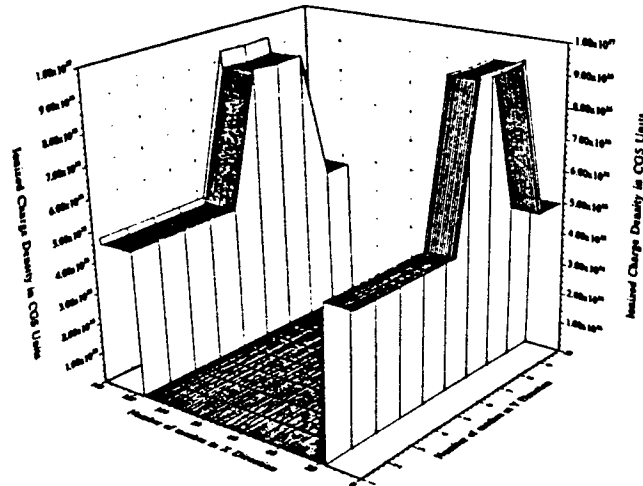


Fig. 23 Steady state ionized impurity profile for unbiased case III device

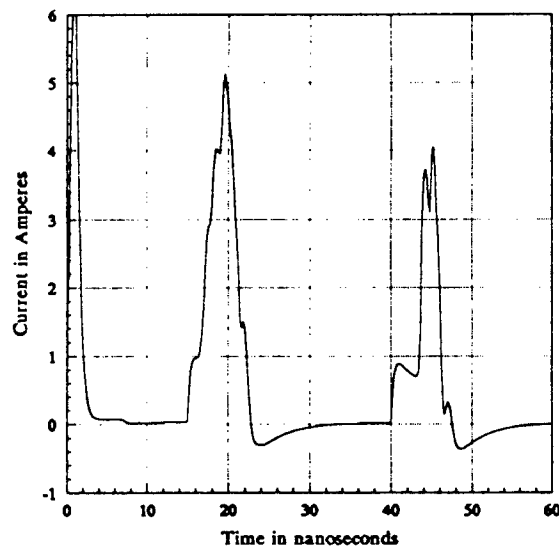


Fig. 24 Transient SAS circuit current for device having case III profile

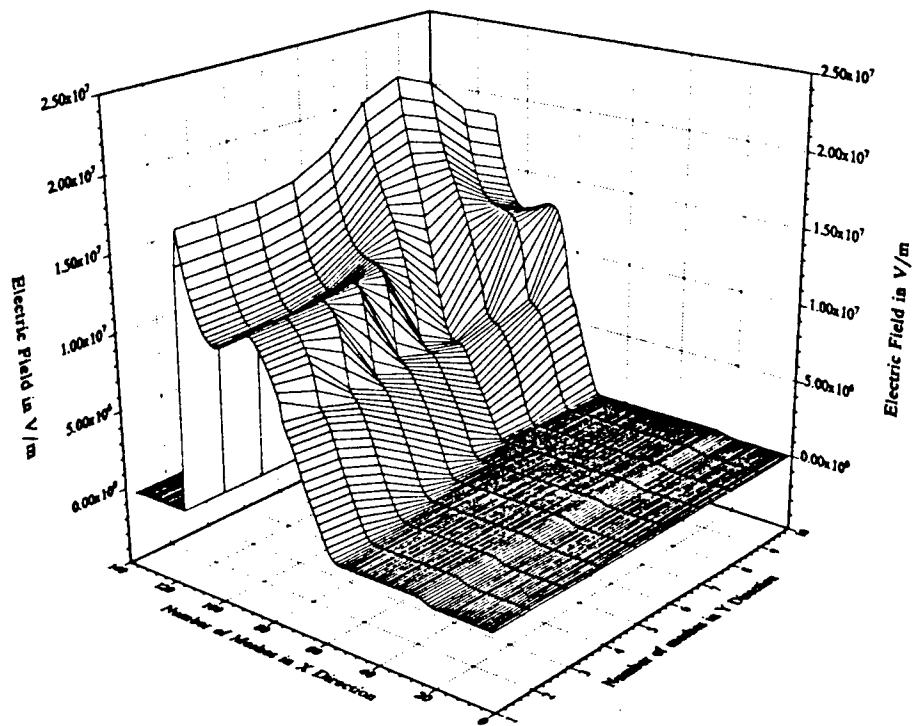


Fig. 25 Longitudinal electric field distribution at 18 ns

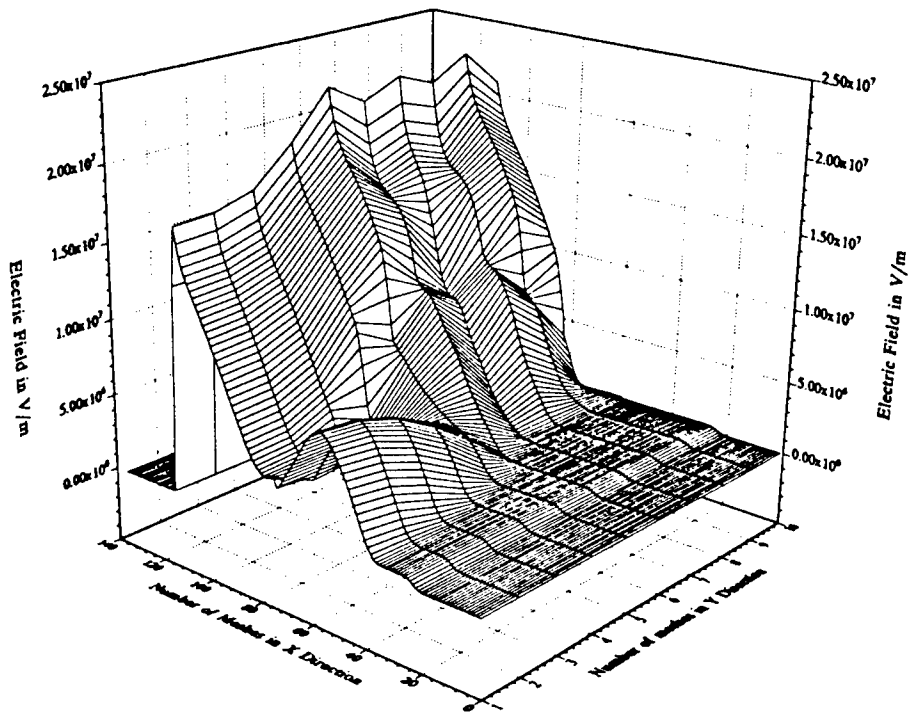


Fig. 26 Longitudinal electric field profile at 20 ns

Finally, plots of the longitudinal conduction current at 20 ns are shown in Figs. 27. The plot indicates that unlike the previous cases, the conduction current is not largest within the  $N^+$  and the  $P^+$  regions. This is due to the relatively negligible electric fields  $E_x$  in these regions which reduces the carrier drift velocities, and hence the conduction current, to negligible levels. Instead, there are two localized areas of large conduction current. These occur within the N-region near the  $P^+$ -N junction at the two transverse ends, and are removed from the asymmetric highly doped strip. These areas of high conduction current are also seen to be moving towards the  $N^+$  region. This movement is brought about by the propagating electric field.

There is some similarity between this situation and that chosen for case I. Both involve convex shaped transverse doping profiles with minima at the two outer boundaries. One might therefore expect the conduction current distributions to be somewhat similar. However, a comparison of Figs. 27 and 15 shows that this is not the case. For example, while case I exhibits a partial conductive filament at the central axis, most of the conduction current in Fig. 27 occurs towards the two boundaries away from the center. This difference can be attributed to the following features: (i) The existence of a much stronger transverse diffusive process as compared to case I, due to the sharper gradient in the doping profile. This diffusion works to force mobile carriers away from the higher doped asymmetric longitudinal strip, towards the outer boundaries more efficiently. (ii) The presence of much higher values of the maximum electric fields  $E_x$  throughout the  $P^+$ -N junction as compared to case I. The doping for case III is the same or higher than that of case I for all points. The higher fields lead to exponential increases in the ionization coefficients.

The two factors mentioned above work to produce the following sequence within the N-region. As the turn-on voltage ramp is applied, the mobile carriers that lie just outside the  $P^+$ -N depletion region begin moving. This produces a conduction current wave and the free carrier density begins to increase within regions to the right. However, the process of diffusion which is strong in this case (but not for case I), forces the excess carriers away from the asymmetric high doped longitudinal strip and towards the outer boundaries. With time, the internal electric fields increase leading to larger values of  $E_{max}$  at the  $P^+$ -N junction boundary and the fields expand deeper into the N-region. The former initiates the impact ionization process and promotes electron injection into the N-region. The latter enhances the local drift velocity values, significantly increasing the drift velocity and hence the conduction current. However, since the electric field does not move as fast nor does it increase as much over the asymmetric strip, the growth in the drift velocity is not quite as large. Besides, strong carrier diffusion forces the mobile carriers away from the strip and towards the two boundaries.

The occurrence of a crest in the conduction current of Fig. 27 signifies the formation and movement of single electronic wavepacket. The production of only a single wavepacket or electronic swarm is influenced by the internal polarization effect. As the electrons get injected into the N-region from the  $P^+$ -N junction following impact ionization, the value of the maximum electric field begins to collapse due to the polarization. This reduces the fields below the impact ionization threshold, and prevents the subsequent and continuous launching of electron waves into the N-region. As a result, only one swarm or packet of electrons is injected into the N-region. Furthermore, the

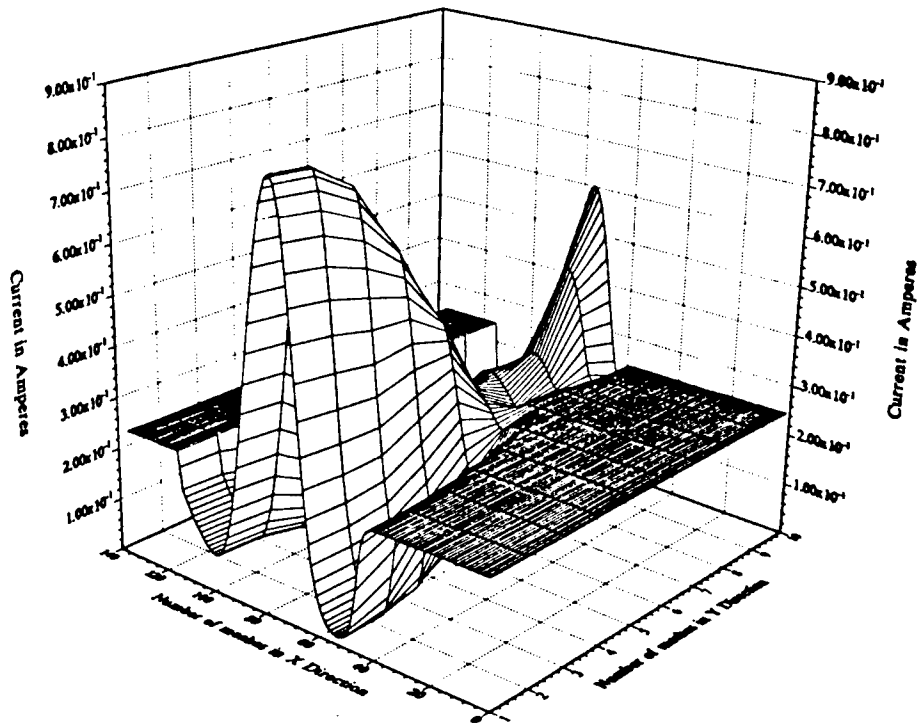


Fig. 27 Snapshot of the longitudinal conduction current within the SAS device at 20 ns

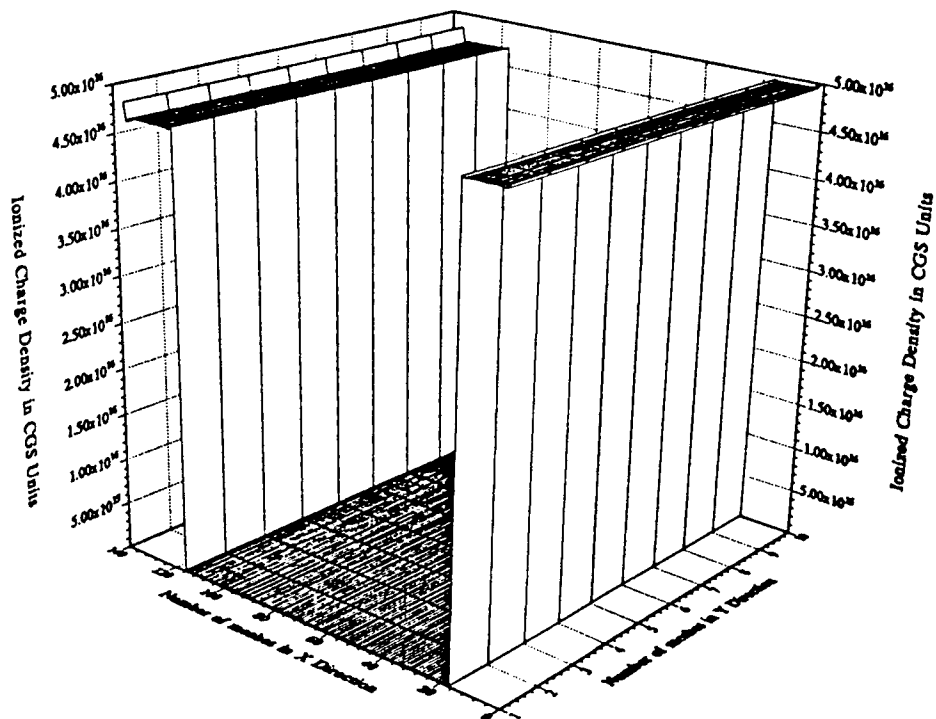


Fig. 28 Ionized impurity profile in steady state for unbiased case IV device

reduction in the applied bias at 20 ns, also has the effect of shutting off the impact ionization process.

#### **TWO-DIMENSIONAL RESULTS AND ANALYSIS: CASE IV**

Finally, 2D simulation results for an SAS device having a uniform dopant profile along the transverse direction were also obtained for completeness. Fig. 28 shows the density of internal immobile charge, which has no variations along the transverse direction as expected. The transient current of Figure 29 shows a behavior somewhat similar to that of Fig. 9. The growth and propagation of an electric field wave starting from the P<sup>+</sup>-N junction is evident in Figs. 30 and 31. Again there are no variations along the transverse axis due to the uniformity of the dopant profile. This leads to near-zero transverse electric fields  $E_y$  within the device at all times as shown in Fig. 32. Finally, the conduction current distributions within the simulated SAS device at two different times during the applied voltage pulse are shown in Figs. 33 and 34. From the plot of Fig. 33 it can be seen that the conduction currents within the P<sup>+</sup> and N<sup>+</sup> regions are almost equal and uniform. Since a high density of free carriers is available in these regions, the drift (and hence the conduction current) component dominates and is nearly equal to the total current  $I_T$ . Requirement of current continuity and the conservation of total current  $I_T$  therefore dictates that the conduction currents in the P<sup>+</sup> and N<sup>+</sup> regions nearly equal  $I_T$  and hence match each other. The current within a portion of the N-region that lies towards the N-N<sup>+</sup> boundary is also composed mainly of the drift current. This region is just beyond the P<sup>+</sup>-N depletion boundary, and has a supply of free electrons available for conduction. Even though their densities are slightly lower than those within the N<sup>+</sup> and the P<sup>+</sup> regions, a larger drift velocity driven by higher electric fields compensates for the difference. This occurs because the electric field increases more quickly in the N-region than in either of the P<sup>+</sup> or N<sup>+</sup> regions. However, the absence of free within the depletion region near the P<sup>+</sup>-N junction, leads to near-zero conduction current levels. This is clearly evident in Fig. 33. At a later time of 20 ns, the process of avalanching and electron injection over the P<sup>+</sup>-N junction changes the conduction current distribution. As the electric field at the P<sup>+</sup>N junction increases and crosses the impact ionization threshold during the voltage ramping, a wave of electrons is injected into the N-region. This produces two effects: (i) The drift component is increased within the N-region lying near the P<sup>+</sup> boundary, and (ii) The rate of increase in the electric field is lowered. This decrease in the rate can also be viewed as a polarization effect. Suppression of the electric field due to this polarization effect, prevents the subsequent launching of electron waves into the N-region. Furthermore, turning off the applied voltage at 20 ns, also precludes a continuous and steady electron injection. As a result, only one swarm or packet of electrons are injected into the N-region. A high conduction current is associated with this electron packet as it moves in the N-region towards the N<sup>+</sup> side. This appears in the snapshot picture of Fig. 34 as the crest of a conduction current wave located near the P<sup>+</sup>-N boundary.

#### **SUMMARIZING CONCLUSIONS**

In this research, a two-dimensional simulator for the SAS device has been developed based on the drift-diffusion model. It represents the first attempt to obtain accurate device performance predictions and the anticipated

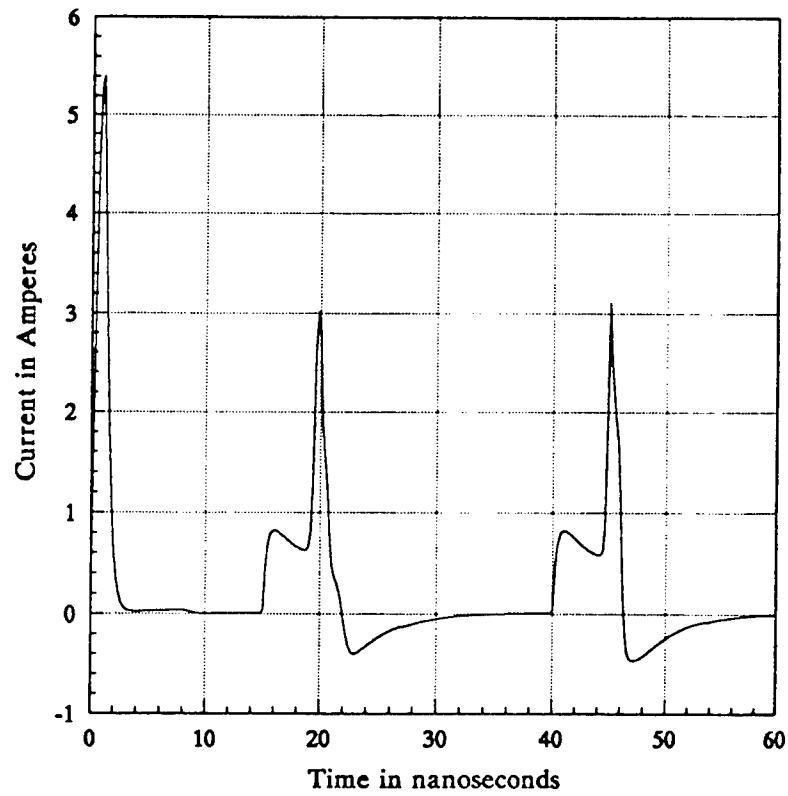


Fig. 29 Transient circuit current waveform for the case IV SAS device

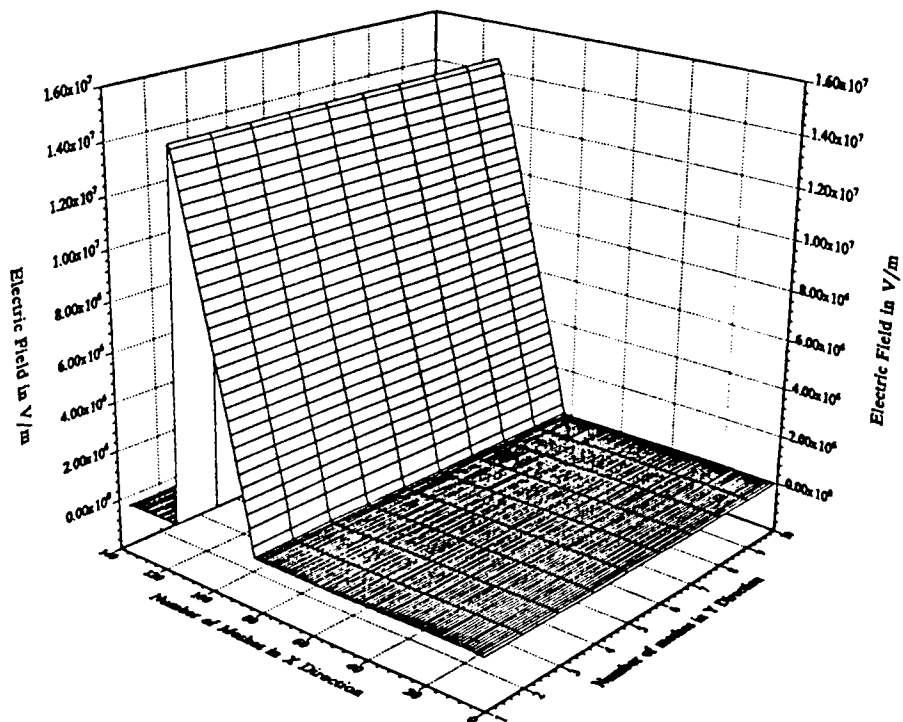


Fig. 30 Longitudinal electric field distribution at 10 ns

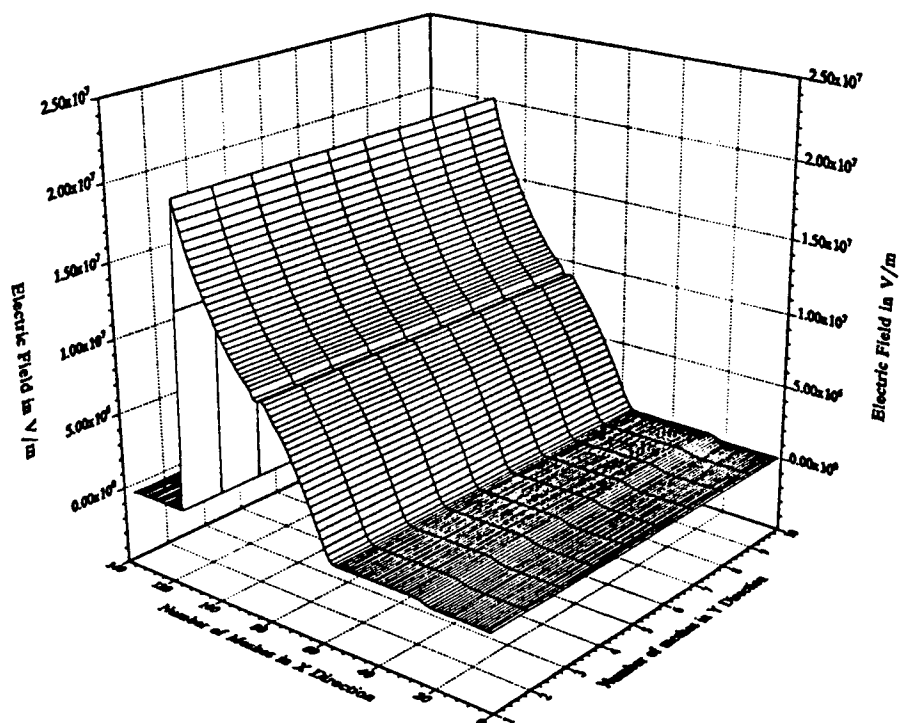


Fig. 31 Longitudinal electric field profile at 20 ns

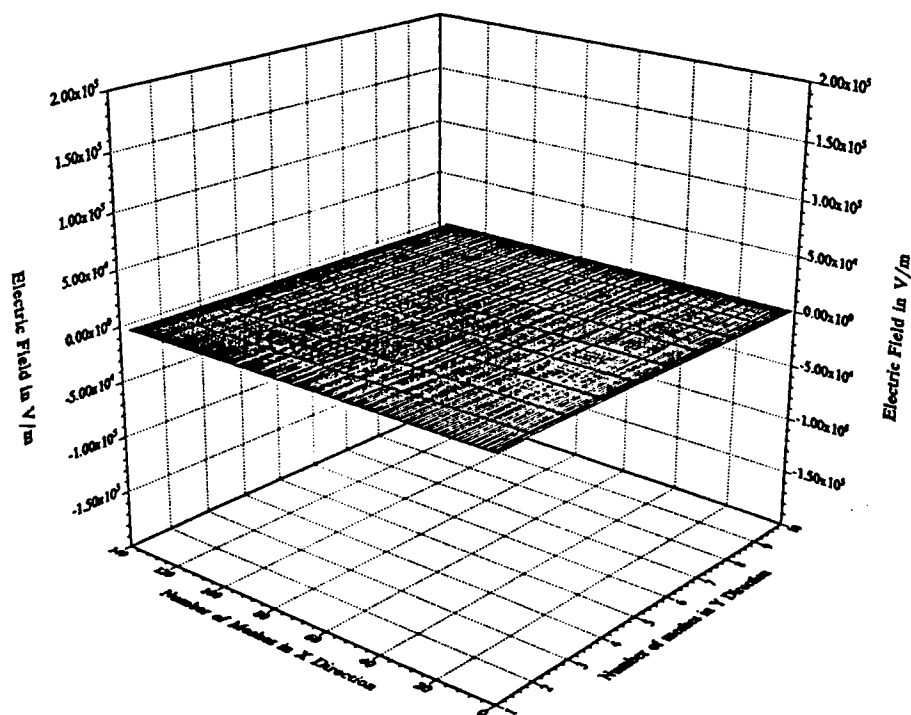


Fig. 32 Transverse electric field distribution within the case IV device at 10 ns

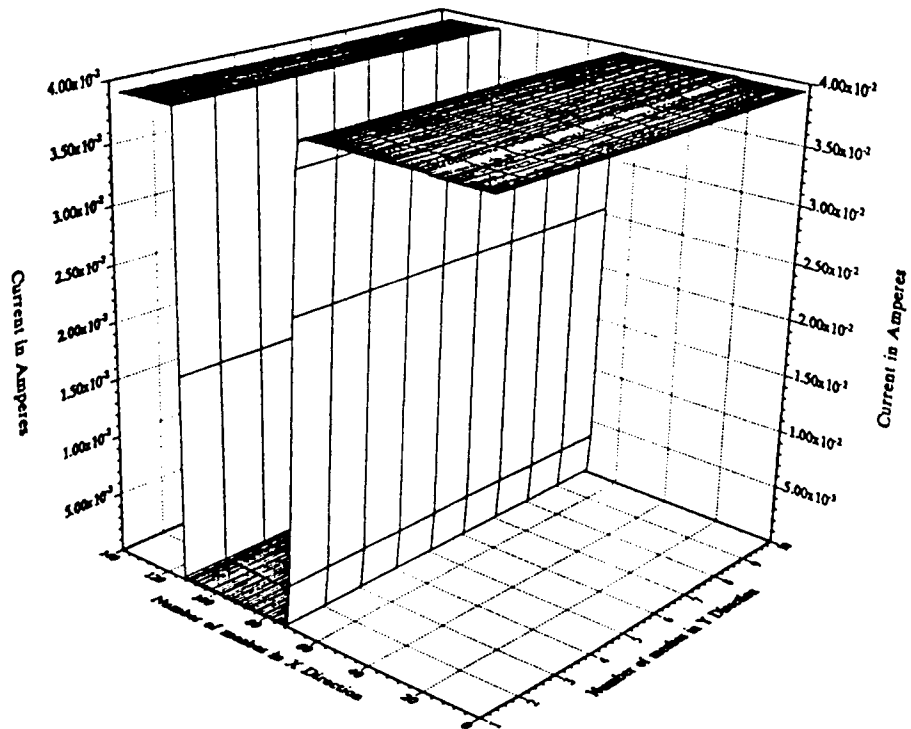


Fig. 33 Conduction current distribution within the SAS device at 18 ns

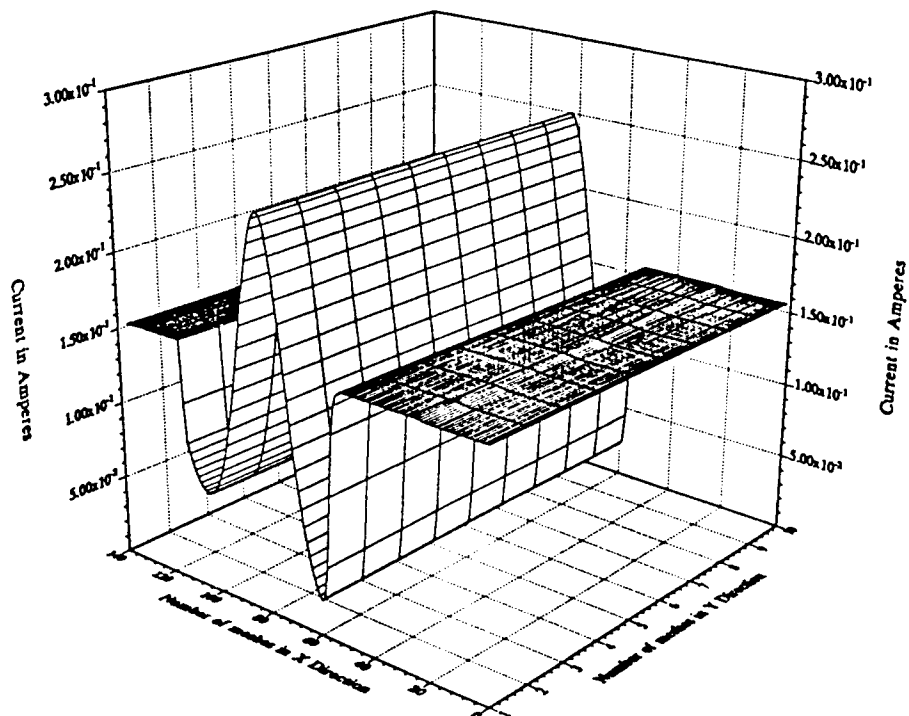


Fig. 34 Conduction current distribution at 20 ns

transient response. The 2D semiconductor model was successfully implemented into a numerical code. The role of transverse variations in the doping profile were then analyzed by obtaining the transient current characteristics. Four different doping profiles were studied through the numerical simulations. The dynamics of development, growth and propagation of internal electric field waves were also analyzed. These studies provide useful insight into the physics of the avalanche process. Finally, predictions of potential current filamentation within the device for a given doping profile were obtained. Simulation data for the conduction current distribution within the device at various time instants, clearly showed the possibility of filamentary mode growth.

A number of important conclusions can be drawn from the results presented in the previous chapter. The main deductions and salient features are as listed below.

- (1) The dopant densities are seen to strongly affect the circuit currents by controlling the device conductance. Both the magnitude and the temporal shape can vary dramatically with changes in the doping profiles. In general, the current magnitudes are higher for larger doping. This is the combined result of two factors: (i) An increased conductance which reduces the overall resistance in the circuit, and (ii) the increased value of the electric field at the p-n junction which enhances impact ionization.
- (2) Current pulses having durations in the sub-nanosecond range were seen to result upon the application of much broader voltage pulses. However, there seems to be a trade-off between current pulse sharpness and the potential for instability linked to current filamentation. Sharp and narrow current pulses, are associated with the growth of filamentary currents. The sharp pulses were the direct result of strong impact ionization and avalanche action. However, the avalanche process can be very non-uniform due to doping variations giving rise to localized surges in the conduction current. Though such localized current may not be detrimental over a short duration, the device could be destroyed during repetitive operation as a result of prolonged internal heating. The absence of sharp current pulses, on the other hand, provides for more stable operation.
- (3) Evidence of a distinct electric field wave propagating from the cathode to the anode of the SAS device was presented through the various simulations. The movement and propagation of the electric field wave was seen to be non-uniform in general, and dependent on the doping variations along the transverse dimension. Larger values of the doping created a slower moving wave since the associated depletion regions did not increase quite as rapidly.
- (4) Associated with a propagating electric field wave, was a travelling conduction current. For "near-uniform" profiles along the transverse direction, the conduction current was seen to develop over regions of highest doping density, and to propagate away towards the anode. Furthermore, this conduction current was due to mobile electrons. This result seems to suggest that slight increases in the dopant density over the central portions of the SAS device could potentially be detrimental. The corresponding conduction current increases and possible temperature enhancements over the central portion, would be more difficult to control or quench. Dopant density increases near the outer surfaces or peripheral regions might present a less acute

problem since the associated temperature enhancements could be controlled through external cooling. Fortunately, the doping profiles resulting from the diffusion process naturally provide such doping enhancements over the peripheral regions.

- (5) Carrier diffusion was seen to be important for profiles having strong gradients in the doping profiles. For instance, results of the previous section showed that localized areas of high conduction currents could arise in regions with moderate doping. This was caused by rapid transverse diffusion. This suggests that there is an optimal gradient of the doping along the transverse direction which would lead to a more uniform current flow. Since "near-uniform" profiles cause filaments over regions of highest doping, while sharp gradients give rise to filaments over regions of relatively low doping, a moderate gradient would lead to a more even current distribution.
- (6) The impact ionization and avalanching processes within the SAS device are caused by holes rather than electrons. During the turn-on transient, holes move from the N-region towards the P<sup>+</sup> side of the junction in response to the voltage pulse. The reason that holes dominate the carrier generation process as compared to electrons, is associated with the doping densities on either side of the P<sup>+</sup>-N junction. The minority electron densities on the P<sup>+</sup> side are relatively much smaller than the minority hole densities on the N-side. Consequently, on applying the voltage ramp, more minority holes are able to traverse the high field region at the P<sup>+</sup>-N junction boundary from the N-side, than minority electrons from the P<sup>+</sup>-side. As a result, carrier generation is facilitated mainly by the overwhelming population of moving minority holes.
- (7) Finally, the SAS devices were seen to require at least 25 ns to make a complete recovery to their original state following a voltage pulse. This time is expected to increase with the transverse dimensions of the device. Such increments in the transverse device dimensions may be necessary for enhancing the current carrying capability. However, by increasing the transverse dimensions, the recovery time would be adversely affected.
- (8) As regards the doping of the N<sup>+</sup> and P<sup>+</sup> contact regions, the simulation data suggests that increases in the concentration would lead to enhancements in the circuit currents. The process of impact ionization would also increase due to the higher values of the electric fields at the junction. Hence, a high doping density of about  $10^{18} \text{ cm}^{-3}$  at the P<sup>+</sup> and N<sup>+</sup> end regions, appears to be a desirable goal. These levels can realistically be attained through high temperature diffusion.

## SCOPE FOR FUTURE RESEARCH WORK

The research presented here focussed on developing numerical simulation codes for the two-dimensional modeling of the SAS switches. This technology has shown promise over other optical based switching approaches. The simulations developed here were meant to analyze a simple device geometry and to provide insight into the physics of device operation. The model was thus a first step towards the development of a more powerful two-dimensional device simulator. However, many other complicated features could be incorporated as additions to

enhance the utility and applicability of the simulator. Including the enhancements would constitute the next set of research tasks. A summary of the various tasks and the scope of future research are listed below.

- (i) Development of an enhanced two-dimensional model to include non-uniform device cross-sections. The non-uniform cross sections may be due to the planar processing techniques used during the fabrication process. In such a case, the two metallic contacts to the device would typically be placed on the same front surface. The cross-sections could also be non-uniform to suppress surface flash-over and dielectric breakdown. In order to avoid surface flash-over, for instance, the path length between the anode and cathode has to be increased as much as possible. Tapered trapezoidal cross-sections have been proposed in this regard to reduce the magnitude and the location of the maximum internal electric field distribution within the device.
- (ii) Inclusion of more complex external circuits. Elements such as inductors need to be included for more realistic simulations. Such inductive elements could either be part of an actual pulse shaping circuit or may be associated with the self- and mutual-inductances of the connecting wires.
- (iii) Allowing for more complicated variations in the doping profiles along the transverse direction. Such variations could include localized clumps and clusters, point defects and other profiles lacking translational symmetry along both the longitudinal and transverse directions. This would also reveal the potential for current filamentation due to the presence of localized traps.
- (iv) The numerical simulations could also be performed for a class of other voltage waveforms. In the present study only one waveform was used throughout. Furthermore, the magnitudes of the peak turn-on voltage, its temporal shape, and turn-on slope could be varied for a more extensive evaluation.
- (v) In this study, only  $P^+-N-N^+$  structures were examined. As an extension, other possibilities such as the  $P^+-P-N^+$  or the  $P^+-I-N^+$  structures could be analyzed as well.
- (vi) This work focussed on the transient electrical response of a single SAS device. However, for applications requiring voltage scaling, a number of such SAS devices may have to be used in a serially stacked mode. Evaluating the performance of such a composite stacked arrangement could be another direction for extending the current simulations.
- (vii) A final area of future research in connection with the SAS shaper devices might be to extend the analysis to heterojunction structures. Instead of having an all-Silicon device, the potential benefits of a Si-Ge heterojunction structure could be examined.

## REFERENCES

1. I. V. Grekhov, Solid-State Electronics **32**, 923-930 (1989).
2. Ihor Vitkovitsky, in *High Power Switching*, (Van Nostrand Reinhold Company, New York, 1987).

3. R. D. Ford, I. Vitkovitsky, and M. Khan, *Trans. Electrical Insulation* **EI-20**, 29 (1985).
4. R. D. Ford and I. M. Vitkovitski, in *Proceedings of the Workshop on Solid State Switches for Pulsed Power*, edited by W. M. Portnoy and M. Kiristiansen, (Texas Tech Univ. Press, Lubbock, TX, 1983), pp. 309-326.
5. J. B. Gunn, *Solid State Commun.*, **1**, 88 (1963).
6. I. V. Grekhov and A. F. Kardo-Sysoev, *Sov. Tech. Phys. Lett.* **5**, 395 (1979); I. V. Grekhov, A. F. Kardo-Sysoev, and L. S. Kostina, *Sov. Tech. Phys. Lett.* **5**, 399 (1979).
7. I. V. Grekhov, V. M. Efanov, A. F. Kardo-Sysoev, and S. V. Shenderei, *Sov. Tech. Phys. Lett.* **9**, 527 (1983).
8. I. V. Grekhov and A. F. Kardo-Sysoev, L. S. Kostina, and S. V. Shenderei, *Sov. Phys. Tech. Phys.* **26**, 984 (1981).
9. I. V. Grekhov, A. Gorbatyuk, L. S. Kostina, S. V. Korotkov, and N. S. Yakovtchuk, *Solid State Electronics* **26**, 1132 (1983).
10. R. P. Joshi, AFOSR Technical Report, Phillips Laboratory, August 1995.
11. B. L. Gelmont and M. Shur, *Sov. Phys. JETP Lett.* **11**, 350 (1970).
12. J. B. Gunn, *IBM J. Res. Dev.* **8**, 141 (1964).
13. J. Stoer and R. Bulirsch, in *Introduction to Numerical Analysis*, (Springer-Verlag, N. York, 1980).
14. R. J. Focia, E. Schamiloglu, C. Fleddermann, W. Nunnally, and J. Gaudet, *Proc. of the IEEE Pulsed Power Conference*, Albuquerque, N. Mexico, Vol. I, 592 (1995).

**THEORY OF WAVE PROPAGATION IN A TIME - VARYING MAGNETOPLASMA  
MEDIUM AND APPLICATIONS TO GEOPHYSICAL PHENOMENA**

**Dikshitulu K. Kalluri  
Professor  
Department of Electrical Engineering**

**University of Massachusetts Lowell  
1 University Avenue  
Lowell, MA 01854**

**Final Report for:  
Summer Research Extension Program  
Phillips Laboratory / Geophysics Directorate**

**Sponsored by:  
Air Force Office of Scientific Research  
Bolling Air Force Base, DC**

**and**

**Phillips Laboratory / Geophysics Directorate**

**December 1996**

# **THEORY OF WAVE PROPAGATION IN A TIME – VARYING MAGNETOPLASMA MEDIUM AND APPLICATIONS TO GEOPHYSICAL PHENOMENA**

**Dikshitulu K. Kalluri  
Professor  
Department of Electrical Engineering  
University of Massachusetts Lowell**

## **Abstract**

Using one dimensional theory, several aspects of electromagnetic wave transformation in a dynamic magnetized plasma are considered. They may be grouped under the following categories

1. Effects of finite rise time and range length on the reflection coefficients of a dynamic inhomogeneous plasma medium.
2. Alteration of pulse duration in a dynamic magnetized plasma medium
3. Green's function and perturbation technique for a switched time - varying magnetoplasma medium
4. Application of the theoretical results developed in 1 - 3 to the investigation of lightning induced ionospheric effects and other geophysical phenomena connected with dynamic magnetized plasma medium. This effort will continue in active collaboration with my focal point .

# THEORY OF WAVE PROPAGATION IN A TIME - VARYING MAGNETOPLASMA MEDIUM AND APPLICATIONS TO GEOPHYSICAL PHENOMENA

Dikshitulu K. Kalluri

## 1. General Introduction

A brief review and references to the previous work on the theory of wave propagation in a time - varying magnetoplasma medium are given in this section. A comprehensive account may be found elsewhere [1].

### 1.1 Switched Isotropic Plasma Medium: A and B waves

Jiang [2] investigated the effect of switching suddenly an unbounded isotropic cold plasma medium. Since the plasma was assumed to be unbounded, the problem was modeled as a pure initial value problem. The wave propagation in such a medium is governed by the conservation of the wave number across the time discontinuity and consequent change in the wave frequency. Rapid creation of the medium may be approximated as a sudden switching of the medium. The main effect of switching the medium is the splitting of the original wave ( henceforth called incident wave, in the sense of incidence on a time discontinuity in the properties of the medium ) into new waves whose frequencies are different from the incident wave. Recent experimental work [3] - [5] and computer simulation [6] demonstrated the frequency-upshifting of microwave radiation by rapid plasma creation.

In any practical situation, the plasma is bounded and the problem can no longer be modeled as a pure initial value problem. Kalluri [7] dealt with this aspect by considering the reflection of a traveling wave when an isotropic cold plasma is switched on only over  $z > 0$  half-space. Kalluri has shown that the reflected field in free space is comprised of two components, A and B. The A component is due to reflection at the spatial discontinuity at  $z = 0$  formed at  $t = 0$ . Its frequency is the same as that of the incident wave. The temporal discontinuity gives rise to two additional waves in the plasma. These are called B waves. One of them propagates in the negative  $z$ -direction, and it is this wave which undergoes partial transmission into free space. The frequency of the B component is different from that of the incident wave.

Kalluri et al. [8] recently brought the solved problem closer to the practical situation by considering the switched plasma medium as a slab of width  $d$  ( Figure 1). A qualitative picture of the reflected and transmitted waves is given in the figure. If the incident wave frequency  $\omega_0$  is less than the plasma wave frequency  $\omega_p$ , i.e.  $\omega_0$  is in the stop band of the medium, the transmitted wave will be a B wave of the new [2] frequency  $\omega_1 = (\omega_0^2 + \omega_p^2)^{1/2}$ .

The solution of the slab problem was complex but it would be more complex if the posed problem was to be brought even closer to the practical situation i.e., the problem of switching a space-varying and time-varying plasma of finite extent. However, since the B waves are generated in the plasma their basic nature in terms of the frequency shift, power and energy in them and how they are damped can all be studied qualitatively by considering the switching of the unbounded medium.

## 1.2 Switched Unbounded Magnetoplasma Medium: L, R, O and X Waves

It is known [9] that the presence of a static magnetic field will influence the frequency shift etc. Rapid creation of a plasma medium in the presence of a static magnetic field may be approximated as the sudden switching of a magnetoplasma medium. An idealized mathematical description of the problem is given next. A uniform plane wave is traveling in free space along  $z$  direction and it is assumed that at  $t = 0^-$ , the wave occupies the entire space. A static magnetic field of strength  $B_0$  is assumed to be present throughout. At  $t = 0$  the entire space is suddenly ionized thus converting the medium from free space to a magnetoplasma medium. The incident wave frequency is assumed to be high enough that the effects of ion-motion may be neglected.

The strength and the direction of the static magnetic field effect the number of new waves created, their frequencies, and the power density of these waves. Some of the new waves are transmitted waves ( waves propagating in the same direction as the incident wave ) and some are reflected waves ( waves propagating in the opposite direction to that of the incident wave ). Reflected waves tend to have less power density.

A physical interpretation of the waves may be given in the following way. The electric and magnetic fields of the incident wave and the static magnetic field accelerate the electrons in the newly created magnetoplasma, which in turn radiate new waves. The frequencies of the new waves and their fields can be obtained by adding contributions from the many electrons whose positions and motions are correlated by the collective effects supported by the magnetoplasma

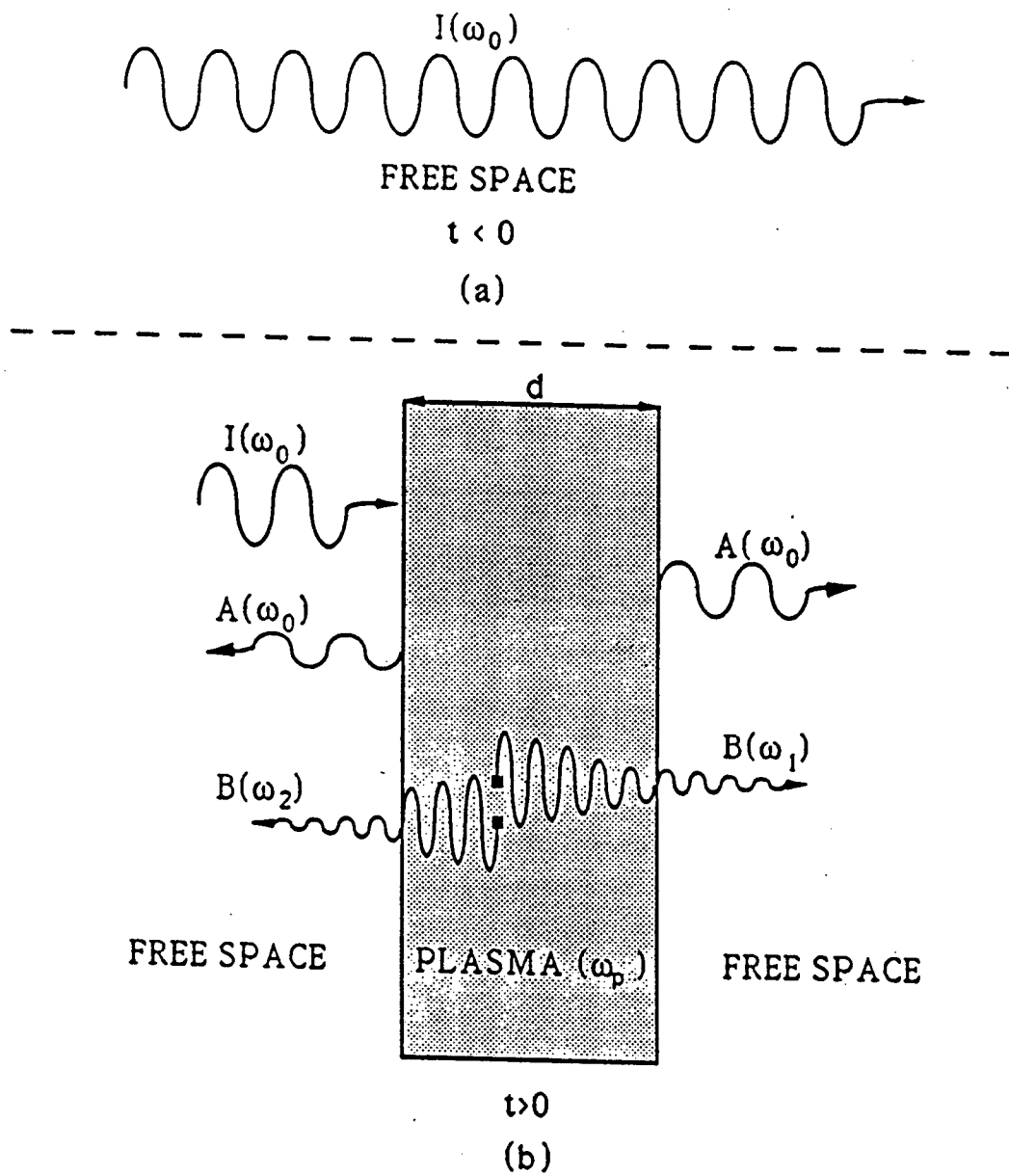


FIG. 1 A and B Waves

medium. Such a detailed calculation of the radiated fields seems to be quite involved. A simple, but less accurate, description of the plasma effect is obtained by modeling the magnetoplasma as a dielectric medium whose refractive index is computed through magnetoionic theory [10]. The frequency of the new waves are constrained by the requirements that the wave number ( $k_0$ ) is conserved over the time discontinuity and the refractive index  $n$  is that applicable to the type of wave propagation in the magnetoplasma. This gives a conservation [11] law  $k_0 c = \omega_0 = n(\omega) \omega$  from which  $\omega$  may be determined. Solution of the associated electromagnetic initial value problem gives the electric and magnetic fields of the new waves. Using this approach the general aspects of wave propagation in a switched magnetoplasma medium were discussed earlier [9],[12],[13] for the cases of L, R and X incidence [10].

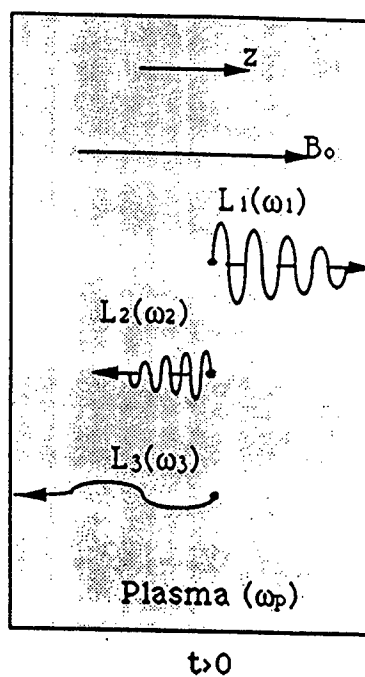
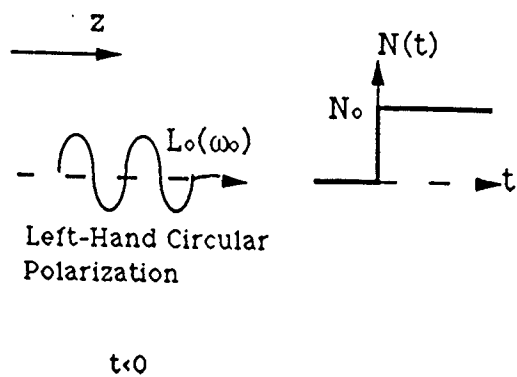
L incidence is an abbreviation used to describe the case where the incident wave has left - hand circular polarization and the static magnetic field is in the  $z$  direction ( Fig. 2 (a)). Three new waves with left - hand circular polarization labeled as L1, L2 and L3 are generated by the medium switching. L1 is a transmitted wave. R incidence refers to the case where the incident wave has right - hand circular polarization and the static magnetic field is in the  $z$  direction . The medium switching , in this case, creates three R waves labeled as R1, R2 and R3. R1 and R3 are transmitted waves. The frequencies of the R waves are the roots of the cubic characteristic equation [9]:

$$\omega_n^3 - \omega_b \omega_n^2 - (\omega_0^2 + \omega_p^2) \omega_n + \omega_0^2 \omega_b = 0 \quad (1.2.1)$$

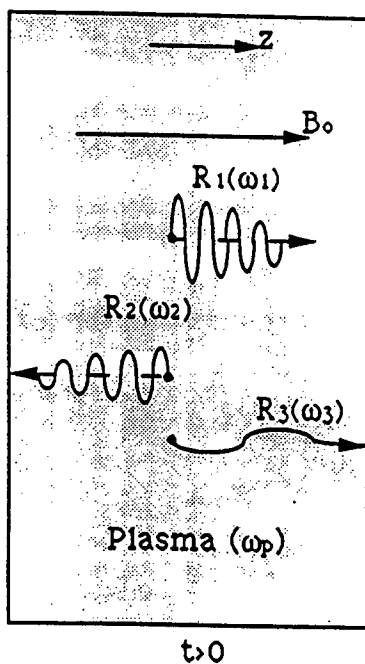
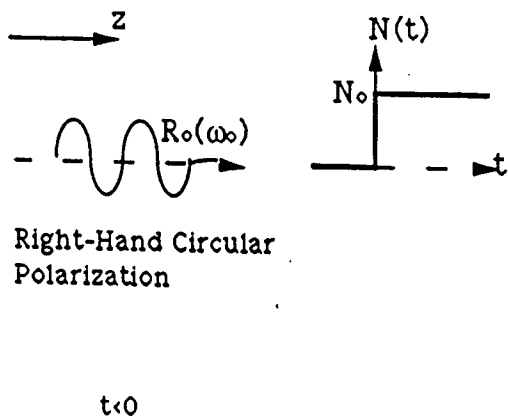
In the above  $\omega_b$  is the electron gyrofrequency and the incident wave variables are denoted by zero subscript. A negative value for  $\omega_n$  [9] indicates that the wave is a reflected wave i.e. , it propagates in a direction opposite to that of the source ( incident ) wave. If the source wave is right-going, then the reflected wave will be left-going.

X incidence refers to the case where the electric field of the incident wave is in the  $x$  direction and the static magnetic field is in the  $y$  direction. The medium switching in this case creates four extraordinary waves labeled as X1, X2, X3 and X4. X1 and X2 are transmitted waves. The frequencies of these waves are :

$$\omega_n^4 - \omega_n^2 (\omega_0^2 + \omega_b^2 + 2 \omega_p^2) + (\omega_p^4 + \omega_0^2 (\omega_b^2 + \omega_p^2)) = 0 \quad (1.2.2)$$



(a)



(b)

FIG. 2 L and R Waves

### 1.3 Some Remarkable Effects

The main effect of suddenly switching a magnetized medium is the splitting of the source wave into new waves whose frequencies are either upshifted or downshifted. A slow switching of the medium modifies the frequency and amplitude [14], [15] of the source wave. For certain choice of the parameter change of the switched medium, some remarkable effects like frequency shifting with power intensification [16], [17] and conversion of the whistler wave into a wiggler magnetic field occur.

This report contains a brief discussion of the new results obtained during the execution of the SREP 95 proposal. Several of these results are being prepared for publication in refereed journals.

## 2. Effect of Variation of Electron density in Space and Time

### 2.1 Introduction

A sudden creation of plasma half space considered in [7] is a mathematical idealization of a rapid creation of a plasma medium with a sharp boundary. Here the square of the plasma frequency  $\omega_p^2(z, t)$  is given by

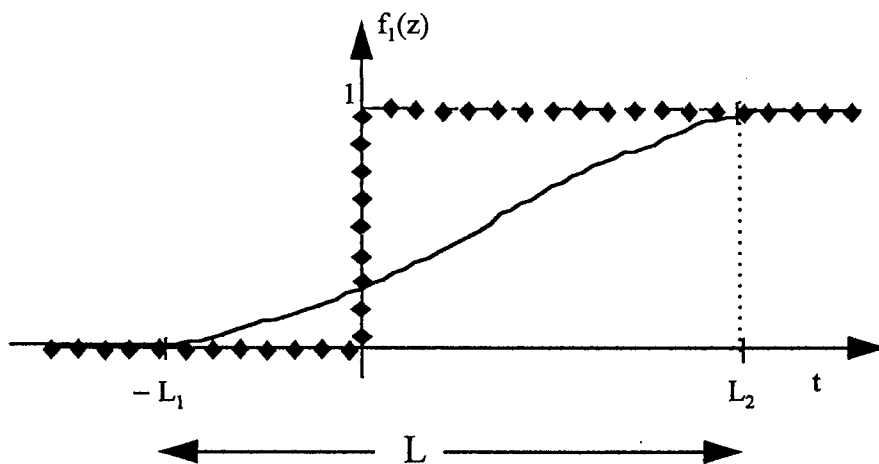
$$\omega_p^2(z, t) = \omega_{p0}^2 u(z) u(t) \quad (2.1.1)$$

where  $u(\cdot)$  is a step function. The steady state reflected field in free space is comprised of A and B waves (section 1) and the reflection coefficients  $R_A$  and  $R_B$  are given in [7].

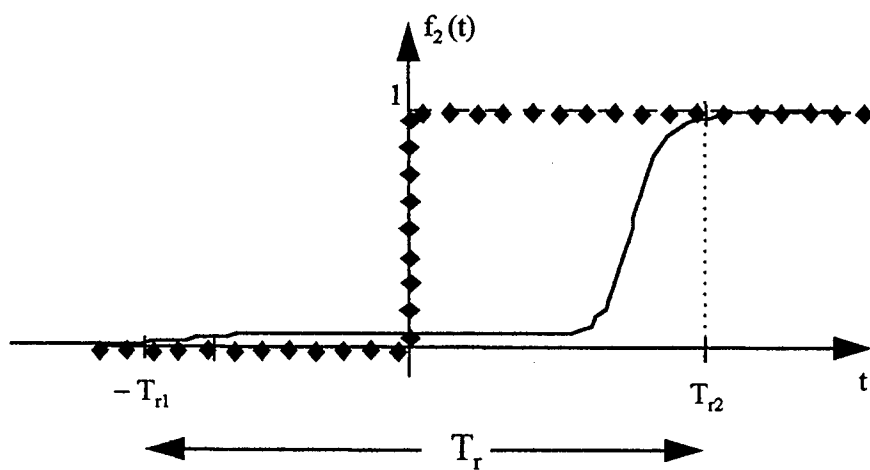
A more realistic dynamic plasma medium problem should model the  $\omega_p^2(z, t)$  profile by

$$\omega_p^2(z, t) = \omega_{p1}^2 + (\omega_{p2}^2 - \omega_{p1}^2) f_1(z) f_2(t) \quad (2.1.2)$$

where  $\omega_{p1}$  is the plasma frequency of the medium 1 as  $z \rightarrow -\infty$  and  $t \rightarrow -\infty$  and  $\omega_{p2}$  is the plasma frequency of the medium 2 as  $z \rightarrow \infty$  and  $t \rightarrow \infty$  and  $f_1(z)$  and  $f_2(t)$  functions describe the transition of the plasma frequency from its asymptotic values. Figures 3 (a) and 3 (b) show a non periodic change of the plasma frequency from medium 1 to medium 2 over a length scale (range length)  $L$  and a time scale  $T_r$  (rise time). Let the source monochromatic plane wave with



(a)



(b)

◆ reference step profile  
| arbitrary profile

**FIG. 3** (a) Spatial profile (b) Temporal profile

frequency  $\omega_1$  be propagating in z direction in medium 1 of plasma frequency  $\omega_{p1}$ . The wave number  $q_{11}$  of the source wave is given by:

$$q_{11} = \omega_1 \sqrt{\mu_0 \epsilon_1(\omega_1)} = \frac{1}{c} \sqrt{\omega_1^2 - \omega_{p1}^2} \quad (2.1.3)$$

The Instantaneous frequencies ( $\pm \omega(t)$ ) of the transmitted and reflected B waves satisfy the equation

$$\omega^2(t) = \omega_1^2 + \omega_p^2(t) - \omega_{p1}^2 \quad (2.1.4)$$

and the asymptotic values of these frequencies ( $\pm \omega_2$ ) are given by

$$\omega_2 = \sqrt{\omega_1^2 + (\omega_{p2}^2 - \omega_{p1}^2)} \quad (2.1.5)$$

A profile approximation of (2.1.2) valid for many practical problems is to restrict (2.1.2) to a finite rise time  $T_r$  and a finite range length  $L$ . The limiting case of  $L$  approaching zero and  $T_r$  approaching zero will give the step profile function:

$$\omega_p^2(z, t) = \omega_{p1}^2 + (\omega_{p2}^2 - \omega_{p1}^2) u(z) u(t) \quad (2.1.6)$$

The steady-state solution for this profile is easily written by generalizing the results given in [7] and are discussed in the subsection 2.2. The effects of non zero values for  $L$  and  $T_r$  on the reflection coefficients  $R_A$  and  $R_B$  of A and B waves are discussed in the subsections 2.3 and 2.4. An approximate analysis of the problem may be done by noting that the range length  $L$  primarily affects  $R_A$  and the rise time  $T_r$  primarily effects  $R_B$ . The problem may thus be decomposed into two simpler problems. The first problem assumes a time - invariant space -varying profile with range length  $L$ . The second problem assumes a space - invariant time -varying profile with rise time  $T_r$ . Solution of each of the problems involves the following steps.

Step1 Obtain the scattering coefficients  $R$  and  $T$  for the reference step profile.

- Step 2 Obtain the Green's function for the step profile
- Step 3 Obtain the equation for the correction terms  $\Delta R$  and  $\Delta T$  in terms of the Green's function and the solution for the reference profile. Obtain a perturbation series solution valid for arbitrary profiles.
- Step 4 Obtain a simple approximation for  $\Delta R$  and  $\Delta T$  based on the dominant term in the series valid for a small value for the range length  $L$  or the rise time  $T_r$ .

The details of these derivations [18] - [19] are omitted from this report and the results are given in the subsections 2.2 - 2.4.

## 2.2 Results for the Step profile

The wave number of the transmitted A wave in medium 2 of frequency  $\omega_1$  is given by

$$q_{21} = \omega_1 \sqrt{\mu_0 \epsilon_2(\omega_1)} = \frac{1}{c} \sqrt{\omega_1^2 - \omega_{p2}^2} \quad (2.2.1)$$

and the reflection coefficient of the A wave is given by

$$R_A = R_{A12} = \frac{q_{11} - q_{21}}{q_{11} + q_{21}} \quad (2.2.2)$$

The frequency  $\omega_2$  of the B wave is given by

$$\omega_2 = (\omega_1^2 + \omega_{p2}^2 - \omega_{p1}^2)^{1/2} \quad (2.2.3)$$

The normalized electric field amplitude  $e_{BN} / E_0$  (normalized with respect to the incident wave amplitude) of the negative B wave of frequency  $(-\omega_2)$  and wave number  $q_{11}$ , created in the switched medium is given by

$$E_{BN} = \frac{e_{BN}}{E_0} = \frac{\omega_2 - \omega_1}{2\omega_2} \quad (2.2.4)$$

The reflection coefficient  $R_B$  is given by multiplying (2.2.4) with the transmission coefficient  $T_{A21}$ :

$$T_{A21} = \frac{2q_{11}}{q_{12} + q_{11}} \quad (2.2.5)$$

$$R_B = \frac{\omega_2 - \omega_1}{2\omega_2} \frac{2q_{11}}{q_{12} + q_{11}} \quad (2.2.6)$$

In the above  $q_{12}$  is the wave number of the B wave of frequency  $\omega_2$  in medium 1:

$$q_{12} = \omega_2 \sqrt{\mu_0 \epsilon_1(\omega_2)} = \frac{1}{c} \sqrt{\omega_2^2 - \omega_{p1}^2} = \frac{1}{c} \sqrt{\omega_1^2 + \omega_{p2}^2 - 2\omega_{p1}^2} \quad (2.2.7)$$

### 2.3 Correction due to finite rise time

The correction to  $E_{BN}$  due to an arbitrary electron density profile of small rise time  $T_r$  is given by

$$\Delta E_{BN} = \int_{-T_{r1}}^{T_{r2}} d\tau \Delta \omega_p^2(\tau) \frac{1 + j\tau E_{BP}}{j} \quad (2.3.1)$$

where

$$E_{BP} = \frac{\omega_1 + \omega_2}{2\omega_2} \quad (2.3.2)$$

$$\Delta \omega_p^2(t) = \omega_p^2(t) - \tilde{\omega}_p^2(t) \quad (2.3.3)$$

and  $\omega_p^2$  is the reference step profile. If we choose the origin so that the area under the  $\Delta \omega_p^2$  curve is zero, (2.3.1) simplifies to

$$\Delta E_{BN} = \frac{\omega_1 + \omega_2}{2\omega_2} \int_{-T_{r1}}^{T_{r2}} d\tau \Delta \omega_p^2(\tau) \tau \quad (2.3.4)$$

If, furthermore, the profile is linear

$$\Delta E_{BN} = - \frac{\omega_2 + \omega_1}{2\omega_2} \frac{\omega_2^2 - \omega_1^2}{24} T_r^2 \quad (2.3.5)$$

and

$$\Delta R_B = T_{A21} \Delta E_{BN} \quad (2.3.6)$$

## 2.4 Correction due to finite range length L

The correction to  $R_A$  due to an arbitrary profile of small range length  $L$  is given by

$$\Delta R_A = \frac{2 q_{11}}{j (q_{11} + q_{21})^2} \int_{-L_1}^{L_2} d\zeta \Delta q^2(\zeta) - \frac{4 q_{11} q_{21}}{(q_{11} + q_{21})^2} \int_{-L_1}^{L_2} d\zeta \zeta \Delta q^2(\zeta) \quad (2.4.1)$$

where

$$\Delta q^2(z) = q^2(z) - \tilde{q}^2(z) \quad (2.4.2)$$

and  $q^2(z)$  is the reference step profile. If we choose the origin so that the area under the  $q^2$  curve is zero, (2.4.1) simplifies to

$$\Delta R_A = - \frac{4 q_{11} q_{21}}{(q_{11} + q_{21})^2} \int_{-L_1}^{L_2} d\zeta \zeta \Delta q^2(\zeta) \quad (2.4.3)$$

If, furthermore, the  $q^2(z)$  profile is linear (see Figure 4), we get

$$\Delta R_A = -4 q_{11} q_{21} R_A \frac{L^2}{24} \quad (2.4.4)$$

$$\Delta R_A = -\frac{1}{6} R_A \left(1 - \frac{\omega_p^2}{\omega_1^2}\right)^{1/2} \left(1 - \frac{\omega_p^2}{\omega_2^2}\right)^{1/2} \left(\frac{\omega_1 L}{c}\right)^2 \quad (2.4.5)$$

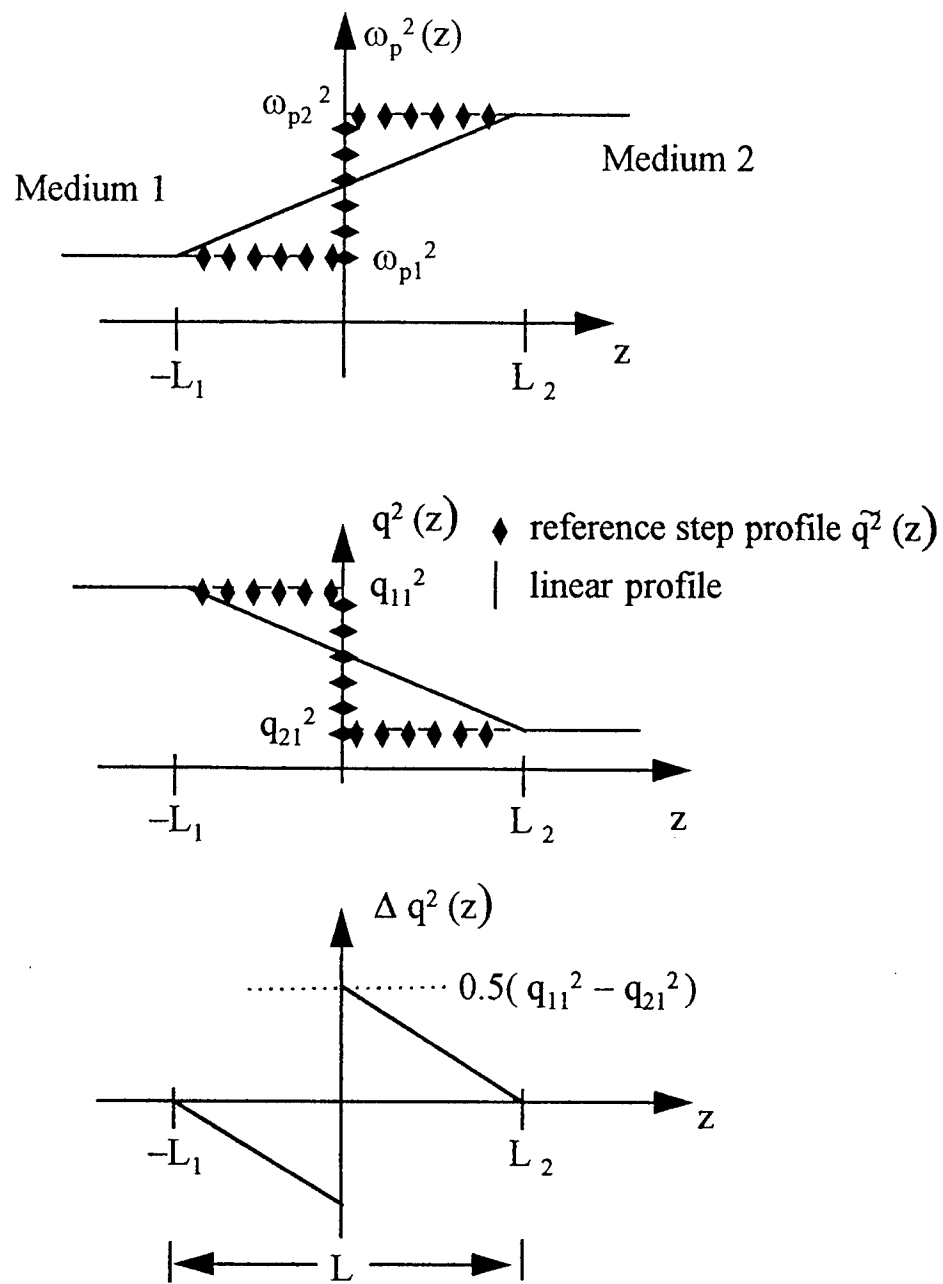


**FIG. 4** Linear Profile

### 3. Pulses and Wave Packets in Switched Anisotropic Plasma Medium

#### 3.1 Introduction

In section 1, the effect of switching a magnetoplasma medium on a monochromatic plane wave is reviewed. In this section we consider the effect of switching the medium on a monochromatic pulse. Let  $\omega_0$  be the frequency,  $k$  the wave number,  $L_0$  the length,  $T_0$  the duration of the monochromatic pulse traveling in  $z$  direction in free space ( Figure 5 a ). At  $t = 0$  let the medium be converted to a magnetoplasma whose parameters are  $\omega_b$  and  $\omega_p$ . The effects of these parameters on the frequencies and amplitudes of the new B pulses will be the same as those on the monochromatic plane wave and are discussed in [1], [9], [12]. At a temporal discontinuity the pulse length  $L_0$  is conserved. However the pulse duration is altered. A geometrical interpretation of the change in the pulse duration for O, R and X pulses is given in the Figures 5, 6 and 7 respectively.

#### 3.2 Pulse Duration

The pulse duration and the pulse length for the  $n$  th wave are related by

$$T_n = \frac{L_0}{v_{gr n}} \quad (3.2.1)$$

where  $v_{gr n}$  is the group velocity of the  $n$  th wave. For the source pulse in free space, the group velocity is  $c$  and

$$T_0 = \frac{L_0}{c} \quad (3.2.2)$$

From the dispersion relation, the group velocity of the  $n$  th wave ( $d\omega_n/dk$ ) may be obtained. The pulse duration ratio is given by

$$\frac{T_n}{T_0} = \frac{c}{|v_{gr n}|} = \frac{c}{|d\omega_n/dk|} = \frac{1}{|d\omega_n/d\omega_0|} \quad (3.2.3)$$

An increase (decrease) in the group velocity produces a pulse compression( expansion).

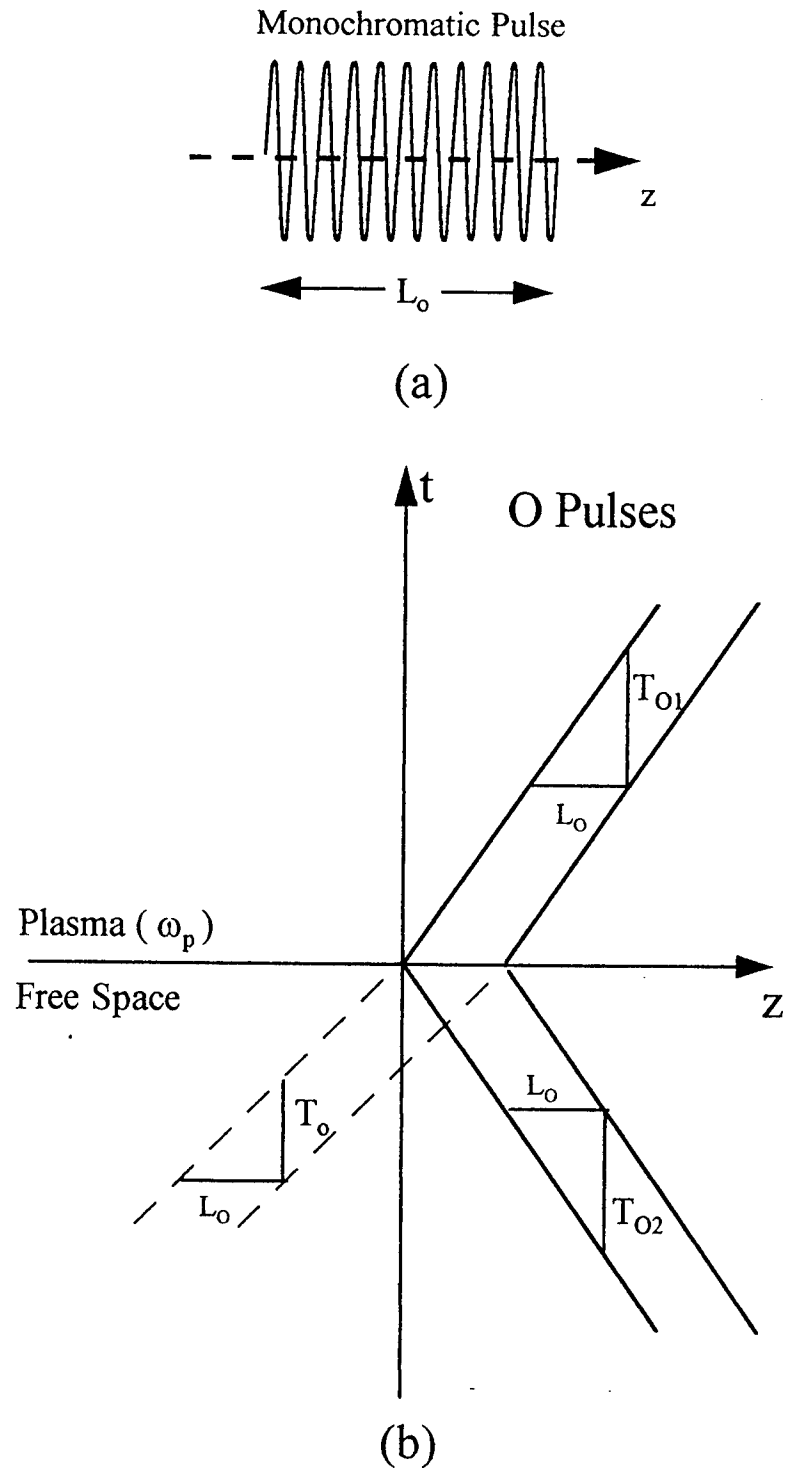


**FIG. 5** (a) Monochromatic source pulse in free space (b) Duration of O Pulses in Plasma

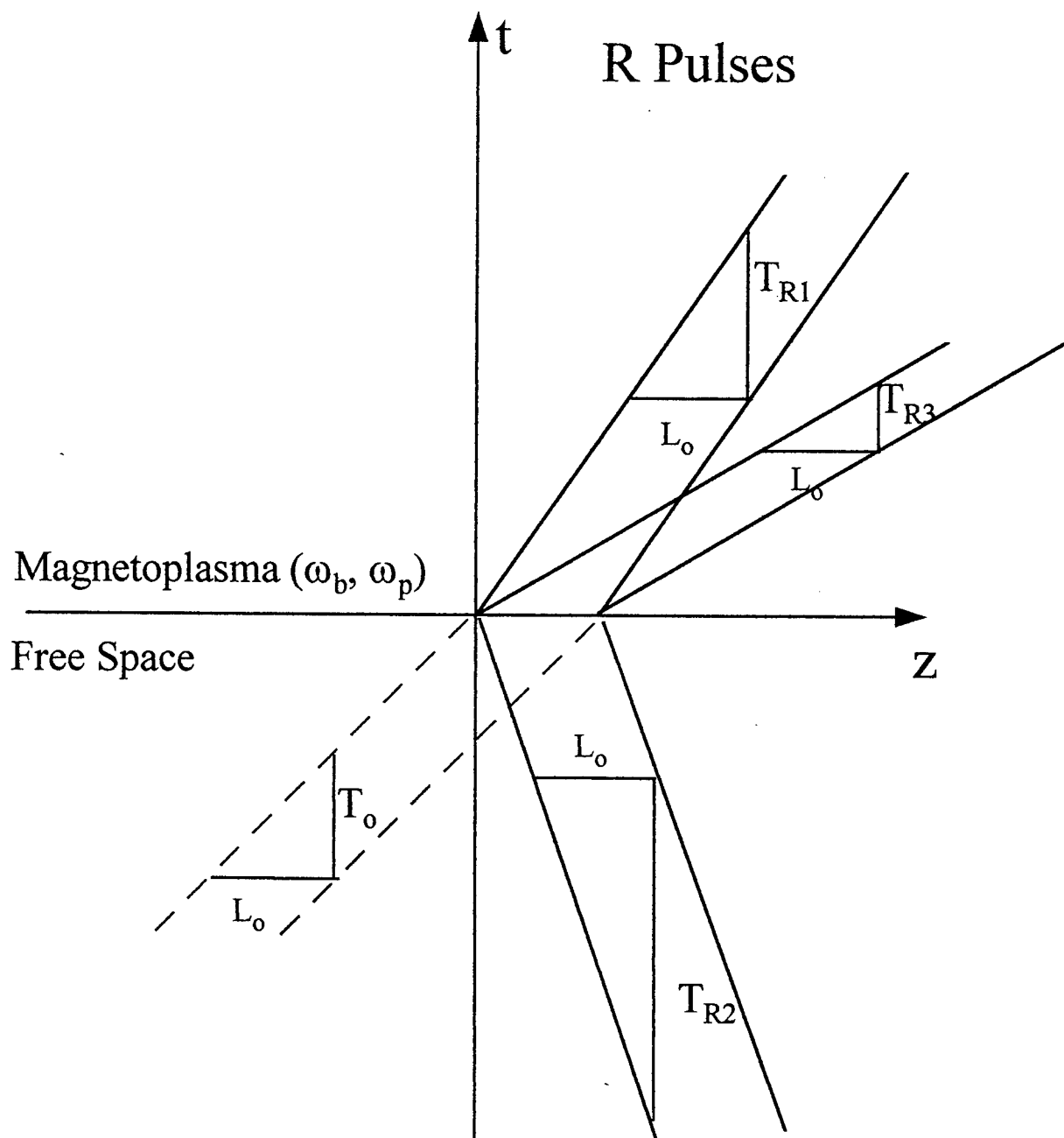
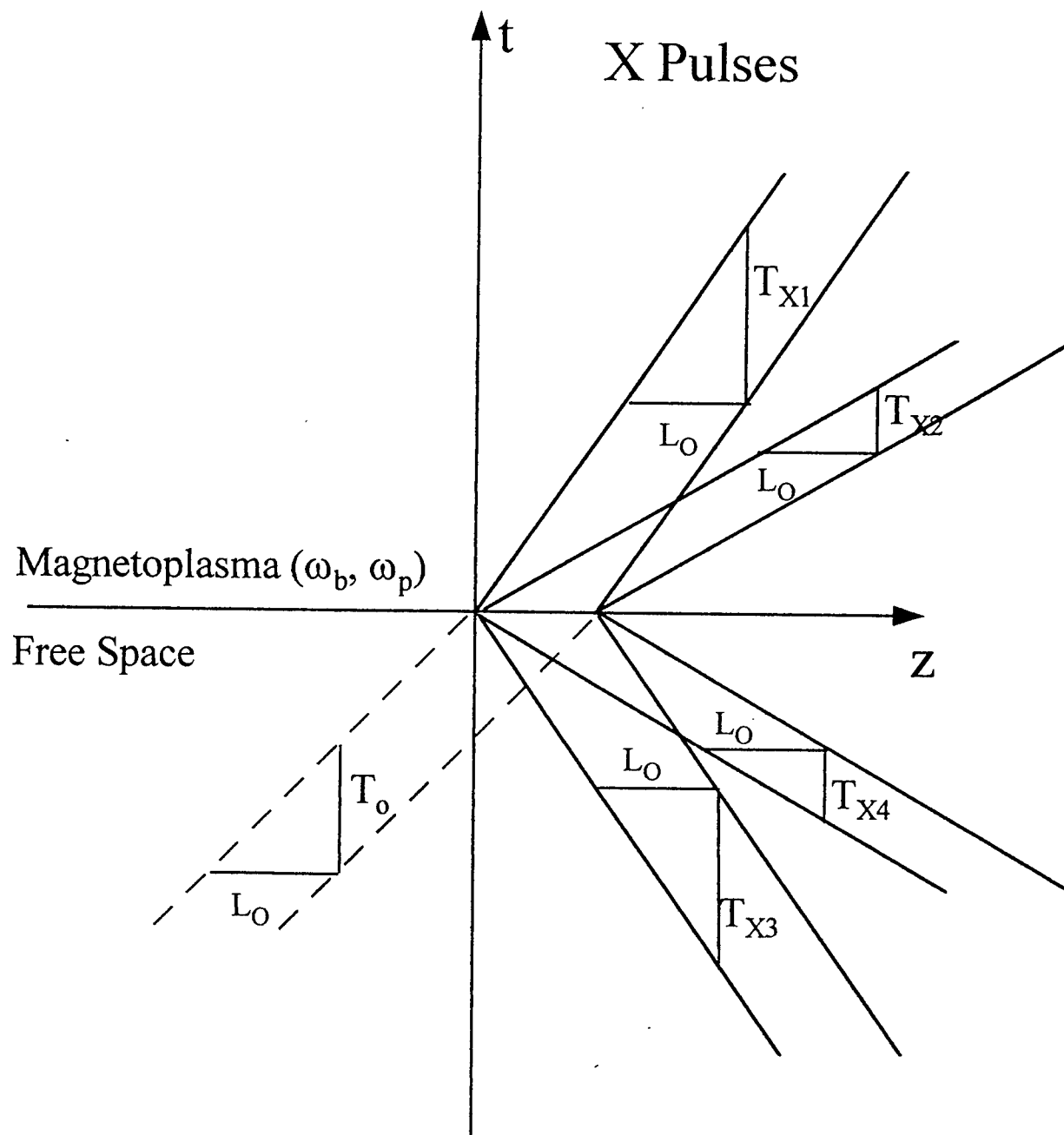


FIG. 6 Duration of R Pulses



**FIG. 7** Duration of X Pulses

For O waves in an isotropic plasma medium the dispersion relation is

$$\omega_n^2 = \omega_0^2 + \omega_p^2 \quad (3.2.4)$$

and

$$\frac{T_{o1,o2}}{T_0} = \frac{\omega_0}{|\omega_n|} \quad (3.2.5)$$

For R waves the dispersion relation is given by [20]

$$\omega_n^3 - \omega_b \omega_n^2 - (\omega_0^2 + \omega_p^2) \omega_n + \omega_0^2 \omega_b = 0 \quad (3.2.6)$$

and

$$\frac{d \omega_n}{d \omega_0} = \frac{2 \omega_0 (\omega_n - \omega_0)}{3 \omega_n^2 - 2 \omega_n \omega_b - \omega_0^2 \omega_p^2} \quad (3.2.7)$$

For X waves the dispersion relation is given by

$$\omega_n^4 - \omega_n^2 (\omega_0^2 + \omega_b^2 + 2 \omega_p^2) + (\omega_p^4 + \omega_0^2 (\omega_b^2 + \omega_p^2)) = 0 \quad (3.2.8)$$

and

$$\frac{d \omega_n}{d \omega_0} = \frac{\omega_0}{\omega_n} \frac{\omega_n^2 - \omega_b^2 - \omega_p^2}{2 \omega_n^2 - (\omega_0^2 + \omega_b^2 + 2 \omega_p^2)} \quad (3.2.9)$$

### 3.3 Numerical Results and Discussion

The top portions of Figures 8 - 12 show the variation of frequency of the B pulses as a function of the frequency  $\omega_0$  of the source pulse in free space. The frequencies are normalized by choosing

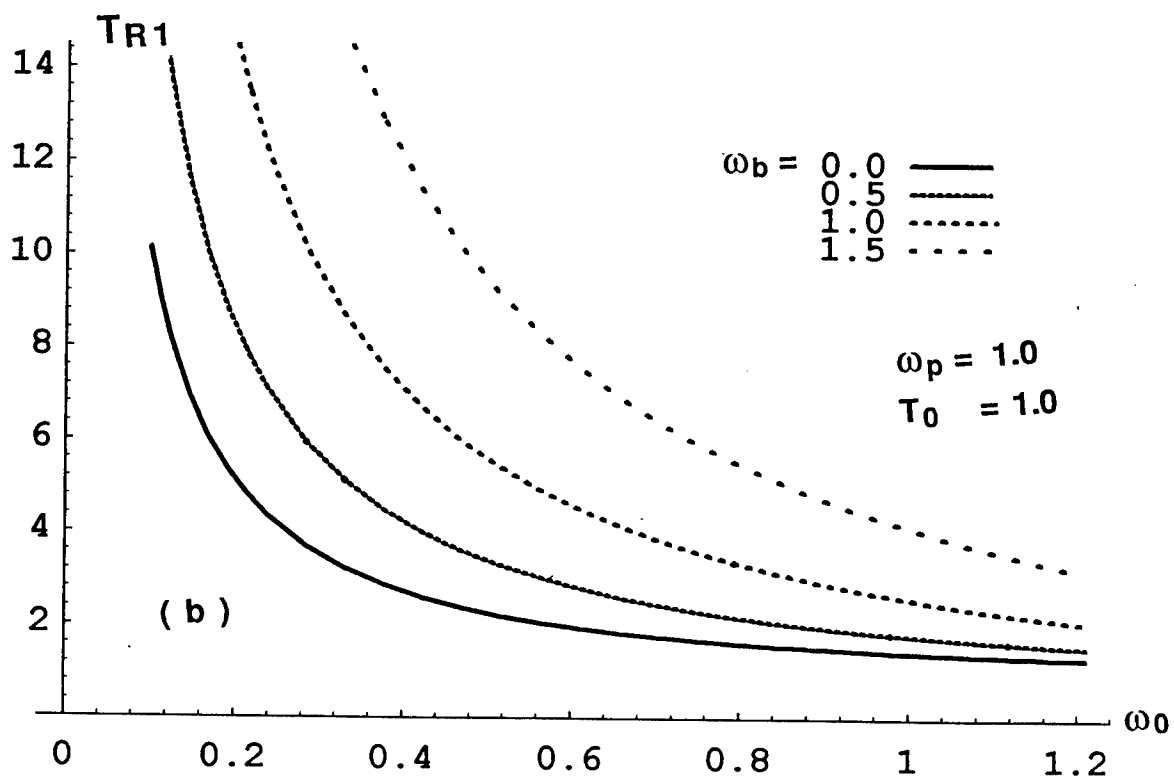
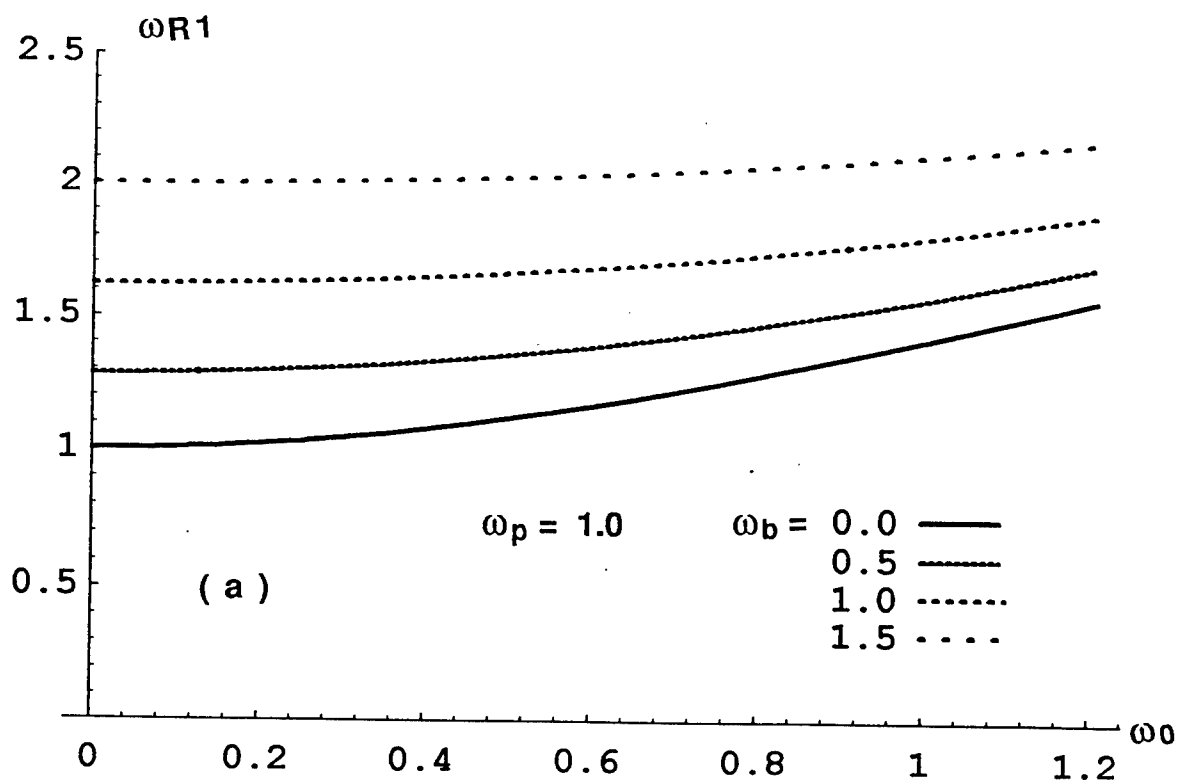


FIG. 8 R1 pulse: (a) pulse frequency vs. source frequency  
 (b) pulse duration vs. source frequency

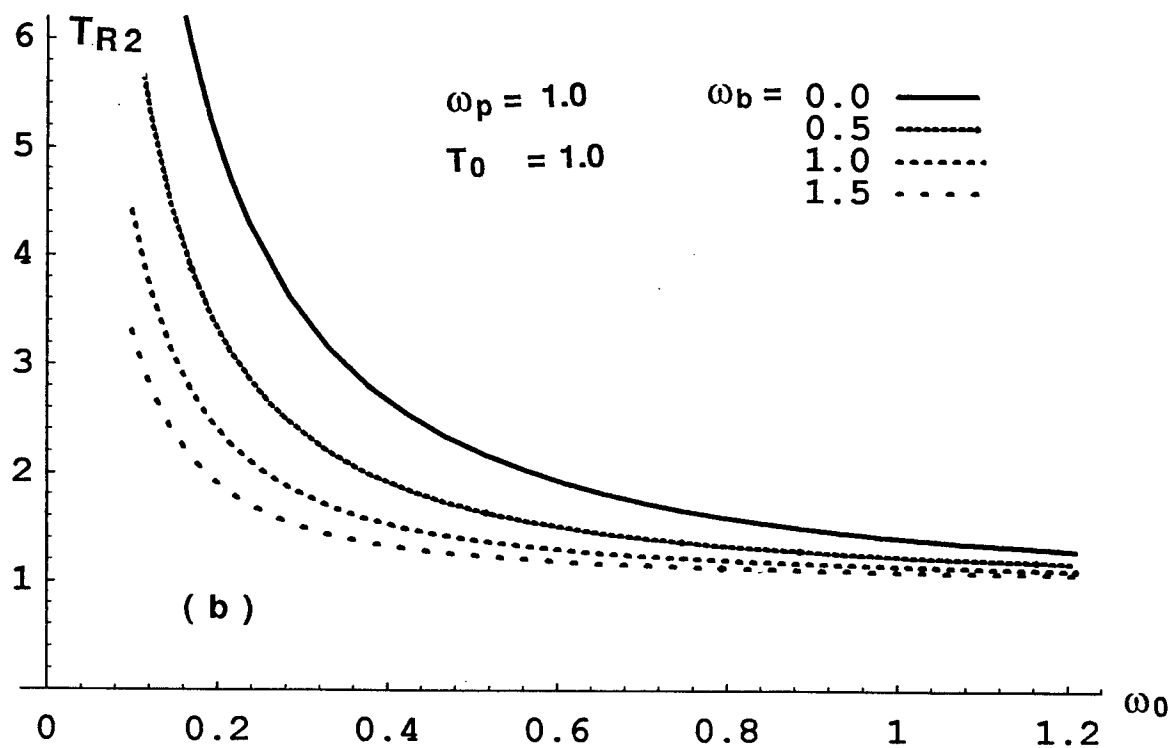
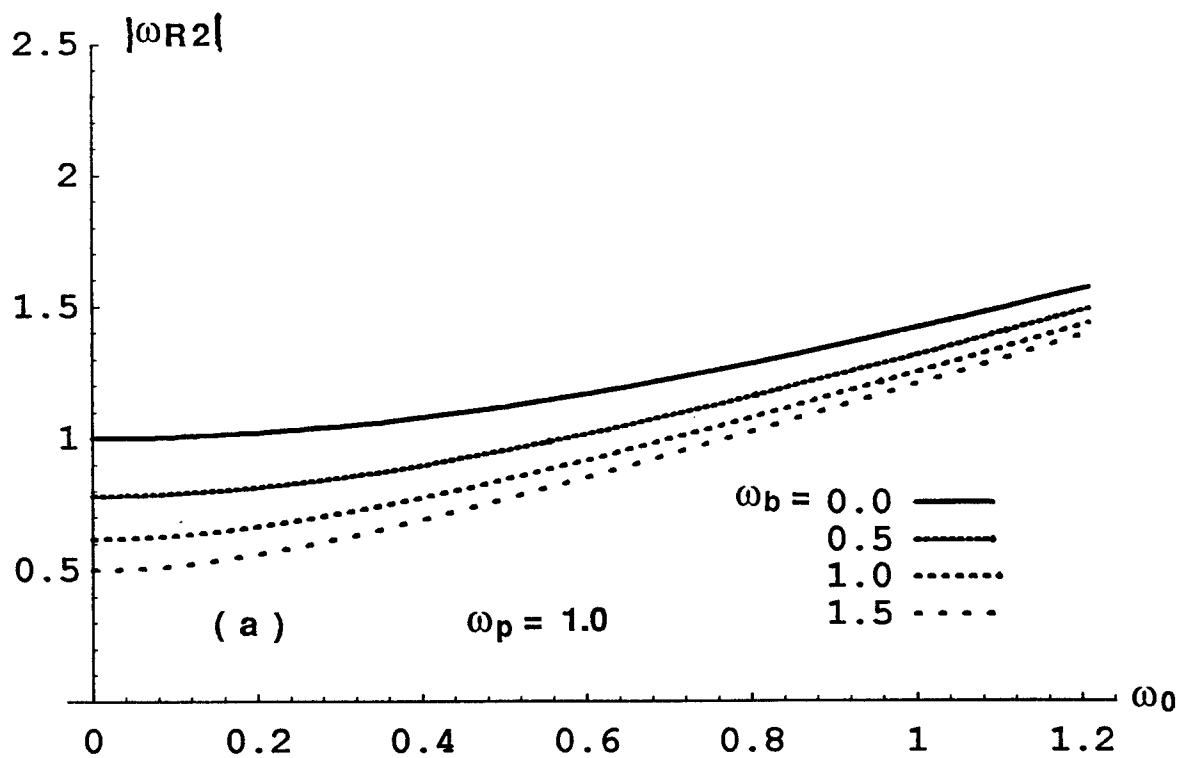


FIG. 9 R2 pulse: (a) pulse frequency vs. source frequency  
(b) pulse duration vs. source frequency

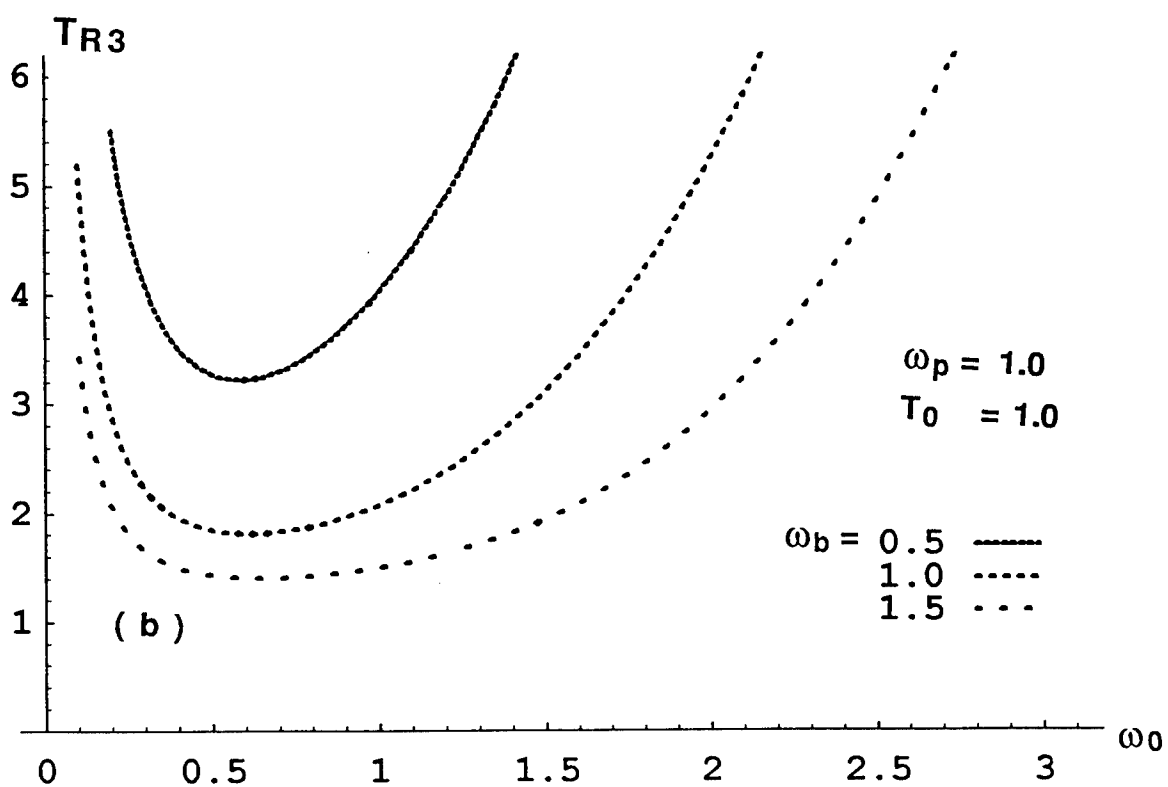
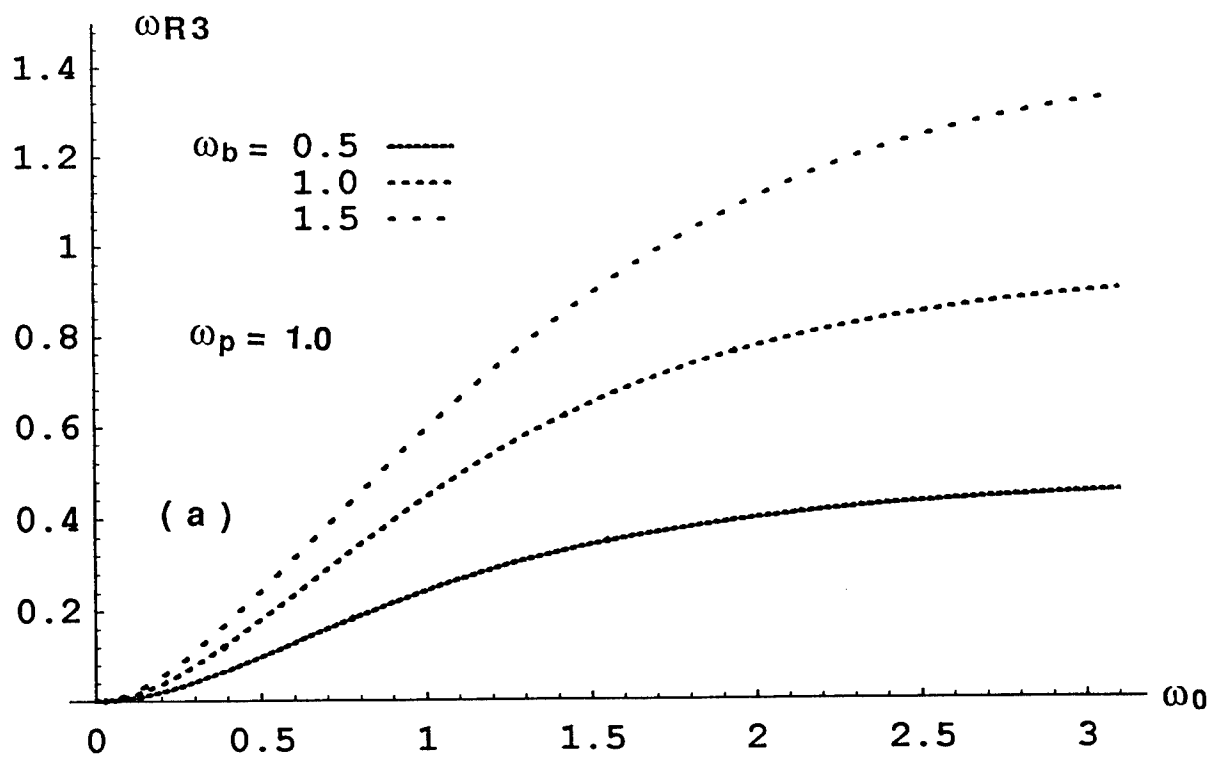


FIG. 10 R3 pulse: (a) pulse frequency vs. source frequency  
(b) pulse duration vs. source frequency

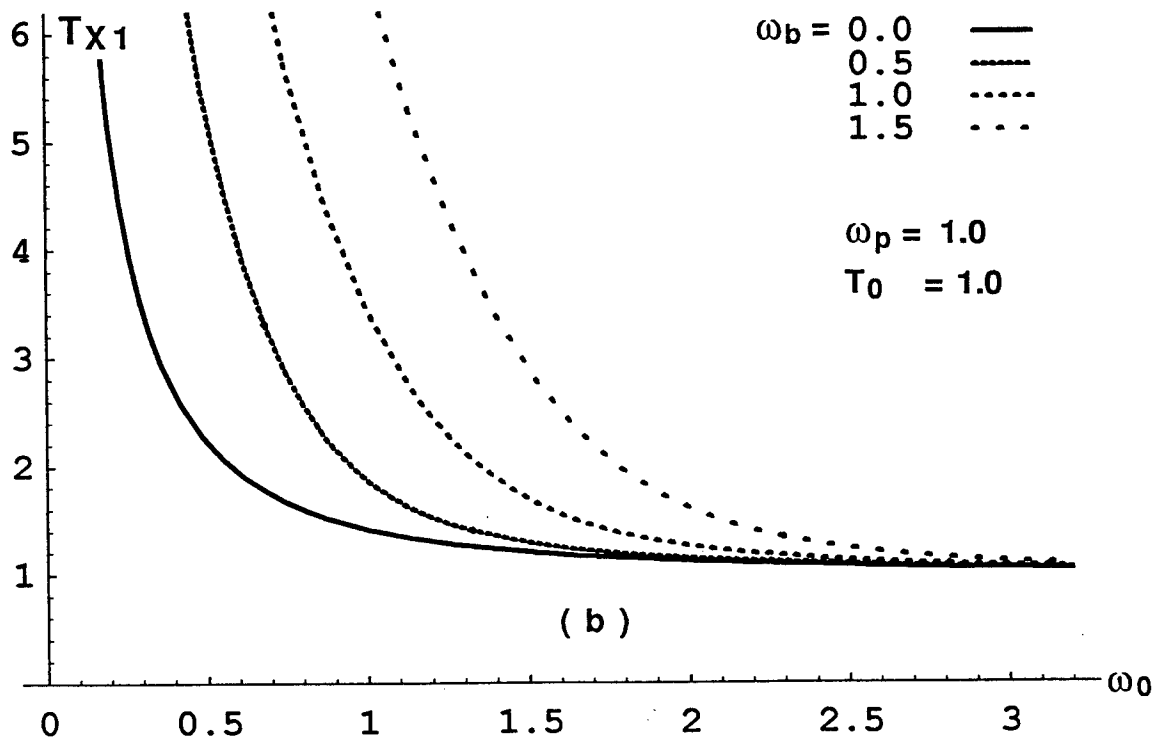
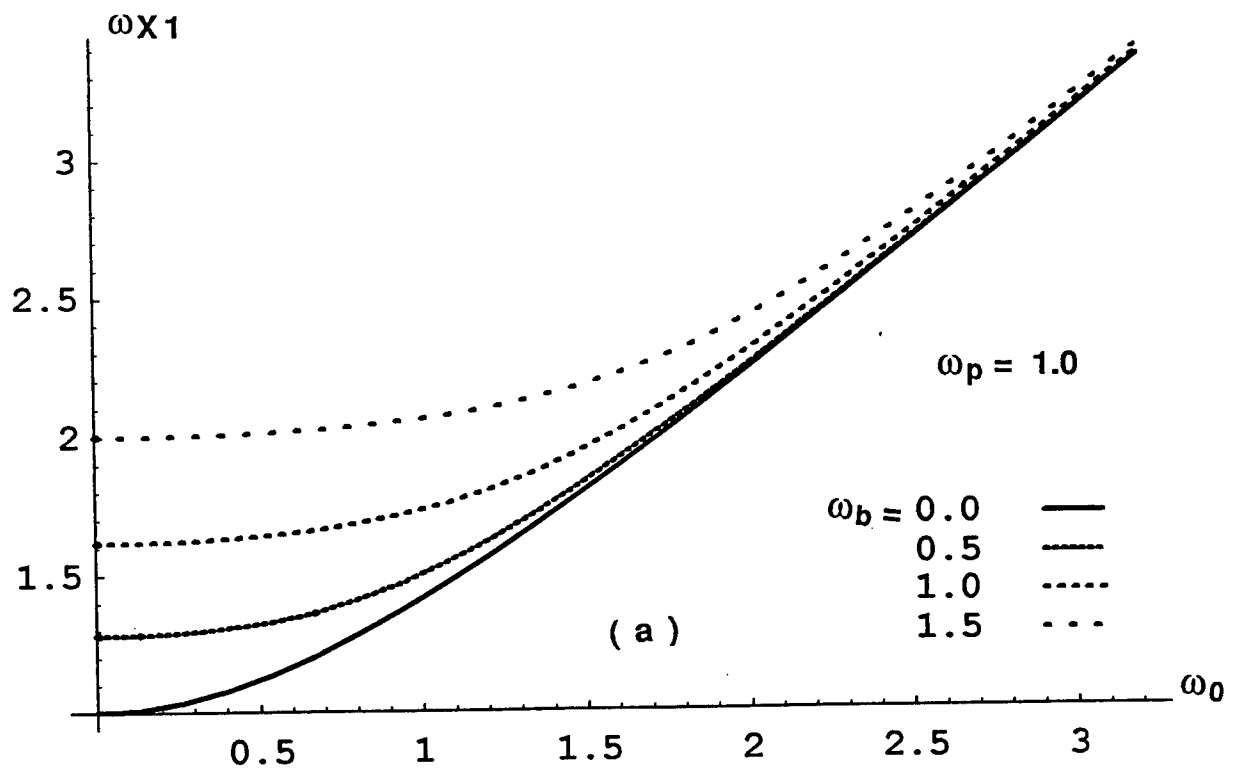
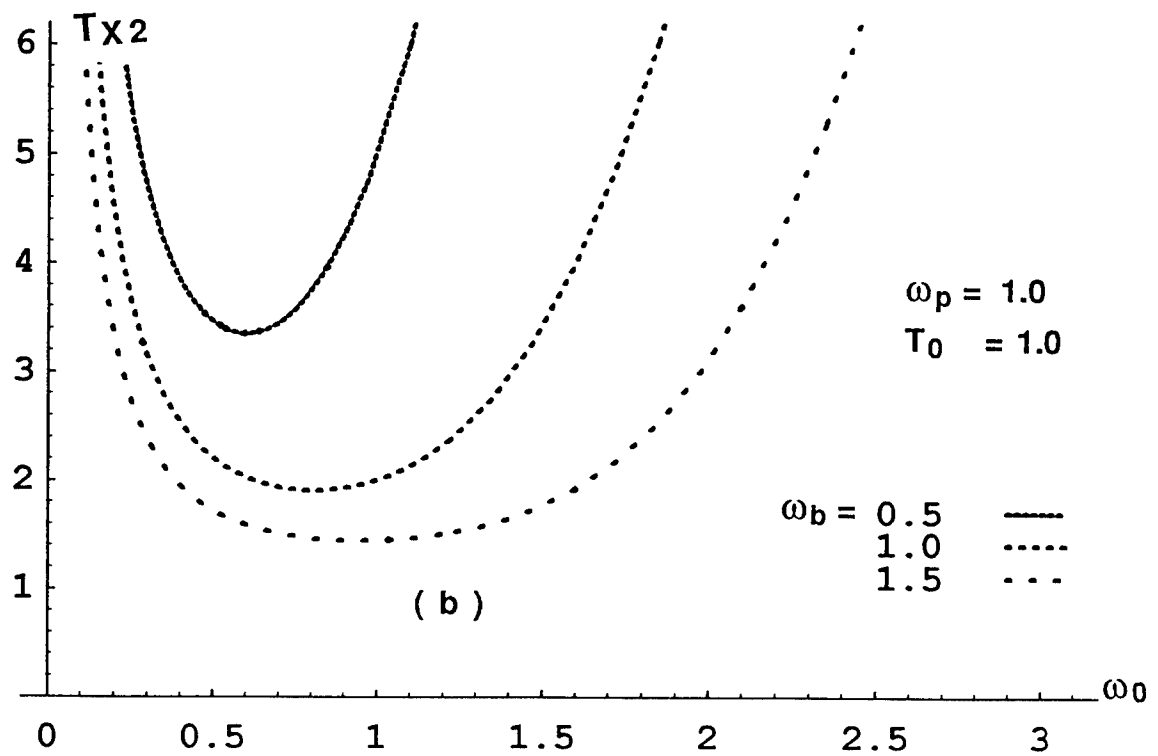
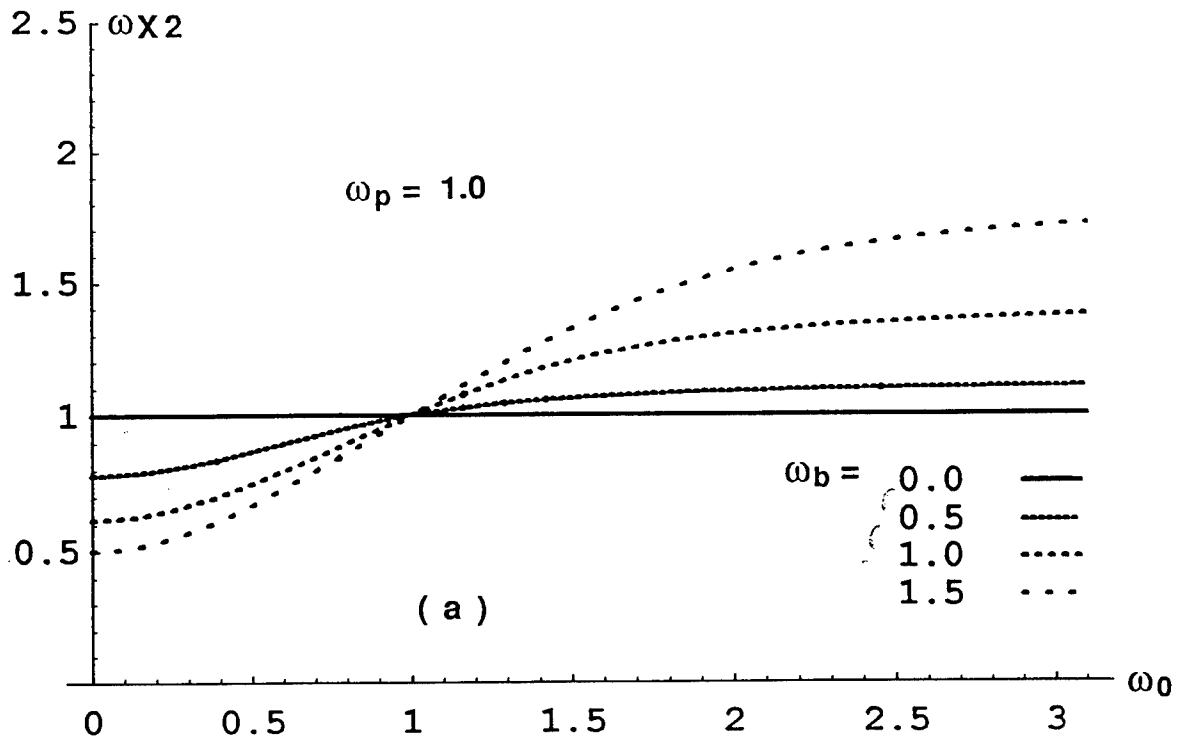


FIG. 11 X1 pulse: (a) pulse frequency vs. source frequency  
(b) pulse duration vs. source frequency



**FIG. 12** X2 pulse: (a) pulse frequency vs. source frequency  
(b) pulse duration vs. source frequency

the plasma frequency parameter  $\omega_p = 1.0$ . The gyrofrequency parameter  $\omega_b$  is varied from 0 to 1.5 in steps of 0.5. The slope of the pulse frequency vs. source frequency curve is proportional to the group velocity and the pulse duration is inversely proportional to the magnitude of this slope. The bottom portions of these curves describe the variation of the pulse duration of the various B pulses. Pulse duration is normalized by choosing  $T_0 = 1$ . The R1 and X1 curves for  $\omega_b = 0$  describe the O1 pulse. The following interesting points may be noted:

1. Pulse duration ratio for R1 and X1 pulses asymptotically reaches unit value as  $\omega_0$  tends to infinity. For large values of  $\omega_0$  the plasma has very little effect.
2. R2 is a reflected pulse and its graph for the pulse duration is qualitatively similar to the R1 graph. O2, X3, X4 pulses are also reflected pulses and their graphs are the same as those for O1, X1, X2 pulses respectively.
3. R3 and X2 pulses are generated only in a switched anisotropic plasma medium and their behavior is strongly influenced by the  $\omega_b$  parameter. Their pulse duration goes through a minimum and the minimum point is strongly influenced by the  $\omega_b$  parameter.

It is suggested that the principle of the change in the pulse duration may be used to diagnose dynamically the time - varying parameters of an anisotropic medium.

The extension of the results, to the case where the source pulse is in another anisotropic medium rather than in free space, is straight forward. Replace  $\omega_0$  by  $\omega_1$  where  $\omega_1$  satisfies the dispersion relation ( 4.3.2 ) for the first anisotropic medium. The pulse duration  $T_1$  of the source wave is obtained by using  $v_{gr 1}$  in ( 3.2.1 ). The pulse duration for the B pulses in the second anisotropic medium may be obtained by using  $d\omega_{2n}/d\omega_1$  in ( 3.2.3 ) where  $\omega_{2n}$  satisfies the dispersion relation ( 4.3.4 ) in medium 2.

#### **4. Green's Function and Perturbation Technique for a Switched Anisotropic Medium.**

##### **4.1 Introduction**

The steps involved in obtaining a solution for profiles of finite rise time are outlined in subsection 2.1. However, in the anisotropic case, the problem is more difficult to solve since the differential equation for the fields are of higher order. The technique is illustrated by solving the R wave

problem. The formulation assumes that medium 1 is also anisotropic. However the illustrative example assumes that the medium 1 is free space ( $\omega_{p1} = 0$ ).

#### 4.2 Solution for a step profile: R Wave

Let the source R wave of frequency  $\omega_1$  be traveling in anisotropic medium 1 whose parameters are  $\omega_{p1}$  and  $\omega_b$ . At  $t = 0$  the plasma frequency is changed to  $\omega_{p2}$ .

The differential equation for the  $h$  field for  $t > 0$  is given by (4.2.1) in which we use the symbol  $h_0$  as the solution for the reference profile  $\tilde{\omega}_p^2(t)$  :

$$\frac{d^3 h_0}{dt^3} - j\omega_b \frac{d^2 h_0}{dt^2} - \left[ k^2 c^2 + \omega_{p2}^2 \right] \frac{dh_0}{dt} - jk^2 c^2 \omega_b h_0 = 0, t > 0 \quad (4.2.1)$$

where

$$k^2 c^2 = n_1^2 \omega_1^2 \quad (4.2.2a)$$

$$n_1^2 = 1 - \frac{\omega_{p1}^2}{\omega_1 (\omega_1 - \omega_b)} \quad (4.2.2b)$$

Equation (4.2.1) subject to the initial conditions

$$h_0(0) = H_0 \quad (4.2.3a)$$

$$\dot{h}_0(0) = j\omega_1 H_0 = j \frac{kc}{n_1} H_0 \quad (4.2.3b)$$

$$\ddot{h}_0(0) = -\omega_1^2 H_0 = -\frac{k^2 c^2}{n_1^2} H_0 \quad (4.2.3c)$$

may be solved by the Laplace transform method and the result is

$$\frac{h_0(t)}{H_0} = \mathcal{L}^{-1} \frac{(s + j\omega_1)(s - j\omega_b) + [\omega_{p2}^2 + (n_1^2 - 1)\omega_1^2]}{s^3 - j\omega_b s^2 + (n_1^2 \omega_1^2 + \omega_{p2}^2)s - jn_1^2 \omega_1^2 \omega_b} \quad (4.2.4)$$

The denominator  $D(s)$  on the right side of (8.2.4) may be written as

$$D(s) = \prod_{n=1}^3 (s - j\omega_{2n}) \quad (4.2.5)$$

where  $\omega_{2n}$  are the roots of

$$\omega^3 - \omega_b \omega^2 - (\omega_1^2 n_1^2 + \omega_{p2}^2) \omega + \omega_1^2 n_1^2 \omega_b = 0 \quad (4.2.6)$$

The Laplace inverse of (4.2.4) gives

$$\frac{h_0(t)}{H_0} = \sum_{n=1}^3 S_{2n} \exp(j\omega_{2n}t) \quad (4.2.7)$$

$$S_{2n} = \frac{(\omega_{2n} + \omega_1)(\omega_{2n} - \omega_b) - [\omega_{p2}^2 + (n_1^2 - 1)\omega_1^2]}{\prod_{m=1, m \neq n}^3 (\omega_{2n} - \omega_{2m})} \quad (4.2.8)$$

### 4.3 Green's function for the Step Profile

Green's function is the solution of (4.3.1):

$$\frac{d^3 G}{dt^3} - j\omega_b \frac{d^2 G}{dt^2} + [n_1^2 \omega_1^2 + \omega_p^2(t)] \frac{dG}{dt} - jn_1^2 \omega_1^2 \omega_b G = \delta(t - \tau) \quad (4.3.1)$$

The appropriate Green's function, in the domain  $-\infty < t < 0$  is built up of functions  $\exp(j\omega_{1m}t)$  where  $\omega_{1m}$  are the roots of the polynomial equation:

$$F_1(\omega) = \omega^3 - \omega_b \omega^2 - (n_1^2 \omega_1^2 + \omega_{p1}^2) \omega + n_1^2 \omega_1^2 \omega_b = 0 \quad (4.3.2)$$

One of the roots of the cubic (4.3.2) is  $\omega_1$ , say

$$\omega_{11} = \omega_1 \quad (4.3.3)$$

In the region  $0 < t < \infty$ , the Green's function is built up from function  $\exp(j\omega_{2n}t)$  where  $\omega_{2n}$  are the roots of

$$F_2(\omega) = \omega^3 - \omega_b \omega^2 - (n_1^2 \omega_1^2 + \omega_{p2}^2) \omega + n_1^2 \omega_1^2 \omega_b = 0 \quad (4.3.4)$$

From causality

$$G(t, \tau) = 0, \quad t < \tau \quad (4.3.5)$$

For  $t > \tau$  the solution may be written by considering separately the following regions of  $(t, \tau)$  space:

$$\text{Case 1} \quad t > \tau, \quad t < 0, \tau < 0$$

$$G(t, \tau) = \sum_{m=1}^3 H_{Am} \exp[j\omega_{1m}(t-\tau)] \quad (4.3.6)$$

$H_{Am}$  may be determined from the requirements of the continuities of  $G$  and the first derivative of  $G = \dot{G}$ , and a unit discontinuity of the second derivative of  $G = \ddot{G}$  at  $t = \tau$ :

$$G(\tau^+, \tau) = G(\tau^-, \tau) = 0 \quad (4.3.7a)$$

$$\sum_{m=1}^3 H_{Am} = 0 \quad (4.3.7b)$$

$$\dot{G}(\tau^+, \tau) = \dot{G}(\tau^-, \tau) = 0 \quad (4.3.8a)$$

$$\sum_{m=1}^3 j\omega_{1m} H_{Am} = 0 \quad (4.3.8b)$$

$$\ddot{G}(\tau^+, \tau) - \ddot{G}(\tau^-, \tau) = 1 \quad (4.3.9a)$$

$$\sum_{m=1}^3 -\omega_{1m}^2 H_{Am} = 1 \quad (4.3.9b)$$

Note that the second term on the left side of ( 4.3.9a ) is zero. From ( 4.3.7b ), ( 4.3.8b ) and ( 4.3.9b ),

$$H_{Am} = - \frac{1}{\prod_{p=1, p \neq m}^3 (\omega_{1m} - \omega_{1p})} \quad (4.3.10)$$

**Case 2**  $t > \tau, t > 0, \tau < 0$

The impulse source in medium 1 generates the three waves given by ( 4.3.10 ). These waves travel and encounter the temporal discontinuity of the medium at  $t = 0$ . Each of these waves generates three waves on encountering the temporal discontinuity of the medium at  $t = 0$ , the scattering coefficients for unit excitation being given by ( 4.2.8 ). Since the frequency of the  $m$ th wave is  $\omega_{1m}$  and the excitation strength of the  $m$ th wave is  $H_{Am} \exp(-j\omega_{1m}\tau)$ , the Green's function may be written as

$$G(t, \tau) = \sum_{m=1}^3 H_{Am} \exp(-j\omega_{1m}\tau) \sum_{n=1}^3 S_{2n1m} \exp[j\omega_{2n1m}t] \quad (4.3.11)$$

where

$$S_{2n1m} = \frac{(\omega_{2n1m} + \omega_{1m})(\omega_{2n1m} - \omega_b) - [\omega_{p2}^2 + [(n_{1m}^2 - 1)\omega_{1m}^2]]}{\prod_{p=1, p \neq n}^3 (\omega_{2n1m} - \omega_{2p1m})} \quad (4.3.12a)$$

$$n_{1m}^2 = 1 - \frac{\omega_{p1}^2}{\omega_{1m}(\omega_{1m} - \omega_b)} \quad (4.3.12b)$$

In the above,  $\omega_{2n1m}$  is the  $n$ th root of ( 4.3.4 ) when  $\omega_1$  is replaced by  $\omega_{1m}$ .  $H_{2n1m}$  is the scattering coefficient of the  $n$ th wave of frequency  $\omega_{2n1m}$  excited in medium 2 by the  $m$ th wave of frequency  $\omega_{1m}$  in medium 1. If  $\omega_{2n1m}$  is positive the scattering coefficient is a transmission coefficient and if  $\omega_{2n1m}$  is negative the scattering coefficient is a reflection coefficient. It may be

noted that as  $n$  varies from 1 to 3 and  $m$  varies from 1 to 3,  $\omega_{2n1m}$  will have 9 values. In actuality there are only three distinct values for a given  $k$  as can be seen from ( 4.3.4 ) and ( 4.3.12c ):

$$k^2 c^2 = n_1^2 \omega_1^2 = n_{1m}^2 \omega_{1m}^2 \quad (4.3.12c)$$

The other 6 values coincide with one of the three distinct values.

### Case 3 $t > \tau, t > 0, \tau > 0$

In this case, the impulse occurs in medium 2. The generated waves do not encounter the temporal discontinuity at  $t = 0$ . Therefore

$$G(t, \tau) = \sum_{m=1}^3 H_{Bm} \exp [j \omega_{2m} (t - \tau)] \quad (4.3.13)$$

where

$$H_{Bm} = - \frac{1}{\prod_{p=1, p \neq m}^3 (\omega_{2m} - \omega_{2p})} \quad (4.3.14)$$

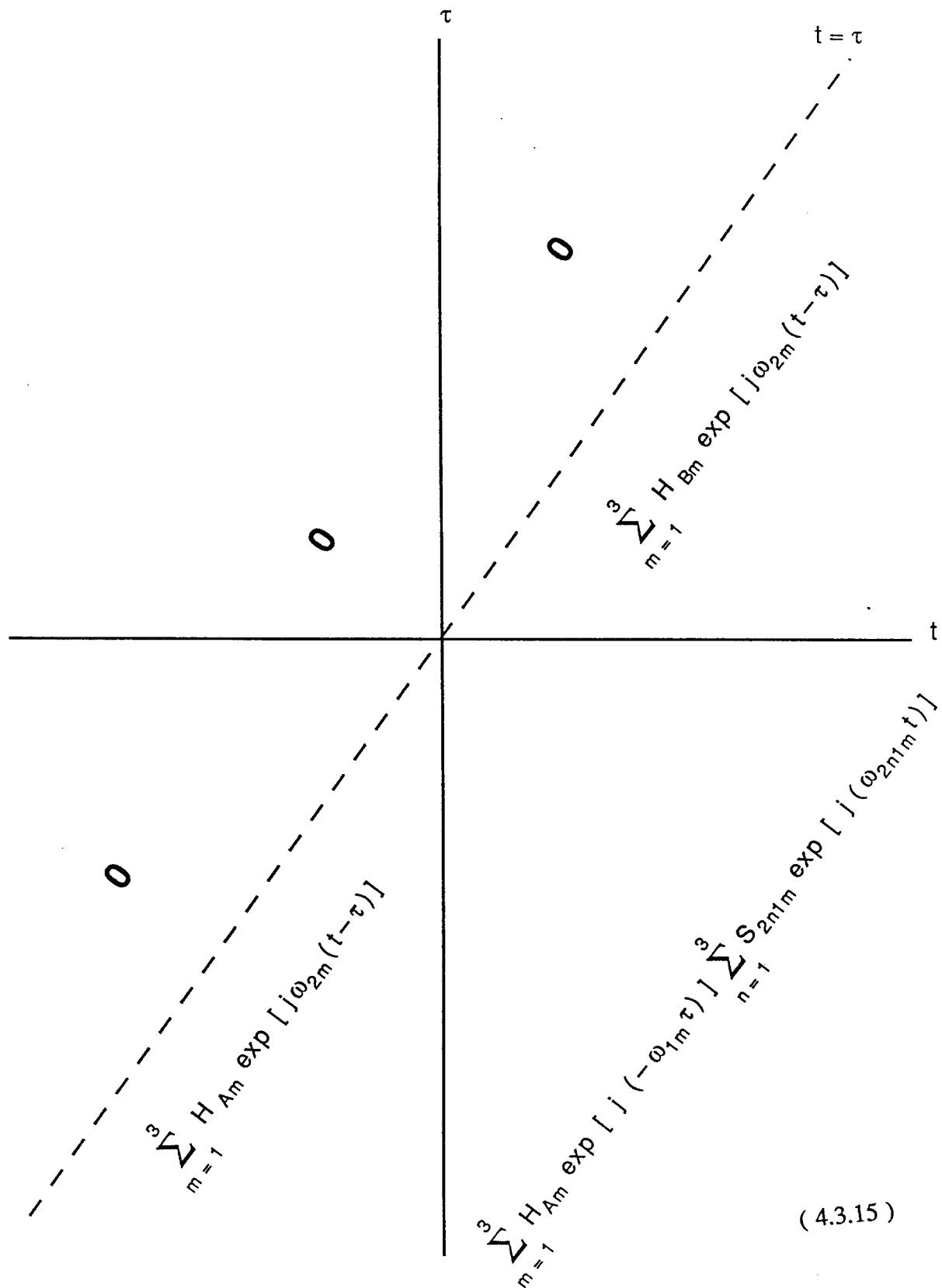
Explicit expressions for  $G(t, \tau)$  valid for various regions of  $(t, \tau)$  plane are given in ( 4.3.15) on the next page .

## 4.4 Perturbation Technique

Proceeding on the lines of [18] for the isotropic case we can show that the  $n$ th order correction term  $h_n$  may be obtained by solving ( 4.4.1 ):

$$\begin{aligned} \frac{d^3 h_n}{dt^3} - j \omega_b \frac{d^2 h_n}{dt^2} + \left[ n_1^2 \omega_1^2 + \tilde{\omega}_p^2(t) \right] \frac{dh_n}{dt} - j n_1^2 \omega_1^2 \omega_b h_n \\ = - \Delta \omega_p^2(t) \frac{dh_{n-1}}{dt} \end{aligned} \quad (4.4.1)$$

where



(4.3.15)

$$h = h_0 + h_1 + h_2 + \dots + h_n + \dots \quad (4.4.2a)$$

and

$$\Delta \omega_p^2(t) = \omega_p^2(t) - \tilde{\omega}_p^2(t) \quad (4.4.2b)$$

The first order correction term may then be written as

$$h_1(t) = \int_{-\infty}^{\infty} d\tau \left[ -\Delta \omega_p^2(\tau) \right] \dot{h}_0(\tau) G(t, \tau) \quad (4.4.3)$$

Since

$$\frac{h_0(t)}{H_0} = \exp [j\omega_1 t], t < 0 \quad (4.4.4a)$$

$$\frac{h_0(t)}{H_0} = \sum_{n=1}^3 S_{2n} \exp [j\omega_{2n} t], t > 0 \quad (4.4.4b)$$

for a finite rise time ( see FIG. 3b )

$$\begin{aligned} \frac{h_1(t)}{H_0} = & \int_{-Tr1}^0 d\tau \left[ -\Delta \omega_p^2(\tau) \right] j\omega_1 \exp [j\omega_1 \tau] \\ & \left[ \sum_{m=1}^3 H_{Am} \exp [-j\omega_{1m} \tau] \sum_{n=1}^3 S_{2n1m} \exp [-j\omega_{2n1m} t] \right] \\ & + \int_0^{Tr2} d\tau \left[ -\Delta \omega_p^2(\tau) \right] \\ & \left[ \sum_{n=1}^3 j\omega_{2n} S_{2n} \exp [j\omega_{2n} \tau] \right] \left[ \sum_{m=1}^3 H_{Bm} \exp [j\omega_{2m} (t-\tau)] \right] \quad (4.4.5) \end{aligned}$$

#### 4.5 Sample Calculation for a Linear Profile

A linear profile for  $\omega_p^2(t)$  function is assumed. The computations for the illustrative example are simplified by choosing  $T_{r1} = 0$  and  $T_{r2} = T_r$ . This will entail some loss of accuracy if the exponential functions  $\exp(x)$  are approximated by only two terms  $(1+x)$  in (4.4.5). However for a linear profile the integration can be carried out analytically without making such an approximation and the loss of accuracy is thus avoided. For the linear profile with  $T_{r1} = 0$

$$\Delta \omega_p^2(t) = -(\omega_{p2}^2 - \omega_{p1}^2) \left(1 - \frac{t}{T_r}\right) \quad (4.5.1)$$

and from (4.4.5)

$$\frac{h_1(t)}{H_0} = \int_0^{T_r} d\tau \left[ (\omega_{p2}^2 - \omega_{p1}^2) \left(1 - \frac{\tau}{T_r}\right) \right] \left\{ \begin{array}{l} \left[ \sum_{n=1}^3 j \omega_{2n} S_{2n} \exp [j \omega_{2n} \tau] \right] \\ \left[ \sum_{m=1}^3 H_{Bm} \exp [j \omega_{2m} (t - \tau)] \right] \end{array} \right\} \quad (4.5.2)$$

For the R wave the left side of (4.5.2) may be expressed as

$$\frac{h_1(t)}{H_0} = \Delta H_{BN} \exp(j \omega_{21} t) + H_{BP1} \exp(j \omega_{22} t) + H_{BP2} \exp(j \omega_{23} t) \quad (4.5.3)$$

where  $\omega_{21}$  is taken as negative (R2 wave),  $\omega_{22}$  positive (R1 wave), and  $\omega_{23}$  positive (R3 wave) and less than  $\omega_{22}$ . Thus  $\Delta H_{BN}$  is the correction to the amplitude of the magnetic field of the R2 wave due to the finite rise time  $T_r$ . Equating the coefficients of  $\exp(j \omega_{2n} t)$  on the left hand side and the right hand side of (4.5.2) we get an expression for  $\Delta H_{BN}$

$$\Delta H_{BN} = (\omega_{p2}^2 - \omega_{p1}^2) H_{B1} \int_0^{T_r} d\tau \left(1 - \frac{\tau}{T_r}\right) \exp(-j \omega_{21} \tau) \left[ \sum_{n=1}^3 j \omega_{2n} S_{2n} \exp [j \omega_{2n} \tau] \right] \quad (4.5.4)$$

Evaluating this definite integral on the right side we get

$$\Delta H_{BN} = (\omega_{p2}^2 - \omega_{p1}^2) H_{B1} \left\{ \begin{aligned} & \frac{S_{21} j \omega_{21} T_r}{2} + \\ & S_{22} \left[ -\frac{\omega_{22}}{\omega_{22} - \omega_{21}} - \frac{j \omega_{22} \exp [j (\omega_{22} - \omega_{21}) T_r - 1]}{T_r (\omega_{22} - \omega_{21})^2} \right] + \\ & S_{23} \left[ -\frac{\omega_{23}}{\omega_{23} - \omega_{21}} - \frac{j \omega_{23} \exp [j (\omega_{23} - \omega_{22}) T_r - 1]}{T_r (\omega_{23} - \omega_{21})^2} \right] \end{aligned} \right\} \quad (4.5.5)$$

The normalized magnetic field ( including the correction term of the R2 wave as a function of  $T_r$  is given by

$$H_{R2}(T_r) = H_{B1} + \Delta H_{BN}(T_r) \quad (4.5.6)$$

and the power reflection coefficient  $\rho$  of the R2 wave is given by

$$\rho_{R2} = \frac{\text{Re}(e_{R2} h_{R2}^*)}{\text{Re}(e_1 h_1^*)} = \frac{|\omega_{21}|}{\omega_1} |H_{R2}|^2 \quad (4.5.7)$$

Figure 13 shows  $\rho$  vs.  $T_r$  for various values of the gyrofrequency. Here  $\omega_{p1}$  is assumed to be zero. Since the medium 1 is free space the source frequency  $\omega_1$  is designated as  $\omega_0$  and the asymptotic plasma frequency in the second medium  $\omega_{p2}$  is designated as  $\omega_p$ . All frequencies are normalized by assuming  $f_0 = \omega_0 / 2\pi = 1$ . Thus  $T_r$  is normalized with respect to the period of the source wave. The plasma frequency  $f_p = \omega_p / 2\pi$  is taken to be 1.2.

The solid line curve, which has the parameter  $f_b = 0$ , is the graph for the isotropic case. Comparison of this curve with the results obtained from the exact solution for the isotropic case for a linear profile[18] shows that the perturbed solution, obtained here, is valid for  $T_r < 0.2$ . For larger values of  $T_r$ , the solution can of course be improved by taking more terms in the perturbation series. For very large values of  $T_r$  ( slow switching ), the perturbation solution must be based on a different Green's function. Such a Green's function has to be developed by using a different

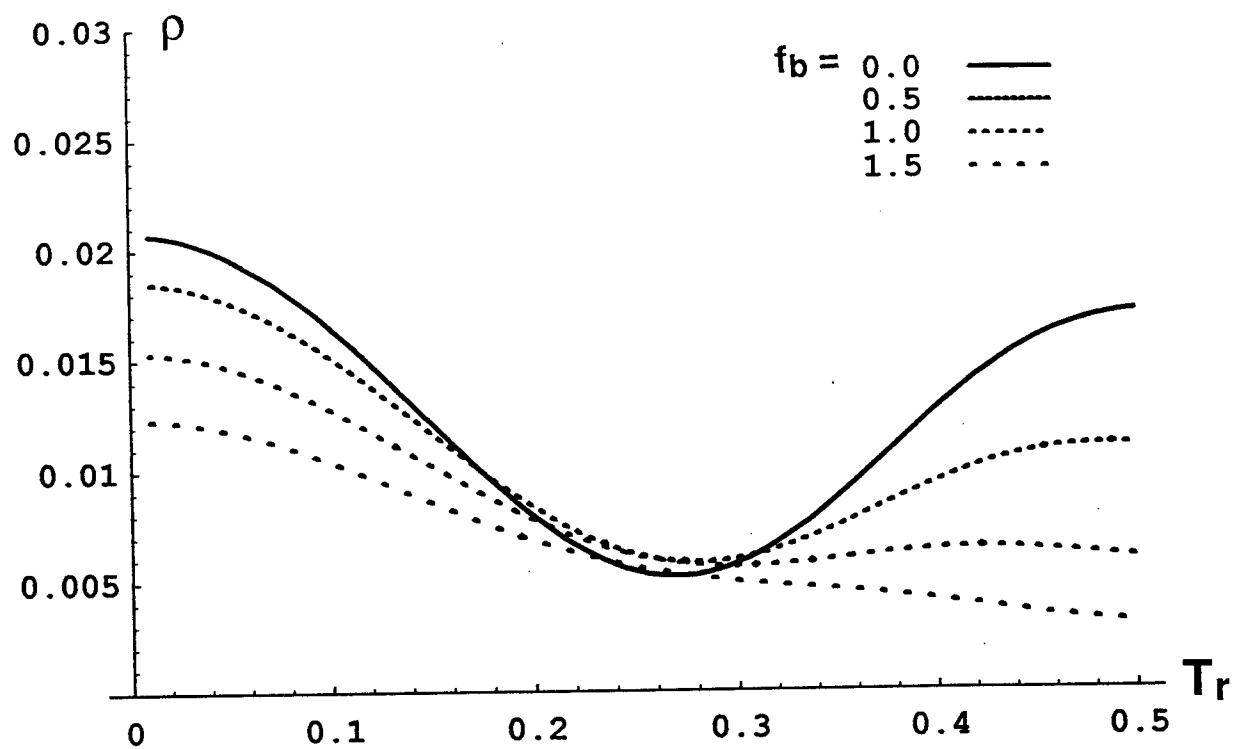


**FIG. 13** R2 wave: power reflection coefficient vs. rise time.  
The variables are normalized, see text

reference profile that is appropriate to slow switching. A starting point for such a development is the WKB solution [14], [15].

## 5. Application to Lightning Induced Ionospheric Effects

### 5.1 Introduction

Lightning induced effects cause a temporary enhancement of ionization [ 21]. Such transient plasmas have a time - varying plasma frequency  $\omega_p ( t )$  with a rise time  $T_r$ . There is considerable interest in the ionospheric community to investigate the recently discovered ' Sprites ' phenomena [ 21] - [23] which are red emissions in the lower D region induced by the lightning discharges from a cloud to the ground. The preliminary indications are that the ' Sprite ' is a plasma with electron density enhanced by about a  $10$  to  $10^3$  / cc. The rise time is about 100 microseconds. However the bulk of the ionization may be taking place in a shorter time duration ( see Figure 3 ) and the effective rise time may be much less than 100 microseconds. The evolution of the electron density in the ' Sprite ' can be diagnosed by tracking from the ground the instantaneous frequency of the upshifted reflected wave with a suitable instrument [24]. If the source frequency is very high ( as in the case of incoherent scatter radar ), the reflection coefficient is negligible and the wave can not be detected by the most sensitive receiver. A source wave in VLF is suitable and in this case the rise time is comparable to the period of the source wave.

### 5.2 Illustrative example

The data for the illustrative example is chosen so as to be relevant in principle to VLF diagnostics of the time evolution of the electron density induced by the lightning. The source frequency  $f_0$  is chosen to be 25 kHz in the VLF range. The plasma frequency is assumed to increase from  $f_{p1} = 0$  to  $f_{p2}$  Hz in a rise time of  $T_r$  seconds. Figure 14 shows a three dimensional picture of the square of the reflection coefficient magnitude (  $| R |^2$  ) obtained by an exact solution for a linear profile of the electron density [18] with a rise time of  $T_r$  seconds. The graph shows that the reflected wave is of sufficient strength for a VLF source wave and can be detected by a suitable receiver.

A question whether the sprite is a plasma or whether the red emissions are caused by processes other than ionization may be answered by diagnosing the B waves or pulses

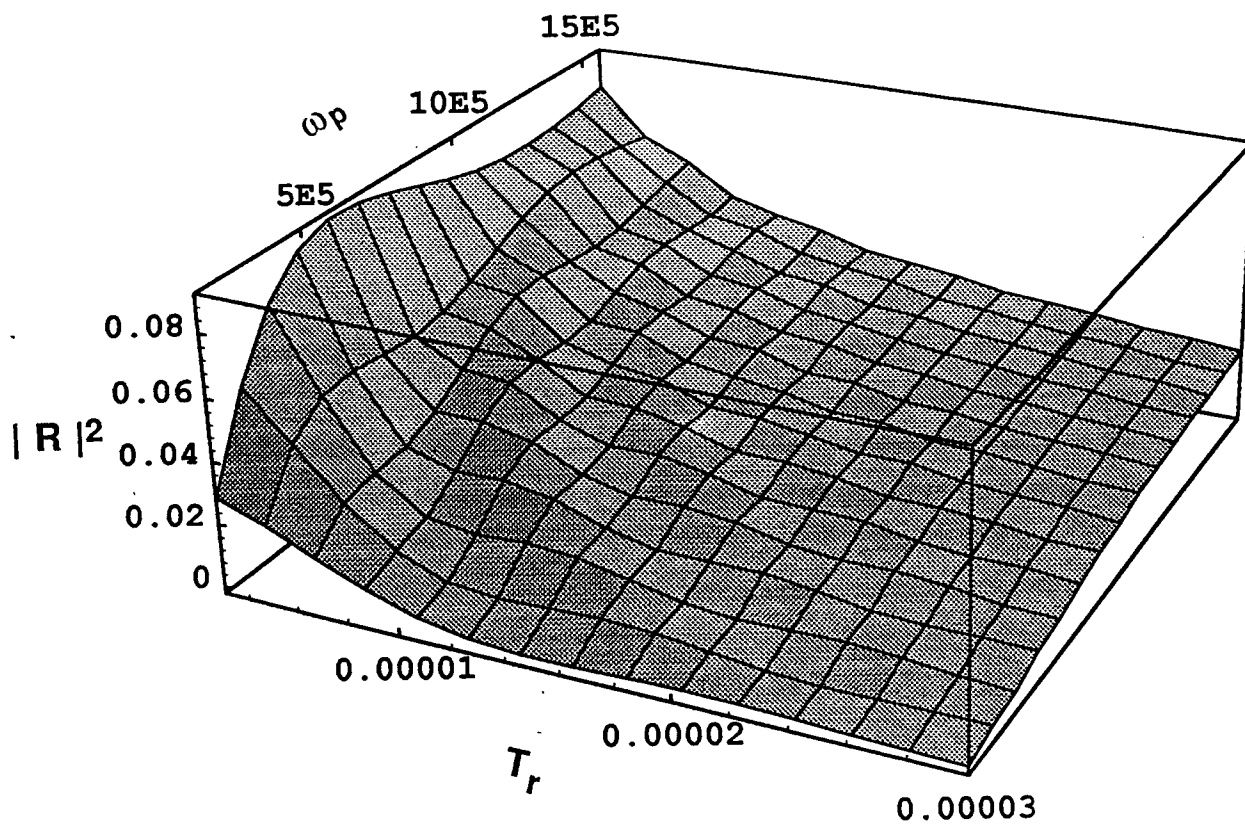


**FIG. 14** Isotropic Plasma: 3 - D graph of the square of the reflection coefficient amplitude for a linear profile obtained through the exact solution. The independent variables are: rise time ( $T_r$ ) in sec. and plasma frequency ( $\omega_p$ ) in rad / sec.

### 5.3 Other Applications

In addition to the 'Sprites', observation of several other lightning induced geophysical phenomena like 'Blue Jets', 'Elves' are reported in the literature. Also ionospheric disturbances in E and F layers require the consideration of dynamic changes in the parameters of a magnetized plasma.. Alteration of the pulse duration in an anisotropic media discussed in section 3 may be a good diagnostic measurement for these time - varying plasmas. These aspects are being explored in active collaboration with my focal point .

## 6. Conclusion

Using one dimensional theory, several aspects of electromagnetic wave transformation in a dynamic magnetized plasma are considered. They may be grouped under the following categories

1. Effects of simultaneous variation of the electron density in space and time
2. Alteration of pulse duration in a dynamic magnetized plasma medium
3. Green's function and perturbation technique for a switched time - varying magnetoplasma medium
4. Application of the theoretical results developed in 1 - 3 to the investigation of lightning induced ionospheric effects. This effort will continue in active collaboration with my focal point .

One dimensional models have shown that the dynamic changes of the parameters of a magnetoplasma have a remarkable effect on a source wave. The next step is to investigate in more depth the realistic three dimensional problems with the help of Finite Difference Time Domain Numerical Technique.

## REFERENCES

- [1] D. K. Kalluri, *Frequency Shifting by a Transient Manetoplasma Medium*, research monograph under preparation
- [2] C. L. Jiang, *IEEE Transactions on Antennas and Propagation*, vol. AP - 23, pp.83 - 90 ( 1975 )
- [3] M. Rader, F. Dyer, A. Matas and I. Alexeff, 1990 IEEE International Conference on Plasma Science 21 - 23 May 1990, CA, Conference Record-Abstracts published by Institute of Electrical and Electronic Engineers, p.171.
- [4] S. P. Kuo, Y. S. Zhang and A. Q. Ren, 1990 IEEE International Conference on Plasma Science 21 - 23 May 1990, CA, Conference Record - Abstracts published by Institute of Electrical and Electronic Engineers, p. 171.
- [5] C. S. Joshi, C. E. Clayton, K. Marsh, D. B. Hopkins, A. Sessler and D. Whittum, *IEEE Trans. Plasma Science*, vol. 18, pp 814 - 818 (1990 ).
- [6] S. C. Wilks, J. M. Dawson and W. B. Mori, *Physical Review Letters*, vol. 61, pp. 337 - 340 (1988 ).
- [7] D. K. Kalluri, *IEEE Transactions on Plasma Science*, vol. 16, pp. 11 - 16, ( 1988 ).
- [8] D. K. Kalluri, V. R. Goteti , *Journal of Applied Physics*, vol. 72, pp. 4575 - 4580 ( 1992 )
- [9] D. K. Kalluri, *IEEE Trans. Antennas and Propagat.* vol. 37, pp. 1638 - 1642 ( 1989 ).
- [10] H. G. Booker, *Cold Plasma Waves*, ( Hingham, MA: Kluwer, 1984 )
- [11] D. K. Kalluri, 1990 IEEE International Conference on Plasma Science 21 - 23 May 1990, CA, Conference Record-Abstracts published by Institute of Electrical and Electronic Engineers, p. 129.
- [12] V. R. Goteti and D. K. Kalluri, *Radio Science*, vol. 25, pp. 61 - 72 ( 1990 ).
- [13] D. K. Kalluri and V. R. Goteti, *IEEE Trans. Plasma Science*, vol. 18, pp.797 - 801 ( 1990 )
- [14] D. K. Kalluri, V. R. Goteti and Andrew Sessler, *IEEE Transactions on Plasma Science*, vol. 21, pp. 70 - 76 ( 1993 )r,
- [15] J. H. Lee, T. Huang and D. K. Kalluri, " Modification of an electromagnetic Source Wave by a time - varying switched plasma medium, " under revision for publication in *IEEE Transactions for Plasma Science*
- [16] D. K. Kalluri, *Journal of Applied Physics*, vol. 79, pp. 3895 – 3899 ( 1996)
- [17] D. K. Kalluri, *Journal of Applied Physics*, vol. 79, pp. 6770 – 6774 ( 1996)

- 
- [ 18] D. K. Kalluri, T. Huang and K. M. Groves, " Green's function for a switched plasma medium and a perturbation technique for the study of wave propagation in a transient plasma with a small rise time, " under revision for publication in *IEEE Transactions for Plasma Science*
  - [19] J. Lekner, *Theory of Reflection*, Boston: Kluwer, 1987.
  - [20] D. K. Kalluri, *IEEE Transactions on Plasma Science*, vol. 21, pp. 77 – 81 (1993 )
  - [21] J. V. Rodriguez, U. S. Inan and T. F. Bell , , *Geophysical Research Letters*, vol. 19, p. 2067 ( 1992 )
  - [22] D. D. Sentman, E. M. Wescott, D. L. Osborne, D. L. Hampton and M. J. Heavner,*Geophysical Research Letters*, Vol. 22, p. 1205 ( 1995 )
  - [23] H. L. Rowland, R. F. Fernsler, J. D. Huba and P. A. Bernhardt , *Geophysical Research Letters*, Vol. 22, p. 361( 1995 )
  - [24] K. Fitzgerald ( 1988 ), *IEEE Spectrum*, Vol. 25, No. 1, p. 49 ( 1988 )

**THERMAL ANALYSIS FOR THE APPLICATION OF HIGH POWER LASERS IN  
LARGE-AREA MATERIALS PROCESSING**

**Jian Xie  
Ph.D Candidate  
and  
Aravinda Kar  
Assistant Professor  
Center for Research and Education in Optics and Lasers (CREOL)**

**University of Central Florida  
4000 Central Florida Boulevard  
Orlando, FL 32816**

**Final Report for:  
Summer Faculty Research Program  
Phillips Laboratory**

**Sponsored by:  
Air Force Office of Scientific Research  
Bolling Air Force Base, DC**

**and  
  
Phillips Laboratory**

**February 1997**

---

THERMAL ANALYSIS FOR THE APPLICATION OF HIGH POWER LASERS IN  
LARGE-AREA MATERIALS PROCESSING

Jian Xie, Ph.D Candidate  
and  
Aravinda Kar, Assistant Professor  
Center for Research and Education in Optics and Lasers (CREOL)  
University of Central Florida

Abstract

The development of high power Chemical Oxygen-Iodine Laser (COIL) by US Air Force Phillips Laboratory makes the large-area materials processing possible. The flexible transmission of COIL beam by optical fibers enhances its application. One of the applications of COIL large-area materials processing is paint removal from aircraft, which is considered as a most potential technique to replace the expensive and waste-generated conventional chemical and mechanical methods. In order to understand the new technique better, a mathematical modeling of paint removal by COIL beam from aircraft is developed. The cross-sectioned shape of paint after laser irradiation and the temperature of aircraft body surface are calculated by the modeling. The effect of laser parameters on the paint removal process is also discussed. An optimum laser power at which the relative more paint is removed and the surface temperature is not so high is found and it is affected by other parameters but is not relative to laser modes. Based on the results derived from the modeling, uniform distribution of power density is suggested for laser large-area materials processing.

# THERMAL ANALYSIS FOR THE APPLICATION OF HIGH POWER LASERS IN LARGE-AREA MATERIALS PROCESSING

Jian Xie and Aravinda Kar

## Introduction

One of the applications of laser large-area materials processing is laser paint removal from aircraft. All aircraft with painted surfaces must be stripped and repainted on an average four-year cycle [1]. Chemical stripping and mechanical abrasion are most often used for paint removal from aircraft [1,2]. However, the use of toxic chemicals and considerable hand scraping result in a large expenditure of personnel hours and the creation of serious air and water pollution. Paint removal is one of the seven most costly elements of maintaining US Naval aircraft [3]. The resulting waste disposal problem has become increasingly important in recent years [1-3].

Using lasers to remove surface coatings from aircraft has been a promising technique since the early 1980s. Cost was the first drive force for developing the technology. Dramatic cost saving will be realized while providing enhanced safety for maintenance personnel [3]. A survey of all potential paint removal processes in 1986 revealed that laser technique had more potential saving than any other processes. Laser paint removal eliminates the environmental hazards associated with chemical methods, reduces waste removal to only paint residue, and allows removal from all types of aircraft substrates. Waste can be minimized to 0.5% of that generated by present chemical stripping techniques, and contained and concentrated in an environmentally acceptable form. In addition, laser paint removal will avoid problems associated with the effects of incompletely removed or neutralized corrosive substances remaining in aircraft faying surfaces or seams after chemical removal [1]. Non-laser automated removal methods such as aqua stripping, dry ice crystals, granulated plastic and abrasive wheat germ pellets may cause surface deformation, surface hardening, and other intrusive and impact-related problems [1]. Another reason to use laser paint removal is that the removal of new high-performance coatings by chemicals ( usually methylene chloride) becomes increasingly difficult. Some of new coatings are resistant to removing and you can begin to realize the dilemma now facing the aerospace industry [2,4,5]. This technique, as a secondary consideration, may subsequently be applied to public transit vehicles including trains, buses, and subway cars and extend to

highway bridges, fuel and water tanks, pressure containers, industrial steel buildings and commercial ship hulls. The commercial potential for lasers and other pulse-power methods of coating removal is considerable. It would result in a savings of approximately \$3 billion per year amount relative to conventional sand blasting [2]. U.S. Navy awarded a contract to build two automated laser paint stripping (ALPS) systems for the stripping of F-14 Fighter and H-3, H46, and H53 helicopters [1].

Both pulsed [1-3,5,6] and CW[2,3] lasers are used for paint removal. CO<sub>2</sub>, Nd:YAG and Excimer lasers are major types of laser for the application [1-3,5,6]. Young *et al.* compared the performance of coating removal with several high power techniques including pulsed and CW, CO<sub>2</sub> and Nd:YAG lasers, and electron beam. The results show that CW Nd:YAG, pulsed Nd:YAG and CO<sub>2</sub> lasers have good performance in removal efficiency [2]. Raiber *et al.* investigated the effect of energy density, pulse frequency as well as other laser parameters on ablating process of paint from aerospace materials with a XeCl-laser [6]. Schweizer and Werner introduced an industrial 2 kW TEA CO<sub>2</sub> laser system for paint removal from aircraft [5]. The description of other laser depaint systems can be found in Refs. 1, 3 and 7. Hickey and Hise developed a color image processing and vision system for an automated laser paint stripping system, which could discriminate between substrates of various colors and textures and paints ranging from semi-gloss grays to high gloss red, white and blue [7]. Stubbier *et al.* investigated the possibility of Excimer laser removal of hard coatings such as TiN or WC from tools [8]. Li *et al.* demonstrated the technical feasibility and basic phenomena of laser removal of embedded contamination down to depths of 0.1-4 mm thick in construction materials such as concrete, brick, plaster/mortar, stones and stainless/carbon steels [9]. Pantelakis *et al.* tested the mechanical behavior of 2024 Al alloy subjected to paint stripping by Excimer, CO<sub>2</sub>, Nd:YAG laser radiation and plasma etching [10]. Their results show that there is no significant degradation in yield and ultimate tensile strength, but in tensile ductility and toughness. The highest degradation results from the use of the plasma etching and Excimer laser, and the lowest reduction from Nd:YAG and CO<sub>2</sub> lasers. There is also a considerable extension in fatigue life.

To make the technique possible and improve the productivity, the high power laser is required [1,5]. The use of CO<sub>2</sub>, Nd:YAG and Excimer lasers for this application has been reported [1-3,5,6]. The chemical oxygen-iodine laser (COIL) may be another good choice for paint removal because it has a short wavelength

( $\lambda=1.315\ \mu\text{m}$ ) close to Nd:YAG laser ( $\lambda=1.06\ \mu\text{m}$ ) and higher power than Nd:YAG laser. COIL can be transmitted by optical fibers instead of the mirror and tube system for CO<sub>2</sub> laser. Unfortunately, no application of COIL in paint removal was reported.

The chemical oxygen-iodine laser (COIL) is still under development and the Phillips Laboratory at the Kirtland Air Force Base is carrying out pioneering research in this area. McDermott, *et al.* invented the COIL in 1977 at the Air Force Weapons Laboratory which is now a part of the Phillips Laboratory [11]. It is the shortest wavelength ( $\lambda= 1.315\ \text{mm}$ ), high power chemical laser ever developed. Truesdell, *et al.* demonstrated the engineering scalability of a supersonic gas flow COIL with the 39 kW RotoCOIL device at the U. S. Air Force's Phillips Laboratory in 1989 [12]. This device used compact, rotating-disk, wetted-wall chemical reactors to generate large quantities of singlet delta oxygen, and then mixed the oxygen with iodine using a stacked supersonic nozzle array [13]. Fujii, *et al.* [14,15] and Wani, *et al.* [16] at Kawasaki Heavy Industries, Ltd., in Japan demonstrated the operation of a COIL for long duration with the operation of a 1 kW subsonic gas flow COIL for 2 hours. At the Phillips Laboratory, sustained high power operation of a supersonic COIL was demonstrated with operation at 9 kW for 2 minutes [17] and at 430 W for 13 minutes on a compact COIL test stand [18]. Further details on COIL development and on the theoretical operation of COIL can be found in Truesdell, *et al.* [12] and Avizonis and Truesdell [19], respectively. Fujioka reviewed the transmission of a COIL beam through optical fibers in 1991 to examine the industrial applications of such beam delivery systems [20].

Some work on further application of the COIL has been carried out recently in Phillips Laboratory. Under the AFOSR 1995 and 1996 summer research program, Dr. A. Kar, from Center for Research and Education in Optics and Lasers in University of Central Florida, worked with Dr. J. E. Scott and Dr. W. P. Latham from Phillips Laboratory. During these time, an extensive theoretical and experimental research were carried out to understand some of the basic principles of thick section cutting with multimode and rectangular COIL beams. Two mathematical models were developed. One of them is based on a simple energy balance to account for the changes in average temperature of the substrate, which is classified as the average temperature model. The second model is based on a more accurate energy balance to account for the pointwise variation of temperature in the substrate, which is classified as the heat conduction model. In

the experimental studies, various process parameters such as the laser power, assist gas nozzle size and the assist gas pressure were varied. Some of the results of these studies have been already presented in the form of a poster in a workshop, and the other data have been published in *Journal of Applied Physics* and *Journal of Laser Applications* and International Conferences. These results are also summarized in reports that have been submitted to the Research and Development Laboratory (RDL) of AFOSR program office.

Although the laser has been consider as a most potential technique for paint removal, the current state of the technology indicates that they are a decade or more off in the future [4]. The proper understanding for the laser paint removal mechanism is essential and important. In this study, a mathematical model of COIL paint removal from aircraft body (aluminum alloy) was developed. The mechanism of laser paint removal could be understood and the effect of laser modes and parameters on paint removal process could be determined by this model. The temperature rise on aircraft surface is also calculated, which is particularly important because we wish to remove the paint without damaging the aircraft body.

#### Mathematical Model

The beam that comes out of a typical COIL cavity is rectangular in shape, and is consisted of several

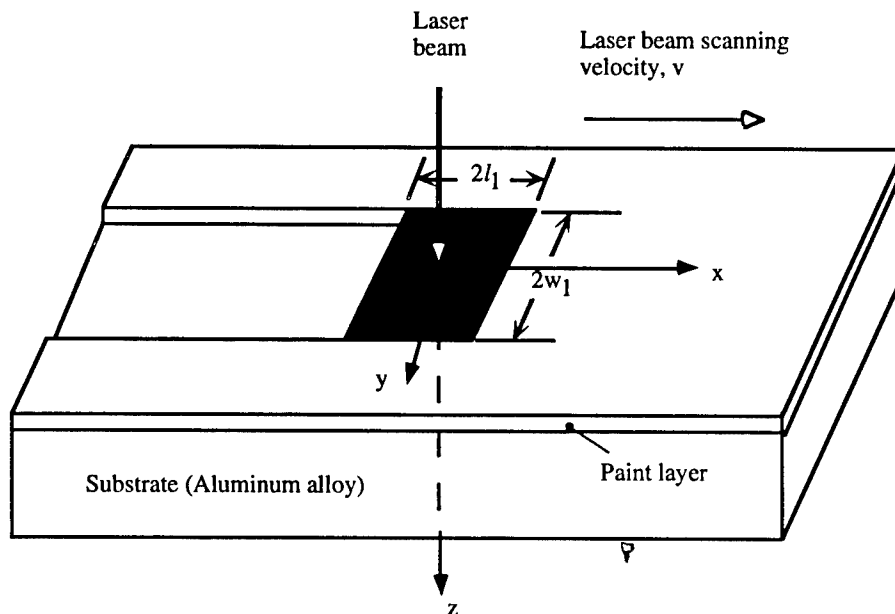


FIG. 1. Laser beam geometry and coordinate system for the mathematical model.

modes. The heating characteristics of a multimode beam is different from that of a Gaussian mode ( $TEM_{00}$ ) beam. The geometric configuration of COIL paint removal is showed in Fig. 1. A rectangular laser beam with a half width of  $w_l$  and a half length  $l_l$  moves in a velocity of  $v$  in  $x$  direction. The paint under the laser irradiation is heated and removed by vaporizing.

From physical point of view, the laser paint removal is a process of melting and vaporizing of paints [2,3 5,6,9]. To make the problem clearer, we first consider the one-dimensional melting and vaporizing of paint under laser irradiation with a power density  $I$  as shown in Fig. 2.  $H_1$  and  $H_2$  are vaporizing depth and melting depth, respectively, which change with laser-paint interaction time  $t$ . The arrows in Fig. 2 indicate the heat flux in or out at boundaries. The substrate is aircraft body made of aluminum or aluminum alloy.  $I_{sub}$  is the heat conduction loss by substrate.

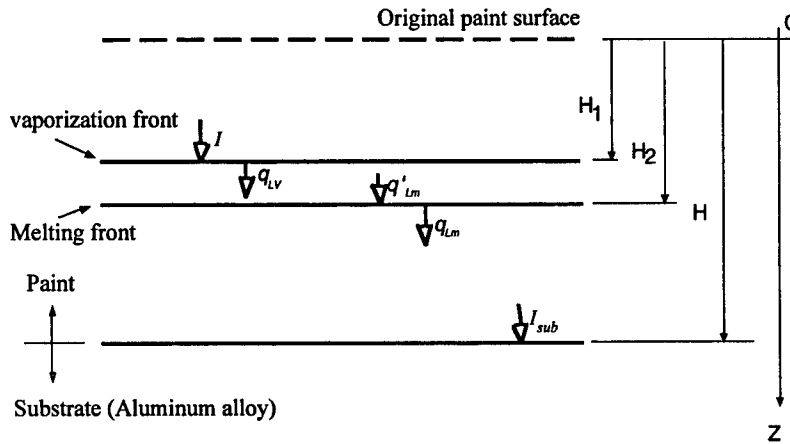


FIG. 2. Heat flux in paint melting and vaporizing process at a site with laser intensity  $I$

The phase change occurs in the liquid-vapor and solid-liquid interfaces and can be described by Stefan condition as follows

$$\rho L_v \frac{dH_1}{dt} = I - q_{LV} \quad \text{at } z=H_1 \quad (1)$$

$$\rho L_m \frac{dH_2}{dt} = q'_{Lm} - q_{Lm} \quad \text{at } z=H_2 \quad (2)$$

where  $L_m$  and  $L_v$  are the latent heats of melting and vaporizing, respectively. In quasi-steady state of paint melting and vaporizing, the liquid-vapor interface is moving down in a same speed as solid-liquid interface [21], e.g.,

$$\frac{dH_1}{dt} = \frac{dH_2}{dt} \quad (3)$$

In this case, the temperature distribution in liquid layer is almost linear and the heat transferred into the liquid ( $q'_{Lm}$ ) layer should be same as the heat transferred out the liquid layer ( $q_{LV}$ )

$$q'_{Lm} = q_{LV} \quad (4)$$

Rearranging the Eqs. (1-2) based on Eqs. (3-4), we obtain

$$q_{LV} = \frac{L_m I + L_v q_{Lm}}{L_m + L_v} \quad (5)$$

In the practical paint removal process in Fig. 1 (quasi-steady-state two-dimensional problem), the above equations are still available by changing the interaction time  $t$  to locations in  $x$  axis

$$t = \frac{l_1 - x}{v} \quad (6)$$

The heat flux  $q_{LM}$  can be taken as  $I_{sub}$  because the energy used to rise the temperature of the solid paint is negligible because it is small compared to the large amount of latent heats of melting and vaporizing.

Considering the effect of the different interaction time at different locations, we can assume

$$q_{Lm} = I_{sub} \frac{l - x}{2l} \quad (7)$$

Since the linear temperature distribution in liquid layer in quasi-steady state, the heat flux  $q_{LV}$  can be expressed by

$$q_{LV} = k_l \frac{T_v - T_m}{H_2 - H_1} \quad (8)$$

The thickness of liquid layer ( $H_1$ - $H_2$ ) can be derived from Eqs. (5), (7) and (8)

$$H_2 - H_1 = \frac{k_l (L_v + L_m) (T_v - T_m)}{L_m I + L_v I_{sub} (l_1 - x) / (2l_1)} \quad (9)$$

Substituting Eqs. (5-7) into Eq. (1) and integrating it, the vaporizing depth is given by

$$H_1 = \frac{1}{\rho v(L_v + L_m)} \int_x^{l_1} (I - I_{sub} \frac{l_1 - x}{2l_1}) dx \quad (10)$$

We need to know the intensity distribution of COIL beam for the calculating of vaporizing depth. The laser intensity,  $I$ , is given by

$$I = \sum_{m=0}^M \sum_{n=0}^N I_{mn} \quad (11)$$

where  $M$  and  $N$  are the largest mode number of the beam in the  $x$  and  $y$  directions, respectively.  $I_{mn}$  is the intensity of the rectangular beam of  $m$ -th and  $n$ -th order modes, which is given by

$$I_{mn} = I_0 H_m^2 \left( \frac{\sqrt{2}x}{l_{10}} \right) H_n^2 \left( \frac{\sqrt{2}y}{w_{10}} \right) \exp \left( -\frac{2x^2}{l_{10}^2} \right) \exp \left( -\frac{2y^2}{w_{10}^2} \right) \quad (12)$$

$$\text{where } I_0 = \frac{2AP_{mn}}{\pi 2^{m+n} m! n! l_{10} w_{10}} \quad (13)$$

and  $P_{mn}$  is the total power of the laser beam of  $m$ -th and  $n$ -th order modes.  $l_{10}$  and  $w_{10}$  are, respectively, the half-length and half-width of the Gaussian mode. If  $l_1$  and  $w_1$  are, respectively, the half-length and half-width of the spot for the beam with TEM<sub>mn</sub> mode,  $l_1$  and  $w_1$  are related to Gaussian spot size by the expressions,

$$l_1 = l_{10} \sqrt{2m+1} \quad \text{and} \quad w_1 = w_{10} \sqrt{2n+1}. \quad A \text{ is the absorptivity of the workpiece. } H_m \text{ and } H_n \text{ are,}$$

respectively,  $m$ -th and  $n$ -th degree Hermite polynomials for the  $m$ -th and  $n$ -th order modes of the laser beam.

An  $(m+1)$ -th degree Hermite polynomial in  $x$  can be written as

$$H_{m+1}(x) = 2xH_m(x) - 2mH_{m-1}(x) \quad (14)$$

where  $H_0(x) = 1$  and  $H_1(x) = 2x$ .

The heat flux reached to substrate surface,  $I_{sub}$ , has similar intensity distribution with  $I$  and it is the difference between original heat input by laser beam and the heat dissipated by melting, vaporizing and heating of paint, so

$$I_{sub} = (I_{sub})_0 H_m^2 \left( \frac{\sqrt{2}x}{l_{10}} \right) H_n^2 \left( \frac{\sqrt{2}y}{w_{10}} \right) \exp \left( -\frac{2x^2}{l_{10}^2} \right) \exp \left( -\frac{2y^2}{w_{10}^2} \right) \quad (15)$$

$$\text{where } (I_{sub})_0 = I_0 \left[ 1 - \frac{-\rho[L_v + L_m + c_p(T_v - T_0)] \frac{dH_1}{dt}}{I_{ave}} \right] \quad (16)$$

$$I_{ave} = \frac{A \sum_m \sum_n P_{mn}}{(2l_1)(2w_1) / \sqrt{(2m+1)(2n+1)}} \quad (17)$$

The  $(dH_1/dt)$  can be represented approximately as  $(H/\tau)$ , where the interaction time

$$\tau = \frac{2l_1}{v} \quad (18)$$

Therefore, the heat flux reached to substrate surface can be represented by both Eq. (15) and the following equation

$$(I_{sub})_0 = I_0 \left[ 1 - \frac{\rho[L_v + L_m + c_p(T_v - T_0)]}{A \sqrt{(2m+1)(2n+1)} \sum_m \sum_n P_{mn}} (2w_1)vH \right] \quad (19)$$

So far, the distribution of laser intensity  $I$  and heat flux in substrate surface  $I_{sub}$  have been obtained and the vaporizing and melting depths can be calculated numerically from Eqs. (9,10).

During the laser irradiation, a portion of the laser energy is dissipated by paint removal and the rest is conducted to substrate (aluminum alloy) which causes the temperature rise of substrate. The surface temperature is what we pay more attention to because we wish to remove the paints completely without damaging the substrate (no melting occurs). The temperature distribution in substrate is calculated based on a 3-dimensional heat conduction model subjected to the heat flux  $I_{sub}$  as follows.

The governing equation for the temperature distribution in substrate is given by

$$\alpha \left( \frac{\partial^2 T}{\partial x^2} + \frac{\partial^2 T}{\partial y^2} + \frac{\partial^2 T}{\partial z^2} \right) = -v \frac{\partial T}{\partial x} \quad (20)$$

for  $-\infty \leq x \leq \infty$ ,  $-\infty \leq y \leq \infty$ , and  $0 \leq z \leq \infty$ . Here  $\alpha$  is the thermal diffusivity of the workpiece, which is defined by  $\alpha = k_{sub}/(\rho c)$ , where  $k_{sub}$  and  $c$  are the thermal conductivity and specific heat of the substrate respectively.  $v$  is the velocity of the laser beam in the  $x$  direction. Eq. (20) is written in a

moving Cartesian coordinate system whose origin lies at the center of the beam. The temperature  $T$ , which represents  $T(x,y,z)$ , in Eq. (20) is the dimensionless temperature of the workpiece, and is defined by

$$T = \frac{T_1 - T_0}{T_m - T_0} \quad (21)$$

where  $T_1$ ,  $T_0$  are the actual and initial temperature of the substrate respectively.  $T_m$  is the melting point of paints. The boundary conditions for Eq. (20) are given by

$$T \rightarrow 0 \text{ as } x \rightarrow \pm\infty \quad (22a, b)$$

$$T \rightarrow 0 \text{ as } y \rightarrow \pm\infty \quad (22c, d)$$

$$T \rightarrow 0 \text{ as } z \rightarrow \infty \quad (22e)$$

$$k \frac{\partial T}{\partial z} = -\frac{1}{T_m - T_0} I_{sub} \text{ at } z = 0 \quad (22f)$$

let us define

$$T = T_2 \exp(-bx), \text{ where } b = \frac{v}{2\alpha} \quad (23)$$

Substituting Eq. (23) into Eq. (20), we obtain

$$\frac{\partial^2 T_2}{\partial x^2} + \frac{\partial^2 T_2}{\partial y^2} + \frac{\partial^2 T_2}{\partial z^2} = -b^2 T_2 \quad (24)$$

The boundary conditions for  $T_2$  are same as those given by the conditions (22a-e). However, due to Eq. (23), boundary condition (22f) takes the following form:

$$\frac{\partial T_2}{\partial z} = -\sum_{m=0}^M \sum_{n=0}^N a_{mn} f_m(x) g_n(y) \quad \text{at } z = 0 \quad (25)$$

where

$$a_{mn} = \frac{(I_{sub})_0}{k(T_m - T_0)} \quad (26a)$$

$$f_m(x) = H_m^2 \left( \frac{\sqrt{2}x}{l_{10}} \right) \exp \left( bx - \frac{2x^2}{l_{10}^2} \right) \quad (26b)$$

$$g_n(y) = H_n^2 \left( \frac{\sqrt{2}y}{w_{10}} \right) \exp \left( -\frac{2y^2}{w_{10}^2} \right) \quad (26c)$$

Using the following Fourier transform pair

$$\text{Integral transform: } \bar{T}_2(p, q, z) = \int_{-\infty}^{\infty} dx \exp(ipx) \int_{-\infty}^{\infty} dy \exp(iqy) T_2(x, y, z) \quad (27a)$$

$$\text{Inversion formula: } T_2(x, y, z) = \frac{1}{4\pi^2} \int_{-\infty}^{\infty} dp \exp(-ipx) \int_{-\infty}^{\infty} dq \exp(-iqy) \bar{T}_2(p, q, z) \quad (27b)$$

the solution of Eq. (24) that satisfies the boundary condition (25) and the conditions as

$x \rightarrow \pm\infty$ ,  $y \rightarrow \pm\infty$ , and  $z \rightarrow \infty$ , can be written as

$$T_2(x, y, z) = \frac{1}{4\pi^2} \sum_{m=0}^M \sum_{n=0}^N a_{mn} \int_{-\infty}^{\infty} dp \exp(-ipx) \bar{f}_m(p) \int_{-\infty}^{\infty} dq \exp(-iqy) \bar{g}_n(q) \frac{\exp\left(-\sqrt{p^2 + q^2 + b^2} z\right)}{\sqrt{p^2 + q^2 + b^2}} \quad (28)$$

where  $\bar{f}_m(p)$  and  $\bar{g}_n(q)$  are Fourier transforms of  $f_m(x)$  and  $g_n(y)$ , respectively, which are given by

$$\bar{f}_m(p) = \int_{-\infty}^{\infty} dx \exp(ipx) f_m(x) \quad (29a)$$

$$\bar{g}_n(q) = \int_{-\infty}^{\infty} dy \exp(iqy) g_n(y) \quad (29b)$$

Noting that the Fourier inverse transform ( $F^{-1}$ ) of  $\frac{\exp\left(-\sqrt{p^2 + q^2 + b^2} z\right)}{\sqrt{p^2 + q^2 + b^2}}$  is given by

$$\begin{aligned} \mathbf{F}^{-1} \left\{ \frac{\exp\left(-\sqrt{p^2 + q^2 + b^2} z\right)}{\sqrt{p^2 + q^2 + b^2}} \right\} &= \frac{1}{4\pi^2} \int_{-\infty}^{\infty} dp \exp(-ipx) \int_{-\infty}^{\infty} dq \exp(-iqy) \bar{g}_n(q) \frac{\exp\left(-\sqrt{p^2 + q^2 + b^2} z\right)}{\sqrt{p^2 + q^2 + b^2}} \\ &= \frac{1}{2\pi} \frac{\exp\left(-b\sqrt{r^2 + z^2}\right)}{\sqrt{r^2 + z^2}}, \quad \text{where } r = \sqrt{x^2 + y^2} \end{aligned} \quad (30)$$

and applying the convolution theorem to Eq. (28), we can obtain an expression for  $T_2(x,y,z)$  which can be substituted into Eq. (23) to obtain the following expression for the dimensionless temperature  $T(x,y,z)$ .

$$T(x,y,z) = \frac{\exp(-bx)}{\pi} \sum_{m=0}^M \sum_{n=0}^N a_{mn} \int_0^{\infty} r' dr' f_m(x - r' \cos \theta) \int_0^{\pi} d\theta g_n(y - r' \sin \theta) \frac{\exp\left(-b\sqrt{r'^2 + z^2}\right)}{\sqrt{r'^2 + z^2}} \quad (31)$$

The integrals in Eq. (31) are numerically evaluated by using the trapezoidal rule for numerical integration to calculate the temperature distribution for various process parameters.

We need to know the thermophysical properties of paints and substrate (aluminum) for numerical calculating. Unfortunately, few data are found by searching the relative literature and by contacting some paint manufacturers and research centers of materials properties in Purdue University and Illinois Institute of Technology. The basic components of a paint consist of film-forming substances, resins, plasticizers and pigments [22]. The polymer film formers can either be macromolecular products or low molecular mass compounds that react to form macromolecules on curing. Increasing molecular mass of the polymer film formers results in improved mechanical properties of the film until a limiting values is reached. The polymer film former of the first group are represented by cellulose nitrate or vinyl chloride co-polymers. The second group includes polyurethanes or epoxy resins. Too much resin produces hard and brittle coatings whereas too much plasticizer produces soft films. Since only small amounts of resins and plasticizers are used, they also may be classified as paint additives. Therefore, the physical properties of paint is mainly determined by the polymer film. Since it is lack of thermophysical properties of paints, we may use the data of polymers as an estimation.

However, it is also difficult to find all of the thermophysical properties of a polymer. Fortunately, the thermophysical properties of almost all polymers are close, so we can choose the average values of most polymers. The thermophysical properties of polymers are collected in Appendix. The thermophysical properties of aluminum [23,24] and polymers [see Appendix] used for numerical calculation are listed in Table 1.

Table 1 Thermophysical properties of polymers (Appendix) and aluminum [23,24]

	<i>Polymers</i>	<i>Aluminum</i>
Density $\rho$ (kg/m <sup>3</sup> )	1200	2700
Specific heat $c_p$ ( $\times 10^3$ J/kg-K)	2.0	0.899
Latent heat of melting ( $\times 10^5$ J/kg)	0.65	0.97
Latent heat of vaporization ( $\times 10^5$ J/kg)	2.72	112.97
Melting temperature (K)	473	933
Thermal decomposition temperature (K)	593	
Thermal conductivity (W/mK)	0.2	92
Thermal diffusivity ( $\times 10^{-6}$ m <sup>2</sup> /s)	0.1	38

## Results and Discussion

The vaporizing depth of paint and temperature of substrate surface are calculated numerically by Eqs. (10) and (31) with different process parameters and laser modes. The absorptivity is quite high for paint [25] and is taken to be 80% in this study. The paint thickness of 1 mm is chosen in the calculation.

The power density distribution of TEM<sub>31</sub> COIL beam with a 10 mm in width and length is shown in

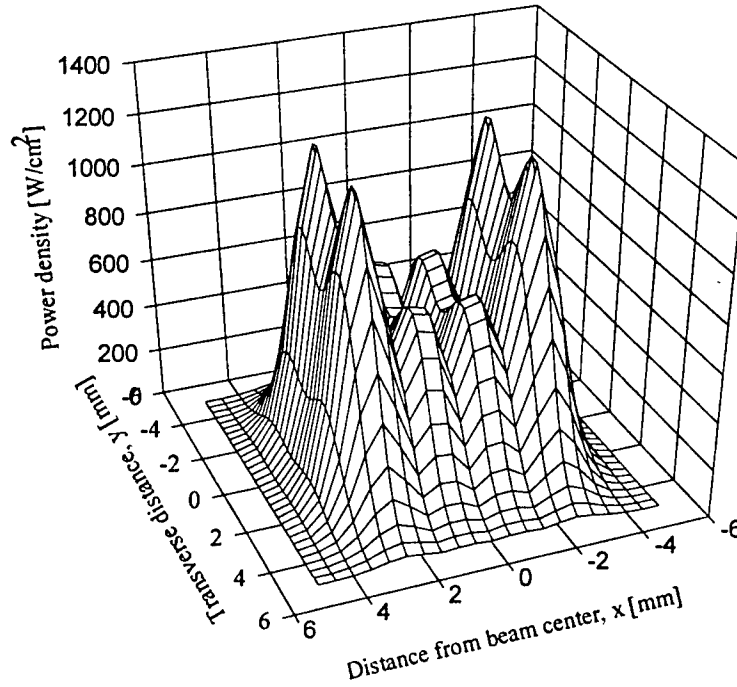


FIG. 3. Three-dimensional distribution of power density of a COIL beam (TEM<sub>31</sub>, P=450 W,  $2l_1=2w_1=10$  mm)

Fig. 3. It should be noted that  $M=3$  and  $N=1$  correspond to  $m=0,1,2,3$  and  $n=0,1$  respectively. For the beam having  $m=0,1,2,3$  and  $n=0,1$ , it means that the beam has 4 and 2 modes in the  $x$  and  $y$  directions respectively. Due to the particular choice of the power distribution in each mode given by Table II, the intensity is low at the beam center and it becomes maximum near the edges of the beam in both  $x$  and  $y$  directions as shown in Fig. 3. There are 4 major peaks of power density at corners and 4 minor peaks in the center. The paint front under the  $TEM_{31}$  COIL beam irradiation and the temperature distribution of substrate surface in the area of laser beam are shown in Figs. 4 and 5.

Table II Power distribution for  $TEM_{31}$  COIL beam (W)

		$n$	
		0	1
$m$	0	7.5	7.5
	1	30	30
	2	75	75
	3	112.5	112.5

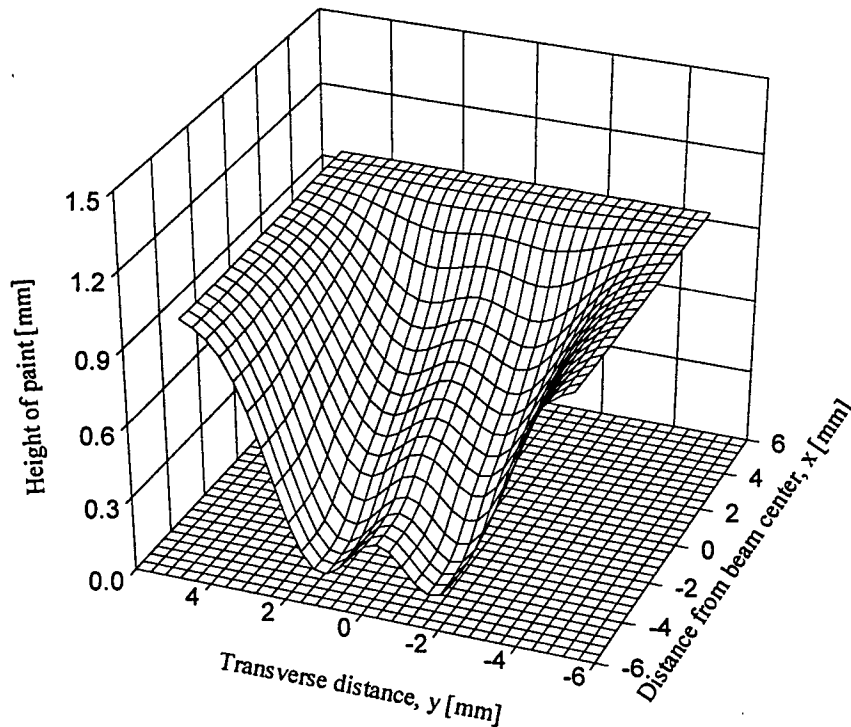


FIG. 4. Variation of hight of paint when COIL beam scans in  $x$  direction ( $TEM_{31}$ ,  $P=450$  W,  $v=10$  cm/s,  $2l_1=2w_1=10$  mm)

At the front edge of laser spot in Fig. 4, the paint begins to be heated and nothing is removed. When the laser beam moves in  $x$  direction, the paint under the laser irradiation is heated up to melting, even vaporizing melting and the paint is vaporized continually. There are two valleys because there are two peaks of the power density in this region. At the rear edge of laser spot, the cross section of the paint looks like a letter "W". Paint cannot be removed at the both sides of laser spot because of the low power density. The temperature distribution of substrate surface is related to both the peaks of power density and thickness of paint. The highest temperatures are located around rear peak of power density as shown in Fig. 5.

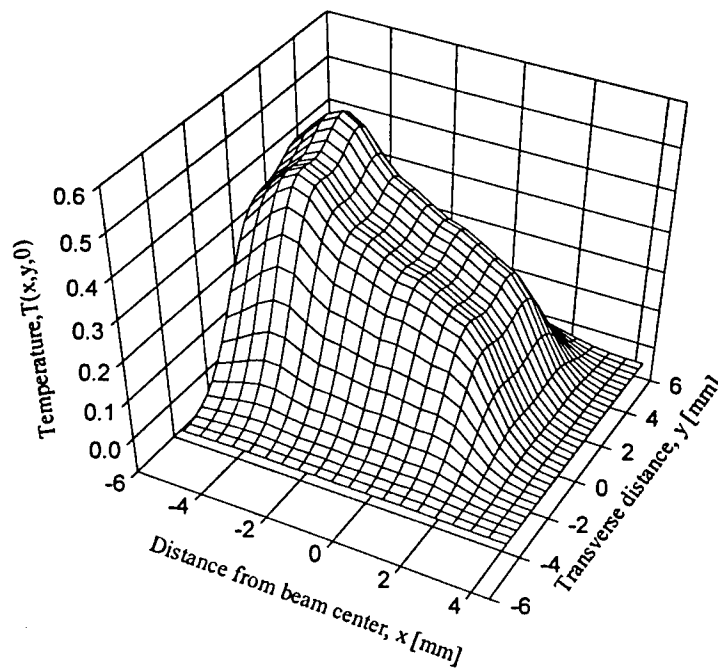


FIG. 5. Three-dimensional distribution of normalized surface temperature (TEM<sub>31</sub>, P=45 W, v=10 cm/s, 2l<sub>i</sub>=2w<sub>i</sub>=10mm)

The final cross-sectioned shapes of paint after TEM<sub>31</sub> COIL beam scanning is like a letter "W" when the laser power is not strong enough. The paint will be vaporized completely around the center of laser spot when the laser power increases as shown in Fig. 6. It can be seen from the figure that the paint in the central area is removed when the laser power is high enough (about 500 W). However, the removed width of paint in the central region cannot be expected to increase greatly with the increasing of laser power. The effect of scanning speed of laser beam on the paint removal is shown in Fig. 7. The removed width

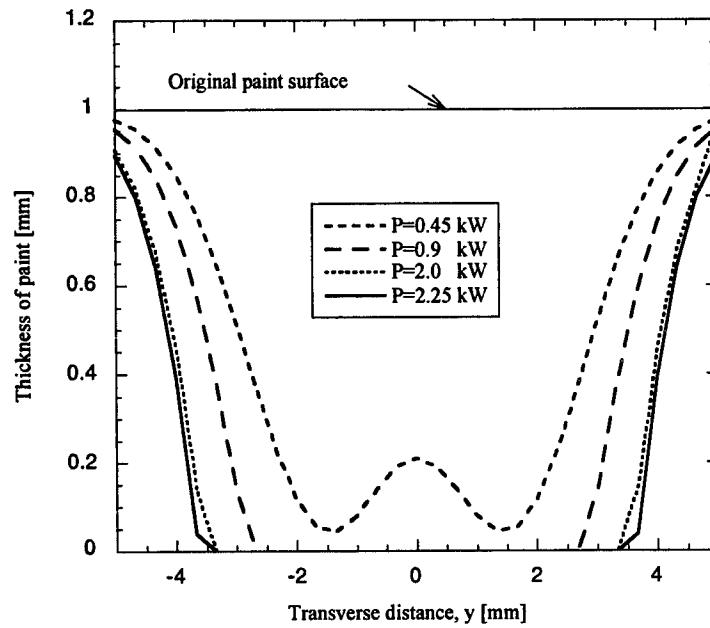


FIG. 6. Variation of cross-sectioned shape of paint with laser power ( $TEM_{31}$ ,  $v=10$  cm/s,  $2l_1=2W_1=10$  mm)

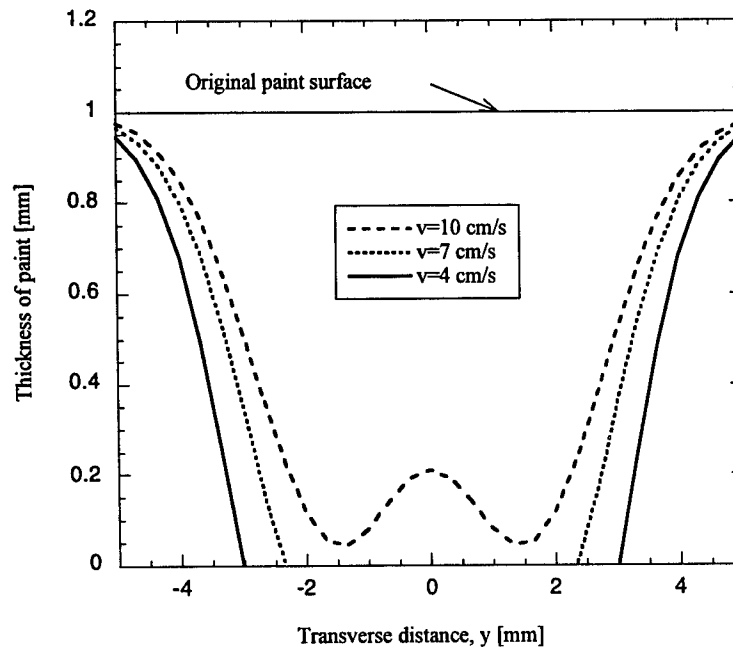


FIG. 7. Variation of cross-sectioned shape of paints with scanning speed ( $TEM_{31}$ ,  $P=450$  W,  $2l_1=2W_1=10$  mm)

increase with the decrease in laser scanning speed. However, we do not wish to reduce the speed too much because the high efficiency of paint removal is what we need.

When the laser power and other process parameters are kept as constant and only the width of laser beam is increasing, the removed width of paint increases as shown in Fig. 8. This means that the wider beam should be chosen to remove the more paint when the laser power is high enough. If the width of laser beam is kept unchanged and the high laser power is applied, the rest of laser power other than that used to vaporize the paint will be utilized to heat up the substrate and may cause the damage of substrate such as melting and degrading of mechanical properties. Similar situation occurs when the laser power is increased and other parameter are kept constant as shown in Fig. 6. The increase in removed width of paint is limited even the laser power increases dramatically. The increased amount of laser energy is conducted to substrate for heating up the substrate. Our aim is to remove the paint completely without damaging the substrate and the further heating of substrate should be avoided.

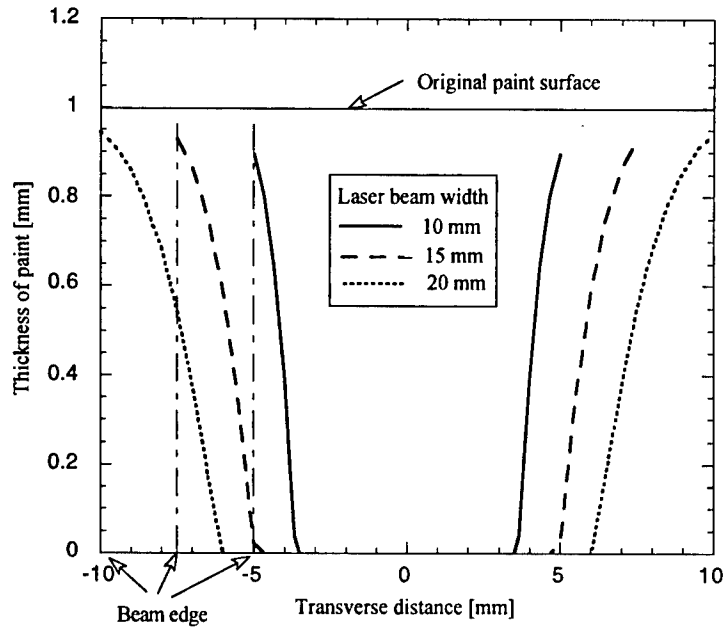


FIG. 8. Cross-sectioned shape of paint at different width of laser beam  
(TEM<sub>31</sub>, P=2.25 kW, v=10 cm/s, 2l=10 mm)

The removed width of paint and the highest temperature on substrate surface for different laser power are summarized in Fig. 9. This figure indicates that the surface temperature increase greatly and removed

width of paint has a limited increase when the laser power is high. In the situation shown in Fig. 9, an optimum laser power is found to be about 1 kW as the removed width of paint increases is not expected to increase a lot with increasing laser power but the higher power than 1 kW will causes the rapid rise in surface temperature. There is a maximum removed width of paint at which the surface temperature reaches the melting point of substrate. The maximum removed width of paint is about 6.4 mm in Fig. 9. When the laser power is less than a minimum value which is about 500 W in Fig. 9, the laser power is not strong enough to vaporize the paint completely from substrate. Similarly, we believe that there is a optimum laser power when other parameters such as scanning speed, beam width and length etc. changes. The relative-wider area paint is removed and the temperature of substrate surface is not high when the optimum laser power is applied. The optimum laser power can be identified by the model developed in this study.

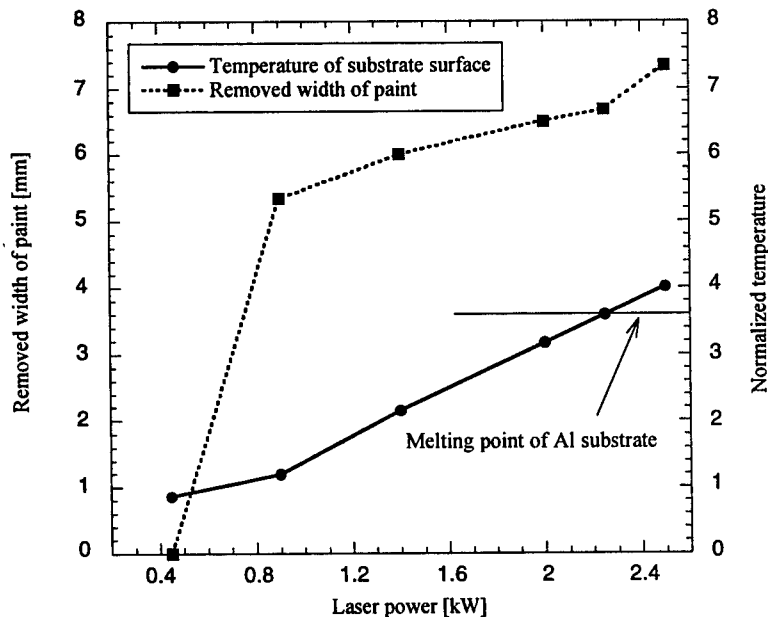


FIG. 9. Variation of removed width and highest normalized temperature of substrate surface with laser power ( $TEM_{31}$ ,  $v=10$  cm/s,  $2l=2W_1=10$  mm)

We have discussed the paint removal by  $TEM_{31}$  COIL beam. The  $TEM_{00}$  mode, e.g., Gaussian beam, is often used in laser materials processing. The three-dimensional distribution of square COIL Gaussian beam is shown in Fig. 10, which is a little different from circle Gaussian beam in edges. The paint front irradiated by square COIL Gaussian beam is shown in Fig. 11. It is easy to understand that more paint is

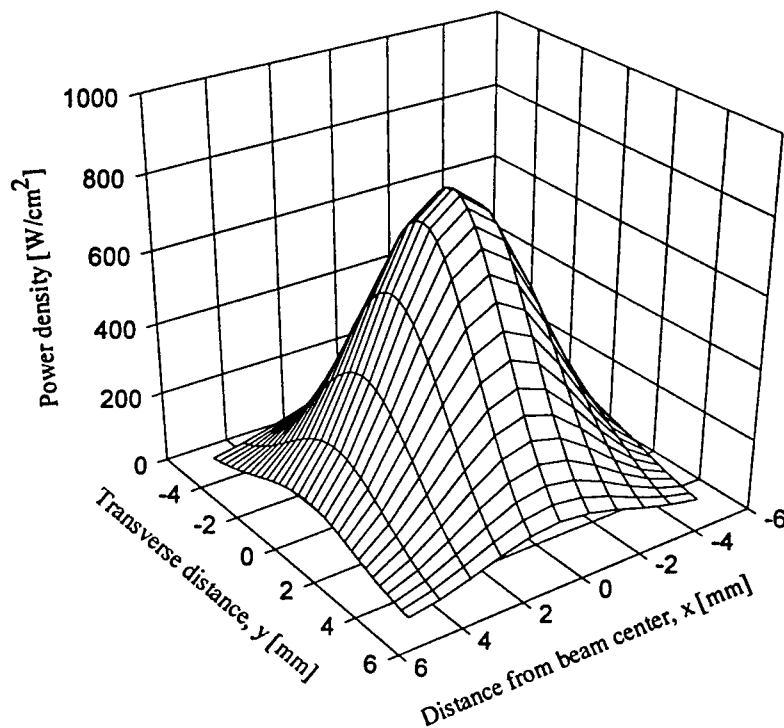


FIG. 10. Three-dimensional distribution of power density for  $TEM_{00}$  COIL beam (Power 400 W)

removed in rear edge than front edge of laser spot and the paint valley is located at the center of rear edge of beam. The cross section of paint is similar to the Gaussian distribution. However, the highest surface temperature is a little behind the center of the square beam in the  $x$  direction.

It is interesting to compare the effect of  $TEM_{00}$  and  $TEM_{31}$  modes on the process of paint removal. First we make a plot of cross-sectioned shape of paint changed with laser power for  $TEM_{00}$  COIL beam as shown in Fig. 12. There is a similar trend as  $TEM_{31}$  that the removed width increases in a limited value when the

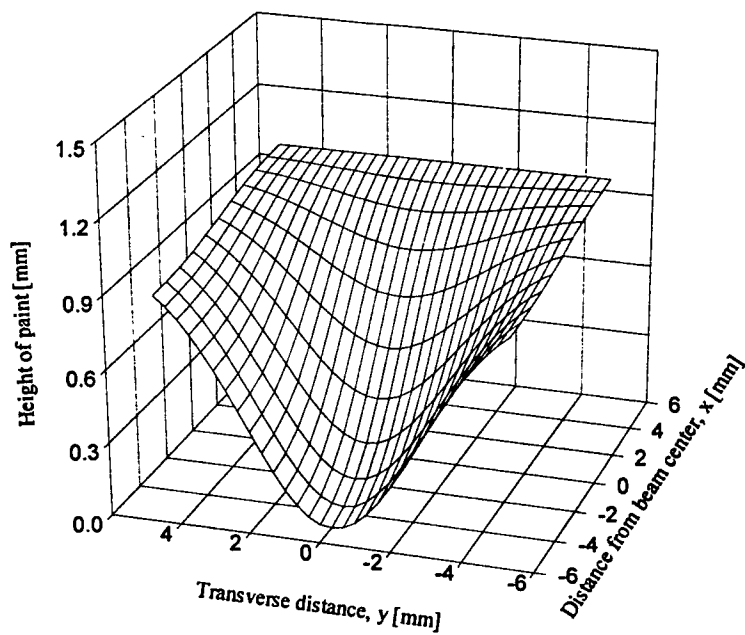


FIG. 11. Cross-section of paint after  $TEM_{00}$  COIL beam radiation  
( $P=400$  W,  $v=10$  cm/s,  $2l_1=2w_1=10$  mm)

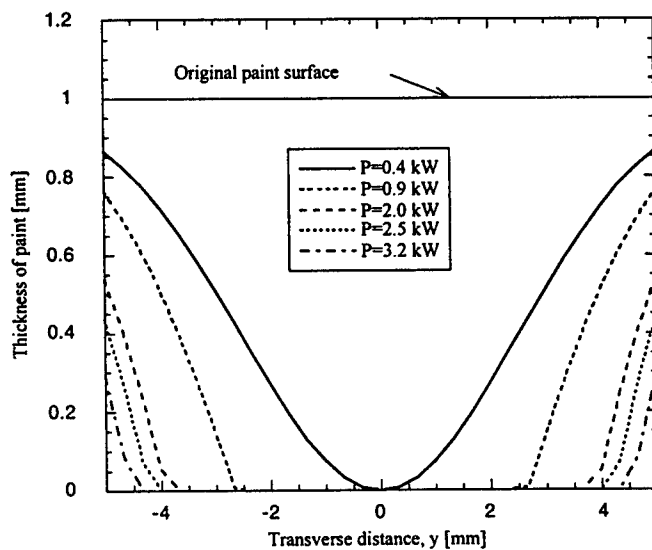


FIG. 12. Variation of cross-sectioned shape of paint with laser power  
( $TEM_{00}$ ,  $v=10$  cm/s,  $2w_1=2l_1=10$  mm).

laser power is high. Much of laser energy is dissipated to heat up the substrate. Similarly, we believe that there is an optimum laser power at which the relative more paint is removed but the substrate temperature is not high. The optimum laser power of  $TEM_{00}$  is found to be about 1 kW same as that of  $TEM_{31}$ . This indicates that the optimum laser power is not relative with laser mode.

The removed width of paint and temperature of substrate surface for  $TEM_{31}$  and  $TEM_{00}$  COIL beams are compared in Figs. 13 and 14. The removed widths of paint for  $TEM_{31}$  and  $TEM_{00}$  beams are almost same when the laser power is below the optimum power, but the width of  $TEM_{00}$  is a little higher than that of  $TEM_{31}$  when the higher power is applied (Fig. 13). This is because that the power density of  $TEM_{00}$  in the both side edges is a little higher than that of  $TEM_{31}$ . However, the temperature of substrate surface caused by  $TEM_{31}$  beam irradiation is always higher than by  $TEM_{00}$ . This situation is caused by the higher values at the peak of power density in  $TEM_{31}$  which can be seen clearly by comparing their distributions of power density in Figs. 3 and 10. To avoid the high temperature of substrate surface and remove more paint,

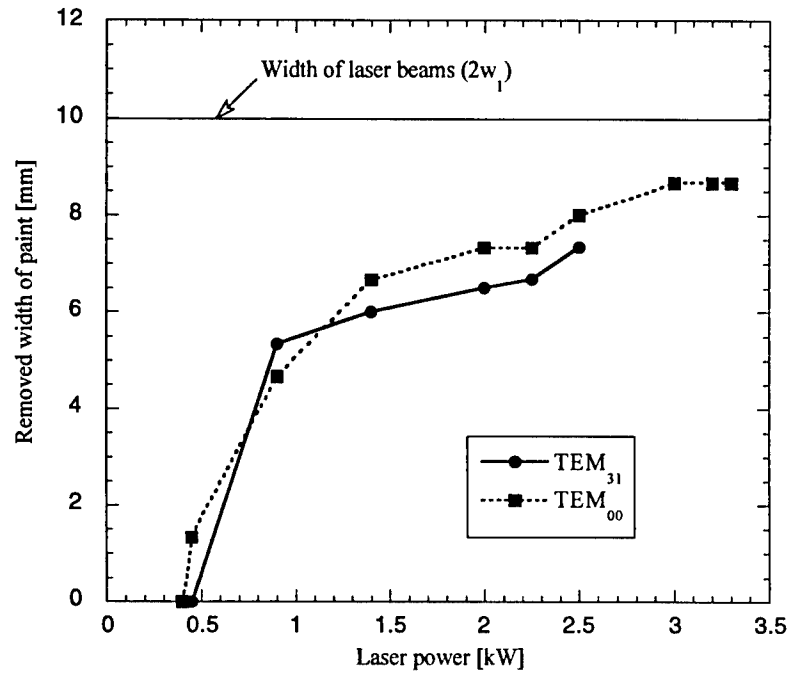


FIG. 13. Variation of removed width of paint with laser power ( $v=10$  cm/s,  $2l_1=2w_l=10$  mm).

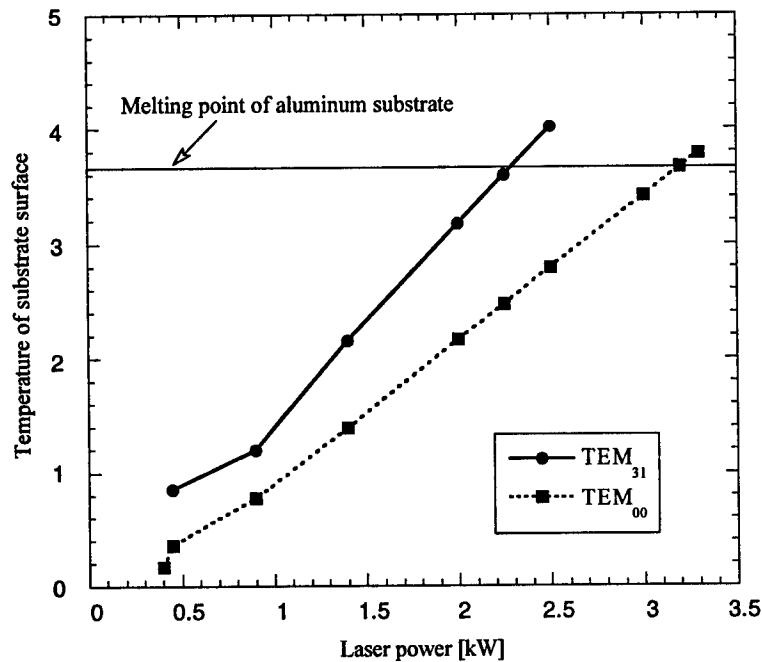


FIG. 14. Variation of normalized temperature of substrate surface with laser power ( $v=10$  cm/s,  $2l_1=2w_1=10$  mm)

the uniform distribution of power density is needed. That is, the beam quality with "flat top" or uniform energy density distribution is very important for large-area surface treatment [5, 26].

In this study, the process of laser paint removal is presented and the temperature of substrate surface is estimated. However, the effect of laser heat on mechanical properties of substrate should be investigated further. Experiments has showed that the degradation in ductility of aircraft body has been found [10]. A detail investigation on the effect of laser power, scanning speed , and laser mode on mechanical properties should be carried out. This investigation will indicate if the degradation is acceptable by practical service of aircraft. The further improvement to this model by both experimental and theoretical study is also important to predict the process accurately.

## Conclusions

- (1) A mathematical model for laser paint removal is developed in this study. This model can be used to estimate the processing of paint removal and the effect of laser parameters on process. The temperature of substrate surface is also calculated numerically by the model.
- (2) The cross-sectioned shape of paint is like a letter of "W" after  $TEM_{31}$  COIL beam irradiation and it is similar to Gaussian distribution after  $TEM_{00}$  beam irradiation when the laser power is low. The paint around the center of beam rear edge is removed completely by vaporizing when laser power is high enough.
- (3) The removed width of paint and the temperature of substrate surface increase with the increase in laser power and decrease in beam scanning speed and beam width. There is optimum laser power at which the relative more paint is removed and the temperature is not high. The optimum value is affected by other process parameters and is not relative to laser mode.
- (4) The removed width of paints by both  $TEM_{31}$  and  $TEM_{00}$  COIL beam are close to each other, but the  $TEM_{31}$  beam causes higher temperature rise on substrate surface.
- (5) The uniform distribution of power density is good for large-area surface treatment. The high value of peak power density may damage the substrate or cause the further degradation in properties of substrate.

## References

- [1] J. F. Foley, Automated Laser Paint Stripping, Metal Finishing, Vol. 90, 1992, pp. 48-50.
- [2] C. M. Young, W. M. Moeny, R. D. Curry, K. McDonald and J. T. Bosma, Application of Lasers and Pulsed Power to Coating Removal, in *Novel Applications of Lasers and Pulsed Power*, edited by R. D. Curry, Proceedings of SPIE-The International Society for Optical Engineering, Vol. 2374, San Jose, California, 1995, pp. 2-9.
- [3] P. Lavoie, Laser Paint Stripping Offers Control and Flexibility, Laser Focus World, November, 1994, pp. 75-80.
- [4] K. E. Abbott, Dry Media Blasting for the Removal of Paint Coatings on Aerospace Surfaces, Metal Finishing, Vol. 94, 1996, pp. 33-35.

- [5] G. Schweizer and L. Werner, Industrial 2 kW TEA CO<sub>2</sub> Laser for Paint Stripping of Aircraft, in *Gas Flow and Chemical Lasers*, edited by W. L. Bohn, and H. Hugel, Proceedings of SPIE-The International Society for Optical Engineering, Vol. 2502, Germany, 1994, pp.57-62.
- [6] A. Raiber, B. Plege, R. Holbein, Paint-Stripping with a XeCl-laser: Basic research and Processing Techniques, in *Gas Flow and Chemical Lasers*, edited by W. L. Bohn, and H. Hugel, Proceedings of SPIE-The International Society for Optical Engineering, Vol. 2502, Germany, 1994, pp. 670-675.
- [7] J. M. Hickey III and L. E. Hise, Color Image Processing and Vision System for an Automated Laser Paint Stripping System, in *Intelligent Robots and Computer Vision XIII: Algorithms and Computer Vision*, edited D. P. Casasent, Proceedings of SPIE-The International Society for Optical Engineering, Vol. 2353, Boston, Massachusetts, 1994, pp. 503-512.
- [8] E. Schubert, K. Schtte, A. Emmel, and H. W. Bergmann, Excimer Laser Assisted TiN and WC Removal from Tools as a Novel Decoating Technology, in *Gas Flow and Chemical Lasers*, edited by W. L. Bohn, and H. Hugel, Proceedings of SPIE-The International Society for Optical Engineering, Vol. 2502, Germany, 1994, pp. 656-663.
- [9] L. Li, W. M. Steen, P. J. Modern, J. T. Spencer, Laser Removal of Surface and Embedded Contamination on/in Building Structures, in *Laser Materials Processing and Machining*, Proceedings of SPIE-The International Society for Optical Engineering, Vol. 2246, Frankfurt, Germany, 1994, pp. 84-95.
- [10] Sp. G. Pantelakis, Th. B. Kermanidis, and Haidemenopoulos, Mechanical Behavior of 2024 Al Alloy Specimen Subjected to Paint Stripping by Laser Radiation and Plasma Etching, *Theoretical and Applied Fracture Mechanics*, Vol. 25, 1996, 139-146.
- [11] W. E. McDermott, N. R. Pchelkin, D. J. Benard and R. R. Bousek, *Appl. Phys. Lett.* **32**, 469 (1978).
- [12] K. A. Truesdell, C. A. Helms and G. D. Hager, "COIL Development in the USA," 25th Plasmadynamics and Lasers Conference, AIAA 94-2421, June 1994.
- [13] J. E. Scott, J. L. R. Shaw, K. A. Truesdell, G. D. Hager and C. A. Helms, "Design Considerations for the Chemical Oxygen-Iodine Supersonic Mixing Nozzle," 25th Plasmadynamics and Lasers Conference, AIAA 94-2436, 1994.
- [14] H. Fujii, S. Yoshida, M. Iizuka and T. Atsuta, *J. Appl. Phys.* **66**, 1033 (1989).

- [15] H. Fujii and T. Atsuta, "Current Status of Industrial COIL Development," Third International Workshop on Iodine Lasers and Applications, SPIE Vol. 1980, Bechyne Castle, Czechoslovakia, pp. 148-152, 1992.
- [16] F. Wani, N. Naitou, T. Nagai, M. Iizuka, H. Tsuji and H. Fujii, in Proceedings of Laser Advanced Materials Processing (LAMP '92), Niigata, Japan, pp. 127-132, June 1992.
- [17] K. A. Truesdell, T. Lonergan, C. Wisniewski, K. Healey, J. Scott and C. Helms, "COIL Thermal Management," 25th Plasmadynamics and Lasers Conference, AIAA 94-2441, June 1994.
- [18] S. Phipps, C. A. Helms and K. A. Truesdell, "Compact CW Supersonic Chemical Oxygen Iodine Laser (COIL)," 25th Plasmadynamics and Lasers Conference, AIAA 94-2453, June 1994.
- [19] P. V. Avizonis and K. A. Truesdell, "Historical Perspectives of the Chemical Oxygen-Iodine Laser (COIL)," 25th Plasmadynamics and Lasers Conference, AIAA 94-2416, June 1994.
- [20] T. Fujioka, *Infrared Phys.* **32**, 81 (1991).
- [21] C. L. Chan and J. Mazumder, One-dimensional Steady-state Model for Damage by Vaporization and Liquid Expulsion due to Laser-material Interaction, *J. Appl. Phys.*, Vol. 62, 1987, pp. 4579-4586.
- [22] D. Stoye, *Paints, Coatings and Solvents*, VCH GmbH, Weinheim, 1993, pp.3-7.
- [23] E. A. Brandes, editor, *Smithells Metals Reference Book*, 6th ed., Butterworths, Boston, 1983.
- [24] Y.S. Touloukian and C.Y. Ho, *Thermophysical Properties of Selected Aerospace Materials, Part II: Thermophysical Properties of Seven Materials*, Purdue University, 1977.
- [25] J.A. Hopkins, V.V. Semak and M.H. McCay (1994), in *Laser Material Processing*, Proc. ICALEO'94, Vol. 2500, Edited by T.O. McCay, A.Matsunawa and H.Hugel, Laser Institute of America, Orlando, Florida, pp.838-845.
- [26] B. Godard, P. Murer, P. Laborde, M. Stehle, J. Bonnet, D. Pigache, A 10 J×100 Hz XeCl Laser for Large Surface Treatment, *Lasers and Electro-Optics Europe*, Amsterdam, Netherlands, 1994, p. 81.

## Appendix Thermophysical Properties of Polymers

### (1) Thermal conductivity (W/mK)

Polymer	Thermal Conductivity (W/mK)	Reference
Epoxy resin	0.2	[A-7],[A-11]
Polyethylene	0.2	[A-2]
LDPE	0.33	[A-2]
HDPE	0.65	[A-2]
PTEF	0.3	[A-11]
Polyvinyl carbazole	0.16	[A-12] (p. 972)
TAC polyester	0.18	[A-12] (p. 976)
Natural and synthetic rubber	0.21-0.32	[A-12] (p. 972)
Polyvinyl chloroxide	0.17 at 300-500 K	[A-12] (p. 1086)
Polystyrene	0.16	[A-12] (p. 1090)

The thermal conductivity of polymers is in the range of 0.15-0.45 W/mK [A-6]. It is in about 0.15-0.3 W/mK for most polymers as shown in Fig. A-1 [A-6].

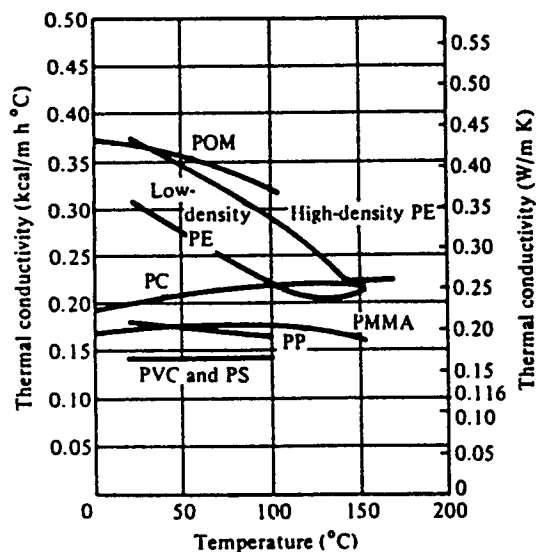


FIG. A-1. Thermal conductivity versus temperatures

## (2) Thermal diffusivity

Polymers	Thermal Diffusivity ( $10^{-6} \text{ m}^2/\text{s}$ )	Reference
EP	0.06	[A-11]
HDPE	0.9	[A-11]
Natural rubber	0.04-0.15 at 300-500 K	[A-12] (p. 1058)
Synthetic rubber	0.06-0.16	[A-12] (p. 1060)
Polyvinyl chloride	0.09	[A-12] (p. 1082)
Polyvinyl cabazole	0.1	[A-12] (p. 1082)
Phenolic resin	0.125	[A-12] (p. 1082)
TAC polyester	0.115	[A-12] (p. 1082)

## (3) Melting temperature

Polymer	Melting Temperature ( $^{\circ}\text{C}$ )	Reference
PVDC	198-205	[A-3]
Poly(vinyl chloride)	200-220	[A-5]
Polytetrafluoroethylene	310-340	[A-4]
Polyvinlidene fluoride	210	[A-9]
Polypropylene	176	[A-9]
Nylon-6	225	[A-9]
PVC	180	[A-9]
Polystyrene	230	[A-9]
Polymethylene	108-136	[A-10]

## (4) Thermal decomposition temperature

Polymer	Thermal Decomposition Temperature ( $^{\circ}\text{C}$ )	Reference
Poly(methl methacrylate) in $\text{H}_2$	310	[A-4]
in Air	242	[A-4]
Polystyrene in $\text{H}_2$	337	[A-4]
Polystyrene filled with $\text{SiO}_2$ in $\text{H}_2$	337	[A-4]
Phenol-formaldehyde resin in $\text{H}_2$	432	[A-4]
Benzhydrylated cellulose in Air	280-310	[A-4]

## (5) Specific heat

Polymer	Specific Heat (J/gK)	Reference
polyethylene	2.3 at room temperature	[A-10]
	2.9 at 12-140 °C	[A-10]
Polyvinyl carbazole	1.24	[A-12] (p. 970)
Cresol resin	1.6	[A-12] (p. 1004)
Nylon	1.3 at room temperature	[A-12] (p. 1047)
	2.09 at 100 °C	[A-12] (p. 1047)
	2.50 at 180 °C	[A-12] (p. 1047)
Synthetic rubber	1.5	[A-12] (p. 1054)
Silicon resin	1.36 at 300-650 K	[A-12] (p. 1072)
Phenyl silane resin	1.4-2.1 at 300-650 K	[A-12] (p. 1074)
PVC resin	1.25	[A-12]
Poly(vinyl chloride)	$C_p = 0.248 + 8.46 \times 10^{-4} T$ (Cal/°Cg <sup>3</sup> )	
	at 20-120 °C	[A-5]

#### (6) Latent heat of fusion

Polymer	Latent Heat of Fusion (J/g)	Reference
Vinylidene Chloride (VDC)	65-82	[A-3]
PVDC	43-47	[A-3]
PE	176-213	[A-4]

#### (7) Latent heat of evaporation

	Latent heat of evaporation (J/g)	Reference
Vinylidene Chloride Monomer	272	[A-3]

#### (8) Heat of Combustion

Polymer	Heat of Combustion (kJ/g)	Reference
Rubber	40	[A-10]
Polyisobutylene	47	[A-10]
Polypropylene	46	[A-10]
Polystyrene	41	[A-10]
ABS	36	[A-10]
Polyformaldehyde	17	[A-10]
Poly(vinyl chloride)	18	[A-10]

Poly(methyl methacrylate)	25	[A-10]
---------------------------	----	--------

(9) Density

Paint or Polymer	Density	Reference
An Aliphatic Polyurethane Gloss	14.709 lbs/gal	[A-8]
Titanium Dioxide Pigmented Paint (Federal Standard Color 17875)		
Polyethylene	0.92-0.96 g/cm <sup>3</sup>	[A-10]
Phenolic resin	1.30 g/cm <sup>3</sup>	[A-12] (p. 980)
Natural and synthetic rubber	1.2-1.7 g/cm <sup>3</sup>	[A-12] (p. 1051)
TAC Polyester	1.23 g/cm <sup>3</sup>	[A-12] (p. 974)

(10) Selected thermophysical properties for paints

Thermal conductivity	0.2	W/mK
Thermal diffusivity	$0.1 \times 10^{-6}$	m <sup>2</sup> /s
Melting temperature	200	°C
Thermal decomposition temperature	320	°C
Specific heat	2.0	J/gK
Latent heat of fusion	65	J/g
Latent heat of vaporization	272	J/g
Density	1.2	g/cm <sup>3</sup>

[A-1] D. Stoye, Paints, Coatings and Solvents, VCH mbH, Weinheim, 1993, pp.3-7.

[A-2] D. Porter, Group Interaction Modelling of Polymer Properties, Dow Benelux, N.V., The Netherlands, 1995, pp. 241.

[A-3] R. A. Wessling, Polyvinylidene Chloride, Gordon & Breach Science, New York, 1977, pp. 7, 70, 81, 106.

[A-4] R. F. Schwenker, Jr., Thermoanalysis of Fibers and Fiber-Forming Polymers, John Wiley & Sons, New York, pp.81, 90, 128.

[A-5] J. V. Koleske and L. H. Wartman, Poly(vinyl chloride), Gordon & Breach Science, New York, 1969, pp. 62, 65.

[A-6] P. C. Powell, Engineering with Polymer, Chapman and Hall, London, 1983, pp. 240-243.

[A-7] H. Lee and K. Neville, Handbook of Epoxy Resins, McGraw-Hill, New York, 1967, p.6-32.

- [A-8] U.S. Paint Company, St. Louis, MO, personal communication.
- [A-9] Handbook of Polymer Science and Technology, Vol. 1: Synthesis and Properties, Ed. N. P. Cheremisinoff, Marcel Dekker, New York and Basel, 1989, p. 495.
- [A-10] Handbook of Polymer Science and Technology, Vol. 2: Performance Properties of Plastics and Elastomers, Ed. N. P. Cheremisinoff, Marcel Dekker, New York and Basel, 1989, pp. 207, 352, 355, 363.
- [A-11] G. Hartwig, Polymer Properties at Room and Cryogenic Temperatures, Plenum, New York and London, 1994, pp. 110, 112, 114.
- [A-12] Y. S. Touloukian and C. Y. Ho, Thermophysical Properties of High Temperature Solid Materials, Vol. 6, Part II: Oxidment, Polymer and Composite, Macmillan, New York, 1967.

Analytical Noise Modeling and Optimization of a Phasor-Based  
Phase Reconstruction Algorithm

Thomas F. Krile  
Professor  
and  
James L. Fox  
MSEE  
Department of Electrical Engineering

Texas Tech University  
Lubbock, TX 79409

Final Report for:  
Summer Research Extension Program  
Phillips Laboratory

Sponsored by:  
Air Force Office of Scientific Research  
Bolling Air Force Base, DC

and  
Phillips Laboratory

December 1996

# ANALYTICAL NOISE MODELING AND OPTIMIZATION OF A PHASOR-BASED PHASE RECONSTRUCTION ALGORITHM

Thomas F. Krile  
Professor  
James L. Fox  
MSEE  
Department of Electrical Engineering  
Texas Tech University

## Abstract

An important procedure in the areas of adaptive optics and speckle imaging is to reconstruct an estimate of an incident wavefront's phase field, given measurements of the incident field's phase differences. Optimal linear procedures for this phase reconstruction are well known, and a newer phasor-based technique has recently been introduced. In a typical phase reconstruction algorithm, forming a weighted sum of phases and/or phase differences is an often-repeated operation, and the phasor-based approach minimizes the problem of  $2\pi$  phase ambiguities at points of zero field amplitude by averaging phasor paths instead of phase/phase difference paths. While there are general analytical models available for studying the performance of linear reconstructors in the presence of phase measurement noise, no such models exist for the phasor-based case. Until now, noise studies of the new phasor-based reconstruction technique were done using computer simulations with randomly generated noise data.

In this paper, an analytical technique for finding the probability density function (pdf) of the output noise, and thence the noise variance and noise gain, for phasor-based path averaging systems is developed. Variable path weights have been incorporated as inputs to the output noise pdf algorithm which characterizes the phasor-based reconstructor. These path weights have been optimized to minimize the output noise variance, and robustness and optimality results are compared to those obtained using path weights derived from optimal linear techniques.

# ANALYTICAL NOISE MODELING AND OPTIMIZATION OF A PHASOR-BASED PHASE RECONSTRUCTION ALGORITHM

Thomas F. Krile

James L. Fox

## I. INTRODUCTION

An important procedure in the areas of adaptive optics and speckle imaging is to reconstruct an estimate of an incident wavefront's phase field, given measurements of the incident field's phase differences. In adaptive optics systems, the phase field information is then used to compensate for atmospheric disturbances [1]. In the case of speckle imaging, the phase field information is used, along with intensity measurements, to reconstruct the complex far field pattern of the original object, which is then Fourier transformed to obtain an estimate of the object[2,3].

Two methods of phase reconstruction that are currently used are linear [1,4] and nonlinear (phasor-based) [2] reconstruction. This paper concentrates on the effect that phase measurement noise has on these two methods of phase reconstruction. Until recently, noise studies of a new non-linear phasor-based reconstruction technique were done using computer simulations with randomly generated noise data. These studies indicated that, as far as noise performance is concerned, the non-linearity introduced into the reconstruction process by the phasor-based approach leads to markedly different (inferior) noise behavior than that for the non-phasor (linear) case for a range of input noise variances [5,6,].

This paper will present an analytical method for finding the probability density function (PDF) and variance of the output noise of the phasor-based reconstructor[7]. Variable path weights have been added as inputs to the output noise PDF program which characterizes the non-linear reconstructor. These path weights have been optimized to minimize the output noise variance and results are compared to those obtained using path weights derived from optimal linear techniques. The robustness of the output noise

variance with respect to the input noise variance estimates will also be examined. Section II of this paper discusses the development of the linear and phasor-based noise models. From these models, the probability density function of  $\Phi_n$ , the reconstructor output noise, will be developed in Section III. Next, Section IV will discuss the method for finding the optimal phasor-based weights for the reconstructor. Section V will present a comparison of the noise performances of each of the two reconstructors (phasor and non-phasor). Noise gain, optimality of the phasor weights and robustness to input noise estimations will also be mentioned. Conclusions are given in Section VI.

## II. NOISE MODEL DEVELOPMENT

### 2.1. LMS Phase Reconstruction Model

The least mean square (LMS) phase reconstruction method uses a weighted sum of phases and/or phase differences to reconstruct the wavefront of an incident waveform from its reflected speckle pattern. A problem with this method of wavefront reconstruction is the occurrence of  $2\pi$  phase ambiguities at points of zero phase field amplitude in the measured speckle pattern. For this reason, the technique of averaging phasor paths instead of phase/phase difference paths has been studied [5]. Unfortunately, this is a non-linear process, as far as noise is concerned, and produces a significantly different noise behavior than that for the non-phasor case. A common operation for finding the phase,  $\Phi_{i,j}$ , from its surrounding phase and phase differences is shown in Figure 2.1. This figure represents a small portion of the reflected speckle pattern. In the figure,  $S^x_{k,l} = \Phi_{k,l+1} - \Phi_{k,l}$  and  $S^y_{k,l} = \Phi_{k+1,l} - \Phi_{k,l}$ . The subscript terms represent the y- and x-direction phase measurement matrix coordinates, the S's represent the measured phase differences and the  $\Phi$  terms represent the phase in the speckle pattern.

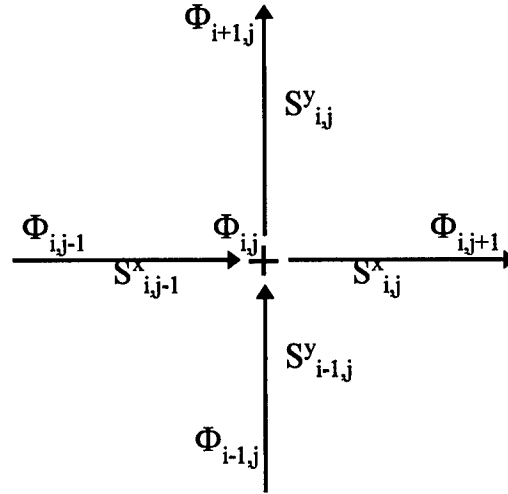


Figure 2.1. Paths for the phase and phase difference measurements are shown here [5].

The common linear LMS estimator for  $\Phi_{i,j}$  is shown in equation (1).

$$\begin{aligned} \Phi_{i,j} = & w_1 \cdot (\Phi_{i,j-1} + S^x_{i,j-1}) + w_2 \cdot (\Phi_{i-1,j} + S^y_{i-1,j}) + \\ & w_3 \cdot (\Phi_{i+1,j} - S^y_{i,j}) + w_4 \cdot (\Phi_{i,j+1} - S^x_{i,j}). \end{aligned} \quad (1)$$

In equation (1), if all noise variances of the phase and phase differences are assumed to be equal, then all of the path weight terms,  $w_n$ , will also be equal with a value of 0.25. This will accomplish the goal of minimizing the variance of  $\Phi_{i,j}$ . It was assumed that each of the noise terms are additive, uncorrelated, and represent normally distributed random variables with a variance of  $\sigma_n^2$ . Considering these assumptions, the mean square error of  $\Phi_{i,j}$  can be found to be  $E^2 = \sigma^2 = (1/2) \sigma_n^2$ .

## 2.2. Phasor-based Phase Reconstruction Model

In phasor form, equation (1) can be rewritten as [5]:

$$\begin{aligned}\Phi_{i,j} = & \text{Arg}(w_1 \cdot \exp[j(\Phi_{i,j-1} + S_{i,j-1}^X)] + w_2 \cdot \exp[j(\Phi_{i-1,j} + S_{i-1,j}^Y)] + \\ & w_3 \cdot \exp[j(\Phi_{i+1,j} - S_{i,j}^Y)] + w_4 \cdot \exp[j(\Phi_{i,j+1} - S_{i,j}^X)]). \end{aligned} \quad (2)$$

Similarly, the noise portion of  $\Phi_{i,j}$  can be written as:

$$\begin{aligned}\Phi_n = & \text{Arg}(w_1 \cdot \exp[j \sum_{i=1}^2 n_i] + w_2 \cdot \exp[j \sum_{j=1}^2 n_j] + \\ & w_3 \cdot \exp[j \sum_{k=1}^2 n_k] + w_4 \cdot \exp[j \sum_{l=1}^2 n_l]), \end{aligned} \quad (3)$$

where the  $n$ 's are normally distributed, independent, zero-mean random variables with a variance of  $\sigma_n^2$ . As shown in equation (4), equation (3) can be rewritten in trigonometric form as:

$$\Phi_n = \text{Tan}^{-1}(X/Y), \quad -\pi \leq \Phi_n \leq \pi, \quad (4)$$

where  $X$  and  $Y$  are defined as follows:

$$X = w_1 \cdot \sin\left(\sum_{i=1}^2 n_i\right) + w_2 \cdot \sin\left(\sum_{j=1}^2 n_j\right) + w_3 \cdot \sin\left(\sum_{k=1}^2 n_k\right) + w_4 \cdot \sin\left(\sum_{l=1}^2 n_l\right) \quad (5)$$

and

$$Y = w_1 \cdot \cos\left(\sum_{i=1}^2 n_i\right) + w_2 \cdot \cos\left(\sum_{j=1}^2 n_j\right) + w_3 \cdot \cos\left(\sum_{k=1}^2 n_k\right) + w_4 \cdot \cos\left(\sum_{l=1}^2 n_l\right) \quad (6)$$

### III. PDF OF $\Phi_n$

#### 3.1. Introduction

In order to help characterize the output noise of the reconstructor, the probability density function (PDF) of  $\Phi_n$  from equation (4) must be found. Due to the complex nature of  $\Phi_n$ , it would be quite difficult to directly find its PDF. Therefore, the  $\Phi_n$

expression was broken down into smaller, more manageable parts. The PDF's of each of these smaller expressions were found and then used to indirectly calculate the PDF of  $\Phi_n$ .

### 3.2. PDF of Sine and Cosine Terms

The first of the simpler PDF's to be found is that of each of the sine terms in equation (5). The argument of each of the sine terms is denoted by  $T$ , where  $T$  is the summation of two independent, normally distributed,  $N(0, \sigma_n^2)$ , random variables. Due to the nature of these noise terms, and assuming that the noise variances within a path are equal,  $T$  is found to be a normally distributed,  $N(0, 2\sigma_n^2)$ , random variable. From this development, the PDF of  $U=w \cdot \sin(T)$  is shown in equation (7) and derived in Appendix A.

$$f_u(u) = \left[ 1/\sqrt{(4\pi\sigma_n^2(w^2-u^2))} \right] \sum [\exp(-T^2/(4\sigma_n^2))]. \quad (7)$$

Here the summation includes all  $T$ 's such that  $T=\arcsin(u/w)$  and  $u$  ranges from  $-w$  to  $w$ . The PDF in equation (7) approaches a zero-mean normal distribution with a variance of  $2\sigma_n^2$  for small values of  $\sigma_n^2$  and, as  $\sigma_n^2$  increases, the PDF approaches  $1/(\pi \sqrt{(w^2-u^2)})$ . The latter form is that of the PDF of a general sinusoid with uniformly distributed phase angle. Figure 3.1 shows how this PDF changes as the noise variance,  $\sigma_n^2$ , increases.

Through a similar development, the probability density function of each cosine term,  $V=w \cdot \cos(T)$ , in equation (6) is found to be:

$$f_v(v) = \left[ 1/\sqrt{(4\pi\sigma_n^2(w^2-v^2))} \right] \sum [\exp(-T^2/(4\sigma_n^2))]. \quad (8)$$

This time the summation is taken to include all  $T$ 's such that  $T=\arccos(v/w)$ , where  $v$  ranges from  $-w$  to  $w$ . The PDF,  $f_v(v)$ , approaches a delta function,  $\delta(v-w)$ , as  $\sigma_n^2$  approaches zero. For larger values of  $\sigma_n^2$ , the PDF approaches  $1/(\pi \sqrt{w^2-v^2})$ . Figure 3.2 shows how  $f_v(v)$  changes as the noise variance,  $\sigma_n^2$ , increases.

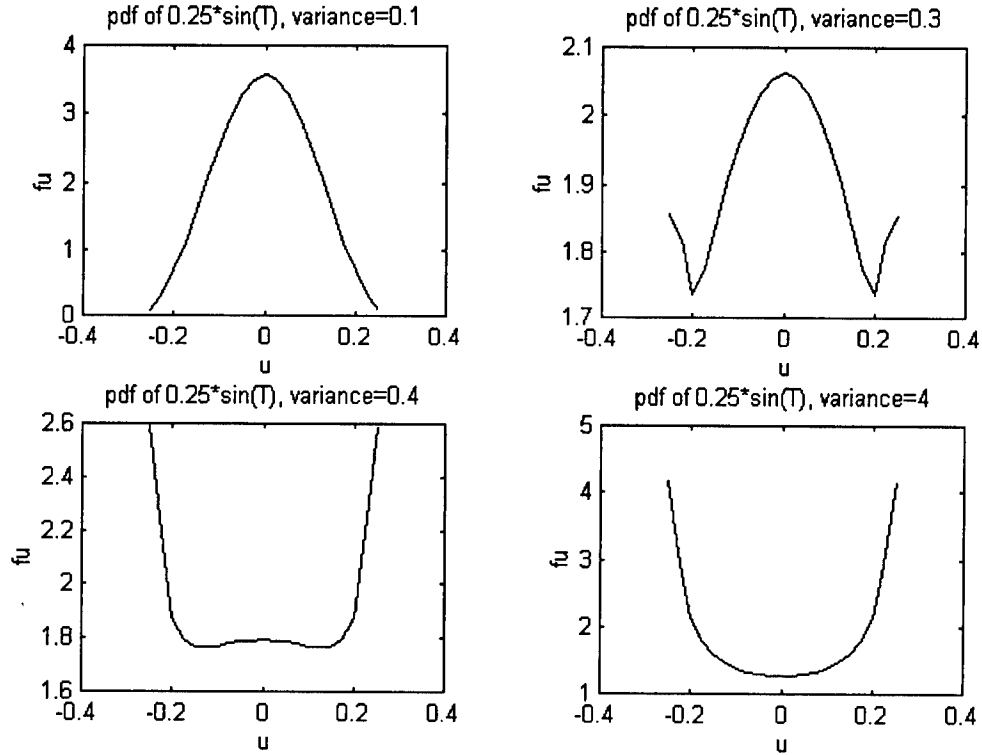


Figure 3.1. The PDF of  $U=w \cdot \sin(T)$  versus  $\sigma_n^2$ .

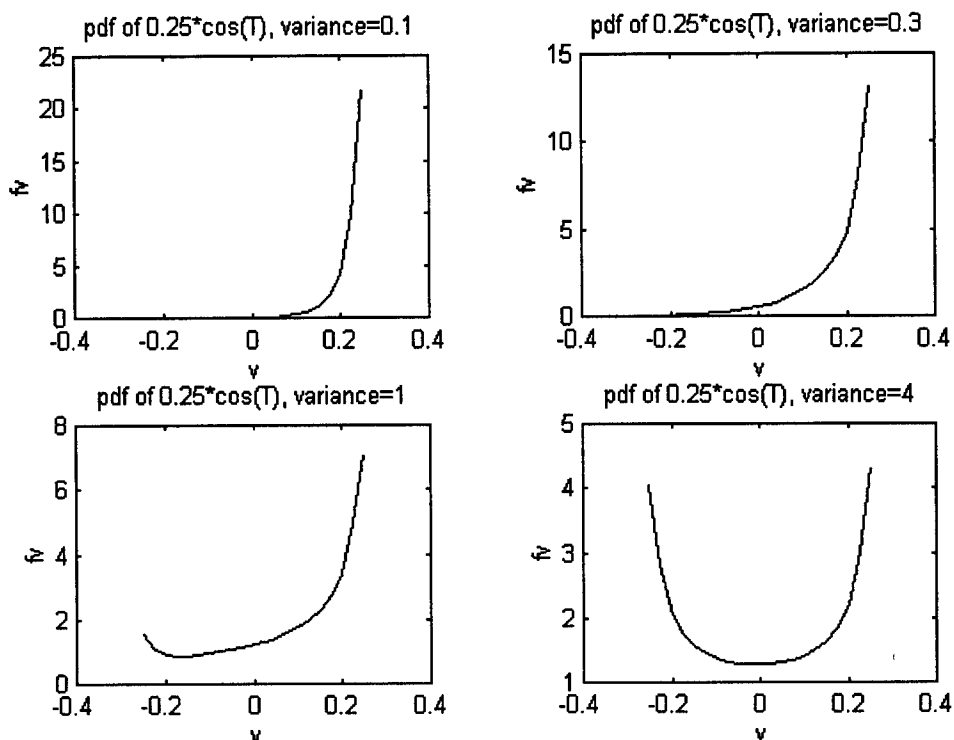


Figure 3.2. The PDF of  $V=w \cdot \cos(T)$  versus  $\sigma_n^2$ .

### 3.3. PDF of Sum of Sine and Cosine Terms

Remembering that  $X$  and  $Y$  are the summation of four sine and cosine terms, respectively, the PDF's of  $X$  and  $Y$  can now be found. Since each of the four sine terms in  $X$  are independent, the PDF of  $X$  is simply the four-fold convolution of the PDF's of each of the sine terms. Likewise, the PDF of  $Y$  is the four-fold convolution of the PDF's of each of the cosine terms. All of the noise terms in the arguments of the sine and cosine terms are assumed to be equal. Figure 3.3 shows the PDF's of  $X$  for various noise variances. The PDF of  $X$  varies from Gaussian for small  $\sigma_n^2$  to a triangularly-shaped PDF as  $\sigma_n^2$  increases.

Figure 3.4 shows the PDF's of  $Y$  for various noise variances. As can be seen from the figure, the PDF of the sum of four  $0.25 \cdot \cos(T)$  terms is approximately a delta function,  $\delta(y-1)$ , for small input variances, and evolves into a somewhat triangularly-shaped PDF, as seen also in Figure 3.3, as the input noise variance increases. Thus, for large  $\sigma_n^2$ , the  $X$  and  $Y$  PDF's look the same.

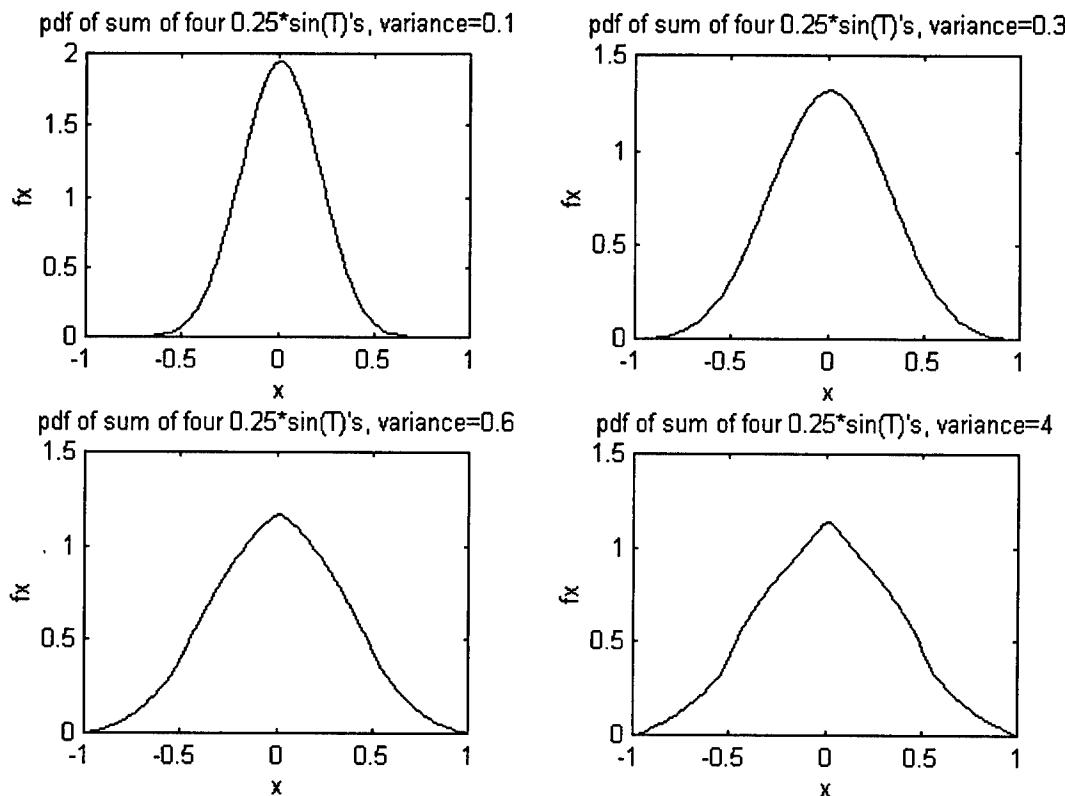


Figure 3.3. Probability density function of  $X$  as the noise variance increases.

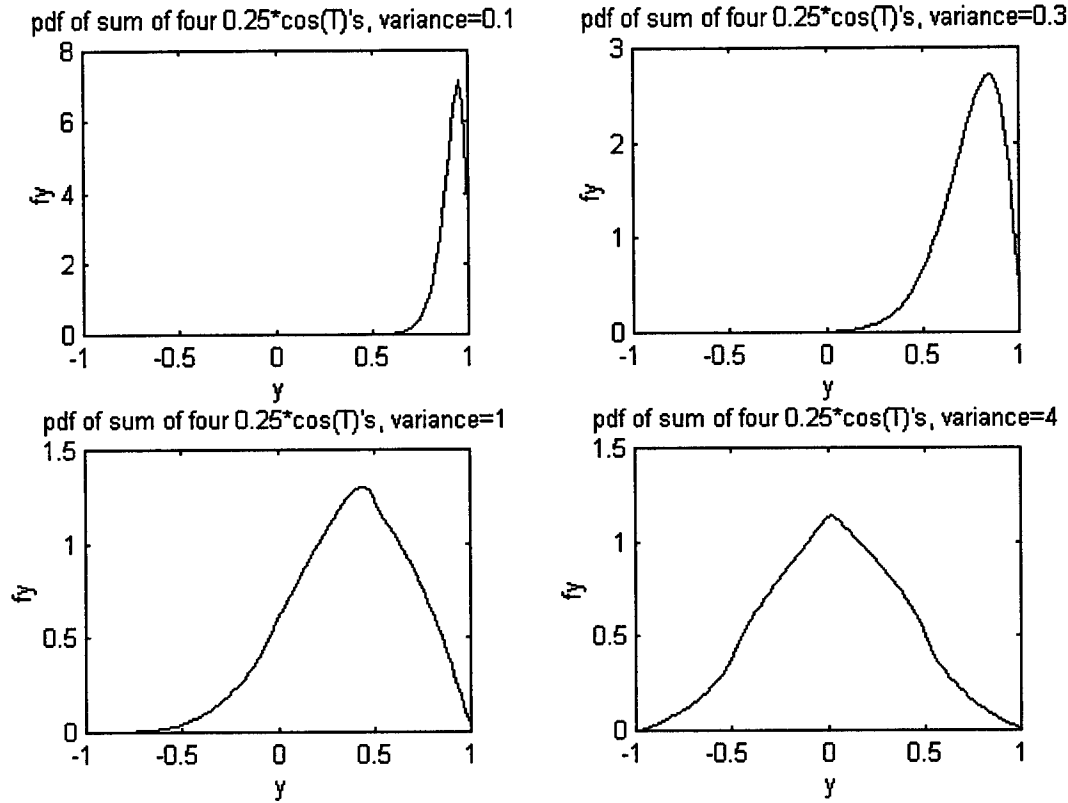


Figure 3.4. Probability density function of Y as the noise variance increases.

### 3.4. PDF of Z

Now, since the PDF's of X and Y have been found, the next step is to find the PDF of  $Z=X/Y$ . To do this, an auxiliary random variable will be defined as  $M=Y$ . The development of the PDF of Z is demonstrated here.

$$Z=X/Y=G_1(x,y).$$

Define an auxiliary variable

$$M=Y=G_2(x,y),$$

so

$$X=Z \cdot Y=Z \cdot M.$$

$$\text{Then} \quad f_{zm}(z,m) = \frac{f_{xy}(x,y)}{|J^{-1}|},$$

where  $J^{-1}$  denotes the inverse Jacobian as shown below.

$$|J^{-1}| = \begin{vmatrix} dG_1/dx & dG_1/dy \\ dG_2/dx & dG_2/dy \end{vmatrix} = \begin{vmatrix} 1/Y & -X/Y^2 \\ 0 & 1 \end{vmatrix} = \frac{1}{|Y|} = \frac{1}{|M|}$$

$$\text{Therefore,} \quad f_{zm}(z,m) = |m| \cdot f_{xy}(m \cdot z, m)$$

$$\text{where,} \quad f_{xy}(x,y) = f_x(x) \cdot f_y(y),$$

when  $X$  and  $Y$  are independent.

Then, to find  $f_z(z)$ , the variable  $m$  is integrated out, as follows.

$$f_z(z) = \left( \int_{-\infty}^{\infty} |m| \cdot f_{xy}(m \cdot z, m) \, dm \right),$$

$$\text{or} \quad f_z(z) = \left( \int_{-\infty}^{\infty} |m| \cdot f_x(m \cdot z) \cdot f_y(m) \, dm \right). \quad (9)$$

Equation (9) represents the probability density function of  $Z=X/Y$ . Figure 3.5 shows how the PDF of  $Z$  varies as the input noise variance,  $\sigma_n^2$ , increases. For small  $\sigma_n^2$ 's,  $f_z(z)$  has a Gaussian distribution. As  $\sigma_n^2$  increases, the PDF approaches a Cauchy distribution.

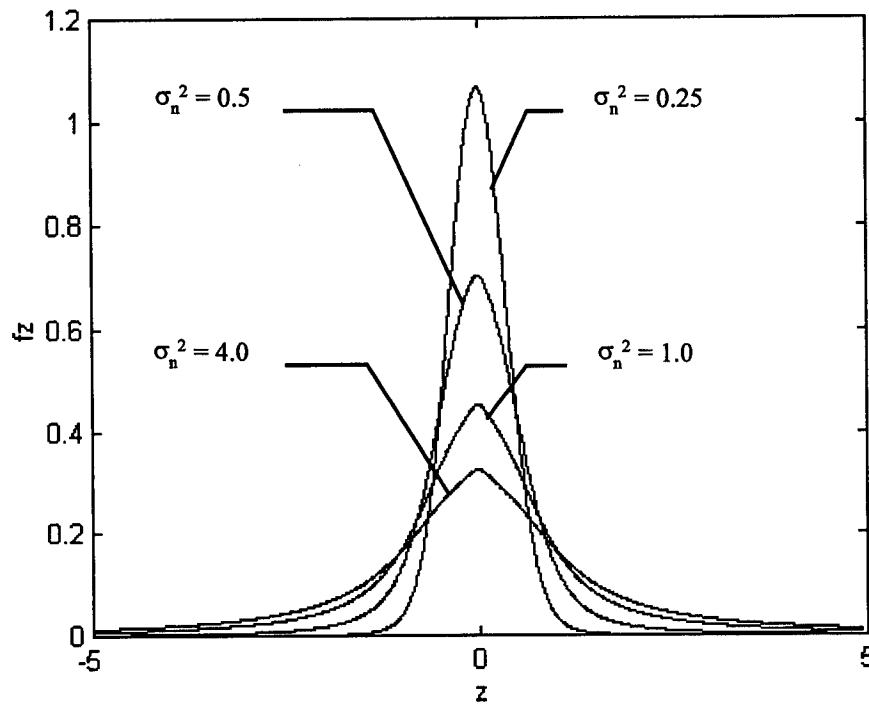


Figure 3.5. This is the PDF of  $Z = X/Y$  for various values of  $\sigma_n^2$ .

### 3.5. PDF of ArcTan(Z)

Now, the PDF of  $\Phi_n = \text{ArcTan}(Z)$ , from equation (4), must be found. Since the inverse tangent function returns only values in the range of  $-\pi/2$  to  $\pi/2$ , the four-quadrant inverse tangent function must be used in order to return values in the range of  $-\pi$  to  $\pi$ , as desired. This is done by dividing  $f_x(x)$  and  $f_y(y)$  into their positive and negative parts, and then using these new PDF's to recalculate  $f_z(z)$ . The new PDF's for X and Y are shown in equations (10) and (11), respectively.

$$f_x(x) = f_{x-}(x) + f_{x+}(x), \quad (10)$$

$$f_y(y) = f_{y-}(y) + f_{y+}(y). \quad (11)$$

Using equations (10) and (11), the PDF of  $Z$  shown in equation (9) can be rewritten as shown in equation (12).

$$f_z(z) = \left( \int_{-\infty}^{\infty} |m| \cdot ([f_{x+}(m \cdot z) + f_{x-}(m \cdot z)] \cdot [f_{y+}(m) + f_{y-}(m)]) dm \right)$$

$$= f_{z++}(z) + f_{z+-}(z) + f_{z-+}(z) + f_{z--}(z). \quad (12)$$

Now, a new random variable is defined to be  $P = \Phi_n = \tan^{-1}(Z)$ , and its PDF can be found to be:

$$f_p(p) = f_z(\tan(p)) \cdot |1 + \tan^2(p)|,$$

$$\text{or } f_p(p) = \begin{cases} (f_{z--}(\tan(p))) \cdot |1 + \tan^2(p)|, & -\pi \leq p \leq -\pi/2 \\ (f_{z++}(\tan(p)) + f_{z+-}(\tan(p))) \cdot |1 + \tan^2(p)|, & -\pi/2 \leq p \leq \pi/2 \\ (f_{z-+}(\tan(p))) \cdot |1 + \tan^2(p)|, & \pi/2 \leq p \leq \pi. \end{cases} \quad (13)$$

The PDF of  $P$  varies from a normal distribution,  $N[0, \sigma_n^2/2]$  for small  $\sigma_n^2$  to uniform  $U[-\pi, \pi]$  as  $\sigma_n^2$  increases, as shown in Figure 3.6.

Now, a method for finding an expression for the PDF of the output noise of a path-averaging, phasor-based phase reconstructor as a function of the input noise variance and path weights has been found.

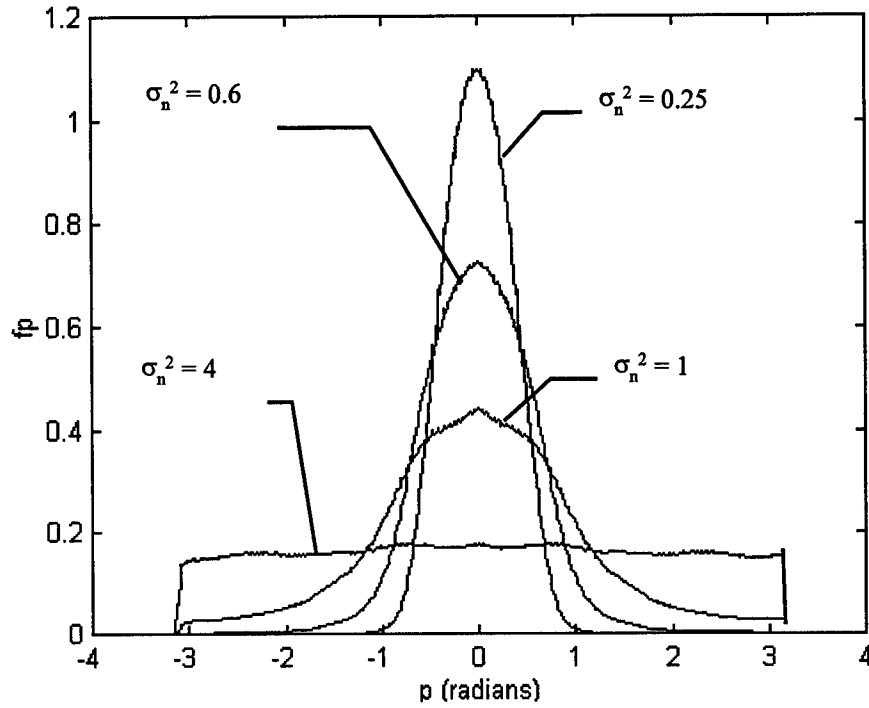


Figure 3.6. Probability density function of  $P=\Phi_n$  for several  $\sigma_n^2$ .

The next step is to find the variance of  $\Phi_n$ . Since  $\Phi_n$  is a zero-mean random variable, the variance,  $\sigma_\Phi^2$ , can be found from the PDF of  $P$  by using equation (14):

$$\sigma_\Phi^2 = \left( \int_{-\infty}^{\infty} p^2 \cdot f_p(p) dp \right). \quad (14)$$

This is the PDF of the output noise of the phasor reconstructor.

Until now, the model has used four paths in order to reconstruct the phase information, as shown in Figure 2.1. It is now convenient to consider the case where only two paths are used in the reconstructor. For the 2-path case, the two paths in the x-direction are assumed to have the same noise variance and the two paths in the y-

direction are assumed to have the same noise variance, but different from the x-direction. Therefore, both  $w_i$ 's in the x-direction would have the same value and both  $w_i$ 's in the y-direction would have the same value. The conversion process from a 4-path problem to a 2-path problem, for the linear reconstructor case is demonstrated in the beginning of Appendix B. Below are the 2-path equations for the phasor case corresponding to equations (5) and (6).

$$X = w_x \cdot \left[ \sin \left( \sum_{i=1}^2 n_i \right) + \sin \left( \sum_{j=1}^2 n_j \right) \right] + w_y \cdot \left[ \sin \left( \sum_{k=1}^2 n_k \right) + \sin \left( \sum_{l=1}^2 n_l \right) \right] \quad (15)$$

$$\text{and } Y = w_x \cdot \left[ \cos \left( \sum_{i=1}^2 n_i \right) + \cos \left( \sum_{j=1}^2 n_j \right) \right] + w_y \cdot \left[ \cos \left( \sum_{k=1}^2 n_k \right) + \cos \left( \sum_{l=1}^2 n_l \right) \right]. \quad (16)$$

Using optimal linear weights for the x- and y-directions,  $w_x$  and  $w_y$ , and equation (14), the output variance of the phasor-based reconstructor has been calculated for several different input noise variances. These output variances are shown in Figure 3.7 and tabulated in Appendix C. For this figure, the input noise variances in the x- and y-direction were varied independently from 0.25 up to 4.0. The optimal linear weights for the reconstructor as a function of the input noise variances are found according to equations (17) and (18), and are derived in Appendix B.

$$w_x = \frac{\sigma_y^2}{2 \cdot (\sigma_y^2 + \sigma_x^2)} \quad (17)$$

$$w_y = \frac{\sigma_x^2}{2 \cdot (\sigma_y^2 + \sigma_x^2)} \quad (18)$$

As can be seen in Figure 3.7, the output noise variance of the phasor-based reconstructor using optimal linear weights has a maximum of approximately 3.3. This maximum occurs whenever  $\sigma_x^2$  and  $\sigma_y^2$  are both greater than approximately 2.

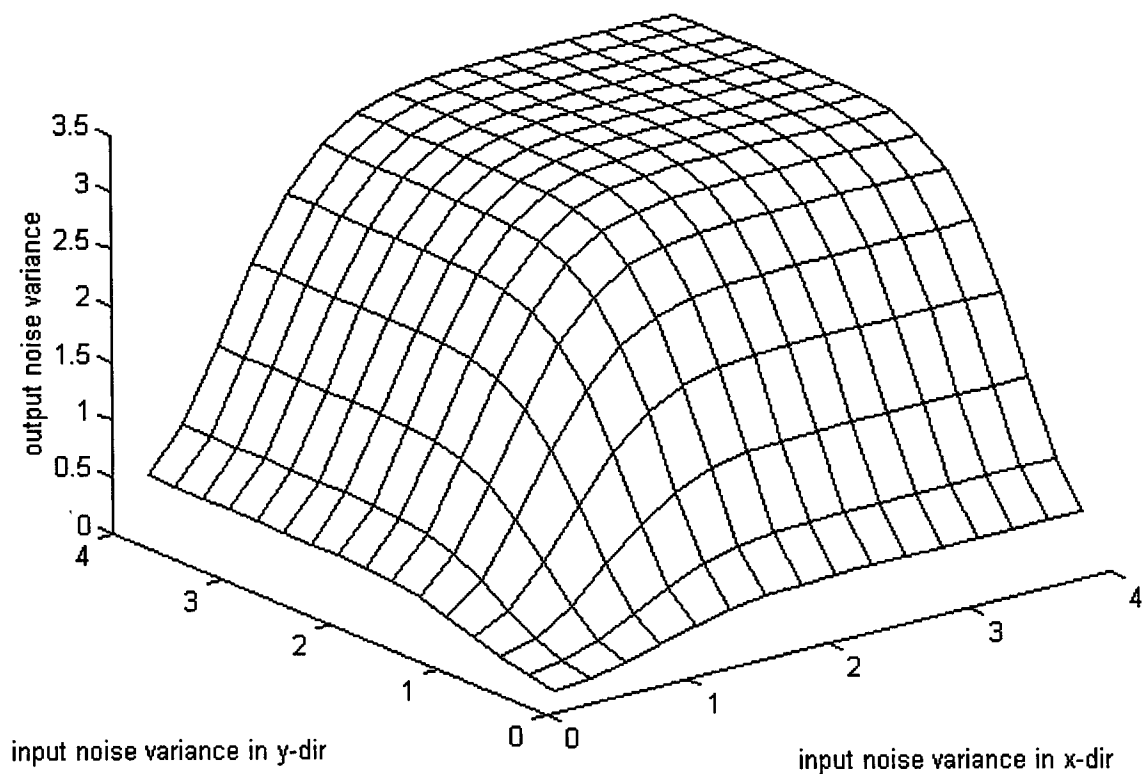


Figure 3.7. Output noise variance as a function of the input noise variances in the x- and y-directions using optimal linear weights in the phasor reconstructor.

#### IV. FINDING OPTIMAL PHASOR-BASED WEIGHTS

Using the PDF of  $\Phi_n$  developed in the last chapter, the optimal phasor-based weights for the reconstructor can be found for a given set of input noise variances. This was done by varying the optimal linear-based weights (used for Figure 3.7) slightly until the resultant output noise variance was minimized.

Now suppose that the optimal phasor-based weights are to be found for input noise variances of  $\sigma_x^2=0.5$  and  $\sigma_y^2=0.25$ . The first step is to find the optimal linear-based weights corresponding to these input noise variances. From equations (17) and (18), the linear-based weights can be found to be:  $w_x = 1/6 = 0.166$  and  $w_y = 1/3 = 0.333$ . To find the optimal phasor-based weights, these values for  $w_x$  and  $w_y$  are varied locally about their original values (i.e.,  $w_x$  is varied from 0.1 to 0.2, which forces  $w_y$  to vary from 0.4 down to 0.3 since the two weights must sum to 0.5). Within the new range of the weights, the values of  $w_x$  and  $w_y$  that produce the minimum phasor reconstructor output noise variance are the optimal phasor-based weights if the range of variation is large enough to give a minimum. Figure 4.1 shows the variance of the output noise when optimal phasor-based weights are used in the phasor reconstructor. As can be seen, the output variance of the reconstructor is nearly always smaller in the phasor weight case than that for the non-phasor weight case (Figure 3.7) for a given input noise variance. There are, however, unexplained ‘ripples’ in the phasor weight output variance plot shown in Figure 4.1 compared to the ‘smooth’ optimal linear weight case plot of Figure

3.7. It should be noted that these 'ripples' are also seen in Monte-Carlo simulations of the output variance, so they are probably a result of system nonlinearities rather than artifacts of computational inaccuracies.

The data that was used to generate the plot in Figure 4.1 is shown in Appendix C. Also, Appendix D shows optimal phasor-based x-direction weights and the optimal linear-based x-direction weights. The optimal y-direction weights can be found as described in Appendix D. As the data shows, the optimal phasor-based x-direction weights are nearly always smaller than the optimal linear-based x-direction weights for a given set of input noise variances in the x- and y-directions.

Figure 4.2 shows the difference of the output variance of the phasor reconstructor with optimal linear weights and the output variance of the same reconstructor with optimal phasor weights. The data from this figure is shown in Appendix C. Figure 4.2 shows that the output noise variance of the phasor reconstructor with optimal linear weights is nearly always greater than the output noise variance of the same reconstructor using optimal phasor weights. It should be noted that there are a few cases, namely for small input noise variance, for which this is not the case.

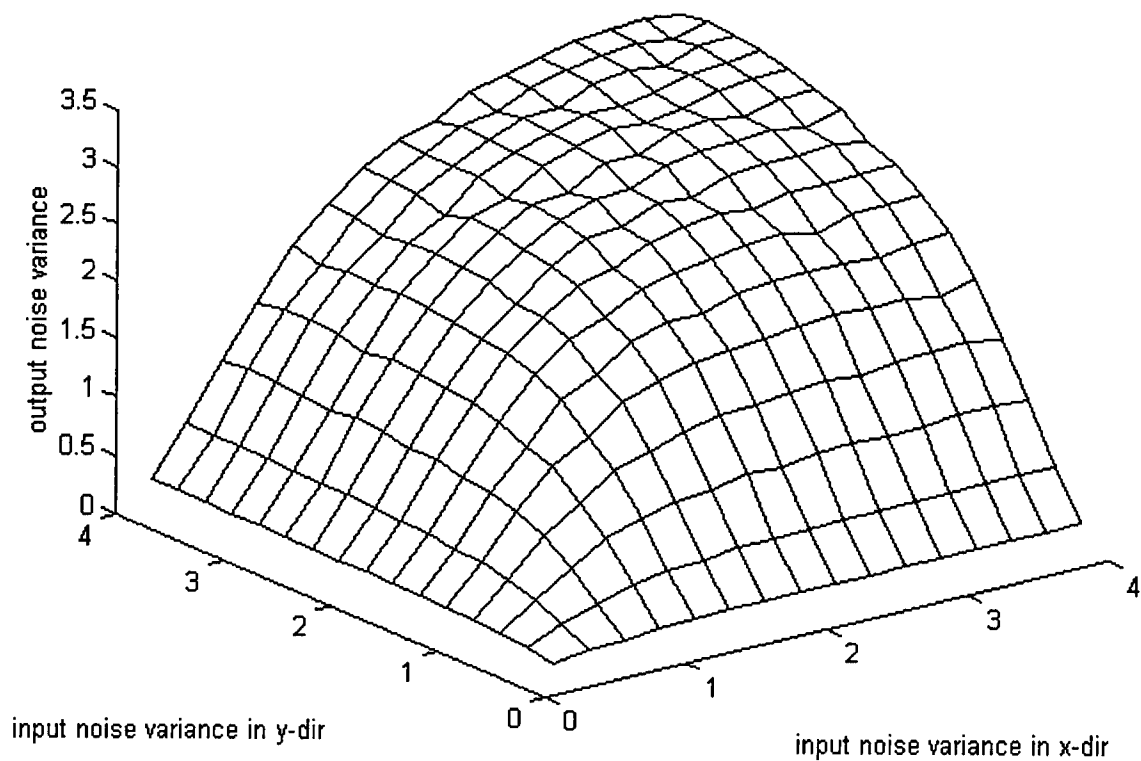


Figure 4.1. Output noise variance using optimal phasor-based weights in the phasor reconstructor.

linear weight output variance minus phasor weight output variance

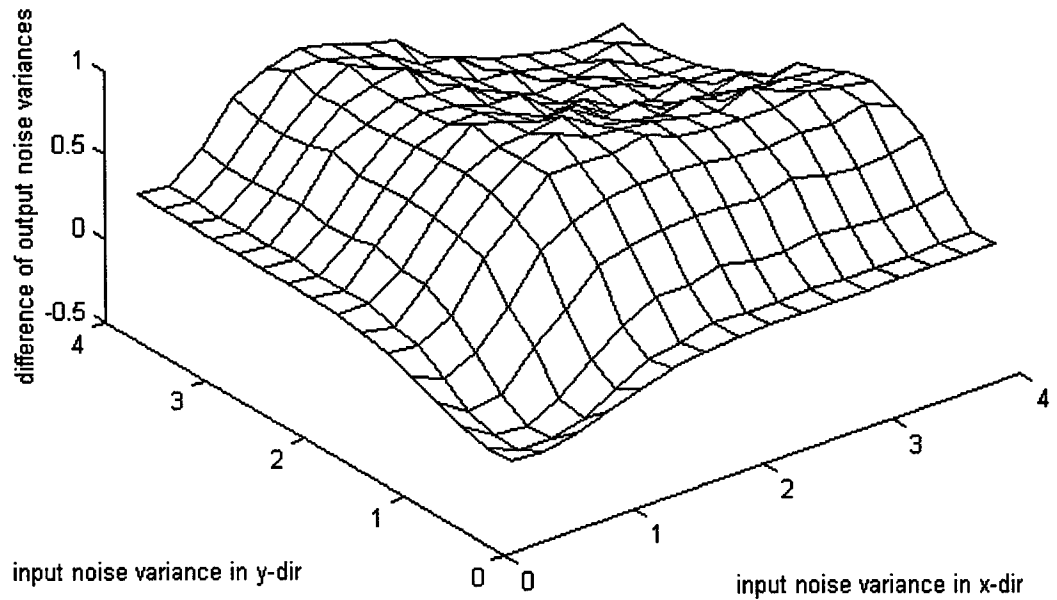


Figure 4.2. This figure shows the difference of Figures 3.7 and 4.1. This is the output noise variance of the phasor reconstructor with optimal linear weights minus the output noise variance of the phasor reconstructor with optimal phasor weights.

## V. NOISE PERFORMANCE: PHASOR VERSUS NON-PHASOR

There are several ways that the noise performance of the reconstructors can be analyzed. The three methods of comparison that will be discussed are noise gain, optimality of weights and robustness to errors in the input noise variance estimates.

### 5.1 Noise Gain

The noise gain is defined as the ratio of the output noise variance and the input noise variance of the reconstructor. Figure 5.1 compares the noise gains of the phasor-based and non-phasor-based reconstructors where the input noise variances in the x- and y-directions are equal and optimal linear weights are used in both. From Figure 5.1, it can be seen that the two reconstructors have nearly identical noise gains when the input noise variance,  $\sigma_n^2$ , is less than approximately 0.3. The noise gain is defined as  $E^2/\sigma_n^2 = 1/2$  for the non-phasor case and  $\sigma_\phi^2/\sigma_n^2$  for the phasor case [7]. As  $\sigma_n^2$  increases, the noise gain of the phasor-based reconstructor grows significantly larger than the non-phasor reconstructor. The phasor-based noise gain will again equal the non-phasor noise gain when  $\sigma_n^2$  is approximately 6.58. Therefore, for the range of  $\sigma_n^2$  that we are interested in, the phasor-based reconstructor noise gain is larger than the gain of the linear-based reconstructor.

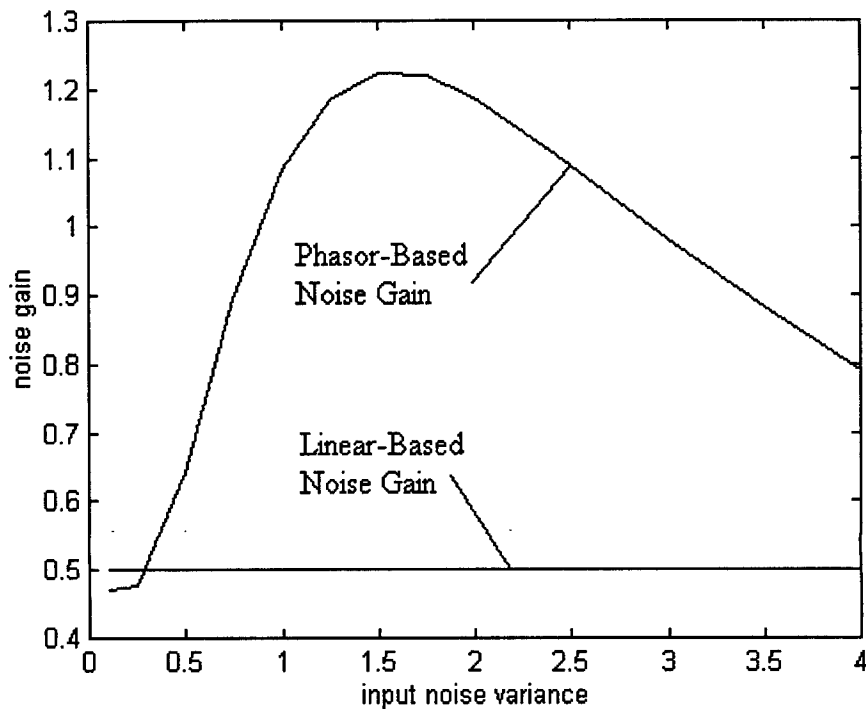


Figure 5.1. This is a comparison of the noise gains of the two different reconstructors. The phasor-based reconstructor has a larger noise gain than the non-phasor based reconstructor over most of this range of input noise variances.

### 5.2 Robustness

It is shown in Figure 5.2 that the phasor-based reconstruction approach is, in general, more robust to errors in the input noise variance estimations than is the linear-based approach. This can be seen by noting that the phasor-case curve is wider and more 'shallow' than the non-phasor curve. This means that a small variation in the input noise variance will produce only a small variation in the phasor-based reconstructor output noise variance.

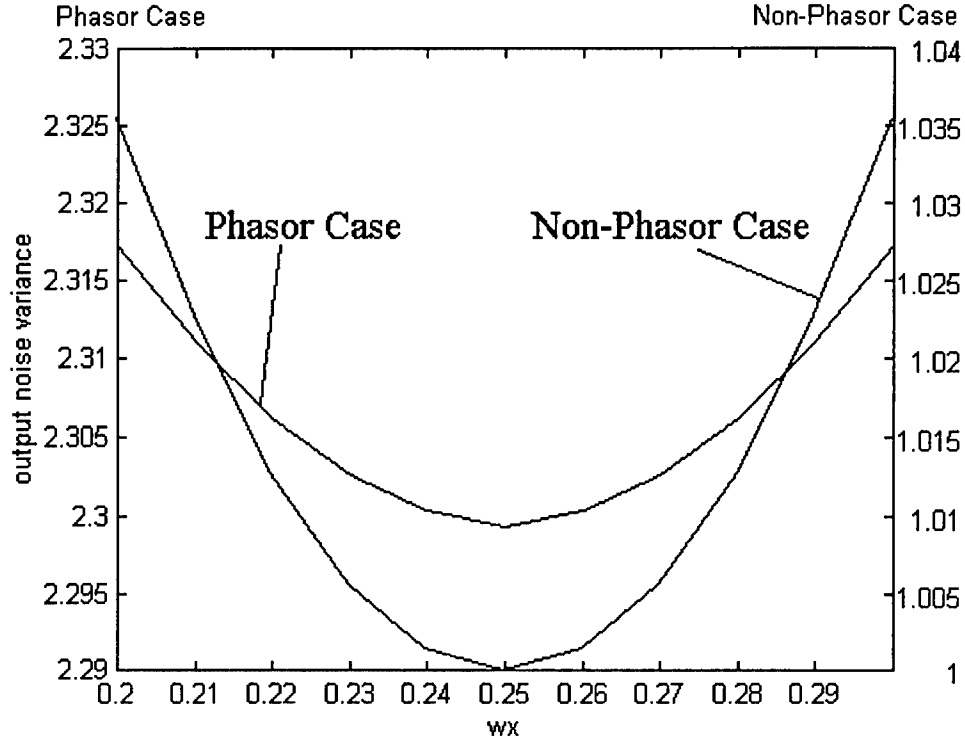


Figure 5.2 Plot shows that robustness of the phasor-based reconstructor compared to the linear-based reconstructor. The phasor-based technique is much more robust than the linear-based, as can be seen from the wider curve. For this plot,  $\sigma_x^2=2$  and  $\sigma_y^2=2$ .

### 5.3 Optimality

Figure 5.3 is an example that shows that, for the phasor reconstructor, the linear weights are not always optimal. The optimal linear x-direction weight for the linear reconstructor is 0.2 for the case shown in Figure 5.3. But from the figure, it can be seen that the optimal phasor-based x-direction weight for the phasor reconstructor is 0.18. Therefore, the optimal phasor weights are the weights of choice if the output variance from the phasor reconstructor is to be minimized. The optimality of the phasor weights for large  $\sigma_x^2$  and  $\sigma_y^2$  can also be realized by noting that the maximum value of Figure 4.1, ( $\sim 3.0$ ), is smaller than the maximum value of Figure 3.7, ( $\sim 3.3$ ). For Figure 5.2 and

Figure 5.3 the linear reconstructor output variance was found according to the method shown in Appendix B.

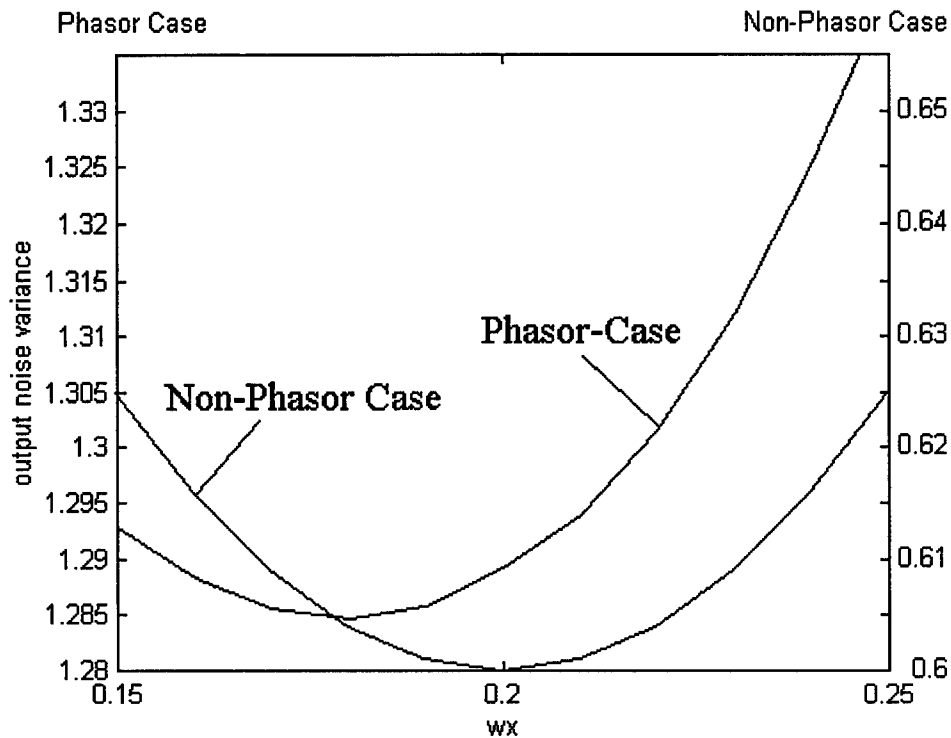


Figure 5.3. Plot shows that a phasor-based x-direction weight can be found which is more optimal than the optimal linear x-direction weight for a given input noise variance. For this plot,  $\sigma_x^2=1.5$  and  $\sigma_y^2=1.0$ .

Figures 5.4 and 5.5 show the output noise variances of the two reconstructors as the x-direction weight is varied. For the case in Figure 5.4,  $\sigma_x^2 = 3.75$  and  $\sigma_y^2 = 0.25$ . Once again, the optimal linear-based x-direction weight is not the same as the optimal phasor-based x-direction weight. For the case of Figure 5.5,  $\sigma_x^2 = 3.75$  and  $\sigma_y^2 = 3.75$ . In this case, since both input noise variances are equal, the optimal phasor-based weight is

the same as the optimal non-phasor-based weight. The figure also shows that the phasor case is much more robust to errors in input noise variance than is the non-phasor case.

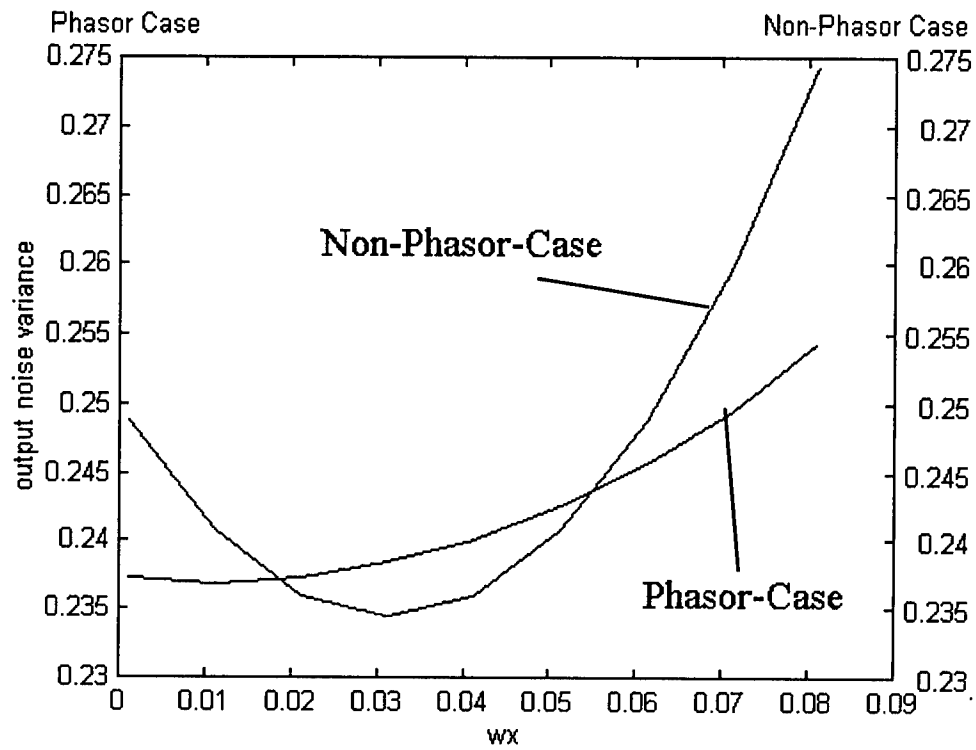


Figure 5.4. Plot shows the difference of the optimal x-direction weights for the phasor and non-phasor reconstructors for  $\sigma_x^2 = 3.75$  and  $\sigma_y^2 = 0.25$ .

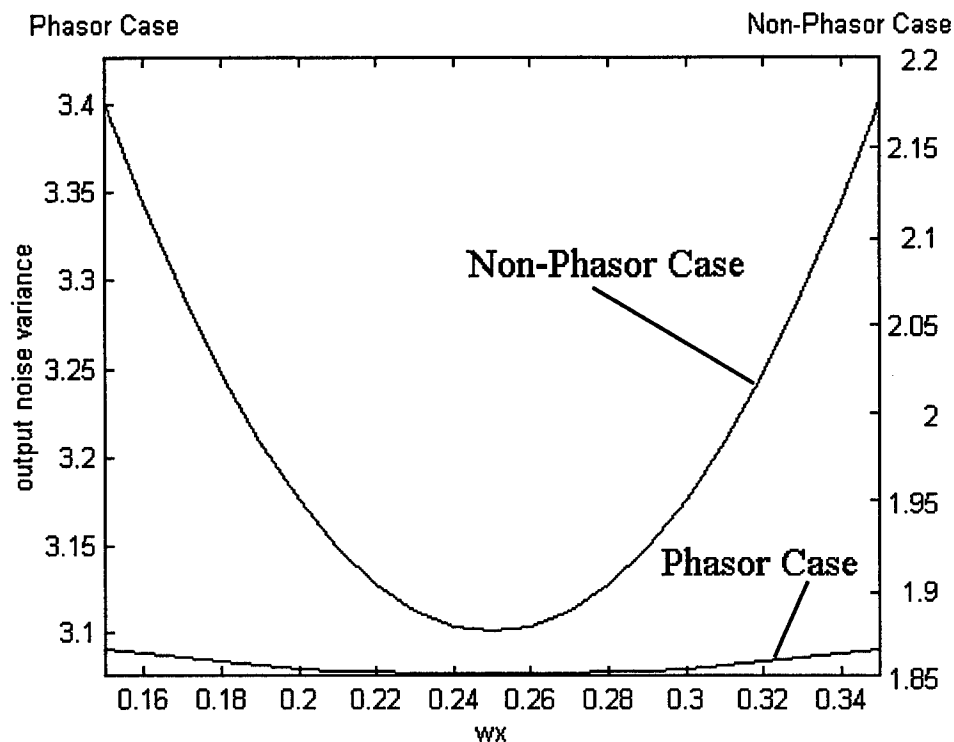


Figure 5.5. Plot where there is no difference between the optimal phasor-based x-direction weight and the optimal non-phasor-based x-direction weight since both input noise variances are equal. In this case  $\sigma_x^2 = 3.75$  and  $\sigma_y^2 = 3.75$ .

## VI. CONCLUSIONS AND FUTURE WORK

The traditional least mean square (LMS) phase reconstructor is susceptible to  $2\pi$  phase ambiguities at points of zero phase field amplitude when applied to speckle field patterns. A phasor-based phase reconstructor has been proposed in hopes of eliminating this problem. The goal of this paper was to analyze the output noise characteristics of path averaging operations in a phasor-based phase reconstructor. An analytic technique was described for finding the probability density function (PDF) and the variance of the

---

variances were the input parameters to the PDF algorithm. The resulting PDF was used to find the optimal phasor-based weights in order to minimize the output noise variance of the reconstructor. The robustness of the phasor-based reconstructor to errors in the input noise variance approximations was studied. These studies concluded that, in general, the phasor-based reconstructor produced results that were more robust to errors in input noise estimates as compared to the common LMS reconstructor. Also, it was shown that the optimal linear-based weights will not always produce the minimum reconstructor output noise gain when used in the phasor-based reconstructor. For this reason, the optimal phasor-based weights should always be used when using the phasor-based reconstructor. Future work should include investigating the effects of correlated input noise on the reconstructor output noise.

## REFERENCES

- [1] R.H. Hudgin, "Wavefront Reconstruction for Compensated Imaging," J. Opt. Soc. Am., Vol. 67, 375-378, March, 1977.
- [2] P.S. Idell and J.D. Gonglewski, "Image Synthesis from Wave-Front Sensor Measurements of Coherent Diffraction Field," Opt. Letters, Vol. 15, 1309-1311, November 15, 1990.
- [3] R.A. Hutchin, "Sheared Coherent Interferometric Photography: A Technique for Lensless Imaging," Proc. SPIE, Vol. 2029, 161-168, 1993.
- [4] B.R. Hunt, "Matrix Formulation of the Reconstruction of Phase Values from Phase Differences," J. Opt. Soc. Am., Vol. 69, 393-399, March, 1979.
- [5] Krile, Thomas F., "A Study of Noise Effects In Phase Reconstruction From Phase Differences." Final Report for Summer Faculty Research Program, AFOSR (Phillips Laboratory), Research and Development Laboratories, Culver City, CA., 1995.
- [6] Ulibarri, Laura and Gamiz, Victor, "Phillips Laboratory Reconstructor Noise Gain Study," Technical Report for Rockwell Power Systems Company, Document Identification: 93RPS703, 1993.
- [7] Fox, James L. and Krile, Thomas F., "Modeling and Analysis of Path Averaging Noise in Phasor-based Phase Reconstruction," SPIE Proceedings, 2827, 1996.

## APPENDIX A

### DERIVATION OF PDF OF $W \cdot \sin(T)$

The PDF of equation (A1) is to be found:

$$U = G(s) = w \cdot \sin(T) = w \cdot \sin(s). \quad (A1)$$

Since  $U=w \cdot \sin(s)$  is a nonmonotonic function, equation (A2) is used to find its PDF. Where each of the  $s_n$ 's represent a solution to  $s_n = \arcsin(U/w)$ . Since equation (A1) is nonmonotonic, there are an infinite number of  $s_n$  solutions.

$$f_u(u) = \frac{fs(s_0)}{|d G(s) / ds|_{s=s_0}} + \frac{fs(s_1)}{|d G(s) / ds|_{s=s_1}} + \dots \quad (A2)$$

$$\text{where } fs(s) = \frac{1}{\sqrt{2 \cdot \pi \cdot (2 \cdot \sigma_n^2)}} \cdot \exp(-s^2 / (2 \cdot (2 \cdot \sigma_n^2))),$$

$$\begin{aligned} \text{and} \quad \left. \frac{d G(s)}{ds} \right|_{s=s_0} &= \left. \frac{d w \cdot \sin(s)}{ds} \right|_{s=s_0} = w \cdot \cos(s_0) \\ &= \sqrt{w^2 - u^2}, \end{aligned}$$

$$\begin{aligned} \left. \frac{d G(s)}{ds} \right|_{s=s_1} &= \left. \frac{d w \cdot \sin(s)}{ds} \right|_{s=s_1} = w \cdot \cos(s_1) \\ &= w \cdot \cos(\pi - \sin^{-1}(u/w)) = -w \cdot \cos(s_0) \\ &= -\sqrt{w^2 - u^2}, \end{aligned}$$

$$\text{and} \quad s_0 = \sin^{-1}(u/w), \quad s_1 = \pi - s_0, \quad s_2 = 2 \cdot \pi + s_0,$$

$$s_3 = 3 \cdot \pi - s_0, \dots$$

Now, substituting into equation (A2), the PDF of  $G(x)=w \cdot \sin(x)$  is found to be:

$$f_u(u) = \left[ 1/\sqrt{(4\pi\sigma_n^2(w^2-u^2))} \right] \sum [\exp(-T^2/(4\sigma_n^2))].$$

## APPENDIX B

### FINDING THE OPTIMAL LINEAR WEIGHTS

### AND OUTPUT VARIANCE FOR THE LINEAR

### RECONSTRUCTOR

Equation (B1) represents the noise portion of equation 1. The first two terms in equation (B1) represent the x-direction noise and the last two terms represent the y-direction noise terms.

$$\Phi_n = w_1 \cdot \left( \sum_{i=1}^2 n_i \right) + w_2 \cdot \left( \sum_{j=1}^2 n_j \right) + w_3 \cdot \left( \sum_{k=1}^2 n_k \right) + w_4 \cdot \left( \sum_{l=1}^2 n_l \right) \quad (B1)$$

Now, let  $w_1=w_2=w_x$  and  $w_3=w_4=w_y$ ,

$$\text{So } \Phi_n = 2 \cdot w_x \cdot \left( \sum_{i=1}^2 n_i \right) + 2 \cdot w_y \cdot \left( \sum_{j=1}^2 n_j \right)$$

Therefore,  $\sigma_\Phi^2 = 2 \cdot w_x^2 \cdot (2\sigma_n^2) + 2 \cdot w_y^2 \cdot (2 \cdot \sigma_n^2)$ ,

where  $\sigma_n^2$  is the variance of the individual noise terms,  $n_i$ .

Now, assume that the variance of the individual noise terms in the x-direction is  $\sigma_x^2$  and the individual noise terms in the y-direction have variance  $\sigma_y^2$ .

$$\begin{aligned} \text{Then } \sigma_\Phi^2 &= 2 \cdot w_x^2 \cdot (2\sigma_x^2) + 2 \cdot w_y^2 \cdot (2 \cdot \sigma_y^2) \\ &= 4 \cdot (w_x^2 \cdot \sigma_x^2 + w_y^2 \cdot \sigma_y^2). \end{aligned}$$

Since originally,  $w_1+w_2+w_3+w_4=1$ , we now have the constraint  $w_x+w_y=0.5$ , or  $w_y=0.5-w_x$ . Now, to optimize  $\sigma_\Phi^2$ , we set:

$$\begin{aligned}\frac{d\sigma_\Phi^2}{dw_x} &= 0 = \frac{d [4 \cdot (w_x^2 \cdot \sigma_x^2 + (0.5-w_x)^2 \cdot \sigma_y^2)]}{dw_x} \\ &= 4 \cdot (2 \cdot w_x) \cdot \sigma_x^2 + (4) \cdot (-2) \cdot (0.5-w_x) \cdot \sigma_y^2 = 0.\end{aligned}$$

$$\text{Therefore, } w_{x,\text{opt}} = (\sigma_y^2) / (2 \cdot (\sigma_x^2 + \sigma_y^2)) \quad (\text{B2})$$

$$\text{and } w_{y,\text{opt}} = (\sigma_x^2) / (2 \cdot (\sigma_x^2 + \sigma_y^2)). \quad (\text{B3})$$

$$\text{Thus, } \sigma_{\Phi,\text{opt}}^2 = 4 \cdot (w_{x,\text{opt}}^2 \cdot \sigma_x^2 + w_{y,\text{opt}}^2 \cdot \sigma_y^2). \quad (\text{B4})$$

Now, substituting equations (B2) and (B3) into equation (B4) and simplifying,  $\sigma_{\Phi,\text{opt}}^2$  is found to be:

$$\sigma_{\Phi,\text{opt}}^2 = \frac{\sigma_x^2 \cdot \sigma_y^2}{\sigma_x^2 + \sigma_y^2}.$$

This is the output noise variance of the linear reconstructor using optimal linear weights. Equations (B2) and (B3) represent the optimal linear based weights for the x- and y-direction terms in the reconstructor.

# APPENDIX C

## RECONSTRUCTOR OUTPUT

### VARIANCE DATA

This data represents the output noise variance of the phasor reconstructor for optimal linear-based weights when the input noise variances in the x- and y-directions vary from 0.25 up to 4.0. This data is plotted in Figure 3.7.

Table C.1 Phasor reconstructor with optimal linear weights for  $\sigma_x^2$  and  $\sigma_y^2$  varied from 0.25 up to 4.0.

$\sigma_x^2$	0.250	0.500	0.750	1.000	1.250	1.500	1.750	2.000	2.250	2.500	2.750	3.000	3.250	3.500	3.750	4.000
$\sigma_y^2$																
0.250	0.030	0.068	0.127	0.208	0.291	0.356	0.396	0.416	0.425	0.428	0.430	0.430	0.431	0.432	0.433	0.434
0.500	0.068	0.121	0.220	0.372	0.530	0.655	0.732	0.771	0.787	0.794	0.796	0.797	0.797	0.798	0.798	0.800
0.750	0.127	0.220	0.422	0.707	0.981	1.186	1.309	1.371	1.398	1.408	1.411	1.412	1.412	1.412	1.412	1.413
1.000	0.208	0.372	0.707	1.130	1.507	1.776	1.935	2.014	2.048	2.060	2.064	2.065	2.065	2.064	2.064	2.063
1.250	0.291	0.530	0.981	1.507	1.953	2.263	2.444	2.533	2.570	2.584	2.588	2.589	2.589	2.588	2.587	2.586
1.500	0.356	0.655	1.186	1.776	2.263	2.596	2.788	2.883	2.923	2.937	2.942	2.943	2.942	2.941	2.940	2.938
1.750	0.396	0.732	1.309	1.935	2.444	2.788	2.986	3.083	3.124	3.139	3.143	3.144	3.144	3.143	3.141	3.139
2.000	0.416	0.771	1.371	2.014	2.533	2.883	3.083	3.181	3.222	3.237	3.242	3.243	3.242	3.241	3.239	3.237
2.250	0.425	0.787	1.398	2.048	2.570	2.923	3.124	3.222	3.264	3.279	3.284	3.285	3.284	3.283	3.281	3.279
2.500	0.428	0.794	1.408	2.060	2.584	2.937	3.139	3.237	3.279	3.294	3.299	3.300	3.299	3.298	3.296	3.294
2.750	0.430	0.796	1.411	2.064	2.588	2.942	3.143	3.242	3.284	3.299	3.304	3.305	3.304	3.303	3.301	3.299
3.000	0.430	0.797	1.412	2.065	2.589	2.943	3.144	3.243	3.285	3.300	3.305	3.305	3.305	3.304	3.302	3.300
3.250	0.431	0.797	1.412	2.065	2.589	2.942	3.144	3.242	3.284	3.299	3.304	3.305	3.304	3.303	3.301	3.299
3.500	0.432	0.798	1.412	2.064	2.588	2.941	3.143	3.241	3.283	3.298	3.303	3.304	3.303	3.302	3.300	3.298
3.750	0.433	0.798	1.412	2.064	2.587	2.940	3.141	3.239	3.281	3.296	3.301	3.302	3.301	3.300	3.298	3.296
4.000	0.434	0.800	1.413	2.063	2.586	2.938	3.139	3.237	3.279	3.294	3.299	3.300	3.299	3.298	3.296	3.294

This is the raw data from the 'optphase.m' m-file. This data represents the output noise variance of the phasor reconstructor for optimal phasor weights when the input noise variances in the x- and y-directions vary from 0.25 up to 4.0. This data is plotted in Figure 4.1.

Table C.2 Phasor reconstructor with optimal phasor weights for  $\sigma_x^2$  and  $\sigma_y^2$  varied from 0.25 up to 4.0.

$\sigma_x^2$	0.250	0.500	0.750	1.000	1.250	1.500	1.750	2.000	2.250	2.500	2.750	3.000	3.250	3.500	3.750	4.000
$\sigma_y^2$																
0.250	0.115	0.164	0.186	0.204	0.219	0.225	0.230	0.231	0.228	0.234	0.234	0.236	0.234	0.236	0.237	0.232
0.500	0.164	0.293	0.402	0.493	0.541	0.552	0.600	0.591	0.611	0.622	0.616	0.625	0.623	0.629	0.620	0.622
0.750	0.186	0.402	0.607	0.795	0.905	0.975	0.990	1.056	1.029	1.083	1.096	1.063	1.086	1.105	1.100	1.080
1.000	0.204	0.493	0.795	1.000	1.214	1.285	1.397	1.450	1.473	1.494	1.524	1.473	1.525	1.548	1.544	1.499
1.250	0.219	0.541	0.905	1.214	1.394	1.607	1.716	1.788	1.827	1.853	1.886	1.903	1.883	1.902	1.845	1.924
1.500	0.225	0.552	0.975	1.285	1.607	1.749	1.943	2.043	2.040	2.138	2.167	2.177	2.176	2.148	2.193	2.218
1.750	0.230	0.600	0.990	1.397	1.716	1.943	2.051	2.232	2.301	2.342	2.392	2.421	2.348	2.432	2.456	2.462
2.000	0.231	0.591	1.056	1.450	1.788	2.043	2.232	2.299	2.463	2.526	2.562	2.525	2.611	2.608	2.611	2.631
2.250	0.228	0.611	1.029	1.473	1.827	2.040	2.301	2.463	2.500	2.638	2.605	2.731	2.748	2.758	2.775	2.718
2.500	0.234	0.622	1.083	1.494	1.853	2.138	2.342	2.526	2.638	2.661	2.792	2.833	2.857	2.878	2.819	2.901
2.750	0.234	0.616	1.096	1.524	1.886	2.167	2.392	2.562	2.603	2.792	2.788	2.907	2.940	2.888	2.970	2.974
3.000	0.236	0.625	1.063	1.473	1.903	2.177	2.421	2.525	2.731	2.833	2.907	2.888	2.925	3.013	3.042	3.053
3.250	0.234	0.623	1.086	1.525	1.883	2.176	2.348	2.611	2.748	2.857	2.940	2.925	2.967	3.063	3.090	3.105
3.500	0.236	0.629	1.105	1.548	1.902	2.148	2.432	2.608	2.758	2.878	2.888	3.013	3.063	3.029	3.125	3.140
3.750	0.237	0.620	1.100	1.544	1.845	2.193	2.456	2.611	2.775	2.819	2.970	3.042	3.090	3.125	3.078	3.153
4.000	0.232	0.622	1.080	1.499	1.924	2.218	2.462	2.631	2.718	2.901	2.974	3.053	3.105	3.140	3.153	3.115

This is the raw data for the plot shown in Figure 4.2. This data represents the difference of the output noise variance of the phasor reconstructor using optimal linear-based weights minus the output noise variance of the phasor reconstructor using optimal phasor-based weights.

Table C.3 Difference of the data in Table C.1 minus data in Table C.2.

$\sigma_x^2$	0.250	0.500	0.750	1.000	1.025	1.500	1.750	2.000	2.250	2.500	2.750	3.000	3.250	3.500	3.750	4.000
$\sigma_y^2$																
0.250	-0.085	-0.096	-0.058	0.005	0.073	0.131	0.166	0.186	0.197	0.195	0.196	0.194	0.197	0.196	0.196	0.202
0.500	-0.096	-0.172	-0.181	-0.121	-0.011	0.102	0.132	0.179	0.177	0.172	0.180	0.172	0.174	0.169	0.178	0.177
0.750	-0.058	-0.181	-0.185	-0.088	0.076	0.211	0.319	0.315	0.369	0.325	0.315	0.349	0.326	0.307	0.313	0.333
1.000	0.005	-0.121	-0.088	0.130	0.293	0.492	0.538	0.564	0.575	0.566	0.540	0.592	0.540	0.517	0.520	0.564
1.250	0.073	-0.011	0.076	0.293	0.559	0.656	0.727	0.745	0.744	0.731	0.702	0.686	0.706	0.687	0.742	0.663
1.500	0.131	0.102	0.211	0.492	0.656	0.848	0.845	0.840	0.883	0.799	0.775	0.765	0.766	0.793	0.747	0.720
1.750	0.166	0.132	0.319	0.538	0.727	0.845	0.935	0.850	0.823	0.797	0.751	0.723	0.796	0.710	0.685	0.677
2.000	0.186	0.179	0.315	0.564	0.745	0.840	0.850	0.881	0.759	0.711	0.680	0.718	0.632	0.633	0.628	0.607
2.250	0.197	0.177	0.369	0.575	0.744	0.883	0.823	0.759	0.763	0.641	0.679	0.553	0.536	0.525	0.506	0.561
2.500	0.195	0.172	0.325	0.566	0.731	0.799	0.797	0.711	0.641	0.633	0.507	0.467	0.442	0.420	0.477	0.393
2.750	0.196	0.180	0.315	0.540	0.702	0.775	0.751	0.680	0.681	0.507	0.516	0.397	0.364	0.415	0.331	0.325
3.000	0.194	0.172	0.349	0.592	0.686	0.765	0.723	0.718	0.553	0.467	0.397	0.417	0.380	0.290	0.260	0.246
3.250	0.197	0.174	0.326	0.540	0.706	0.766	0.796	0.632	0.536	0.442	0.364	0.380	0.337	0.240	0.211	0.194
3.500	0.196	0.169	0.307	0.517	0.687	0.793	0.710	0.633	0.525	0.420	0.415	0.290	0.240	0.273	0.175	0.157
3.750	0.196	0.178	0.313	0.520	0.742	0.747	0.685	0.628	0.506	0.477	0.331	0.260	0.211	0.175	0.221	0.143
4.000	0.202	0.177	0.333	0.564	0.663	0.720	0.677	0.607	0.561	0.393	0.325	0.246	0.194	0.157	0.143	0.179

## APPENDIX D

### OPTIMAL X-DIRECTION WEIGHTS

#### D.1 Optimal Phasor-Based X-Direction Weights

This data represents the optimal phasor-based x-direction weights for input noise variances in both the x- and y-directions varying from 0.25 up to 4.0. The optimal phasor-based y-direction weights for a given x- and y-direction input noise variance can be found by subtracting the corresponding x-direction weight from 0.5.

Table D.1 Optimal phasor-based x-direction weights.

$\sigma_x^2$	0.250	0.500	0.750	1.000	1.250	1.500	1.750	2.000	2.250	2.500	2.750	3.000	3.250	3.500	3.750	4.000
$\sigma_y^2$																
0.250	0.250	0.333	0.375	0.400	0.427	0.449	0.458	0.464	0.480	0.485	0.478	0.482	0.494	0.497	0.489	0.501
0.500	0.167	0.250	0.300	0.343	0.377	0.395	0.419	0.440	0.459	0.467	0.473	0.479	0.483	0.488	0.491	0.494
0.750	0.125	0.200	0.250	0.296	0.333	0.363	0.380	0.414	0.425	0.435	0.443	0.450	0.456	0.462	0.467	0.471
1.000	0.100	0.157	0.204	0.250	0.288	0.320	0.358	0.383	0.396	0.407	0.417	0.425	0.432	0.439	0.445	0.450
1.250	0.073	0.123	0.168	0.212	0.250	0.283	0.322	0.348	0.371	0.383	0.394	0.403	0.411	0.418	0.425	0.431
1.500	0.051	0.105	0.137	0.180	0.217	0.250	0.289	0.316	0.340	0.363	0.374	0.383	0.392	0.400	0.407	0.414
1.750	0.043	0.081	0.120	0.142	0.178	0.211	0.250	0.287	0.321	0.344	0.356	0.366	0.375	0.383	0.391	0.398
2.000	0.036	0.060	0.086	0.117	0.152	0.184	0.213	0.250	0.285	0.308	0.340	0.350	0.360	0.368	0.376	0.383
2.250	0.020	0.041	0.075	0.104	0.129	0.160	0.179	0.215	0.250	0.303	0.285	0.336	0.346	0.354	0.363	0.370
2.500	0.016	0.033	0.065	0.093	0.117	0.138	0.156	0.192	0.197	0.250	0.272	0.313	0.333	0.342	0.350	0.358
2.750	0.022	0.027	0.057	0.083	0.106	0.127	0.144	0.161	0.185	0.228	0.250	0.271	0.301	0.320	0.339	0.346
3.000	0.019	0.021	0.050	0.075	0.097	0.117	0.134	0.150	0.164	0.187	0.229	0.250	0.280	0.319	0.328	0.336
3.250	0.006	0.017	0.044	0.068	0.089	0.108	0.125	0.141	0.155	0.167	0.199	0.220	0.250	0.309	0.298	0.316
3.500	0.003	0.023	0.038	0.061	0.082	0.100	0.117	0.132	0.146	0.158	0.180	0.181	0.201	0.250	0.299	0.307
3.750	0.011	0.009	0.033	0.055	0.075	0.093	0.109	0.124	0.138	0.150	0.162	0.172	0.202	0.201	0.250	0.308
4.000	-0.001	0.006	0.029	0.050	0.069	0.086	0.102	0.117	0.130	0.142	0.154	0.164	0.184	0.193	0.192	0.240

## D.2 Optimal Linear-Based X-Direction Weights

This data represents the optimal linear-based x-direction weights for input noise variances in both the x- and y-directions varying from 0.25 up to 4.0. The optimal linear-based y-direction weights for a given x- and y-direction input noise variance can be found by subtracting the corresponding x-direction weight from 0.5.

Table D.2 Optimal linear-based x-direction weights.

$\sigma_x^2$	0.250	0.500	0.750	1.000	1.250	1.500	1.750	2.000	2.250	2.500	2.750	3.000	3.250	3.500	3.750	4.000
$\sigma_y^2$																
0.250	0.250	0.333	0.375	0.400	0.417	0.429	0.438	0.444	0.450	0.455	0.458	0.462	0.464	0.467	0.469	0.471
0.500	0.167	0.250	0.300	0.333	0.357	0.375	0.389	0.400	0.409	0.417	0.423	0.429	0.433	0.438	0.441	0.444
0.750	0.125	0.200	0.250	0.286	0.313	0.333	0.350	0.364	0.375	0.385	0.393	0.400	0.406	0.412	0.417	0.421
1.000	0.100	0.167	0.214	0.250	0.278	0.300	0.318	0.333	0.346	0.357	0.367	0.375	0.382	0.389	0.395	0.400
1.250	0.083	0.143	0.188	0.222	0.250	0.273	0.292	0.308	0.321	0.333	0.344	0.353	0.361	0.368	0.375	0.381
1.500	0.071	0.125	0.167	0.200	0.227	0.250	0.269	0.286	0.300	0.313	0.324	0.333	0.342	0.350	0.357	0.364
1.750	0.063	0.111	0.150	0.182	0.208	0.231	0.250	0.267	0.281	0.294	0.306	0.316	0.325	0.333	0.341	0.348
2.000	0.056	0.100	0.136	0.167	0.192	0.214	0.233	0.250	0.265	0.278	0.290	0.300	0.310	0.318	0.326	0.333
2.250	0.050	0.091	0.125	0.154	0.179	0.200	0.219	0.235	0.250	0.263	0.275	0.286	0.296	0.304	0.313	0.320
2.500	0.046	0.083	0.115	0.143	0.167	0.188	0.206	0.222	0.237	0.250	0.262	0.273	0.283	0.292	0.300	0.308
2.750	0.042	0.077	0.107	0.133	0.156	0.177	0.194	0.211	0.225	0.238	0.250	0.261	0.271	0.280	0.289	0.296
3.000	0.039	0.071	0.100	0.125	0.147	0.167	0.184	0.200	0.214	0.227	0.239	0.250	0.260	0.269	0.278	0.286
3.250	0.036	0.067	0.094	0.118	0.139	0.158	0.175	0.191	0.205	0.217	0.229	0.240	0.250	0.259	0.268	0.276
3.500	0.033	0.063	0.088	0.111	0.132	0.150	0.167	0.182	0.196	0.208	0.220	0.231	0.241	0.250	0.259	0.267
3.750	0.031	0.059	0.083	0.105	0.125	0.143	0.159	0.174	0.188	0.200	0.212	0.222	0.232	0.241	0.250	0.258
4.000	0.029	0.056	0.079	0.100	0.119	0.136	0.152	0.167	0.180	0.192	0.204	0.214	0.224	0.233	0.242	0.250

# Mathematical Modeling of Thermionic-AMTEC Cascade System for Space Power

M.A.K. Lodhi  
Professor  
Department of Physics

Texas Tech University  
Lubbock, TX 79409

Final Report for:  
Summer Research Extension Program  
Phillips Laboratory

Sponsored by:  
Air Force Office of Scientific Research  
Bolling Air Force Base, DC

and

Phillips Laboratory

October 1996

---

MATHEMATICAL MODELING OF THERMIONIC-AMTEC  
CASCADE SYSTEM FOR SPACE POWER

M. A. K. Lodhi  
Professor  
Department of Physics  
Texas Tech University

Abstract

A mathematical modeling of the function of a system consisting of a cascade of a thermionic energy conversion (TIEC) device and an alkali metal thermal to electrical conversion (AMTEC) device has been performed. The AMTEC utilizes this reject heat of the TIEC. A mathematical thermal model of the cascade converter has been developed to analyze effects of key parameters such as power level, heat fluxes, temperatures, cascade geometry, etc. In this effort, a 9-node system of nonlinear simultaneous equations has been constructed which is solved by MATHCAD predicting the temperatures of the principal components and the heat flow. Through this study, a better understanding of the thermal coupling of the two converters was gained which helps to produce a more efficient cascade.

# MATHEMATICAL MODELING OF THERMIONIC-AMTEC CASCADE SYSTEM FOR SPACE POWER

M. A. K. Lodhi

## Introduction

The purpose of this study is to investigate the compatibility of such a tandem device which cascades two complementary static devices and to develop a mathematical model for matching the thermal impedances of the two converters resulting in a more efficient cascade.

The cascade consists of a thermionic energy converter (TIEC) and an alkali metal thermoelectric converter (AMTEC). The reason for selecting these converters is for the temperature at which the TIEC rejects its heat is in the range of the temperature suitable for the AMTEC to receive the heat. With little modification, a TIEC can tandem with AMTEC to make a cascade device. To better describe our research, we will give first brief descriptions of the TIEC, the AMTEC, and the cascade.

The goal for static conversion systems has been to identify static converters with efficiencies that are competitive with dynamic system. Alternatively two compatible static devices may be linked together in a tandem form to increase the efficiency for space power system. The purpose of this research is to investigate into the compatibility of such a tandem device which cascades two complementary static devices and develops a mathematical model to help the designing of the matching of the thermal impedances of the two converters resulting in a more efficient cascade. The cascade under investigation consists of a thermionic energy converter (TIEC) and an alkali metal thermoelectric converter (AMTEC). Fortunately the temperature at which TIEC rejects its heat is in the range of the temperature suitable for AMTEC to receive the heat. With little modification a TIEC can tandem with AMTEC to make a cascade device.

A thermionic converter is a static device which converts heat energy into electricity through the surface emission of electrons. Fig. 1 gives a schematic diagram of parts and working of a typical TIEC. It consists of an emitter (or cathode) which at one surface receives heat from a suitable source and emits electrons from the other. A collector (or anode) collects these electrons and is cooled to a lower temperature than the emitter to limit the back emission of electrons. The anode and cathode are connected by electrical leads to supply this generated power to the load.

The rate of the electron emission from the hot metal surface is a function of metal temperature and the work function. The kinetic energy of electrons within the bulk metal increases with increasing temperature allowing a higher fraction of them to escape from the metal surface.

To reduce the space charge effect the gap between the emitter and collector is filled with plasma of cesium vapor. Cesium has the lowest ionization potential and its absorption reduces the surface work function of the electrodes lower than liquid cesium or any metal [1]. The converter stably generated power at  $80\text{kW/m}^2$  ( $8\text{W/cm}^2$ ) with an electrode efficiency of 17% for 5 years in the lab without a failure [2]. The typical temperature of TIEC working are 1600 to 2000K at the receiving end of the heat and 800-1100K at the rejection end [3].

AMTEC is a relatively new type of device based on the principle of concentration cell conceived in late sixties [4,5] as illustrated in Fig. 2. A closed vessel is divided into a high temperature,  $T^2$ , and high pressure region contact with a heat source and low temperature,  $T^1$ , and low pressure region in contact with a heat sink. These regions are separated by a barrier of beta-alumina solid electrolyte (BASE) which has ionic conductivity much larger than the electronic conductivity. The BASE bears a porous metal electrode (anode) which converts the low pressure surface of the BASE. A closed container is partially filled with liquid sodium working fluid. Sodium ions diffuse through the BASE in response to the pressure differential (gradient of Gibbs free energy). Electrical leads are connected with the porous anode and with the high temperature liquid sodium as cathode. When the circuit is closed electrons flow to the porous anode surface through the load producing electrical work. A return line and electromagnetic pump or a wick circulate

the sodium work fluid through AMTEC [4-7]. AMTEC conversions efficiency was reported 19% in 1981 [8] and a power density of  $1\text{ W/cm}^2$  [6]. Its hot region temperature is in the range of 900-1300K [9], quite compatible with the general purpose heat source (GPHS) [10] or the projected Sp-100 nuclear space power reactor [11]. AMTEC is limited to 1350K because of the strength of the BASE. The lower temperature region could be limited to 600K as the condenser temperature increases above 700K the efficiency decreases quite rapidly [1]. AMTEC has high efficiency near Carnot [12], low maintenance and high durability, modular construction and the ability to use high temperature combustion nuclear or solar heat source [13].

#### Cascade Assembly

An assembly of TIEC and AMTEC has been cascaded with a transition piece between the collector of TIEC and AMTEC. The transition piece is surrounded by a trim collar which is heated at a desirable temperature by a heating element. The trim heater is surrounded by a calorimeter. The cascade is schematically shown in Fig. 3. The TIEC is heated by electron bombardment portion of this heat energy into electricity and rejects the rest from the lower end of the emitter. The rejected heat is picked up by AMTEC via the transition piece and converted into electricity.

At the outset the cascade was broken down mathematically into as many nodes as necessary for the complete analysis of the converter. From the conservation of energy, the energy balance equations were developed at each node. We determined nine equations were adequate. These equations are nonlinear in temperature and were solved with the boundary conditions determined at their respective nodes. For solving this set of equations a software called MATHCAD was used.

#### Cascade Modeling

For the purpose of keeping the track of the heat and mass flow the cascade has been broken down into nine different nodes. At each node the boundary conditions are determined for the heat and mass flow through the cascade. This gives rise to nine simultaneous equations with nine temperatures at these nodes to be solved. With the help of the nodal circuit the nine equations are developed and solved for those temperatures. In order to solve these lengthy and complicated equations an iterative procedure is adopted with MATHCAD 5.0. For the iterative solution some initial values of the unknowns are guessed and supplied for the calculations. The final answers do not depend on the initial values supplied. The answers do depend on the parameters used for material properties and radiation loss or heat transfer terms. The radiation terms are in turn dependent on view factors of the geometry of the cascade.

Before solving the nine nodal equations it is essential to estimate the view factors at each node as close as possible to the geometry of the cascade. This is not a trivial job. Various view factors have been evaluated and substituted in the appropriate places in the nodal equations with corresponding portions of the areas of the various components of the cascade. The details of calculation of the view factors is avoided here to be presented for the sake of brevity. The development of these expressions is given as the input and output data of the MATCHED compilation at the outset of the nine simultaneous nodal equations and their solutions.

The model consists of nine nodal equations (using conservation of energy) at strategic locations within the cascade. The nodal points selected on the cascade system were at the emitter, flange, bellows, collector, transition piece, trim collar, AMTEC evaporator (in the high temperature zone), AMTEC condenser (in the low temperature zone), and the calorimeter collar.

Because the cascade is to be used in a vacuum environment, convection heat transfer was assumed to be non-existent in the thermal model. Therefore, the only heat transfer modes considered in the thermal model were conduction and radiation. Since the solid components of the cascade were assumed to be at uniform temperature, the only conduction applied in the thermal modeling was from component to component across contact interfaces. The heat transfer across contact interfaces was actually a combination of conduction and radiation. Since perfect contact between components is virtually impossible, gaps exist in which the only possible avenue for heat transfer is radiation. The lack of a fluid medium to act as an energy transfer mechanism within the contact gaps of the interfaces increases the thermal resistance.

The interfacial heat transfer between the various cascade nodal sections was therefore calculated by assuming the heat flow was equal to the temperature difference across the interface divided by the thermal interfacial resistance. The thermal interfacial resistance was approximated, and it is therefore a candidate for further investigation.

Due to the high temperatures within the device, radiation heat transfer was a major heat transfer mechanism. A major challenge involved in calculating radiation heat transfer is the calculation of the view factors. The radiation view factor is defined as the fraction of the diffuse, uniform radiant energy leaving a surface that is incident on another surface. The view factors are a function of geometry only, due to the assumption of diffuse, uniform radiation. This analysis utilized two geometrically calculated view factors which included parallel disks and cylinder within cylinder [14]. The actual view factors were then derived from these using view factor algebra and enclosure analysis.

## Results

Calculational results from this model with a heat input of 318 W for the electron gun and 126 W for the trim heater are given in Table 1, followed by experimental results. The size of the error vector for the solution given in Table 1 was given by MATHCAD as 0.004.

TABLE 1. Solution to Cascade Nodal Equations.

Temp	Te (K)	Tc (K)	Tf (K)	Tbel (K)	Tb (K)	Ta (K)	Ttrim (K)	Tl (K)	Tcal (K)
Calc	1944	1264	1318	1054	1229	1196	1310	364	928
Exp	1801	1041	1110	NR	933	875	NR	347	1052

## Discussion

In general the main causes for the overprediction temperature are the boundary conditions and the assumed values of thermal resistance at the various material interfaces. All boundaries were assumed to be adiabatic, with the exception of the AMTEC condenser, which was assumed to be in contact with a constant temperature (300 K) heat sink. In reality, none of the boundaries are adiabatic, they radiate heat to the vacuum chamber walls. The only parts of the device where the adiabatic assumption is far from reality are around the heaters. The electron beam heater, while shielded by insulation, appears to have radiated a large amount of heat to the chamber. More significantly, this heater appears to have radiated a great deal of heat to the calorimeter (around the transition piece), causing it to operate at a higher temperature than predicted. The calorimeter itself took out 100 watts more than the trim heater put in, due to minimum flow requirements needed to avoid boiling in the cooling lines. This heat loss, coupled with higher than expected thermal resistances, led to the AMTEC cell operating at a much lower temperature than predicted. We believe that most of the thermal resistance is due to gaps opening up between the collector and the transition piece, due to thermal expansion. The copper plate attached to the AMTEC condenser actually removed 50 watts less than the model predicted, but we still had some trouble avoiding boiling water in the cooling lines.

## Conclusion

The main purpose of this study was to understand the heat flow through the cascade at various points, which has been achieved thus providing a test for the model. The accuracy of this model depends on a number of parameters. Some discrepancies noted between the predicted and observed temperatures in Table I are attributed to: (a) Material properties. These properties were taken from the catalogs of the material properties of standard samples at various

temperature and pressure rather than measuring them actually, and using them for our model. . (b) Thermal contact resistances. A good estimate of thermal contact resistances between various components of TIEC, AMTEC, and other ancillary components is necessary at the projected temperatures and pressures. Although this information has been incorporated as accurately as possible in the model; it is, however, a serious source of error. © Radiation heat transfer (particularly losses). This factor is one of the most important for the model to predict the temperatures. For this reason, the cascade geometry has been studied very carefully. Its geometrical parameters affect the configuration (or view) factors for the various components of the cascade. These quantities have been calculated with mathematical exactitude, though involving some tedious and laborious algebra. This is one of the least sources of error, but the temperature terms arising from the radiation losses vary as the fourth power of temperature and thus could cause a large error for small deviation in temperatures. (d) Nodal analysis of the cascade: At the outset, the cascade was broken down mathematically into as many nodes as necessary for the complete analysis of the converter. In this case there are nine nodes. From conservation of energy, the energy balance equations have been developed at each node. These equations are nonlinear in temperature and have been solved with the boundary conditions determined at the respective nodes. Further increasing of the number of nodal points would yield better agreement at intermediate points.

For solving this set of equations a computer model was developed for a software called MATHCAD. As a sample calculation and a test of the model, a temperature profile for the cascade nodal points was obtained for a set of input energy parameters at the emitter and the trim heater.

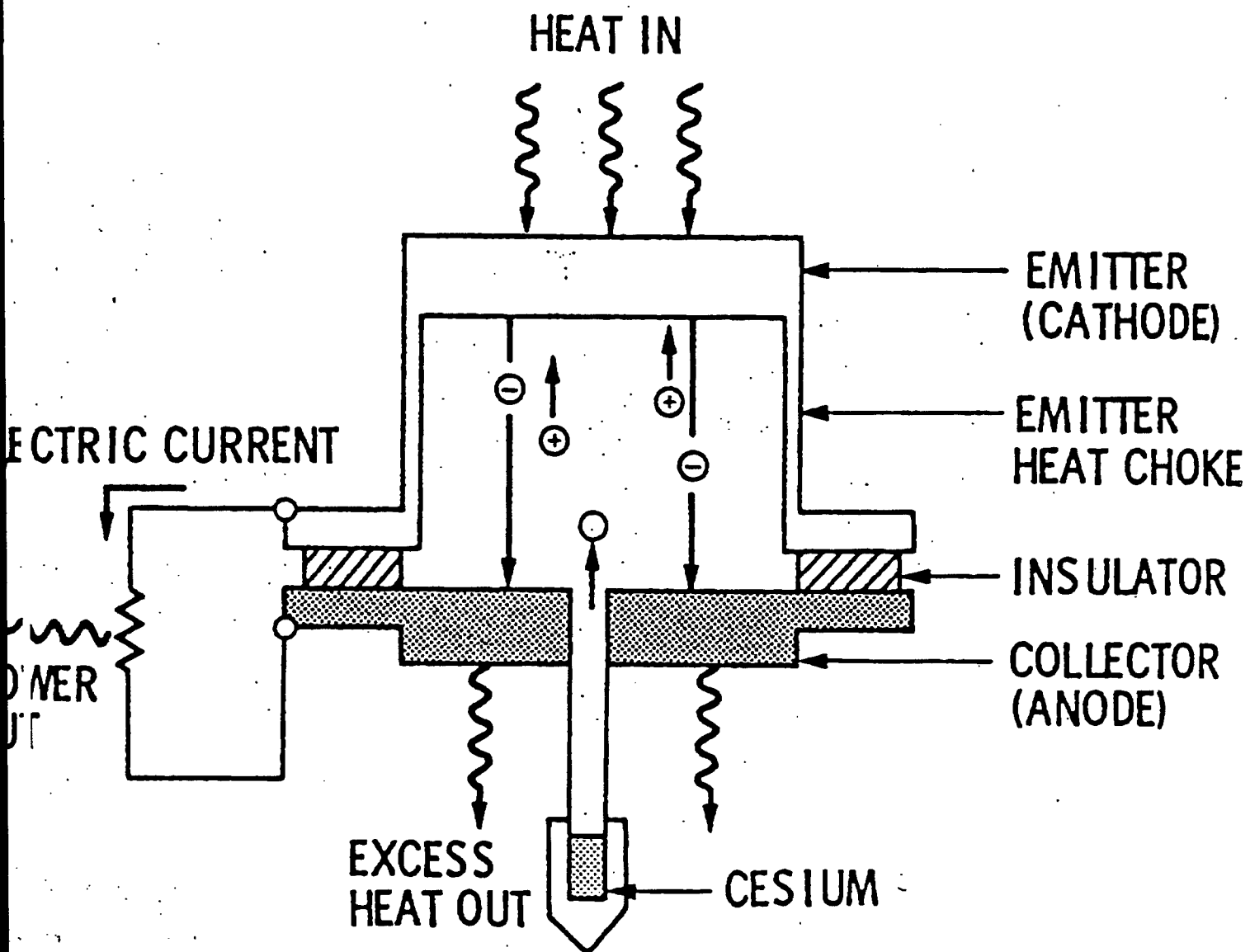
This work was supported in part by the Air Force Office of Scientific Research (AFOSR) and Phillips Laboratory, Kirtland AFB, NM.

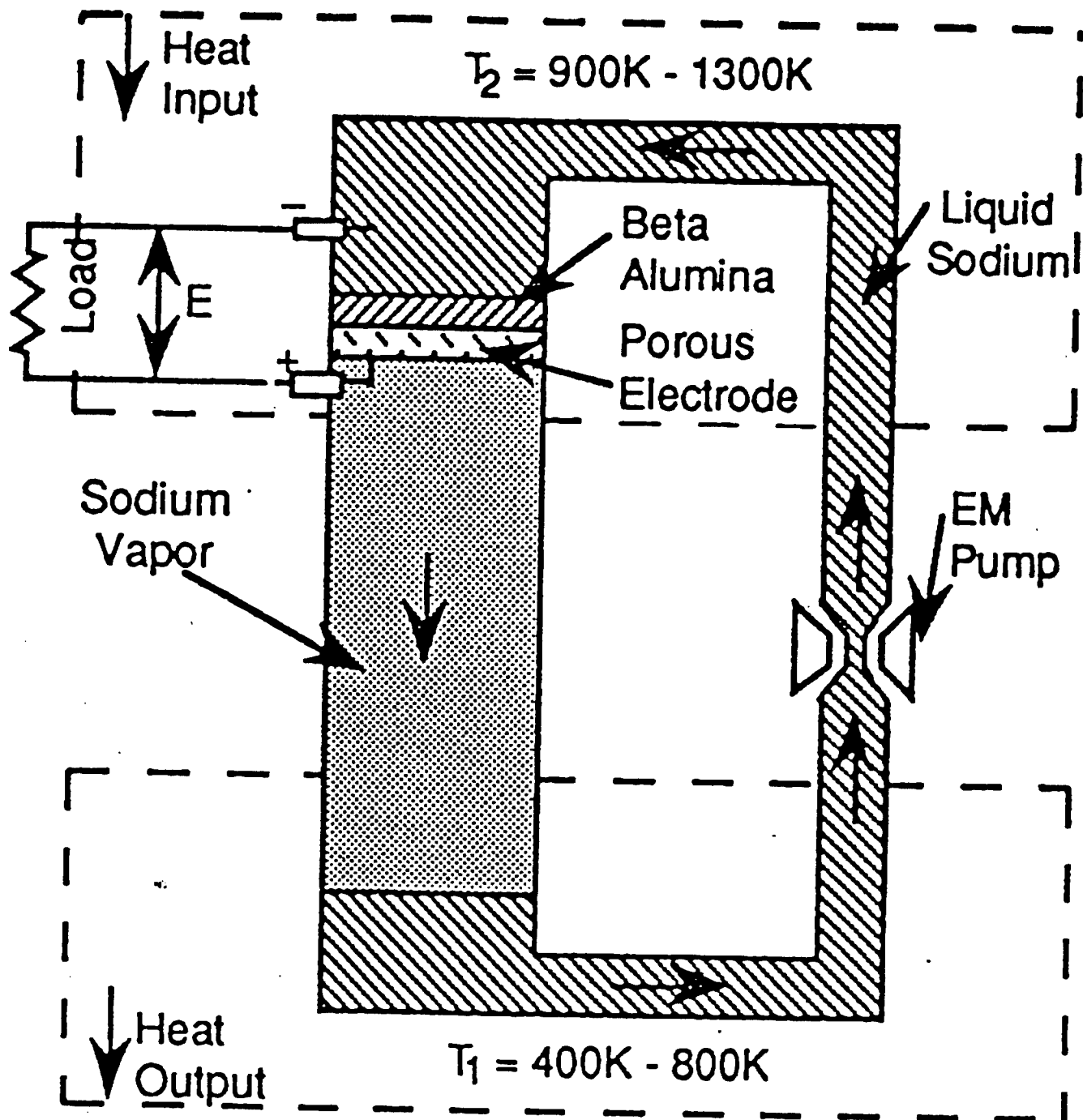
## References

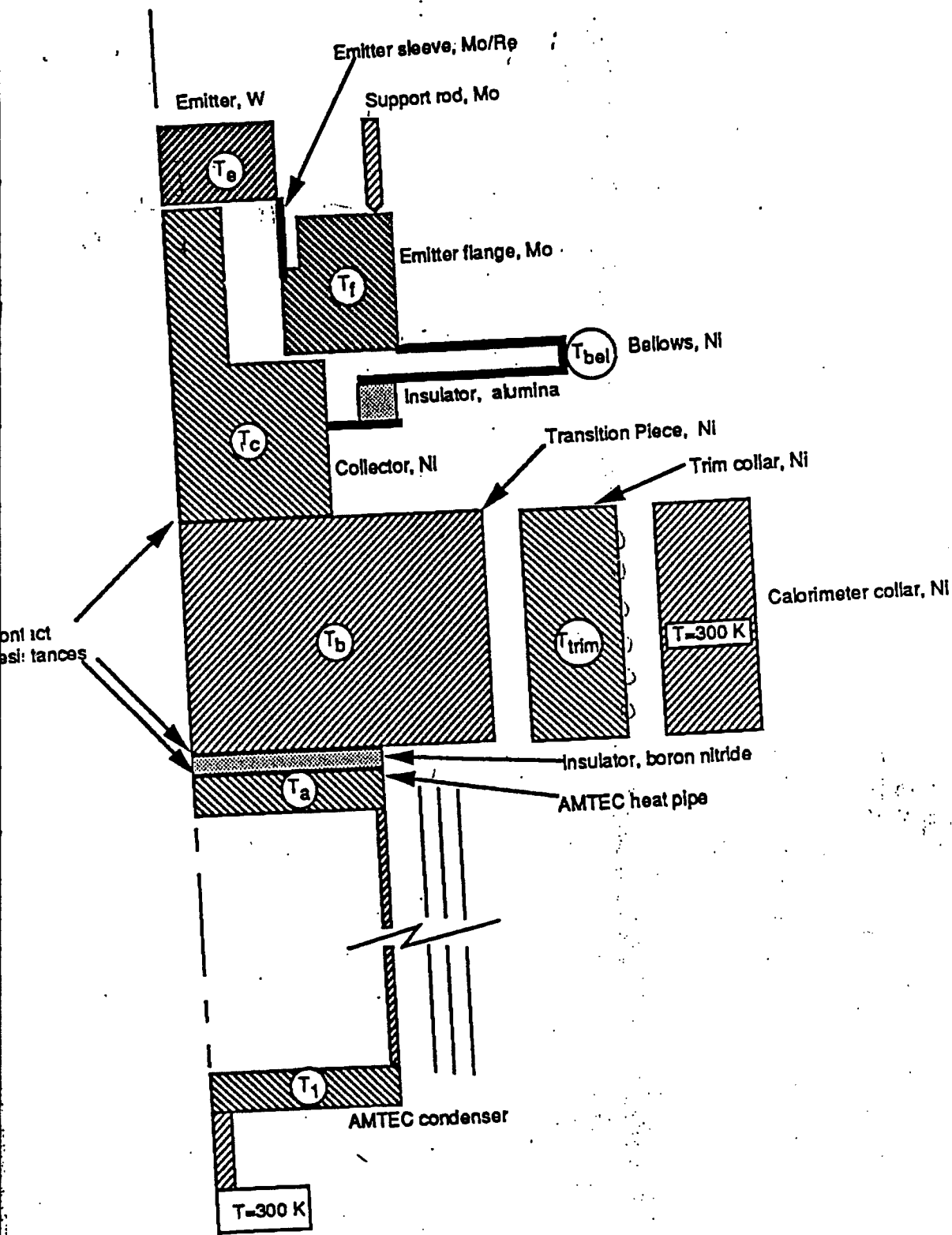
1. R. Ewell and J. Mondt, "Static Conversion Systems", Space Nuclear Power Syst., Ed. M.S. El-Genk and M.D.H. Hoover (Orbit Book Co. Malabar, FL, 1985) pp385-391
2. E.J.Britt and G.O. Fitzpatrick, "Direct Conversion Nuclear Reactor Space Power Sys.." Report No. AFWAL-TR-82-2073, Vol 1
3. R.C.Dahlberg et al, "Review of Thermionic Technology 1983 to 1992," "A Critical Rev of Space Nucl Power and Propulsion 1984-1992", Ed. M.S.El-Genk (AIP Press, NY 1994) pp 121-161
4. J. T. Kummer and N. Weber, U.S. Patent 3,458,356 (1968), Assigned to Ford Motor Co.
5. N. Weber, "A Thermoelectric Device Based on Beta-Alumina Solid Electrolyte", Energy Conversion 14, 1(1974)
6. T.K.Hunt, N.Weber, and T.Cole, "Research on the Sodium Heat Engine", Proc 13th Intersoc Energy Conversion Engineering Conf., SAE, Warrandale, PA (1978) p 201
7. T. Cole, "Thermoelectric Energy Conversion with Solid Electrolyte", Science, 221, 915 (1983)
8. T.K. Hunt, N. Weber, and T. Cole, "High Efficiency Thermoelectric Conversion with Beta" - Alumina Solid Electrolyte: The Sodium Heat Engine", Fast Ionic Transpost in Solids, Ed. J.B. Bates, C.G. Ferrington (N-Holland Co, 1981) p 263
9. C.P. Bankston, T. Cole, S.K. Khanna and A.P Thakoor, "Alkali Metal Thermodynamic Conversion (AMTEC) for Space Nuclear Power Systems", Space Nucl Power Sys., Ed. M.S. El-Genk and M.D. Hoover, (Orbit Co., Malabar, FL, 1985) pp 398-402
10. A. Shock, "Design Evolution and Verification of the General Purpose Heat Source", Proc 15th Intersocieties Energy Conversion Engineering Conf., Vol 2 (AIAA, NY 1980) p 1032
11. D. Budan and F.A. Angelo, "Space Reactor-Past, Present and Future", Proc. 18th Intersocieties Energy Conversion Engineering Conf., Vol (AIChE, NY, 1983) p 61
12. C.B. Vinning, R.M. Williams, M.L. Underwood, M.A. Ryan, and J.W. Suiter, "Reversible Thermodynamic Cycle for AMTEC Power Conversion", Proc. 27th Intersocieties Energy Conversion Engineering Conf., Society of Automobile Engineers, 1992, pp 3: 123-128
13. M.L. Undersoon, et al, "Recent Advances in AMTEC Recirculating Test Cell Performance", Conf. 930103 (AIP, 1993) pp 885-890
14. R. Siegel and J.R. Howell, "Thermal Radiation Heat Transfer", 3rd Ed. (Hemisphere Pub. Corp., Washington, DC, 1992) pp 1032, 1034

# Nomenclature

$T_e$ :	The temperature of the emitter (K)
$T_c$ :	The temperature of the collector (K)
$T_f$ :	The temperature of the flange (K)
$T_{bel}$ :	The temperature of the bellow (K)
$T_b$ :	The temperature of the transition piece (K)
$T_{trim}$ :	The temperature of the trim collar (heater) (K)
$T_l$ :	The temperature of the AMTEC condenser (K)
$T_{cal}$ :	The temperature of the calorimeter (K)
$Q_{input}$ :	The heat input from the electron gun into the emitter (W)
$Q_{trim}$ :	The heat input from trim heater into transition piece (K)







**SCHEMATIC OF THERMAL MODEL OF CASCADE TEC/AMTEC CONVERTER**

Fig 3

**Charles Noel**  
**Report not available at time of publication.**

INCORPORATION OF BOUNDARY CONDITION MODELS INTO THE AIR FORCE  
COMPUTER SIMULATION PROGRAM, MACH

Carlos A. Ordonez  
Assistant Professor  
Department of Physics

University of North Texas  
Denton, TX 76203

Final Report for:  
Summer Research Extension Program  
Phillips Laboratory

Sponsored by:  
Air Force Office of Scientific Research  
Bolling Air Force Base, Washington DC  
and  
University of North Texas  
Denton, Texas

November 1997

---

# INCORPORATION OF BOUNDARY CONDITION MODELS INTO THE AIR FORCE COMPUTER SIMULATION PROGRAM, MACH

Carlos A. Ordonez  
Assistant Professor  
Department of Physics  
University of North Texas

## Abstract

A set of boundary condition models have been developed for the Air Force computer simulation program, MACH. This culminates an important effort carried out by the principle investigator. The models are based on a fully-kinetic self-consistent theory describing the plasma sheath under conditions of space-charge saturation. The phase-space distribution functions for each species of particles are evaluated and velocity moments are taken in order to obtain particle densities, fluxes, temperatures, and energy fluxes. The electric potential profile is determined self-consistently for three different types of profiles. These are a monotonically-decreasing potential, a single-minimum potential associated with a negative surface floating potential, and a single-minimum potential associated with a positive surface floating potential. The electron emission requirements for production of the third potential profile are found to be severe. Particle and energy transport relations are provided only for the first two of the three potential profiles. These relations are supplied for three separate species: plasma electrons, plasma ions, and surface-emitted electrons. At the present time, these boundary condition models are being extended for current-carrying plasma-facing surfaces. It was felt that this extension was sufficiently important to devote the time and resources allocated toward the project to this effort.

# INCORPORATION OF BOUNDARY CONDITION MODELS INTO THE AIR FORCE COMPUTER SIMULATION PROGRAM, MACH

Carlos A. Ordóñez

## I. Introduction

Computer programs, such as MACH, which simulate plasma processes often require boundary conditions in the form of particle and energy transport relations at plasma/surface interfaces. In this report, boundary conditions suitable for incorporation into such computer programs are presented which include the effect of the plasma sheath. The boundary conditions are based on an extension of a fully-kinetic self-consistent theoretical description of the plasma sheath found in Ref. [1]. In Section II, the planar source model is presented and applied to a planar source of half-Maxwellian particles. In Section III, the plasma-electron, plasma-ion, and surface-emitted-electron phase-space distribution functions, and associated densities, fluxes, normalized temperatures, and energy fluxes are provided. In Section IV, the presheath and sheath potentials are evaluated numerically. In Section V, the boundary conditions at the presheath/sheath interface are given along with the simple expressions for the presheath and sheath potentials. Section V is self-contained for easy referral. A concluding summary is found in Section VI.

## II. Planar Source Model

In this section, the planar source model is used to describe the transport of an individual species of charged particles through three types of electric potential profiles under steady-state, collisionless conditions. In order to avoid having to consider the sign of the charged particles, the theory is developed in terms of potential energy profiles. The three potential energy profiles are illustrated in Fig. 1. In all three cases, a planar particle source is located at  $x_0$  which injects particles with a known velocity distribution into the spacial region of interest. The spacial region of interest is located between  $x_0$

and  $x_n$  (at the plasma-facing surface) and particles which reach  $x < x_o$  or  $x > x_n$  are considered lost from the region. The injected-particle velocity distribution function at  $x_o$  is written as  $f_o(v_x, v_y, v_z) \Theta(v_x)$  where the Heaviside step function,  $\Theta$ , is included to indicate that only particles traveling in the positive-x direction are injected at  $x_o$ . As a result of the conservation of energy and momentum, the initial velocity in the x direction of an injected particle at  $x_o$  is related to the particle's velocity in the x direction,  $v_x$ , while the particle is located at position,  $x$ , by

$$v_{ox} = \sqrt{v_x^2 + \frac{2[U(x) - U_o]}{m}} \quad (1)$$

where  $U_o = U(x_o)$  is the particle's potential energy at  $x_o$  and  $m$  is the particle mass. The phase-space distribution function for the charged particles must satisfy the steady-state Vlasov equation,

$$m v_x \frac{\partial f(x, \mathbf{v})}{\partial x} = \frac{\partial U(x)}{\partial x} \frac{\partial f(x, \mathbf{v})}{\partial v_x} \quad (2)$$

while taking into account inaccessible regions in phase-space. In terms of the injected-particle velocity distribution, the phase-space distribution function given by,  $f(x, v_x, v_y, v_z) = f_o(v_{ox}, v_y, v_z)$ , satisfies the steady-state Vlasov equation where  $v_{ox}$  is replaced by the right-hand-side of Eq. (1).

For the first potential energy profile, Fig. 1a, the injected particles encounter an asymmetric potential well. In the collisionless limit, all injected particles pass directly through the region between  $x_o$  and  $x_n$  and travel only in the positive-x direction. Since all particles must have velocities in the x direction greater than  $\sqrt{2[U_o - U(x)]/m}$ , the phase-space velocity distribution function is

$$f(x, v_x, v_y, v_z) = f_o(v_{ox}, v_y, v_z) \Theta \left( v_x - \sqrt{\frac{2[U_o - U(x)]}{m}} \right) \quad (3)$$

For the potential energy profile illustrated in Fig. 1b, particles can be reflected between  $x_o$  and  $x_m$  and then travel past  $x_o$  moving in the negative-x direction. Under

conditions of complete reflection,  $U_m \rightarrow \infty$ , the injected-particle and reflected-particle parts of the phase-space distribution between  $x_o$  and  $x_m$  are symmetric. The only difference for a finite value for  $U_m$  is that particles between  $x_o$  and  $x_m$  with velocities in the positive-x direction greater than,  $\sqrt{2[U_m - U(x)]/m}$ , are not reflected. Consequently, particles traveling in the negative-x direction are restricted to velocities, greater than  $-\sqrt{2[U_m - U(x)]/m}$  and the phase-space distribution function which describes the charged particles between  $x_o$  and  $x_m$  is

$$f(x, v_x, v_y, v_z) = f_o(v_{ox}, v_y, v_z) \Theta \left( v_x + \sqrt{\frac{2[U_m - U(x)]}{m}} \right) \quad (x_o < x < x_m) \quad (4)$$

In the region,  $x_m < x < x_n$ , particles are accelerated in the positive-x direction and are restricted to velocities greater than  $\sqrt{2[U_m - U(x)]/m}$ . Consequently, the phase-space distribution function in this region is

$$f(x, v_x, v_y, v_z) = f_o(v_{ox}, v_y, v_z) \Theta \left( v_x - \sqrt{\frac{2[U_m - U(x)]}{m}} \right) \quad (x_m < x < x_n) \quad (5)$$

The third potential energy profile, Fig. 1c, causes the particle velocity distribution at any location between  $x_o$  and  $x_r$  to occupy two separate velocity regions. One region describes particles moving in the positive-x direction. These particles have a velocity in the x direction greater than  $\sqrt{2[U_o - U(x)]/m}$  and are associated with the phase-space velocity distribution function,

$$f(x, v_x, v_y, v_z) = f_o(v_{ox}, v_y, v_z) \Theta \left( v_x - \sqrt{\frac{2[U_o - U(x)]}{m}} \right) \quad (x_o < x < x_r; \quad v_x > 0) \quad (6)$$

The second region describes particles moving in the negative-x direction. These particles have  $v_x$  values between  $-\sqrt{2[U_n - U(x)]/m}$  and  $-\sqrt{2[U_o - U(x)]/m}$  and are associated with the phase-space distribution function,

$$f(x, v_x, v_y, v_z) = f_o(v_{ox}, v_y, v_z) \Theta \left( v_x + \sqrt{\frac{2[U_n - U(x)]}{m}} \right)$$

$$\times \Theta \left( -v_x - \sqrt{\frac{2[U_o - U(x)]}{m}} \right) \quad (x_o < x < x_r; \quad v_x < 0) \quad (7)$$

Altogether, the phase-space distribution function for particles between  $x_o$  and  $x_r$  can be written as

$$f(x, v_x, v_y, v_z) = f_o(v_{ox}, v_y, v_z) \left[ 1 - \Theta \left( v_x + \sqrt{\frac{2[U_o - U(x)]}{m}} \right) \Theta \left( \sqrt{\frac{2[U_o - U(x)]}{m}} - v_x \right) \right] \\ \times \Theta \left( v_x + \sqrt{\frac{2[U_n - U(x)]}{m}} \right) \quad (x_o < x < x_r) \quad (8)$$

Notice that the velocity distribution at  $x_r$  is the same as at  $x_o$  since  $U(x_r) = U(x_o)$ . Consequently, the phase-space distribution function for particles between  $x_r$  and  $x_n$  is similar to that given by Eq. (4). It is

$$f(x, v_x, v_y, v_z) = f_o(v_{ox}, v_y, v_z) \Theta \left( v_x + \sqrt{\frac{2[U_n - U(x)]}{m}} \right) \quad (x_r < x < x_n) \quad (9)$$

For the three potential energy profiles shown in Fig. 1, the planar particle source located at  $x_o$  is now considered to inject particles having a half-Maxwellian velocity distribution. The half-Maxwellian velocity distribution is

$$f_o(\mathbf{v}) \Theta(v_x) = n_o \left( \frac{\beta}{\pi} \right)^{3/2} e^{-\beta v^2} \Theta(v_x) \quad (10)$$

where  $\beta = m/(2T_o)$ , and  $n_o$  and  $T_o$  are the density and temperature (the latter in energy units) associated with the full-Maxwellian velocity distribution,  $f_o(\mathbf{v})$ . For the potential energy profile shown in Fig. 1a, the phase-space distribution function is given by Eq. (3). For half-Maxwellian injected particles, the phase-space distribution is

$$f(x, \mathbf{v}) = n_o \left( \frac{\beta}{\pi} \right)^{3/2} e^{-\beta v^2 + \psi_{ox}} \Theta \left( v_x - \sqrt{\frac{\psi_{ox}}{\beta}} \right) \quad (11)$$

where  $\psi_{ox} = [U_o - U(x)]/T_o$ . The particle density, particle flux, normalized temperature, and energy flux are

$$n = \int f d^3v = \frac{1}{2} n_o G_1(\psi_{ox}) \quad (12)$$

$$F = \int v_x f d^3v = \frac{n_o}{2\sqrt{\pi}\beta} \quad (13)$$

$$\frac{T}{T_o} = \frac{2\beta}{3} \left[ \frac{\int v^2 f d^3v}{\int f d^3v} - \left( \frac{\int v_x f d^3v}{\int f d^3v} \right)^2 \right] = 1 + \frac{2\sqrt{\psi_{ox}/\pi}}{3G_1(\psi_{ox})} - \frac{2}{3\pi [G_1(\psi_{ox})]^2} \quad (14)$$

and

$$Q = \frac{1}{2} m \int v^2 v_x f d^3v = \frac{(2 + \psi_{ox}) n_o T_o}{2\sqrt{\pi}\beta} \quad (15)$$

Here,  $G_1(x) = e^x \operatorname{erfc}(\sqrt{x})$ , where  $\operatorname{erfc}$  is the complementary error function.

For the potential energy profile shown in Fig. 1b, the phase-space distribution function is given by Eqs. (4) and (5). With half-Maxwellian particles injected at  $x_o$ , the distribution function, density, flux, normalized temperature, and energy flux are

$$\begin{aligned} f(x, \mathbf{v}) &= n_o \left( \frac{\beta}{\pi} \right)^{3/2} e^{-\beta v^2 - \psi_{xo}} \Theta \left( v_x + \sqrt{\frac{\psi_{mx}}{\beta}} \right) \quad (x_o < x < x_m) \\ &= n_o \left( \frac{\beta}{\pi} \right)^{3/2} e^{-\beta v^2 - \psi_{xo}} \Theta \left( v_x - \sqrt{\frac{\psi_{mx}}{\beta}} \right) \quad (x_m < x < x_n) \end{aligned} \quad (16)$$

$$\begin{aligned} n &= \frac{1}{2} n_o e^{-\psi_{mo}} G_2(\psi_{mx}) \quad (x_o < x < x_m) \\ &= \frac{1}{2} n_o e^{-\psi_{mo}} G_1(\psi_{mx}) \quad (x_m < x < x_n) \end{aligned} \quad (17)$$

$$F = \frac{n_o e^{-\psi_{mo}}}{2\sqrt{\pi}\beta} \quad (18)$$

$$\begin{aligned} \frac{T}{T_o} &= 1 - \frac{2\sqrt{\psi_{mx}/\pi}}{3G_2(\psi_{mx})} - \frac{2}{3\pi [G_2(\psi_{mx})]^2} \quad (x_o < x < x_m) \\ &= 1 + \frac{2\sqrt{\psi_{mx}/\pi}}{3G_1(\psi_{mx})} - \frac{2}{3\pi [G_1(\psi_{mx})]^2} \quad (x_m < x < x_n) \end{aligned} \quad (19)$$

and

$$Q = \frac{(2 + \psi_{mx}) n_o T_o e^{-\psi_{mo}}}{2\sqrt{\pi}\beta} \quad (20)$$

where  $\psi_{xo} = [U(x) - U_o]/T_o$ ,  $\psi_{mx} = [U_m - U(x)]/T_o$ ,  $\psi_{mo} = [U_m - U_o]/T_o$ , and  $G_2(x) = e^x \operatorname{erfc}(-\sqrt{x})$ .

With half-Maxwellian particles injected at  $x_o$  into the potential energy profile shown in Fig. 1c, the phase-space distribution function is given by Eqs. (8) and (9). Since the velocity distribution at any location between  $x_o$  and  $x_r$  occupies two separate velocity regions, a separate temperature can be associated with each. In order to evaluate the normalized temperature, the phase-space distribution function given by Eq. (6), which describes particles moving in the positive- $x$  direction, is used. The density, flux, and energy flux are found using the phase-space distribution function given by Eqs. (8) and (9). The relations are

$$\begin{aligned}
f(x, \mathbf{v}) &= n_o \left( \frac{\beta}{\pi} \right)^{3/2} e^{-\beta v^2 + \psi_{ox}} \left[ 1 - \Theta \left( v_x + \sqrt{\frac{\psi_{ox}}{\beta}} \right) \Theta \left( \sqrt{\frac{\psi_{ox}}{\beta}} - v_x \right) \right] \\
&\quad \times \Theta \left( v_x + \sqrt{\frac{\psi_{nx}}{\beta}} \right) \quad (x_o < x < x_r) \\
&= n_o \left( \frac{\beta}{\pi} \right)^{3/2} e^{-\beta v^2 - \psi_{xo}} \Theta \left( v_x + \sqrt{\frac{\psi_{nx}}{\beta}} \right) \quad (x_r < x < x_n) \quad (21)
\end{aligned}$$

$$\begin{aligned}
n &= n_o \left[ G_1(\psi_{ox}) - \frac{1}{2} e^{-\psi_{no}} G_1(\psi_{nx}) \right] \quad (x_o < x < x_r) \\
&= \frac{1}{2} n_o e^{-\psi_{no}} G_2(\psi_{nx}) \quad (x_r < x < x_n) \quad (22)
\end{aligned}$$

$$F = \frac{n_o e^{-\psi_{no}}}{2 \sqrt{\pi} \beta} \quad (23)$$

$$\begin{aligned}
\frac{T}{T_o} &= 1 + \frac{2 \sqrt{\psi_{ox}/\pi}}{3 G_1(\psi_{ox})} - \frac{2}{3 \pi [G_1(\psi_{ox})]^2} \quad (x_o < x < x_r; \quad v_x > 0) \\
&= 1 - \frac{2 \sqrt{\psi_{nx}/\pi}}{3 G_2(\psi_{nx})} - \frac{2}{3 \pi [G_2(\psi_{nx})]^2} \quad (x_r < x < x_n) \quad (24)
\end{aligned}$$

and

$$Q = \frac{(2 + \psi_{nx}) n_o T_o e^{-\psi_{no}}}{2 \sqrt{\pi} \beta} \quad (25)$$

### III. Presheath and Sheath Description

Illustrations of three possible electric potential profiles within a presheath and sheath are shown in Fig. 2 and are given in order of increasing fluxes of emitted electrons from the plasma-facing surface. The first profile, Fig. 2a, is a monotonically decreasing potential which occurs if, for example, the wall surface emits no electrons. The second and third profiles, Figs. 2b and 2c, occur in space-charge saturated sheaths. Notice that with a sufficient flux of emitted electrons, the electrically-floating wall gains a positive potential with respect to the plasma. This phenomenon, which is illustrated in Fig. 2c, has been experimentally observed.[2] For all three profiles, half-Maxwellian plasma electrons and ions are injected at  $x_p$  while half-Maxwellian surface-emitted secondary and thermionic electrons are injected at  $x_s$ . The relations describing plasma electrons, plasma ions, and surface-emitted electrons within the presheath and sheath are derived following a procedure similar to that described in Section II and given below. The notation used is as follows. Location subscripts:  $p$  - edge-plasma/presheath interface;  $b$  - presheath/sheath interface;  $m$  - electric potential minimum;  $r$  - the location in Fig. 2c where the electric potential equals that at  $x_p$  ( $x_r$  is not shown in Fig. 2);  $s$  - sheath/surface interface; and  $x$  - location along the  $x$  coordinate. Two adjacent location subscripts means the difference in values at the two locations. For example,  $\phi_{ms} = \phi_m - \phi_s$ . Particle subscripts:  $e$  - plasma electrons;  $i$  - plasma ions; and  $\delta$  - surface-emitted electrons. Symbols:  $\phi$  - the electric potential;  $e$  - the unit charge; and  $Z$  - the ion charge state. Definitions:  $\beta_e = m_e/(2T_{pe})$ ;  $\beta_i = m_i/(2T_{pi})$ ;  $\beta_\delta = m_e/(2T_{s\delta})$ ;  $\psi_e = U_e/T_{pe} = -e\phi/T_{pe}$ ;  $\psi_i = U_i/T_{pi} = Ze\phi/T_{pi}$ ; and  $\psi_\delta = U_\delta/T_{s\delta} = -e\phi/T_{s\delta}$ .

Plasma electrons within the potential profile shown in Fig. 2a are described by:

$$f_e(x, \mathbf{v}) = n_{pe} \left( \frac{\beta_e}{\pi} \right)^{3/2} e^{-\beta_e v^2 - \psi_{xpe}} \Theta \left( v_x + \sqrt{\frac{\psi_{sxe}}{\beta_e}} \right) \quad (26)$$

$$n_e = \frac{1}{2} n_{pe} e^{-\psi_{spe}} G_2(\psi_{sxe}) \quad (27)$$

$$F_e = \frac{n_{pe} e^{-\psi_{spe}}}{2\sqrt{\pi}\beta_e} \quad (28)$$

$$\frac{T_e}{T_{pe}} = 1 - \frac{2\sqrt{\psi_{sxe}/\pi}}{3G_2(\psi_{sxe})} - \frac{2}{3\pi [G_2(\psi_{sxe})]^2} \quad (29)$$

and

$$Q_e = \frac{(2 + \psi_{sxe}) n_{pe} T_{pe} e^{-\psi_{spe}}}{2\sqrt{\pi}\beta_e} \quad (30)$$

Plasma electrons within the potential profiles shown in Figs. 2b and 2c are described by:

$$\begin{aligned} f_e(x, \mathbf{v}) &= n_{pe} \left( \frac{\beta_e}{\pi} \right)^{3/2} e^{-\beta_e v^2 - \psi_{spe}} \Theta \left( v_x + \sqrt{\frac{\psi_{mxe}}{\beta_e}} \right) \quad (x_p < x < x_m) \\ &= n_{pe} \left( \frac{\beta_e}{\pi} \right)^{3/2} e^{-\beta_e v^2 - \psi_{spe}} \Theta \left( v_x - \sqrt{\frac{\psi_{mxe}}{\beta_e}} \right) \quad (x_m < x < x_s) \end{aligned} \quad (31)$$

$$\begin{aligned} n_e &= \frac{1}{2} n_{pe} e^{-\psi_{mpe}} G_2(\psi_{mxe}) \quad (x_p < x < x_m) \\ &= \frac{1}{2} n_{pe} e^{-\psi_{mpe}} G_1(\psi_{mxe}) \quad (x_m < x < x_s) \end{aligned} \quad (32)$$

$$F_e = \frac{n_{pe} e^{-\psi_{mpe}}}{2\sqrt{\pi}\beta_e} \quad (33)$$

$$\begin{aligned} \frac{T_e}{T_{pe}} &= 1 - \frac{2\sqrt{\psi_{mxe}/\pi}}{3G_2(\psi_{mxe})} - \frac{2}{3\pi [G_2(\psi_{mxe})]^2} \quad (x_p < x < x_m) \\ &= 1 + \frac{2\sqrt{\psi_{mxe}/\pi}}{3G_1(\psi_{mxe})} - \frac{2}{3\pi [G_1(\psi_{mxe})]^2} \quad (x_m < x < x_s) \end{aligned} \quad (34)$$

and

$$Q_e = \frac{(2 + \psi_{mxe}) n_{pe} T_{pe} e^{-\psi_{mpe}}}{2\sqrt{\pi}\beta_e} \quad (35)$$

Plasma ions within the potential profiles shown in Figs. 2a and 2b are described by:

$$f_i(x, \mathbf{v}) = n_{pi} \left( \frac{\beta_i}{\pi} \right)^{3/2} e^{-\beta_i v^2 + \psi_{pxi}} \Theta \left( v_x - \sqrt{\frac{\psi_{pxi}}{\beta_i}} \right) \quad (36)$$

$$n_i = \frac{1}{2} n_{pi} G_1(\psi_{pxi}) \quad (37)$$

$$F_i = \frac{n_{pi}}{2\sqrt{\pi}\beta_i} \quad (38)$$

$$\frac{T_i}{T_{pi}} = 1 + \frac{2\sqrt{\psi_{pxi}/\pi}}{3G_1(\psi_{pxi})} - \frac{2}{3\pi [G_1(\psi_{pxi})]^2} \quad (39)$$

and

$$Q_i = \frac{(2 + \psi_{pxi}) n_{pi} T_{pi}}{2\sqrt{\pi\beta_i}} \quad (40)$$

Plasma ions within the potential profile shown in Fig. 2c are described by:

$$\begin{aligned} f_i(x, \mathbf{v}) &= n_{pi} \left(\frac{\beta_i}{\pi}\right)^{3/2} e^{-\beta_i v^2 + \psi_{pxi}} \left[ 1 - \Theta\left(v_x + \sqrt{\frac{\psi_{pxi}}{\beta_i}}\right) \Theta\left(\sqrt{\frac{\psi_{pxi}}{\beta_i}} - v_x\right) \right] \\ &\quad \times \Theta\left(v_x + \sqrt{\frac{\psi_{sxi}}{\beta_i}}\right) \quad (x_p < x < x_r) \\ &= n_{pi} \left(\frac{\beta_i}{\pi}\right)^{3/2} e^{-\beta_i v^2 - \psi_{xpi}} \Theta\left(v_x + \sqrt{\frac{\psi_{sxi}}{\beta_i}}\right) \quad (x_r < x < x_s) \end{aligned} \quad (41)$$

$$\begin{aligned} n_i &= n_{pi} \left[ G_1(\psi_{pxi}) - \frac{1}{2} e^{-\psi_{spi}} G_1(\psi_{sxi}) \right] \quad (x_p < x < x_r) \\ &= \frac{1}{2} n_{pi} e^{-\psi_{spi}} G_2(\psi_{sxi}) \quad (x_r < x < x_s) \end{aligned} \quad (42)$$

$$F_i = \frac{n_{pi} e^{-\psi_{spi}}}{2\sqrt{\pi\beta_i}} \quad (43)$$

$$\begin{aligned} \frac{T_i}{T_{pi}} &= 1 + \frac{2\sqrt{\psi_{pxi}/\pi}}{3G_1(\psi_{pxi})} - \frac{2}{3\pi [G_1(\psi_{pxi})]^2} \quad (x_p < x < x_r; \quad v_x > 0) \\ &= 1 - \frac{2\sqrt{\psi_{sxi}/\pi}}{3G_2(\psi_{sxi})} - \frac{2}{3\pi [G_2(\psi_{sxi})]^2} \quad (x_r < x < x_s) \end{aligned} \quad (44)$$

and

$$Q_i = \frac{(2 + \psi_{sxi}) n_{pi} T_{pi} e^{-\psi_{spi}}}{2\sqrt{\pi\beta_i}} \quad (45)$$

For the description of surface-emitted electrons, particle and energy fluxes are defined as positive in the negative-x direction. Surface-emitted electrons within the potential profile shown in Fig. 2a are described by:

$$f_\delta(x, \mathbf{v}) = n_{s\delta} \left(\frac{\beta_\delta}{\pi}\right)^{3/2} e^{-\beta_\delta v^2 + \psi_{sx\delta}} \Theta\left(v_x - \sqrt{\frac{\psi_{sx\delta}}{\beta_\delta}}\right) \quad (46)$$

$$n_\delta = \frac{1}{2} n_{s\delta} G_1(\psi_{sx\delta}) \quad (47)$$

$$F_\delta = \frac{n_{s\delta}}{2\sqrt{\pi}\beta_\delta} \quad (48)$$

$$\frac{T_\delta}{T_{s\delta}} = 1 + \frac{2\sqrt{\psi_{sx\delta}/\pi}}{3G_1(\psi_{sx\delta})} - \frac{2}{3\pi [G_1(\psi_{sx\delta})]^2} \quad (49)$$

and

$$Q_\delta = \frac{(2 + \psi_{sx\delta}) n_{s\delta} T_{s\delta}}{2\sqrt{\pi}\beta_\delta} \quad (50)$$

Surface-emitted electrons within the potential profiles shown in Figs. 2b and 2c are described by:

$$\begin{aligned} f_\delta(x, \mathbf{v}) &= n_{s\delta} \left( \frac{\beta_\delta}{\pi} \right)^{3/2} e^{-\beta_\delta v^2 - \psi_{xs\delta}} \Theta \left( v_x - \sqrt{\frac{\psi_{mx\delta}}{\beta_\delta}} \right) \quad (x_p < x < x_m) \\ &= n_{s\delta} \left( \frac{\beta_\delta}{\pi} \right)^{3/2} e^{-\beta_\delta v^2 - \psi_{xs\delta}} \Theta \left( v_x + \sqrt{\frac{\psi_{mx\delta}}{\beta_\delta}} \right) \quad (x_m < x < x_s) \end{aligned} \quad (51)$$

$$\begin{aligned} n_\delta &= \frac{1}{2} n_{s\delta} e^{-\psi_{ms\delta}} G_1(\psi_{mx\delta}) \quad (x_p < x < x_m) \\ &= \frac{1}{2} n_{s\delta} e^{-\psi_{ms\delta}} G_2(\psi_{mx\delta}) \quad (x_m < x < x_s) \end{aligned} \quad (52)$$

$$F_\delta = \frac{n_{s\delta} e^{-\psi_{ms\delta}}}{2\sqrt{\pi}\beta_\delta} \quad (53)$$

$$\begin{aligned} \frac{T_\delta}{T_{s\delta}} &= 1 + \frac{2\sqrt{\psi_{mx\delta}/\pi}}{3G_1(\psi_{mx\delta})} - \frac{2}{3\pi [G_1(\psi_{mx\delta})]^2} \quad (x_p < x < x_m) \\ &= 1 - \frac{2\sqrt{\psi_{mx\delta}/\pi}}{3G_2(\psi_{mx\delta})} - \frac{2}{3\pi [G_2(\psi_{mx\delta})]^2} \quad (x_m < x < x_s) \end{aligned} \quad (54)$$

and

$$Q_\delta = \frac{(2 + \psi_{mx\delta}) n_{s\delta} T_{s\delta} e^{-\psi_{ms\delta}}}{2\sqrt{\pi}\beta_\delta} \quad (55)$$

Secondary electron emission occurs when an electron strikes a material surface and causes an ejection of one or more electrons from the surface. This emission process

is characterized by the electron emission coefficient,  $\delta$ , which equals the average ratio of electrons emitted from the surface to electrons incident on the surface. A relation for secondary electron emission suitable for a plasma-facing surface when space-charge saturation is not present within the sheath is[3]

$$\delta(T_{pe}) = \frac{2.6 \delta_{max}}{\sqrt{\pi} r^3} \int_0^\infty \frac{\epsilon^{7/6} (2 + 3\epsilon) e^{-\epsilon/r}}{(1 + \epsilon)^2} d\epsilon \quad (56)$$

where  $r = 0.72 T_{pe}/E_{max}$ , and  $\delta_{max}$  and  $E_{max}$  are material-dependent constants. (Values for  $\delta_{max}$  and  $E_{max}$  are found, for example, in Ref. [4].) When space-charge saturation is present within the sheath,

$$\delta(T_{pe}, \psi_{mse}) = \frac{2.6 \delta_{max} e^{\psi_{mse}}}{\sqrt{\pi} r^3 G_1(\psi_{mse})} \int_{r\psi_{mse}}^\infty \epsilon^{1/6} e^{-\epsilon/r} \left[ \frac{3 + 4\sqrt{r\psi_{mse}\epsilon}}{(1 + \sqrt{r\psi_{mse}\epsilon})^2} - \frac{3 + 4\epsilon}{(1 + \epsilon)^2} \right] d\epsilon \quad (57)$$

provides a suitable relation for secondary electron emission.[3]

The gross flux of emitted electrons at the material surface,  $F_{g\delta}$ , is given by Eq. (48). Consequently, the source density of surface-emitted electrons is

$$n_{s\delta} = 2 \sqrt{\pi \beta_\delta} F_{g\delta} \quad (58)$$

For secondary electron emission,

$$F_{g\delta} = \delta F_e \quad (59)$$

where  $F_e$  is the net flux of plasma electrons (which is the same at any location with the presheath and sheath) striking the surface. Note that the return of secondary electrons to the surface within a space-charge saturated sheath is not considered to result in additional secondary electron emission. Only plasma electrons (which normally will have much larger energies) which strike the surface are considered to produce secondary electrons. For thermionic electron emission, the gross electron flux leaving the surface is given by the Richardson-Dushman equation,

$$F_{g\delta} = A T_{s\delta}^2 e^{-\Phi/T_{s\delta}} \quad (60)$$

where  $\Phi$  is the work function of the plasma-facing surface at temperature,  $T_{s\delta}$ , and  $A$  is a material-dependent constant. (Values for  $A$  are found, for example, in Ref. [5].) In order to use the same description for both secondary electron emission and thermionic electron emission, Eqs. (58) and (59) can be combined to give,

$$n_{s\delta} = 2 \sqrt{\pi \beta_\delta} \delta F_e \quad (61)$$

where, for thermionic electrons,

$$\delta = \frac{A T_{s\delta}^2 e^{-\Phi/T_{s\delta}}}{F_e} \quad (62)$$

should be used while for secondary electrons, Eqs. (56) and (57) are suitable.

#### IV. Evaluation of the Sheath and Presheath Potentials

A number of conditions are implemented in order to evaluate the sheath and presheath potentials. The first two conditions are that the total current density to the electrically-floating surface is zero (for a steady-state solution) and that the charge density at the presheath/sheath interface is zero. The third condition is that the spacial integral of the charge density in the presheath is zero. This requires the presheath to be globally quasineutral. It should be noted, however, that a manifestation of the presheath model used here is that the presheath is not locally quasineutral except at the presheath/sheath interface. The fourth condition, which applies only when space-charge saturation takes place within the sheath, is that the electric field at the electric potential minimum is zero.

The first condition, zero current density, requires  $Z F_i = F_e - F_\delta$ . With Eqs. (28), (33), (38), (43), (48), (53), and (61), this condition provides the relations,

$$\alpha = e^{-\psi_{spe}} (1 - \delta) \sqrt{\frac{\eta}{\tau_i}} \quad (63)$$

$$\alpha = e^{-\psi_{mpe}} (1 - \delta e^{-\psi_{ms\delta}}) \sqrt{\frac{\eta}{\tau_i}} \quad (64)$$

and

$$\alpha = e^{\psi_{spi} - \psi_{mpe}} (1 - \delta e^{-\psi_{ms\delta}}) \sqrt{\frac{\eta}{\tau_i}} \quad (65)$$

which correspond to the potential profiles shown in Figs. 2a, 2b, and 2c, respectively. Here,  $\alpha = Z n_{pi}/n_{pe}$  is a parameter called the neutralization factor,  $\eta = m_i/m_e$ , and  $\tau_i = T_{pi}/T_{pe}$ .

In order to implement the second and third conditions, the charge density,  $\rho = e(Z n_i - n_e - n_\delta)$ , between  $x_p$  and  $x_b$  is needed. The charge density can be written as a set of three relations in terms of  $\alpha$  corresponding to the three potential profiles using Eqs. (27), (28), (32), (33), (37), (42), (47), (52), and (61). Substituting for  $\alpha$  the right-hand sides from Eqs. (63-65) provides,

$$\frac{2\rho e^{\psi_{spe}}}{e n_{pe}} = (1 - \delta) \sqrt{\frac{\eta}{\tau_i}} G_1(\psi_{pxi}) - G_2(\psi_{sxe}) - \frac{\delta}{\sqrt{\tau_\delta}} G_1(\psi_{sx\delta}) \quad (66)$$

$$\frac{2\rho e^{\psi_{mpe}}}{e n_{pe}} = (1 - \delta e^{-\psi_{ms\delta}}) \sqrt{\frac{\eta}{\tau_i}} G_1(\psi_{pxi}) - G_2(\psi_{mxe}) - \frac{\delta}{\sqrt{\tau_\delta}} e^{-\psi_{ms\delta}} G_1(\psi_{mx\delta}) \quad (67)$$

$$\begin{aligned} \frac{2\rho e^{\psi_{mpe}}}{e n_{pe}} = & (1 - \delta e^{-\psi_{ms\delta}}) \sqrt{\frac{\eta}{\tau_i}} [2e^{\psi_{spi}} G_1(\psi_{pxi}) - G_1(\psi_{sxi})] \\ & - G_2(\psi_{mxe}) - \frac{\delta}{\sqrt{\tau_\delta}} e^{-\psi_{ms\delta}} G_1(\psi_{mx\delta}) \end{aligned} \quad (68)$$

where  $\tau_\delta = T_{s\delta}/T_{pe}$ . The second condition, zero charge density at the presheath/sheath interface, requires the right-hand-sides of the above relations to equal zero at  $x_b$ . This written as

$$(1 - \delta) \sqrt{\frac{\eta}{\tau_i}} G_1(\psi_{pbi}) = G_2(\psi_{sbe}) + \frac{\delta}{\sqrt{\tau_\delta}} G_1(\psi_{sb\delta}) \quad (69)$$

$$(1 - \delta e^{-\psi_{ms\delta}}) \sqrt{\frac{\eta}{\tau_i}} G_1(\psi_{pbi}) = G_2(\psi_{mbe}) + \frac{\delta}{\sqrt{\tau_\delta}} e^{-\psi_{ms\delta}} G_1(\psi_{mb\delta}) \quad (70)$$

and

$$(1 - \delta e^{-\psi_{ms\delta}}) \sqrt{\frac{\eta}{\tau_i}} [2 e^{\psi_{spi}} G_1(\psi_{pbi}) - G_1(\psi_{sbi})] = G_2(\psi_{mbe}) + \frac{\delta}{\sqrt{\tau_\delta}} e^{-\psi_{ms\delta}} G_1(\psi_{mb\delta}) \quad (71)$$

The third condition, that the spacial integral of the charge density in the presheath is zero, requires zero electric fields at  $x_p$  and  $x_b$ . With no electric fields at the edge-plasma/presheath interface and at the presheath/sheath interface, it can be shown (see, for example, Eq. (36) of Ref. [1]) that  $\int_{\phi_p}^{\phi_b} \rho d\phi = 0$  or, equivalently,  $\int_{\psi_{pe}}^{\psi_{be}} \rho d\psi_{xe} = 0$ . Consequently, with Eqs. (66-68), the third condition requires

$$(1 - \delta) \sqrt{\frac{\eta}{\tau_i}} \int_{\psi_{pe}}^{\psi_{be}} G_1(\psi_{pxi}) d\psi_{xe} = \int_{\psi_{pe}}^{\psi_{be}} G_2(\psi_{sxe}) d\psi_{xe} + \frac{\delta}{\sqrt{\tau_\delta}} \int_{\psi_{pe}}^{\psi_{be}} G_1(\psi_{sx\delta}) d\psi_{xe} \quad (72)$$

$$\begin{aligned} & (1 - \delta e^{-\psi_{ms\delta}}) \sqrt{\frac{\eta}{\tau_i}} \int_{\psi_{pe}}^{\psi_{be}} G_1(\psi_{pxi}) d\psi_{xe} \\ &= \int_{\psi_{pe}}^{\psi_{be}} G_2(\psi_{mxe}) d\psi_{xe} + \frac{\delta}{\sqrt{\tau_\delta}} e^{-\psi_{ms\delta}} \int_{\psi_{pe}}^{\psi_{be}} G_1(\psi_{mx\delta}) d\psi_{xe} \quad (73) \\ & (1 - \delta e^{-\psi_{ms\delta}}) \sqrt{\frac{\eta}{\tau_i}} \left[ 2 e^{\psi_{spi}} \int_{\psi_{pe}}^{\psi_{be}} G_1(\psi_{pxi}) d\psi_{xe} - \int_{\psi_{pe}}^{\psi_{be}} G_1(\psi_{sxi}) d\psi_{xe} \right] \\ &= \int_{\psi_{pe}}^{\psi_{be}} G_2(\psi_{mxe}) d\psi_{xe} + \frac{\delta}{\sqrt{\tau_\delta}} e^{-\psi_{ms\delta}} \int_{\psi_{pe}}^{\psi_{be}} G_1(\psi_{mx\delta}) d\psi_{xe} \quad (74) \end{aligned}$$

Since the electric field is zero at the presheath/sheath interface, the fourth condition, which requires the electric field at the electric potential minimum to be zero, is equivalent to requiring the spacial integral of the charge density between the presheath/sheath interface and the potential minimum to be zero. Hence, the fourth condition is similar to the third except that it applies only to the profiles shown in Figs. 2b and 2c and that it applies between  $x_b$  and  $x_m$ . Using Eqs. (67) and (68) for the charge density between  $x_b$  and  $x_m$ , the fourth condition requires,

$$(1 - \delta e^{-\psi_{ms\delta}}) \sqrt{\frac{\eta}{\tau_i}} \int_{\psi_{be}}^{\psi_{me}} G_1(\psi_{pxi}) d\psi_{xe}$$

$$= \int_{\psi_{be}}^{\psi_{me}} G_2(\psi_{mxe}) d\psi_{xe} + \frac{\delta}{\sqrt{\tau_\delta}} e^{-\psi_{ms\delta}} \int_{\psi_{be}}^{\psi_{me}} G_1(\psi_{mx\delta}) d\psi_{xe} \quad (75)$$

$$(1 - \delta e^{-\psi_{ms\delta}}) \sqrt{\frac{\eta}{\tau_i}} \left[ 2 e^{\psi_{spi}} \int_{\psi_{be}}^{\psi_{me}} G_1(\psi_{pxi}) d\psi_{xe} - \int_{\psi_{be}}^{\psi_{me}} G_1(\psi_{sxi}) d\psi_{xe} \right]$$

$$= \int_{\psi_{be}}^{\psi_{me}} G_2(\psi_{mxe}) d\psi_{xe} + \frac{\delta}{\sqrt{\tau_\delta}} e^{-\psi_{ms\delta}} \int_{\psi_{be}}^{\psi_{me}} G_1(\psi_{mx\delta}) d\psi_{xe} \quad (76)$$

The integrals in Eqs. (72-76) are given by the two indefinite integrals,

$$\int G_1(x) dx = G_1(x) + 2 \sqrt{\frac{x}{\pi}} \quad (77)$$

and

$$\int G_2(x) dx = G_2(x) - 2 \sqrt{\frac{x}{\pi}} \quad (78)$$

along with  $\psi_i = -Z \psi_e / \tau_i$  and  $\psi_\delta = \psi_e / \tau_\delta$ . The electric potential at one location must also be defined. Hereafter, the electric potential at the presheath/sheath interface shall be defined as zero,  $\psi_{be} = 0$ . With  $\psi_{be} = 0$ ,  $\psi_{se}$  gives the normalized sheath potential drop (as a positive value for a monotonically decreasing potential) and  $\psi_{pe}$  gives the normalized presheath potential drop (as a negative value). For a monotonically decreasing potential (Fig. 2a), Eqs. (69) and (72) are solved simultaneously for the two unknown parameters,  $\psi_{pe}$  and  $\psi_{se}$ . For a space-charge saturated sheath, the three unknown parameters,  $\psi_{pe}$ ,  $\psi_{me}$  and  $\psi_{se}$ , are solved simultaneously using Eqs. (70), (73), and (75) if the surface has a negative floating potential with respect to the edge plasma and Eqs. (71), (74), and (76) if the surface has a positive floating potential. In order to determine the transition from the potential profile in Fig. 2a to that in Fig. 2b (this transition occurs at the onset of space-charge saturation), Eqs. (70), (73), and (75) are solved simultaneously for  $\delta$ ,  $\psi_{pe}$  and  $\psi_{se}$  under the condition,  $\psi_{me} = \psi_{se}$ . In order to determine the transition from the potential profile in Fig. 2b to that in Fig. 2c, Eqs. (70), (73), and (75) are solved simultaneously for  $\delta$ ,  $\psi_{pe}$  and  $\psi_{me}$  under the condition,  $\psi_{se} = \psi_{pe}$ .

Once the values for the normalized potentials are known, the profile of the electric potential within the presheath and sheath is evaluated using Poisson's equation. The procedure is outlined in Ref. [1]. Eq. (39) of Ref. [1] is written here as

$$\frac{x}{\lambda_{D(p)}} = \int_{\psi_{pe}}^{\psi_{xe}} \left[ \int_{\psi'_{pe}}^{\psi'_{xe}} \frac{2\rho(\psi''_{xe})}{e n_{pe}} d\psi''_{xe} \right]^{-1/2} d\psi'_{xe} \quad (x_p < x < x_m) \quad (79)$$

where  $x_p = 0$ ,  $\lambda_{D(p)}$  is the Debye length in the edge plasma, and  $2\rho(\psi''_{xe})/(e n_{pe})$  is given by Eqs. (66-68). The inner integral of this relation is evaluated in closed form while the outer is evaluated numerically. The results are then inverted to obtain  $\psi_{xe}$  as a function of  $x$ . Fig. 2 shows actual self-consistent calculations of different electric potential profiles. (The vertical dimensions are different for each of the three profiles shown in Fig. 2. The horizontal dimensions are the same, however, and the width of the curve in Fig. 2a is  $27 \lambda_{D(p)}$ .) The profiles are calculated for a thermal ( $\tau_i = 1$ ) hydrogen ( $Z = 1, \eta = 1836$ ) plasma which is bounded by an electron-emitting surface (with  $\tau_\delta = 0.2$ ). The profiles are shown in order of increasing values for the electron emission coefficient:  $\delta = 0$  for Fig. 2a,  $\delta = 15$  for Fig. 2b, and  $\delta = 1000$  for Fig. 2c. The values for the normalized potentials calculated for each of the profiles are:  $\psi_{pe} = -0.34$  and  $\psi_{se} = 2.5$  for Fig. 2a;  $\psi_{pe} = -0.43$ ,  $\psi_{me} = 0.29$  and  $\psi_{se} = -0.28$  for Fig. 2b; and,  $\psi_{pe} = -0.53$ ,  $\psi_{me} = 0.31$  and  $\psi_{se} = -1.1$  for Fig. 2c. The onset of space-charge saturation occurs at  $\delta = 0.88$ ,  $\psi_{pe} = -0.43$ , and  $\psi_{me} = \psi_{se} = 0.29$  while the transition from a negative to a positive surface floating potential occurs at  $\delta = 31$ ,  $\psi_{pe} = \psi_{se} = -0.43$ , and  $\psi_{me} = 0.29$ .

## V. Boundary Conditions

The boundary conditions provided in this section are those which occur at the presheath/sheath interface. This location is both quasineutral and electric-field free. For brevity, location subscripts are not used in this section since quantities which were previously location dependent are now only considered at the presheath/sheath interface. The boundary conditions at the presheath/sheath interface are the pressure terms,  $\langle v_y^2 \rangle$ ,

$\langle v_z^2 \rangle$  and  $\langle v_x^2 \rangle - \langle v_x \rangle^2$ , the plasma flow velocity,  $\langle v_x \rangle$ , and the energy flow term,  $\langle v^2 v_x \rangle$ . Using relations from Section III, the boundary conditions are written in terms of the electron and ion plasma temperatures ( $T_e$  and  $T_i$ ) at the presheath/sheath interface, the temperature ( $T_\delta$ ) associated with electrons emitted at the plasma-facing surface, the ratio ( $\tau_i$ ) of ion to electron plasma temperatures at the edge plasma, the normalized presheath ( $\psi_{pe}$ ), sheath ( $\psi_{se}$ ), and minimum ( $\psi_{me}$ ) potentials, the electron and ion masses ( $m_e$  and  $m_i$ ) and the ion charge state ( $Z$ ). Using relations in Section IV, the normalized potentials are evaluated numerically and the values obtained are fit in terms of  $Z$ ,  $\tau_i$ , the electron emission coefficient ( $\delta$ ), which equals the ratio of surface-emitted electron flux to plasma electron flux incident on the surface, the ratio ( $\eta$ ) of ion to electron mass, and the ratio ( $\tau_\delta$ ) of the temperature associated with electrons emitted at the surface to the electron plasma temperature at the edge plasma. Of the three types of electric potential profiles shown in Fig. 2, the third is expected to be rare since, for  $\tau_\delta \leq 0.1$ , the electron emission coefficient must be very large,  $\delta > 10^3$ , to produce the type of potential profile shown in Fig. 2c (with  $\tau_i \sim 1$ ). For this reason, only boundary conditions for the electric potential profiles shown in Figs. 2a and 2b are presented. Also, all calculations of normalized potentials are carried out using the same  $\tau_\delta$  value,  $\tau_\delta = 0.01$ . This is appropriate since, for  $\tau_\delta \leq 0.1$ , the normalized potentials are essentially independent of  $\tau_\delta$ .

For use of the boundary conditions,  $\tau_i$  is the only non-local parameter needed. The value for  $\tau_i$  should be evaluated at one of two possible locations depending on which of the two has a shorter path length to the wall surface (the path length should be along a magnetic field line if a magnetic field is present). One location is an ion mean-free-path away from the wall surface while the other location is where the maximum temperature occurs along the magnetic field line. The first of these two locations applies when no magnetic field is present or when the source of presheath ions is predominantly either ionization or diffusion parallel to a magnetic field; the second method applies when

diffusion perpendicular to a magnetic field provides most of the presheath ions.

Two of the boundary conditions, the second and third pressure terms, can be written in terms of another boundary condition, the first pressure term. They are  $\langle v_z^2 \rangle = \langle v_y^2 \rangle$  and

$$\langle v_x^2 \rangle - \langle v_x \rangle^2 = \frac{3T}{m} - 2 \langle v_y^2 \rangle \quad (80)$$

The other boundary conditions are determined separately for plasma electrons, plasma ions, and surface-emitted electrons. (For surface-emitted electrons,  $\langle v_x \rangle_\delta$  and  $\langle v^2 v_x \rangle_\delta$  are defined as positive in the negative-x direction.) For the electric potential profile shown in Fig. 2a, the boundary conditions are

$$\langle v_y^2 \rangle_e = \frac{T_e}{m_e \chi_{se}} \quad (81)$$

$$\langle v_x \rangle_e = \frac{\sqrt{2 \langle v_y^2 \rangle_e / \pi}}{e^{\psi_{se}} \operatorname{erfc}(-\sqrt{\psi_{se}})} \quad (82)$$

$$\langle v^2 v_x \rangle_e = 2(2 + \psi_{se}) \langle v_y^2 \rangle_e \langle v_x \rangle_e \quad (83)$$

$$\langle v_y^2 \rangle_i = \frac{T_i}{m_i \chi_{pi}} \quad (84)$$

$$\langle v_x \rangle_i = \frac{\sqrt{2 \langle v_y^2 \rangle_i / \pi}}{e^{\psi_{pi}} \operatorname{erfc}(\sqrt{\psi_{pi}})} \quad (85)$$

$$\langle v^2 v_x \rangle_i = 2(2 + \psi_{pi}) \langle v_y^2 \rangle_i \langle v_x \rangle_i \quad (86)$$

$$\langle v_y^2 \rangle_\delta = \frac{T_\delta}{m_e} \quad (87)$$

$$\langle v_x \rangle_\delta = \frac{\sqrt{2 \langle v_y^2 \rangle_\delta / \pi}}{e^{\psi_{s\delta}} \operatorname{erfc}(\sqrt{\psi_{s\delta}})} \quad (88)$$

and

$$\langle v^2 v_x \rangle_\delta = 2(2 + \psi_{s\delta}) \langle v_y^2 \rangle_\delta \langle v_x \rangle_\delta \quad (89)$$

where the following definitions are used:

$$\chi_{se} = 1 - \frac{2 \sqrt{\psi_{se}/\pi}}{3 e^{\psi_{se}} \operatorname{erfc}(-\sqrt{\psi_{se}})} - \frac{2}{3 \pi [e^{\psi_{se}} \operatorname{erfc}(-\sqrt{\psi_{se}})]^2} \approx \ln(2.51 \psi_{se}^{0.042}) \quad (90)$$

$$\chi_{pi} = 1 + \frac{2 \sqrt{\psi_{pi}/\pi}}{3 e^{\psi_{pi}} \operatorname{erfc}(\sqrt{\psi_{pi}})} - \frac{2}{3 \pi [e^{\psi_{pi}} \operatorname{erfc}(\sqrt{\psi_{pi}})]^2} \approx \ln(2.05 \psi_{pi}^{-0.013}) \quad (91)$$

$\psi_{pi} = -Z \psi_{pe}/\tau_i$ , and  $\psi_{s\delta} = T_e \psi_{se}/(T_\delta \chi_{se})$ . The approximations for  $\chi_{se}$  and  $\chi_{pi}$  are accurate to within 2% for  $0.1 < \psi_{se} < 10$  and  $0.01 < \psi_{pi} < 100$ , respectively. For the normalized sheath and presheath potentials, the following two expressions are recommended:

$$\psi_{se} = \ln [0.2725 (1 - \delta) \sqrt{\eta} \tau_i^{-0.092} Z^{-0.44}] \quad (92)$$

$$\psi_{pe} = -\ln \left[ 1.43 \left( \frac{Z}{\tau_i} \right)^{0.195} \right] \quad (93)$$

These expressions are fits to numerically-determined values using the values: 1, 10, and 100 times the proton-to-electron mass ratio (1836) for  $\eta$ ; 1/3, 1, and 3 for  $\tau_i$ ; 1, 2, and 3 for  $Z$ ; and, 0 and 1/2 for  $\delta$ . The numerically-determined values were calculated using all possible combinations of  $\eta$ ,  $\tau_i$ ,  $Z$ , and  $\delta$  except combinations which simultaneously involved  $Z = 1$  and  $\eta = 1836$ . The expressions for  $\psi_{se}$  and  $\psi_{pe}$  agree to within 4% and 7%, respectively, with the numerically-determined values. Notice that the relation for the sheath potential has the usual,  $\ln[(1 - \delta) \sqrt{\eta}]$ , dependence given elsewhere.[6,7]

The onset of space-charge saturation and the corresponding transition from a monotonically decreasing potential (e.g. Fig. 2a) to a potential profile with a potential minimum (e.g. Fig. 2b) takes place if the electron emission coefficient reaches a sufficiently large value. A suitable expression which provides the value of the electron emission coefficient at the transition between profiles is

$$\delta_c = 1 - 7.7 \tau_i^{0.1} \sqrt{\frac{Z}{\eta}} \quad (94)$$

This expression is a fit to values determined numerically for the same combinations of  $\eta$ ,  $\tau_i$ , and  $Z$  which were used for the  $\psi_{se}$  and  $\psi_{pe}$  fits. The  $\delta_c$  fit is remarkably accurate being within 0.1% of the numerically-determined values.

If the electron emission coefficient, as determined using Eq. (56) for example, is larger than  $\delta_c$ , boundary conditions associated with the potential profile shown in Fig. 2b should be used. For the potential profile shown in Fig. 2b, the boundary conditions are the same as those for Fig. 2a except with subscript,  $s$ , replaced by subscript,  $m$ . For the normalized sheath minimum and presheath potentials under space-charge saturation conditions (Fig. 2b), the following two expressions are recommended:

$$\psi_{me} = \ln(1.63 \eta^{0.01}) \quad (95)$$

and

$$\psi_{pe} = -\ln \left[ 1.51 \left( \frac{Z}{\tau_i} \right)^{0.209} \right] \quad (96)$$

These two expressions agree to within 5% and 6%, respectively, with numerically-determined values using the combinations of  $\eta$ ,  $\tau_i$ , and  $Z$  used for the  $\delta_c$  fit along with  $\delta = \delta_c$  and  $\delta = 10$ . Note that these expressions are independent of  $\delta$  for  $\delta \geq \delta_c$ . Thus, a specific relation for the electron emission coefficient under conditions of space-charge saturation [e.g. Eq. (57)] is not needed for calculating the associated boundary conditions. It should also be mentioned that trapping of slow charge-exchange ions within the potential well surrounding the potential minimum has been found to be responsible for reducing space-charge saturation.[2] When that is the case, it is probable that the sheath potential profile is adequately described by using an effective electron emission coefficient which is smaller than the actual one. If so, then for situations in which  $\delta > \delta_c$ , the boundary conditions presented here are unaffected by ion trapping since the sheath minimum and presheath potentials are not dependent on  $\delta$ . Nevertheless, a more detailed study of the effects of ion trapping on space-charge saturation appears warranted.

## VI. Concluding Summary

A fully-kinetic self-consistent theory describing the plasma sheath under conditions of space-charge saturation has been presented. The phase-space distribution functions for each species of particles have been evaluated and velocity moments have been taken in order to obtain particle densities, fluxes, temperatures, and energy fluxes. The electric potential profile has been determined self-consistently for three different types of profiles. These are a monotonically-decreasing potential, a single-minimum potential associated with a negative surface floating potential, and a single-minimum potential associated with a positive surface floating potential. The electron emission requirements for production of the third potential profile were found to be severe. For this reason, boundary conditions have been provided only for the first two of the three potential profiles. Boundary conditions on velocity moments have been supplied for three separate species: plasma electrons, plasma ions, and surface-emitted electrons. These boundary conditions can be combined as needed for use in multi-fluid and single-fluid (MHD) applications. The boundary conditions are in terms of sheath and presheath potential drops and simple expressions have been provided for these potential drops. Once the potential drop expressions are inserted into the boundary conditions, the boundary conditions are in terms of the three species' temperatures,  $\tau_i$ , the ion-to-electron plasma temperature ratio,  $Z$ , the ion charge state,  $\eta$ , the ion-to-electron mass ratio, and  $\delta$ , the electron emission coefficient.

In order to determine the value of  $\delta$  at which the transition between the first two potential profiles occurs, the following expression was developed:  $\delta_c = 1 - 7.7 \tau_i^{0.1} \sqrt{Z/\eta}$ . This expression gives the value of the electron emission coefficient at the onset of space-charge saturation. For  $\delta < \delta_c$ , the following expressions are recommended for the sheath and presheath potentials normalized to the electron-plasma temperature:  $\ln[0.2725 (1 - \delta) \sqrt{\eta} \tau_i^{-0.092} Z^{-0.44}]$  and  $\ln[1.43 (Z/\tau_i)^{0.195}]$ . For  $\delta \geq \delta_c$ , recommended expressions for the normalized sheath minimum and presheath potentials are, respectively,  $\ln(1.63 \eta^{0.01})$  and  $\ln[1.51 (Z/\tau_i)^{0.209}]$ . The conditions these expressions for  $\delta_c$  and the normalized

---

potential are expected to be suitable for are: a temperature associated with the emitted electrons which is less than one tenth that associated with the plasma electrons;  $1/3 \leq \tau_i \leq 3$ ;  $1 \leq Z \leq 3$ ; and  $1836 \leq \eta \leq 100 \times 1836$ .

## References

- [1]C. A. Ordonez, Phys. Fluids B, **4** 778 (1992).
- [2]T. Intrator, M. H. Cho, E. Y. Wang, N. Hershkowitz, D. Diebold, and J. DeKock, J. Appl. Phys. **64**, 2927 (1988).
- [3]C. A. Ordonez and R. E. Peterkin, Jr., J. Appl. Phys., **79** 2270 (1996).
- [4]E. W. Thomas in *Data Compendium for Plasma-Surface Interactions*, (Nuclear Fusion, Special Issue, 1984) p. 94.
- [5]K. Ertl and R. Behrisch in *Physics of Plasma-Wall Interactions in Controlled Fusion*, ed. D. E. Post and R. Behrisch (Plenum, New York, 1986) p. 515.
- [6]P. C. Stangeby in *Physics of Plasma-Wall Interactions in Controlled Fusion*, ed. D. E. Post and R. Behrisch (Plenum, New York, 1986) p. 41.
- [7]R. N. Franklin and W. E. Han, Plasma Phys. and Cont. Fus., **30** 771 (1988).

## Figure Captions

Fig. 1. The particle potential energy profiles considered in Section II. A planar source of particles is located at  $x_o$  which emits particles in the positive- $x$  direction. For the potential energy curve shown in (a),  $U(x_m) < U(x_n) < U(x_o)$  and all particles originating at  $x_o$  travel past  $x_n$ . For the potential energy curve shown in (b),  $U(x_o) < U(x_m)$ ,  $U(x_n) < U(x_m)$ , and a fraction of the particles originating at  $x_o$  reach a turning point between  $x_o$  and  $x_m$  and pass back through  $x_o$ . For this potential energy profile,  $U(x_n) < U(x_o)$  is also possible. For the potential energy curve shown in (c),  $U(x_m) < U(x_o) < U(x_n)$ ,  $U(x_o) = U(x_r)$ , and a fraction of the particles originating at  $x_o$  reach a turning point between  $x_r$  and  $x_n$  and pass back through  $x_o$ .

Fig. 2. Illustrations of possible electric potential profiles (solid curves) in the presheath and sheath for (a) no space-charge saturation, (b) space-charge saturation and a surface floating potential which is negative with respect to the edge plasma (at  $x \leq x_p$ ), and (c) space-charge saturation and a positive surface floating potential. Although not apparent as a result of the limited resolution of the plots, the electric field is zero at  $x_p$  and  $x_b$ . The dotted lines are provided to guide the eye.

Figure 1

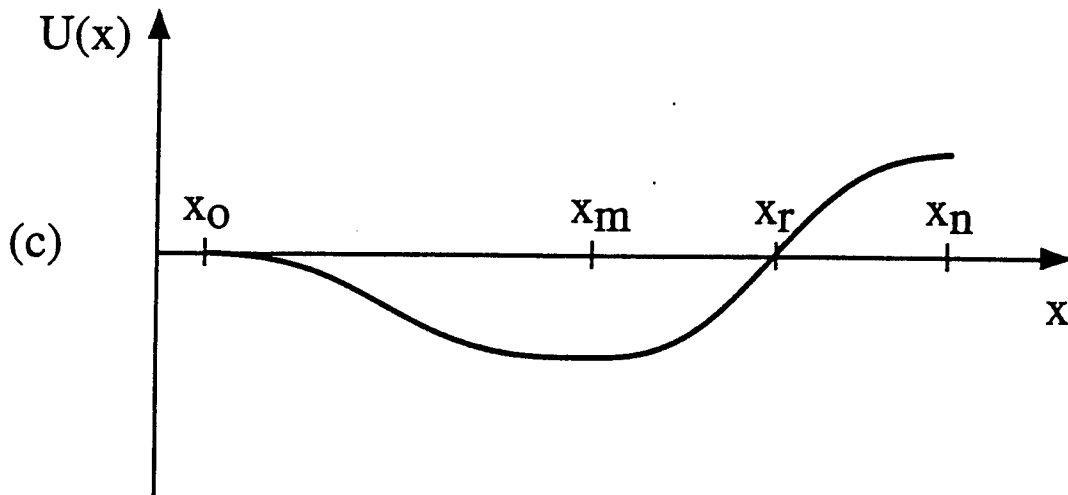
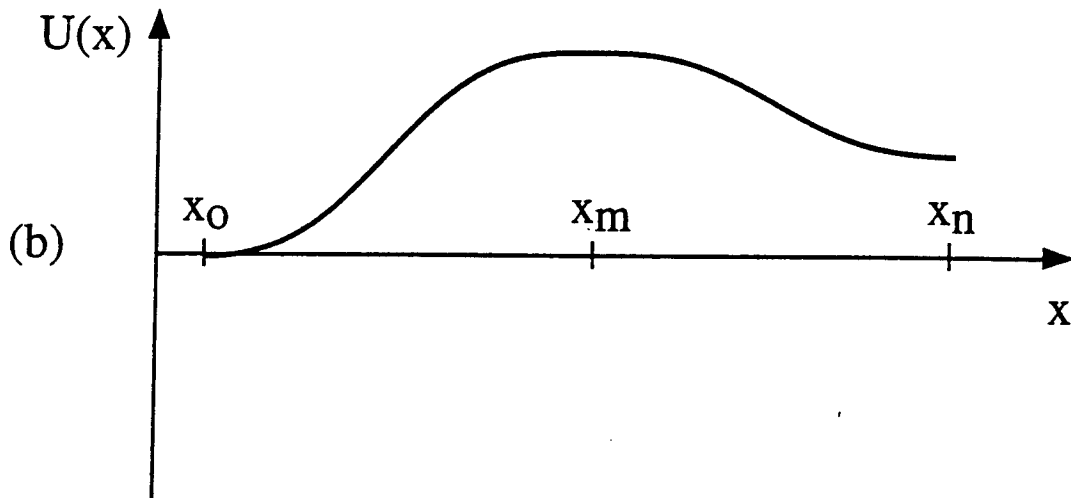
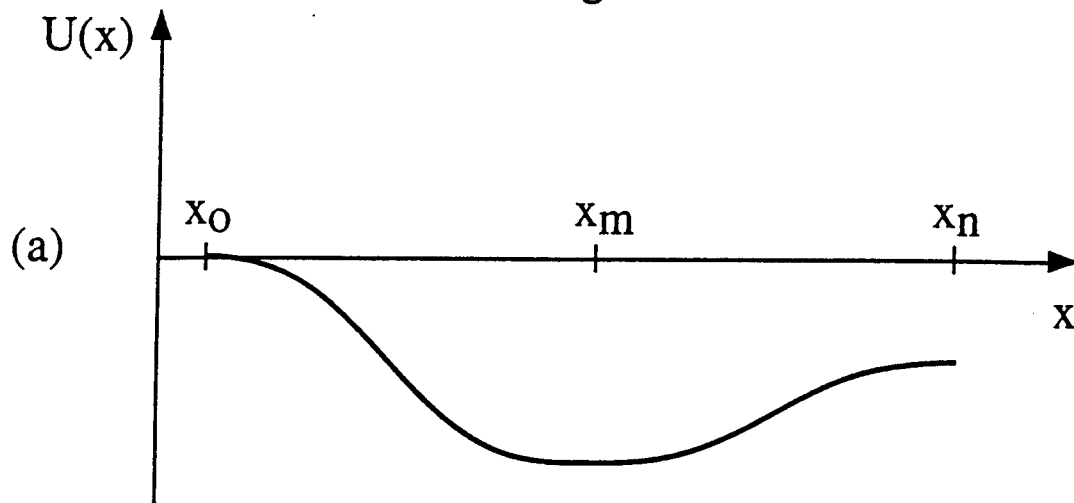
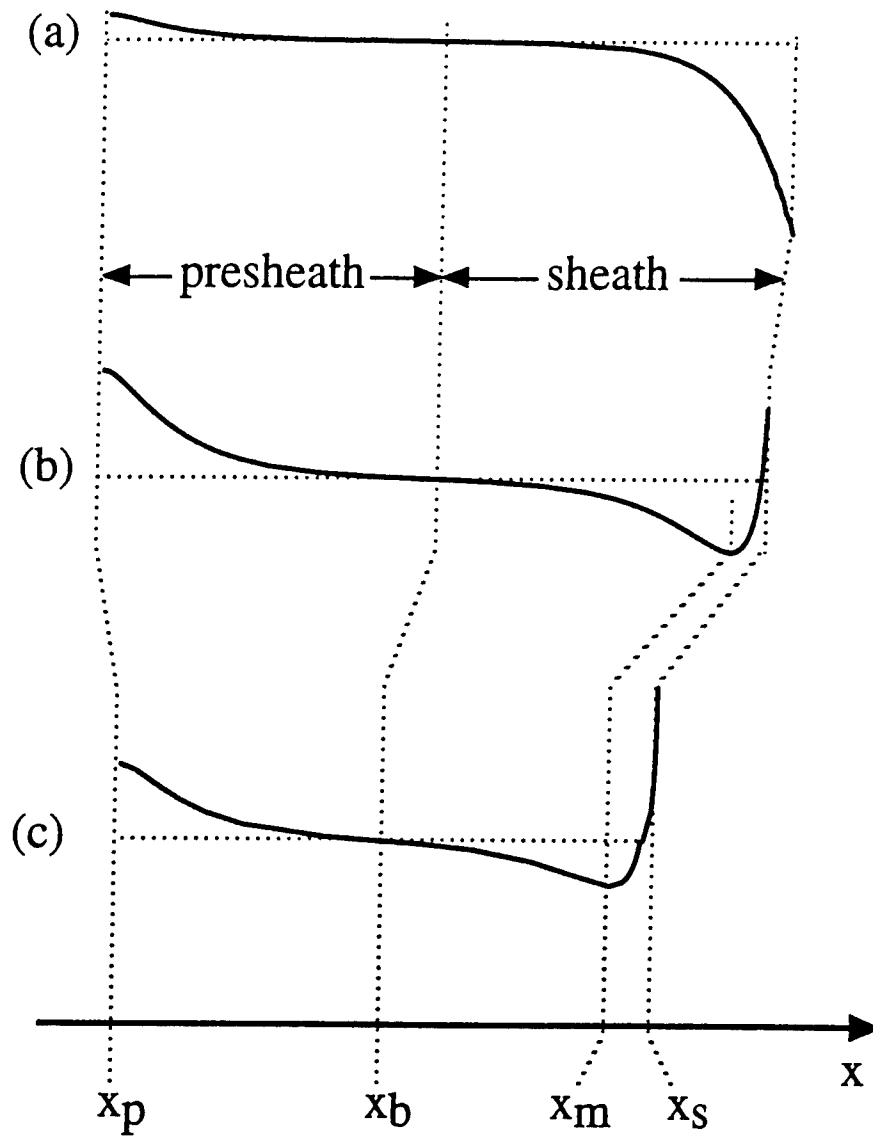


Figure 2



Analysis of the Structure and Motion of Equatorial Depletion Bands  
Using Optical All-sky Images

R. Pickett  
Professor  
Department of Psychology  
and  
G. S. Sales and A. Gee

University of Massachusetts Lowell  
Lowell, MA

Final Report for:  
Summer Research Extension Program  
Phillips Laboratory

Sponsored by:  
Air Force Office of Scientific Research  
Bolling Air Force Base, DC

and  
Phillips Laboratory

June 1997

Analysis of the Structure and Motion of Equatorial Depletion Bands  
Using Optical All-sky Images

R. Pickett  
Professor  
Department of Psychology  
and  
G. S. Sales and A. Gee

Abstract

This project has been concerned with finding an improved approach to analyzing the volumetric structure of equatorial depletion bands. These north-south oriented bands of depleted optical emission (630.0 nm) appear in the F-region of the ionosphere in the night sky in the vicinity of the magnetic equator. They arise behind the sunset terminator and slowly travel eastward. At any specific site, two or three of these depletions can be observed at intervals during the evening. The critical interest motivating the present work is that these regions of depleted emission in the ionosphere can severely disrupt line-of-sight radio signals that pass through them from navigation and communications satellites.

## 1. Introduction

This project has been concerned with finding an improved approach to analyzing the volumetric structure of equatorial depletion bands. These north-south oriented bands of depleted optical emission (630.0 nm) appear in the F-region of the ionosphere in the night sky in the vicinity of the magnetic equator. They arise behind the sunset terminator and slowly travel eastward. At any specific site, two or three of these depletions can be observed at intervals during the evening. The critical interest motivating the present work is that these regions of depleted emission in the ionosphere can severely disrupt line-of-sight radio signals that pass through them from navigation and communications satellites. To better understand, predict and contend with these disruptions, it is important to learn as much as possible about the volumetric structure of these regions. Information on the volumetric structure has been obtained to date, primarily from analyses of ground-based radar soundings. Volumetric information has also been derived from analyses of differences in the character of line-of-sight radio signals between those that “look” through the depletion and those that do not. The use of multiple satellites in different positions, potentially reveals different aspects of the depletions volumetric structure. However, the problem with both of these current approaches is that they provide only crude and sparse data.

The present project explores the possibility of deriving more fine-grained information from analyses of ground-based optical images. Considerable amounts of optical data are available, much of it simultaneous with the radar sounding and signal disturbance observations. To date, however, analyses of the optical data have been aimed at mining only two dimensional information on the depletions, i.e., with respect to aspects such as depletion width, lateral position and motion. But, the light intensity recorded at each pixel in these images can be considered the integral of the emission along the line of sight from the pixel position in the image plane through the imager optics and out through the F-layer. Using an appropriate model of the electron density of the F-region and computing the implied line-of-sight emission intensity, one should be able to infer aspects of the volumetric shape of these depletions that account for the distribution of intensity at the image plane. Required is a model to generate the idealized

intensity distribution that would occur at the image plane for particular settings of *altitudinal and volumetric parameters of idealized depletion regions*. Smoothed versions of the empirical image data can then be compared to the idealized images, and parameters of the model can then be adjusted to maximize the fit of the ideal image to the empirical image. The required parameter settings of the model can then serve as measures of the volumetric structure of the real depletion. Such was the logic of the present project, and we pursued it in three main steps.

1. First, develop a model for generating line-of-sight emission and attendant intensities in the image plane as a function altitude and volumetric parameters.

2. Second, *obtain smoothed cross-sections of the sequence of images of three actual depletion bands* and conduct various analyses of the position, shape and motion of these cross-sections as a function of time.

3. Third, use the model to generate synthetic images, taking cross-sections of model generated images corresponding to those we obtained on actual images and determined what settings of the model parameters was required to maximize goodness-of-fit between the actual and the synthetic profiles.

In Section 2 below we present the relevant technical background:

- a. *On the general characteristics of equatorial depletion bands*
- b. On the physics and chemistry of the F-region and on the mechanisms that form the depletion bands;
- c. On the imaging system - its optical and electronic features that must be considered when translating pixel intensities at each point in the image to actual emissions.

In Section 3, we report on development of the model. In Section 4, we report on the empirical and model-based analyses that we conducted on the three selected depletions. In Section 5 we present a summary of the results and our overall conclusions and recommendations.

## 2. Technical Background

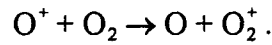
### 2.1. General Characteristics of Equatorial Depletion Bands

At the magnetic equator and beginning after sunset, a series of relatively narrow, north-south oriented bands of electron density depletion in the F-region of the ionosphere appear at the western horizon and drift slowly eastward. At a particular site two or three are born at intervals during the evening hours. These depletions, typically 100 to 200 km wide are directly associated with bubbles of low density, low altitude plasma that form and rise at the magnetic equator. The origin of the bubbles in the vicinity of the magnetic equator is described in detail by Kelly (*The Earth's Ionosphere*) in terms of the growth of *Rayleigh-Taylor instabilities in the lower F-region, i.e. around 250 km*. The more dense ionization is forced out of the bubble volume as it rises into the plasma region above 250 km. The bubbles rise to about 750 km at the equator and spread north and south by more than 1000 km, aligned with and following the earth's down-heading magnetic field lines. Agua Verde, Chile, the observing site for the depletions used in this project, is some 1200 km south of the magnetic equator, and the bubbles have curved down along the field lines at this point to about 300 km altitude. The resulting elongated regions of depleted emission are seen as dark bands when viewed from the ground against the background of normal 630.0 nm airglow of about 40 to 50 Rayleighs at these latitudes.

### 2.2. Physics and Chemistry of the F-Region

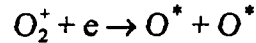
Optical emissions are generated in the high atmosphere by a variety of chemical processes. One of the most useful emission lines arises from excited atomic oxygen at a wavelength of 630.0 nm (red line). This emission tracks the density of electrons in the interval from 250 to 300 km in the F-region of the ionosphere. During the daytime when solar UV is available to ionize atomic species at altitudes in the F-region, equal numbers of electrons and positively charged atomic oxygen ions are produced. After sunset, with no significant ionization sources present, two chemical processes act sequentially to remove the electrons and the  $O^+$  ions, resulting in a decay of the lower F-region and the emission of photons, specifically at 630.0 nm.

The first of these processes involves charge exchange between the  $O^+$  ions and the neutral molecular oxygen to form neutral atomic oxygen and an  $O_2^+$  ion. The chemical expression for this reaction is:



It proceeds at a laboratory measured rate  $k_1 = 2 \times 10^{-11} \text{ cm}^6 \text{ s}^{-1}$ . The number of  $\text{O}^+$  ions lost in a unit volume per second is  $k_1 \cdot n[\text{O}^+] \cdot n[\text{O}_2]$ . A typical value for this rate of disappearance of  $\text{O}^+$  ions in the F-region at 300 km is around  $200 \text{ s}^{-1}$ .

The second process is the dissociative recombination reaction described by the expression:



where  $\text{O}^*$  is one of several possible forms of excited atomic oxygen. The rate constant for this reaction is  $k_2 = 2.2 \times 10^{-7} (300/\text{Te})^{0.8} \text{ cm}^6 \text{ s}^{-1}$ . At 300 km, with an electron temperature  $\text{Te} = 900 \text{ K}$ , this rate is about  $9.13 \times 10^{-8} \text{ cm}^6 \text{ s}^{-1}$ , considerably faster than the charge exchange reaction.

This means that as soon as the charge exchange reaction occurs, it is immediately followed by a recombination reaction effectively removing the electron and positive ion and, at the same time, leaving behind two excited neutral atomic oxygen atoms which ultimately radiate photons, with a high probability, at the 630.0nm red line. Actually these excited atomic oxygen atoms are in a forbidden state with a relatively long half life of 110 s, which is important in terms of the quenching process discussed below.

Reasonable standard models for the neutral  $\text{O}_2$  and  $\text{N}_2$  density and neutral temperature profiles used in our modeling effort are given in Figures 1 and 2.

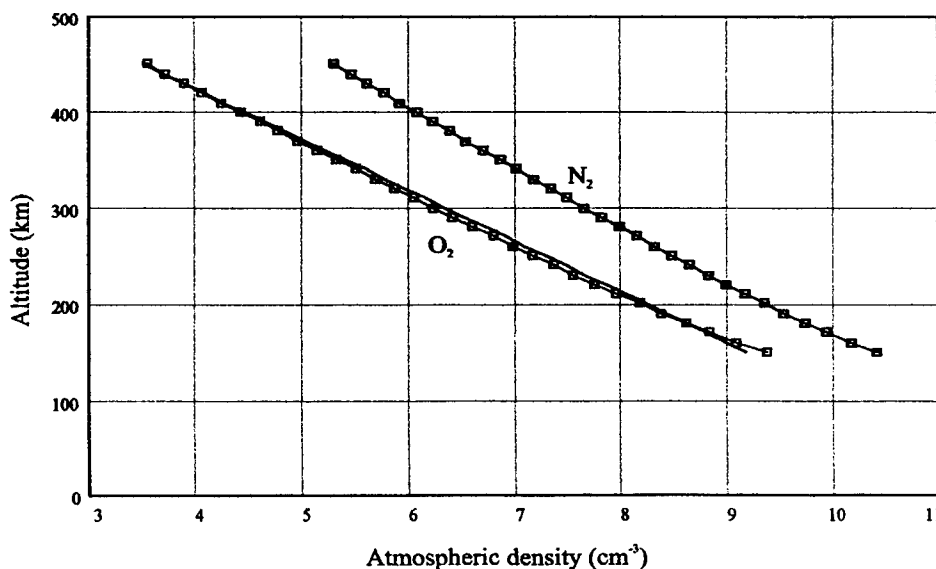


Figure 1. Model of the density of the neutral constituents (molecular oxygen and nitrogen) the atmosphere vs. altitude.

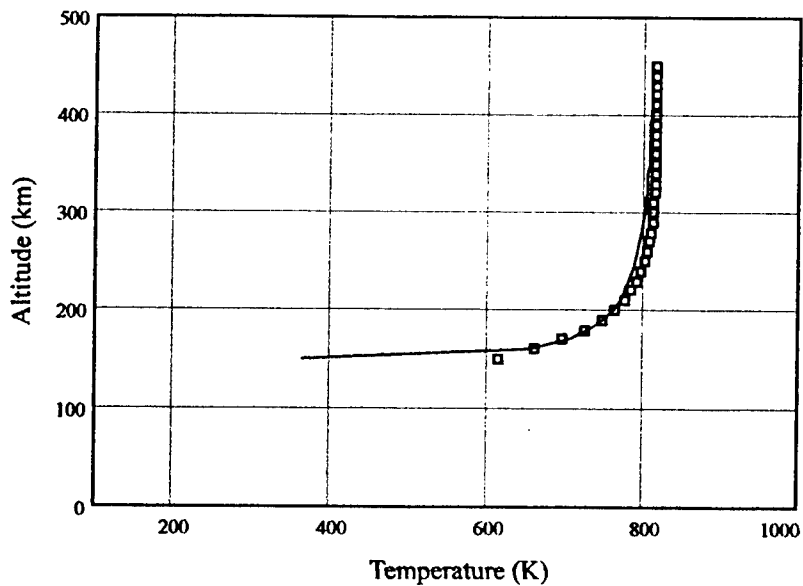


Figure 2. Model of the neutral atmospheric temperature vs. altitude.

The vertical electron density profile for the background ionosphere (as opposed to inside the depletion bands) is illustrated in Figure 3.

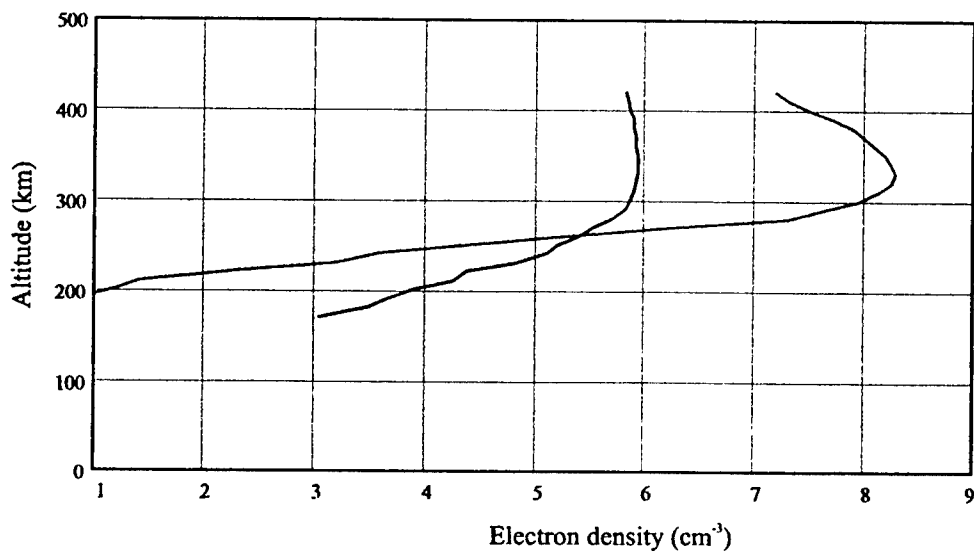


Figure 3. Assumed background ionospheric electron density vs. altitude for Agua Verde, Chile on Oct. 1, 1994 at 01 UT.

Another important factor in calculating the background airglow emission is the so called "quenching" process which deactivates the excited atomic oxygen atoms by collisions with other constituents of the atmosphere before the excited atom is able to

radiate. The approach presented by Sheehan (private communication) is used here; considering only collisions between the excited atomic oxygen atoms and  $O_2$ ,  $N_2$  and electrons. The resulting expression for the volumetric emission rate for 630.0 nm photons, taking into account both the chemical excitation processes and the collisions which prevent the radiative emission is:

$$\epsilon = \frac{0.86 k_2 n(O_2) n_e}{1 + \frac{k_3 n(N_2) + k_4 n(O_2) + k_5 n_e}{6.81 \times 10^3}} \quad (1)$$

where  $k_3$ ,  $k_4$  and  $k_5$  are the collisional deactivation rates for  $N_2$ ,  $O_2$  and electrons, respectively. Actually in the region below 300 km, where quenching is important, collisions with the neutral  $N_2$  dominate. Figure 4 shows the calculated volumetric emission rate for the 630.0 nm airglow using the above atmospheric models.

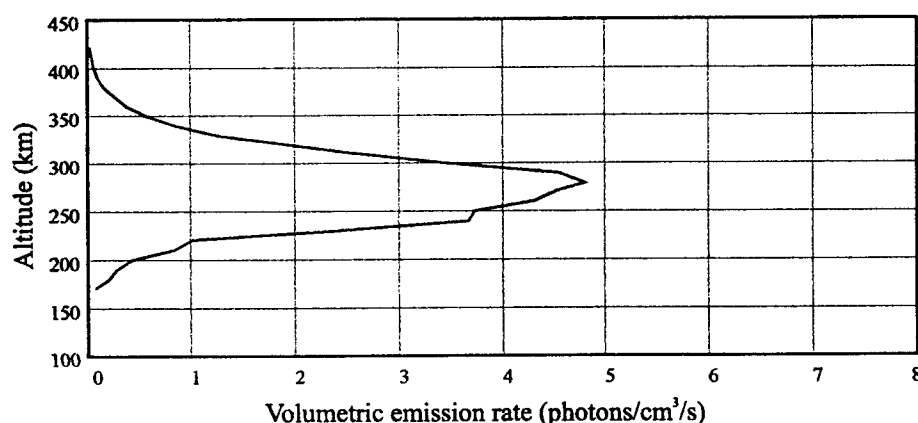


Figure 4. Calculated background volumetric emission rate at 630.0 nm.

Under these conditions the peak emission originates in the vicinity of 285 km falling off by a factor of five in  $\pm 50$  km.

The volumetric emission fall-off below the peak results from the rapid quenching of the excited oxygen atoms by collision with the dominant neutral constituents of the atmosphere before the  $O^*$  can radiate. The decreased emission above 300 km results from the rapidly decreasing density of molecular oxygen, resulting in less charge exchange, resulting in less excited atomic oxygen and, therefore, less emission.

The integrated vertical emission of 630.0 nm is about 42.2 R at Agua Verde, which corresponds well with other observations of mid-latitude airglow.

The all-sky imager, in viewing a full 180° about the local zenith, integrates the volumetric emission along each “look” angle, and the resultant intensity is located at a unique position on the “film” plane, as discussed in detail in Section 2.3.

### 2.3. Ground-Based Optical Imaging System

The HAARP all-sky scanning photometer system records images in a 256 x 256 pixel format, with 12 bits of stored information per pixel, and scans up to four wavelengths every minute. As discussed above, these optical images result from “airglow” emissions that occur principally between 250 km and 300 km in altitude.

The imager uses a lens system that has the capability to “photograph” the entire sky from horizon-to-horizon. The emissions involved here are relatively weak and require several levels of amplification to achieve a recordable image. A CCD detector is used with the 256 x 256 pixels followed by an intensifier with a variable gain control. This system has been calibrated by the developers of the HAARP imager system, KEO Associates. To convert the measured counts to a photon emission rate measured in Rayleighs (one Rayleigh corresponds to a photon flux of  $10^6/\text{cm}^2/\text{s}$ ), the calibration curves, which depend on gain setting and exposure time, were taken from documentation supplied KEO Associates (private communication), who built the system.

For the analysis of the depletion images, it is important to establish the geometrical relationships between the recorded optical image and the location and motions of the emitting sources in the ionosphere. This analysis was carried out assuming the emitting sources in the F-region are at an altitude of 300 km. Of the 256 x 256 pixels on the CCD image plane, pixel #128 represents looking overhead and pixels #1 and #256 represent the horizon. The relationship is expressed as:

$$\psi = \arcsin\left(\frac{p - 128}{128}\right) \quad (3)$$

where  $\psi$  is the look angle from the site to the source measured from the vertical, and  $p$  is the pixel number. The geometry is illustrated in Figure 5.

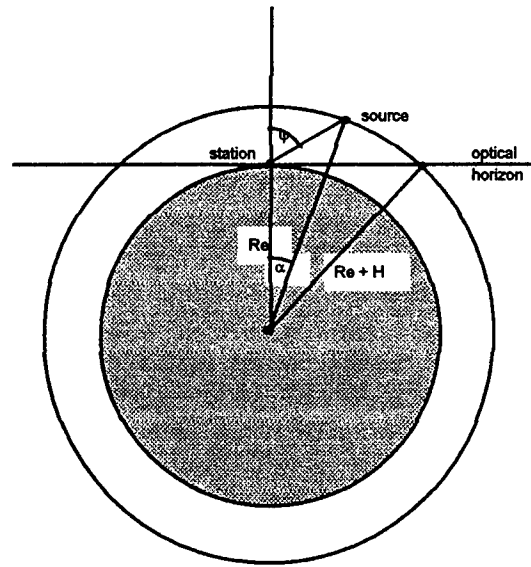


Figure 5. Simplified all-sky image geometry assuming the emitting layer is at altitude  $H$ . To relate the pixel position  $p$  to the distance of the emitting source from the site a second expression for the look angle,  $\psi$ , and the earth central angle,  $\alpha$ , is derived as:

$$\psi = \arctan \left( \frac{\sin \alpha}{\cos \alpha - \gamma} \right) \quad (4)$$

where  $\gamma = R_e/R_e + h$ , where  $h=300$  km in this situation.

Eliminating the look angle,  $\psi$ , between these two equations yields an expression relating the earth central angle,  $\alpha$ , to the pixel number. Finally, the distance of the emitting source from the site is  $D = \alpha R_e$ . A plot of  $D$  vs.  $p$  is shown in Figure 6.

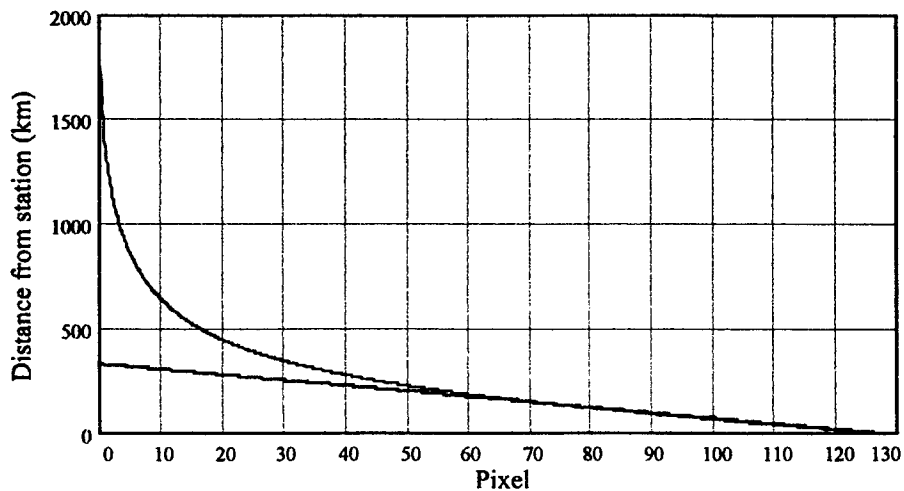


Figure 6. Relationship of the ground distance of an emitting source to pixel position. The straight line fit illustrates the linearity of the image from overhead (pixel 128) out almost half way across the image (pixel 60).

As an example, an object on the horizon at an altitude of 300 km lies some 1700 km from the site. The relationship between distance and pixel number is quite linear from pixel #128 (the overhead position) out to  $\pm 68$  pixels.

Finally, it is important to know the velocity with which a source moves over the image, assuming a constant angular velocity of the actual source measured at the center of the earth. This can be applied to either depletions, which typically move from west to east, or to stars in the background, which move from east to west as the earth rotates. Here the expression for the apparent velocity is:

$$v_a(\alpha) = v \frac{60 \times D}{1000 \times (R_e + H)} \frac{1}{\sqrt{\left(\frac{\sin(\alpha)}{\cos(\alpha) - \gamma}\right)^2 + 1}} s(\alpha) \quad (6)$$

where,  $s(\alpha) = \frac{d}{d\alpha} \psi(\alpha)$  .

For a typical depletion band at an altitude of 300 km moving at a speed of 80 m/s the apparent velocity across the image is shown in Figure 7.

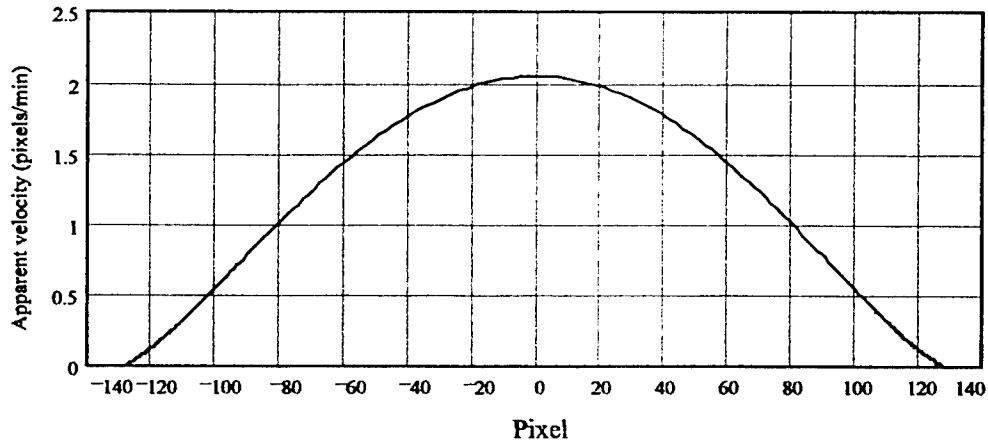


Figure 7. The apparent source velocity (pixels/min) vs. pixel position for a source at 300 km moving with a constant velocity of 80 m/s in the west to east direction.

At the center of the image, the depletion moves at the maximum speed of about 2 pixels/minute. The apparent speed is less as the source moves closer to the edges of the image, i.e., nearer to the horizon.

### 3. Model of Electron Density Depletions

We designed this model to represent the electron density distribution within the depletion region in terms of the altitude  $z$  in kilometers, and longitude  $L$  in degrees, measured from the longitude of the center of the depletion  $L_o$ . It is represented as:

$$n_e(z,L) = n_{\infty} C(L) \exp \left[ - \left[ \frac{z - z_m(L)}{D(L)} \right]^2 \right]$$

where  $z_m(L)$  is the peak altitude as a function of longitude within the depletion,

$z_o$  is the peak height in the background F-layer,

$D(L)$  is the height scale within the depletion,

$D_o$ , the height scale in the background ionosphere outside the depletion,

$D_c$  is the height scale at the center of the depletion,

$C(L)$  is the electron density scale factor.

The expressions for these parameters are:

$$z_m(L) = (z_{\max} - z_o) \exp \left[ - \left( \left| \frac{L - L_o}{2F} \right| \right)^{2p} \right] + z_o$$

$$D(L) = (D_c - D_o) \exp \left[ - \left( \left| \frac{L - L_o}{2F} \right| \right)^{2p} \right] + D_o$$

$$C(L) = (df - 1) \exp \left[ - \left( \left| \frac{L - L_o}{2F} \right| \right)^{2p} \right] + 1$$

where  $F$  is the depletion width, measured in degrees longitude, and  $p$  is the steepness factor affecting the transition of the three structural parameters from depletion to the background ionosphere.

Figure 8 shows a longitudinal cut through the band which is assumed uniform in the north/south direction, i.e., it is assumed that the depletion is aligned with the magnetic field.

In Figure 8,  $L_0=289$  degrees,  $z_0=440$  km,  $D=30$  km,  $F=0.45$  km and  $p=6$ .

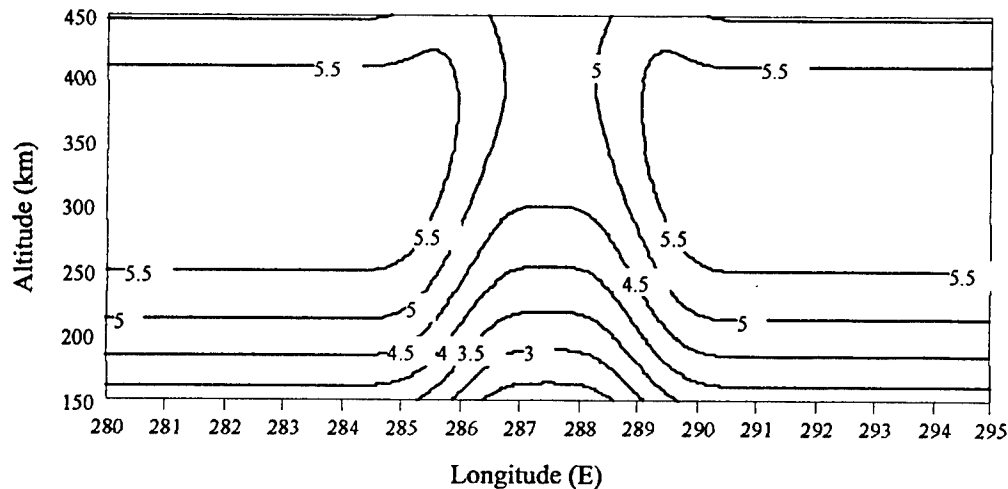


Figure 8. Two dimensional electron density distribution along an east-west line combining the background ionosphere described earlier with a model of the depletion region. The contour are log (electron density).

In this particular model, the peak electron density of  $1.6 \times 10^6 \text{ cm}^{-3}$  is at an altitude of 340 km in the background ionosphere, while within the depletion, the peak is at 400 km with a density of  $2.0 \times 10^5 \text{ cm}^{-3}$ . Although the parameters of the background ionosphere are measured by the vertical soundings, the electron density profile within the depletion can only be modeled consistent with the observations of the optical imager and other ancillary information. Direct measurement by the sounder within the depletion is not possible, as will be discussed later.

Using these electron density profiles and the model for the neutral atmosphere, the volumetric emission rate of 630.0 nm can be calculated using Equation (1). Then the integrated emission can be calculated for each ray path from the all-sky imager through the emitting volume.

## 4. Analyses of Observed Depletion Bands

### 4.1. Observed Depletion Bands

The depletions we analyzed were recorded during the field campaign conducted in late September and early October, 1994 as part of the MISETA program by Phillips Laboratory using the HAARP all-sky imager. The observing site at Agua Verde (25.5 S, 70.1W) lies almost on the same magnetic field line as the Jicamarca Ionospheric Observatory on the magnetic equator in Peru. This allows the incoherent scatter radar observations at Jicamarca recorded at the same time to be directly linked with our observations.

Only the nights of October 1 and October 3, 1994 showed depletion activity. The image recording started shortly after sunset (at approximately 00 UT) when the sky became sufficiently dark to detect the background airglow and continued until the airglow intensity became undetectable, around local midnight, when the background F-region ionization had sufficiently decayed. Figure 9 shows the all-sky image for October 1 at xxxx UT using the 630.0 nm filter. The dark band is the depleted region viewed against the background airglow emission.

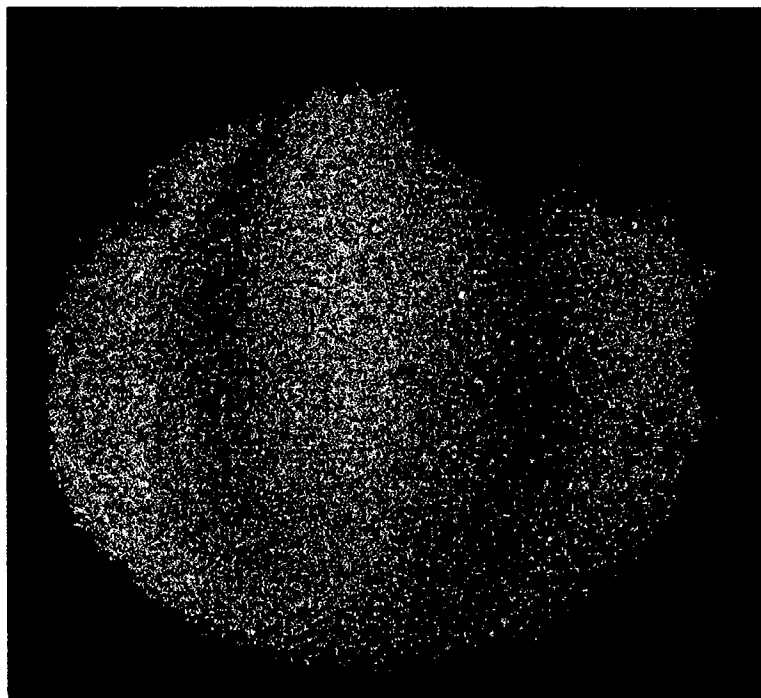


Figure 9. All-sky image at 630.0 nm made at Agua Verde, Chile on Oct. 1, 1994 at 0130 UT. Visible are two dark depletion bands extending north-south across the image.

#### 4.2. Analysis of the Shape and Motion of the Depletions Bands

One of the most obvious characteristics of the equatorial depletions is their west to east motion. After sunset when these depletions begin to form as bubbles rising over the magnetic equator, they begin to drift eastward as a result of a vertical electric field in the F-region. This  $\mathbf{ExB}$  motion drives them across the all-sky image at velocities of the order of 100 m/s.

The depletions were tracked for approximately 100 minutes on Oct. 1, 1994 and for only about 35 minutes on Oct. 3, 1994. Depletions only appeared on these two nights. This relatively short duration was caused by the general weakening of the background emission. As discussed earlier, this makes the depletions almost invisible as the background emission becomes as dark as the depletion.

Using the recorded one minute sequence of optical images at a wavelength of 630.0 nm, we processed a cut through the north-south center of each image, averaging across the 256 pixels using seven rows #125 through #131 to generate an smoothed east-west cut through the image. A typical cut is shown in Figure 10 where we see two low emission depletion bands, one in the western sky and a second one near overhead.

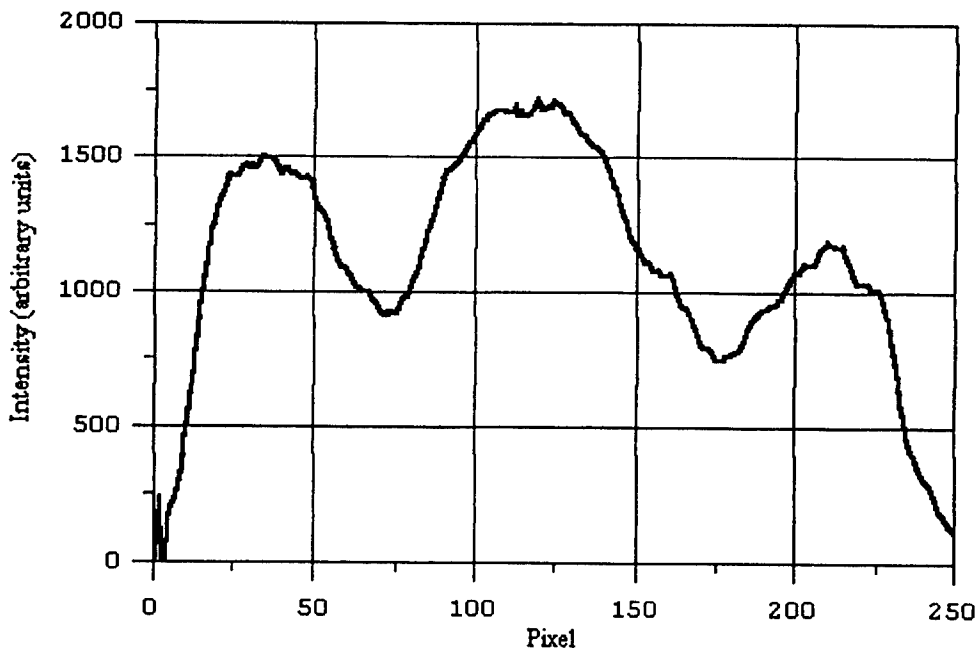


Figure 10. All-sky image intensity across the center in the east-west direction for Oct. 1, 1994 at 0130 UT (see Figure 9).

The amplitudes are the integrated emission intensity measured in Rayleighs. For the data collected during the MISETA campaign, the gain of the intensifier was held at 2

and the exposure time was a constant 4 seconds. This results in a conversion factor of 40 recorded counts = 1 Rayleigh. With these images, which are one minute apart, the depletions can be tracked by generating a contour plot of emission intensity as a function of pixel number and time. The horizontal cuts are stacked vertically as a function of time and the resulting composite plots for Oct. 1, 1994 are shown in Figure 11. We see, as a function of time, the motion of the depletions from west to east. When the coordinates of the depletion are in pixel numbers, there is a distortion caused by the all-sky lens, making the depletions appear narrower when they are far from the center of the image. This effect was illustrated earlier in Figure 7 where the horizontal distances and velocity are compressed near the edges of the image. The entire time sequence is shown including those times when the depletions are near the edges of the image. The "S" shaped dark low intensity bands show the motion of the depletions as they move across the all-sky image. In these plots it is also possible to see the motion of individual bright stars and the milky way as these features progress from east to west as the earth rotates.

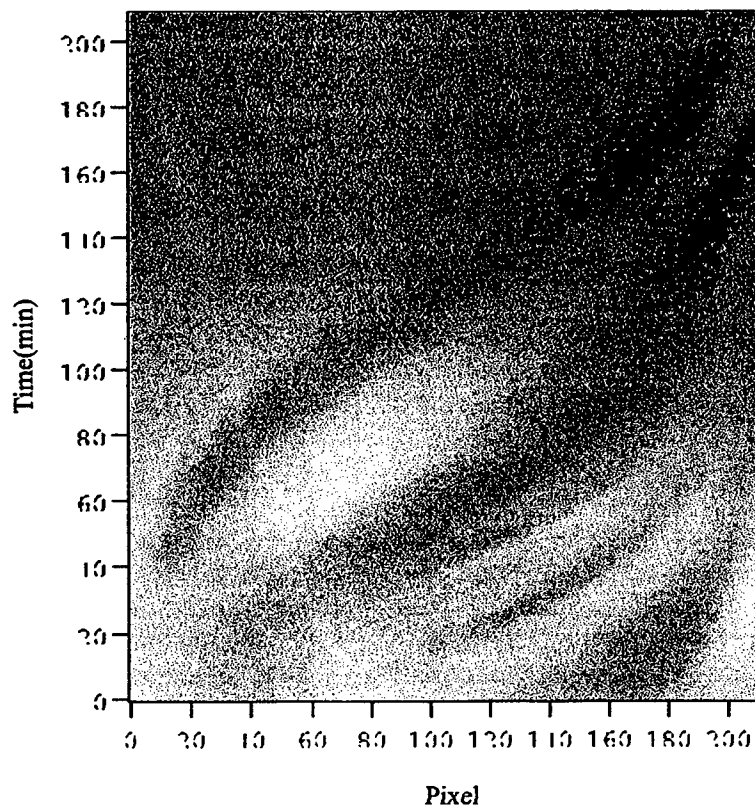


Figure 11. Composite of crosscuts from the Agua Verde, 630.0 nm images for Oct. 1, 1994 showing the motion of depletions as they move from west to east. The origin for the time axis is at 00UT.

As part of this analysis, the intensity cuts across the center of the image were again smoothed to remove the noisy characteristics of the amplified optical signal by fitting these data points with a cubic spline interpolation. We then used the location of its minimum to determine the centers of the depletion bands, and we determined the widths of these depletions by using the separation of the inflection points on both sides of the minimum. The difference, in pixels, between the two inflections was then converted to the width of the depletion in kilometers using Equations 3 and 4.

Fitting these cross-cut data with the cubic spline technique and searching for the local minima resulted in the curves, shown in Figure 12. Each curve represents the position of the minimum associated with each depletion of the four depletions as they move across the field of view as a function of time. The time origin for each curve is 00 UT. When the depletions are within the linear region of the optical image, the slope of the curve is related to the mean drift velocity of that depletion.

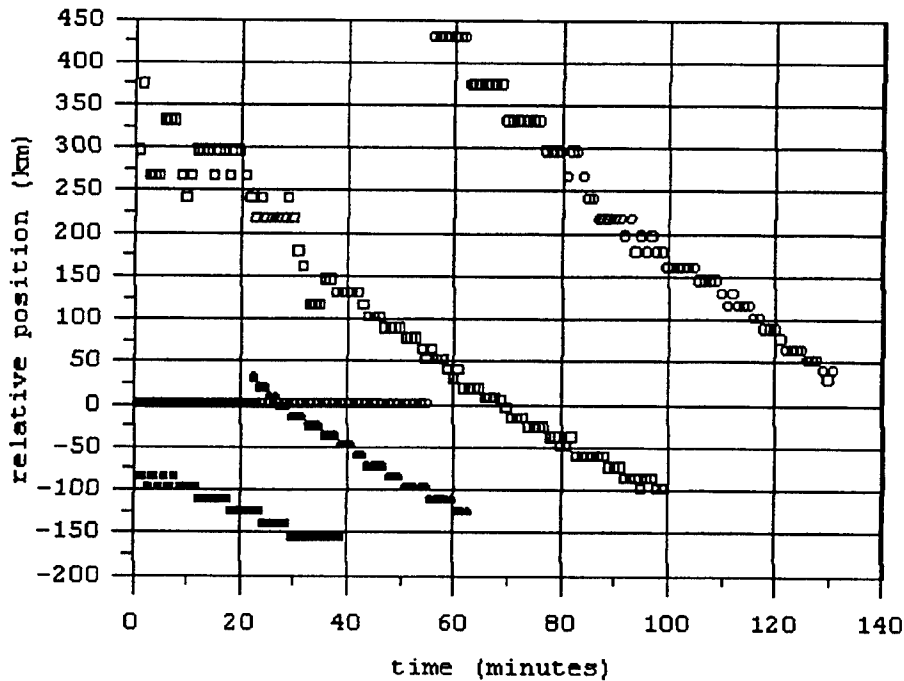


Figure 12. Motion of the depletion centers as a function of time.

For the two main depletions observed on October 1, the velocity was 67 m/s averaged over their observed lifetime. Only relatively small noise-like fluctuations are

observed in the velocity of these two depletions. The width of these depletions was, on the average, 120 km.

The geometrical velocity variation discussed in the previous section of this report is not apparent on these plots, since the scaled data were restricted to the more central, linear portion of the image, purposefully excluding those times when the 180 degree lens distortion significantly slows the apparent motion of the depletion, as was seen in Figure 7.

#### **4.3. Model-based Analysis**

Using our model based approach we produced synthetic image cross-sections that fit as closely as possible the cross-sections obtained the actual depletions at 00xx and 00yy UT . Figure 13a shows the results when a depletion is almost overhead with the synthetic cross-section adjusted and shifted to align with it.

The underlying physical situation for the model adjusted to fit the empirical depletions are shown in Sections *b* and *c* of Figure 13. In Section *b* we show the two dimensional structure of the electron density required to achieve the fit to the empirical data, both the background and within the depletion and Section *c* shows the derived volumetric emission profile.

These two physical descriptions constitute the end product sought in this project. They provide, using an inverse analysis technique, new continuous information on the volumetric structure of the depletions available in optical all-sky images. We conducted a quantitative analysis using this model-based approach to produce synthetic image cross-sections that fit as closely as possible the cross-sections obtained from the actual depletions.

Figure 13.

We have overlaid the actual cross-sections onto the calculated emission intensity across the center of the image. The model was shifted to align the minimum of the measurements with the minimum of the simulated emissions. The important quantitative comparisons are:

1. The background intensity level.

2. The minimum intensity within the depletion.
3. *The slope of the transition between the two regions.*

The background airglow level was first matched by modifying the measured ambient electron density profile within reasonable bounds. When this was completed, attention was turned to the structure of the electron density depletion, and the adjustable parameters discussed in Section 3 are varied, again in a reasonable manner to match the slopes of the emission profile, and most importantly, the emission level within the depletion. The program resides within IBM Data Explorer and provides a set of “knobs” and a real-time interactive capability to accomplish this fitting process.

To ensure that the measured intensity at the darkest part of the depletion is an actual emission level above the system-minimum-detectable intensity, several images were scanned to determine the distribution of measured intensities. The important result is that the HAARP imaging system seems capable of measuring down to approximately 10 R or less and the residual emission within the depletion is real reaching 15 to 20 R.

## **5. Conclusions**

We have developed new analysis tools that can be used to describe the structure and motion of equatorial depletion bands. We are able to process and analyze relatively large amounts of optical all-sky photometer imagery, particularly in this case, equatorial depletion bands. This processing technique involves smoothing (using spatial averaging only) and curve fitting, making it possible to use simple mathematical methods to determine the speed and structure sizes of the depletion bands.

We also developed a simulation technique that makes it possible to infer some of the characteristics of the 3-D structure of the depletion bands based on the 2-D optical images. The basic parametric electron density model we developed on the Silicon Graphic work station provides for real-time control of the parameters and for visual feedback effects on the image emission intensity profile, either as a full 2-D all-sky image, or as a cross-cut through the image that can be compared with the smoothed empirical image data.

It appears that the depletions observed on the two nights during the MISETA campaign in Chile, away from the magnetic equator, are relatively shallow. Emission

within the depletion is only a factor of 2 down from the ambient airglow. This may result from the relatively long time since these depletions formed and to fill-in by diffusion. But, other observations have shown that the electron density within these regions is highly irregular at these times and clearly causes scattering and scintillation on radio signals passing through these bands (Sales et al., 1996).

At this point, the number of depletions recorded and analyzed is very small, making it difficult to draw reliable conclusions concerning the structure of the equatorial depletion bands, but some insight has already been gained. Although it appears that the internal shape of the depletion band is remarkably stable as the bands drift after they are formed, we have observed some changes on October 3, a change in the character of the spread-F that initially was associated with irregularities within the depletion band, ultimately evolved into general lower F-region spread-F, as the band "grew old".

Several areas for future research have become obvious. Besides collecting and processing additional data to build up the data base, we ought to consider adding an optical site closer to the magnetic equator, possibly 600 km south, to catch the earlier development of these bands before they reach a stable configuration. It is during these early stages that the irregularities, observed by radio wave scattering, are formed. The observations at an intermediate site may shed light on the mechanisms for the formation and maintenance of these internal irregularities within the depletion. An important question is whether analysis of the structural changes within the depletion band, as observed by the optical system, such the steepening of the walls affects the formation of these small and medium scale irregularities?

The general approach we have developed in this program for getting more information out of the optical data should help in answering these questions.

**Dimos Poulikakos**  
**Report not available at time of publication.**

**GIGAHERTZ MODULATION AND ULTRAFAST GAIN BUILD UP IN  
IODINE LASERS**

**Jeff Nicholson**

Graduate Student

**Wolfgang Rudolph**

Associate Professor

Department of Physics and Astronomy

The University of New Mexico

Albuquerque, NM 87131

Report for:

Faculty Summer Research Extension Program

Phillips Laboratory

Sponsored by:

Air Force Office of Scientific Research

and

Phillips Laboratory, Albuquerque

December 1996

---

# GIGAHERTZ MODULATION AND ULTRAFAST GAIN BUILD UP IN IODINE LASERS

**Jeff Nicholson**

Graduate Student

**Wolfgang Rudolph**

Associate Professor

Department of Physics and Astronomy

The University of New Mexico

Albuquerque, NM 87131

## Abstract

A photolytic iodine laser is shown to have a 13.59 GHz modulation in the laser radiation when simultaneous lasing of two hyperfine transitions is obtained. The necessary gain tuning required to achieve dual line lasing is accomplished through the use of a magnetic field. In addition, we investigate the possibility of using a nonlinear mirror to increase the gain coupling between the two transitions.

# GIGAHERTZ MODULATION AND ULTRAFAST GAIN BUILD UP IN IODINE LASERS

Jeff Nicholson and Wolfgang Rudolph

## 1 Introduction

Gas lasers have received attention because of their ability to operate at very high cw power levels with good beam quality, and also because they possess an active media that is not as susceptible to damage as solid state materials. One example of high power gas lasers, the Chemical Oxygen Iodine Laser (COIL), has been shown to operate at power levels as high as 40 kW [1].

Modulation of these high power lasers at gigahertz frequencies is desirable. Not only does one obtain higher peak intensities in a modulated laser beam, but one can think of a gigahertz modulated laser beam as a radar wave with an optical carrier. Thus, one can envision producing a radar signal that propagates with the qualities of a coherent optical wave. Modulating a laser at gigahertz frequencies with active elements is difficult because of the high bandwidth requirements. In addition, the high intracavity powers of, for example, COIL, impose extreme damage threshold requirements on intracavity elements.

An alternative is to force the laser to operate on two different hyperfine transitions of atomic iodine simultaneously. If the radiation in the two transitions is temporally coherent, the intensity of the laser will be modulated at a frequency equal to the frequency separation of the two transitions.

Furthermore, previous experiments and computer simulations have shown that energy extraction in high power iodine amplifiers can be improved by amplifying a pulse whose spectrum consisted of two separate frequencies coincident with the two strongest transitions of atomic iodine and suggested that the output of such an amplifier would indeed be modulated at gigahertz frequencies [2, 3].

An atomic iodine laser operates on the  $^2P_{1/2} - ^2P_{3/2}$  magnetic dipole transition of atomic iodine, with a wavelength of  $1.315 \mu\text{m}$  (see Fig. 1). The strongest of its six hyperfine transitions, and the one that typically lases is the  $F' = 3$  to  $F'' = 4$ . The gain of the second strongest transition, the  $F' = 2$  to  $F'' = 2$ , is more than twice as small as that of the 3-4. The two transitions are separated by 13.59 GHz.

Applying a magnetic field to atomic iodine causes Zeeman splitting of the energy levels,

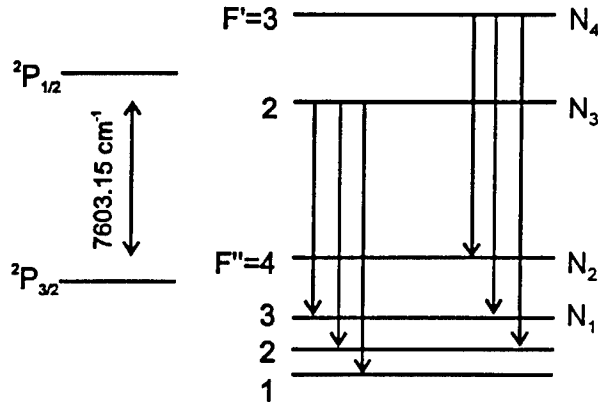


Figure 1: Energy levels and allowed transitions of atomic iodine. The numbers on the right side of the diagram are the designations used in the computer simulations.

removing their degeneracies. For small magnetic fields ( $< \text{Kilogauss}$ ) the frequencies of the hyperfine transitions are not shifted significantly [4]. For this reason, the transitions are still referred to as the 3-4 and 2-2 transitions, even under the influence of a magnetic field. The gain of the two transitions can be equalized without the need of intracavity elements by applying a magnetic field of approximately 350 Gauss perpendicular to the polarization of the laser [5]. With a smaller magnetic field, the 3-4 transition dominates, with a stronger field, the 2-2.

## 2 Experimental Results and Discussion

In this paper, we show the modulation in the laser radiation that results from the simultaneous lasing of the 2-2 and 3-4 transition in an iodine laser. The experiments were performed with a photolytic iodine laser, a convenient tool for performing small scale experiments which can later be scaled up to the high power COIL. A sketch of the experimental apparatus is shown in Fig. 2. The laser consisted of a cell of  $\text{CF}_3\text{I}$  at 8 Torr pumped by a KrF excimer laser producing 250 mJ in 20 ns pulses at 248 nm. As a result of the absorption at 248 nm,  $\text{CF}_3\text{I}$  dissociates into  $\text{CF}_3$  and iodine, with. 92% of the iodine produced in the excited state ( $\text{I}^*$ ) [6].

An aperture in the cavity forced oscillation on a single transverse mode. At 8 torr iodine is primarily Doppler broadened with a Doppler width of approximately 250 MHz [7] and the free spectral range of the cavity was 150 MHz, therefore, the laser operated on either one or two longitudinal modes. A typical gain switched pulse is shown in the inset of Fig. 2. The

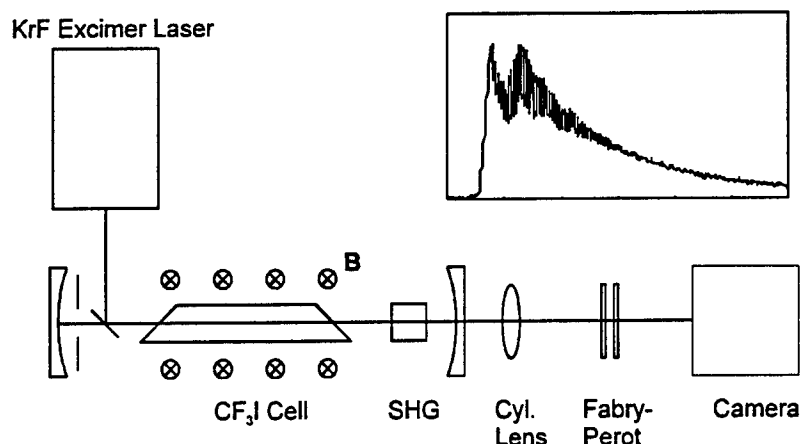


Figure 2: The experimental setup. Inset: a typical gain-switched iodine laser pulse showing longitudinal mode beating.

fast beating shown, with a period of approximately 6 ns, is longitudinal mode beating.

A set of ferrite ceramic permanent magnets was used to apply a magnetic field to the gain cell perpendicular to the polarization of the laser. The strength of the magnetic field was tuned by varying the distance between the magnets and the gain cell. This produced a magnetic field of up to a Kilogauss that varied less than 10% over the mode volume of the iodine laser.

The single shot spectrum of the iodine pulse was measured with a Fabry-Perot interferometer. The free-spectral-range of the interferometer was 39 GHz, and the resolution was approximately 2 GHz at  $1.315 \mu\text{m}$ . Therefore, while the interferometer was capable of distinguishing the hyperfine transitions, it was not able to resolve individual longitudinal modes. A cylindrical lens was used to focus into the Fabry-Perot and produce line fringes.

The temporal profile of the iodine laser pulses was recorded with a streak camera with a resolution of 5 ps. When used in conjunction with the Fabry-Perot interferometer, the streak camera was able to time-resolve the spectral content of the laser pulse. This provided details about the temporal overlap of the laser radiation due to the two different hyperfine transitions.

Because the cameras were not sensitive in the infrared, a  $\text{LiIO}_3$  crystal was used to frequency double the laser radiation to 657.5 nm. Both intracavity and extra-cavity doubling was investigated. Extra-cavity doubling had the advantage of ease of alignment. Placement of the crystal in the cavity, however, becomes important when considering the effect of the nonlinear crystal in conjunction with the laser resonator outcoupler to create a nonlinear

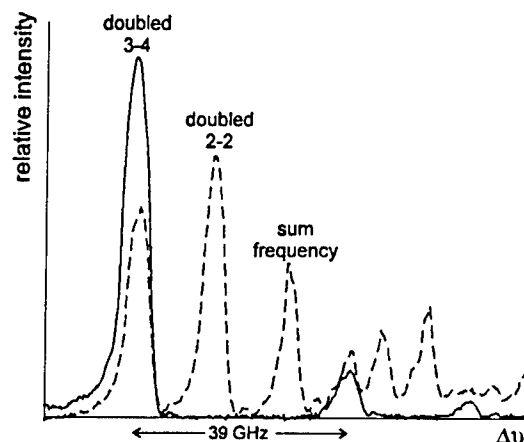


Figure 3: Fabry-Perot fringes without magnetic field (solid line) and with a 400 G magnetic field (dashed line) applied to the active medium.

mirror as explained below.

Fig. 3 shows the Fabry-Perot fringes obtained from the interferometer. The solid curve shows the fringes due to the 3-4 line when there was no magnetic field on the gain cell. The dotted curve shows the fringes obtained when a magnetic field of approximately 400 Gauss was applied to the gain cell, perpendicular to the laser oscillation. Two-line lasing is clearly visible. Because of the second harmonic generation, the doubled 2-2 line appears 27 GHz below the doubled 3-4 line. The sum frequency occurs halfway between the doubled 3-4 and 2-2 lines.

The temporal dependence of the two laser lines for two typical pulses is shown in Fig. 4. The solid curves show the 3-4 line and the dashed curves the 2-2.

The two curves represent typical pulses observed. Because of the single shot nature of the laser, and because no attempt was made to stabilize the excimer pump or the iodine laser in any way, a certain amount of variation in the laser pulses from shot to shot was observed. Both lines tended to operate with either one or two longitudinal modes an equal amount of time and independent of the magnetic field strength. In addition, when the magnetic field was such that both hyperfine transitions lased, there was a variation in the temporal overlap of the two transitions from shot to shot. Typical shot to shot fluctuations in the iodine laser pulse energy were less than 10%.

Although the 2-2 and the 3-4 transitions do not share any energy levels (see Fig. 1), there are fast relaxations among the upper and lower hyperfine levels that tend to equalize the populations. Population in the upper hyperfine levels is equalized through collisions

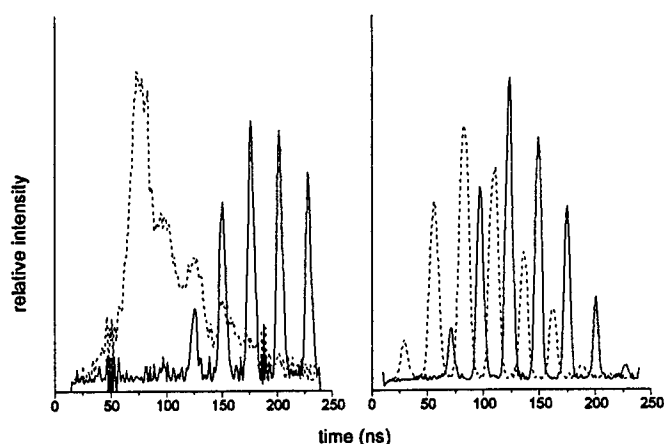


Figure 4: Temporal dependence of the 3-4 (solid line) and the 2-2 (dashed line) transitions as measured by the streak camera for two different laser pulses.

with ground state iodine and can take place with a time constant on the order of tens of nanoseconds; relaxation among the lower hyperfine levels proceeds more directly through collisions with any species in the gain cell, and has a time constant of a few nanoseconds [8]. If the gain of the two transitions is not exactly equal, the stronger will build up first, and collisional relaxations will remove the population from the weaker, effectively decreasing the gain of the weaker transition even further. Any small change in the magnetic field away from the crossing point in the gain of the transitions leads to one of the transitions dominating over the other [9]. This meant that simultaneous lasing of both transitions was only seen in a narrow range of magnetic field strength. Strong lasing of both transitions was observed from approximately 360 to 390 Gauss (corresponding to moving the permanent magnet 0.5 cm). However, within this region, there was always a certain amount of temporal overlap because the relaxations among hyperfine levels forced the gain of the two transitions to be approximately equal in order to observe lasing of both transitions. Fig. 4a depicts the approximate minimum amount of temporal overlap observed. Fig. 4b shows a more typical case. Although the 2-2 transition is the first to build up in both pulses of Fig. 4, this could be changed by tuning the magnetic field strength, and pulses where the 3-4 transition dominated were also observed by simply adjusting the position of the permanent magnet.

In Fig. 4a, the 3-4 transition shows beating from multiple longitudinal modes, whereas the 2-2 transition has only a single longitudinal mode. In contrast, both the 3-4 and the 2-2 transitions show longitudinal mode beating in Fig. 4b. Fig. 4 illustrates an inherent problem in producing the desired 13.6 GHz modulation. In order to have a maximum depth

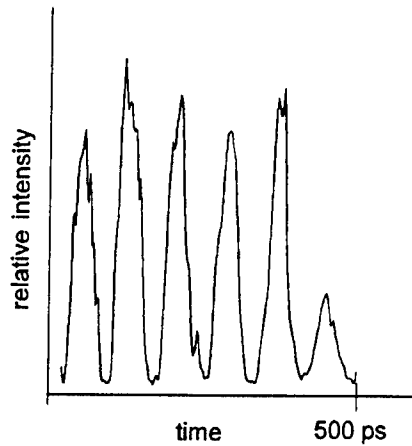


Figure 5: Gigahertz mode beating of the laser output.

of modulation over the entire length of the laser pulse, the two frequencies must overlap temporally and be of equal intensity. In Fig. 4a, the temporal overlap of the 3-4 and 2-2 is only partial. In the case of Fig. 4b, even though the envelopes of the two transitions overlap, longitudinal mode beats in each of the transitions do not. Therefore, this pulse would not show a substantial spectral component at 13.6 GHz.

When the magnetic field was adjusted for optimum temporal overlap of the 3-4 and 2-2 transitions, and the pulse is viewed with a fast streak camera with a resolution of 5 ps, a clear 13.6 GHz modulation is observed, as is shown in Fig. 5. This data was taken with the second harmonic generation performed extra-cavity.

Another possibility to record the GHz modebeating is the mixing of the optical signal with a local oscillator. To this aim we detected the second harmonic of the iodine laser with a 20 ps photodiode. Since the diode is a quadratic detector the current exhibits the 13.6 GHz modulation. This current was mixed with a local oscillator tunable around 13.6 GHz so that the resulting difference frequency could be detected directly by a 400 MHz oscilloscope. Figure locoscill shows an oscilloscope trace. The laser operated at two longitudinal modes on each hyperfine transition which explains the modulation of the beat amplitude.

### 3 Potentials of a nonlinear mirror for mode coupling

The 13.6 GHz modulation is observed without any extra coupling between the 3-4 and 2-2 transitions. However, because of the above mentioned shot to shot variation in the overlap of the two transitions and to ease the requirements of tuning the magnetic field, an additional

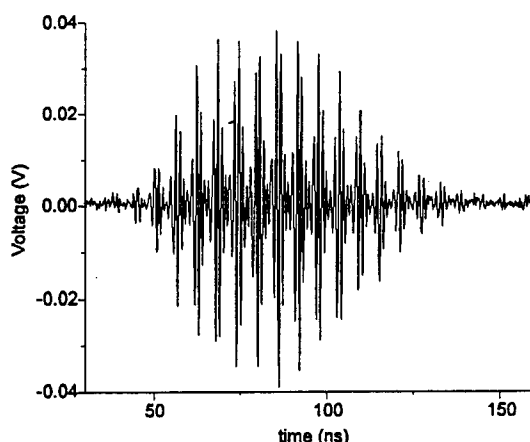


Figure 6: Signal after mixing the output of a 20 ps photodiode illuminated by the second harmonic of the iodine laser with a local oscillator tuned to 14 GHz.

coupling between the transitions is desirable. The possibility of using a nonlinear mirror to equalize the gain of the two transitions was investigated. A schematic of the mirror is shown in the inset of Fig. 7. Such a mirror was first used to mode-lock a Nd:YAG laser [10]. The nonlinear mirror consists of a second harmonic crystal, and a dichroic mirror as the outcoupler for the resonator. Typical reflectivities for the outcoupler are 90% for the fundamental frequency and 100% for the second harmonics. The distance between the mirror and the second harmonic crystal is such that the difference in the index of refraction for fundamental and sum frequencies introduces a  $\pi$  phase change between the two upon re-entrance into the crystal. The  $\pi$  phase change means that after converting IR to red in the first pass through the nonlinear crystal and reflecting off the outcoupler, the red is converted back to IR in the second pass through the crystal. The result is an energy transfer from the stronger laser line to the weaker.

A computer simulation was developed in order to investigate the degree of effective gain coupling possible with the nonlinear mirror. The computer simulation was based on the usual rate equations for describing the interaction with the gain medium and the outcoupler [11],

$$\frac{d}{dt}N_4 = -\sigma_1 F_1 (N_4 - N_2) + \frac{1}{\tau_u} (N_3 - N_4), \quad (1)$$

$$\frac{d}{dt}N_2 = \sigma_1 F_1 (N_4 - N_2) + \frac{1}{\tau_l} (N_1 - N_2), \quad (2)$$

$$\frac{d}{dt}N_3 = -\sigma_2 F_2 (N_3 - N_1) - \frac{1}{\tau_u} (N_3 - N_4), \quad (3)$$

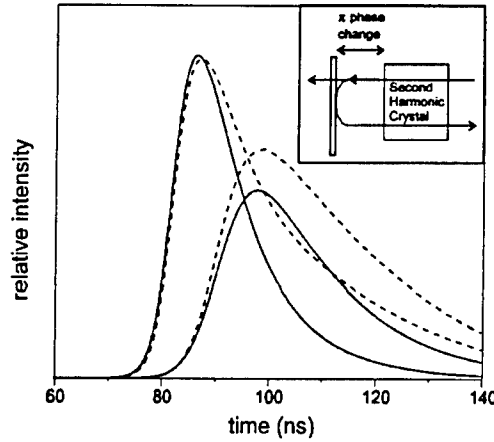


Figure 7: Simulation of the nonlinear mirror. Solid curves are the 2-2 and 3-4 (stronger) transitions without the nonlinear mirror. Dashed curves are with the nonlinear mirror. The inset shows a schematic of the mirror. Reflectivities for the dichroic outcoupler are 90% for the IR and 100% for the red.

$$\frac{d}{dt}N_1 = \sigma_2 F_2 (N_3 - N_1) - \frac{1}{\tau_l} (N_1 - N_2), \quad (4)$$

$$\frac{d}{dt}F_1 = \sigma_1 c F_1 (N_4 - N_2) - \frac{F_1}{\tau_r}, \quad (5)$$

$$\frac{d}{dt}F_2 = \sigma_2 c F_2 (N_3 - N_1) - \frac{F_2}{\tau_r}, \quad (6)$$

where  $\sigma_1$  and  $\sigma_2$  are stimulated emission cross section for the 3-4 and 2-2 transitions,  $F_1$  and  $F_2$  are the photon flux of the 3-4 and 2-2 transitions,  $\tau_u$  and  $\tau_l$  are the time constants for relaxation among upper and lower hyperfine levels, and  $\tau_r$  is the resonator lifetime. The various populations  $N_i$  refer to the designations on the right side of Fig. 1. Because of the short pump pulse, the simulation is started with the pumping process completed and the population already in the excited state. In addition, the time scale of the iodine laser pulse was much faster than any chemical kinetics in the active medium (such as quenching of  $I^*$  due to the formation of  $I_2$ ) [12] and all such chemical processes were ignored in the rate equation model. As in other rate equation models of atomic iodine lasers, the  $F'' = 2$  and  $F'' = 1$  levels are lumped into the lower laser levels because of the fast relaxation among the lower hyperfine levels [13]. The model assumed the laser operated on a single longitudinal mode.

Between two time steps (the resonator round trip time) the photon flux was modified to account for the interaction with the nonlinear mirror. The interaction of the laser radiation with the  $LiIO_3$  crystal was modeled using the coupled wave equations for second harmonic

and sum frequency generation. The equations for the complex field amplitude are [14]

$$\frac{d}{dz}\tilde{A}_1 = \mu\tilde{A}_1^*\tilde{A}_{D1} + \mu\tilde{A}_{SF}\tilde{A}_2^*, \quad (7)$$

$$\frac{d}{dz}\tilde{A}_2 = \mu\tilde{A}_2^*\tilde{A}_{D2} + \mu\tilde{A}_{SF}\tilde{A}_1^*, \quad (8)$$

$$\frac{d}{dz}\tilde{A}_{D1} = \mu\tilde{A}_1^2, \quad (9)$$

$$\frac{d}{dz}\tilde{A}_{D2} = \mu\tilde{A}_2^2, \quad (10)$$

$$\frac{d}{dz}\tilde{A}_{SF} = \mu\tilde{A}_1\tilde{A}_2. \quad (11)$$

The subscripts 1 and 2 again refer to the 3-4 and 2-2 transitions, D1 and D2 refer to the doubled frequencies, and SF to the sum frequency.  $\mu$  is a nonlinear coefficient, proportional to the nonlinear susceptibility  $\chi^{(2)}$ . The actual equations used in the computer program were the separate equations for the real field amplitude  $A$  and phase  $\phi$  (see, for example, [15]), where  $\tilde{A} = Ae^{i\phi}$ .

The simulation first calculated the effect of the gain media using Eqs. (1) - (6), starting from spontaneous emission. Then the first passage through the nonlinear crystal was computed using Eqs. (7) - (11). At this point, part of the energy at the fundamental frequencies (approximately 10%) was coupled out of the cavity, and an additional phase change was introduced between the fundamental and second harmonic frequencies. The second passage through the crystal was then calculated. Because the second harmonic and sum frequency were not resonated, any remaining energy in the red was lost to the laser. For this reason, when the phase change after the first passage through the nonlinear crystal was set to  $2\pi$ , for high enough values of  $\mu$  the laser was driven below threshold and was shut off prematurely.

Results from the simulation are summarized in Fig. 7. The solid lines show the temporal dependence of the 2-2 and 3-4 transitions when there is no nonlinear crystal in the cavity and the gain cross section of the 2-2 transition is 90% of the 3-4 transition. The dashed lines show the profiles when the crystal is placed in the cavity. In both cases, the smaller pulse is the 2-2 and the larger is the 3-4. All curves have been normalized to the peak of the 3-4 pulse obtained with no nonlinear mirror. The case with the nonlinear mirror shows a relative increase in the 2-2 profile compared to the 3-4, demonstrating the coupling ability of the nonlinear mirror.

The expected depth of the hyperfine mode beating is given by the visibility of the gigahertz

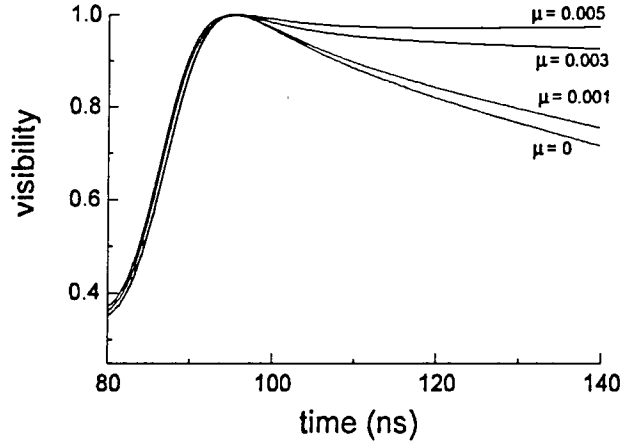


Figure 8: The visibility of the GHz mode beating as a function of time for different nonlinear coefficients.

modulation in the total photon flux:

$$V(t) = \frac{F_{max}(t) - F_{min}(t)}{F_{max}(t) + F_{min}(t)} = \frac{2\sqrt{F_1(t)F_2(t)}}{F_1(t) + F_2(t)}, \quad (12)$$

where the total photon flux is given by  $F(t) \propto |\tilde{A}_1(t) + \tilde{A}_2(t)|^2$ .  $F_{max}(t)$  and  $F_{min}(t)$  are the maximum and minimum values obtained at time  $t$  due to the gigahertz modulation.  $V(t)$  is plotted in Fig. 8 for several values of the nonlinear coefficient  $\mu$ . With an increasing nonlinear coefficient, the visibility of the fringes remains near the maximum value of one in the tail of the pulse, meaning the depth of modulation remains close to 100% for the length of the pulse. The peak value of  $\mu = 0.005$  corresponds to a single pass conversion efficiency from IR to red of approximately 80%.

It was demonstrated that the nonlinear mirror can increase the coupling between the two hyperfine transitions in our pulsed iodine laser. In a cw iodine laser, such as a flashlamp pumped iodine laser or a COIL, the possibilities of the nonlinear mirror can be extended even further. First, one could use the simple photolytic iodine laser described above to generate a seed pulse for a COIL. This way, a magnetic field can be used to tune the gain of the COIL to the region of optimal overlap of the 2-2 and 3-4 transitions. The seed pulse can then provide the maximum depth of modulation without any intracavity elements in the COIL. In a cw flashlamp pumped iodine laser, the nonlinear mirror could be used for both coupling the hyperfine transitions together and mode-locking of the longitudinal modes. Mode-locking occurs in the nonlinear mirror because longitudinal modes in the first pass through the nonlinear crystal undergo sum frequency generation, and on the second

pass the difference frequency generation produces new modes separated by the longitudinal mode spacing and with the phase locked to the original modes [15]. Thus, not only is the peak intensity enhanced even further, but it is expected that, in a manner analogous to mode-locking longitudinal modes under a single transition, the nonlinear mirror will lock the longitudinal modes of both hyperfine transitions together, eliminating the problem shown in Fig. 4b. A planned extension to the computer simulation to check this assumption is to allow more than one longitudinal mode to oscillate.

In conclusion, we have demonstrated an intrinsic gigahertz modulation that occurs in an atomic iodine laser. The gain of two different hyperfine transitions can be equalized through the use of a magnetic field, allowing them to lase simultaneously and beat together. Additional coupling of these transitions is desired to achieve consistent operation and can be achieved through a nonlinear mirror based on intracavity sum frequency generation.

## References

- [1] K. A. Truesdell, S. L. Lamberson, and G. D. Hager. A history of COIL in the U.S. *AIAA 23rd Plasmadynamics and Lasers Conference*, 1992.
- [2] V. A. Katulin, V. Yu. Nosach, and A. L. Petrov. Investigation of the characteristics of the preamplifier stages of a short-pulse iodine laser. *Soviet Journal of Quantum Electronics*, 9(2):1692, 1979.
- [3] Taro Uciyama and Klaus J. Witte. Theoretical analysis of the performance of an atomic iodine laser amplifier chain. *IEEE Journal of Quantum Electronics*, QE-18(5):885-897, 1982.
- [4] I. M. Belousova, B. D. Bobrov, V. M. Kiselev, V. N. Kurzenkov, and P. I. Krepostnov.  $I^{127}$  atom in a magnetic field. *Opt. Spectrosc.*, 37(1):20-24, 1974.
- [5] M. A. Kelly, J. K. McIver, R. F. Shea, and G. D. Hager. Frequency tuning of a CW atomic iodine laser via the Zeeman effect. *IEEE J. Quantum Electron.*, QE-27:263-273, 1991.
- [6] G. N. A. Van Veen, T. Baller, A. E. De Vries, and M. Shapiro. Photofragmentation of  $CF_3I$  in the A band. *Chemical Physics*, 93:277-291, 1985.

- [7] G. Brederlow, E. Fill, and K. J. Witte. *The high-power iodine laser*. Springer, Berlin, 1983.
- [8] W. Thieme and E. Fill. Hyperfine relaxation in the iodine photodissociation laser. *Optics Communications*, 36(5):361–365, 1981.
- [9] J. W. Nicholson, W. Rudolph, and G. Hager. Using laser dynamics to probe the relaxation of an anisotropic velocity distribution of excited iodine. *Journal of Chemical Physics*, 104(10):3537–3545, 1996.
- [10] K. A. Stankov. A mirror with an intensity-dependent reflection coefficient. *Appl. Phys. B*, 45:191–195, 1988.
- [11] A. E. Siegman. *Lasers*. University Press, Oxford, 1986.
- [12] C. C. Davis, R. J. Pirkle, R. A. McFarlane, and G. J. Wolga. Output mode spectra, comparative parametric operation, quenching, photolytic reversibility, and short-pulse generation in atomic iodine photodissociation lasers. *IEEE Journal of Quantum Electronics*, QE-12(6):334, 1976.
- [13] V. A. Alekseev, T. L. Andreeva, V. N. Volkov, and E. A. Yukov. Kinetics of the generation spectrum of a photodissociation iodine laser. *Soviet Physics JETP*, 36(2):238, 1973.
- [14] R. W. Boyd. *Nonlinear Optics*. Academic Press, 1992.
- [15] K. A. Stankov, V. P. Tzolov, and M. G. Mirkov. Frequency-domain analysis of the mode-locking process in a laser with a second-harmonic nonlinear mirror. *Optics Letters*, 16(9):639–641, 1991.

Inversion of Atmospheric Radiance Measurements for the Measurement  
of Temperature, Turbulence, and Velocity

David W. Watt  
Associate Professor  
Department of Mechanical Engineering

Andrew D. Litch  
Undergraduate Student of Mechanical Engineering

Kingsbury Hall

The University of New Hampshire  
Durham, NH

Final Report for:  
Summer Research Extension Program  
Phillips Laboratory

Sponsored by:  
Air Force Office of Scientific Research  
Bolling Air Force Base  
Washington, D.C.

and

Phillips Laboratory

October 1997

---

## **Inversion of Atmospheric Radiance Measurements for the Measurement of Temperature, Turbulence, and Velocity**

### **Abstract**

Obtaining atmospheric parameters from radiance measurements consists of ill-conditioned problems that require appropriate inversion methods. This report analyzes the solution methods for atmospheric temperature, turbulence, and velocity profiles from the inversion of multi-spectral radiance measurements. The following inversion methods are presented and evaluated for the attainment of atmospheric parameters: direct linear, direct non-linear, Tikhonov-Miller, Generalized Singular Value Decomposition (GSVD), Truncated Singular Value Decomposition (TSVD), and Damped Singular Value Decomposition (DSVD). The last five are a special breed of inversion techniques known as regularization methods. These methods can handle ill-conditioning well if a suitable regularization parameter is chosen. Several methods are evaluated for choosing this parameter, including the L-Curve criterion, Generalized Cross Validation (GCV), Quasi-Optimality criterion, and the Discrepancy principle.

The results from numerical simulations using all these techniques are analyzed. The regularization methods are the most promising inversion techniques for this application because the solutions are more stable than the direct methods, and because it reduces output error, given an appropriate regularization parameter. Inversions for temperature using the Quasi-Optimality criterion proved to be more successful than the other parameter selection techniques. Solutions for atmospheric turbulence, however, had very limited success. Therefore, solving for velocity profiles, which depends upon turbulence parameter results, is not feasible and thus was not studied.

## **1. Introduction**

Passively emitted atmospheric radiance in the lower atmosphere (below 30 km) depends on the composition of the gas phase, the concentrations of aerosols, cloud cover, precipitation, and the local temperature. The composition of the atmosphere varies dramatically in the vertical direction; the density and temperature diminish causing different chemical species to be present in different proportions. In the lateral direction, the effects of large weather systems and topography cause spatial variations in the structure of the atmosphere over lateral scales on the orders of ten to hundreds of kilometers. In addition to these large scale variations, there are local structural variations in the atmosphere caused by a variety of dynamic processes and commonly grouped together under the name of turbulence.

Turbulent motion in the atmosphere occurs on scales of millimeters to hundreds of meters; this motion results from the breakdown of large scale coherent motion in the atmosphere (such as thermal plumes or gravity waves) into randomly oriented vortical motions often referred to as eddies. The effect of turbulence is to enhance the transfer of heat, mass, and momentum from the surface into the atmosphere and to enhance mixing of aerosols throughout the atmosphere. As a consequence of this activity, the temperature field (and to a lesser extent the chemical concentration fields) take on a spatially random, self-similar structure with a range of scales. As a result of the thermal structural variations, the atmospheric radiance and the local refractive index both display variations characterized by the length scale of the temperature fluctuations. The physical nature of atmospheric radiation has been the subject of much research, and resulting models have been incorporated into the LOWTRAN, MODTRAN, HITRAN, and FASCODE atmospheric radiance codes. These codes are designed to predict the absorptance and radiance with moderate to very high spectral resolution and to account for a wide range of atmospheric

---

conditions, scattered sunlight, or other ambient factors. These models treat the atmosphere as a relatively small number of layers, each having different properties. Experimentally, atmospheric radiance is measured using filtered radiometers or Fourier Transform Spectrometry (FTS).

The physics of atmospheric radiation and the techniques of radiation measurement are well understood, but the use of radiation for the determination of atmospheric parameters is not. One motivation for developing suitable techniques is the reduction in cost of such devices as windshear detectors. A passive device would be less expensive than the lasers and radar currently used in windshear detectors. There is an infrared device made by Turbulence Prediction Systems in Colorado that uses radiation to detect large temperature gradients in front of an aircraft, associating those with large velocity changes. This device, however, does not explicitly solve for turbulence or velocities. The difficulty associated with obtaining these parameters, as well as temperature, is that the radiative nature of the atmosphere is similar for different wavelengths and because the radiation signal can be heavily attenuated. This results in ill-conditioned mathematical problems. The theory and simulations associated with this report were carried out in hopes of overcoming these problems and accurately determining atmospheric temperature, turbulence, and velocity profiles.

## 2. Theory and Modeling

The formation of radiance images can be modeled by considering an imaging radiometer staring into the atmosphere. The image plane of the radiometer has an array of detectors, and the detector has an imaging volume defined by the imaging lens, aperture, and detector. The atmosphere within the imaging volume can be considered to be a series of parallel slices perpendicular to the optic axis. The composition (and therefore the radiative properties) of the atmosphere can vary along the view axis, but it should be essentially constant within an individual slice. The temperature field may also vary significantly along the view axis. In addition, temperature fluctuations due to turbulence are present within an individual slice.

Planck's Law is the fundamental equation for relating radiant energy and temperature. It gives the radiance intensity  $B$  at wavelength  $\lambda$  for a black body at temperature  $T$ , where  $c_1$  and  $c_2$  are constants.

$$B(\lambda, T) = c_1 \lambda^{-5} \exp\left(\frac{c_2}{\lambda T} - 1\right) \quad (1)$$

The constituent species in each differential slice emit a fraction of the black body intensity. If the combined spectral absorptivities of each species is  $\alpha$ , and assuming  $\alpha$  is equal to the emissivity, then the intensity  $I$  from passively emitted radiation in an imaging volume striking a detector is given by

$$I_\lambda(x, y) = \int_0^\infty B(\lambda, T(x \frac{z}{F}, y \frac{z}{F}, z)) \alpha(\lambda, z) \exp\left(-\int_0^z \alpha(\lambda, z') dz'\right) dz \quad (2)$$

where  $x$  and  $y$  are the coordinates of a particular detector cell in the array of detectors,  $z$  is the optical axis distance through the imaging volume, and  $F$  is the focal length of the imaging lens of the radiometer. The exponential term is the attenuation of the radiance image from the absorption

of the atmosphere. Scattering effects are ignored. Equation 2 can be linearized with a Taylor series about an assumed or first guess temperature profile. If  $T_o(z)$  is the assumed profile, and if

$$K(\lambda, z) = \left. \frac{\partial B}{\partial T} \right|_{T=T_o(z)} a(\lambda, z) \exp\left(-\int_0^z a(\lambda, z') dz'\right) \quad (3)$$

then equation 2 becomes

$$I_\lambda(x, y) - \int_0^\infty K(\lambda, z) [B(\lambda, T_o(x \frac{z}{F}, y \frac{z}{F}, z)) \left( \left. \frac{\partial B}{\partial T} \right|_{T=T_o(z)} \right)^{-1} - T_o(x \frac{z}{F}, y \frac{z}{F}, z)] dz = \int_0^\infty K(\lambda, z) T(x \frac{z}{F}, y \frac{z}{F}, z) dz \quad (4)$$

A radiometer can measure  $I_\lambda$  at multiple wavelengths (about 30). Databases such as MODTRAN can give  $a(\lambda, z')$  at a high spectral resolution and at distinctive atmospheric conditions. Therefore, the left hand side consists of known, or measured, quantities. The spatial fluctuations in temperature produce corresponding spatial fluctuations in the measured radiance. Assuming the temperature fluctuations are small compared to the mean temperature, equation 2 becomes

$$\delta I_\lambda(x, y) = \int_0^\infty K(\lambda, z) \delta T(x \frac{z}{F}, y \frac{z}{F}, z) dz \quad (5)$$

where the fluctuation quantities are relative to the mean. The structure function developed by Kolmogorov can be used to relate the temperature fluctuations to turbulent intensity<sup>6</sup>. The turbulence of a convective medium can be quantified by the temperature structure parameter  $C_T$ . If the distance between any two arbitrarily spaced points is  $r$ , then the ensemble average of the temperature fluctuations can be represented by

$$\langle [\delta T(r)]^2 \rangle = C_T^2 r^{\frac{2}{3}} \quad (6)$$

As the turbulence intensity increases, then by equation 5 the radiation fluctuations will increase in magnitude. The temperature difference of a point relative to the mean temperature at any  $z$  is approximately equal to the average of all the differences in temperature between any two points at the same  $z$ . Thus equation 5 becomes

$$\langle \delta I_{\lambda}^2 \rangle \cong \int_0^{\infty} C_T^2(z) w(z)^{\frac{2}{3}} [K(\lambda, z)]^2 dz \quad (7)$$

where  $w$  is the width of a slice at optic axis distance  $z$ .

Equation 4 provides a basis for obtaining temperature profiles from the radiance measurements, whereas equation 7 provides a basis for obtaining temperature structure parameter profiles, which characterize turbulence, from the radiance fluctuations.

The effect of the ambient fluid velocity field for short time intervals can be examined in the context of Taylor's "frozen turbulence" assumption. This hypothesis states that the small scale features of an atmospheric turbulent flow field change slowly compared to the mean flow<sup>3</sup>. So the temperature field deforms slowly with respect to the overall velocity. Therefore, over a short time interval  $t$ , the temperature fluctuations evolve as  $\delta T(x, y, z, t) = \delta T(x + U\tau, y + V\tau, z, t + \tau)$ , where  $U$  and  $V$  are the velocities normal to the optic axis. In addition to the frozen turbulence assumption, it is assumed that the motion parallel to the optic axis results in a negligible magnification change. Based on these assumptions, the short-time evolution of the radiance images depends only on the motion normal to the optic axis. The effect of the velocity components can be seen explicitly from the cross-correlation of two radiance images,  $I_{1,\lambda}$  and  $I_{2,\lambda}$ , separated by a small time interval. The cross-correlation function  $R$  is given by

$$R_{\lambda,11}(u, v) = \int_{-\infty}^{\infty} \int_{-\infty}^{\infty} \delta I_{1,\lambda}(x, y) \delta I_{2,\lambda}(x + u, y + v) dx dy \quad (8)$$

where  $u$  and  $v$  are the spatial shifts in the detector plane. The velocity at any location  $z$  along the optic axis has an apparent magnitude when viewed in the image plane that is scaled by the magnification  $F/z$ . The displacement of an object at a location  $z$  will move across the detector by an amount  $u'(z) = (F/z)U(z)\tau$  and  $v'(z) = (F/z)V(z)\tau$ . Thus equation 8 becomes

$$R_{\lambda II}(u, v) = \int_0^\infty \int_{-\infty}^\infty \int_{-\infty}^\infty [K(\lambda, z)]^2 \delta T(x \frac{z}{F}, y \frac{z}{F}, z) \delta T([x + u'(z)] \frac{z}{F}, [y + v'(z)] \frac{z}{F}, z) dx dy dz \quad (9)$$

If the spatial in-plane cross-correlation of the temperature field is expressed in terms of the temperature structure function and the correlation coefficient  $c_{TT}$ , then the above expression becomes

$$R_{\lambda II}(u, v) = \int_0^\infty [K(\lambda, z)]^2 C_T^2 w(z)^{\frac{2}{3}} c_{TT}([u'(z)] \frac{z}{F}, [v'(z)] \frac{z}{F}, z) dz \quad (10)$$

Once the temperature cross-correlations  $c_{TT}$  are obtained, the in-plane velocity components can be found from the displacement of the correlation peaks for each location  $z$ .

The integrals in the above equations are definite, and  $T(z)$ ,  $C_T$ , and  $c_{TT}$  appear only in the integrand of one side of the equation. Thus, equations 4, 7, and 10 are Fredholm integral equations of the first kind. In a more general form, this type of equation is represented as

$$g(y) = \int_a^b K(y, x) f(x) dx \quad (11)$$

where  $g(y)$  is the given or measured function,  $f(x)$  is the function being sought, and  $K(y, x)$  is the kernel or weighting function. In figure 1, the kernels are discrete because they contribute only at one value of  $x$ . Since only one kernel contributes to  $g(y)$  at a given  $x$ , it is an ideal situation for extracting  $f(x)$  from a set of measurements.

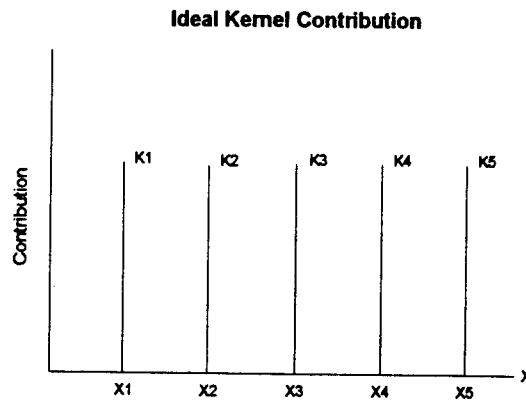


Figure 1: Ideal, independent kernels

On the other hand, figure 2 shows kernel functions with non-discrete narrow profiles. These produce a slightly blurred  $f(x)$ .

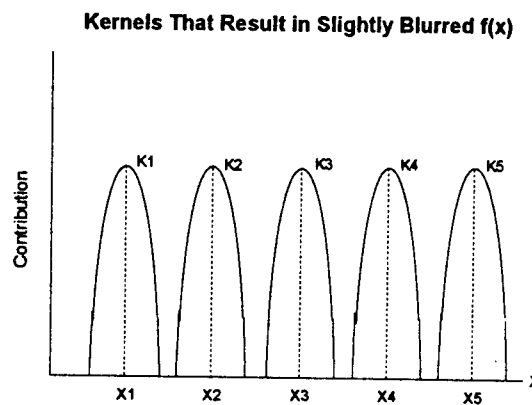


Figure 2: Close to ideal kernels

However,  $f(x)$  can be sharpened with an appropriate inversion method. In real inversion problems, the kernels, such as the ones in figure 3, are often non-zero over the entire range of  $x$ , or have smooth or common maximums. Relative contributions of the kernels are more difficult to discern, and the kernels are more interdependent. The task of inversion becomes more formidable.

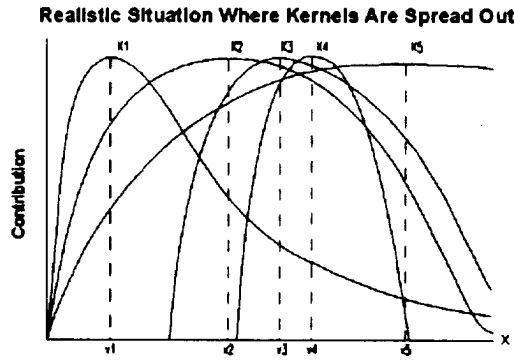


Figure 3: Interdependent kernels

The kernels in these may cause the solution  $f(x)$  to be unstable or oscillatory due to small changes or errors in the input. Hence, Fredholm equations of the first kind are often ill-conditioned, and this property greatly complicates inversion problems.

One method for finding  $f(x)$  is by direct linear inversion. If there are  $M$  discrete measurements and  $N$  number of points in the domain of  $x$ , then a quadrature of equation 11 is

$$g_i = \sum_{j=1}^N K_{ij} f_j \Delta x \quad i = 1, 2, \dots, M \quad (12)$$

If  $A_{ij} = K_{ij} \Delta x$  and  $g_j$  and  $f_j$  are defined as vectors  $\mathbf{g}$  and  $\mathbf{f}$  respectively, then

$$\mathbf{A} \mathbf{f} = \mathbf{g} \quad (13)$$

$$\mathbf{f} = \mathbf{A}^{-1} \mathbf{g} \quad (14)$$

Error due to the quadrature is generally very small and is not considered. The multiplication of  $\mathbf{A}^{-1}$  and  $\mathbf{g}$  will only work when  $\mathbf{A}$  is square and the number of measurements equals the number of rows in  $\mathbf{A}$ . Furthermore,  $\mathbf{A}$  is often singular or near singular in ill-conditioned problems. Singular Value Decomposition (SVD), however, can help to rectify these problems.

SVD can decompose  $\mathbf{A}$  into a  $M \times N$  column-orthogonal matrix  $\mathbf{U}$ , an  $N \times N$  diagonal matrix  $\mathbf{W}$  containing singular values, and the transpose of an  $N \times N$  orthogonal matrix  $\mathbf{V}$ . After zeroing the reciprocals of the small singular values to reduce round-off error in the sets of equations, the solution that will best minimize the least squares residual is

$$\mathbf{f} = \mathbf{V} \left[ \text{diag} \left( \frac{1}{\omega_i} \right) \right] (\mathbf{U}^T \mathbf{g}) \quad (15)$$

where  $\omega_j$ 's are the singular values<sup>1</sup>. SVD will only work with  $M$  greater than or equal to  $N$ ; however, by augmenting  $\mathbf{A}$  and  $\mathbf{g}$  with zeros so that  $\mathbf{A}$  becomes a square matrix, the process will work to give a possible and useful, but never a unique solution.

Another method for finding  $f(x)$  is by direct non-linear inversion. Equation 11 is no longer of importance because it is linear. A general form of equation 2 is

$$g(y) = \int_a^b K(y, x, f(x)) dx \quad (16)$$

The Newton-Raphson method for finding  $f(x)$  can be used by letting

$$F_i(f_1, f_2, \dots, f_N) = \left( \sum_{j=1}^N K_{ij}(f_j) \Delta x \right) - g_i = 0 \quad i = 1, 2, \dots, M \quad (17)$$

and if

$$J_{ij} \equiv \frac{\partial F_i}{\partial f_j} \quad (18)$$

then the iterative formula is

$$\mathbf{f}_{\text{new}} = \mathbf{f}_{\text{old}} - \mathbf{J}^{-1} \mathbf{F} \quad (19)$$

The process is stopped when  $\|\mathbf{F}\|$  is small enough. To apply Newton-Raphson,  $M$  and  $N$  must be equal.  $\mathbf{J}$  and  $\mathbf{F}$  can be augmented with zeros to make  $M$  and  $N$  equal if SVD is used.

Another inversion method involves imposing an additional constraint on  $f(x)$  to limit the set of possible solutions. This is called a regularization method. There exist a handful of regularization methods, but their general structure will be explained below.

If there exists some a priori knowledge about  $f(x)$ 's shape, then a reasonable constraint on  $f(x)$  might be its measure of smoothness. The additional condition is arbitrary, because the measurements give no evidence that  $f(x)$  is smooth.

Let  $r(\mathbf{f})$  be a positive scalar measure of the roughness of  $\mathbf{f}$ . If  $r(\mathbf{f})$  is zero, then the resulting  $\mathbf{f}$  is completely smooth as given by the measure of  $r(\mathbf{f})$ . A least squares criterion minimizes  $\|\mathbf{A}\mathbf{f} - \mathbf{g}\|$ , whereas a regularization method minimizes  $\|\mathbf{A}\mathbf{f} - \mathbf{g}\| + \gamma r(\mathbf{f})$ .  $\gamma$  is a regularization parameter that can be varied from zero to infinity. As  $\gamma$  approaches infinity, the minimization goes to  $r(\mathbf{f}) = 0$  regardless of  $\mathbf{g}$ . In a purely least squares problem,  $\gamma$  equals zero, and the solution depends completely on  $\mathbf{g}$ . Therefore,  $\gamma$  is a parameter that can be arbitrarily set as a trade-off between smoothness and agreement with the measurements.

Most measures of smoothness are simple quadratic combinations of the  $f_i$ . The measures of smoothness are the sums of squares of differences computed at every  $i$ . Let  $\mathbf{B}$  be a matrix such that  $\mathbf{B}\mathbf{f}$  contains in its elements values that are squared and summed to give  $r(\mathbf{f})$ . Suppose it is an *a priori* belief that  $\mathbf{f}$  is a second degree polynomial, then the third derivative of  $\mathbf{f}$ 's components should equal zero. If  $\mathbf{B}\mathbf{f}$  is to have elements proportional to a third derivative, then  $\mathbf{B}$  must be the third difference matrix.

$$\mathbf{B} = \begin{bmatrix} -1 & 3 & -3 & 1 & 0 & 0 & 0 & \cdots & 0 \\ 0 & -1 & 3 & -3 & 1 & 0 & 0 & \cdots & 0 \\ \vdots & & & & \ddots & & & & \vdots \\ 0 & \cdots & 0 & 0 & -1 & 3 & -3 & 1 & 0 \\ 0 & \cdots & 0 & 0 & 0 & -1 & 3 & -3 & 1 \end{bmatrix} \quad (20)$$

In the case of inversion for atmospheric temperature, there is sufficient statistical data in MODTRAN or other sources to provide average temperature profiles which can be used for difference operators of  $\mathbf{B}$ . In this case, not all the rows in  $\mathbf{B}$  would be the same, but would depend upon the fit to the MODTRAN data.

The quadratic measure  $q$  of  $\sum(-f_i + 3f_{i+1} - 3f_{i+2} + f_{i+3})^2$  is given by the square of the norm of  $\mathbf{Bf}$ .

$$q(\mathbf{f}) = (\mathbf{Bf})^T \mathbf{Bf} = \mathbf{f}^T \mathbf{B}^T \mathbf{Bf} \quad (21)$$

Suppose  $\mathbf{L} = \mathbf{B}^T \mathbf{B}$ , then the minimization is of the quantity  $(\mathbf{Af} - \mathbf{g})^T (\mathbf{Af} - \mathbf{g}) + \gamma \mathbf{f}^T \mathbf{Lf}$ . This is a constrained extremum problem with  $\gamma$  as an undetermined Lagrangian multiplier. For all  $i$ ,

$$\frac{\partial}{\partial f_i} (\mathbf{f}^T \mathbf{A}^T \mathbf{Af} - \mathbf{g}^T \mathbf{Af} - \mathbf{f}^T \mathbf{A}^T \mathbf{g} + \gamma \mathbf{f}^T \mathbf{Lf}) = 0 \quad (22)$$

which simplifies to

$$\mathbf{f} = (\mathbf{A}^T \mathbf{A} + \gamma \mathbf{L})^{-1} \mathbf{A}^T \mathbf{g} \quad (23)$$

For regularization methods, equation 23 is not usually solved by inverting the coefficient matrix, but by using SVD, or LU factorization if the ill-conditioning has been removed by changing to a suitable basis through the introduction of the side constraint.

Within the realm of regularization methods, several were compared for the solution of atmospheric parameters from simulated radiance measurements. One method called Tikhonov-Miller regularization is simply a solution of equation 23 with a conventional numerical technique such as LU factorization or SVD. Two methods called Truncated Singular Value Decomposition (TSVD) and Damped Singular Value Decomposition (DSVD) solve equation 23 in parts by minimizing the roughness term subject to minimizing the residual term.

In addition, these two methods derive a new problem with a well-conditioned rank deficient coefficient matrix<sup>2</sup>. For TSVD and DSVD, a truncation parameter  $k$  plays an similar role to  $\gamma$ .

For TSVD; the rank deficient matrix is achieved by truncation of  $\mathbf{A}$ . By truncating the SVD expansion, the smaller singular values (the ones beyond the cutoff at  $k$ ) are set to zero thereby reducing the sensitivity of the solution to the input. The truncated SVD expansion is

$$\mathbf{A}_k = \sum_{i=1}^k \mathbf{u}_i \mathbf{w}_i \mathbf{v}_i^T \quad (24)$$

where  $k \leq N$  and  $\mathbf{u}$ ,  $\mathbf{w}$ , and  $\mathbf{v}$  are elements of the matrices of the SVD. DSVD is slightly more sophisticated than TSVD because it zeroes the smaller singular values of the SVD expansion by smoothing the cutoff point at  $k$ . Thus equation 15 would be multiplied by appropriate filter factors that gradually zero out smaller singular values.

A fundamental problem of regularization methods is their dependence upon choosing a suitable parameter for providing a fair balance between both parts of the minimization. The quality of the solution depends heavily upon the choice of a regularization parameter, and there are several techniques for prescribing a reasonable choice. These techniques in conjunction with the aforementioned regularization techniques were considered. The techniques are called Generalized Cross-Validation (GCV), L-Curve criterion, the Quasi-Optimality criterion, and the Discrepancy principle. These techniques inspect the spectrum of regularized solutions as a function of the regularization parameter. Each one uses different functions, but all suggest using parameters that correspond to unique points on the function curve.

As stated by Hansen<sup>2</sup>, Generalized Cross-Validation works on the knowledge that if an arbitrary element of  $\mathbf{g}$  is removed, then the resulting solution should predict this well, and a selected regularization parameter should be independent of an orthogonal transformation of  $\mathbf{g}$ .

$$GCV(\gamma) \equiv \frac{\|\mathbf{A}\mathbf{f}(\gamma) - \mathbf{g}\|_2^2}{(\text{trace}(\mathbf{I} - \mathbf{A}\mathbf{A}^1))^2} \quad (25)$$

is the function given by Hansen where  $\mathbf{A}^1$  (related to the pseudo-inverse) is a matrix which produces the solution  $\mathbf{f}(\gamma)$  when multiplied with  $\mathbf{g}$ . The  $\gamma$  suggested by this approach is the one that minimizes  $GCV(\gamma)$ .

The L-curve criterion computes the curvature of the curve ( $\log \|\mathbf{A}\mathbf{f}(\gamma) - \mathbf{g}\|_2$ ,  $\log \|\mathbf{L}\mathbf{f}(\gamma)\|$ ), where  $\gamma$  varies the position along the curve. The curve is generally L shaped because of its appearance on a log scale and because the two halves of the regularization are separately sensitive to changes in  $\gamma$ , producing a point, or a value of  $\gamma$ , where there is a fair balance between the two different types of error. It is at this  $\gamma$  where there is maximum curvature, and the L-Curve criterion suggests using that  $\gamma$  for the regularization problem.

The Quasi-Optimality criterion minimizes the function

$$Q \equiv \gamma \left\| \frac{d\mathbf{f}(\gamma)}{d\gamma} \right\|_2 \quad (26)$$

This method, like the L-Curve criterion, attempts to balance residual error and the side constraint error, but the procedure is different<sup>4</sup>.

The Discrepancy principle suggests choosing a regularization parameter so that the residual norm is below an error estimate when one is known. In the case of radiance measurements, radiometer devices typically have associated with them a noise level that can be used to make this error estimate. The regularization using the Discrepancy principle is a least squares problem with the error constraint.

### 3. Initial Simulations

There are many techniques to choose from when consulting the literature on inversion methods. The results can be vastly different when a greater number of methods are considered, and many of these methods are based on subjective criteria. Hence, numerical testing of multiple methods is essential for finding an optimal one to solve the particular problem at hand.

The inversion methods mentioned above were applied to the discretized versions of the radiance equations and evaluated by numerical simulation. An initial set of simulations for the inversion for temperature profiles were done to compare the traditional numerical linear algebra techniques to that of regularization. Since Tikhonov-Miller is representative of most regularization methods, it was chosen as a comparison to direct linear inversion and non-linear, iterative, inversion.

The initial simulations assume that the measurements are taken with a radiometer having 25 wavelength channels, a bandwidth of 0.05% of the wavelength, a focal length of 400 millimeters, and a detector width of 5 millimeters. An exponential function was used to simulate a plausible line shape for each wavelength. The absorption data comes from a MODTRAN database assuming a US standard atmosphere. Twenty-five equally spaced wavelengths in the range of 9.65 to 9.90 microns are used in the simulations. These wavelengths were selected subjectively from contour plots showing weighting functions for the entire spectrum. Wavelengths were selected such that their weighting functions were as dissimilar as possible. The weighting functions for wavelengths in the range of 9.65 to 9.90 microns appeared to vary sufficiently to warrant their selection.

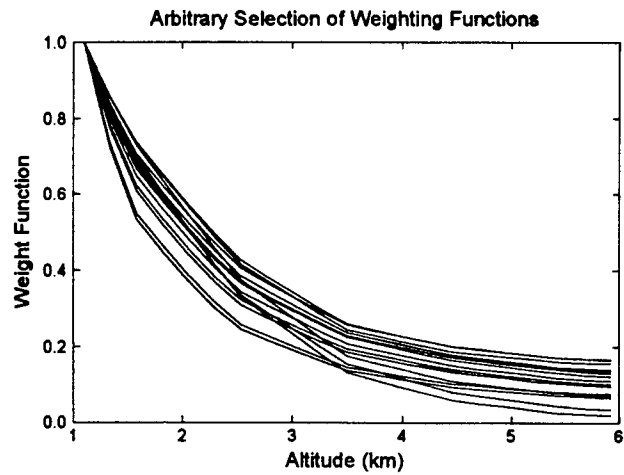


Figure 4: Weighting functions for 9.65 to 9.90 microns

A plot of the weighting functions for these wavelengths is shown in figure 4. Because the goal of initial set of simulations was to compare classes of inversion techniques, optimal selection of weighting functions was not a key factor. Simulations described later use a more objective approach. The arbitrary parabolic temperature profile shown in figure 5 is used to generate the intensity measurements. The assumed temperature profile is a parabola as well.

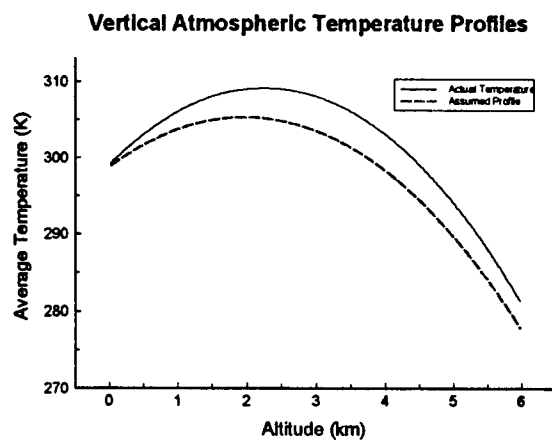


Figure 5: Arbitrary temperature profiles

6 km of vertical atmosphere are considered in measurement generation and inversion. The resolution sought for the temperature profile is 20 m. Since there are more unknowns than equations, the problem is certainly not injective ( $\mathbf{A}$  has a trivial null space so there is no unique solution), but this situation is 'remedied' by the use of SVD.

There are three signal to noise ratios, SNR, that are compared in the preliminary simulations: 100, 20, and 10. Comparing the effects of noise levels is of particular interest because this is an ill-conditioned problem. The solution may be unstable or oscillatory due to small changes or errors in the input. Therefore, to evaluate the initial results, the following indicators of quality of solution are calculated for each inversion method. The absolute error,  $\varepsilon$ , represents a measure of the accuracy of the calculated profiles.

$$\varepsilon = \sqrt{\frac{1}{N} \sum_{i=1}^N (T_i^{\text{actual}} - T_i^{\text{calculated}})^2} \quad (27)$$

The bias,  $B$ , is the difference between the average and the true values. The temperature profile calculated with  $\text{SNR} = \infty$ ,  $T_i^o$ , is used as the "average value" in these simulations.

$$B = \sqrt{\frac{1}{N} \sum_{i=1}^N (T_i^{\text{actual}} - T_i^o)^2} \quad (28)$$

The standard deviation,  $S$ , of the calculated temperatures around the biased temperature profile  $T_i^o$  represents a measure of the precision of the calculated profiles.

$$S = \sqrt{\frac{1}{N} \sum_{i=1}^N (T_i^{\text{calculated}} - T_i^o)^2} \quad (29)$$

Equations 27-29 are applied to all three inversion methods in the initial simulations. The Tikhonov-Miller method, however, depends on the regularization parameter  $\gamma$ , so values for equations 27-29 in this case must be computed as a function of  $\gamma$ .

The direct linear inversion method produces the temperature profiles seen in figure 6 for the four signal to noise ratios. There are prominent oscillations in the output around the actual temperature profile. As expected, the amplitude of these oscillations increases as the signal to noise ratio decreases.

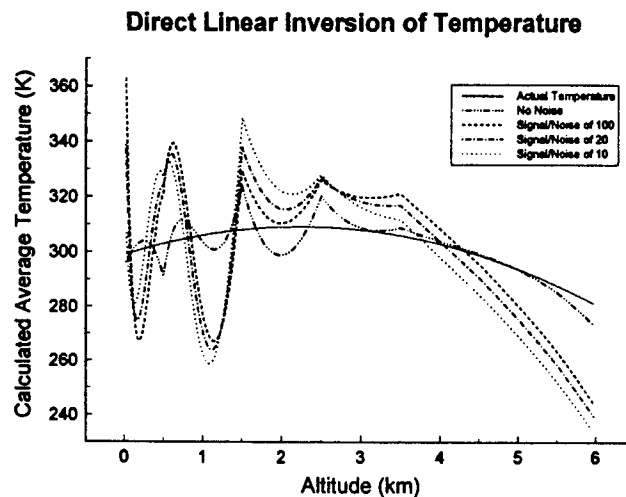


Figure 6: Direct inversion using SVD

The direct non-linear inversion method shown in figure 7 exhibits much smaller oscillations than the linear method. Note the scale of the graph in figure 6 is much larger than the scale of the graph in figure 7. The oscillations from the direct method indicate that the eigenvalues of the kernel matrix are too small for the solution to be stable. The high degree of kernel interdependence results in small eigenvalues. Although SVD can help invert the kernel matrix by finding the singular values, small changes in the measurements still result in large changes in the solution because they are multiplied by large eigenvalues in the inverse kernel matrix.

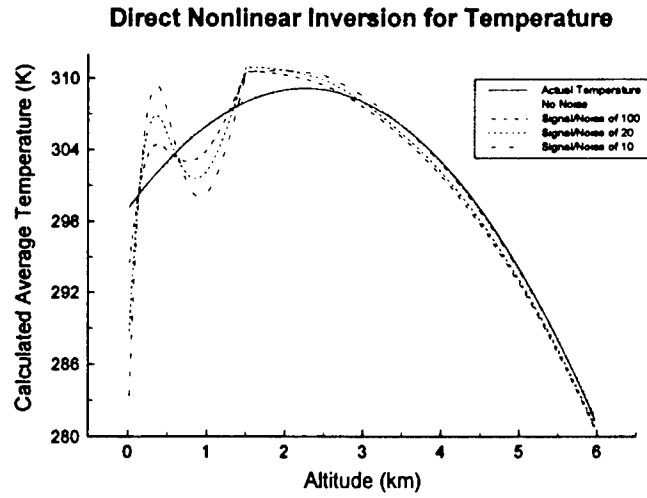


Figure 7: Non-linear inversion using Newton-Raphson

Table 1 gives the values for equations 27-29 generated from the direct methods. The standard deviations show the non-linear method is more precise, and the increase in precision error with SNR decrease is greater using the linear method.

Table 1: Root Mean Squared Values from Direct Inversion Methods

R.M.S. Value	Linear SNR = 100	Non-Linear SNR = 100	Linear SNR = 20	Non-Linear SNR = 20	Linear SNR = 10	Non-Linear SNR = 10
Bias Error (K)	4.63	0.11	4.63	0.11	4.63	0.11
Standard Deviation (K)	17.04	1.33	18.30	1.93	21.77	2.64
Absolute Error (K)	18.54	1.33	19.70	1.93	22.95	2.64

The same is true regarding each method's accuracy, given by the absolute error. Also, the non-linear method shows equal standard deviation and absolute error because of its low bias error. Hence, the direct non-linear method is more accurate and more precise than the direct linear method, but each method is susceptible to producing oscillations from noise.

The root mean squared values must be computed as a function of the regularization parameter for the Tikhonov-Miller method. The simulations computed values for equations 27-29 with  $\gamma$

ranging from  $10^{-6}$  to  $10^{10}$ . In figure 8, the bias error for each noise level has a minimum value associated with  $\gamma$ . The minimum values are all approximately zero, and each noise level exhibits two plateaus of bias error, one at 4.75 K, and one around 2 K.

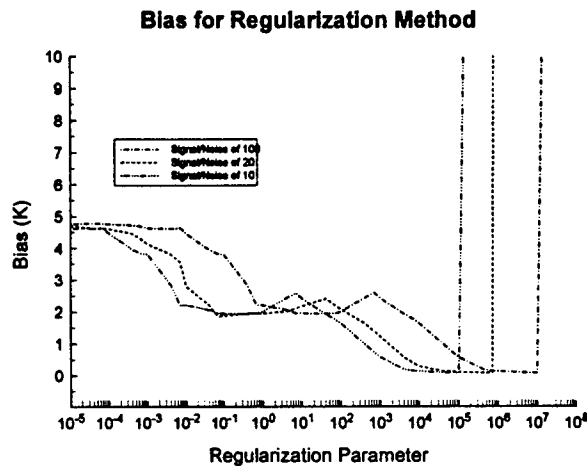


Figure 8: Bias errors for Tikhonov regularization

After the minimum values, the bias errors increase rapidly to extremely large values. The standard deviations, shown in figure 9, demonstrate the effects of regularization on the inversion.

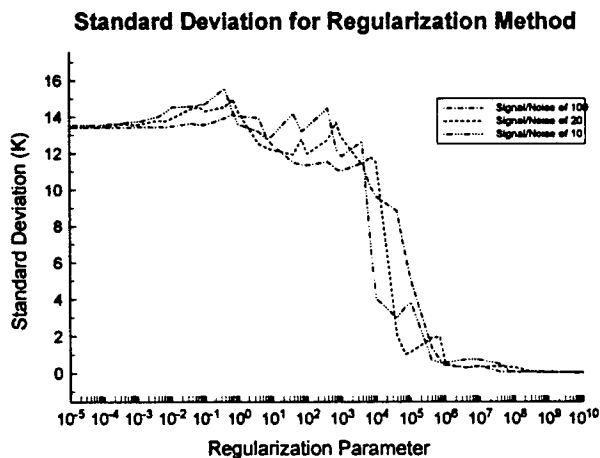


Figure 9: Standard deviations for Tikhonov regularization

The standard deviations range from initial values of 13.8 K to final values of 0 K. The standard deviations become zero because  $\gamma$  becomes large, so the minimization is primarily on the smoothing functional. The smoothing functional does not depend on the measurements, so there

is no difference between the temperature profiles with and without the noise. The standard deviations are high initially because  $\gamma$  is small and the emphasis of the minimization is instead on the residual. The absolute error plots in figure 10 are much like the bias plots; they have minimums at about the same regularization parameters and increase rapidly after the minimums.

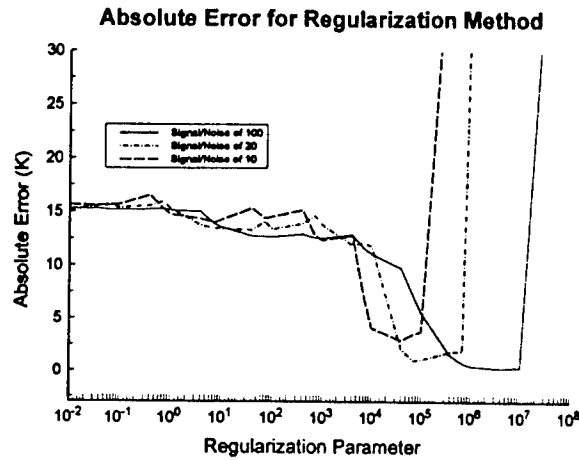


Figure 10: Absolute error for Tikhonov regularization

However, there is a sharp dip in each error before the minimums, unlike the plateaus of the bias errors. The errors given in table 2 are almost the same as those from the direct non-linear inversion.

Table 2: Values at Minimum Absolute Error for Regularization Method

Values at Minimum Absolute Error	SNR = 100	SNR = 20	SNR = 10
Bias Error (K)	0.09	0.12	0.09
Standard Deviation (K)	0.30	1.02	2.99
Absolute Error (K)	0.26	1.03	2.94
Regularization Parameter	4E6	7E4	4E4

In a real situation, the difficulty of picking  $\gamma$  so that the error happens to be at the minimum absolute error is a disadvantage of a regularization method, because the absolute error is a function of the unknown true solution. The simulations shown later will demonstrate the effect of the different 'objective' techniques for choosing an optimal regularization parameter.

The regularization produces the temperature profiles in figure 11 when  $\gamma$  is such that there is minimum absolute error. Compared to the direct inversion methods, there is no instability inherent in the profiles. This is the case at any value of  $\gamma$  above about 0.1.

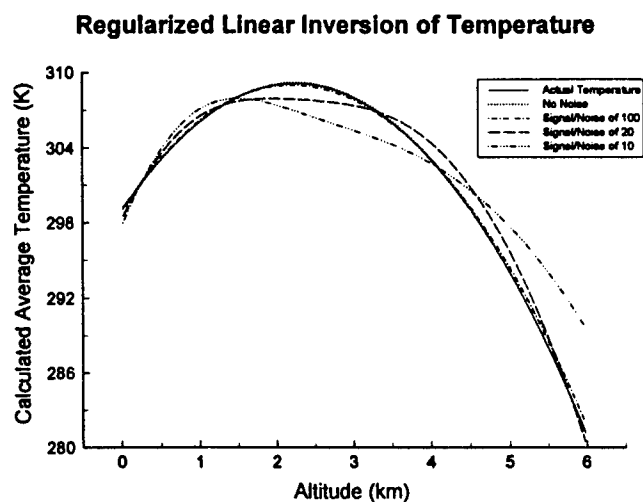


Figure 11: Tikhonov regularization for temperature profiles

#### **4. Optimal Wavelength Selection**

The problem of choosing optimal wavelengths such that the weighting functions are least interdependent amounts to an optimization problem of the determinant. Which thirty or so wavelengths taken in aggregate out of about five thousand possible spectral lines produce a coefficient matrix with the highest determinant? To answer this question, Applied Statistics algorithm AS295 was used as an optimization routine<sup>5</sup>. This algorithm uses a Fedorov exchange routine to exchange candidates with existing selections until no further increase in the determinant can be obtained. The normalized weighting functions for one particular simulation are shown in figure 12. The routine selects a spread of weighting functions. The centroids of these weighting functions are dispersed showing how the row vectors span the measurement space as best as they can from the candidate weighting functions. The rapid decay in the functions shows the heavy attenuation by the atmosphere. This set is far from the ideal situation as shown in figure 1, but any attempt to improve the conditioning of a problem such as this is worth the effort. The optimization of wavelengths procedure was used on the next set of simulations.

## 5. Final Simulations

Since it was found that a regularization method is more suited to this type of problem, Tikhonov-Miller, TSVD, and DSVD regularization were compared in simulations using the L-Curve, GCV, and Quasi-Optimality parameter selection methods. The Discrepancy principle, which has its own regularization procedure, was also compared. These simulations solve for the temperature structure parameter,  $C_T$ , as well. In order to facilitate comparison and plotting of multiple regularization methods, the following simulations used the Matlab tools developed by Hansen by integrating them with the existing C code<sup>2</sup>. Several cases were examined where the imaging volume's optic axis is parallel to the ground. In this situation, the absorption coefficient in the radiance equations does not change with  $z$ . The simulations used a signal to noise ratio of 100, a bandwidth of .05% of the wavelength, a focal length of 400 millimeters, and a detector width of 5 millimeters. Except for the SNR, these parameters do not significantly affect the quality of the results. These simulations only consider about one kilometer of atmosphere in order to reduce the number of unknowns. This was done because of the inaccurate results obtained for the temperature structure parameter, as shown later. If the solution methods for cannot find  $C_T$  with 25 unknowns, than they certainly will not with 300. Twenty-five wavelengths are used from the output of the Fedorov exchange algorithm. No prevalent wavelength range was noted; the wavelengths spanned the spectrum from 2 to 18 microns. An equal number of atmospheric slices and wavelengths were used. Arbitrary profiles such as the ones shown in the plots were used for generation of the radiance measurements.

The results shown by the plots below indicate Quasi-Optimality criterion to be a clear cut winner for regularization parameter selection for this problem. As stated before, there is no theoretical reason as to why one or more of these methods would prevail over another, but from simulation to simulation, the Quasi-Optimality criterion consistently picks a parameter which gives more accurate results than the other methods. Figures 13-16 show results for the vertical case. Inversions for temperature shown in figures 13,14, and 16 have high amplitude oscillations because the parameter selection method did not pick an optimal  $\gamma$ .

The inversions for temperature using Quasi-Optimality produce solution profiles with root mean squared errors no higher than 1.5 K for assumed profile average deviations as high as 20 K. The structure parameter profiles are better for the L-Curve and Discrepancy criterion, but even using the Quasi-Optimality criterion the results are on average 300 percent off from the actual solution. The attempt to resolve information from small, similar radiance fluctuations is even more ill-conditioned than the inversions for temperature. Attempts to produce larger temperature fluctuations in the simulations by increasing the actual structure parameter magnitude yields profiles with different numbers but the same trends. As shown, the Tikhonov, TSVD, and DSVD methods each perform approximately the same, so there is no advantage to using one over another for this problem. The horizontal case simulations shown in figures 17-20 show similar findings about the regularization methods and parameter selection techniques.

The solution for correlation coefficients in equation 10 relies on accurate temperature structure parameter profiles. Because of the inaccurate structure parameter results in all cases, no attempt was made to invert correlations of radiance images to find velocity components.

#### **4. Conclusions**

A regularization method is better suited to handle the ill-conditioned nature of atmospheric radiance inversion problems than a direct inversion method. The direct linear method is unacceptable. The results show high magnitudes of error and large oscillations. The direct non-linear method succeeds in reducing error. Nonetheless, the output is still sensitive to small changes or errors in the measurements. A regularization method, however, employs an a priori constraint of smoothness on the solution that reduces or eliminates the instability with a correctly chosen regularization parameter.

All regularization techniques presented were tested on the problem of finding atmospheric temperature profiles and temperature structure parameter profiles. Regularization parameter selection techniques were compared for each of the regularization methods. The Quasi-Optimality criterion consistently gives more accurate results than the other three selection procedures: L-Curve criterion, the Discrepancy principle, and Generalized Cross Validation. Temperature solutions using Quasi-Optimality criterion were within 1.5 K whereas other parameter selection techniques gave unstable results. Temperature structure parameter profiles also benefit the most from the Quasi-Optimality criterion, but lack in accuracy by about 300 percent in the best case. Therefore, inversions for velocity would be futile. From the methods tested, it appears that solutions for atmospheric turbulence and velocity from passive radiance measurements by means of a radiometer device are unfeasible.